R-06-98

Groundwater flow and transport modelling during the temperate period for the SR-Can assessment

Forsmark area – version 1.2

Lee Hartley, Andrew Hoch, Peter Jackson, Steve Joyce,
Rachel McCarthy, William Rodwell, Ben Swift
Serco Assurance

Niko Marsic, Kemakta Konsult AB

December 2006

Svensk Kärnbränslehantering AB
Swedish Nuclear Fuel
and Waste Management Co
Box 5864
SE-102 40 Stockholm Sweden
Tel 08-459 84 00
+46 8 459 84 00
Fax 08-661 57 19
+46 8 661 57 19

ISSN 1402-3091
SKB Rapport R-06-98

Groundwater flow and transport modelling during the temperate period for the SR-Can assessment

Forsmark area – version 1.2

Lee Hartley, Andrew Hoch, Peter Jackson, Steve Joyce,
Rachel McCarthy, William Rodwell, Ben Swift
Serco Assurance

Niko Marsic, Kemakta Konsult AB

December 2006

Executive summary

Nuclear waste in Sweden is handled by Svensk Kärnbränslehantering AB, the Swedish Nuclear Fuel and Waste Management Company, SKB. Within SKB's programme for spent nuclear fuel management, an interim storage facility and a transportation system are already in operation. SKB's concept for the final stage of the nuclear fuel cycle, based on several decades of research and development, is to place spent fuel inside a cast iron insert inside copper canisters. These are then deposited in a repository, about 500 m deep in saturated, granitic rock, with the canisters surrounded by bentonite clay. This method is referred to as the KBS-3 concept.

Two principal remaining tasks in SKB's programme are to locate, build and operate i) the deep repository and ii) an encapsulation plant in which the spent fuel will be emplaced in canisters to be deposited in the deep repository.

SKB is currently carrying out site investigations for a deep repository in the municipalities of Östhammar and Oskarshamn. The investigations will be conducted in two stages; an initial site investigation (ISI) phase followed, if the expected site suitability is confirmed, by a complete site investigation (CSI) phase. The aim is to build a deep repository at one of these candidate sites, provided that the bedrock and other relevant conditions are found to be suitable. An application to build a deep repository will be made at the end of 2009 according to the current timetable.

The favoured alternative for the location of the encapsulation plant is at Oskarshamn, where it would operate in conjunction with the existing interim storage facility. An application to build an encapsulation plant will be made in 2006.

The final planning application requires a report on the long-term safety of the deep repository, referred to as SR-Site, which will be based on data from the completed site investigations. This is an obvious requirement for the application to build the repository. SR-Can is a preparatary stage for the SR-Site report. The main[1] purposes are to obtain a first assessment of long-term safety of a repository at the Forsmark and Laxemar sites, based on data from the initial site investigation stage, and to foster a dialogue with concerned authorities regarding interpretations of applicable regulations. SR-Can will be based on site data from the initial site investigation phase.

The overall purposes of the safety assessment SR-Can are the following:

1. Primarily, to investigate whether canisters of the envisaged type are suitable for disposal in repositories at Forsmark and Laxemar, given the host rock conditions at the sites in so far as they can be specified after the initial site investigation phase.
2. Secondarily, to provide feedback to design development, to SKB's R&D programme, to further site investigations and to future safety assessment projects.

An Interim report of the SR-Can project was published in 2004 to demonstrate the methodology to be used in the assessment, so that it could be reviewed and commented prior to use. There groundwater flow and transport modelling were performed using the Forsmark site as an illustration and based on data from the Version 1.1 site descriptive modelling. Here, numerical simulations of groundwater flow at the Forsmark site make use of the Version 1.2 update of the

[1] The SR in the acronym SR-Can stands for Safety Report and Can is short for canister. This title of the present report was chosen since it was originally intended to support the application to build an encapsulation plant. As a result of the formal consultation process with concerned authorities regarding safety assessments during SKB's site investigation phase, such a report is no longer required for that application. For practical reasons, this altered purpose of the SR-Can report has not been reflected in a change of the name of the report, since it is long well established.

site descriptive model as well as enhancements in the methodology to support the final SR-Can report.

The methodology for the assessment of the groundwater pathway makes use of both continuum porous medium (CPM) and discrete fracture network (DFN) models on a range of scales to investigate the groundwater flow and radionuclide transport from a deep disposal facility to the biosphere. SKB's methodology refers to three scales of modelling, these being 'regional' (~10 km), 'local' (~1 km) and 'repository/block' (10–100 m). Using models at these scales it is necessary to simulate the transient, variable-density groundwater flow in sufficient detail to enable the groundwater flux and radionuclide transport paths to be determined. For example, flows from deposition holes into adjacent small-scale fractures represent one release route for radionuclides into the geosphere. Further transport through fractures of increasing size, up to regional-scale fracture zones, is the most likely route through the geosphere to the biosphere. Due to significant developments both in computational tools and in hardware it has been possible to integrate some of these scales and include more detail in each individual model. However, due to the requirement to simulate processes such as transients, rock matrix diffusion, and thermal effects, it was still necessary to use several types of model to address the relevant issues. Key outputs from the modelling are the groundwater flux through the repository, the definition of flow-paths and values for parameters describing the transport of radionuclides along the paths. The results from the groundwater flow modelling will feed into the assessment of radionuclide transport,and ultimately into biosphere calculations of radiological risks to man.

The focus of the study described in this report has been to perform numerical simulations of the geosphere from post-closure and throughout the temperate period up until the beginning of the next permafrost period around 9,000 AD. Together with providing quantitative results for the immediate temperate period following post-closure, these results are also intended to give a qualitative indication of the evolution of the groundwater system during future temperate periods within an ongoing cycle of glacial/inter-glacial events. Additional calculations were performed to assess the impact of the effects of gas and heat generation in the repository on groundwater flow.

The groundwater pathway

As part of the assessment of the groundwater pathway models on two different scales were constructed: regional-scale transient porous medium models, and more detailed repository-scale steady-state models using both DFN and CPM representations. The regional-scale was used to assess the effects of transient processes such as land-rise and the evolution of hydro-geochemistry coupled to groundwater flow, as well as to perform a sensitivity study of transport performance measures (PMs) to conceptual and parameter uncertainties. The repository-scale modelling was performed with much more detail to resolve the flow around individual deposition holes and calculate flow-paths to the surface for input to performance assessment (PA) calculations. For all models, transport was characterised by four main PMs for each canister position in terms of travel-time, initial Darcy velocity, path-length and F-quotient along flow-paths started from each canister position. Additional PMs were derived for the repository-scale models such as distances and travel-times in the EDZ and tunnels.

The important transport parameter flow-wetted surface a_r can be estimated based either on the frequency of Posiva Flow Log (PFL) identified flow-anomalies, or based on simulation using the Hydro-DFN derived in SDM F 1.2. Based on the PFL data, ar=0.3 m^2/m^3 in the bedrock above and East of deformation zone ZFMNE00A2, and a_r=0.05 m^2/m^3 in the bedrock below and West of ZFMNE00A2. The corresponding values based on simulations of DFN connectivity are 0.2 m^2/m^3 and 0.03 m^2/m^3, respectively. The simulations also predict an average spacing of water-bearing fractures along a vertical borehole in the same volumes to be about 28 m and 174 m, respectively.

The regional-scale modelling was a natural continuation of the site-modelling study for F 1.2. However, several small but significant improvements were made since the model used there to ensure it honoured observed site conditions more realistically. More specific to safety assessment, a decision was made here to use the alternative case (AC) geological structural model as the central case since this case tends to give shorter flow-paths at future times once the shoreline retreats, and hence its use is conservative. A key aspect of the study was to analyse two alternative conceptual models for hydraulic property assignment based on either an equivalent continuum porous medium model (ECPM) using stochastic Hydro-DFN properties within specified hydrogeological domains, or a simpler continuum porous medium (CPM) model using homogeneous hydraulic properties within specified hydrogeological domains. Transient simulations of coupled groundwater flow and reference water transport with rock matrix diffusion were performed from 8,000 BC until the 2,020 AD at which time a representation of the repository was introduced instantaneous, and then simulations carried on until 9,000 AD. The most significant transient changes were found to take place between 2,020 AD and 3,000 AD as the shoreline retreats from very close to the site to a few kilometres away. Some discharge points at the coast follow the retreat of the shoreline, though a significant number of shorter paths to the immediate surface remain. More moderate changes occur later on as the shoreline retreats further to several kilometres from the site. Representative times were selected at 2,020 AD, 3,000 AD and 9,000 AD to quantify PMs for use in the streamline based far-field (FARF31) PA transport calculations.

For the regional homogeneous CPM model the median travel-time is about 4,000 years, initial Darcy velocity is about $1.3 \cdot 10^{-6}$ m/y, and a F-quotient of about $5 \cdot 10^{7}$ y/m for a release at 2,020 AD. For the ECPM model with a lower fracture transmissivity beneath ZFMNE00A2, the median travel-time is about 2,500 years, an initial velocity of about $5 \cdot 10^{-6}$ m/y, and a F-quotient of about $1.6 \cdot 10^{7}$ y/m for a release at 2,020 AD. For this case, at later times, median travel-time increases by about an order of magnitude, initial velocity increases slightly, while path-length and F-quotient both rise by about an order of magnitude. Hence, the present time is likely to give the highest risk based on a porous medium model since all discharge areas are close to the site at this time. Both of these cases are consistent with the hydraulic data and predict PMs that are similar, though risk is likely to be slightly higher for the ECPM case based on an underlying DFN. There are some other differences between the models, such as flow is more channelised in the ECPM model due to heterogeneities, and flow tends to be shallower in the ECPM model.

A more comprehensive set of sensitivities have been considered in this study than was possible in the site-modelling study for F 1.2. For example, variants in the geological model have shown that deformation zones outside the candidate area affect flow velocities downstream of the repository area with the flow-paths being generally shorter for the AC model than the BC model. Another uncertainty is whether the lower hydraulic conductivity seen in the candidate area is due to lower fracture transmissivity or fracture intensity. Based on two variants, one on fracture intensity and one on fracture transmissivity, which both match the observed hydraulic data, the case with lower fracture intensity gives slightly higher initial Darcy velocity and lower F-quotient, but has very poor fracture connectivity. Alternatives were considered to the Hydro-DFN properties by using different relationships between fracture transmissivity and length. A case was considered with a semi-correlated model. This gave travel-times and F-quotients that were two orders of magnitude lower for many paths, and a significantly larger spread in flow-paths and exit locations. Part of the reason is slightly higher block-scale hydraulic conductivities for this case. Another is thought to be that the heterogeneity in this model will tend to shorten flow channels making connections easier to the surface than to the horizontal boundaries, and so favour the vertical path straight up rather than the longer path to the shoreline. Similar results were observed for a case with no correlation between fracture transmissivity and length. The results are significant since they suggest that heterogeneity or a lack of correlation tends not only to disperse particles and exit locations, but also to shorten paths by making long horizontal flow-paths less likely.

Detailed repository-scale models have been used to derive near-field and far-field performance measures for input to PA calculations. Two main types of conceptual models, DFN and CPM, have been applied to model the entire repository and flow in the bedrock around each deposition hole down to the scale of a few metres or less. As an advance on the methodology used in the interim SR-Can assessment, variable-density flow calculations have been implemented in DFN models so that the effects of buoyancy-driven flow due to the presence of salinity are represented consistently in both DFN and CPM conceptual models. Since the PA calculations use a streamline concept for the far-field modelling in FARF31, groundwater flow and flow-paths are calculated at an appropriate series of representative times with boundary conditions and the salinity distribution being interpolated on to the steady-sate repository-scale models from transient regional-scale coupled groundwater flow and salt transport models. Properties of both the CPM and DFN models have been developed since the site modelling of SDM F 1.2 to incorporate a multi-domain definition of properties that is more realistic and better reflects the observed spatial variability in fracture and hydraulic properties at the site.

The use of different conceptual models has allowed us to quantify the sensitivity to the choice of model. For Forsmark it is found that the two types of model yield quite different results. This stems from the fact that the bedrock within the repository candidate area is very sparsely fractured with generally poor connectivity. In consequence, a DFN model predicts a very disjoint flow system with poor connections, areas of stagnant flow, tortuous flow-paths such that significant flow and transport is restricted to the deterministic deformation zones and the larger stochastic fractures. The lack of connectivity horizontally over long distances restricts long flow-paths from forming, and hence flow tends to be much localised and discharge from the repository is mainly to the immediate surface above. Transport is mainly sensitive to the structural model and occurrence of large stochastic fractures, while transient processes such as shoreline retreat are less influential. In contrast, a CPM model with isotropic hydraulic properties allows flow connections in all directions, and although the CPM bulk hydraulic properties are equivalent on a large-scale (100 m), the detailed flow and transport is very different. Generally in the CPM model flow is more homogeneous with flow around all deposition holes and longer flow-paths many of which reach the shoreline. In this case, results are sensitive to the position of the shoreline, and flow-paths less dominated by the geological structural model. To implement a representation of a sparse fracture network in a porous medium model one would have to use a fine-scale heterogeneous ECPM model that captures the intact block between the water conducting fractures, and this may not be practicable. This intrinsic difference between the two types of model has possible implications for the site-modelling also as it may affect the interpretation of interference tests and tracer tests.

In terms of the performance measures, the CPM model predicts travels times with a median over 10^3 years, while the DFN model median is less than 10^2 years; Initial velocity has a median around 10^{-6} m/y in the CPM model with small variability, while the DFN predicts a median around 10^{-5} m/y but with a standard deviation nearly one order of magnitude; The F-quotient has a median just under 10^8 y/m for the CPM model, and under 10^7 y/m for the DFN model with a standard deviation of about 0.8 in log10-space. Generally, the DFN representation is a worse scenario, but it does have some positive aspects also. For example, the DFN model predicts there is advection away from the canister via a fracture that intersects the deposition hole for only about 40% of canisters, and of these only about 15% have a significant transmissivity (greater than 10^{-9} m^2/s). Similarly, there are stagnant flow conditions in parts of the EDZ and tunnel that amounts to about 40% of the canisters. Hence, for many canisters there are essentially no advective routes for radionuclides to escape.

Sensitivities have been considered to the tunnel and EDZ properties as well as the relationship used between fracture transmissivity and length. The sensitivity to the backfill and EDZ properties is not great since the system of deposition tunnels is arranged orthogonal to the head gradients. Therefore flow tends to be limited by what the fracture system can supply and paths have to leave the tunnel or EDZ after relatively short distance to find a flow-path to the surface through the fracture network. For the semi-correlated and uncorrelated transmissivity DFN

variants higher percentages of canisters have connected fractures of significant transmissivity (greater than 10^{-9} m^2/s) intersecting the deposition holes, 18–20%. The percentage of particles starting in stagnant flow areas increases to 67–74% for the two variants. This is indicative of flow being more heterogeneous for the variants and there being fewer advective pathways through the model, as was found in the equivalent ECPM regional models. Therefore, the results are moderately sensitive to the relationship used for the transmissivity to length relationship, and the semi-correlated and uncorrelated models may give moderately worse results than the correlated model in terms of inputs to PA, although fewer particles escape to the surface for these cases.

For the current fracture model, avoiding locations where fractures intersect the full perimeter of a tunnel seems to be a sufficient test for screening out the worst deposition hole locations without having to perform flow tests of fracture transmissivity in deposition pilot holes.

Gas migration and its effects on groundwater flow

The consequences of the production of gas from iron corrosion in a small proportion of canisters that potentially have manufacturing defects allowing water ingress were addressed.

Gas is generated in defective canisters by anaerobic corrosion of the cast iron insert as a result of water ingress through the defect. The rate of gas generation is determined by the iron corrosion rate, the iron surface area exposed to water, and the availability of water. Assuming that the whole surface of the iron insert is exposed to an unlimited supply of water, the rate of hydrogen production would be $2.1 \cdot 10^{-2}$ m^3y^{-1} at STP. This is an upper bound to the rate of gas production from a canister as in practice water availability will be limited by the flow capacity of the bentonite, the build up of gas pressure in the canister opposing water ingress through the defect, and the capacity of the geosphere to supply groundwater. The generation rate is unlikely to exceed ~10^{-3} m^3y^{-1} at STP, and the build of gas pressure is likely to reduce the rate to less than ~10^{-4} m^3y^{-1} at STP. Bear in mind that no gas escapes from the defective canister until the gas pressure has reached at least hydrostatic. Gas generation will continue, but possibly only at these very low rates, for at least 250,000 years.

Gas released from a defective canister needs to pass through the bentonite buffer if it is to escape from the vicinity of the canister. Even at the constrained gas generation rates discussed above, gas transport through the bentonite by diffusion in solution from the small defect will be inadequate to remove all the gas generated. However, if the gas pressure opens a gap between the canister and the buffer into which the gas can spread, the contribution of diffusion of dissolved gas to gas transport through the buffer may become more significant. In any event, is expected that, if the gas pressure rises sufficiently, movement of a free gas phase through the bentonite buffer will occur.

Once the gas has passed through the bentonite, it might collect in the tunnel and the EDZ associated with the tunnel, and it might enter the fracture network either from the tunnel or directly from the deposition hole. Some of the gas will dissolve in the groundwater and be transported away by the groundwater flow. However, the groundwater flow at the repository depth is very slow, and it is unlikely that gas generated at the upper bound generation rate of $2.1 \cdot 10^{-2}$ m^3y^{-1} at STP could all dissolve and be transported away in groundwater flowing through the neighbourhood of the repository. If, as seems quite probable for most defective canisters, the gas release rate is 1–2 orders of magnitude less than the upper bound, it is possible that much if not all of the gas could be transported away in solution.

Should the gas not all dissolve, simple estimates show that the gas transport capacity of the fracture network, assuming that it is sufficiently connected between the location of the defective canister and the surface, should be more than adequate to easily transport the gas to the surface without any significant increase in gas pressure in the neighbourhood of the repository.

Should free gas phase migration be sustained between the repository and the surface, this would be capable of transporting volatile radionuclides relatively rapidly from the repository to the surface. The only significant such radionuclides identified in the waste canisters are ^{14}C and ^{222}Rn. Direct release of the volatile ^{14}C in defective canisters to the surface has been previously assessed as not causing a significant radiological hazard and so the capacity of migrating gas to transport this radionuclide is immaterial. Similar conclusions were reached for ^{222}Rn release, although it may be desirable to assess the consequences of ^{222}Rn release into an occupied dwelling.

Migrating gas may also affect the movement of groundwater and hence the transport of dissolved radionuclides. Such transport is mitigated by the following observations:

- With a small defect, it is not possible to get release of dissolved radionuclides and gas at the same time. The situation may be different if a large hole develops.
- Gas migration can only affect transport of dissolved radionuclides released from a nearby different canister, and the probability of two defective canisters being present close together must be quite small.
- Migrating gas is only likely to affect groundwater flows in the neighbourhood of a small number of canisters local to the canister generating gas, and there is a low probability that one of these also may be defective and releasing radionuclides.

The effects of heat generation on groundwater flow

Based on porous medium calculations it is concluded that thermal effects can potentially have a moderate impact on groundwater flow and transport from a repository. The flow-paths can be significantly modified in the immediate vicinity of the repository. The potential effects are greatest for radionuclides released from the repository shortly after repository closure though such releases are very unlikely. However, the discharge locations are not greatly effected, because these are determined by the location of surface water bodies, which are determined by lows in the surface topography and the shoreline. Possibly the most important impact of thermal effects might be due to their effect on the groundwater viscosity, which might be reduced by about a factor of two in a region around the repository for many thousands of years, and in consequence Darcy velocity might be increased by a factor of two. This effect possibly ought to be taken into account in the PA transport calculations.

Contents

1 Introduction

1.1 SKB's programme for spent fuel and the SR-Can project

Nuclear waste in Sweden is handled by Svensk Kärnbränslehantering AB, the Swedish Nuclear Fuel and Waste Management Company, SKB. Within SKB's programme for spent nuclear fuel management, an interim storage facility and a transportation system are already in operation. SKB's concept for the final stage of the nuclear fuel cycle, based on several decades of research and development, is to place spent fuel inside a cast iron insert inside copper canisters. These are then deposited in a repository, about 500 m deep in saturated, granitic rock, with the canisters surrounded by bentonite clay. This method is referred to as the KBS-3 concept.

Two principal remaining tasks in SKB's programme are to locate, build and operate i) the deep repository and ii) an encapsulation plant in which the spent fuel will be emplaced in canisters to be deposited in the deep repository.

SKB is currently carrying out site investigations for a deep repository in the municipalities of Östhammar and Oskarshamn. The investigations will be conducted in two stages; an initial site investigation (ISI) phase followed, if the expected site suitability is confirmed, by a complete site investigation (CSI) phase. The aim is to build a deep repository at one of these candidate sites, provided that the bedrock and other relevant conditions are found to be suitable. An application to build a deep repository will be made at the end of 2009 according to the current timetable.

The favoured alternative for the location of the encapsulation plant is at Oskarshamn, where it would operate in conjunction with the existing interim storage facility. An application to build an encapsulation plant will be made in 2006.

The final planning application requires a report on the long-term safety of the deep repository, referred to as SR-Site which will be based on data from the completed site investigations. This is an obvious requirement for the application to build the repository. SR-Can is a preparatary stage for the SR-Site report. The main purposes are to obtain a first assessment of long-term safety of a repository at the Forsmark and Laxemar sites, based on data from the initial site investigation stage, and to foster a dialogue with concerned authorities regarding interpretations of applicable regulations. SR-Can will be based on site data from the initial site investigation phase and SR-Site on data from the complete site investigation.

1.2 SR-Can: scope and objectives

The overall purposes of the safety assessment SR-Can are the following:

1. Primarily, to investigate whether canisters of the envisaged type are suitable for disposal in repositories at Forsmark and Laxemar, given the host rock conditions at the sites in so far as they can be specified after the initial site investigation phase.
2. Secondarily, to provide feedback to design development, to SKB's R&D programme, to further site investigations and to future safety assessment projects.

An Interim report of the SR-Can project was published in 2004 /SKB 2004a/ to demonstrate the methodology to be used in the assessment, so that it could be reviewed and commented prior to use. As part of that work, groundwater flow and transport modelling was performed /Hartley et al. 2004/ using the Forsmark site as an illustration and based on data from the Version 1.1 site descriptive modelling (SDM) /SKB 2004b/.

The work reported here provides numerical simulations of groundwater flow at the Forsmark site to support the final SR-Can report. As such, it builds on the methodology developed in the interim study, but considers a more comprehensive set of simulations and includes features and processes in more detail than was performed previously. In addition, it uses an update of the site-modelling based on data from Version 1.2 /SKB 2005b/.

The methodology developed in the interim assessment of the groundwater pathway makes use of both continuum porous medium (CPM) and discrete fracture network (DFN) models on a range of scales to investigate the groundwater flow and radionuclide transport from a deep disposal facility to the biosphere. There it was stated that the modelling should address the effects of variable groundwater density and transients. Significant transients occur naturally as a consequence of changes in climate states associated with glacial events and during the construction, operation (e.g. dewatering by pumping) and immediate post-closure phases of the repository. Key outputs from the modelling are the groundwater flux through the repository, the definition of flow-paths and values for parameters describing the transport of radionuclides along the paths. The results from the groundwater flow modelling will feed into the assessment of radionuclide transport using the PROPER code, and ultimately into biosphere calculations of radiological risks to man.

SKB's methodology refers to three scales of modelling, these being 'regional' (~10 km), 'local' (~1 km) and 'repository/block' (10–100 m). Using models at these scales it is necessary to simulate the transient, variable-density groundwater flow in sufficient detail to enable the groundwater flux and radionuclide transport paths to be determined. For example, flows from deposition holes into adjacent small-scale fractures represent one release route for radionuclides into the geosphere. Further transport through fractures of increasing size, up to regional-scale fracture zones, is the most likely route through the geosphere to the biosphere. Research into ways of effectively coupling the geosphere and biosphere through near-surface and surface hydrology models is ongoing within the SKB programme. Due to significant developments both in computational tools and in hardware it has been possible to integrate some of these scales and include more detail in each individual model. However, due to the requirement to simulate processes such as transients, rock matrix diffusion, and thermal effects, it was still necessary to use several types of model to address the relevant issues.

The focus of the study described in this report has been to perform numerical simulations of the geosphere from post-closure and throughout the temperate period up until the beginning of the next permafrost period around 9,000 AD. Together with providing quantitative results for the immediate temperate period following post-closure, these results are also intended to give a qualitative indication of the evolution of the groundwater system during future temperate periods within an ongoing cycle of glacial/inter-glacial events. Additional calculations were performed to assess the impact of the effects of gas and heat generation in the repository on groundwater flow.

The output from the groundwater flow models forms some of the important input to repository performance assessment (PA) calculations. These outputs are described as performance measures (PMs) and are generally tables of data associated with the exit location, canister-flux, travel-time, and F-quotient along paths for particles released at or around each of the canister locations within the repository. These PMs provided a means for quantifying the sensitivity of the PA input to various features, uncertainties and processes. Hence, they provide a way of answering some of the key questions to be asked of the groundwater flow and transport modelling, such as:

1. What is the distribution of groundwater discharge areas and how does this evolve in the future?
2. What are the distributions of (PMs), and how do these evolve in the future?
3. Under what conditions do the backfilled tunnels and engineered damage zone (EDZ) acts as potential pathways for groundwater flow?
4. What are the key sensitivities of PMs to model parameters?

5. What uncertainties in the Version 1.2 site descriptive modelling (SDM) have the greatest impact on PMs?
6. What effect do uncertainties in the conceptual model for groundwater flow have on PMs?

Gas migration through the geosphere, and any consequences it might have, is assessed as part of this project as an update to an earlier gas assessment /Wikramaratna et al. 1993/. In particular, the following questions are addressed:

1. What are the principal sources of gas generation and what amounts of gas are likely to be produced?
2. How much of the produced gas will dissolve in groundwater in the repository engineered system and be transported away in solution?
3. Does the DFN contain connected fracture networks of sufficient flow capacity to transport generated gas from canisters to surface, either as a result of flow as a dissolved gas, or more likely as a free gas-phase flow driven by buoyancy forces (or possibly an elevated pressure around the canister)?
4. If two-phase flow conditions are created, as expected from the results of previous studies, what will be the nature of the gas flow regime?
5. What are the implications of gas migration for modelling of the transport of radionuclides dissolved in groundwater?

Finally, the effects of heat generated by a spent fuel repository are addressed by numerical simulations to address the following questions:

1. Are the discharge areas modified by a potential 'thermal fountain' above the repository?
2. Will thermal flows pull cooler saline waters from depth to replenish water rising from the repository, and cause a potential saline upconing?
3. For how long will thermal effects be significant?

1.3 Setting and limitations

The setting for groundwater flow modelling for Forsmark Version 1.2 (abbreviated to F 1.2) has been identified in the site modelling performed by /Hartley et al. 2005/ and /Follin and Stigsson 2005/. The suggested regional area is oriented 45° NE and has an area of 15 km by 11 km as shown in Figure 1-1. Forsmark Version 1.1, or F 1.1, groundwater flow and transport modelling was based on very limited site hydraulic and hydro-geochemical data, principally that from borehole KFM01A. It also used a preliminary structural model with transmissivities of the deterministically modelled deformation zones based on sparse hydraulic data from the bedrock characterisation of the SFR facility (located outside the candidate area).

The data freeze F 1.2 represents a significant advance in the site investigations and understanding. Additional cored boreholes KFM02A–05A distributed throughout the candidate area gave fracture intensities from boremap data, Posiva flow-log (PFL) hydraulic data, together with Pipe-string system (PSS) packer-test data in KFM01A–KFM03A (locations shown in Figure 1-1). This stimulated considerable modelling activity to condition Hydro-DFN model parameters to successfully reproduce the field observations. The result was a set of Hydro-DFN parameters for the bedrock between deterministic deformation zones, along with variants based on uncertainty in assumptions such as the fracture size distribution and a correlation between fracture transmissivity and radius. Further, site investigations suggested significant spatial variations in the bedrock fracturing. The most significant being lower fracture intensity inside a 'tectonic lens' of high mechanical rock strength associated with the rock domains RFM029 and RFM017 as included in Figure 1-1. Another characteristic proposed is lower fracture intensity below zone ZFMNE00A2. This gives rise to models of much greater complexity than were considered in F 1.1.

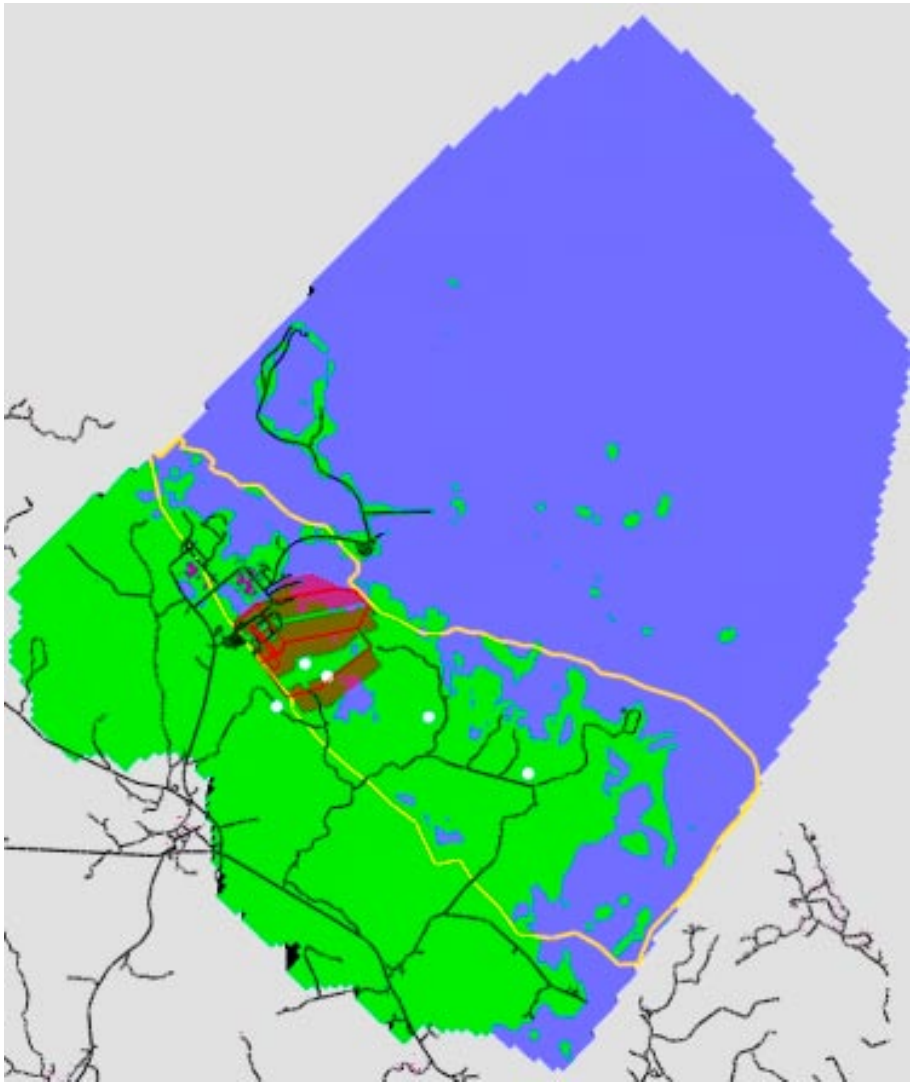

Figure 1-1. *Location of regional-scale area (green=land, blue=sea) from F 1.2 modelling. The repository footprint is shown in red, roads in black, and the approximate extent of the tectonic lens corresponding to rock domain RFM017 and RFM029 lies within the yellow curve. The positions of cored boreholes are shown in white. The cross-section X-XX is used in Figure 2-21.*

Three new alternative geological models were produced for F 1.2 based on different levels of confidence in interpretation of the large-scale geological structures. These cases are:

1. A base case (BC) was provided based on high confidence structures local to the site between the Singö deformation zone (DZ) and Eckarfjärden DZ. One of the key features of this model is the presence of several extensive sub-horizontal DZs within the candidate area.
2. A variant case (VC) was developed that considers an extension of some sub-horizontal zones beyond the candidate area.
3. An alternative case (AC) case was proposed with the inclusion of many low confidence sub-vertical lineaments outside the candidate area.

In addition to these considerations of the sensitivity to various structural models, hydraulic data gathered in DZs suggested a concept that hydrogeological properties for the hydraulic conductor domains (HCDs) vary with depth and according to the dip of structures. In the F 1.2 site modelling simulations of flow-paths were performed based on the present day groundwater flow patterns only. This indicated low sensitivity to the structural model used, but this conclusion has to be treated with caution since it may not hold when one considers the future evolution

of the groundwater system as the land continues to rise in the future due to post-glacial rebound. Hence, the study reported here had to re-visit the sensitivity to the structural model.

Importantly, far greater quantities of hydro-geochemical data were available for calibration in the F 1.2 than for F 1.1. These were provided for cored boreholes KFM01A, KFM02A, KFM03A, KFM04A, and KFM05A and for a series of shallower percussion drilled boreholes. Further, the data were provided in terms of interpreted mixing fractions for reference waters, concentrations of major ions, stable isotope ratios and tritium concentrations in addition to the salinity data that had been supplied previously. This enabled a more sophisticated and comprehensive calibration of the groundwater flow models than was possible previously. However, the data still has its limitations. Firstly, data at elevations below –500 m is very sparse and so the location of deep Brine water is uncertain. Secondly, as of data freeze F 1.2, data had not been made available for the rock matrix, which makes it difficult to quantify the role of rock matrix diffusion in transport of natural tracers. Still, the new data motivated the development of transient groundwater flow models coupled to transport of multiple reference waters of the paleo-hydrogeological situation from 8,000 BC until 2,000 AD. All these models were either continuum porous medium (CPM) or equivalent continuum porous medium (ECPM) models based an underlying DFN model, and were on the regional-scale with grid resolution only going down to 50 m. Time constraints placed on the site-modelling exercises meant it was not possible within those studies to consider as a wide a range of uncertainties as were considered important, and hence some additional sensitivity studies were completed here.

For this study it is necessary to continue the transient simulations up to 9,000 AD to consider the future evolution of the site in the temperate period, and to consider models with a much higher resolution to represent flow around individual deposition holes and in the adjoining tunnels and EDZ. It should be noted the periods involving the open repository and resaturation are not considered here. They are dealt with elsewhere in the SR-Can project /Svenson 2005/.

1.4 Organisation of work and structure of report

The approach taken was to use the regional-scale CPM/ECPM models developed in the site-scale modelling to address issues relating to the future evolution of the site. A wider variety of variant simulations were run to better quantify sensitivities than was possible in the site modelling. In the site modelling, sensitivities were measured in terms of both the calibration against hydraulic data and current hydro-geochemistry data, as well as transport PMs based on releasing particles in the current groundwater flow situation from a regular grid of points within the site release-area. In SR-Can, sensitivities were measured solely in terms of transport PMs for particles released at the 6,824 canister locations, but at different release times in the future also. Measuring sensitivities in this way, the regional-scale models were used to rank the most important sensitivities. This is a useful exercise in its own right, but it also helped identify which key variants should be propagated in to the second stage of modelling where much more detailed models were used to consider flow-paths with greater resolution. For practical reasons only a restricted set of cases could be considered with detailed models.

The detailed models include the use of discrete fracture network (DFN) models or combined CPM/DFN to give a more realistic and accurate description of flow in the vicinity of a repository and represent flow-paths through a fracture system. Two different types of combined model are used to build confidence in the approach by quantifying how sensitive flow-paths and related quantities such as F-quotient are to assumptions made about how to nest models and represent the repository.

Significant advances since the interim assessment in the capabilities of combined models have made it possible to model variable-density flow in DFN and/or combined models. It is also possible to construct much larger models containing many thousands of deposition holes and around 1 million of the surrounding fractures, whereas in the interim assessment it was only possible to model a few hundred deposition holes at a time. The former option addresses some

problems encountered in how to define boundary conditions in DFN models to approximate variable-density flow, while the latter option makes it possible to provide input to PA for the entire repository rather than just a fraction.

Calculations to support the assessment of gas migration have been performed based on analytical models using data from the numerical groundwater flow calculation as input.

Assessment of thermal effects was performed by extending the regional-scale CPM and ECPM models to include heat generation and conduction as a transient numerical simulation for future times. Additional discretisation around the repository was incorporated into the models to represent the heat source more accurately.

All the work presented in this report was conducted by the *CONNECTFLOW Team* involving modelling experts from Serco Assurance and Kemakta Konsult using the CONNECTFLOW code that is developed and maintained by /Serco Assurance 2005abc/.

This report presents the general concepts and methodology used in groundwater flow simulations in Section 2. Regional-scale flow simulations using CPM and ECPM models and the ranking of sensitivities are described in Section 3. The more detailed repository-scale modelling to give PMs for input to PA calculations is reported in Section 4. Assessment of gas generation and migration is covered in Section 5. The impact of thermal effects on groundwater flow are analysed in Section 6. Implications for flow-paths moving in a transient flow-field are also quantified in Section 6. The work is summarised in Section 7

A glossary of abbreviations used in the report is included in Appendix A. Statistics of PMs for the regional-scale modelling are tabulated in Appendix B. Appendix C presents tables of PMs derived from the detailed modelling for use in PA calculations. The development and verification of a facility for modelling variable-density flow in DFN models is described in Appendix D. A study of the effects of spalling is included in Appendix E. The development and testing of a new capability to model heat transport coupled to groundwater flow and transport of reference waters is reported in Appendix F.

2 Hydrogeological concepts, methodology and data from site modelling

2.1 Conceptual model types

There are two main types of groundwater flow model relevant to a description of the granitic bedrock at Forsmark: continuum porous medium (CPM) models and discrete fracture network (DFN) models. CPM groundwater flow models treat the rocks through which the groundwater flows as a continuum characterised by quantities defined at all points in a 3D region; DFN models explicitly model the water conducting fractures through which groundwater flows in some rocks, and are characterised by quantities associated with the fractures. For crystalline hard rocks groundwater flow generally takes place through an interconnected network of fractures. However, the candidate rock under consideration at Forsmark is so tight that it is hard to observe flows in some boreholes above the measurement limit, which is not indicative of an interconnected network of water bearing fractures. This makes it difficult to validate and interpret a conceptual model for groundwater flow. Flow may occur in localised areas through a sparsely connected fracture network, or at very low rates through a system of micro-fractures and pores. Hence, there is some uncertainty over the most appropriate conceptual model at this stage in the site investigations. For this reason both types of concept, CPM and DFN, will be considered in this project.

At suitable scales the overall flow through a fracture network can be modelled (to a reasonable approximation) using CPM models by appropriate choice of bulk properties (e.g hydraulic conductivity and kinematic porosity). Such models tend to be heterogeneous and have anisotropic block properties in order to represent an underlying stochastic DFN model. Here and elsewhere in SKB's SDM exercises these models are referred to as Equivalent Continuum Porous Medium (ECPM) models.

2.1.1 Continuum porous medium (CPM) representation

CPM models are considered the appropriate models for certain types of rock in which flow is predominantly through an interconnected network of pores in the rock matrix, such as many sandstones, or for soils and unconsolidated deposits. The model assumes continuity in 3D and hence a high degree of connectivity between points in the model domain. Connectivity is only reduced when very low conductivity layers or flow barriers are incorporated in the model. The flow through such models is modelled by Darcy's Law, which relates the specific discharge (volumetric flux) to the driving force, i.e. the pressure gradient and/or buoyancy force.

To keep consistency with SDM F 1.2, the term CPM model is used to refer specifically to models with properties which are uniform within defined rock volumes with spatial heterogeneity only arising due to the implicit representation of fracture zones. This type of model was developed in the site modelling by the DarcyTools (DT) Team and is reproduced here in CONNECTFLOW. The distinction between rock volumes was based on either different rock domains (e.g. rock domains RFM029 and RFM017 associated with the 'tectonic lens') or depth below surface. Figure 2-1 shows an example of a CPM model used in regional-scale modelling. The top figure shows how the 'rock types' are defined in CONNECTFLOW on which hydraulic properties are specified. The lower figure shows the distribution of hydraulic conductivity based on the hydraulic properties of the rock and the implicit representation of higher conductivity fracture zones. The finite-elements coloured, red, orange and yellow in the lower figure all correspond with higher hydraulic conductivity associated with deformation zones, while the background rock has a green colour since hydraulic conductivity is uniform between the fracture zones within a rock volume. A lower uniform background hydraulic conductivity is used in the tectonic lens (dark green colour in the lower figure).

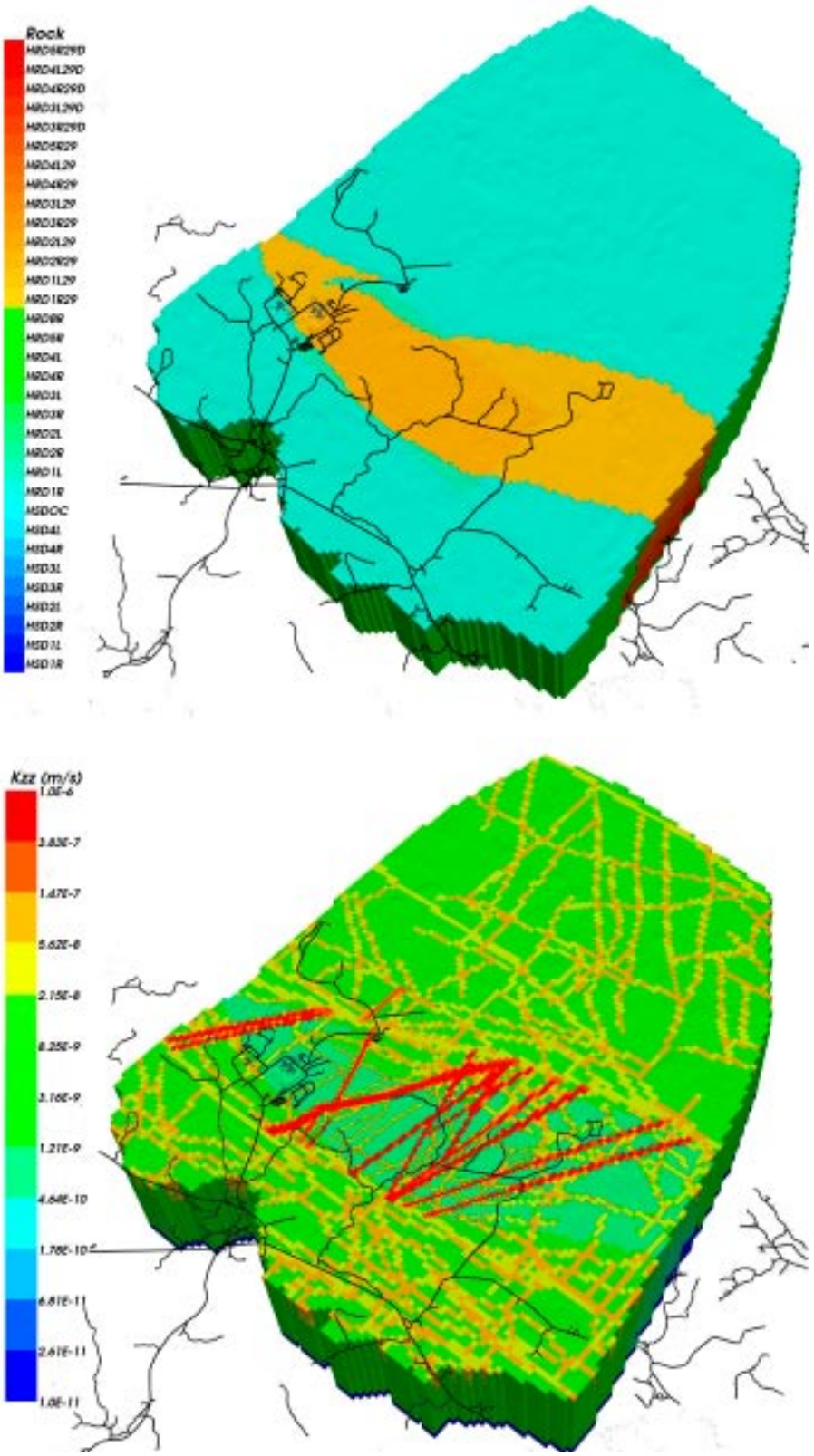

Figure 2-1. *An example of a CPM regional-scale model. Top: each finite-element is coloured by 'rock types' defined within the CONNECTFLOW model. Those coloured red to orange are associated with RFM029/017, while other rock types are coloured blue to green. Bottom: each element is coloured by vertical hydraulic conductivity. Roads and buildings are added in black.*

2.1.2 Discrete fracture network representation (DFN)

The discrete fracture network (DFN) concept assumes flow through a fractured rock is predominantly through an inter-connected network of flow-conductive fractures with groundwater moving from one fracture to another at the intersections between them. The properties of the network are usually characterized in terms of:

- Spatial distribution (e.g. Poisson, fractal, clustered around points or lineaments).
- Fracture intensity (and its spatial variation).
- Number of fracture sets distinguished by orientation.

The properties of deterministic or stochastic individual fractures are primarily:

- Length.
- Orientation (strike and dip).
- Transmissivity (and possibly spatial variability within the plane).
- Transport aperture.
- Storativity.

In CONNECTFLOW, fractures are rectangular, or may be right-angle triangles where a complex surface has been triangulated into many pieces. For stochastic fractures, the properties are sampled from probability distribution functions (PDFs) specified for each fracture set. The properties may be sampled independently or correlated.

The DFN concept is very useful since it naturally reflects the individual flow conduits in fractured rock, and the available field data. However, to understand flow and transport on the regional-scale it is often necessary to consider larger-scale bulk properties in the context of an ECPM continuum concept. This requires methods (i) to convert the properties of a network of discrete fractures of lengths less than the continuum blocks into equivalent continuum porous medium (CPM) block properties, known as upscaling, and (ii) to represent larger scale features such as fracture zones by appropriate properties in a series of continuum blocks, i.e. a downscaling method. The implementation of upscaling and downscaling in CONNECTFLOW is described in Sections 2.1.3 and 2.2.2, respectively.

As part of the site modelling a parameterisation of a Hydro-DFN model was developed using the field data for F 1.2. The purposes of the Hydro-DFN modelling exercise were:

- Checking the fracture distributions in the boreholes based on the Geo-DFN.
- Deriving transmissivity distributions to match the observed flows in the Posiva flow-log (PFL) and Pipe-string system (PSS) data.
- Deriving the statistical distributions of equivalent continuum porous medium (ECPM) properties on specified block scales for addressing design issues using flux-based upscaling.
- Creating realisations of the regional-scale ECPM model based on upscaling regional-scale DFN models.

An example of a DFN model generated on the local-scale for F 1.2 is shown in Figure 2-2. Here fractures are generated in a local-scale area within a cube 2.3 km by 2.3 km by 1.1 km. It includes both stochastic fractures that are square combined with deterministic fracture zones that are defined as more complex non-planar surfaces.

2.1.3 Equivalent continuum porous medium (ECPM) representation

In order to assess the implications of the DFN model on flow and transport on the regional-scale, it is often necessary for practical reasons to convert the DFN model to an ECPM model with appropriate properties. The resulting parameters are a directional hydraulic conductivity

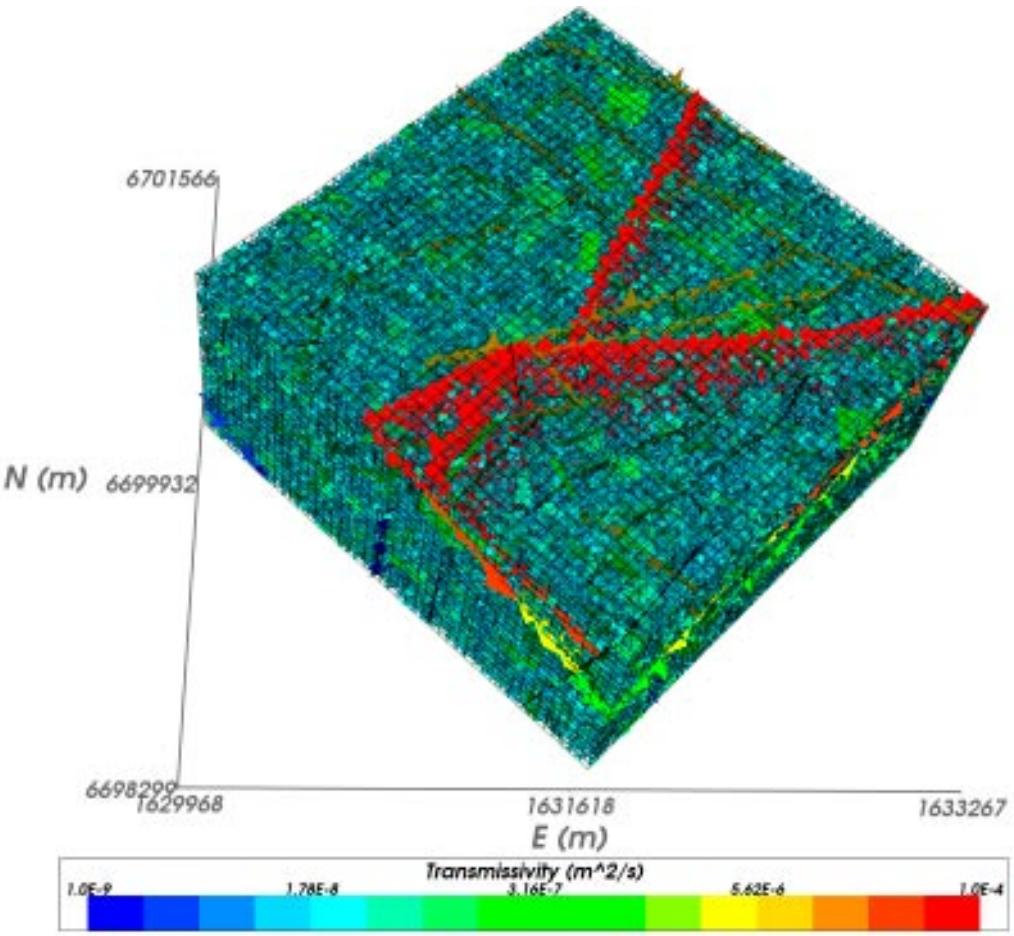

Figure 2-2. *An example of a local-scale DFN model showing stochastic fractures and higher transmissivity deterministic fracture zones coloured by log(transmissivity). Here, fractures are generated within a grid of cells with 50 m side.*

tensor, fracture kinematic porosity and other transport properties (such as the fracture surface area per unit volume). In CONNECTFLOW a flux-based upscaling method is used that requires several flow calculations through a DFN model in different directions.

Figure 2-3 shows an illustration of how flow is calculated in a DFN model (a 2D network is shown for simplicity). To calculate equivalent hydraulic conductivity for the block shown, the flux through the network is calculated for a linear head gradient in each of the axial directions. Due to the variety of connections across the network, several flow-paths are possible, and may result in cross-flows non-parallel to the head gradient. Cross-flows are a common characteristic of DFN models and can be approximated in an ECPM by an anisotropic hydraulic conductivity. In 3D, CONNECTFLOW uses six components to characterise the symmetric hydraulic conductivity tensor. Using the DFN flow simulations, the fluxes through each face of the block are calculated for each head gradient direction. The hydraulic conductivity tensor is then derived by a least-squares fit to these flux responses for the fixed head gradients. Other authors /La Pointe et al. 1995/ have only considered the components of the equivalent hydraulic conductivity parallel to the coordinate axes using a head difference between opposite faces and no-flow on the other faces. This leads to a very poor representation of blocks in which the network connections, and hence flow, are mostly between adjacent faces rather than between opposite faces. The effective hydraulic conductivity assigned to such blocks may be essentially zero, even though the flow-paths through the block may contribute significantly to the overall flow through the network.

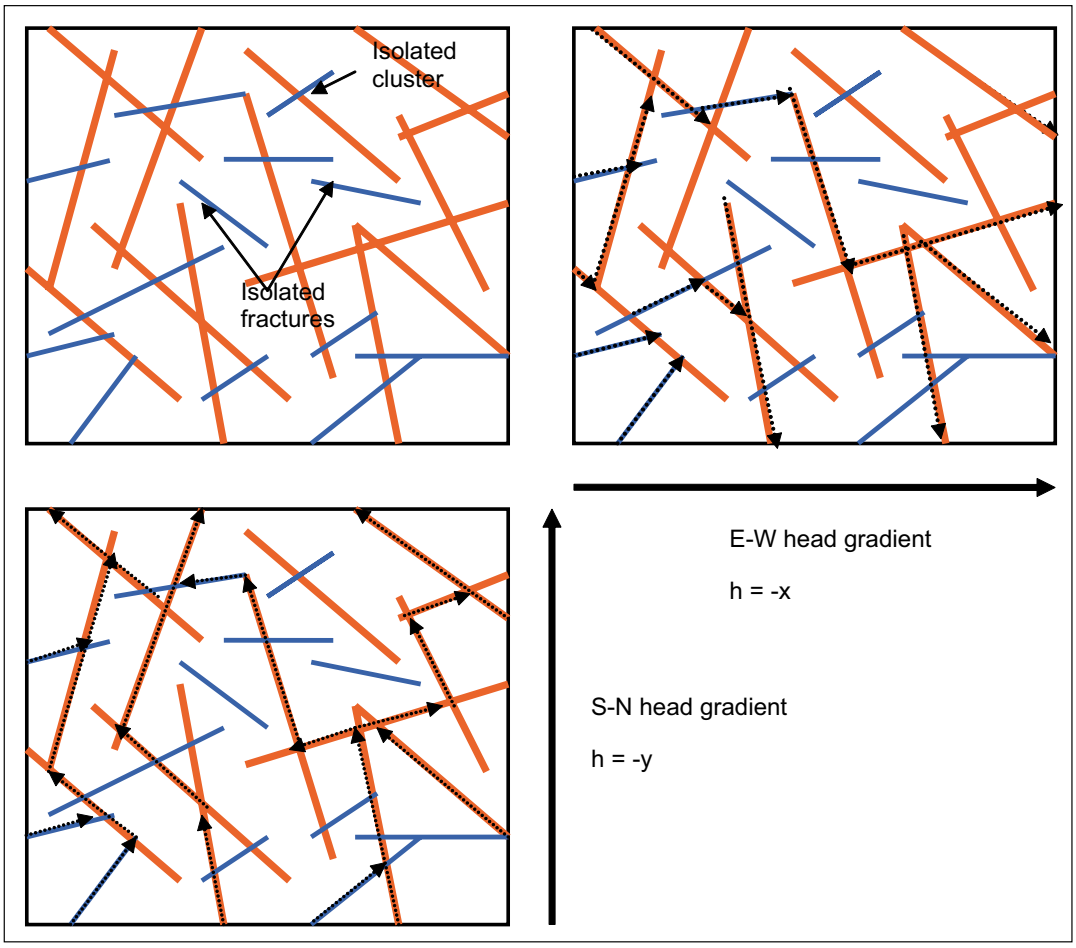

Figure 2-3. *2D illustration of flow through a network of fractures. A random network of fractures with variable length and transmissivity is shown top left (orange fractures are large transmissivity, blue are low). Top right: flow-paths for a linear head gradient E-W decreasing along the x-axis. Bottom left: flow-paths through the network for a linear head gradient S-N decreasing along the y-axis.*

In 3D, the blocks have to be hexahedra (cuboids), but the upscaling method can be applied to an array of sub-blocks within a much larger DFN domain by performing the upscaling on each sub-block in sequence. The upscaling method is typically used in one of two ways:

1. To obtain the statistical distribution of hydraulic conductivity on a given block scale a DFN model is generated for a much larger domain, and then ECPM properties are calculated for an array of sub-blocks of equal size and shape to give an ensemble of properties.
2. To obtain an ECPM model for a local- or regional-scale grid, a DFN model is generated within the grid domain, and the upscaling is performed within each grid element to derive the ECPM properties element by element.

A detailed description of the upscaling method to calculate the ECPM hydraulic conductivity tensor is given in /Jackson et al. 2000/. Briefly, the method can be summarised by the following steps:

- Define a sub-block within a DFN model.
- Identify the fractures that are either completely inside or cut the block.
- Calculate the connections between these fractures and their connection to the faces of the block.
- Specify a linear head gradient parallel to each coordinate axis on all the faces of the block.

- Calculate the flow through the network and the flux through each face of the block for each axial head gradient.
- Fit a symmetric anisotropic hydraulic conductivity tensor that best fits (least-squares) the flux response of the network.
- Fracture kinematic porosity is calculated as the sum (over all fractures that are connected on the scale of the block) of fracture area within the block multiplied by the transport aperture of the fracture.

Hence, to calculate the ECPM properties for a finite-element grid with 1 million elements, say, involves 3 times 1 million DFN flow calculations. One important aspect of this approach is that the properties are calculated on a particular scale, that of the blocks, and that a connectivity analysis of the network is performed only on the scale of the block. Bulk flows across many blocks will depend on the correlation and variability of properties between blocks.

One refinement of the upscaling methodology is to simulate flow through a slightly larger domain than the block size required for the ECPM properties, but then calculate the flux responses through the correct block size. The reason for this is to avoid over-prediction of hydraulic conductivity from flows through fractures that just cut the corner of the block but that are unrepresentative of flows through the in-situ fracture network. This method is illustrated in Figure 2-4. The area around the block is known as a 'guard-zone', and an appropriate choice for its thickness is about a fracture radius. The problem is most significant in sparse heterogeneous networks in which the flux through the network of fractures is affected by 'bottlenecks' through low transmissivity fractures, and is quite different to the flux through single fractures.

An example of an ECPM model used in the regional-scale modelling is illustrated by Figure 2-5. In most areas this model is similar to that shown in Figure 2-1, except for inside rock domains RFM029 and RFM017 where the properties are based on a stochastic DFN model that has been upscaled element-by element giving rise to heterogeneities in the background properties that reflect the stochastic nature of the underlying DFN. Note the higher hydraulic conductivity in fracture zones crossing the tectonic lens. This reasons for this are discussed in Section 2.3.4.

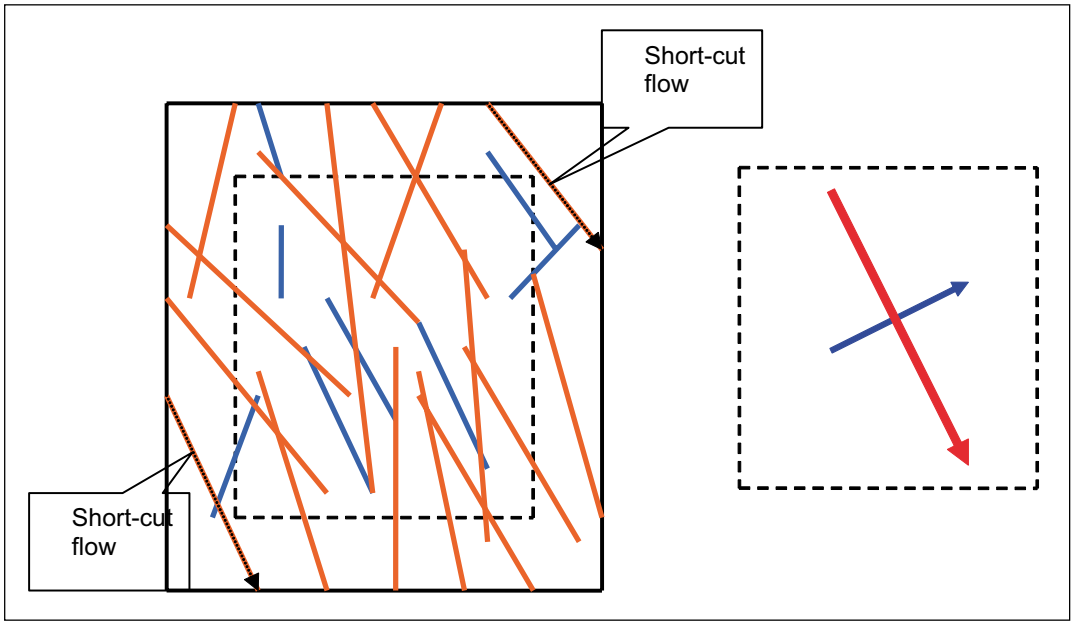

Figure 2-4. *2D sketch of how block-scale hydraulic conductivity can be over-estimated using a linear head gradient by high transmissivity fractures that cut across a corner of the block. By simulating flow through a larger domain, but only calculating the flux through the required block size (dashed block) then fluxes more consistent with flow through an in-situ network are obtained. The ECPM hydraulic conductivities are then calculated for the dashed block to give principal components (right). The red arrow is the maximum component, blue the minimum.*

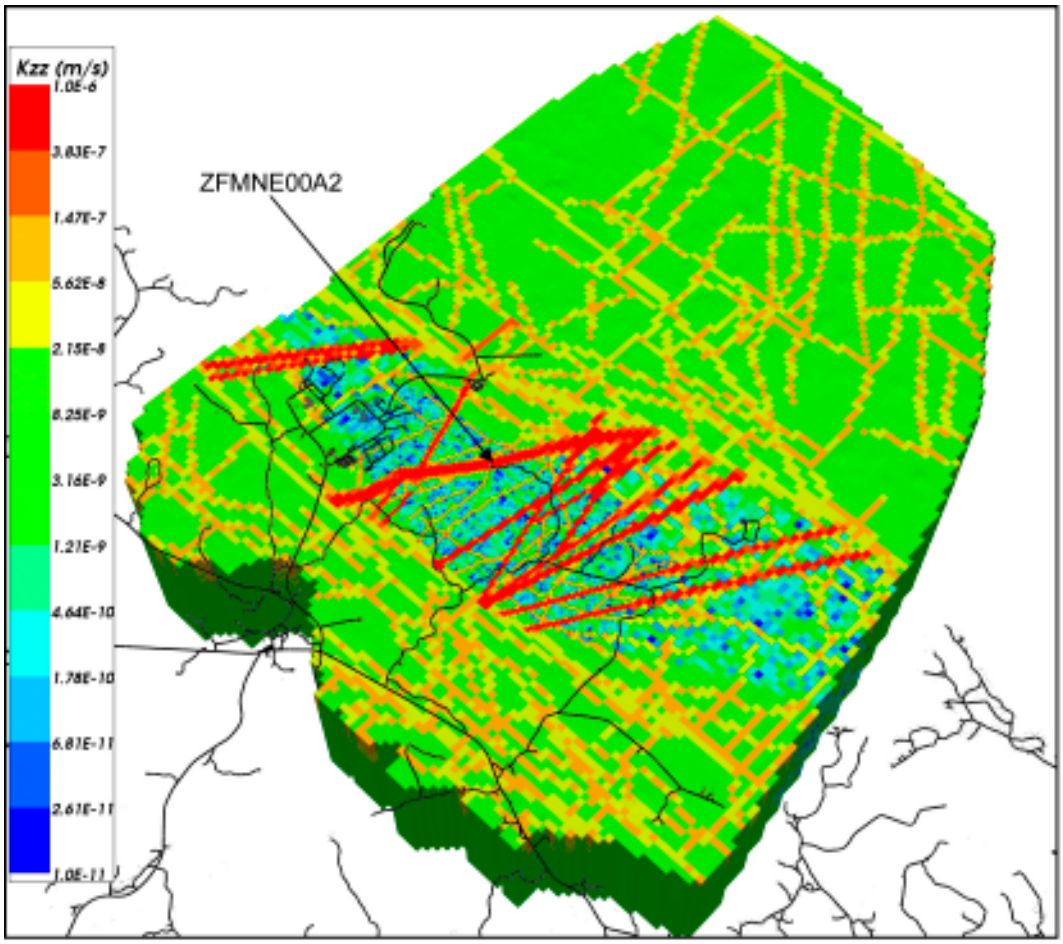

Figure 2-5. *An example of an ECPM regional-scale model. Each finite-element is coloured by vertical hydraulic conductivity. Only the heterogeneous area in the centre has background properties based on an upscaled DFN model within rock domains RFM029/017. Roads and buildings are added in black.*

2.1.4 Combined CPM/DFN models

In addition, to the ability to create distinct models based on the concepts described above, CONNECTFLOW offers the option to construct combined models that integrate sub-models of different types. That is, the model can be split into 2 different domains: one that uses the CPM concept, and one that uses the DFN concept. However, DFN and CPM sub-models have to be exclusive, i.e. the approaches cannot be used simultaneously in any part of the domain.

Two quite different examples are included below to illustrate some of the possible models that can be constructed. Figure 2-6 shows an example of a combined model where a local-scale DFN model is nested within a larger regional-scale ECPM model. The DFN sub-model is used to provide detailed flow and transport calculations around a repository, while the ECPM sub-model provides a representation of the regional-scale flow pattern that control the boundary conditions on the DFN model. The interface between these two sub-models is on the six faces of the DFN model.

The converse example is to nest a CPM sub-model within a DFN sub-model as shown in Figure 2-7. In this case, a CPM sub-model is used to represent flow in backfilled access and deposition tunnels, while the surrounding fractured rock is represented by a DFN sub-model. The interface between the two sub-models has a complex geometry corresponding to the outer surface of the tunnel system.

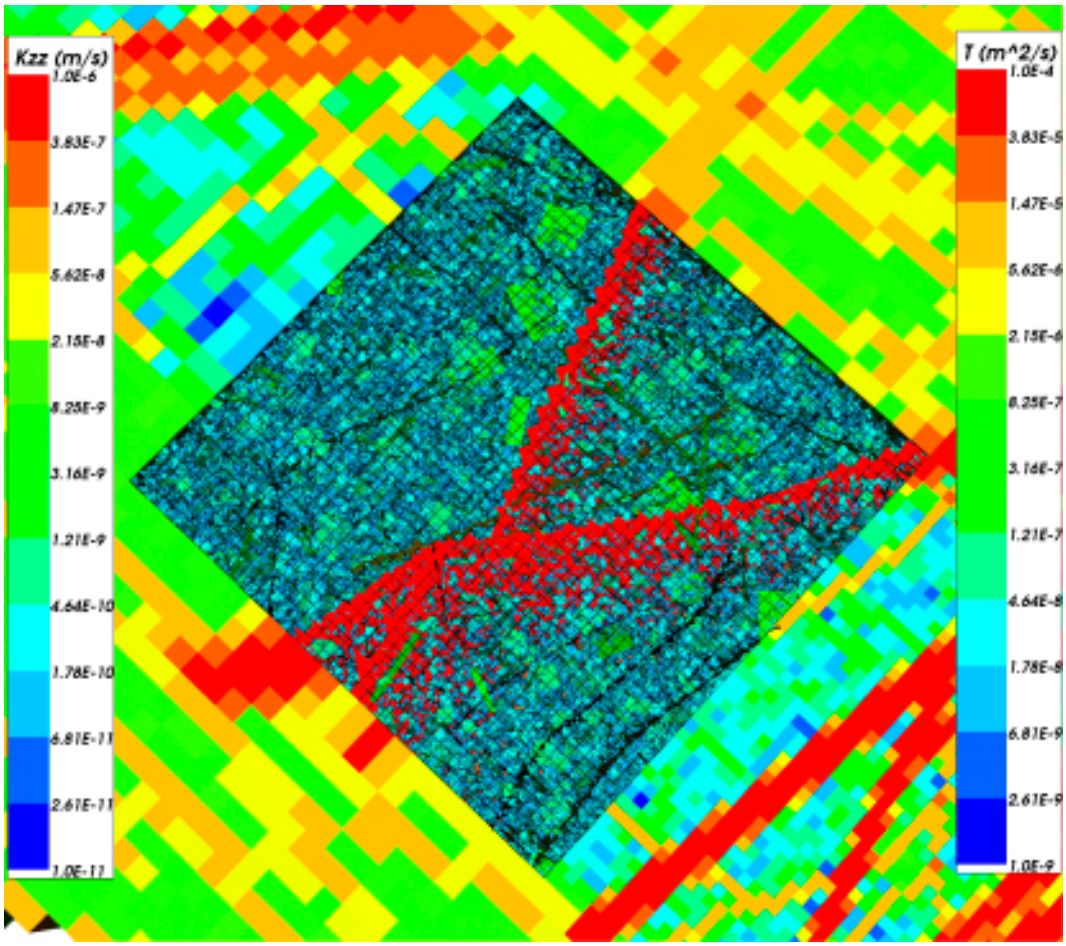

Figure 2-6. *An example of a combined ECPM/DFN CONNECTFLOW model using a DFN sub-model to represent the detailed fractures around a repository and nested within a larger regional-scale ECPM sub-model. In this map view fractures are coloured by transmissivity while elements are coloured by vertical hydraulic conductivity. Here, the interface between the two sub-models is on the boundary of the DFN model.*

In summary, combined models make it possible to represent different regions in different ways and then combine the regions into a single model. This is different from the case where discrete fracture objects co-exist in the same space with a porous medium model of the rock matrix. Representations of the interaction between fractures and the rock matrix within the same domain can be represented in CONNECTFLOW by modelling rock matrix diffusion (RMD) within CPM/ECPM models, but it should be recognised that this is quite a different issue. It may be noted that RMD of salinity is not represented within the DFN domain, whilst RMD within the fracture system of radionuclides can be accounted for either in the particle tracking algorithm or later in the PROPER radionuclide transport calculations.

In a combined DFN/CPM model, flow in the DFN and CPM models is nested formally by internal boundary conditions at the interface between the two sub-models. These boundary conditions are implemented as equations that ensure continuity of pressure and conservation of mass at the interface between the two sub-regions. On the DFN side of the interface, these boundary conditions are defined at nodes that lie along the lines (traces) that make up the intersections between fractures and the interface surface. On the CPM side, the boundary conditions are applied to nodes in finite-elements that abut the interface surface. Thus, extra equations are added to the discrete system matrix to link nodes in the DFN model to nodes in the finite-element CPM model. Figure 2-8 shows this configuration. By using equations to ensure both continuity of pressure and continuity of mass, then a more rigorous approach to nesting is obtained than by simply interpolating pressures, say, between separate DFN and CPM models.

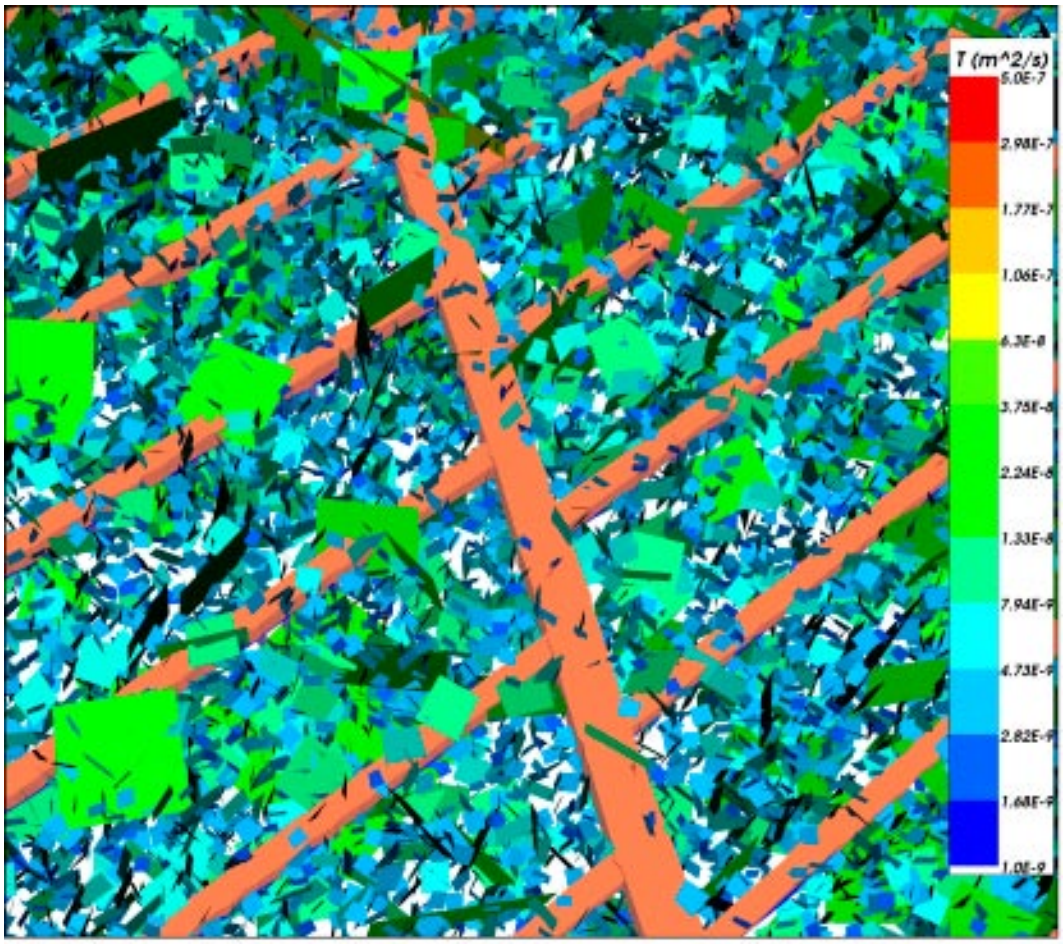

Figure 2-7. *An example of a combined DFN/CPM CONNECTFLOW model using a CPM sub-model of deposition and access tunnels nested within a DFN sub-model. Some fractures have been removed to reveal the tunnels. Here, the interface between the two sub-models is on the boundary of the CPM model.*

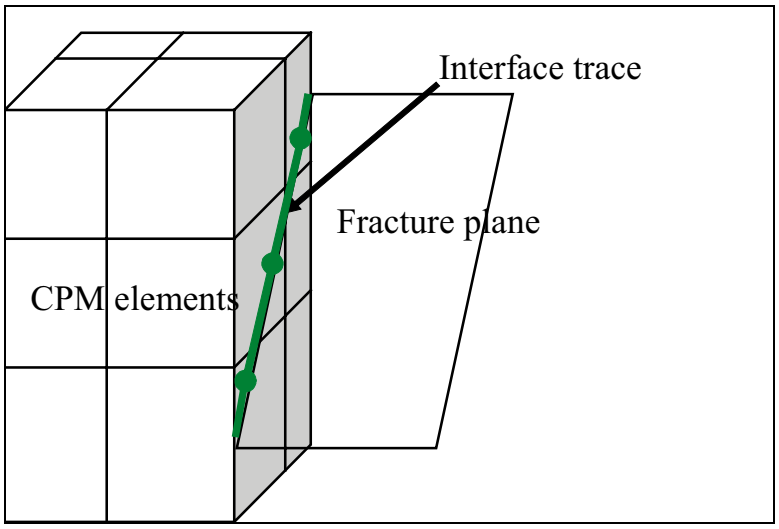

Figure 2-8. *Sketch of coupling between DFN and CPM sub-models. A finite-element CPM mesh is shown on the left. The right hand surface is intersected by a single fracture plane. Extra equations are used to link the DFN to the CPM. These equations are applied at fracture global nodes (dark green points) in the fracture plane along the intersection (dark green line).*

In order to construct nested models of the same fractured rock (mixing DFN and CPM sub-models), then the data used for the DFN and CPM models should be self-consistent. For example, if a repository scale DFN model is nested within a ECPM model, then flow statistics on an appropriate scale (the size of the elements in the ECPM model) need to be consistent. This is achieved by the fracture upscaling techniques described in Section 2.1.3.

The steps in coupling the two regions are:

1. Calculate the intersections of fractures with the boundary of the DFN region.
2. Select the surfaces of the DFN region that abut the CPM region and specify a coupling type boundary condition.
3. For each fracture that intersects these DFN region surfaces, identify the CPM finite-elements that abut the fracture. A single fracture may abut several elements, or several fractures may abut the same element.
4. Add extra equations to the discrete system matrix to link the pressure values at nodes on the fracture intersects with the pressure values in the adjoining finite-elements.
5. Solve the discrete system matrix.

Hence, extra internal boundary conditions have to be specified for a CONNECTFLOW model to link DFN and CPM regions.

A particle tracking algorithm is used in combined models to represent advective transport of solutes. In CPM models, particles are tracked in a deterministic way by moving along a discretised path with the local finite-element velocity-field. In DFN models, a stochastic 'pipe' network type algorithm is used. Particles are moved between pairs of fracture intersections stepping from one intersection to another. At any intersection there may be several possible destinations that the particle may potentially moved to next as flow follows different channels through a fracture. A random process weighted by the mass flux between pairs of intersections (connected by a 'pipe') is used to select which path is followed for any particular particle. Hence, there is an explicit hydrodynamic dispersion process built into the transport algorithm used in the DFN. The time taken to travel between any two intersections, the distance travelled and flow-wetted surface are calculated for each pipe based on flow rates and geometries. In a combined model, particles are traced through both DFN and CPM regions continuously using the appropriate algorithm according to the region the particle is currently in. An example of this is shown in Figure 2-9. The implication is that particle tracks are deterministic until they enter a DFN sub-model, and are then stochastic afterwards, even if the particle goes back into a CPM sub-model.

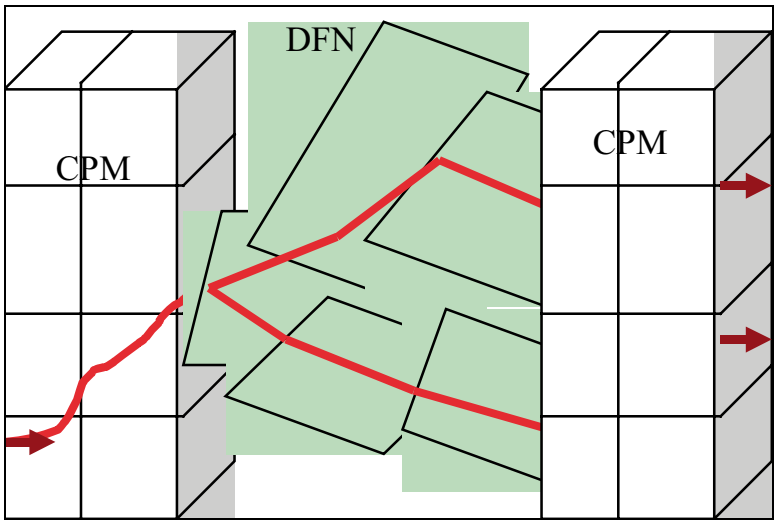

Figure 2-9. *Illustration of particle tracking through a combined DFN/CPM to show the different particle tracking methods in the two regions: deterministic in CPM, stochastic in DFN.*

2.2 Modelling methodology

As mentioned at the beginning of Section 2.1, a key uncertainty is the appropriate conceptual model for groundwater flow in the tight rocks within the candidate area at Forsmark. In the site modelling F 1.2 it was concluded that there was insufficient data to make a firm decision on the most appropriate conceptual model. Therefore, in SR-Can we adopt a modelling methodology that maintains the two alternative model concepts that were developed in the site modelling:

- **Alternative 1** uses an ECPM model with heterogeneous properties based on the use of an underlying discrete fracture network (DFN) concept, which explicitly represents fractures within the rock mass and calculates flows through the individual fractures and between fractures at intersections. Using DFN models it is possible to integrate statistically-generated, smaller-scale fractures with large-scale deterministic deformation zones. From these DFN models, it is then possible to generate equivalent continuum porous medium (ECPM) models by converting the flow properties of blocks of the fracture network into the equivalent properties for a porous medium block of the same size. This conceptual model is based on the upscaled regional DFN including sub-block scale fractures derived for SDM F 1.2 developed by the CONNECTFLOW Team to carry out the modelling as it allows both DFN and ECPM representations to be used independently or combined in a single model. Some variants on the DFN model used for the site modelling are made here to improve the match to borehole hydraulic data by introducing spatial variations in the DFN properties.
- **Alternative 2** uses a CPM model based on multi-component homogenous properties derived for SDM F 1.2 as developed by the DarcyTools Team. This considers a more conceptually simple model based on bulk properties measured in the Pipe-stream system (PSS) packer-test interval data (e.g. 100 m packer sections). This concept was considered a valuable alternative given the difficulties in measuring flow in the fracture system within parts of the candidate area such as the lower parts of KFM01A.

Since there are very few measured flows above the detection limit in the repository area below about 300 m depth, then it is difficult to parameterise hydraulic properties in the vicinity of the repository. For the DFN based Alternative 1 concept, parameters from the Hydro-DFN models developed to match the data from the site boreholes are extrapolated in several different ways to deal with uncertainties in the hydraulic properties around the repository. Thus, the site-scale DFN model considered here is more sophisticated in considering spatial variability of the DFN that was not possible in the site modelling due to time constraints. In the CPM based Alternative 2 concept, the hydraulic conductivity is to set to the detection limit of the 100 m PSS interval data, which is about 10^{-11} m/s. The latter approach is conservative in the sense that the detection limit is certainly higher than the hydraulic conductivity of the deep rock in KFM01A, for example, but it may not be so for the entire repository volume due to heterogeneities. The original site modelling DFN based model gave hydraulic conductivities that were too high in KFM01A. However, in this study by reducing the fracture transmissivity or fracture intensity in the candidate area, then a much better match has been attained. Further, these two modified DFN models both give hydraulic and hydro-geochemical profiles that are consistent with the Alternative 2 CPM model. Thus, for the current site data there isn't a firm basis for promoting one concept over the other.

The two concepts have their own advantages. Alternative 1 is probably the more realistic, at least for parts of the bedrock, since there is evidence from boreholes such as KFM03A that when flow does occur it can be tied to water-bearing fractures. A number of assumptions were made and uncertainties identified in developing the Hydro-DFN from the supporting geological and hydraulic data, and hence the DFN approach allows us to quantify the effects of the uncertainties on PA calculations. Alternative 2 is a much simpler and homogeneous so it is easier to interpret the results from this model and the effects of additional processes such as thermal. The only real sensitivities relevant to this model are the initial and boundary conditions, but these were dealt with in the site modelling.

Since it is required that flow and transport be considered on a variety of scales from the canister (a few metres) to the several kilometres associated with shoreline movements over the next 7,000 years, then a key issue in the modelling is how to integrate or 'nest' these scales. Important aspects that have to be considered in how to go about nesting different scales are:

1. How to nest different scales of model either as 'embedded' models where different scales or types of model are combined and are linked by internal boundary conditions or as separate models where boundary conditions have to be transferred from the larger scale to the small;
2. How to represent features such as fracture zones that cross the boundary consistently between the different scales.
3. How to model processes such as variable-density flow on the different scales.
4. How to represent transient processes on the different scales.
5. How to perform particle tracking continuously across the different scales.

Aspects 1, 2 and 3 are dealt with in Sections 2.2.1, 2.2.2 and 2.2.5, respectively. In respect to transients (Aspect 4), the site modelling has already developed a methodology for understanding the current hydrogeological situation by regional-scale modelling of the paleo-hydrogeology over the last 10,000 years. For SR-Can we continue this approach to calculate the evolution of groundwater flow at the Forsmark site up to 9,000 AD and also the transport of dissolved species in the groundwater. For more detailed fine-scale models it is not practicable to consider transient processes in a continuous manner. Instead several 'snapshots' in time are considered chosen on the basis of distinct changes in the groundwater flow pattern as calculated in the regional-scale modelling. The methodology used for transport (Aspect 5) is described in Section 2.2.4. A final aspect is how to represent the repository, and this is covered in Section 2.2.5.

2.2.1 Nesting of models

Several different methods of nesting different scales of model have been applied in this project. The methods fall into two main types: either embedded models where only a single model is constructed, but areas of the model have a finer resolution or different type of model (e.g. DFN) and internal boundary conditions are required to ensure continuity of variables and conservation of flux; or two separate scales of model where boundary conditions have to be transferred more manually from the larger scale to the small. In CONNECTFLOW the embedded method is used to nest fine-scale CPM models inside coarser CPM models, or to nest DFN models inside CPM models, or vice versa. The second method we call 'combined' models to make a distinction. A schematic of how the nesting works in shown in Figure 2-10. Some real examples of both embedded and combined models have already been given in Section 2.1. The embedded method of nesting has the advantage that it ensures both continuity of variables and fluxes at the interface between the two scales, whereas separate models only ensure continuity of variables.

Because of the complex requirements of this project a variety of nesting methods had to be used and often combined. Figure 2-11 presents an illustration of the overall workflow and interactions between models. Boxes are used to indicate distinct types of model, and arrows to show the flow of data between them. All phases of the process are shown including those from the site-modelling from geological data and data interpretation to site investigation modelling to repository-scale modelling through to PA calculations. The models described by the green boxes are the ones constructed as part of this project and described in this report. The right-hand branch of models represent those based on Alternative 1 using a DFN concept, while the left-hand branch reflects the Alternative 2 set of models. In both cases, regional-scale models of the transient evolution of groundwater flow and geochemistry are used to supply boundary conditions at selected times to finer scale models. For each alternative, fine-scale models that represent the flow down to the scale of individual deposition holes and the surrounding tunnels and EDZ are used to provide accurate and realistic input to PA calculations.

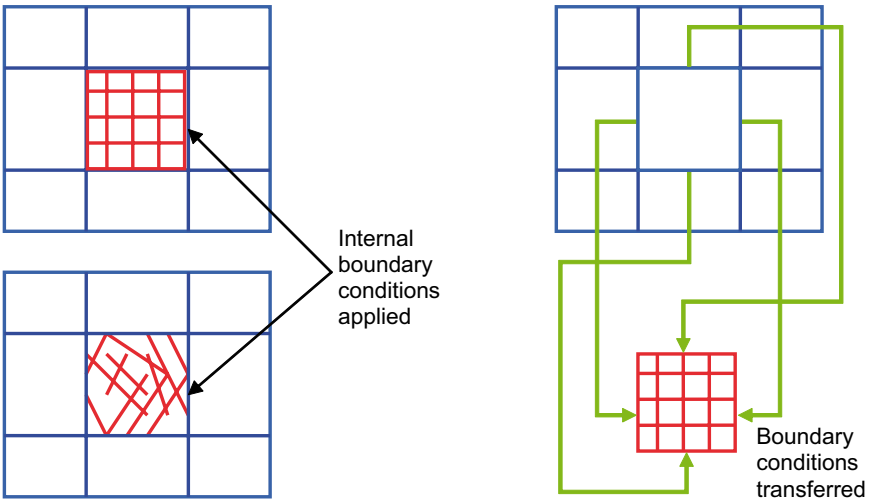

Figure 2-10. *Examples of different methods for nesting models. Top left: an embedded fine-scale CPM model inside a coarser CPM model. Bottom left: a combined fine-scale DFN model inside a coarser CPM model. Right: two separate CPM models with boundary conditions transferred from the larger to smaller scale.*

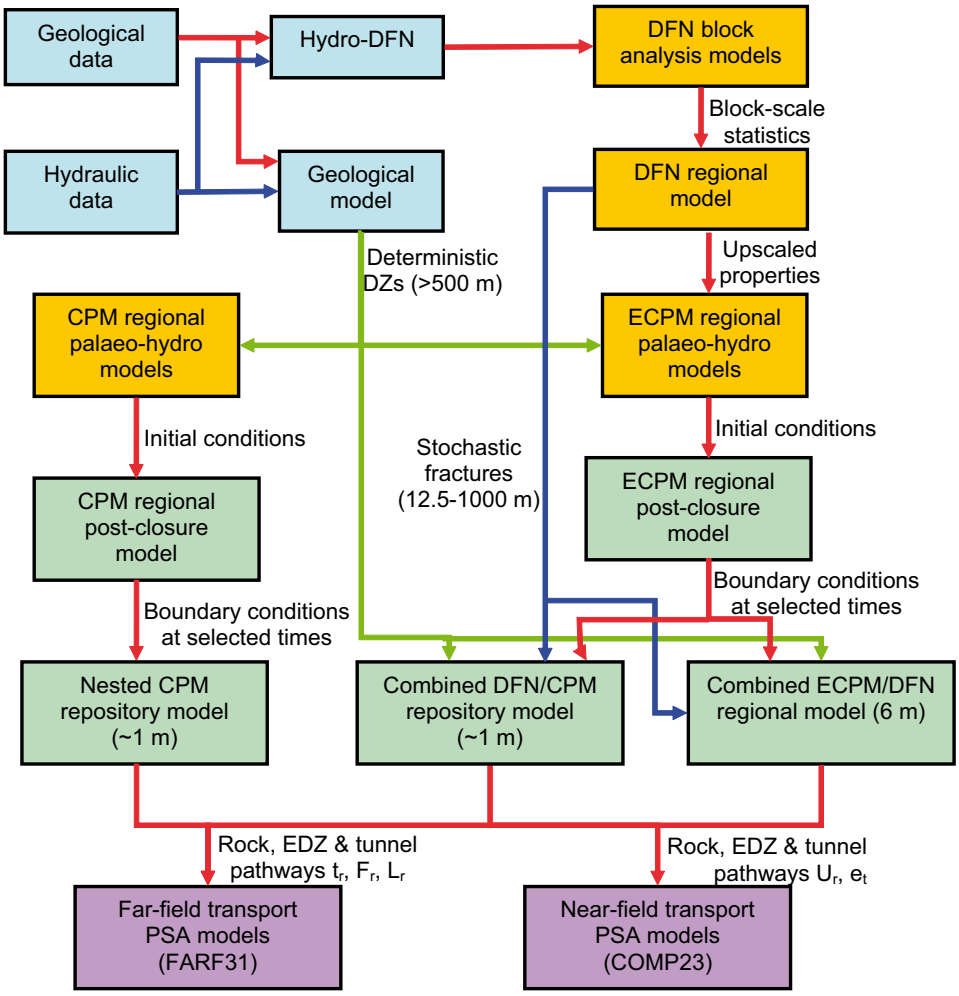

Figure 2-11. *Schematic illustration of model chain developed for the SR-Can methodology. Models coloured blue were supplied as part of the site modelling (SDM) F 1.2 Exercise. Models coloured orange were an overlap between work as part the HydroNet Modelling Group within SDM and SR-Can. Models coloured green have been created solely within SR-Can. Models coloured purple relate to the PA modelling phase of SR-Can.*

For Alternative 1, two slightly different types of model are constructed to cross-check the approach of calculating groundwater pathways and associated PMs in DFN models. The first is to use a detailed repository-scale model that models the repository explicitly as a CPM surrounded by a DFN models with fractures down to a scale of order 1 m radius to resolve the release of particles from a canister and then advected through surrounding rock. However, this type of model has a limited domain, so it cannot necessarily model transport to ground surface for all flow-paths, particularly long horizontal paths. Hence, a second type of combined model is constructed where a local-scale DFN model is nested within a regional-scale ECPM model with the repository modelled as equivalent fractures with appropriate properties. In this case, it is only possible to include fractures down to a radius of order 3 m (6 m length). This means it is possible to track all particles continuously through the local and regional domains, but some retention in small fractures around the repository is possibly lost. Hence, these two types of model can be used to compliment each other in quantifying the sensitivities to the approximations necessary for practical reasons.

2.2.2 Representation of deformation zones (DZs) and the implicit representation of fracture zones (the 'IFZ' method)

For Forsmark 1.2, the basic concept is that fractures exist on a continuous range of length scales, which motivates a methodology to generate sub-lineament-scale fractures stochastically on scales between tens of metres to about 1 km, and then combine this DFN by superposition with the larger scale deterministic DZs. The approach used to represent the DZs was different in DFN and CPM/ECPM models. In CPM and ECPM models the DZs were represented by modifying the hydraulic properties of any finite-elements intersected by one or more zones to incorporate the structural model in terms of the geometry and properties of zones using the Implicit Fracture Zone (IFZ) method in CONNECTFLOW as described in /Marsic et al. 2001/. In a CPM model, properties are homogeneous within a set of defined sub-domains prior to superposition of the DZs. Afterwards the hydraulic properties vary from element to element if intersected by a DZ, as shown in Figure 2-1 (bottom). In a ECPM model, the methodology is to first create one or more realisations of the stochastic network on the regional-scale and then, using the upscaling methods described in Section 2.1.3, to convert this to a realisation of the ECPM model, minus the DZs. The ECPM model properties are then modified to incorporate the effect of the DZs as shown in Figure 2-5. The IFZ method is described below.

The IFZ downscaling method identifies which elements are crossed by a fracture zone and combines a hydraulic conductivity tensor associated with the fracture zone with a hydraulic conductivity tensor for the background stochastic network. For each element crossed by the fracture zone the following steps are performed:

1. The volume of intersection between the fracture zone and the element is determined.
2. The hydraulic conductivity tensor of the background rock is calculated in the coordinate system of the fracture zone.
3. The combined conductivity tensor of the background rock and the fracture zone is calculated in the coordinate system of fracture zone.
4. The effective hydraulic conductivity tensor that includes the effect of the fracture zone is determined in the original coordinate system.

The methodology is illustrated diagrammatically in Figure 2-12. In 3D, the resultant hydraulic conductivity is a 6-component symmetric tensor in the Cartesian coordinate system. The tensor can be diagonalised to give the principal components and directions of anisotropy.

Similarly, a combined scalar block-sale porosity is calculated for the element based on combining the fracture zone porosity and the background block-sale porosity using a weighting either based simply on either the relative volume or on relative transmissibility (total channel flow capacity, which is transmissivity times flow length [m^3s^{-1}]). The latter weighting can be suitable for transport since it weights the combined porosity toward the fracture zone porosity

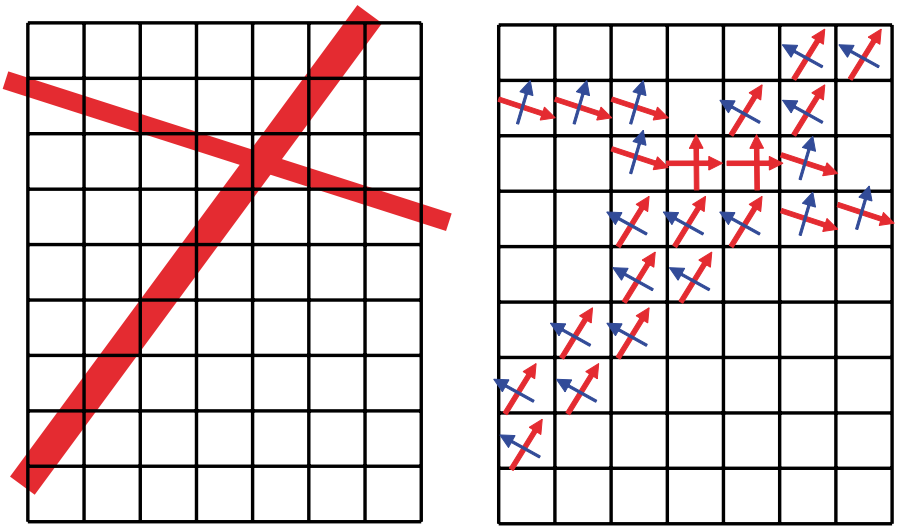

Figure 2-12. *Schematic illustration of the modification of the hydraulic conductivity tensor by the IFZ method. A finite-element grid crossed obliquely by two fracture zones of different thickness (left). The effect on the equivalent continuum porous medium hydraulic conductivity (right). Elements with a large IFZ effect are coloured pink. Ones with a lesser effect, where the fracture zone only crosses one corner, are coloured orange. The principal directions of the resultant anisotropic hydraulic conductivity tensor are shown by arrows (red for major component, blue for minor).*

if this is of a relatively high hydraulic conductivity. The result of this step is to produce a spatial distribution of CPM element properties (hydraulic conductivity tensor and porosity) that represent the combined influence of both the deterministic fractures zones and background stochastic fractures.

It may be noted the term “background conductivity” here means the equivalent conductivity of the stochastic fracture network. No extra component for matrix conductivity or micro-fracturing is added. However, the stochastic DFN is necessarily truncated in some way e.g. based on fracture radius which in consequence means that some elements may not include a connected network of fractures or may only be connected in some directions. To avoid this just being a result of the choice of truncation limit and chance, a minimum block conductivity and porosity is set for any elements that have zero properties following the fracture upscaling and IFZ methods. Appropriate minimum properties were derived in the SDM Hydro-DFN studies by calculating the minimum values seen when the DFN is truncated only at very small fractures relative to the block size, and so are essentially free from the truncation effect.

In DFN models the DZs are modelled as surfaces (i.e. no volume). The surfaces are composed of many rectangular or triangular fractures to discretise the geometry and hydraulic properties. The site modelling F 1.2 prescribed a depth dependent transmissivity that decreased significantly with depth, and which also depends on the dip (gently dipping or vertical) of the zone. Therefore, it was necessary to sub-divide the zones into relatively small sub fractures to represent the property variations. An example is shown in Figure 2-13.

In combined models it is important to ensure that the DZ geometries are represented consistently where they cross between DFN and CPM models. This is to ensure continuity of flow across the interface where the zone crosses the interface, otherwise artificial barriers to flow may be introduced. It is achieved in CONNECTFLOW by specifying the DZs using the same input file in the DFN and CPM sub-models. The parts of a fracture within each sub-model are calculated automatically. Figure 2-14 shows an illustration of how a large deterministic fracture that crosses between DFN and CPM sub-models can be modelled in such a way as to ensure there is continuity in its representation, and hence in flow between the regions. An example of how this was applied in the SR-Can study is shown in Figure 2-5.

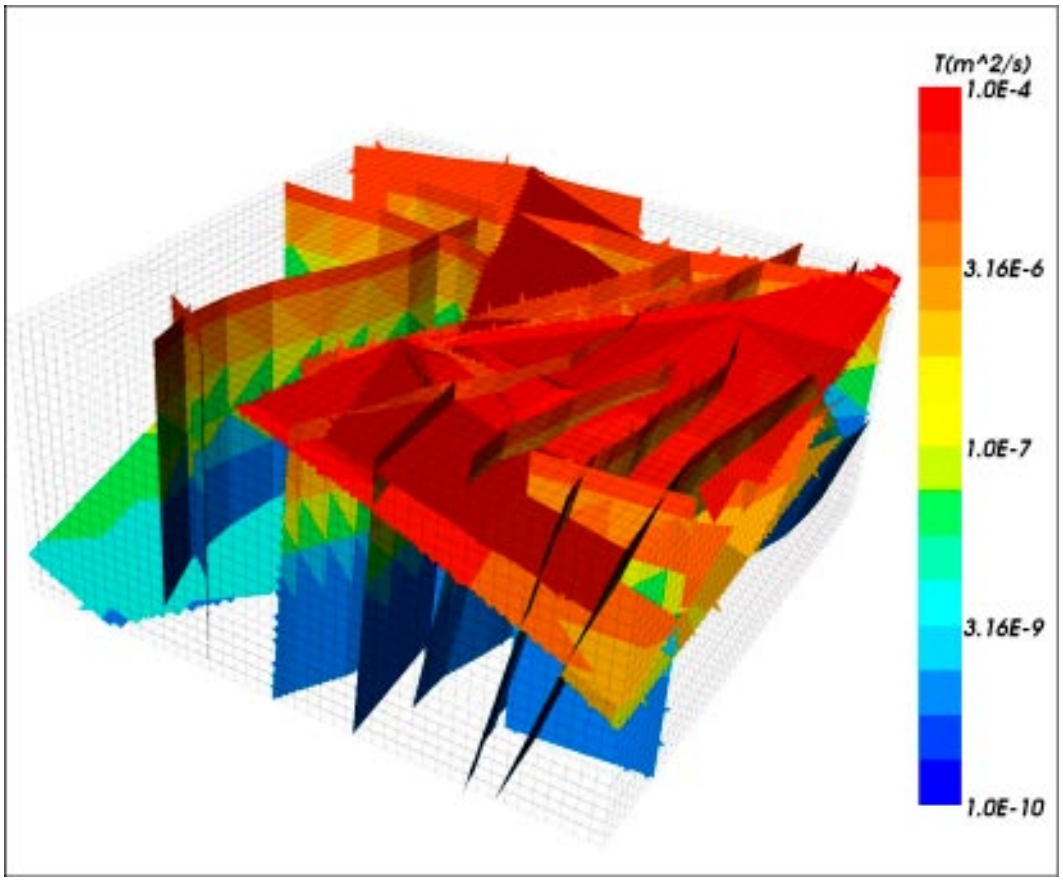

Figure 2-13. *Deformation zones (DZs) modelled as surfaces in a local-scale DFN model with depth dependent transmissivity.*

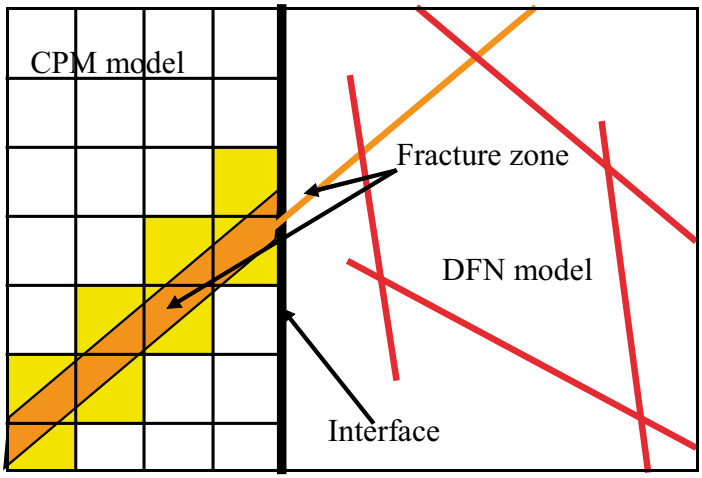

Figure 2-14. *Schematic illustration of continuity of DZs across a CPM/DFN interface in a CONNECT-FLOW model. The DFN region is to the right with a CPM grid to the left. A few fractures are shown in red and orange in the DFN region. The red fractures may be stochastic for example. The orange fracture is a deterministic DZ that crosses the interface. On the DFN side it is shown as a plane, while on the CPM side it is drawn with its actual thickness. The elements crossed by the DZs are coloured yellow. Hydraulic conductivity in these elements will be modified in the IFZ method to represent the effect of the fracture zone on flow and transport.*

2.2.3 Variable density groundwater flow and salt transport

Variations in groundwater composition create variations in groundwater density and hence buoyancy-driven flow that modifies the pattern of groundwater flows. Since gradients in the watertable at Forsmark are relatively weak, then buoyancy forces arising from the presence of salt are significant. Important advances in the modelling capabilities for handling variable-density flow have been made since the interim SR-Can assessment, namely:

1. An option in CPM or ECPM models to simulate flow in a porous medium for groundwater of variable salinity, where the salinity arises from a number of groundwater constituents. This can be modelled either in terms of transport of mass fractions of the basic hydro-geochemical constituents (such as chloride, sodium, oxygen isotope ratio), which are taken to be conservative, or in terms of transport of fractions of selected reference waters. Either way, the transport equations are coupled with the overall mass conservation equation for groundwater. In addition, rock matrix diffusion (RMD) is included in the transport of each groundwater constituent.
2. An option to calculate groundwater flow for specified spatial variations in groundwater density in DFN models and combined models. That is, the groundwater density has to be interpolated onto the fracture system from another model, but then the consistent pressure distribution and flow-field is calculated with buoyancy forces included. The groundwater density is typically interpolated from a CPM or ECPM model at a selected time. Particle tracking through both DFN and combined models with the calculated flow field can then be performed.

The first option was applied in the site modelling to simulate the transport and mixing of four reference waters (Rain 1960, Marine, Glacial, and Brine) in line with the conceptual model for hydro-geochemistry. This helped in the calibration of the model in terms of hydraulic properties and boundary conditions using data from the results of the Mixing and mass-balance modelling (M3) geochemical analysis and the various ionic species, oxygen and hydrogen isotope ratios. However, limitations in data did not justify more than a qualitative calibration of the model. The same option is used here to model the future evolution of groundwater constituents up to 9,000 AD. No only is this necessary for calculating groundwater flow and flow-paths in the future, but it also gives a prediction of how groundwater chemistry will evolve around the repository and some more general indication of how groundwaters evolve over cycles of glacial and inter-glacial periods.

The option also makes it possible to model diffusion of the reference waters between groundwater flowing in fractures and immobile water in the rock matrix between the fractures (RMD). The numerical approach used /Hoch and Jackson 2004/ is based on a method developed by /Carrera et al. 1998/ enhanced to enable potentially larger time steps to be taken. The approach combines an approximation that is accurate for small times with one that is accurate for long times, to give a representation of the diffusion into the rock matrix that is accurate for all times. At early times, the diffusion is represented in terms of the inverse of the square root of time, and at long times it is represented as a series of decaying exponentials. The main parameter that controls the rate of RMD is the facture surface area per volume, a_r [m^2/m^3], which is also the key parameter in determining the F-quotient. Therefore, calibrating models against groundwater constituents in the fracture and matrix systems may help condition the selection of a_r and hence reduced the uncertainties in predictions of F-quotient. Unfortunately, hydro-geochemistry data in the matrix was not available for the F 1.2 data-freeze. In consequence, a_r has to be derived based primarily on fracture hydraulic data such as PFL data (see Section 2.3.3).

The second option addresses an outstanding issue from the interim assessment of how to define boundary conditions for repository-scale or local-scale DFN models when buoyancy-driven flows are significant. In the interim study quite different flow-paths were predicted by DFN models than the corresponding ECPM models, and it was not clear whether this was due to deficiencies in the choice of boundary conditions used to approximate variable-density flows in the DFN or an innate difference in connectivity for flow through a sparse fracture

network compared to a continuum model. Here, groundwater density was exported from the regional-scale ECPM models at selected times and then interpolated onto the fracture systems in either the repository-scale DFN/CPM combined models or the regional-scale ECPM/DFN models and used to calculate the consistent groundwater flow throughout the model, and then flow-paths were computed using particle tracking. This was done at several different instances in time to capture changes in the regional flow boundary conditions. The groundwater density is interpolated on to each fracture intersection and then within each fracture on every finite-element used to discretise the flow in individual fractures, and so variable-density flow is resolved on a fine-scale.

2.2.4 Nesting of transport and calculation of performance measures: travel time (t_r), canister Flux (U_r), pathlength (L_r) and F-quotient (F_r)

A major objective of the SR-Can modelling is to compute groundwater flow-paths from each deposition hole (there are 6,824 in total) to the surface. The approach taken was to track particles moving with the advective flow velocity from release points around the deposition holes until they reach the top surface. In doing this, two key issues that have to be addressed are how to do this when two scales of model are being used, and how to deal with the transient evolution of the flow-field.

There is a potential nesting issue because the repository-scale models are very detailed around the repository but have limited extent. Vertically the model extends from –600 m elevation almost to the surface, –20 m elevation, but does not extend horizontally far beyond the edge of the repository footprint. The vertical path was found to be an important one in the combined DFN/CPM model, but still some paths exit the vertical sides of the model. The solution is to track particles from the release points to the outer boundary of the repository-scale model, and then restart the particle tracking in the corresponding regional-scale model from the points where the particles hit the repository-scale model. PMs such as travel-time are calculated as the cumulative travel-time along both legs of the path. The same approach is used for both nested CPM models and DFN models, although for the DFN model this means starting the particle in the corresponding ECPM regional-scale model.

In terms of transients, it is possible in CONNECTFLOW to track particles as they move through a flow-field that evolves in time. However here it is preferred to use fixed instantaneous flow-fields from selected times in the future to obtain a qualitative assessment of the potential impact of releases at different times or evolutions in the flow-field. The objective is to establish whether flow-paths are sensitive to the retreat of the shoreline and if so whether flow-paths stabilise once the shoreline becomes remote to the site. Part of the reason for taking this approach is a practical one that to consider radionuclide transport for a range of radionuclides each with different retardation rates and different release times becomes a huge sequence of calculations. Hence, in order to compare transport at different release times, and between different concepts and variants, in a simpler and more quantifiable way, we perform a series of particle-tracking calculations at an appropriate set of release times. These release times are chosen carefully to represent different phases when the flow-field appears to be either changing significantly, or when there are periods of relative stability. Hence, for most transport calculations reported here, PMs are calculated based on fixed flow-fields at several selected times. Another motivations is the fact that the radionuclide transport code (FARF31) used in the PA calculations is based on a streamline formulation that assumes a steady-state flow-field.

For the case where the shoreline is retreating away from the site, such that a major discharge area is getting further away in time, then it is expected that flow-paths and travel-times are getting longer, and hence using the instantaneous flow-field at the release time is considered a conservative approximation for the subsequent evolution. When travel-times become longer than the temperate climate period due to retention (e.g. due to sorption), then one needs to consider transport in the wider context of the climate evolution, which is outside the remit of the study reported here. In Section 6, transients arising from heat generation are considered

which create changes in the flow-field over a shorter period of tens to thousands of years. In this case it is more important to consider the sensitivity to moving particles in an evolving transient flow-field and so the effect is quantified with and without heat generation for the two main alternative models.

To provide input to PA calculations tables of performance measures are produced for each case using the four performance measures (PMs). In a continuum model these defined as:

1. Travel-time, $t_r = \sum_l \frac{\varphi \delta l}{q}$, where δl is a step in distance along the path, for example through one finite-element, φ is the kinematic porosity, and q the Darcy velocity.
2. Initial Darcy velocity at the release point (Canister flux), $U_r = U_{0,r}$.
3. Pathlength, $L_r = \sum_l \delta l$.
4. F-quotient, $F_r = \sum_l \frac{a_r \delta l}{q}$, where a_r is the fracture surface area per unit volume.

The subscript "*r*" indicates that the PM is calculated in the rock. That is, they only represent cumulative PMs for those parts of paths within the rock and exclude parts of flow-paths that pass through the EDZ or tunnel backfill. PMs are calculated for legs of paths within the EDZ and tunnels, but these computed as separate PMs for each path and distinguish by a "*EDZ*" or "*t*" subscript, respectively.

In a DFN model the PM definitions are slightly different:

1. Travel-time, $t_r = \sum_f \frac{e_t w_f \delta l}{Q_f}$, where δl is a step in distance along the path, between a pair of fracture intersections, e_{tf} is the fracture transport aperture, w_f is the flow width between the pair of intersections, transport aperture, and Q_f is the flux between the pair of intersections in the fracture.
2. Initial Darcy velocity at the release point (Canister flux), $U_r = \frac{\sum_f Q_f}{h_d}$, where the sum is over fractures intersecting a deposition hole, and h_d is the height of the deposition hole.
3. Pathlength, $L_r = \sum_f \delta l$.
4. F-quotient, $F_r = \sum_f \frac{2 w_f \delta l}{Q_f} = \sum_f \frac{2 t_{rf}}{e_{tf}}$, t_{rf} is the travel time in a fracture along the path.

The results from the particle tracking are then used to produce ensemble statistics for the performance measures, as well as locating the discharge areas. The ensemble is over the set of 6,824 particle start locations, one for each canister, as shown in the F 1.2 repository (Layout D1, see Figure 2-16). Apart from the work done on the repository layout by Design, no further attempt is made to avoid starting particles in either deterministic fracture zones or high transmissivity stochastic fractures in the DFN or ECPM models. In reality such features are likely to be avoided during repository construction, and hence the model may tend to see particles start in a wider range of possible fracture transmissivities than might be encountered in reality.

2.2.5 Flow and transport in the repository and EDZ

The repository is a large hydraulic feature with a potentially large impact on the local groundwater flow given the low hydraulic conductivity of the bedrock. In order to account for these effects it is necessary to represent the repository appropriately in the model. The potential conduits for flow within the repository are the deposition tunnels, access tunnels, ramp and shafts, together with the EDZ around the tunnels created during construction of the repository. The operational and resaturation phases are not considered here, so it is assumed that

we only need consider saturated flow and that all tunnels have been backfilled with a mixture of bentonite and crush rock to give homogeneous properties. For the EDZ, the most realistic scenario suggested by the Design Team is that hydraulic conductivity parallel to the axis of the tunnel will be enhance by about half an order of magnitude over a thickness of 0.3 m, but due to the drill and blast techniques used the EDZ will occur in 5 m sections with intact sections of 0.5 m in-between (see /SKB 1997/, for example). The short intact sections arise due to the cycle of blasting with a short intact section around the cut of the previous blast round. A discontinuous EDZ as such obviously gives very little impact on groundwater flow, since the EDZ is a discontinuous hydraulic feature of small volume and only slightly enhanced conductivity. For this reason the EDZ was neglected in the regional-scale modelling, and in the repository-scale modelling, more pessimistic scenarios were assessed such as a continuous EDZ otherwise it had negligible effect. For both the tunnel backfill and EDZ, values for hydraulic conductivity, porosity, and flow-wetted surface, a_r, were required. Only a single porosity was used for the tunnels and EDZ since RMD of groundwater constituents was neglected in the EDZ and backfill for the groundwater flow modelling. Likewise, a_r was set to zero for the same reason.

In terms of PA calculations, the near-field concept for KBS-3 considers three potential paths for radionuclides to leave the canister:

1. **Path_Q1**, diffusion into the mobile water in fractures surrounding the deposition hole.
2. **Path_Q2,** diffusion into mobile water in the EDZ.
3. **Path_Q3**, diffusion into tunnel pore-water.

In order to study each of these paths, the detailed repository-scale models have to represent the deposition holes, tunnels and EDZ explicitly, and flow-paths have be computed for a release at 3 appropriate positions around each canister. Hence, the PMs defined in Section 2.2.4 are calculated for 3 paths for each canister. It is possible that the 3 particles may follow very similar trajectories, such that T_r, L_r and F_r are similar, but U_r will vary. Further for each path, the PMs are calculated for portions of the path spent in the rock, tunnels, and EDZ separately. Because $a_r=0$ in the tunnel and EDZ, F_{EDZ} and F_T are zero, and therefore only T_{EDZ}, L_{EDZ}, t_t and L_t are calculated. Clearly a_r in the EDZ (and possibly in the tunnel) is none zero in relaity. However, we do not include retention in EDZ and tunnel as retention mechanisms; and hence a_r is assumed to be zero since there is no need to quantify this retention.

Figure 2-15 shows the three pathways considered in the KBS-3 concept. A fourth path, Q4, relates to diffusion through the floor of the tunnel to a fracture, but this is generally found to be negligible compared to the advective pathways.

In terms of the hydraulic properties, the repository is represented implicitly in the regional-scale modelling since the grid resolution only goes down to 50 m, while in the repository-scale the tunnels and EDZ are modelled explicitly, i.e. one or more finite-elements are used to represent each deposition hole and the tunnels sections and EDZ in between. For the transient regional-scale, the model is run from 8,000 BC to 9,000 AD, so the repository is not present in the system until 2,020 AD (assumed), and then the model needs to be modified to include the repository and restarted at this time. All cases are therefore treated as two separate parts, one for the past evolution (8,000 BC–2,020 AD) and one for the future evolution (2,020 AD–9,000 AD). The model for the past evolution is run without any repository included. Using the IFZ method, the Forsmark Repository Layout D1, see Figure 2-16, is then implicitly added to the model at the start of the future evolution (2,020 AD).

The IFZ method uses an input file that defines hydraulic features as tabular features with a specified width and hydraulic properties, and so it is possible to represent the repository as a set of linked feature volumes which are then converted into a continuum representation by modifying the properties on the finite-element grid. Since the refinement of the grid around the repository is 50 m and many of the repository features are much smaller, it is possible to simplify the geometrical representation of the repository without loosing any important information. Hence, all cross-sections in the repository (tunnel, ramps and shafts) are treated

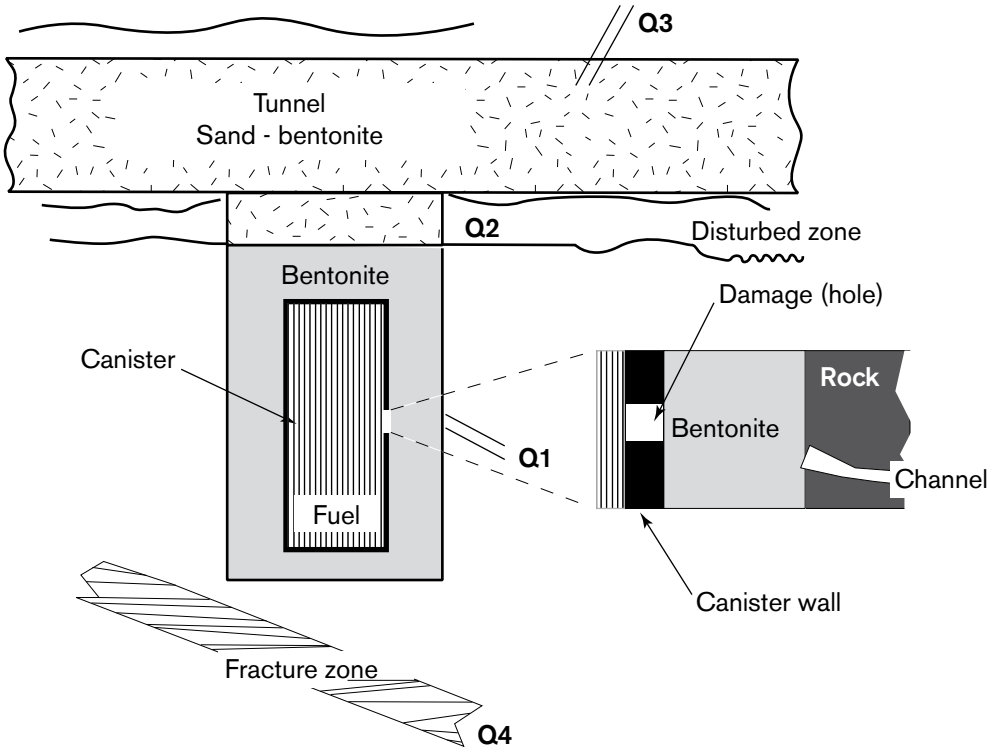

Figure 2-15. *Schematic view of the KBS-3 repository design, showing the small hole in the canister and the location of the various possible transport paths into near-field rock.*

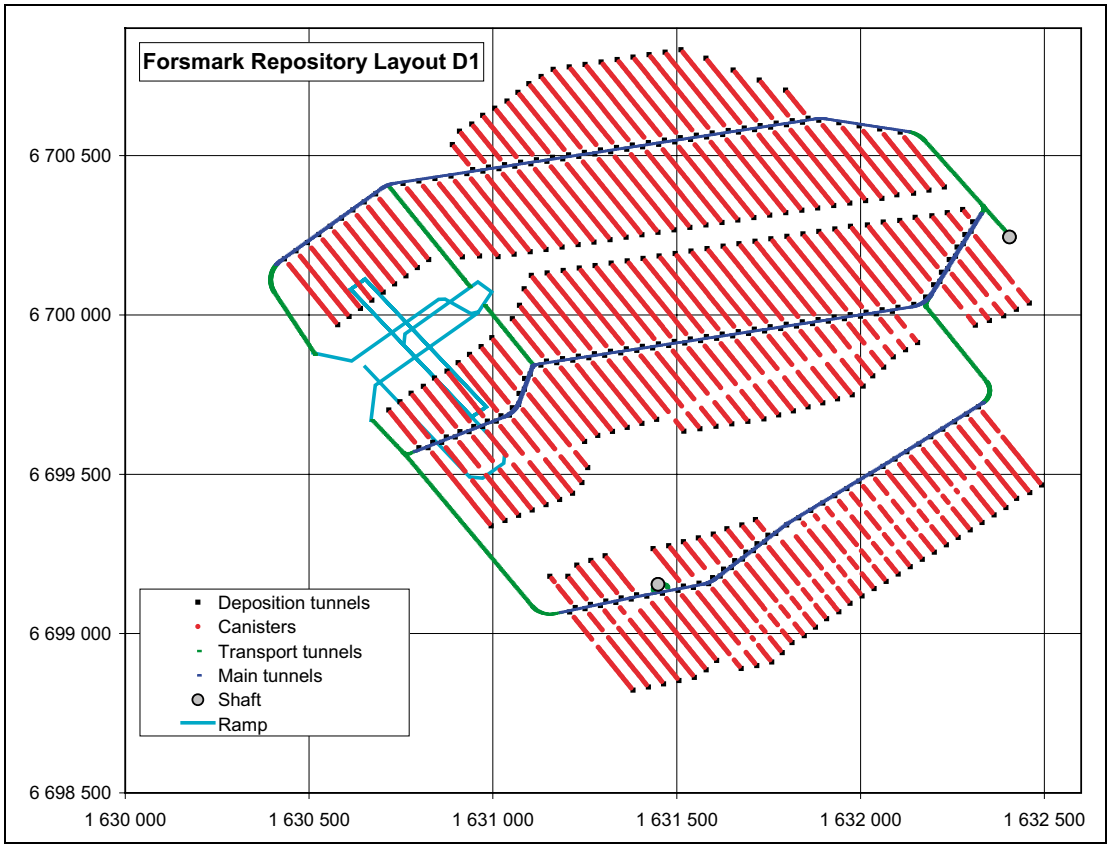

Figure 2-16. *Plan view of the Forsmark Repository Layout D1 (at z=–410 m).*

as rectangular using the dimensions listed in Table 2-1. To simplify the representation in the model, the curved structure of the ramp was simplified by using linear connections instead of more proper bends. Considering the refinement of the grid, the implications of these simplifications are negligible.

The deposition tunnels are defined by a start and an end point for each tunnel. The start point of each deposition tunnel is geometrically connected to the main tunnels. The main tunnels, transport tunnels and the ramp are defined by smaller parts all connected to each other to form a hydraulically connected system. The shafts are two vertical features that should have a diameter of 3 m but are here represented as square sections with the equivalent cross-section area. Neither the deposition holes nor EDZ are represented in the regional-scale continuum models. The hydraulic parameter values assigned to the repository are given in Table 2-2. All different parts of the tunnel and ramp system are assigned the same values. The flow wetted surface is set to zero in the tunnel as retention in the backfill of the tunnel will be handled in the radionuclide transport calculations using FARF31 far-field model within PROPER. This requires inputs of the length and travel-time of flow-paths within the tunnel sections from the detailed repository-scale models, but not an F-quotient.

Since the cross-sectional area is much smaller than that of a 50 m square finite-element and the hydraulic conductivity of the backfill is within one order of magnitude, then the repository has a negligible effect on the regional-scale hydraulic conductivity. However, the porosity of the backfill is five or six orders of magnitude higher than the kinematic porosity of the bedrock, and so this does modify the regional-scale porosity upwards around the repository as shown in Figure 2-17. The result will be slower travel times immediately around the repository at future release times once the repository is included.

In the repository-scale models the EDZ was modelled explicitly as shown in Figure 2-18. In the continuum models the EDZ is modelled by a layer of elements below the base of the tunnel, whereas in the nested DFN/CPM models it is represented as an equivalent fracture beneath the tunnel. The EDZ ‘fracture’ is subdivided into 6 m sections to improve discretisation, and is assumed to be continuous as a conservative approximation. Table 2-3 gives the properties used in the EDZ. An example of how the tunnels are modelled in the nested DFN/CPM model was shown in Figure 2-7.

Table 2-1. Dimensions of different sections of the Forsmark Repository Layout D1 as used in the model.

Section	Width [m]	Height [m]
Deposition tunnel	4.9	5.4
Main tunnel	10.0	7.0
Transport tunnel	7.0	7.0
Ramp	7.0	7.0
Shaft	2.66	2.66

Table 2-2. Summary of hydraulic parameter values used for the Forsmark Repository Layout D1.

Parameter	Value
Tunnel hydraulic conductivity, k	$1.0 \cdot 10^{-10}$ m/s
Deposition hole hydraulic conductivity, k	$1.0 \cdot 10^{-11}$ m/s
Kinematic porosity, n_e	0.35
Flow wetted surface, a_r	0.0 m^2/m^3

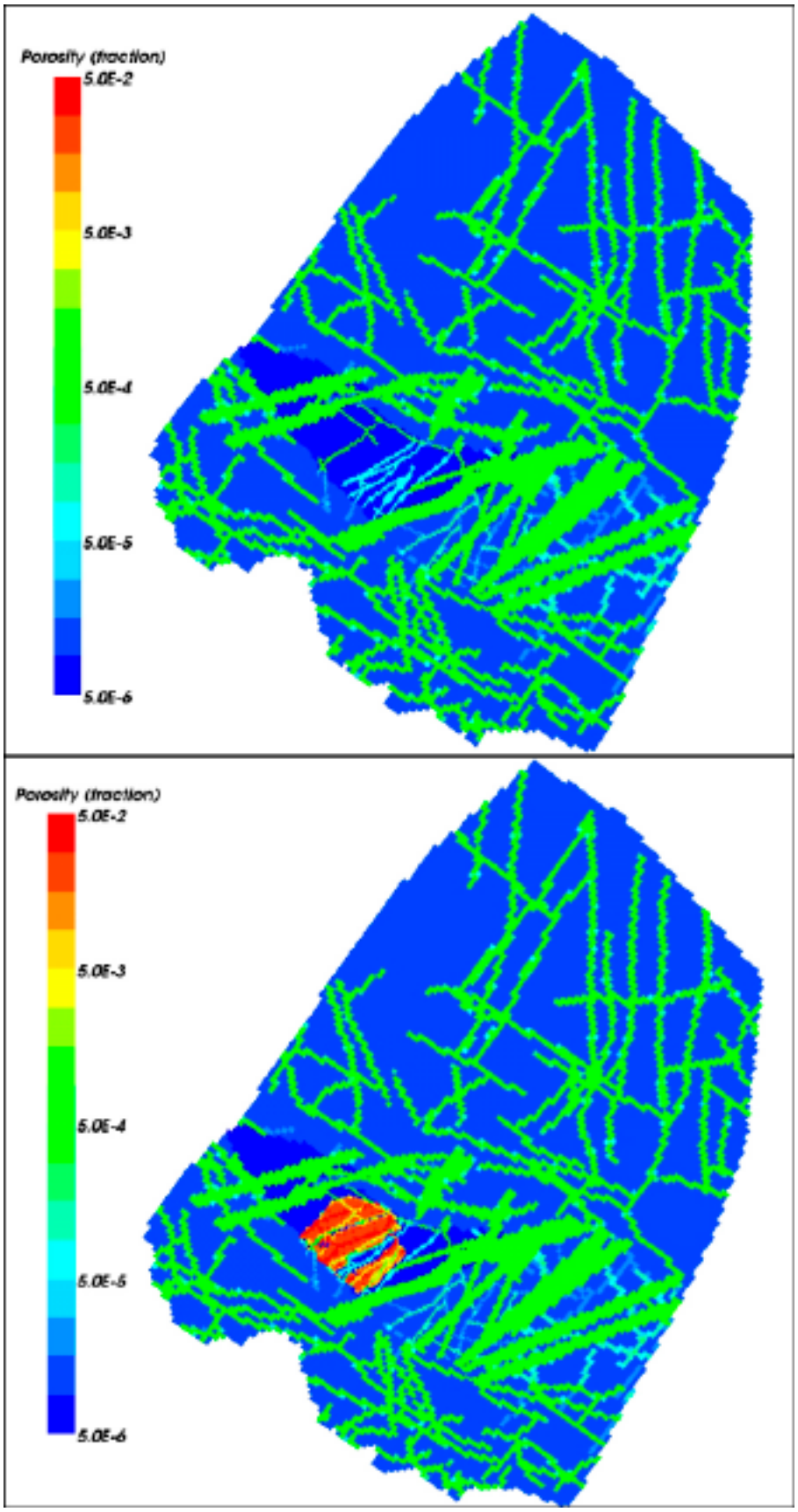

Figure 2-17. *Kinematic porosity in the regional-scale CPM model at repository depth. Top: before 2,020 AD. Bottom: after 2,020 AD with repository added.*

Table 2-3. Summary of hydraulic parameter values used for the EDZ.

Parameter	Value
Thickness	0.3 m
Hydraulic conductivity, k	$3.0 \cdot 10^{-10}$ m/s
Kinematic porosity, n_e	$1.0 \cdot 10^{-4}$
Flow wetted surface, a_r	0.0 m^2/m^3

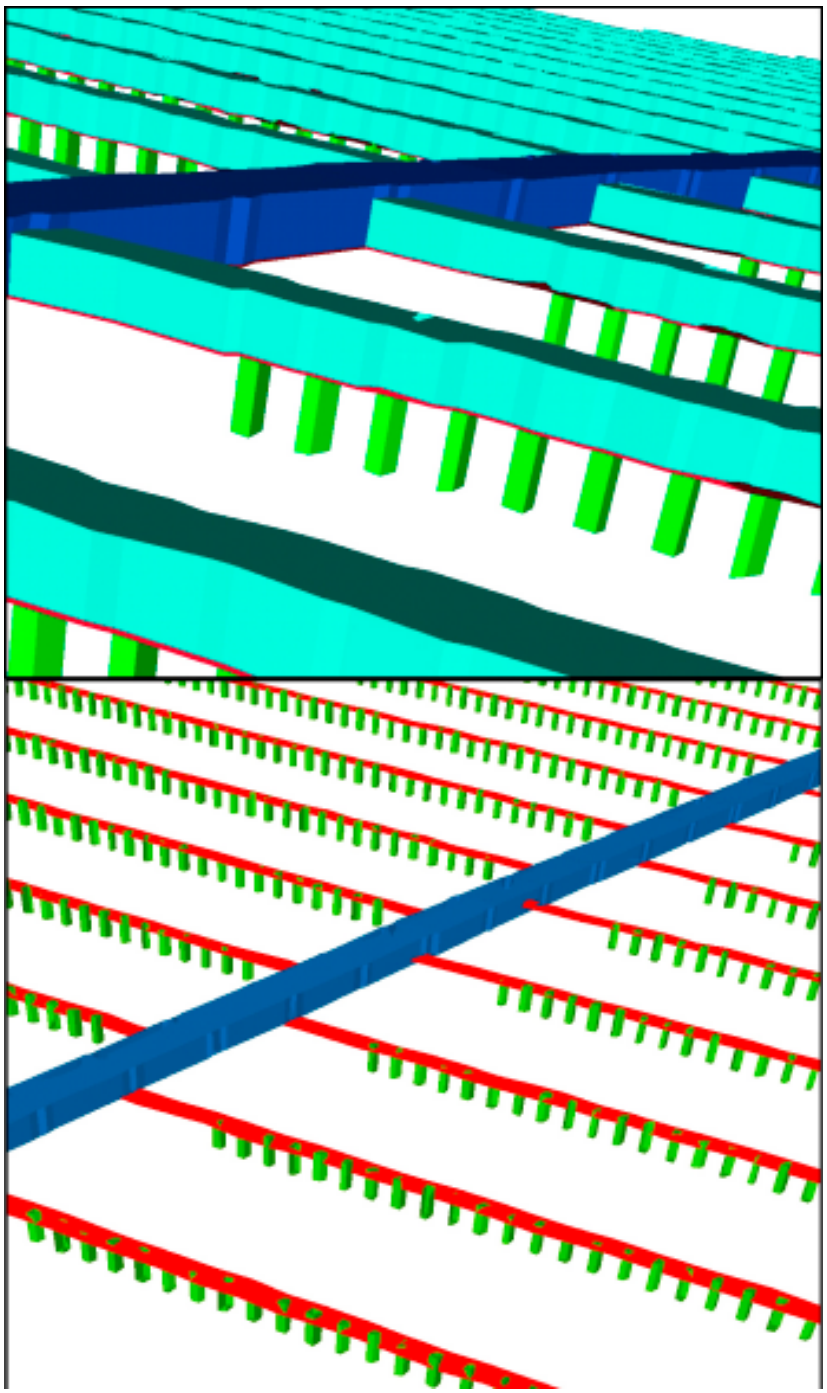

Figure 2-18. *Methods used to represent the tunnels and EDZ in the repository-scale models. Top: the continuum models showing a close up of the tunnels (blue, deposition holes (green) and EDZ (red). Bottom: the combined DFN/CPM model showing the access tunnel (blue), EDZ modelled as a set of equivalent fractures (red), and deposition holes (green).*

Finally, in the regional-scale nested ECPM/DFN both the tunnel system and EDZ are represented by equivalent fractures as shown in Figure 2-19. The EDZ 'fracture' and tunnel 'fractures' are orthogonal to give a hydraulic connection between the tunnels and EDZ. Similarly, the sections of tunnels, ramps and shafts are all linked to ensure they are hydraulically connected.

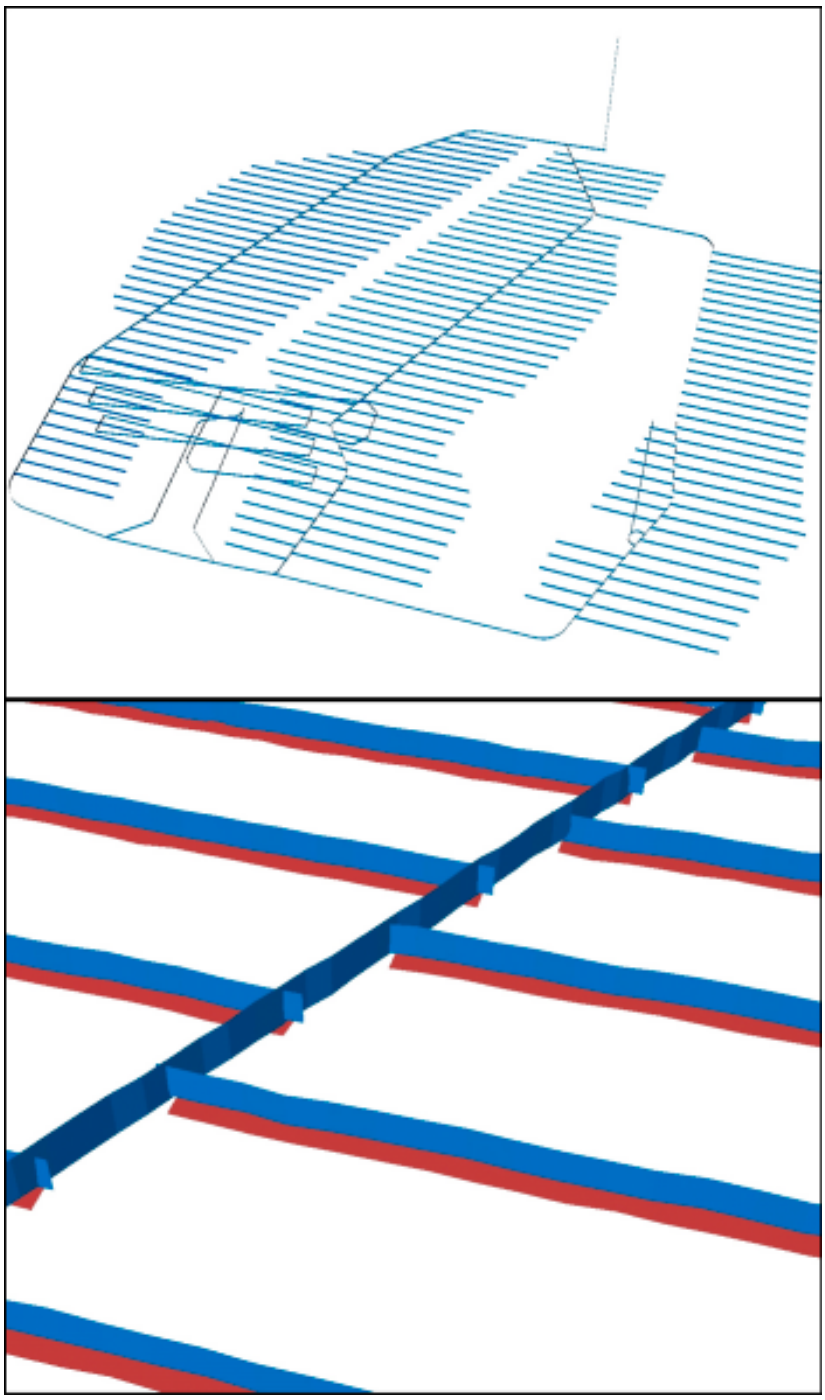

Figure 2-19. *Representation of tunnels and EDZ in regional-scale combined ECPM/DFN model. Top: overall system showing tunnels, ramps and shafts. Bottom: close up of a section of tunnels (blue) and EDZ (red).*

2.2.6 Q-equivalent (Qeq) for input to near-field model (COMP23)

The near-field code COMP23 calculates the non-stationary nuclide transport in the near-field of a repository. The system is divided in to compartments, where the only restriction is that a compartment is formed of the same material. The model, which is a very coarsely discretised Integrated Finite Difference Model, embeds analytical solutions at locations where other models require a very fine discretisation such as entrances and exits from small holes and fractures. In the repository, radionuclides leaking out through a small hole in the canister wall diffuse into the bentonite buffer and may then migrate through various pathways into the flowing water in rock fractures. The pathways are illustrated in Figure 2-15.

For compartments in contact with water flowing in fractures in the rock, the diffusive transport is determined by an equivalent flow-rate, *Qeq* [m^3/yr]. This parameter is a fictitious flow-rate of water that carries a concentration equal to that at the compartment interface. It has been derived by solving the equations for diffusional transport to the passing water by using boundary layer theory /Neretnieks 1979/. The value of *Qeq* is dependent on the geometry of the contact area, the water flux, the flow porosity or fracture aperture and the diffusivity. As part of the SR 97 assessment formulae were derived for a CPM model /Moreno and Gylling 1998/. The formulae are different for a DFN model as detailed below for the three pathways.

Q-equivalent release into fractured rock for the nested model (Q1) for a DFN model

Path Q1 considers release of radionuclides into the fractured rock surrounding the deposition hole, and hence the particle starts within a fracture that intersects the wall of the deposition hole. Several fractures may intersect the canister. For reasons of making a conservative assumption, the flux into all fractures that intersect the canister and contribute to advective flow away from the canister are included in the calculation of *Qeq*. That is, an effective flow-rate is calculated for all fractures that cut deposition hole and are connected to at least one other fracture. These effective flow-rates are summed for the deposition hole to give the total *Qeq*. The equivalent groundwater flow rate for Q_{eq1} can be written as:

$$Q_{eq\,1} = \sum_f \left(2\frac{Q_f}{\sqrt{a_f}} \sqrt{\frac{4D_w t_{wf}}{\pi}} \right), \text{ where } t_{w,f} = \frac{L_f \cdot e_{t,f}}{Q_f / \sqrt{a_f}} \qquad (2\text{-}1)$$

If there are several fractures intersecting a single deposition hole, then a conservative approach to calculate the equivalent groundwater flow-rate requires the flow to be summed across all the fractures. Hence, the equivalent Darcy velocity, U_{r1}, for all fractures intersecting the deposition hole is:

$$U_{r1} = \frac{1}{w_c} \sum_f \frac{Q_f}{\sqrt{a_f}} \qquad (2\text{-}2)$$

where:

- D_w is the diffusivity in water, [m^2/yr],
- t_{wf} is the time the water is in contact with the deposition hole within each fracture, [yr],
- L_f is the length of the fracture intersection with the wall of the deposition hole, [m],
- U_{r1} is the average initial Darcy velocity in the fracture system averaged over the rock volume adjacent to the canister (water flux) [m/yr],
- Q_f is the volumetric flux in the fracture adjacent to the deposition hole [m^3/yr],
- $e_{t,f}$ is the transport aperture of the fracture adjacent to the deposition hole [m],
- a_f is the area of the fracture plane intersecting the hole [m^2],
- w_c is the canister height [m].

Here, D_w was set to 0.0316 m²/yr, and w_c was set to 5 m. All other values were determined in the DFN flow simulations.

Potentially, a damaged zone may form due to spalling in the rock wall in the deposition hole for waste canisters. The zone can have higher conductivity and porosity than the intact rock. In which case, water will be drawn into the damaged zone from fractures that intersect the deposition hole. The water can attain a longer residence time in contact with the buffer in the hole than would otherwise be the case when only the thin fracture contacts the buffer. This may lead to a higher exchange of solutes between the flowing water and the pore water in the buffer /Neretnieks 2006/. The implications of such an effect are quantified for the reference case in Appendix D.

Q-equivalent release into the EDZ (Q2) for a DFN model

Path Q2 considers the release of radionuclides into the EDZ. Here the particles are released within a fracture used to represent the EDZ that surrounds the top of the deposition hole. The equivalent groundwater flow-rate, Qeq_2, is calculated from the flow in the EDZ fracture that cuts deposition hole and are connected to at least one other fracture. These effective flow-rates are summed for the deposition hole to give the total Qeq. The equivalent groundwater flow-rate, Q_{eq2}, can be written as:

$$Q_{eq2} = 2\sqrt{\frac{4D_w L w_E \varepsilon_E \left(Q_E / \sqrt{a_E}\right)}{\pi}} \tag{2-3}$$

The equivalent Darcy velocity, U_{r2}, for flow in the EDZ is:

$$U_{r2} = \frac{Q_E}{w_E \sqrt{a_E}} \tag{2-4}$$

where:

- L is the half circumference of the deposition hole, [m],
- U_{r2} is the average initial Darcy velocity in the EDZ fracture averaged over the fracture cross-sectional area [m/yr],
- Q_E is the volumetric flux in the EDZ fracture between each deposition hole [m³/yr],
- ε_E is the EDZ porosity [m],
- a_E is the horizontal area of the EDZ between each deposition hole [m²],
- w_E is the EDZ thickness [m].

Here, L_E was set to 2.8 m, w_E was set to 0.3 m, and ε_E was set to 10^{-4}. All other values were determined in the DFN flow simulations.

Q-equivalent release into the tunnel (Q3) for a DFN model

Path Q3 considers the release of radionuclides into a fracture that intersects the tunnel. It is assumed that diffusive equilibrium of radionuclides is achieved in the tunnel backfill and diffusion takes place into the water flowing in fractures surrounding the tunnel. Hence, an equivalent flow-rate, Qeq_3, is required for advective flow in the first fracture encountered along the path after a particle is released in the tunnel backfill above the deposition hole. The equivalent groundwater flow-rate, Qeq_3 is calculated from the flow-rate in the first fracture the particle enters after leaving the tunnel. The equivalent groundwater flow-rate, Q_{eq3}, can be written as:

$$Q_{eq3} = 2\sqrt{\frac{4D_w L_f e_{t,f} \left(Q_f / \sqrt{a_f}\right)}{\pi}} \tag{2-5}$$

The equivalent Darcy velocity, U_{r3}, for flow in the EDZ is:

$$U_{r3} = \frac{Q_f}{w_T \sqrt{a_f}} \tag{2-6}$$

where:

- L_f is the length of the fracture intersection with the wall of the tunnel [m],
- U_{r3} is the Darcy velocity in the fracture averaged over the fracture cross-sectional area [m/yr],
- Q_f is the volumetric flux in the fracture adjacent to the tunnel [m^3/yr],
- w_T is the fracture width intersecting the tunnel [m],
- a_f is the area of the fracture plane intersecting the tunnel [m^2],
- $e_{t,f}$ is the transport aperture of the fracture intersecting the tunnel [m].

Here, L_f was set to 7 m, w_f was set to 2.5 m. All other values were determined in the DFN flow simulations.

Q equivalent release into fractured rock for the nested model (Q1) for a CPM model

Path Q1 considers release of radionuclides into the fractured rock surrounding the deposition hole. For a continuum model the Darcy velocity, U_0, is calculated at the initial point. The equivalent groundwater flow rate for Q_{eq1} can be written as:

$$Q_{eq1} = 4 w_c \sqrt{\frac{D_w U_{r0} L \varepsilon_r}{\pi}} \tag{2-7}$$

where:

- D_w is the diffusivity in water, [m^2/y],
- L is the half circumference of the deposition hole, [m],
- U_{r0} is the initial Darcy velocity adjacent to the canister [m/y],
- ε_r is the kinematic porosity of the rock adjacent to the deposition hole [m],
- w_c is the canister height [m].

Here, D_w was set to 0.0316 m^2/y, L was 2.8 m, w_c was set to 5 m, and ε_r was $5 \cdot 10^{-6}$ in the bedrock, though it could have higher vales if the canister was located within a deformation zone in the AC geological model. All other values were determined in the CPM flow simulations.

Q equivalent release into the EDZ (Q2) for a CPM model

Path Q2 considers the release of radionuclides into the EDZ. Here the particles are released within finite-elements used to represent the EDZ that surrounds the top of the deposition hole. The equivalent groundwater flow-rate, Q_{eq2}, can be written as:

$$Q_{eq2} = 4 w_E \sqrt{\frac{D_w L \varepsilon_E U_{E0}}{\pi}} \tag{2-8}$$

where:

- L is the half circumference of the deposition hole, [m],
- U_{E0} is the initial Darcy velocity in the EDZ [m^3/yr],
- ε_E is the EDZ porosity [m],
- w_E is the EDZ thickness [m].

Here, L was set to 2.8 m, w_E was set to 2.0 m, and ε_E was set to 10^{-4}. All other values were determined in the CPM flow simulations.

Q equivalent release into the tunnel (Q3) for a CPM model

Path Q3 considers the release of radionuclides into a fracture that intersects the tunnel. It is assumed that diffusive equilibrium of radionuclides is achieved in the tunnel backfill and advection takes place into fractures surrounding the tunnel. Hence, an equivalent flow-rate, Qeq_3, is required for advective flow from the tunnel into a fracture zone that intersects it. The equivalent groundwater flow-rate, Qeq_3 is calculated from the Darcy velocity in the tunnel assuming the Darcy velocity in the fracture zone is of similar order of magnitude to that in the tunnel (by conservation of mass). The equivalent groundwater flow-rate, Q_{eq3}, can be written as:

$$Q_{eq3} = 4w_z\sqrt{\frac{D_w L_z \varepsilon_r U_{T0}}{\pi}} \qquad (2\text{-}9)$$

where:

- L_z is the length of the fracture zone intersection with the tunnel [m],
- U_{T0} is the initial Darcy velocity in the tunnel [m/y],
- ε_r is the porosity of the fracture zone [m],
- w_z is the fracture zone thickness [m].

Here, L_z was set to 7 m, and ε_r was set to $1\cdot10^{-3}$, w_z was set to 2.5 m. All other values were determined in the CPM flow simulations.

2.3 Data from Site descriptive modelling F 1.2

The data analysis and site modelling is documented in /SKB 2005b/, /Hartley et al. 2005/ and /Follin and Stigsson 2005/. Here, a brief summary of the main assumptions adopted from the site modelling in this study, and key data such as the Hydro-DFN is given. In addition, some new results on a key issue of how to assign values to the flow-wetted surface in transport calculations are reported.

2.3.1 DFN assumptions and concepts

Few characteristics of the DFN can be determined uniquely and directly, so it is necessary to assume a framework of conceptual models, and then derive parameters that best match the field-data.

Continuous power-law length distribution

One of the most difficult fracture characteristics to measure directly in the sub-surface is fracture size. Fracture sizes can be measured on outcrops for fractures on the scale of metres to tens of metres, and additional data are available for lineaments on the scale of 500 m to several kilometres length, but this leaves a gap between the scales. A widely used assumption is one of a continuum of fracturing that spans all scales and that can be described by a power-law relationship between fracture intensity and size. The key parameters for the power-law distribution are the slope and reference radius, r_0. Often the distribution is defined only in a truncated range, $r_{min}<r<r_{max}$ because either the concept is only valid on a certain range or for practical reasons. As for the site modelling, fractures it will be assumed that fractures of radius greater than 560 m (1 km length) will be modelled deterministically having been detected as lineaments or fracture zones, whereas fractures less than 560 m in radius will have to be modelled stochastically based on the Hydro-DFN.

It should be noted that CONNECTFLOW represents fractures as squares, rectangles or triangulated surfaces, and fracture size is defined in terms of side length L. Elsewhere in SKB's programme fractures are represented by discs of radius, r. Assuming a consistent area between both representations implies a conversion $r=L/\sqrt{\pi}$.

A useful formula /Munier 2004/ associated with the power-law distribution is the fracture intensity, P32, for fractures in some truncated length range $r_{max}>r>r_{min}$ based on the $P32_{tot}$ for length range $r>r_0$:

$$P32(r_{\max} > r > r_{\min}) = \frac{P32_{\text{tot}}\left(r_{\max}^{(2-k_r)} - r_{\min}^{(2-k_r)}\right)}{r_0^{(2-k_r)}} \quad (2\text{-}10)$$

where *kr* is the power-law slope. It was used extensively in this work to calculate the fracture intensity of additional small-scale fractures to be added to the regional-scale DFN, for example.

Fracture transmissivity models

In the Forsmark Version 1.1 modelling, a direct correlation between fracture transmissivity and length was assumed. For F 1.2 the uncertainty associated with this assumption was explored. Three alternative transmissivity concepts were considered for F 1.2 (as shown in Figure 2-20):

- Uncorrelated: log-normal distribution for *T,*

  $T = 10^{\mu+\sigma N'(0,1)}$ (2-11)

  where μ is the mean of $\log_{10}(T)$, σ is the standard deviation of $\log_{10}(T)$, and N(0,1) is a normalised normal distribution.

- Correlated: power-law relation between *T* and *r*,

  $T = a \times r^b$ (2-12)

  where *a* and *b* are the factor and exponent respectively describing the power-law relation.

- Semi-correlated: Random lognormal distribution about a mean that is based on a correlation,

  $T = 10^{\log(a \times r^b) + \sigma N'(0,1)}$ (2-13)

  where *a* and *b* are the factor and exponent respectively of the power-law relation between *r* and the mean of $\log_{10}(T)$, σ is the standard deviation of $\log_{10}(T)$, and N'(0,1) is a normalised normal distribution, truncated between –2 and +2.

All three cases were simulated in the development of the Hydro-DFN, but the correlated case was used as the main case. The correlated case was originally proposed in /Dershowitz et al. 2003/. One argument for it is that, at least for deformation zones, the zone width often increases with length, and thus generally the number of individual conductive fractures associated with zone. If the transmissivity distribution for individual fracture is the same, then based on the above assumption it follows that the effective transmissivity for the fracture zone should increase with the length of the fracture zone. Each of these concepts has an associated set of parameters, as given in parentheses above, which were derived in the Hydro-DFN to match the hydrogeological data.

Fracture kinematic porosity models

As part of the modelling, it is intended to derive fracture kinematic porosity as part of the block properties, as these will be needed in the regional flow modelling. There are no new data such as tracer tests to try to interpret, so the model for the porosity of an individual fracture will be based on Äspö Task Force 6c results /Dershowitz et al. 2003/. This approximates a direct correlation between the transport aperture e_t, and the transmissivity, such that:

$e_t = aT^b$

The values for the constants suggested from Äspö Task Force 6c are $a = 0.46$ and $b = 0.5$. For CPM models, these parameters affect the kinematic porosity and hence travel-time for particle tracks. For DFN models, the transport aperture affects travel time directly. In both cases the relationship is linear between transport aperture and travel-time. In this study, explicit

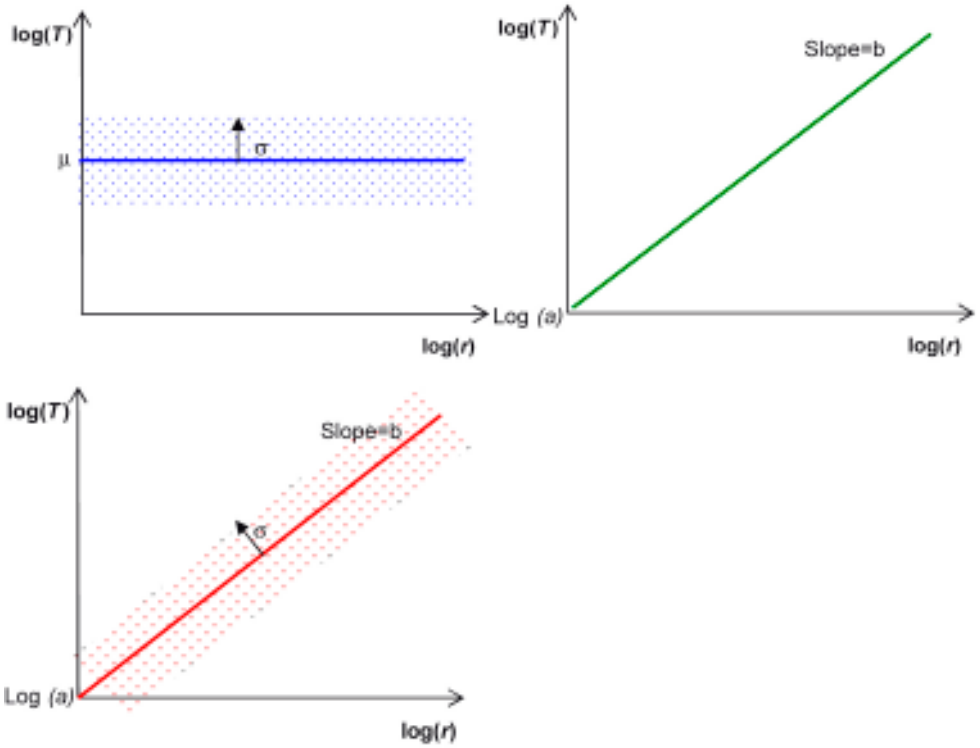

Figure 2-20. *Schematic of transmissivity models, top left to bottom: Uncorrelated, correlated, and semi-correlated. Note that for the Hydro-DFN models, the values of the parameters a and b used for the semi-correlated case are not necessarily the same as those used for the correlated case.*

sensitivities to the transport aperture are only calculated for the deterministic deformation zones. The sensitivity to properties of the background fractures can be estimated simply from the linear relationship.

2.3.2 Hydraulic DFN properties (Hydro-DFN)

Spatial variability and rock volumes

Due to the wide variations in fracture intensity between different borehole sections, coupled with flow measurements found at varying depth the site modelling suggested that different volumes of rock should be considered separately, depending on the fracture intensity measured in different regions within the study area. Hence, a conceptual model was proposed as shown in Figure 2-21 with the rock in the candidate area sub-divided into volumes according to both depth and position relative to the sub-horizontal zone ZFMNE00A2. The location of ZFMNE00A2 at the surface is shown in Figure 2-5. The concept is illustrated on a NW-SE slice through the candidate area as shown in by the section X-XX in Figure 1-1. Two slightly different concepts were derived by the DarcyTools Team using volumes A–D, and by the CONNECTFLOW Team using volumes E–G. The rock outside the tectonic lens is considered to be distinct from these volumes and have its own hydraulic properties. Volumes A–D were used to parameterise the multi-component CPM models based on /Follin and Stigsson 2005/. Volume A is rock above ZFMNE00A2 and below z=–220 m; Volume B is below ZFMNE00A2 and between z=–220 m and z=–360 m; Volume C is above z=–220 m; and Volume D is below ZFMNE00A2 and z=–350 m. In contrast Volumes E–G was used to parameterise the DFN models based on /Hartley et al. 2005/. Volume E is rock above ZFMNE00A2; Volume F is below ZFMNE00A2 and above z=–350 m; Volume G is below ZFMNE00A2 and z=–350 m. The repository lies in either Volume D or at the boundary between Volume F and Volume E, depending on the conceptual model.

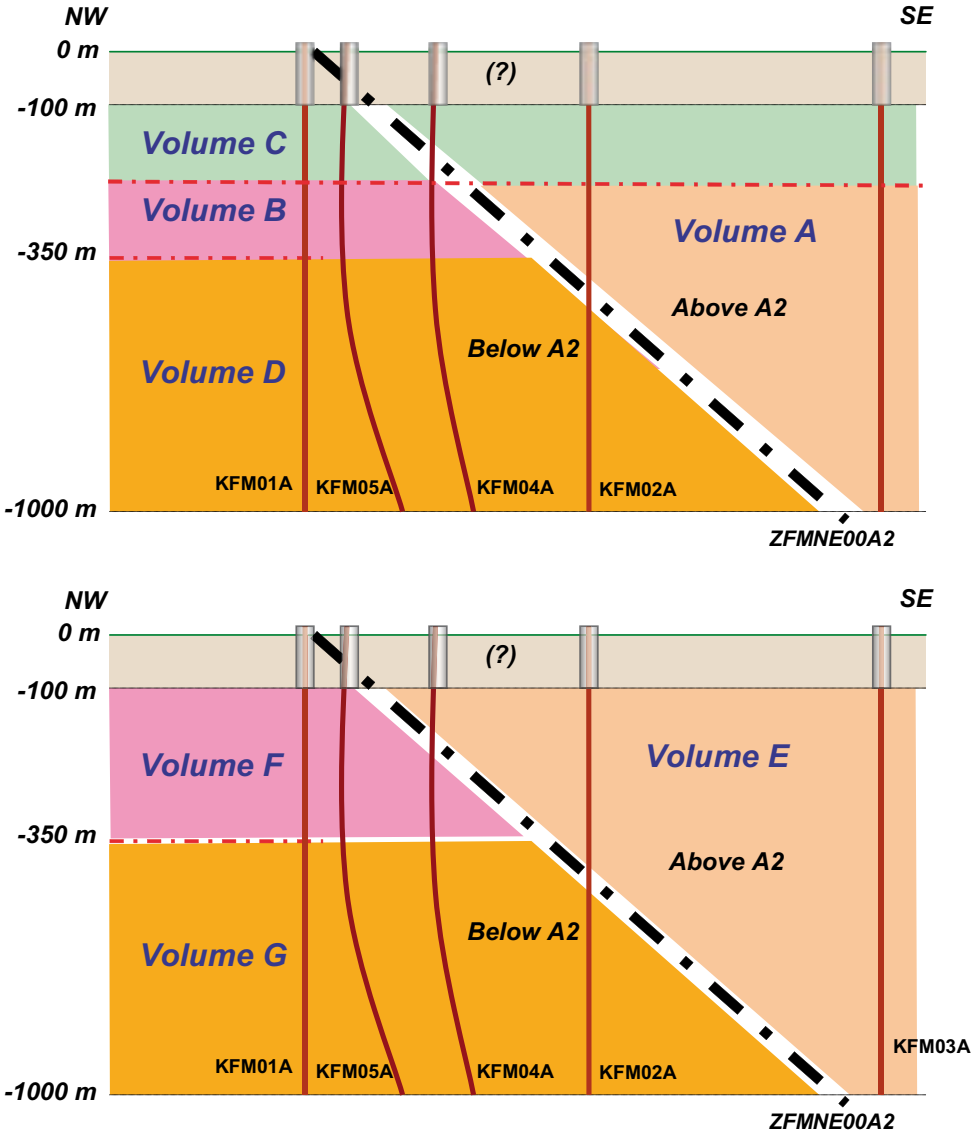

Figure 2-21. *Schematic cross-sections along the line X-XX shown in Figure 1-1 through RFM029 illustrating the division into smaller volumes. The upper conceptualisation was treated by /Follin and Stigsson 2005/ and the lower by /Hartley et al. 2005/. The difference between the two cross-sections concerns the division of Volume F into volumes B and C mainly. Thus, Volumes A and E may be considered equivalent as can Volumes D and G, respectively. Volume C is the most transmissive, whereas Volume D (G) has almost no measurable inflows according to the data available for model version 1.2.*

Hydraulic properties vary significantly between the volumes. For example, Volume E is characterised by a fracture intensity of open fractures around 0.7 m^{-1}, based on borehole KFM03A. The section of KFM02A above ZFMNE00A2 was also considered to be within Volume E. Volume F is described as the upper section of rock, below ZFMNE00A2. It is characterised by high fracture intensity (e.g. fracture intensity of open fractures 3.3 m^{-1} above 386 m in KFM01A). Flow anomalies have been observed in Volume F, e.g. the upper 386 m of KFM01A shows much flow. KFM05A has PFL flow anomalies restricted to only about the top 200 m, suggesting the base of Volume F is uncertain or variable. Volume G is described as the deeper rock that is also found below ZFMNE00A2. It is characterised by low fracture intensity with measurement of almost no flow anomalies. For example, the deeper section of KFM01A (> 412 m) shows a fracture intensity of 0.4 m^{-1}, and the deeper section of KFM02A (> 600 m) shows a fracture intensity of 0.2 m^{-1}; both of these boreholes exhibit almost no measured flow anomalies.

These volumes are applied only inside the tectonic lens. The upper 412 m of KFM04A is found outside the tectonic lens, and also exhibits high fracture intensity of open fractures around 4.6 m^{-1}. It is suggested that the background rock outside the tectonic lens should be analogous to the Volume F conceptual model. The reasons for this are two-fold: firstly, the high fracture intensity outside the tectonic lens is most similar to that found in Volume F, such as the upper part of KFM01A; and secondly, since there are limited data available outside the tectonic lens in the F 1.2 data freeze, a conservative assumption that the rock has high fracture intensity is appropriate, i.e. significant groundwater flow-rates, a hypothesis that was tested in the regional flow modelling.

The top 100 m of the model has no boremap data or hydraulic data available, and hence the properties of this layer should be considered by sensitivity analyses in the regional-scale flow modelling.

Model parameters of the Hydro-DFN Models with uncertainties

A summary of the best-fit parameters derived in the site modelling /Hartley et al. 2005/, using the Geo-DFN fracture orientations for 5 sets, for Volume E, Volume F and Volume G is given in Table 2-4, Table 2-5 and Table 2-6, respectively. Based on the geometrical description of the DFN model – known as the Geo-DFN model – developed by Geology, the percolation threshold below which there is no flow was found to be a fracture intensity of 0.36 m^2m^{-3}. Due to the lack of any PFL anomalies below 400 m in KFM01A, then a P32 equal to the percolation threshold was advocated in the site modelling. However, as we shall see in Table 2-8 there are PFL anomalies elsewhere in Volume G, and taken over all borehole sections in Volume G (KFM01A, KFM02A, KFM04A and KFM05A) gives a P10 for PFL anomalies of about 0.01 m^{-1}. Thus, an increased P32 of 0.45 m^{-1} is proposed in Table 2-6 for Volume G for use in this study since it gives a more consistent value of P10 for connected fractures in a vertical borehole, as will be shown in Section 2.3.3. Table 2-4, Table 2-5 and Table 2-6 also give the hydraulic parameters for each of the three length/transmissivity relationships suggested in Section 2.3.1.

A variant on the Geo-DFN model was also suggested with a greater number of long fractures by altering the slope of the power-law distribution (k_r = 2.75 for all fracture sets). This case requires a lower open fracture intensity for the best fit parameters as shown in Table 2-7. The statistical models used, such as Univariate Fisher and power-law, are documented in /Munier 2004/.

Table 2-4. Description of DFN parameters and Geo-DFN fracture set orientations used for simulation of fractures in Volume E. P32 and the transmissivity model parameters are given for each of the cases, denoted in italics.

Rock domain	Fracture set name	Orientation set pole: (trend, plunge), conc.	Size model, Constants: power-law (r_0, k_r) (m)	Intensity, (P32), valid length interval: r_0, r_{max} (m^2m^{-3})	Relative intensity of P32	Transmissivity model Eq.No, constants T (m^2s^{-1})
RFM029 RFM017	NS	(87, 2) 21.7	(0.28, 2.88)	*130% of open* = 0.90, (0.28, 560)	0.124	*Correlated (excl. DZs):* (*a,b*) ($1.8\cdot10^{-9}$, 1.0) ; *Uncorrelated (excl. DZs):* (*μ,σ*) (–6.5, 0.9); *Semi-correlated (excl. DZs):* (*a,b,σ*) ($5.3\cdot10^{-8}$, 0.6, 1.0)
	NE	(135, 3) 21.5	(0.28, 3.02)		0.291	
	NW	(41, 2) 23.9	(0.28, 2.81)		0.191	
	EW	(190, 1) 30.6	(0.28, 2.95)		0.100	
	HZ	(343, 80) 8.2	(0.28, 2.92)		0.294	

Table 2-5. Description of DFN parameters and Geo-DFN fracture set orientations used for simulation of fractures in Volume F. P32 and the transmissivity model parameters are given for each of the cases, denoted in italics.)

Rock domain	Fracture set name	Orientation set pole: (trend, plunge), conc.	Size model, power-law (r_0, k_r) (m)	Intensity, (P32), valid length interval: r_0, r_{max} (m^2m^{-3})	Relative intensity of P32	Transmissivity model Eq.No, constants T (m^2s^{-1})
RFM029	NS	(87, 2) 21.7	(0.28, 2.88)	26% of open = 1.2, (0.28, 560)	0.110	*Correlated:* (*a,b*) ($1.8\cdot10^{-9}$, 1.0); *Uncorrelated:* (μ, σ) (–6.5, 0.9); *Semi-correlated:* (*a,b,σ*) ($5.3\cdot10^{-8}$, 0.6, 1.0)
	NE	(135, 3) 21.5	(0.28, 3.02)		0.449	
	NW	(41, 2) 23.9	(0.28, 2.81)		0.085	
	EW	(190, 1) 30.6	(0.28, 2.95)		0.049	
	HZ	(343, 80) 8.2	(0.28, 2.92)		0.306	

Table 2-6. Description of DFN parameters and Geo-DFN fracture set orientations used for simulation of fractures in Volume G. P32 and the transmissivity model parameters are given for each of the cases, denoted in italics.

Rock domain	Fracture set name	Orientation set pole: (trend, plunge), conc.	Size model, power-law (r_0, k_r) (m)	Intensity, (P32), valid length interval: r_0, r_{max} (m^2m^{-3})	Relative intensity of P32	Transmissivity model Eq.No, constants T (m^2s^{-1})
RFM029	NS	(87, 2) 21.7	(0.28, 2.88)	100% of open = 0.45, (0.28, 560)	0.110	*Correlated:* (*a,b*) ($1.8\cdot10^{-9}$, 1.0); *Uncorrelated:* (μ, σ) (–6.5, 0.9); *Semi-correlated:* (*a,b,σ*) ($5.3\cdot10^{-8}$, 0.6, 1.0)
	NE	(135, 3) 21.5	(0.5, 3.02)		0.449	
	NW	(41, 2) 23.9	(0.5, 2.81)		0.085	
	EW	(190, 1) 30.6	(0.5, 2.95)		0.049	
	HZ	(343, 80) 8.2	(0.5, 2.92)		0.306	

Table 2-7. Description of variant Geo-DFN parameters used for simulation of fractures to fit the PFL anomalies and PSS data for Volume E (KFM03A). P32 and the transmissivity model parameters are given for each of the cases, denoted in italics.

Rock domain	Fracture set name	Orientation set pole: (trend, plunge), conc.	Size model, power-law (r_0, k_r) (m)	Intensity, (P32), valid length interval: r_0, r_{max} (m^2 m^{-3})	Relative intensity of P32	Transmissivity model Eq.No, constants T (m^2 s^{-1})
RFM029 RFM017	NS	(87, 2) 21.7	(0.28, 2.75)	70% of open = 0.53, (0.28, 560)	0.161	*Correlated, (excl. DZ):* (*a,b*) ($1.8\cdot10^{-9}$, 1.0); *Uncorrelated (excl. DZs):* (μ, σ) (–6.9, 0.9); *Semi-correlated (excl. DZs):* (*a,b, σ*) ($1.8\cdot10^{-8}$, 0.3, 1.0)
	NE	(135, 3) 21.5	(0.28, 2.75)		0.319	
	NW	(41, 2) 23.9	(0.28, 2.75)		0.164	
	EW	(190, 1) 30.6	(0.28, 2.75)		0.076	
	HZ	(343, 80) 8.2	(0.28, 2.75)		0.280	

Hence, the site-modelling concluded the key uncertainties in the Hydro-DFN model were:

- The correlation between transmissivity and length. This has been addressed here by considering three alternative transmissivity models.
- The slope of the power-law distribution, k_r, and hence the need for the variant Geo-DFN model.
- The spatial variability between boreholes making it hard to derive statistics that can be extrapolated away from the borehole.

2.3.3 Fracture connectivity and flow-wetted-surface (FWS)

The flow-wetted-surface, or a_r, is required to calculate the F-quotient along flow-paths in continuum models. There are several possible approaches to estimating a_r. One possibility might have been to obtain a value by calibrating the models of paleo-hydrogeology in terms of the RMD process to estimate a value of a_r that gave a reasonable reproduction of the measured hydro-geochemistry data. Unfortunately, this was not possible due to the sparse data and the lack of hydro-geochemistry data for the rock matrix. Two other possible approaches are either to perform a connectivity analysis of the Hydro-DFN to calculate the fracture intensity of the connected network, $P32_c$, or to use the hydraulic PFL data directly. Starting with the latter approach, Table 2-8 gives a breakdown of the boreholes into the sub-volumes illustrated in Figure 2-21, and the vertical frequency of PFL anomalies in each, $P10_{PFL}$, as well other hydraulic statistics. Two formulae are then needed to estimate a_r. Firstly, $a_r = 2 \times P32_c$, where $P32_c$ is the connected fracture intensity. The factor 2 comes from the two rock surfaces either side of the fracture at which matrix diffusion and sorption can take place. Secondly, $P32_c = \alpha \times P10_c$ relates the areal fracture intensity of connected fractures to the vertical frequency of connected fractures, $P10_c$. The factor α is a function of the geometrical parameters of the DFN model. For a single horizontal set it would be 1.0. For the Hydro-DFN, α is about 2.5, and hence $a_r \approx 5 \times P10_c$. Approximating $P10_c$ by $P10_{PFL}$ implies for Volume E (see KFM03A) values of a_r about 0.3 $m^2\ m^{-3}$ for KFM03A. For Volume F, a_r is about 0.65 to 0.8 $m^2\ m^{-3}$. Volume G is very uncertain giving values of a_r between 0.0 and 0.6 $m^2\ m^{-3}$ with an overall average about 0.05 $m^2\ m^{-3}$.

Table 2-8. Summary table of PFL anomalies. $P10_{PFL}$ is the number of flowing PFL anomalies per unit length of borehole.

Borehole	Sub-volume	Number of PFL anomalies	P10PFL (m^{-1})	Total Transmissivity ($m^2\ s^{-1}$)	Mean K (m/s)
KFM01A	Volume F (< 400 m)	34	0.13	2.0E–07	7.7E–10
	Volume G (> 400 m)	0	0.00	–	–
KFM02A	Volume E (< 414 m, above A2)	75	0.38	1.2E–04	6.2E–07
	ZFMNE00A2 (414 m to 514 m, DZ6)	49	0.48	7.8E–06	7.6E–08
	Volume G (> 514 m, below A2)	1	0.002	2.6E–09	–
KFM03A	Volume E	52	0.06	1.1E–04	1.2E–07
KFM04A	Volume F (< 169 m, above A2)	29	0.48	6.4E–05	1.1E–06
	ZFMNE00A2 (169 m to 242 m, DZ1, DZ2 and DZ3)	26	0.40	8.9E–05	1.4E–06
	Volume G (> 242 m, below A2)	16	0.02	1.5E–06	2.1E–09
KFM05A	Volume F (< 400 m)	25	0.16	1.3E–03	8.0E–06
	Volume G (> 400 m)	2	0.12	1.0E–08	5.9E–10

The other approach is to use the relationship $a_r = 2 \times P32_c$, and calculate $P32_c$ from a connectivity analysis of the Hydro-DFN model. In performing the connectivity analysis it is informative to calculate both $P32_c$ and the vertical frequency of connected fractures, $P10_c$, since this gives an estimate of the number of connected fractures intersecting a vertical deposition hole. $P32_c$ is calculated by generating a network of fractures within a given block-size, removing all isolated fractures and isolated clusters that have no connection to the boundary, removing all dead-end fractures (those with only one intersection), and then the surface area per volume of the remaining fractures is calculated. To calculate $P10_c$, fractures are generated within a given block-size, all isolated and dead-end fractures are removed, and then an array of 25 equally spaced vertical boreholes is used to sample the fracture spacing in the block. This means the total simulated core length is 25 multiplied by the block size. The average vertical fracture spacing is calculated. Since both block-size and the minimum fracture radius truncation affect connectivity, then these parameters are varied to quantify sensitivities.

Using the Hydro-DFN for Volume E (see Table 2-4), the connected $P32_c$ is calculated for a range of different blocks sizes and truncations of the fracture distribution as presented in Table 2-9. In the first row, the table gives the input P32 before removing unconnected and dead-end fractures, followed by $P32_c$. From this table it is clear that the fractures longer than 10 m generally make up a connected network, since $P32_c$ is close to the input P32. For these fractures $P32_c$ is about 0.03–0.04 $m^2\ m^{-3}$. Adding in smaller fractures down to 2 m increases the input P32 to about 0.25 $m^2\ m^{-3}$ but that only increases $P32_c$ to about 0.10 $m^2\ m^{-3}$, and adding fractures down to 0.28 m radius also adds a disproportionately small connected fracture area suggesting the small fractures are poorly connected. Since the limit for significance of the flow in fractures is a transmissivity of about 10^{-9} m^2/s, then the correlated model in Table 2-5 suggests that this corresponds to fractures of about 0.6 m radius (1 m length). Hence, using the r_{min}=1.1 m and block size=500 m entry, the $P32_c$ for water-bearing fractures is about 0.1 $m^2\ m^{-3}$, and a_r is about 0.2 $m^2\ m^{-3}$ in Volume E. This is consistent with the PFL data based approach.

The average vertical fracture spacing in a connected network for Volume E is given in Table 2-10. Using the L_{min}=2 m and block size=500 m entries, the average vertical spacing of flowing fractures is about 28 m Volume E.

It is useful to try to illustrate the fracture connectivity graphically also. Figure 2-22 shows an example of a DFN model generated in a 200 m cube using the data from Volume E. The top two pictures show all fractures in 3D and then the same network, but with isolated fractures removed. Only isolated fractures are removed here, dead-ends remain. The effect is not so clear from this 3D view since the larger fractures still appear to be there, and perhaps only some of the smaller ones have been removed. Now, look at the pictures below which show the same two cases, but using a 2D vertical slice to reveal what's going on inside. The left picture shows all fractures that are generated, and the right those that remain after removing isolated fractures and clusters. The difference is striking. There are large areas that are devoid of connected fractures, and a clear pattern is seen that perhaps half of the large fractures (coloured green to red) remain, but only the small fractures (coloured blue) that intersect or hang-off the large fractures are retained. It means the connected network shows a dendritic like pattern. That is, the connected network is made up of the larger stochastic fractures around 10–20 m, or larger, and any small

Table 2-9. Calculation of connected $P32_c$ for different block-sizes and different length truncations r_{min} in Volume E. Blank cells are too large to compute easily.

	Block size (m)	r_{min} 5.6 m	1.1 m	0.28 m
input P32 ($m^2\ m^{-3}$)	–	0.0569	0.2506	0.9030
$P32_c$ ($m^2\ m^{-3}$)	100	0.0381	0.1083	0.3085
$P32_c$ ($m^2\ m^{-3}$)	200	0.0380	0.1096	–
$P32_c$ ($m^2\ m^{-3}$)	500	0.0338	0.1030	–
$P32_c$ ($m^2\ m^{-3}$)	1,000	0.0288	–	–

Table 2-10. Average vertical fracture spacing in a connected network for different block-sizes and different length truncations r_{min} in Volume E. Blank cells are too large to compute easily.

Block size (m)	Vertical fracture spacing ($P10_c^{-1}$) r_{min} = 5.6 m Mean	r_{min} = 1.1 m Mean	r_{min} = 0.28 m Mean
100	61 m	21 m	9 m
200	66 m	22 m	–
500	76 m	28 m	–
1,000	110 m	–	–

fracture that happen to connect to these. The small fractures do not form a connected network in themselves or provide extra connections in between the large fractures. The pattern of connected fracturing shown here also illustrates that intact 'matrix' blocks between the interconnected networks are very heterogeneous in size and shape. This has important consequences since it means boreholes will show large variability in sections of broken and unbroken core as well as flow and since matrix block size has a very strong influence on the effectiveness of the

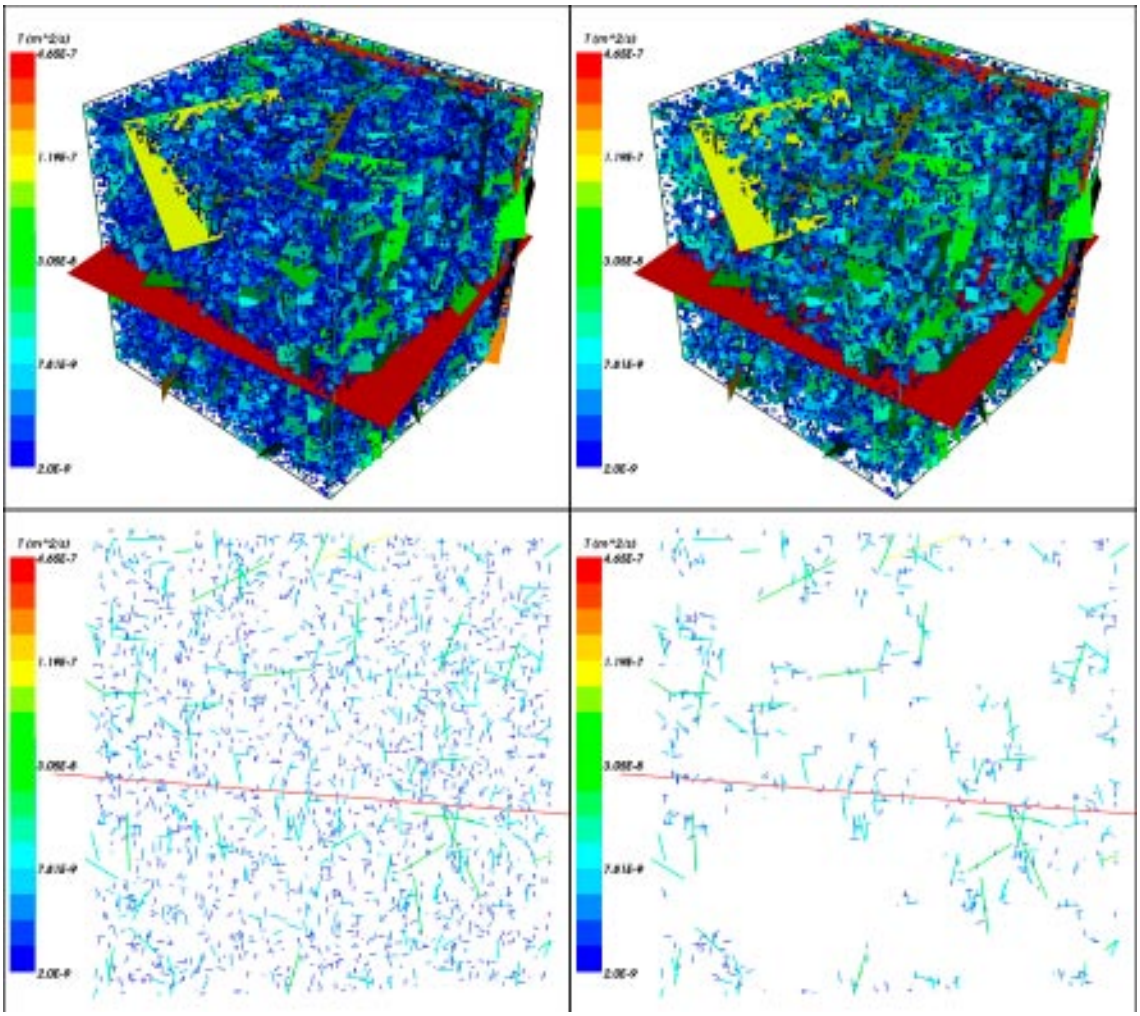

Figure 2-22. *An example of fracture connectivity in a 200 m cube using the fracture network defined for Volume E (see Table 2-4). Top left: Oblique view of fractures within 3D volume; Top right: after removal of isolated fractures; Bottom left: a 2D vertical slice through the network showing all fractures; Bottom right: 2D vertical slice after removing isolated fractures.*

RMD process, then the degree of equilibrium between fracture and matrix hydro-geochemistry will consequently be highly variable. This suggests we have to be cautious to not to assume the interpretation of a few boreholes can be extrapolated over the whole candidate area, and sensitivities have to be considered.

Of more relevance to the repository location are the values of $P32_c$ and $P10_c$ in Volume G as given in Table 2-11 and Table 2-12. Here, the input P32 is half that in Volume E, which results in much poorer connectivity. In Table 2-11 it is seen that $P32_c$ generally reduces with block-size and the addition of smaller scale fractures makes a limited impact on $P32_c$. Using the entry for a 500 m block-size and r_{min} of 1.1 m gives a $P32_c$ of about 0.015 m^2m^{-3}, or a_r of 0.03 m^2m^{-3} for Volume G, which again is consistent with the PFL based approach. The average vertical fracture spacing in a connected network for Volume G is given in Table 2-10. Using the r_{min}=1.1 m and block size=500 m entries, the average vertical spacing of flowing fractures is about 174 m Volume G. However, it can be seen here the block-size has a large impact on the spacing of connected fractures, so one has to be a bit careful. Although the repository is at 410 m depth and therefore one might expect an appropriate block-size for connectivity to be around 500 m, the system of repository tunnels will form a potential source of water and provide extra connectivity. Hence, a cautious estimate for the vertical frequency of water bearing fracture in the presence of the repository might be around 40 m.

2.3.4 Hydraulic conductor domain (HCD) models with uncertainties

Three alternative DZ geometries were supplied by the Geology Group and considered in the site modelling as follows:

1. **Base Case (BC):** containing only high confidence DZs. This contains many sub-horizontal DZs between the Singö DZ and Eckarfjärden DZ that have been identified by drilling and/or reflection seismic techniques. Also, it is assumed that DZs identified in the site area extend no further than the Singö DZ and Eckarfjärden DZ. Only the high confidence lineaments outside of this area are included, see Figure 2-24.
2. **Variant Case (VC):** is similar to the BC model except a few large sub-horizontal zones are extended beyond the Eckarfjärden DZ.
3. **Alternative Case (AC):** contains the DZs included in the BC model with the addition of many regional-scale lineaments, based on lineament and comparison studies, that are potential hydraulic conductors but of lower confidence, see Figure 2-25.

The BC model contains 44 distinct geological DZs, of which 23 are steeply dipping and 21 are gently dipping. The alternative model has an additional 171 DZs, which includes 36 steeply dipping zones DZs between the Singö DZ and Eckarfjärden DZ and 135 steeply dipping DZs outside. The lineaments are all assumed to be vertical. The VC and AC cases, in particular, give an indication of how much effect additional DZs outside of the Singö DZ and Eckarfjärden DZ can have on flow and transport in the local-scale area.

Table 2-11. Calculation of connected $P32_c$ for different block-sizes and different length truncations r_{min} in Volume G. Blank cells are too large to compute easily.

	Block size (m)	r_{min} 5.6 m	1.1 m	0.28 m
input P32 (m^2 m^{-3})	–	0.0284	0.1253	0.4515
$P32_c$ (m^2 m^{-3})	100	0.0159	0.0407	0.0676
$P32_c$ (m^2 m^{-3})	200	0.0172	0.0263	–
$P32_c$ (m^2 m^{-3})	500	0.0121	0.0146	–
$P32_c$ (m^2 m^{-3})	1,000	0.0075	–	–

Table 2-12. Average vertical fracture spacing in a connected network for different block-sizes and different length truncations r_{min} in Volume G. Blank cells are too large to compute easily.

Block size (m)	Vertical fracture spacing ($P10_c$) r_{min} = 5.6 m Mean	r_{min} = 1.1 m Mean	r_{min} = 0.28 m Mean
100	227 m	46 m	40 m
200	192 m	81 m	–
500	291 m	174 m	–
1.000	472 m	–	–

Hydraulic properties were based on an analysis of the measured transmissivity of DZs that gave a dependence on depth /SKB 2005b/. In this, DZs were categorised according to dip to give a correlation between transmissivity of sub-horizontal DZs:

$T_H = \max(4.1 \cdot 10^{-4} \exp(-0.0116 \times \text{depth}), 1 \cdot 10^{-8})$ $m^2 s^{-1}$;

where depth is in metres, and in sub-vertical DZs:

$T_V = \max(4.6 \cdot 10^{-5} \exp(-0.0174 \times \text{depth}), 1 \cdot 10^{-8})$ $m^2 s^{-1}$.

The basic depth trends above were used in the modelling such that gently dipping DZs between the Singö DZ and Eckarfjärden DZ transmissivities were set according to the depth trend for T_H; for steeply dipping DZs transmissivities were set according to the depth trend for T_H. Figure 2-24 to Figure 2-25 show examples of this property assignment. This case was denoted property assignment **HCD1**. However, these general trends are not conditioned to transmissivity of particular borehole test intervals that intersect a DZ, and therefore a localised conditioning of the DZs properties was performed as part of the site modelling to honour the actual test interval data in the boreholes. This locally conditioned deterministic case was denoted **HCD3**.

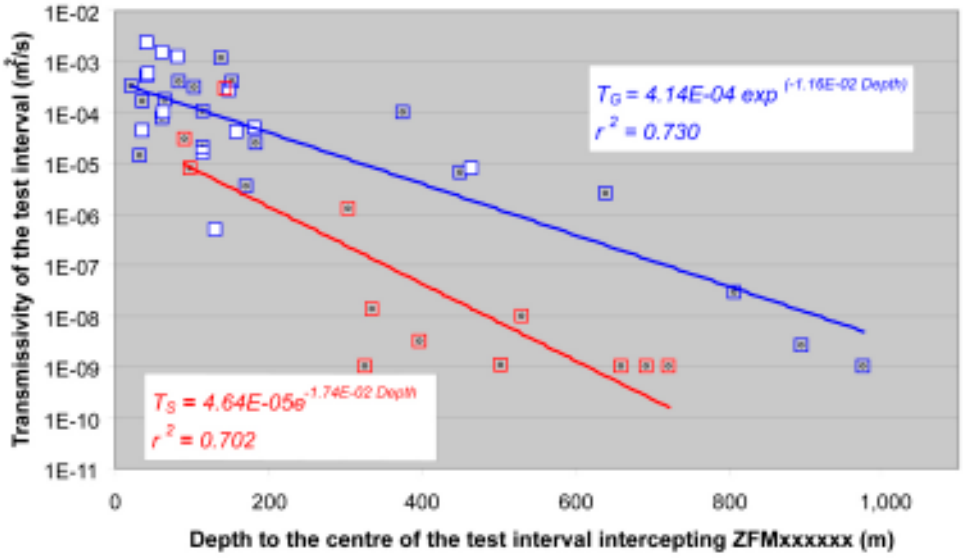

Figure 2-23. *Analysis of depth trends in hydraulic data by /Follin et al. 2005/. Red squares indicate steeply dipping HCDs and blue gently dipping. Blue squares with a white infilling refer to the hydraulic test interpretations associated to the gently dipping deformation zone ZFMNE00A2.*

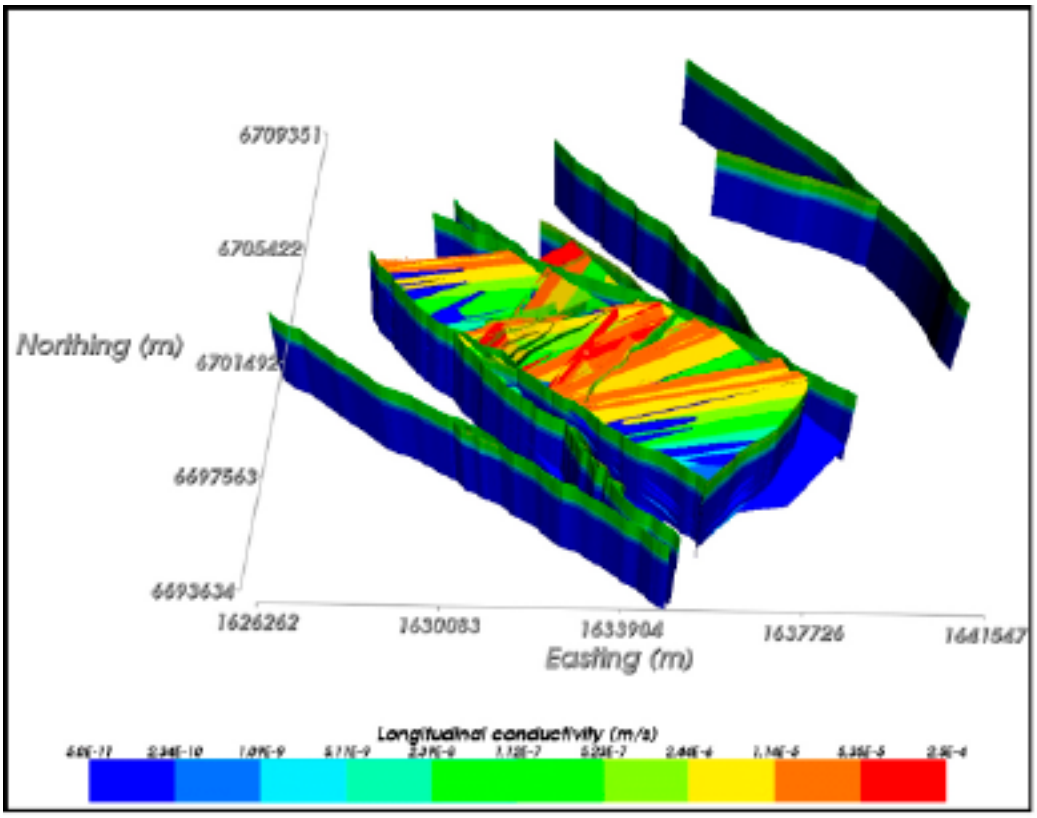

Figure 2-24. *Base Case (BC) HCD model that only includes high confidence zones. DZs are coloured by hydraulic conductivity, which shows the depth dependency of properties.*

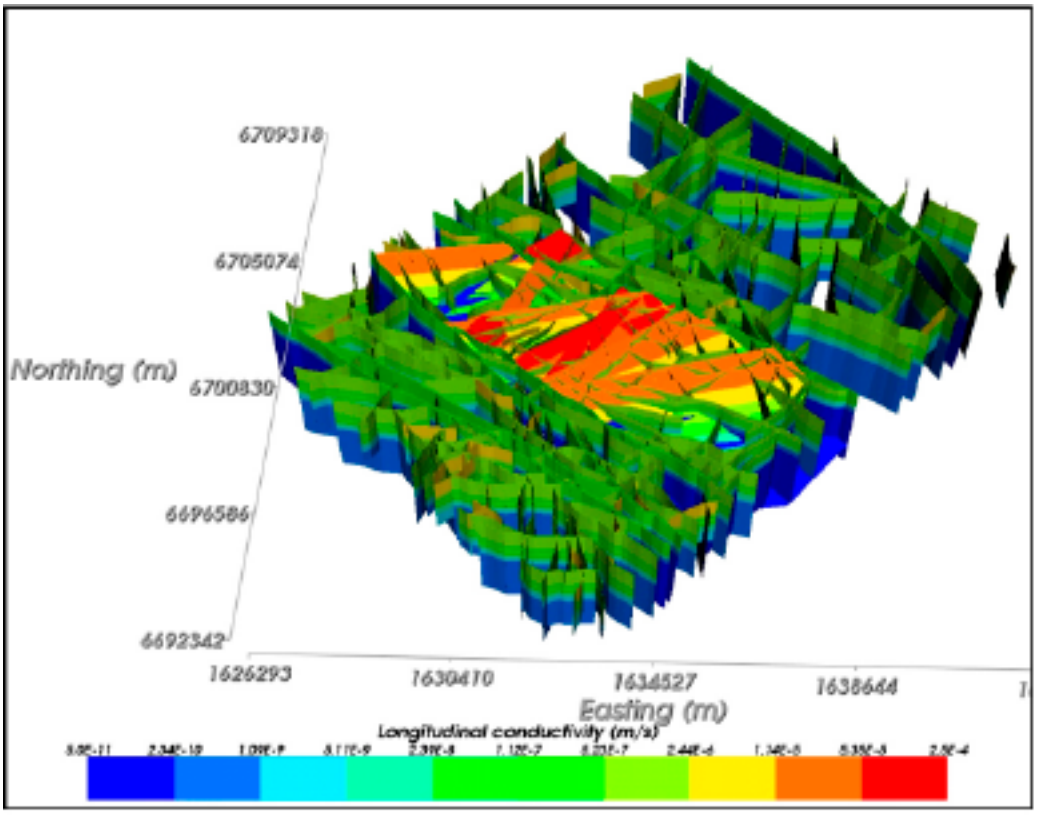

Figure 2-25. *Alternative Case (AC) HCD model, which includes many additional regional-scale lineaments that are of lower confidence. DZs are coloured by hydraulic conductivity, which shows the depth dependency of properties.*

3 Regional-scale modelling of the temperate climatic period (2,020–9,000 years AD)

The continuum modelling for SDM F 1.2 developed a coupled model of groundwater flow and reference water transport with RMD from 8,000 BP to the present-day to study conditions and parameters consistent with measured borehole profiles of hydraulic conductivity and hydro-geochemistry. This supported some conditioning of the model, but still significant uncertainty remains due to a sparsity of borehole data.

As mentioned in Section 2.2 above, one requirement for the safety assessment calculations is to extend the regional-scale ECPM and CPM models developed for SDM F 1.2 to consider the future evolution of flow-paths and groundwater chemistry over the next 7,000 AD (to 9,000 AD). Additional objectives are to use the model to consider a wider range of sensitivities appropriate to safety assessment than was possible in SDM F 1.2, such as to evaluate the effect of grid-resolution on PA measures in more detail, give a preliminary evaluation of the effect of the repository structures and properties on flow, and provide a model that can be extended for assessing the impact of heat generated in the repository. Some of these issues will later be re-quantified and cross-verified against nested models using a DFN concept on the local- and repository-scales in Section 4. However, current capabilities within CONNECTFLOW means that a greater diversity of processes such as transport of reference waters and coupling to heat can be modelled using CPM/ECPM models than in DFN models.

Both alternative conceptual continuum models, ECPM and CPM, will be considered throughout the modelling to quantify conceptual uncertainties. Each model will contain implicit representations of deterministic large-scale fracture zones and repository structures, but the ECPM model obtains its site-scale hydrogeological properties based on and consistent with an underlying DFN.

In SDM F 1.2 it was found that many of the variants considered had a relatively small effect on PA performance measures and exit locations. However, some cases were highlighted as ones that should be retained in SR-Can either because they suggested sensitivity in the results or that they were of sufficient interest that they needed to be demonstrated in the safety assessment. The parameters that proved to have a clear effect on results were the transmissivity/length distribution and the flow-wetted-surface (FWS). Among the other cases of interest are the variant Geo-DFN (using a different fracture radius distribution) and the Alternative Case (AC) geological model.

3.1 Model set-up and specification

3.1.1 Model domain and properties

Following a calibration against hydro-geochemical data the SDM F 1.2 derived a base case with the parameter settings and proposed range of possible values as given in Table 3-1. For the site modelling a distinction is made between the following three hydrogeological units due to different modelling concepts, field investigations, and interpretation techniques are applied to each:

HCD Hydraulic conductor domains – deterministically represented fracture zones of generally relatively high conductivity.

HRD Hydraulic rock domains – the bedrock between the fracture zones.

HSD Hydraulic surface domains – the surface hydrological units.

Table 3-1. Summary of hydraulic parameters and conditions used in SDM F 1.2 base case model with an indication of the possible range of alternative parameters that have either been consider in the site modelling or here in sensitivity studies.

Parameter	Calibration value	Range
Model domain	Regional model – about 15 km (SW-NE) × 11 km (NW-SE) is the minimum	Shown to be sufficient in SDM modelling
Grid resolution	50 m necessary in site-scale	100 m sufficient on regional-scale
Initial condition	Full Glacial 0–500 m; then linear gradient to no Glacial, full Brine at –2,000 m; full Brine below –2,000 m	Full Brine could be even deeper: a linear profile suggests –2,700 m
Top surface flow BC	Topography	A specified infiltration gave similar results IN SDM F 1.2
Top surface waters	Ancylus Ice Lake (Glacial), Littorina Sea (Marine), Baltic Sea/Precipitation with land-rise (Marine diluting with Rain 1960)	Onshore – Ice Lakes could be a mixture of Brine and Rain 1960 Offshore, Littorina could occur at slightly different time or strength
ECPM model Hydraulic conductivity based on Hydro-DFN	Calibrated on short interval PSS and PFL data This had block-scale properties of $K_{50\%}$~$4 \cdot 10^{-10}$ m s^{-1}, $K_{10\%}=1 \cdot 10^{-11}$ m s^{-1}	All conditioned Hydro-DFN models calibrated, but the model is sensitive to changing K by a factor
CPM model Hydraulic conductivity	Based on PFL, mainly KFM01A K=$1 \cdot 10^{-11}$ m s^{-1} in Volume D	Higher values in Volumes A, B and C
Depth dependence	None	A factor 2–10 higher in top 100–200 m and/or factor 2–10 lower below may improve calibration
Kinematic HRD porosity n_{etb}	Based on DFN value, $e_t=0.5T^{0.5}$	Fairly insensitive Can increase by factor 10
Matrix porosity n_m	$4 \cdot 10^{-3}$	$2.5–6 \cdot 10^{-3}$
Geological model	BC	AC case and VC equally likely based on calibration possible here
HCD hydraulic properties	HCD3 = depth dependency but with local conditioning to PSS 100 m data	Consider different depth trend (less conservative) for gently dipping
Kinematic HCD porosity n_{et}	$e_t=5T^{0.5}$	a=1–5 in $t=aT^{b,}$ or could make b higher to be continuous with HRD
FWS, a_r, for RMD	1.0 m^{2}m^{-3}	0.25–1.0 m^{2}m^{-3}
RMD length L_D	1.0 m	1–4 m
Intrinsic diffusion coefficient in matrix D_e	$5 \cdot 10^{-13}$ m^{2}s^{-1}	$1–5 \cdot 10^{-13}$ m^{2}s^{-1}

Hydraulic properties in the ECPM model

In the main, properties along with initial and boundary conditions were taken directly from the base case ECPM from SDM F 1.2 as detailed in Table 3-2. A few enhancements were based on the finalisation of the SDM F 1.2 summary report or due to issue specific to SR-Can. The most significant change was to use the AC geological model as the central case in the simulations reported here. The site modelling suggested flow-paths were not sensitive to the choice of structural model. This can be understood since the structural models are very similar in the local area around the site differing more in the area offshore (seen in Figure 2-24 and Figure 2-25), but for the current shoreline position the deformation zones downstream do not affect flow and particle tracks for the present-day groundwater flow are governed mainly by the site DZs. At future times, when the shoreline retreats, then the lineaments to the north in the AC model tend to cause a shortening of pathlines compared to the BC model as will be demonstrated in Section 3.3. Therefore, to be conservative the AC model is used as the reference case here, and sensitivity studies are made about it. The other main change was to reduce the flow-wetted-surface to 0.25 m^2/m^3 in the tectonic lens based on a connectivity analysis of the Hydro-DFN model (see Section 2.3.3) and some indications, post F 1.2, from hydro-geochemistry data that the fracture and matrix systems are not in equilibrium. Other differences were that for consistency with other transport calculations in SR-Can, the free-water diffusivity was decreased from $5 \cdot 10^{-13}$ to 10^{-13} m^2/s based on an updated specification of the transport parameters to be used generally in SR-Can, and the regional-DFN was modified to include fractures down to L_{min}=12.5 m in the local-scale area so that L_{min} was set to a quarter of the element-size throughout the model rather a constant 25 m. The parameter settings are summarised in Table 3-2. A higher FWS is used in the bedrock outside the tectonic lens since the fracture intensity outside RFM029/017 is higher. For deformation zones, a constant FWS of 0.25 m^2/m^3 was used irrespective of whether the DZ was inside or outside the tectonic lens.

The distribution of hydraulic conductivity was shown in 3D in Figure 2-5. In Figure 3-1 the hydraulic conductivity is shown on several horizontal slices which demonstrate the reduction in transmissivity of DZs with depth. It is noticeable that below –700 m, the DZs do not have a significant effect on hydraulic properties. In consequence, groundwater flow reduces in magnitude below –700 m. These figures also show the marked difference in hydraulic conductivity inside and outside the tectonic lens. Outside the tectonic lens homogeneous properties are used, and the only spatial variability arises from the HCDs.

The kinematic porosity and FWS are shown on a slice at repository depth in Figure 3-2. An important point to note is that a constant value of FWS, as in Table 3-1, is used in the calculations of RMD in the coupled groundwater flow and salt transport equations, whereas for particle-tracking calculations FWS is based on an upscaled regional-scale DFN as is shown in Figure 3-2. The regional-scale DFN assumes a L_{min} of 12.5 m in the local-scale model, which referring to Table 2-9 suggests a FWS for connected fractures of around 0.1 m^2/m^3 as is borne out in Figure 3-2.

Table 3-2. Summary of parameters used in the ECPM model reference case.

Domain	Hydraulic conductivity [m/s]	Kinematic porosity	Matrix porosity	FWS [m^2/m^3] (for RMD)
RFM029/017 (Volumes E–F)	Based on upscaled DFN	Based on upscaled DFN	$3.7 \cdot 10^{-3}$	0.25
Outside RFM029/017	10^{-8} for z>–100 m $5 \cdot 10^{-9}$ for z<–100 m	10^{-4} for z>–20 m 10^{-5} for z<–20 m	$3.7 \cdot 10^{-3}$	1.0
HCD	AC geological model with HCD3 properties from SFM F 1.2	As for HCD3 properties from SFM F 1.2	$3.7 \cdot 10^{-3}$	0.25

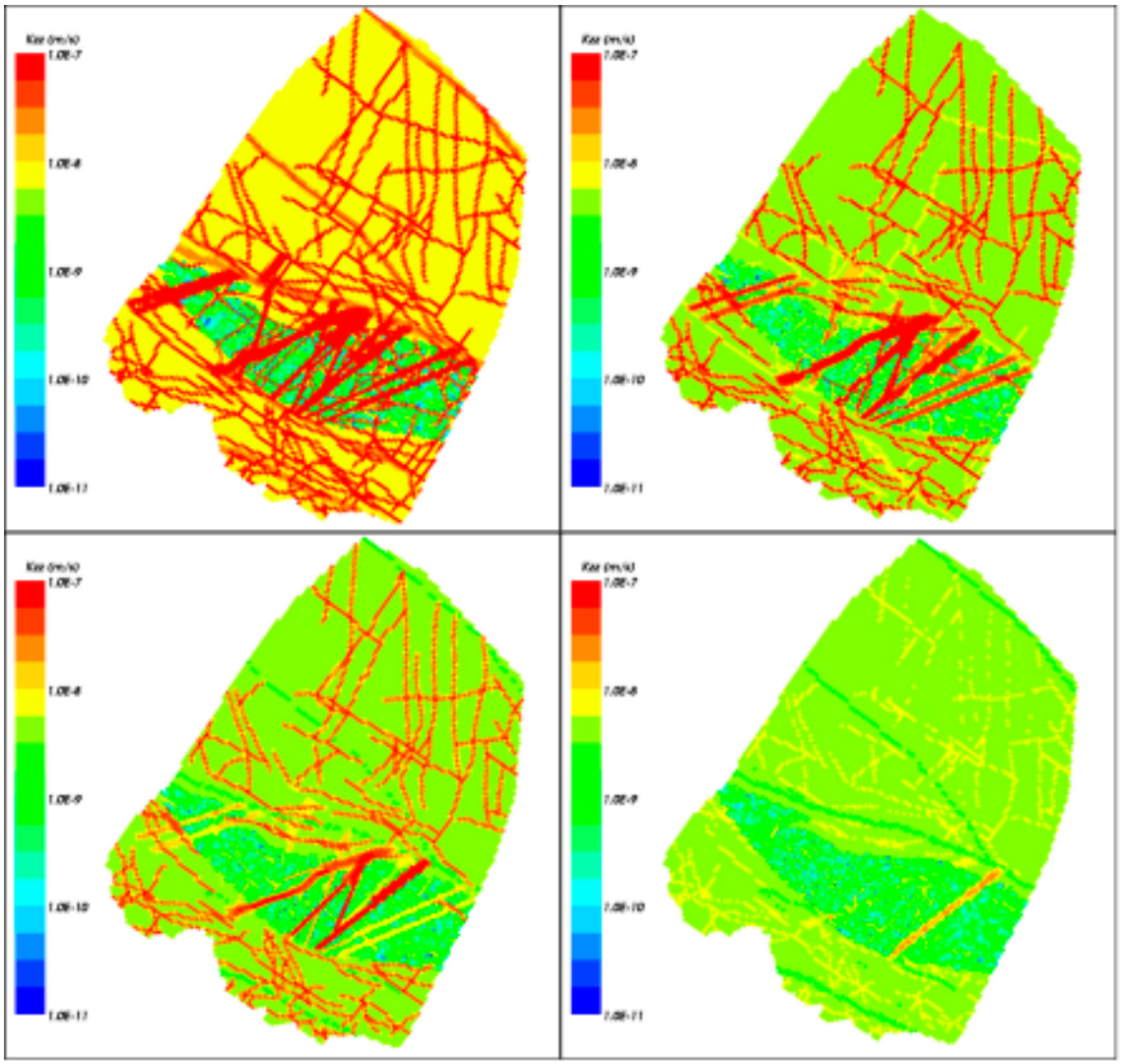

Figure 3-1. *Distribution of vertical hydraulic conductivity on horizontal slices through the ECPM model for the case using the AC geological model. Top left: at z=–80 m. Top right: at z=–250 m. Bottom left: –400 m. Bottom right: z=–700 m.*

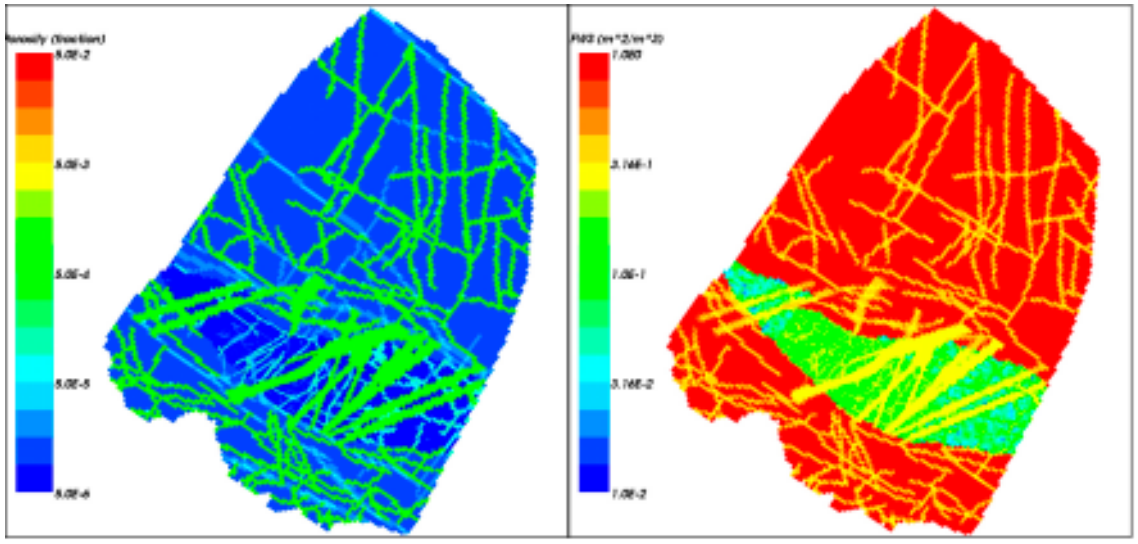

Figure 3-2. *Distribution of kinematic porosity (left) and FWS (right) on a horizontal slice at z=–400 m through the ECPM model for the case using the AC geological model.*

Although the site-modelling prescribed distinct domains as described in Section 2.3.2 initial difficulties were encountered there in implementing what is a relatively complex DFN model. Instead a simpler uniform DFN was used there to derive the hydraulic conductivity for a regional-scale ECPM model since the Hydro-DFN defined for Volume E was used throughout the tectonic lens with the correlated transmissivity model as the central case. Here, we created a regional-scale ECPM model consistent with the site modelling and called it the 'reference case' as a direct continuation of the SDM F 1.2 modelling subject to the modifications listed above, but created a number of more realistic DFN cases that better reflect the current interpretation of the site. The reference case is probably a pessimistic one since the repository area is inside Volume G which is thought to have lower fracture intensity based on boreholes KFM01A and KFM05A than in Volume E based on KFM03A. However, it is felt important to retain the reference case partly for comparison to the site modelling, but also to address the uncertainty in extrapolation of fracture properties over the large volume of the repository given while there are relatively few boreholes in the repository area as of F 1.2. This case essentially takes the pessimistic view that the fracture properties seen in KFM03A are also prevalent in the repository area. More realistic cases were also constructed based on heterogeneous DFN models that have different fracture properties in Volume G, defined as the area in RFM029/017 below z=–350 m and zone ZFMNE00A2, as discussed in Section 3.3. It is entirely clear from the site investigations whether the observed scarcity of flow in Volume G is due to a relatively lower fracture intensity or fracture transmissivity. Reality may be a combination of the two. Hence, two alternative heterogeneous DFNs were considered: one using the Volume G Hydro-DFN defined in Table 2-6 (i.e. about half the fracture intensity); and one using the same fracture intensity as Volume E but with one tenth the fracture transmissivity. Both of these models lead to hydraulic properties consistent with the measured hydraulic data. Of the two, the case with the same fracture intensity, but lower fracture transmissivity will probably give a slightly worse scenario because it will predict flows around a larger number of canisters, although they'll generally be very small.

Hydraulic properties in the CPM model

The CPM model was constructed based on preliminary findings of the DarcyTools Team /Follin and Stigsson 2005/ due to programme timing. A multi-component homogeneous CPM was used based on the sub-domains defined in Figure 2-21, and the properties given in Table 3-3.

The value of FWS used is higher than that used by /Follin and Stigsson 2005/, but was chosen to be the same as for the ECPM model for consistency. The distribution of properties in the CPM is shown in 3D in Figure 2-1. They are also shown in Figure 3-3 on a series of horizontal slice. Porosity and FWS are shown at repository depth in Figure 3-4. Again, FWS is lower in the DZs outside the tectonic lens than in the surrounding rock. This was difficult to avoid without laborious efforts to define a higher FWS for zones outside the tectonic lens than those inside.

Table 3-3. Summary of parameters used in the CPM model base case.

Domain	Hydraulic conductivity [m/s]	Kinematic porosity	Matrix porosity	FWS [m²/m³] (for RMD)
RFM029/017 Volumes A,B and C	$5 \cdot 10^{-10}$	10^{-4} for z>–20 m 10^{-5} for z<–20 m	$3.7 \cdot 10^{-3}$	0.25
RFM029/017 Volume D	10^{-11}	$5 \cdot 10^{-6}$	$3.7 \cdot 10^{-3}$	0.25
Outside RFM029/017	10^{-8} for z>–100 m $5 \cdot 10^{-9}$ for z<–100 m	10^{-4} for z>–20 m 10^{-5} for z<–20 m	$3.7 \cdot 10^{-3}$	1.0
HCD	AC geological model with HCD3 properties from SFM F 1.2	As for HCD3 properties from SFM F 1.2	$3.7 \cdot 10^{-3}$	0.25

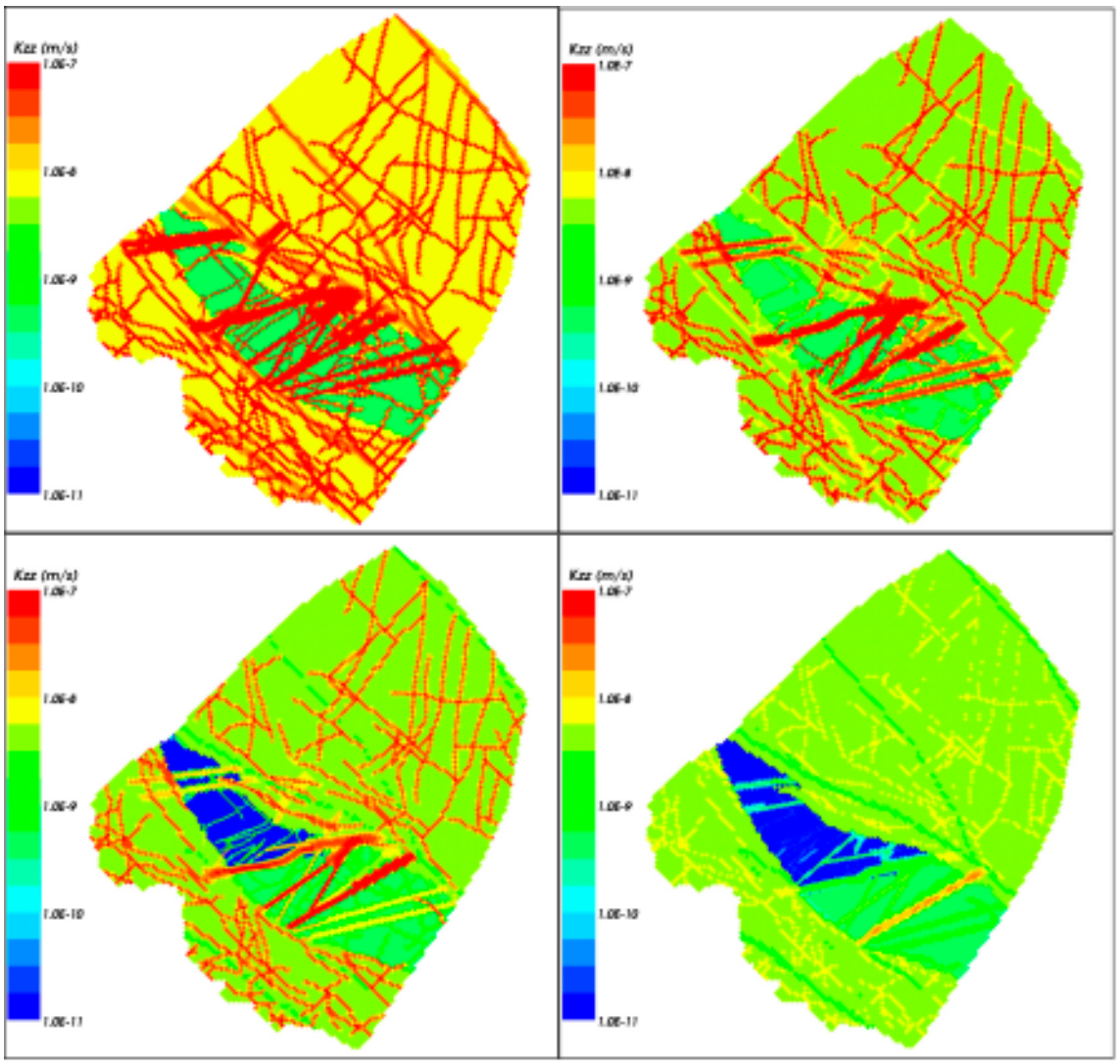

Figure 3-3. *Distribution of vertical hydraulic conductivity on horizontal slices through the CPM model for the case using the AC geological model. Top left: at z=–80 m. Top right: at z=–250 m. Bottom left: –400 m. Bottom right: z=–700 m.*

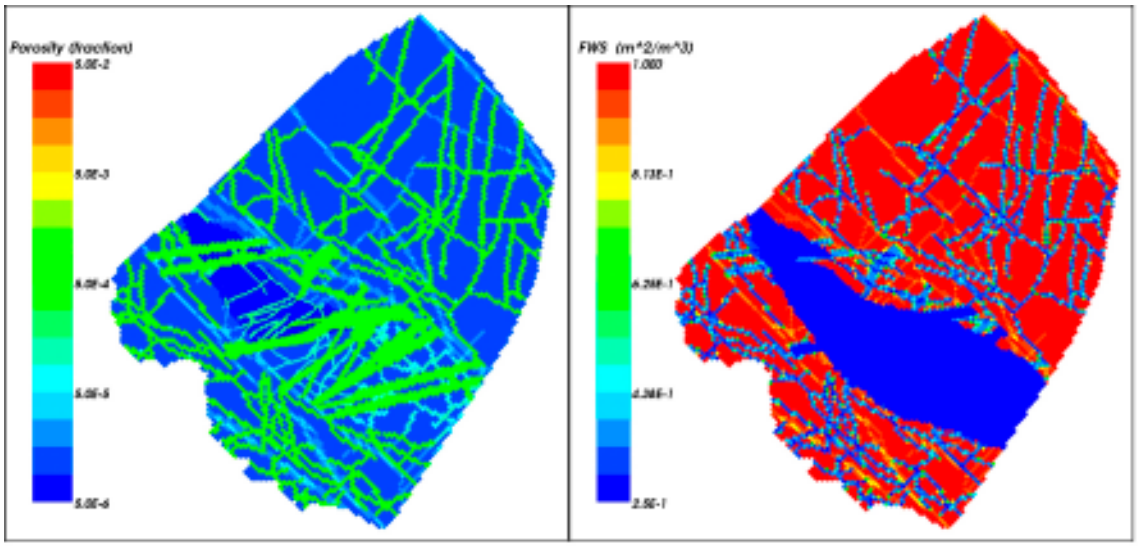

Figure 3-4. *Distribution of kinematic porosity (left) and FWS (right) on a horizontal slice at z=–400 m through the CPM model for the case using the AC geological model.*

3.1.2 Model grid

The regional-scale model grid used in the SR-Can study is nearly identical to the model used in SDM F 1.2, i.e. a 100 m element-size regional model of about 15 km (SW-NE) × 11 km (NW-SE) with a 50 m element-size embedded grid covering the key areas including the potential repository area and the five cored boreholes KFM01A-KFM05A. Some small changes were made to capture the whole of the tectonic lens inside the local-scale refined area. For practical reasons of model size, greater resolution over the whole model domain would be prohibitive for transient multi-component reference water transport problems. However, the capability of using embedded grids in CONNECTFLOW makes it possible to attain greater resolution of properties and numerical accuracy within key areas of the model. Higher vertical resolution was found to be required for the models that included thermal effects in Section 6.

For all the regional-scale models described in this section, the same 50 m embedded grid was used. The improved refinement gives a better representation of both the DZs and the heterogeneity of the HRD between them in the key areas of the Forsmark local-scale area. At the interface between the two levels of refinement, internal boundary conditions are imposed to ensure continuity of variables (pressure and reference water fractions) and conservation mass and reference water flux.

3.1.3 Modelling strategy

By considering both the ECPM and CPM sensitivities to the choice of conceptual model can be quantified. Further sensitivities are considered using the ECPM model as the base case, since it provides a means of quantifying sensitivities to the Hydro-DFN parameters that motivate it. In this way, the regional-scale ECPM is used to rank a range of variants that represent uncertainties in parameters related to the DFN and other hydraulic and transport parameters. Ranking sensitivities helps identify which variants need to be considered in the more detailed nested models, and potentially need to be considered in PA calculations.

3.2 Flow simulations using the ECPM reference case (SC_HCD3_AC_HRD3EC)

A detailed summary of the results for the ECPM reference case are given of as an example of the general behaviour of the groundwater flow hydro-geochemistry within the temperate period.

3.2.1 Description of past evolution

The simulations are started from 8,000 BC and run until 9,000 AD using 20 year time-steps. The period up to 2,000 AD, corresponding to present-day conditions, is here called the ‘past evolution’. In the SDM F 1.2 study, considerable effort was put into calibrating the model against measured data in terms of salinity, reference water mixing fractions, major ions, environmental isotopes and hydraulic conductivity. Since the SR-Can study uses slightly modified models compared to SDM F 1.2 it is necessary to check that the models still calibrate to the same degree as before. It should be noted that model calibration is intentionally qualitative at this stage in the site characterisation since the amounts and quality of the hydro-geochemical does not justify a more quantitaive calibration yet. This section presents the past evolution and calibration results for the ECPM reference case.

Reference waters

The current conceptual understanding of the transient evolution of the surface and groundwaters at Forsmark is illustrated in Figure 3-5. The simulations start during Phase b when the area is covered by the Ancylus Lake, which is a mixture of glacial melt water and meteoric water. This is followed by the Littorina Sea Phase c, whose salinity gradually decreases, and eventually the land emerges from the sea and so becomes exposed to infiltration of modern meteoric water. As discussed in Section 2.2.3, the hydro-geochemical composition of the groundwater is model by conservative transport and mixing of four reference waters (Rain 1960, Marine, Glacial, and Brine).

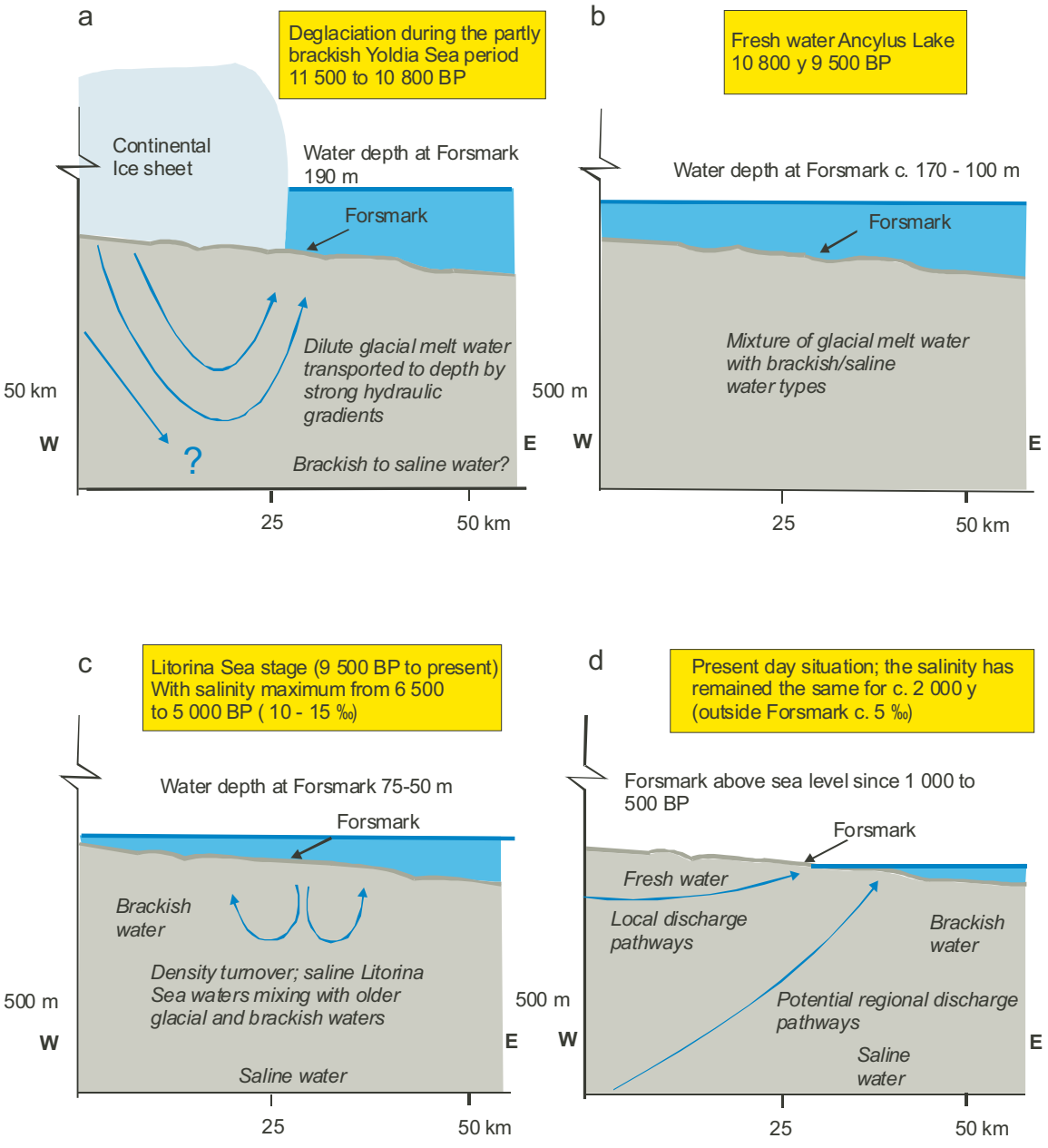

Figure 3-5. *Conceptual postglacial hydro-geochemical scenario model for the Forsmark area. The figures show possible flow lines, density driven turnover events and non-saline, brackish and saline water interfaces. Possible relation to different known postglacial stages such as land uplift which may have affected the hydrochemical evolution of the site is shown: a) deglaciation of the continental ice, b) Ancylus Lake stage, c) Littorina Sea stage, and d) present day Baltic Sea stage. From this conceptual model it is expected that glacial meltwater and deep and marine water of various salinities have affected the present groundwater.*

Figure 3-6 to Figure 3-9 show the calibration of the ECPM reference case against the four interpreted reference water profiles for the cored boreholes KFM01A to KFM05A. The mixing fractions in both the fracture system and matrix are shown. Compared to the SDM F 1.2 study /Hartley et al. 2005/, where there was little difference between the fracture and matrix fractions, there are now large differences between the two fractions. The reason for this is that the reduction in FWS, results in a decreased communication between the fracture and matrix. The calibration is discussed below for each of the cored boreholes separately. Interestingly, in parts of KFM02A and KFM03A the data for Marine water compares better with matrix concentrations than the fracture system. This perhaps confirms a dual-porosity system, though what here is strictly the matrix pore volume may in fact be a network of relatively short fractures and micro-fractures. It perhaps motivates more detailed work with the dual-porosity models in the site-modelling once there is an improved set of hydro-geochemistry data to match to.

KFM01A. Figure 3-6 shows that the calibration in the top 100–200 m is still fairly good compared to SDM F 1.2 even if data suggests slightly less Rain 1960 in the top. There is a sharp transition from Rain 1960 to Marine at about 200 m depth which is confirmed by data. There are small fractions of Rain 1960 present at great depths indicating the presence of fracture zones leading water deep into the rock. The Glacial fraction is only seen at depth and has been replaced mainly by Marine water. Brine is found from depths of about 500 m. There are however no data available below 200 m to confirm model results.

KFM02A. Figure 3-7 shows the model predicts deep penetration of Marine water and substantial flushing of Glacial. Glacial water is predicted at somewhat lower fractions than the data suggests down to 500 m depth. Data also indicates a more gradual transition and faster transport of Rain 1960 and Marine down to 500 m depth, while the models predict a sharp transition around 250 m depth. Again there are no data to confirm the deep profiles of Brine and Glacial waters.

KFM03A. This borehole provides the greatest abundance of data with samples at depths down to 1,000 m. Figure 3-8 shows that data suggests 50% Marine water close to the surface which could not be reproduced by the SDM F 1.2 model. In this model however, FWS has been reduced by a factor 4 and the effect is that although the Marine fraction in the fracture system is still low, the matrix now shows a considerably higher fraction of Marine water close to the surface. The model tends to over-predict the Marine water fraction and under-predict the Rain 1960 at depths below 400 m. The Glacial water profile is predicted reasonably by the ECPM model. It is hard to say anything about the Brine content at depth since data are close to the M3 resolution uncertainty. Even if there are significant uncertainties in the data regarding the M3 analysis, it still suggests that the models could potentially be better calibrated by “fine-tuning” the RMD parameters.

KFM04A. Figure 3-9 shows again that the models reasonably predict the data at 250–300 m depth but cannot reproduce the surface water composition with high fractions of Marine water. There are no data provided below 300 m depth to confirm modelled results.

As was concluded in SDM F 1.2, although the M3 analysis of the reference water fractions provides a very accessible interpretation of the transport and mixing of waters of different origin, it does have to be used with some caution since it is associated with uncertainties of about 10% in each reference waters. Unfortunately, this makes it difficult to use these results for calibration of the model. Instead more focus should be put on the major ions and environmental isotopes. It should be noted that data points shown in the top 100 m are from tube samples, and hence is of a less controlled quality than other data points, and should therefore be viewed with caution.

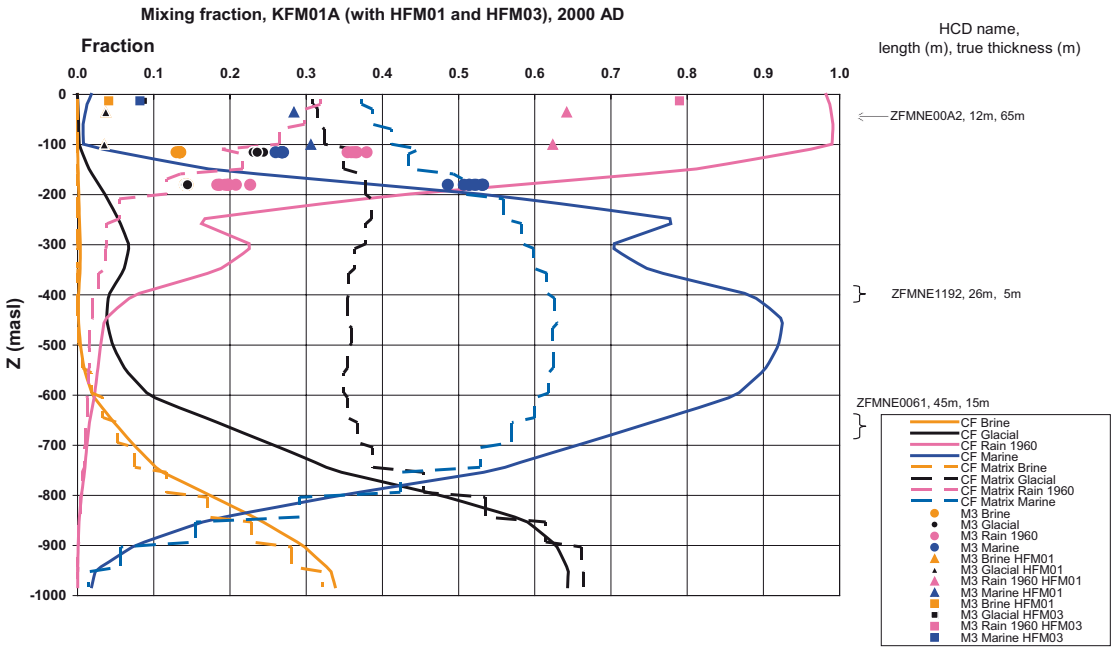

Figure 3-6. *Comparison of 4 reference water fractions in KFM01A for the ECPM reference case. The mixing fractions in the fracture system are shown by solid lines, in the matrix it is dashed, and the data by points.*

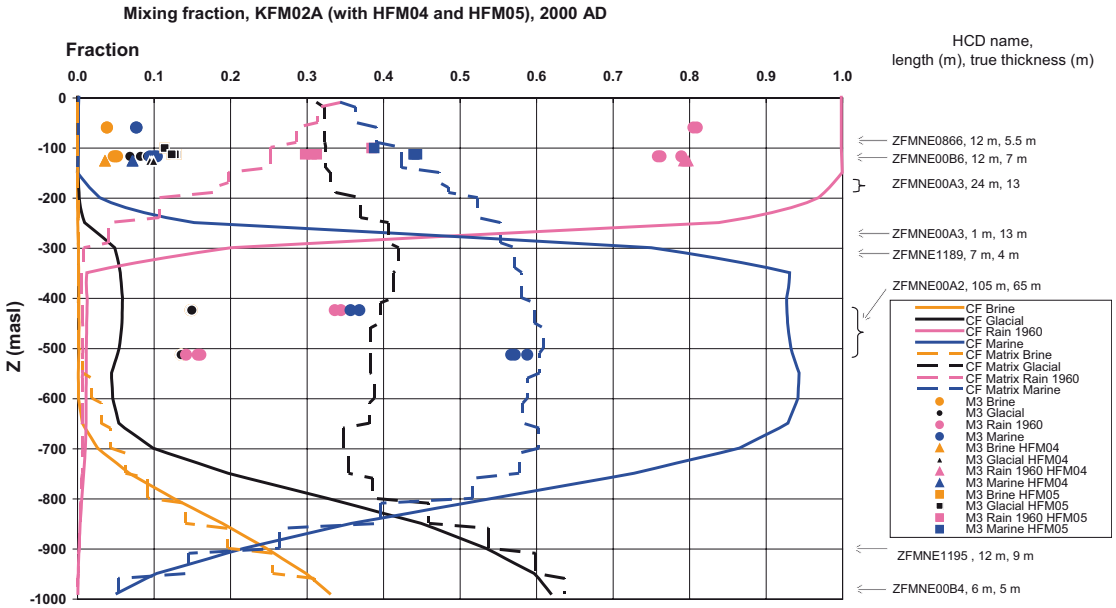

Figure 3-7. *Comparison of 4 reference water fractions in KFM02A for the ECPM reference case. The mixing fractions in the fracture system are shown by solid lines, in the matrix it is dashed, and the data by points.*

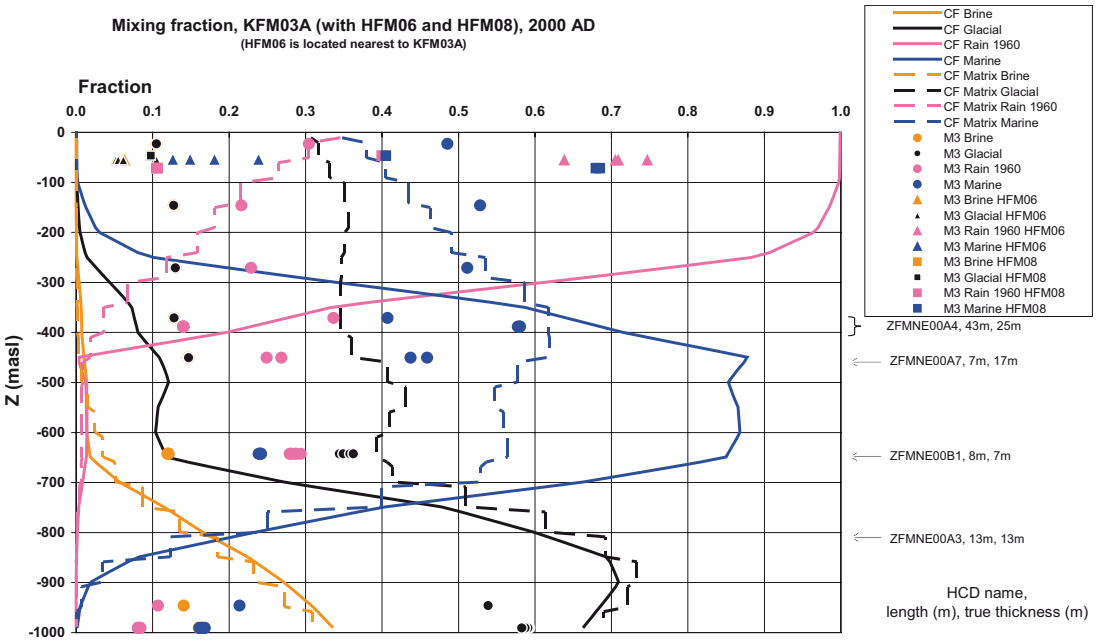

Figure 3-8. *Comparison of 4 reference water fractions in KFM03A for the ECPM reference case. The mixing fractions in the fracture system are shown by solid lines, in the matrix it is dashed, and the data by points.*

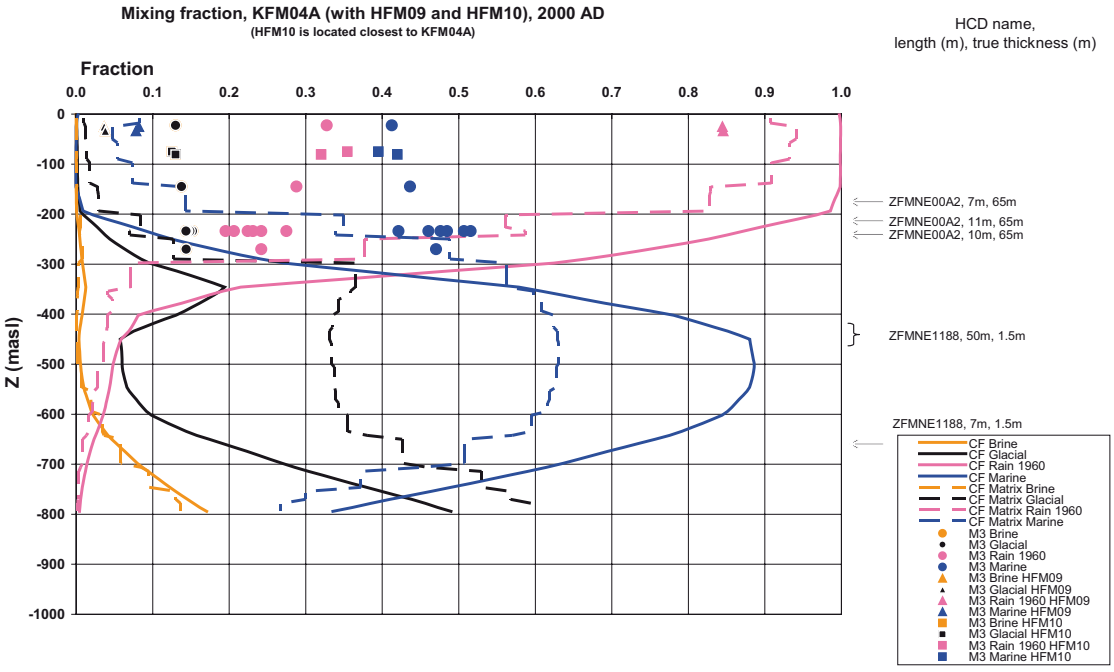

Figure 3-9. *Comparison of 4 reference water fractions in KFM04A for the ECPM reference case. The mixing fractions in the fracture system are shown by solid lines, in the matrix it is dashed, and the data by points.*

Salinity

Figure 3-10 shows the calculated salinity profiles compared to measured data in KFM01A–KFM04A for the ECPM reference case. Salinity closely follows the profile of Brine, although there is also a contribution from the Marine reference water. The results are similar to the SDM F 1.2 study, with a smooth trend of salinity with depth. Except for in KFM02A, the model still under-predicts salinity above 200 m depth. However, it is not clear whether the discrepancy

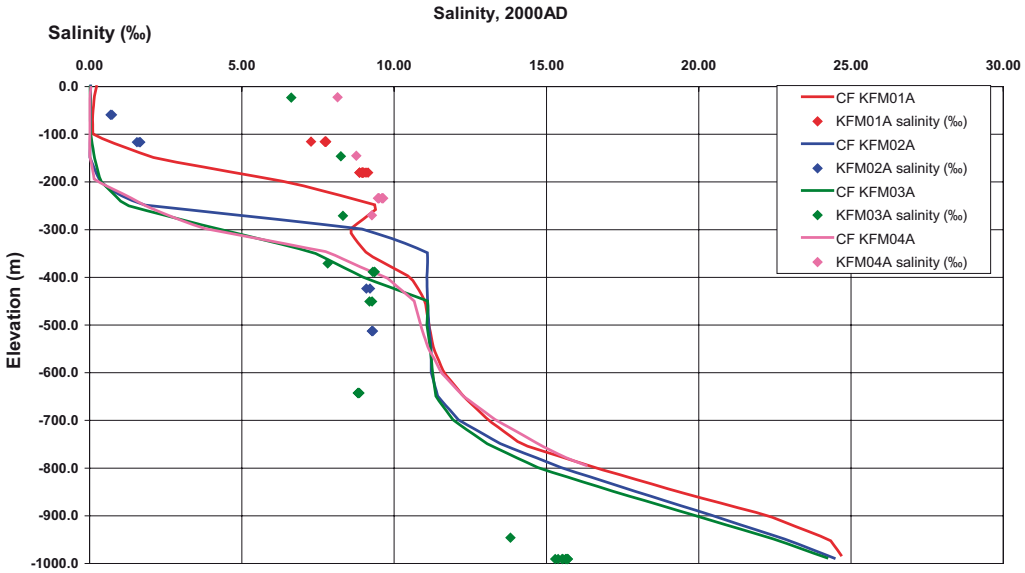

Figure 3-10. *Comparison of salinity (TDS) in KFM01A–KFM04A for the ECPM reference case. The salinity in the fracture system is shown by solid lines and the data by points.*

is due to uncertainties in measurements or if the problems are of a conceptual nature, most likely some of both. The opposite situation occurs at 1,000 m depth (data available only in KFM03A) where the models over-predict salinity. This would suggest the Brine is even deeper and that the initial condition could be modified slightly. As seen before, Marine water is found at high fractions at moderate depths, increasing the overall salinity. It should be noted that freshwater is measured near the surface in KFM02A while salinities similar to that of sea water are measured in KFM01A, KFM03A and KFM04A. Difference in the Quaternary deposits (e.g. recent deposition of clay sediments) has been advanced as one possible explanation.

Major ions and environmental isotopes

Figure 3-11 shows the profiles of the three constituents, $\delta^{18}O$, Cl and Mg in KFM01A–KFM04A for the ECPM reference case. The error bars only indicate the laboratory analysis uncertainty of about 5%. This comparison of relatively conservative ions serves as a complement to the uncertain interpretation in the M3 analysis. Again the profiles are consistent between the boreholes and suggest a smooth trend down the boreholes unlike the M3 data.

$\delta^{18}O$ allows the identification of Glacial water by a large negative ratio and differentiates between Rain 1960 and Glacial freshwaters. The model predictions are generally good where there are corresponding data. The ECPM model suggests a small spike in the profile for $\delta^{18}O$ below 800 m depth. However, below 500 m depth, only data from KFM03A is provided so the model results at this depth stay unconfirmed.

Cl indicates the presence of either Brine or Marine water. Mg is then used to differentiate between saline Marine (high Mg) and Brine (low Mg). The Cl profiles correlate to salinity which was discussed previously.

Mg is used in combination with the Cl profiles to distinguish between salinity originating from Brine (low Mg/Cl ratio) and salinity originating from Marine water (high Mg/Cl ratio). Data suggest a rather sharp transition between these two water types at about 500 m depth. The ECPM model suggests a transition 200 m deeper down so the calibration is not as good as desired. Mg data also gives evidence for Marine water in the near surface for KFM01A, KFM03A and KFM04A. Strictly, Mg is not a conservative tracer which leads to mid depth Mg concentrations being consistently lower than the model predicts. It is suggested that Mg has been removed by ion exchange along the flow paths /SKB 2005a/, and hence the observed Mg values tend to be lower than the model where Mg is approximated as being conserved.

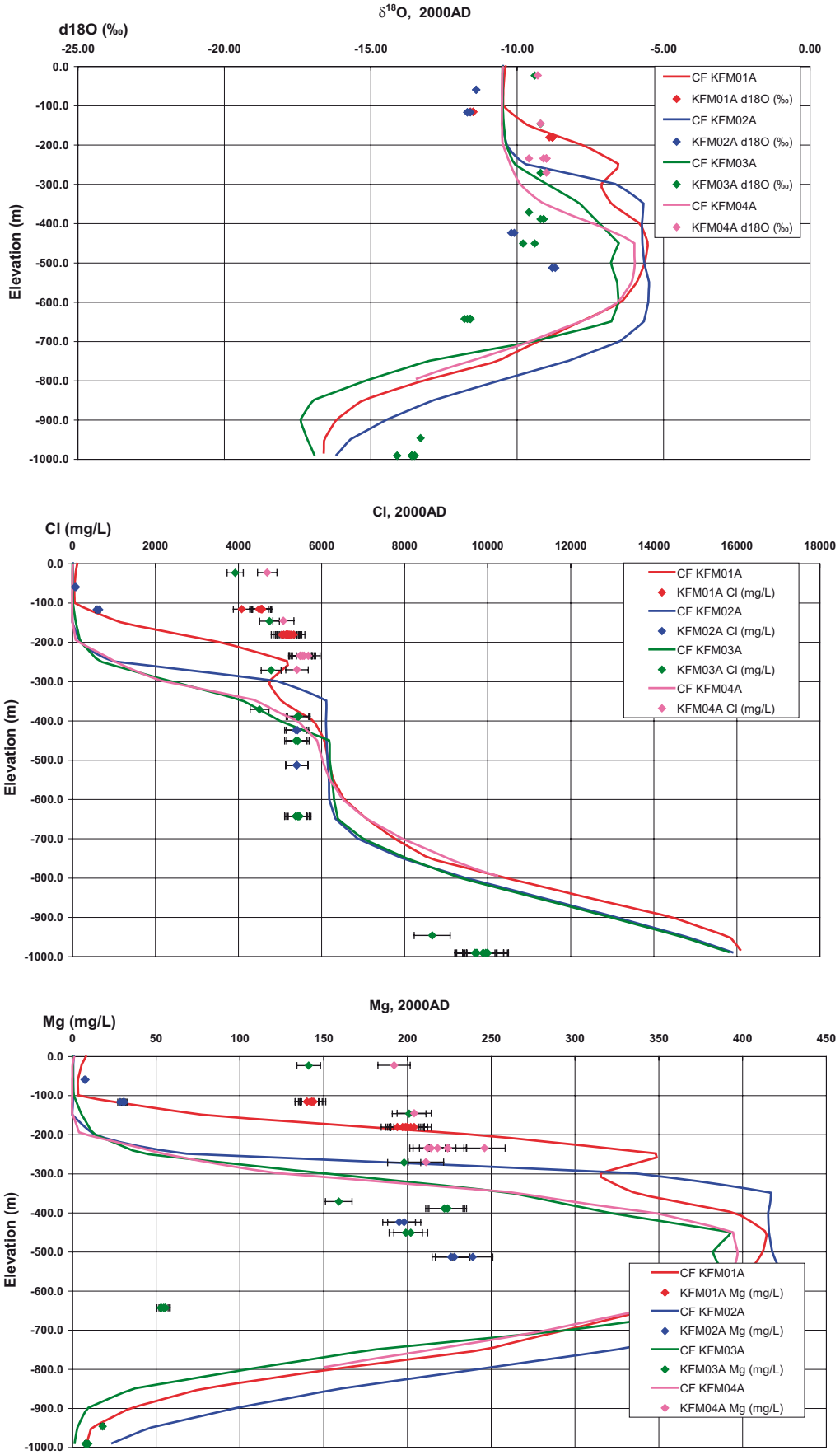

Figure 3-11. Comparison of $\delta^{18}O$, Cl and Mg in KFM01A–KFM04A for the ECPM reference case. Values in the simulated fracture system are shown by solid lines and the data by points.

Comparison of hydraulic conductivities in boreholes

Figure 3-12 to Figure 3-16 show the modelled block hydraulic conductivities in the ECPM reference case for boreholes KFM01A, KFM02A, KFM03A, KFM04A and KFM05A for the top 1,000 m of borehole compared with the interpreted values. KFM01A, KFM02A and KFM03A are compared with the 100 m PSS packer-test data, while KFM04A and KFM05A are compared with the PFL anomaly data converted to an average conductivity over 100 m intervals. In the figures, the depths and thickness of DZs in the geological model are indicated since they correlate strongly with the high conductivity intervals. The models use a 50 m grid refinement throughout the area characterised by boreholes. It is important to comment that the measured hydraulic conductivities are point-wise measurements of the flow through fractures intersecting the line of the borehole and hence are very sensitive to the occurrence of stochastic fractures in the vicinity of the borehole, whereas in the simulations the hydraulic conductivity is the bulk property for either a 50 m or 100 m cube.

The properties of the HCDs have been conditioned to 100 m PSS data, so the intervals with large hydraulic conductivity are reproduced reasonably by the models. This is seen in all five boreholes. The main discrepancy between the measured data and the ECPM model can be found in the less conductive intervals in KFM01A and in KFM02A and KFM05A below ZFMNE00A2. The ECPM model uses an upscaled stochastic DFN model to generate the background hydraulic conductivity. In this reference case, the Hydro-DFN is statistically homogeneous and based on Volume E only, and since this was based on KFM03A it is unsurprising that this borehole gives the best match and over-predicts the hydraulic conductivities in the very tight sections of KFM01A and KFM02A. Another factor is that the calculation of ECPM block properties for a sparse network such as this has a tendency to over-predict connectivity of the network, and therefore the hydraulic conductivity. So if we sample the conductivity as seen along the line of the borehole, we will get a contribution to the modelled conductivity from any fracture within the size of a finite-element, 50 m, even if the fracture does not intersect the borehole. Since no effort is made to condition the positions of fractures to the field-data, even locally, the simulated hydraulic conductivity will inevitably be too high in low conductive intervals of the ECPM model.

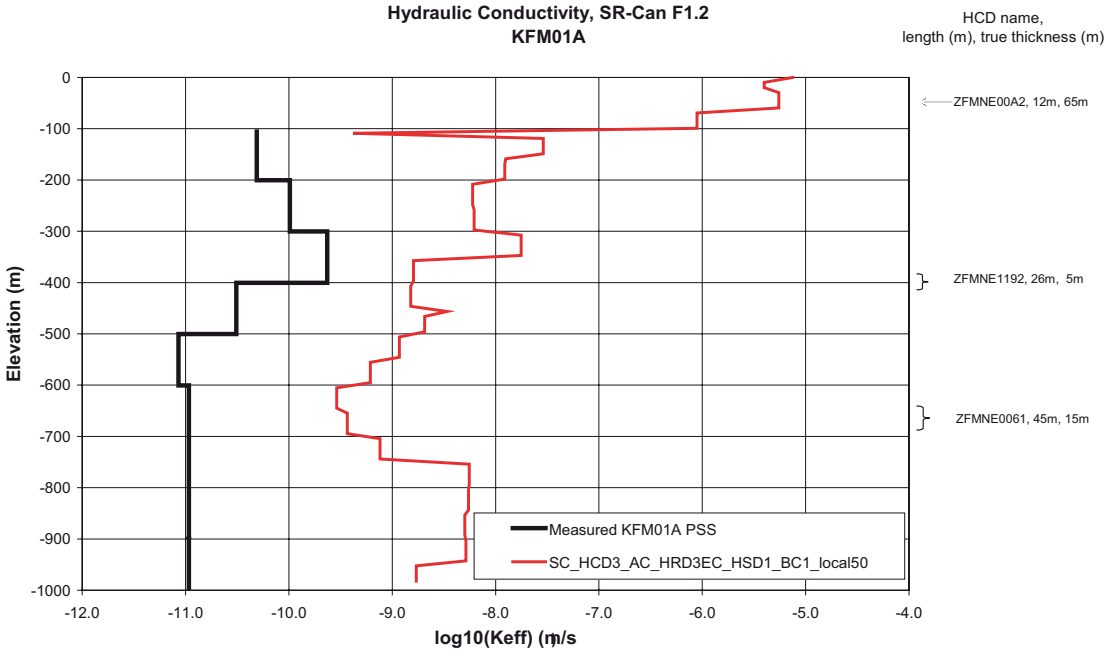

Figure 3-12. *Comparison of hydraulic conductivity in KFM01A for the ECPM reference case. Values simulated in the model are shown by red lines while the measured values in 100 m intervals are shown in black. The detection limit on measurements is about 10^{-11} m/s.*

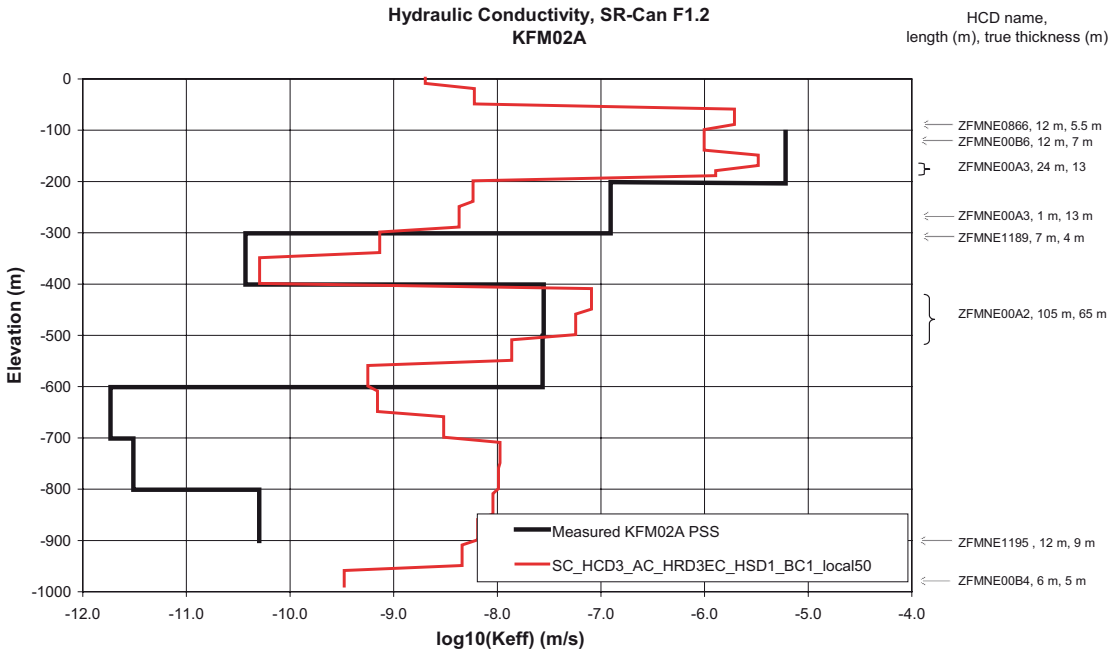

Figure 3-13. *Comparison of hydraulic conductivity in KFM02A for the ECPM reference case. Values simulated in the model are shown by red lines while the measured values in 100 m intervals are shown in black. The detection limit on measurements is about 10^{-11} m/s.*

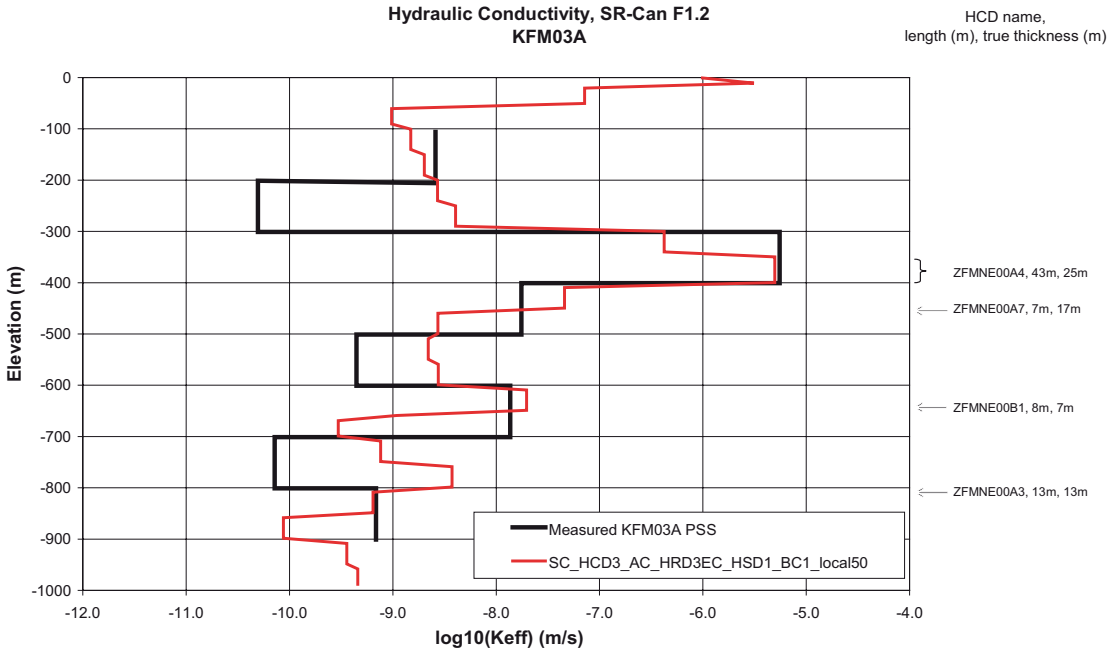

Figure 3-14. *Comparison of hydraulic conductivity in KFM03A for the ECPM reference case. Values simulated in the model are shown by red lines while the measured values in 100 m intervals are shown in black. The detection limit on measurements is about 10^{-11} m/s.*

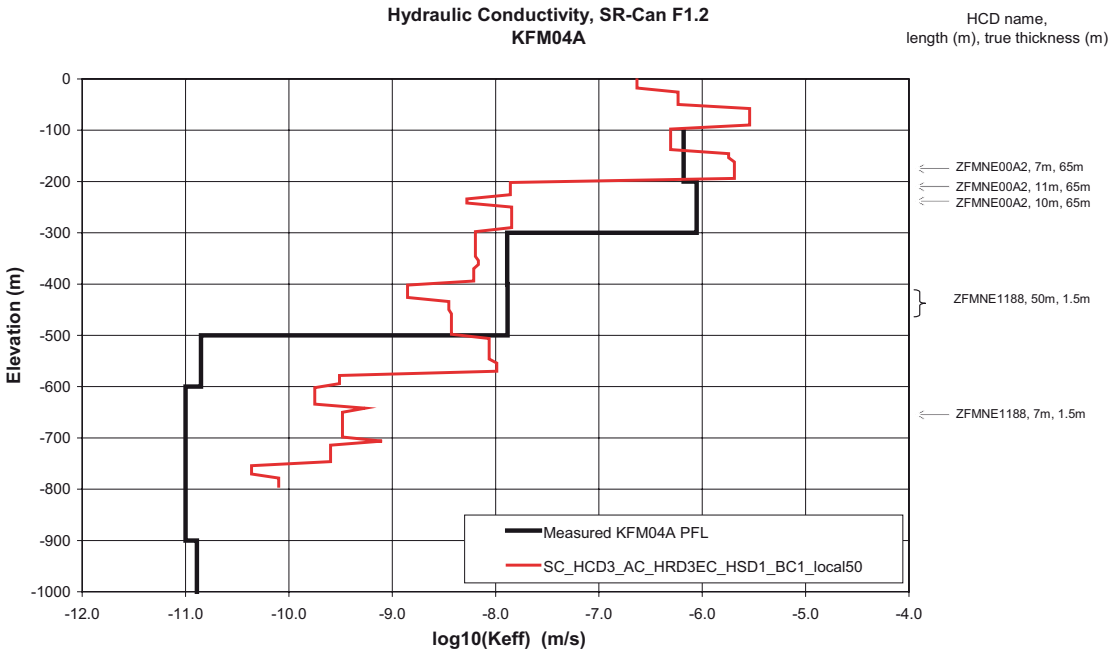

Figure 3-15. *Comparison of hydraulic conductivity in KFM04A for the ECPM reference case. Values simulated in the model are shown by red lines while the measured values in 100 m intervals are shown in black. The detection limit on measurements is about 10^{-11} m/s.*

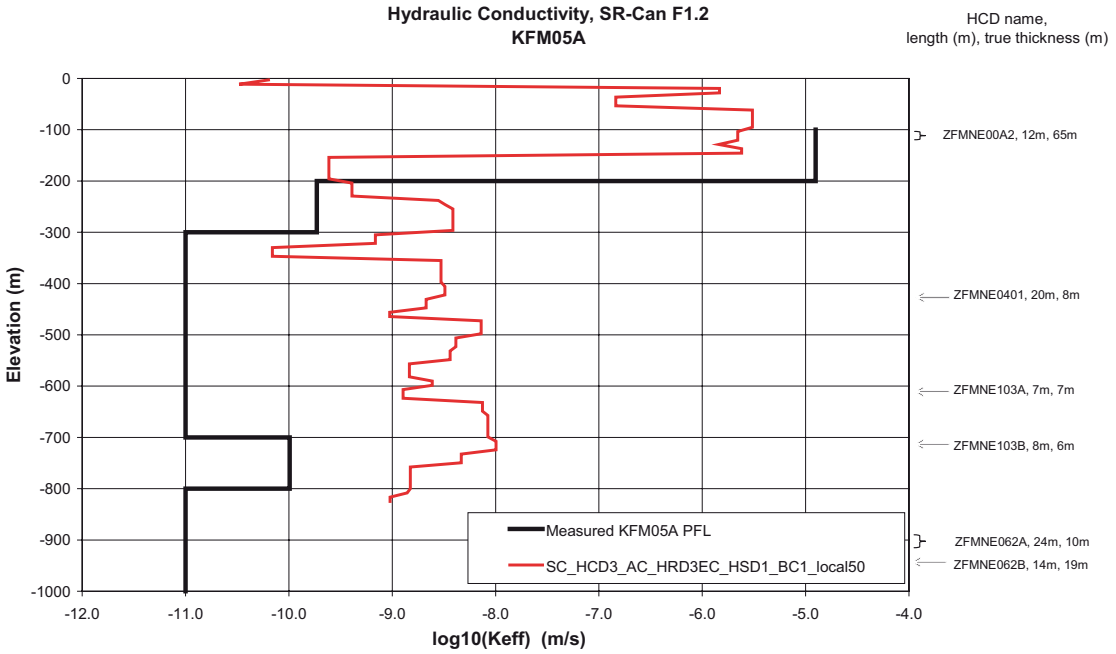

Figure 3-16. *Comparison of hydraulic conductivity in KFM05A for the ECPM reference case. Values simulated in the model are shown by red lines while the measured values in 100 m intervals are shown in black. The detection limit on measurements is about 10^{-11} m/s.*

3.2.2 Description of future evolution

In order to calculate the transient evolution of groundwater flow into the future, predictions were required for the future evolution of the shoreline and the salinity of the Bothnian Sea. The shoreline displacement was needed to be able to set boundary conditions for groundwater pressure on the top surface. The salinity evolution was needed to define boundary conditions on the reference water fractions on the top surface that is covered by the sea. For shoreline displacement, the same curve as used for SDM F 1.2 was used /Påsse 1997/ (see Figure 3-17). Note, this case is based a natural evolution of the climate and is mainly due to post-glacial rebound of the land. It does not consider the effects of climate change. The salinity evolution model was changed from SDM F 1.2 (green curve in Figure 3-17) based on data supplied by Ulrik Kautsky (personal comunication 2005) based on /Gustafsson 2004ab/. Several models were considered as shown in Figure 3-17. The final red curve represents a compromise between the historic evolution used in SDM F 1.2 and the latest predictions of the future evolution. Although there is uncertainty in the future evolution of salinity, it is considered that the groundwater flow results are unlikely to be sensitive to the uncertainty suggested here.

The shoreline evolution has a much greater impact on groundwater flow and PA calculations because of the gentle topographic gradient in the area. Currently, because the site is located at the coast, groundwater flow is generally upwards through the proposed repository area as flow discharges at the coast. In the future, the shoreline retreats quite rapidly due the gentle topographic slope as the land rises. This effect is illustrated in Figure 3-18 with the dark blue areas corresponding to the sea, and the target circle indicating the proposed repository location. Remember the model size is about 15 km by 11 km. It can be seen that even at 3,000 AD the shoreline moves a few kilometres north. At 5,000 AD new lakes are formed to the north, and by 7,000 AD the shore is retreated to the northern boundary of the model where there are a number of deep depressions in the seabed that persistent even to 9,000 AD. These depressions may have been isolated from the main body of the sea by then and become gradually diluted. Implications for PA are a likely evolution of flow from discharge to recharge around the site, and a change in discharge areas to either the retreating shoreline or the newly formed lakes to the north.

The future evolution of the four reference waters Brine, Marine, Glacial and Rain 1960 for the ECPM **reference** Case is shown in Figure 3-19 and Figure 3-20. The distributions of the different water types are presented in vertical slices at three times corresponding to: 2,020 AD, 3,000 AD and 9,000 AD. The fraction of each water type is calculated and the sum of the fractions of the four water types equals one. The corresponding total dissolved solids (TDS) distributions are presented in Figure 3-21.

The Brine distribution is notably stable during the entire range of times. The reason is the low hydraulic conductivities at depth in combination with the depth dependency in HCD properties that approach the background conductivity below about 700 m depth. At 2,020 AD, the Brine profile is close to the initial condition. At later times the Brine is moved only slowly by infiltrating freshwater (Rain 1960).

Marine water is allowed to enter the system through the sea covered areas. The mechanism for infiltration of Marine water is from the fact that it is heavier than the underlying Glacial melt water and hence gradually sinks downwards as a pulse through the system toward the dense Brine. The pulse will sink heterogeneously around the deformation zones since advection is more rapid. This effect can be seen in Figure 3-19 where the Marine water clearly enters some sub-horizontal zones sloping south-east. During the past evolution most of the region has been covered by sea water (Littorina and Baltic) and the result is clearly seen at 2,020 AD and 3,000 AD where we have large fractions of Marine water in the upper part of the model.

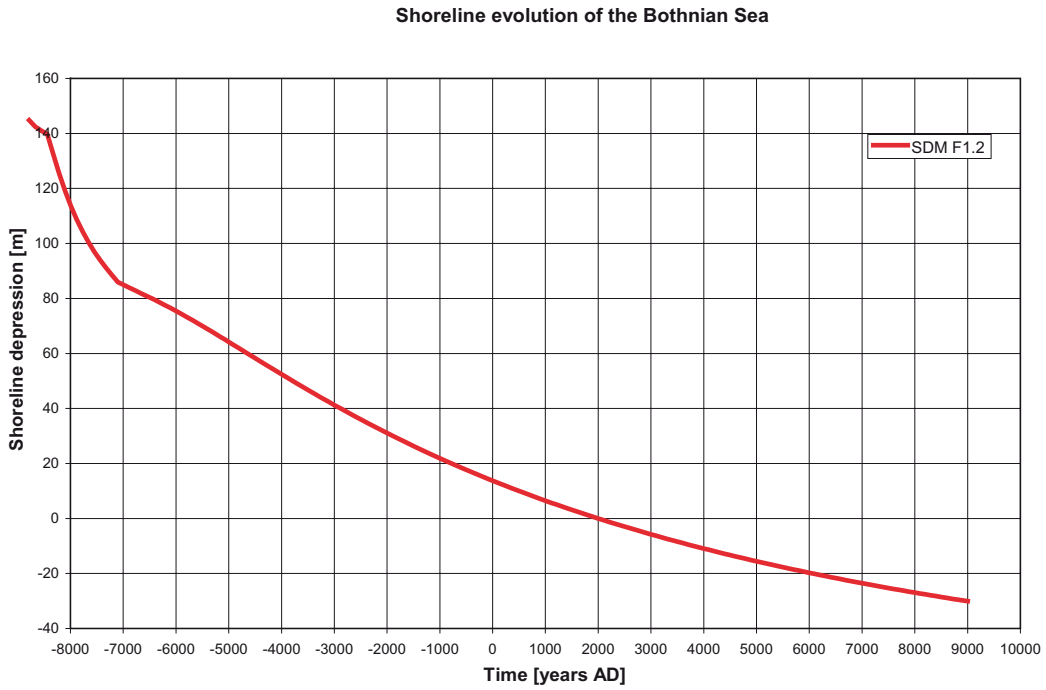

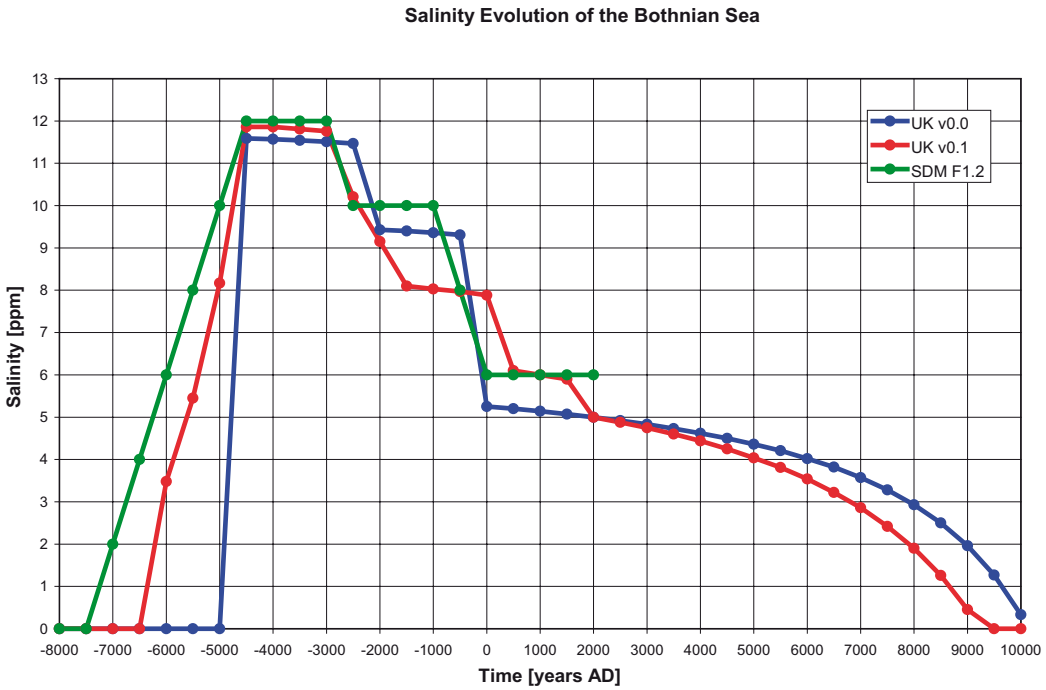

Figure 3-17. *Evolution of shoreline (top) and salinity of the Bothnian Sea (bottom). The red curves are the ones used in SR-Can. For salinity, 2 other curves are shown as proposed in other studies (Ulrik Kautsky, personal communication 2005) and /Påsse 1997/.*

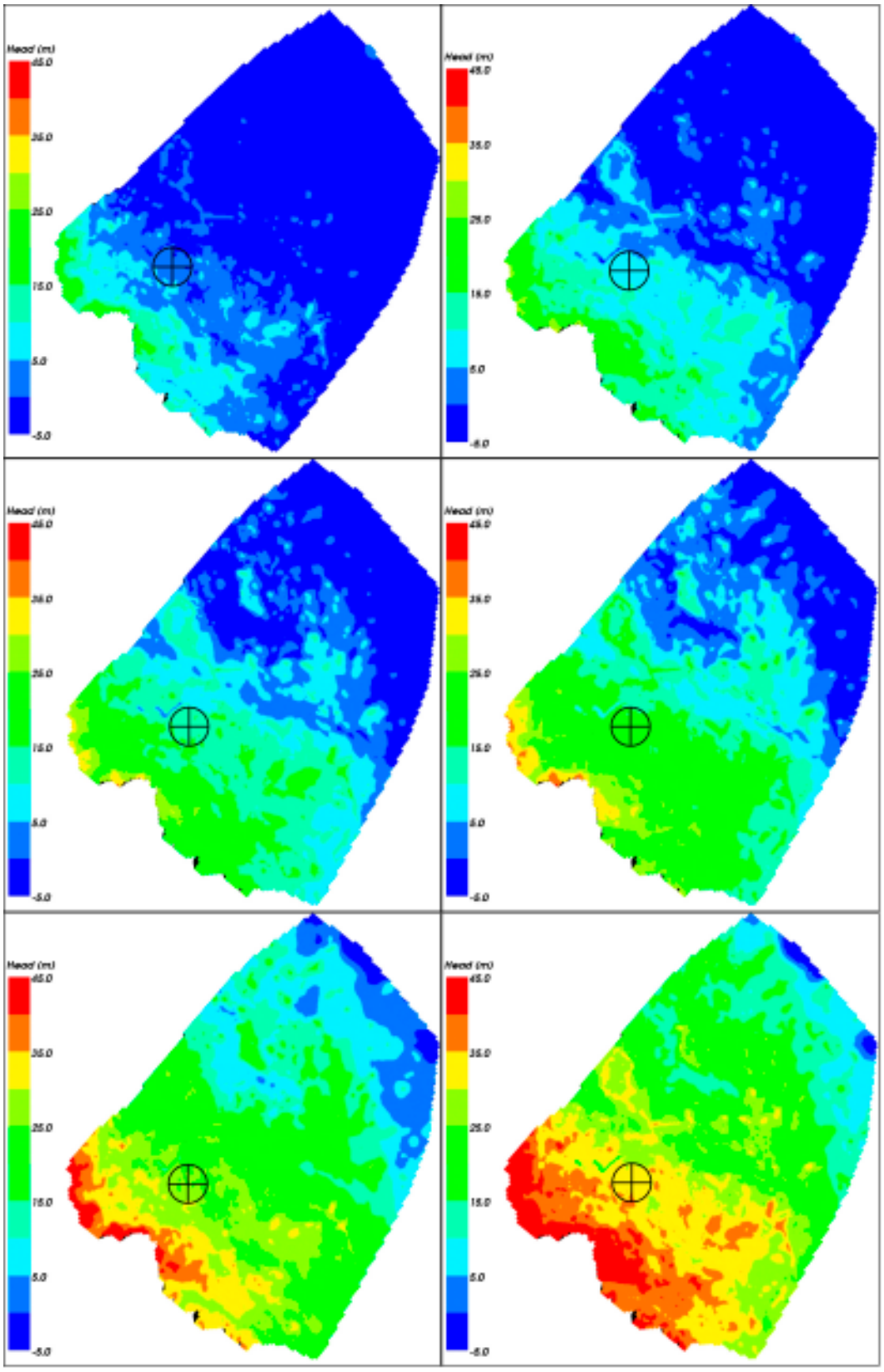

Figure 3-18. *Evolution of head distribution in the future at the surface. From top left to bottom right: 2,000 AD, 3,000 AD, 4,000 AD, 5,000 AD, 7,000 AD, 9,000 AD. The ⊕ symbol shows the approximate repository location.*

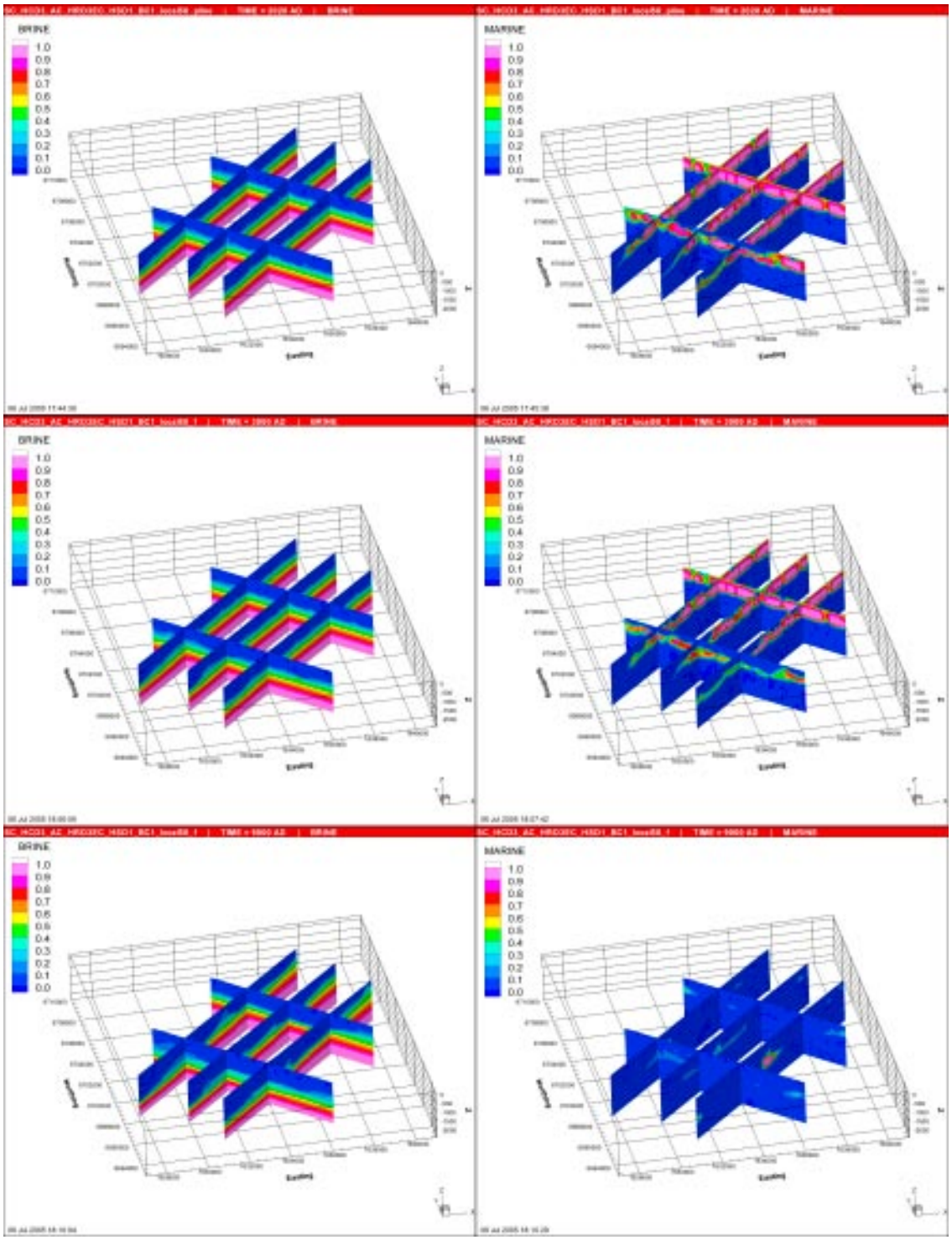

Figure 3-19. *Distribution of Brine (left) and Marine water (right) in vertical slices at times equal to (from top to bottom) 2,020 AD, 3,000 AD and 9,000 AD, for the ECPM reference case.*

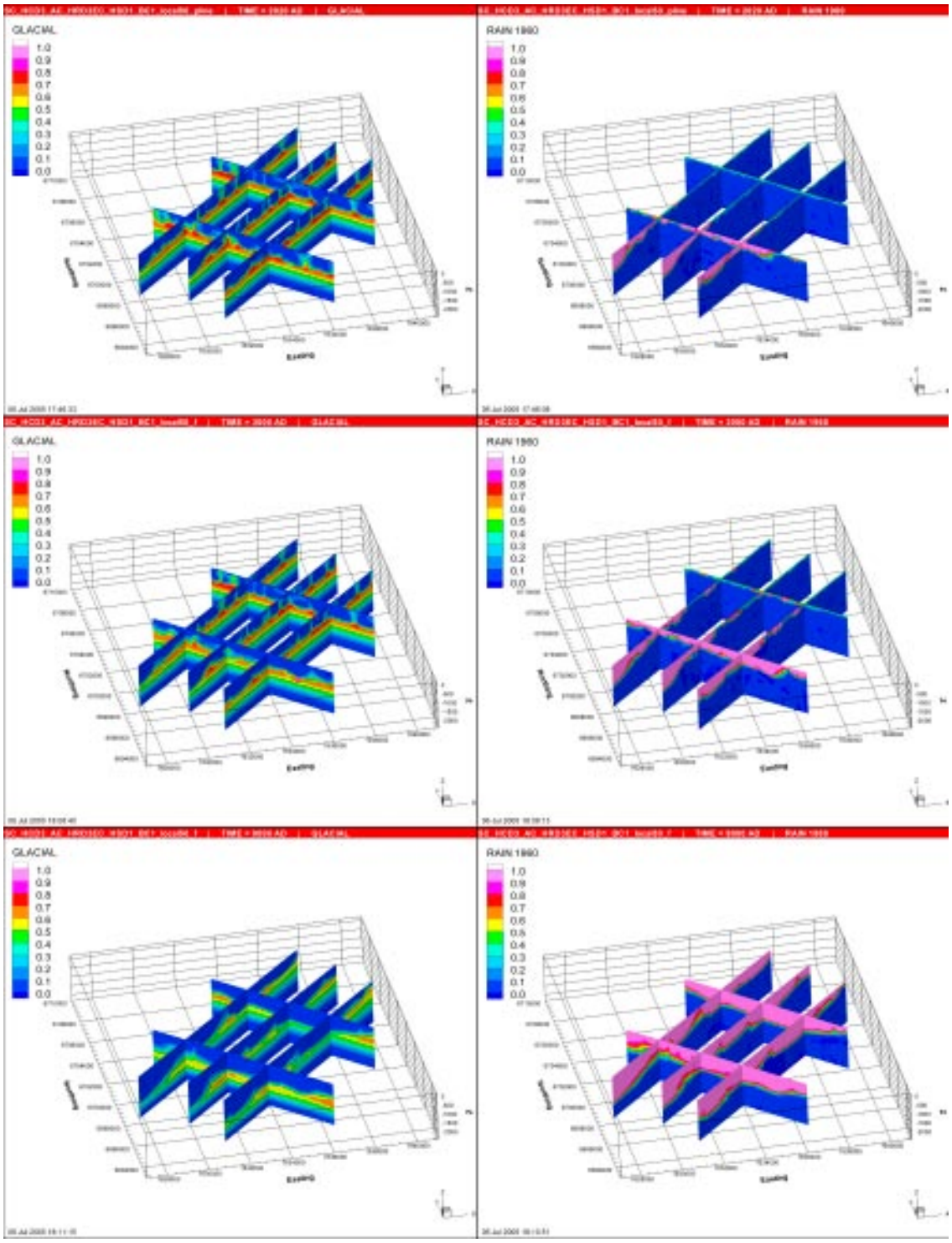

Figure 3-20. *Distribution of Glacial water (left) and Rain 1960 (right) in vertical slices at times equal to (from top to bottom) 2,020 AD, 3,000 AD and 9,000 AD, for the ECPM reference case.*

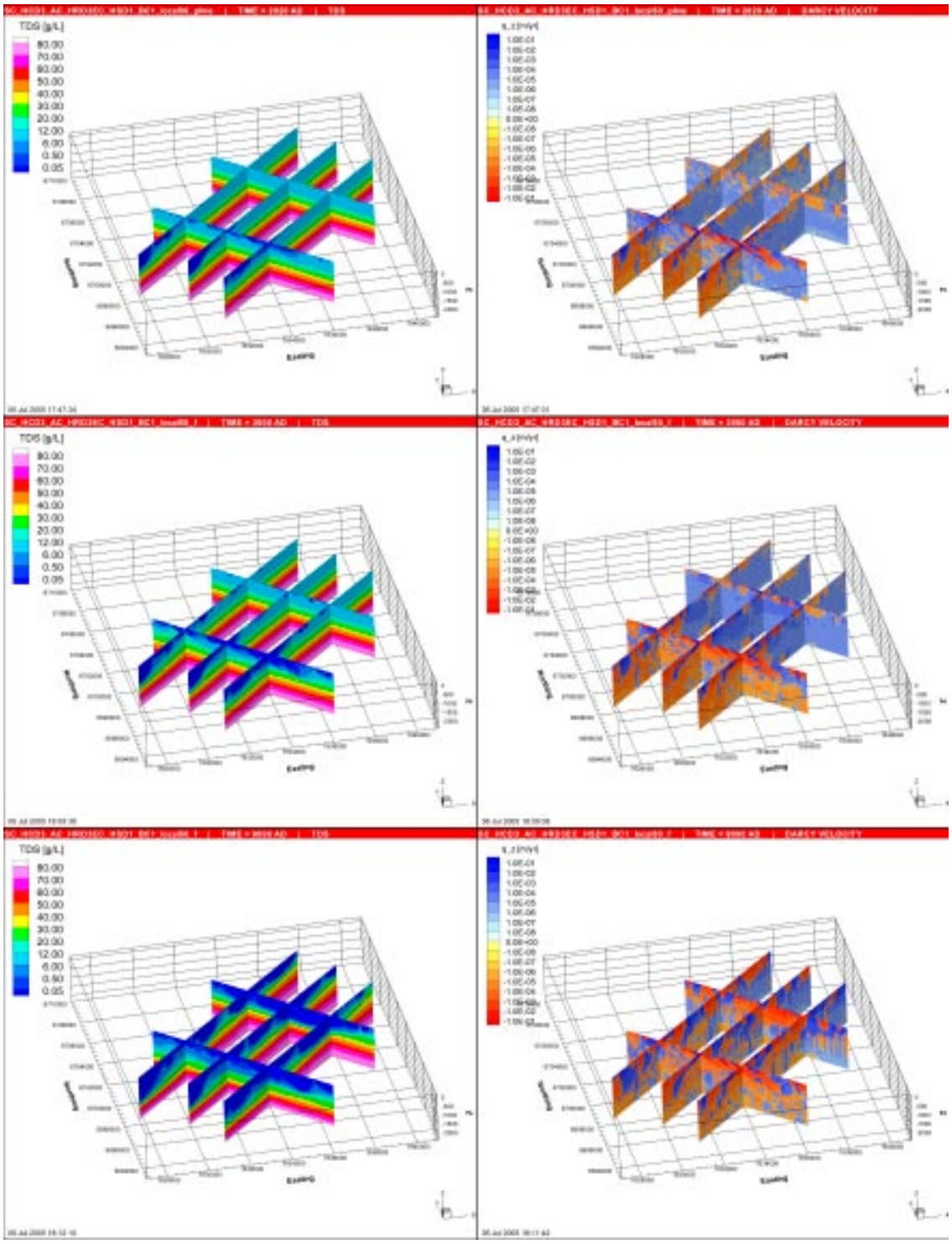

Figure 3-21. *Distribution of TDS (left) and the vertical Darcy velocity, q_z (right; positive flow is upward) in vertical slices at times equal to (from top to bottom) 2,020 AD, 3,000 AD and 9,000 AD, for the ECPM reference case.*

The Marine pulse is generally in the top 500 m. As the land continues to rise above the sea level Rain 1960 is begins to infiltrate the system through the top surface. At 2,020 AD this occurs in the south-west only where we have land, but already at 3,000 AD large parts of the model have emerged from the sea and Rain 1960 effectively replaces the Marine water in the top of the model. By 9,000 AD there are only a few spots of deep Marine water present in the model.

Figure 3-20 shows what is left of the Glacial water at present-day and how this continues to be flushed out. Initially Glacial water fills the top of the model and sits on top of the Brine. Dense Littorina water in combination with a greater water column of seawater in early years results in a higher buoyancy force driving a more rapid flushing of the Glacial water by Marine water. At 2,020 AD almost all Glacial water is gone in the top 600 m. At 9,000 AD the fraction of Glacial water has decreased to 50% at 1,000 m depth. However, there are still some spots in the model with higher fractions of Glacial water which is gradually mixing with the Brine.

At 2,020 AD the south-east of the model is exposed to infiltrating precipitation (Rain 1960 water) that leads to a flushing of the preceding Marine water in the top 300–400 m. The process continues to accelerate as the land rises and at 9,000 AD the entire model area is subject to infiltrating precipitation. At this time Rain 1960 is present at a fraction of 100% down to a depth of about 1,000 m.

The TDS distribution seen in Figure 3-21 is the result of mixing between Brine and Marine water, which has a time varying concentration of salt. The shape of the TDS distribution at 9,000 AD suggests that the dominant part of the salt originates from the Brine and that the early pulse of Littorina and Baltic Sea water has been flushed.

The distribution of the vertical Darcy velocity, presented in Figure 3-21, shows a highly heterogeneous flow field confirming the presence of local flow cells. Flow in the sub-horizontal zones dipping south-east are generally downwards (negative q_z). The predominant flow direction in the parts of the model under the land is downwards as expected, though there are some large discharge areas clearly visible especially as the coast retreats at 9,000 AD. At 9,000 AD land covers most of the model and changes the flow considerably.

3.2.3 Recharge and discharge

In Figure 3-22 the distribution of Darcy velocity is shown on a vertical slice through the repository for three selected times: 2,020 AD, 3,000 AD and 9,000 AD. These times represent when the coast is at the site, when it has moved a few kilometres away, and at the end of the temperate period when the coast is about 10 km away. The velocity is up around 1 to 100 m/y in the surface layers, but drops to about 10^{-5} to 10^{-1} m/y in the bedrock. In the heterogeneous ECPM model, flow follows a complex pattern indicating localized flow cells all over the modelled area. The flow becomes less heterogeneous with depth. A key feature is that at 2,020 AD, flow is upwards at the northern end of the repository discharging at the coast, while at 3,000 AD and 9,000 AD flow is downward and then horizontal in this area. It also increases in magnitude. The reason stems from the edge of the tectonic lens being located just downstream of the repository, so as the shoreline retreats to the north flow is pulled down into the are of relatively high hydraulic conductivity just north of the tectonic lens. The hydraulic conductivity in the area to north of RFM029/017 is thought to be low by analogy to the rock to the south of the site, but is yet to be proven. Flows below 700 m are all below 10^{-4} m/y.

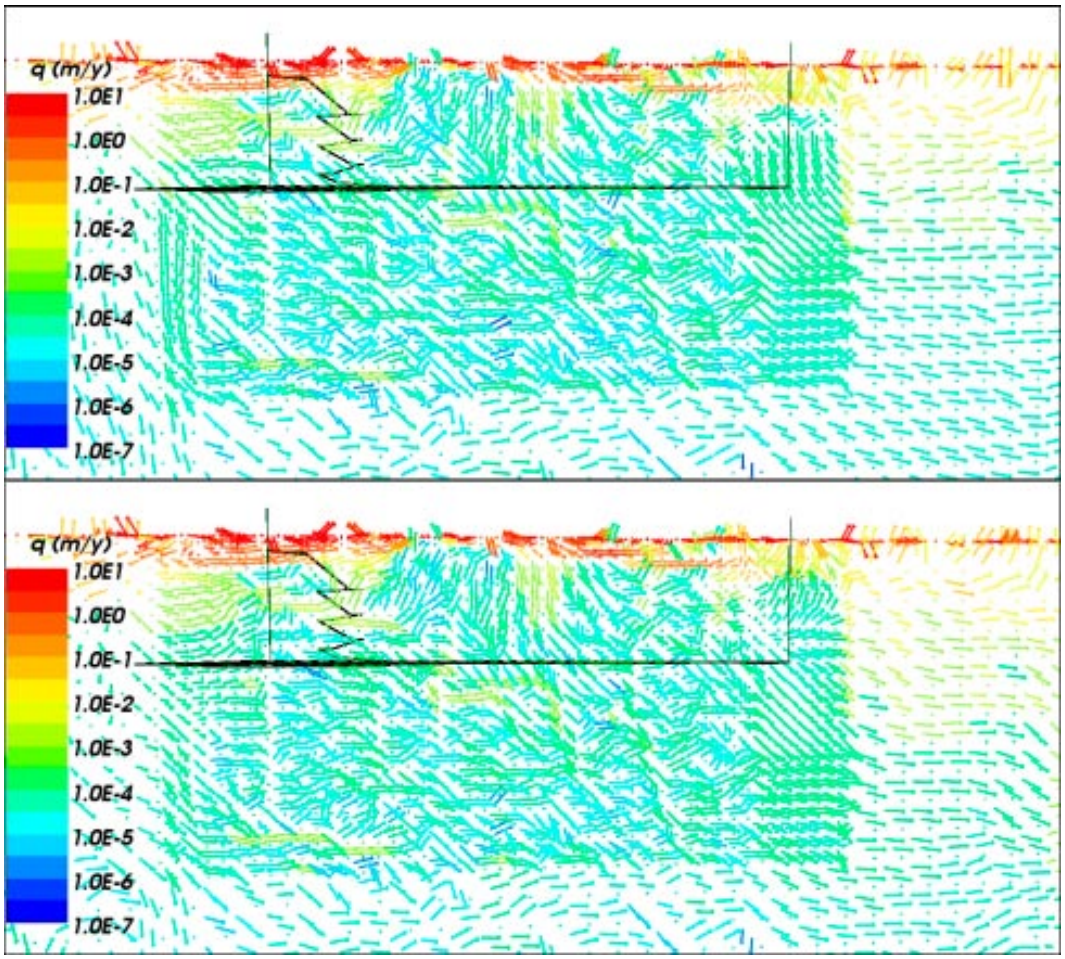

Figure 3-22. *Distribution of the Darcy velocity, q, in the ECPM reference case on a vertical slice from SW (left) to NE (right) through the repository. The repository is shown in black with the two vertical shafts and the ramp to the left. One velocity arrow is drawn per finite-element, which means there is a greater density of arrows in the central region where there is more refinement. From top to bottom: 2,020 AD, 3,000 AD and 9,000 AD. Arrows show the direction of velocity in 3D and the colour indicates the magnitude of the vector.*

The horizontal distribution of flow at repository depth is shown Figure 3-23 at times 2,020 AD, 3,000 AD, 5,000 AD and 9,000 AD in the vicinity of the repository. Again, this reveals the heterogeneity in the flow pattern within the area which is based on an underlying DFN inside RFM029/17. The main change in time occurs in the northern area of the repository as the coast moves away. Initially, velocities are upwards, but of low magnitude. Later, velocity then increases in magnitude and is downwards. There is a suggestion that velocities increase in magnitude slightly in the future. The difference between 5,000 AD and 9,000 AD appear slight suggesting flow stabilises in the repository area around 5,000 AD. High flow areas occur between the western and central set of deposition tunnels and along a band intersecting the southern end of the eastern set of deposition tunnels. There is also an area around the deviation in the western access tunnel.

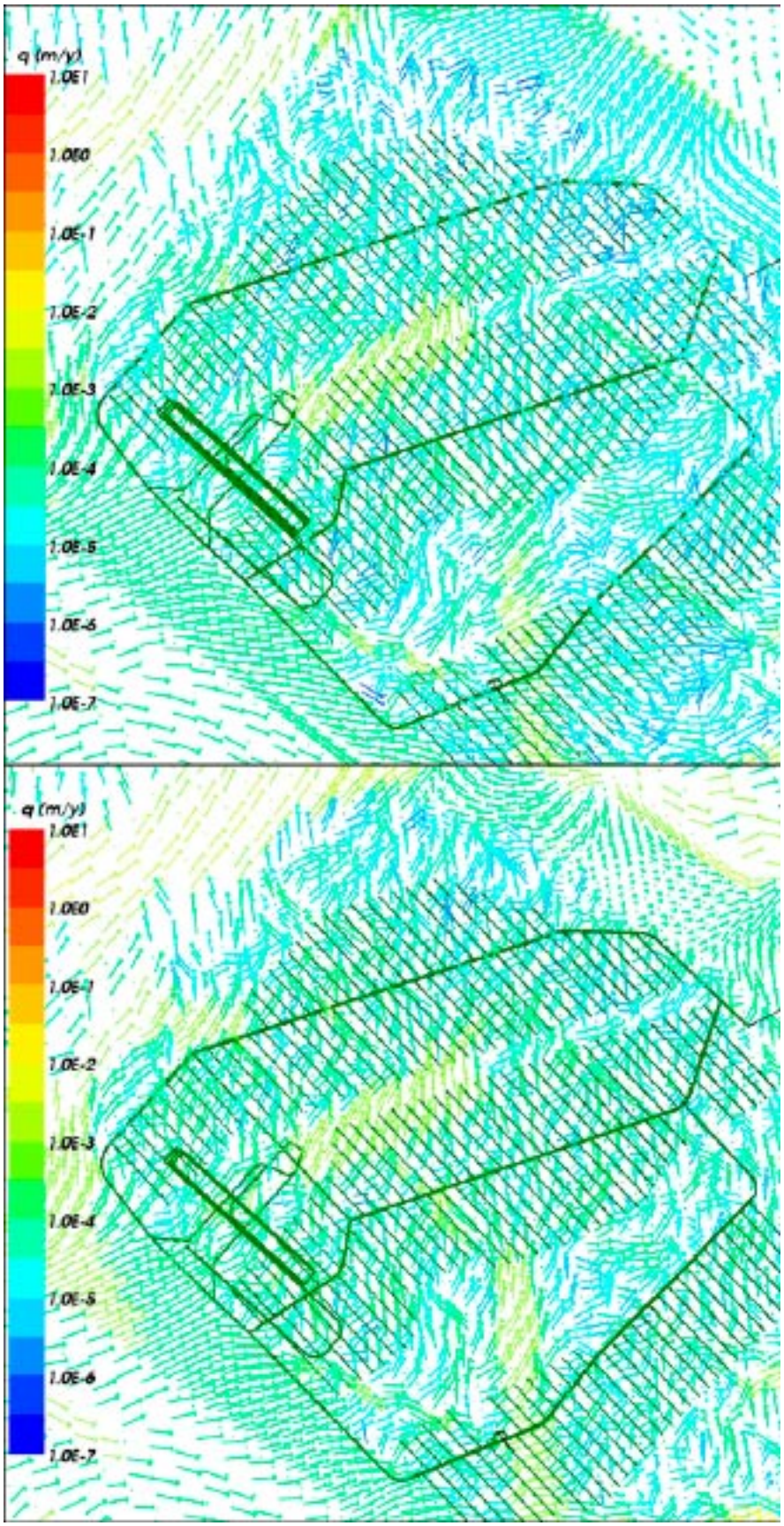

Figure 3-23. *Distribution of the Darcy velocity, q, in the ECPM reference case on a horizontal slice through the repository (shown superimposed). One velocity arrow is drawn per finite-element, which means there is a greater density of arrows in the central region where there is more refinement. Top: 2,020 AD. Bottom: 3,000 AD. Arrows show the direction of velocity in 3D and the colour indicates the magnitude of the vector.*

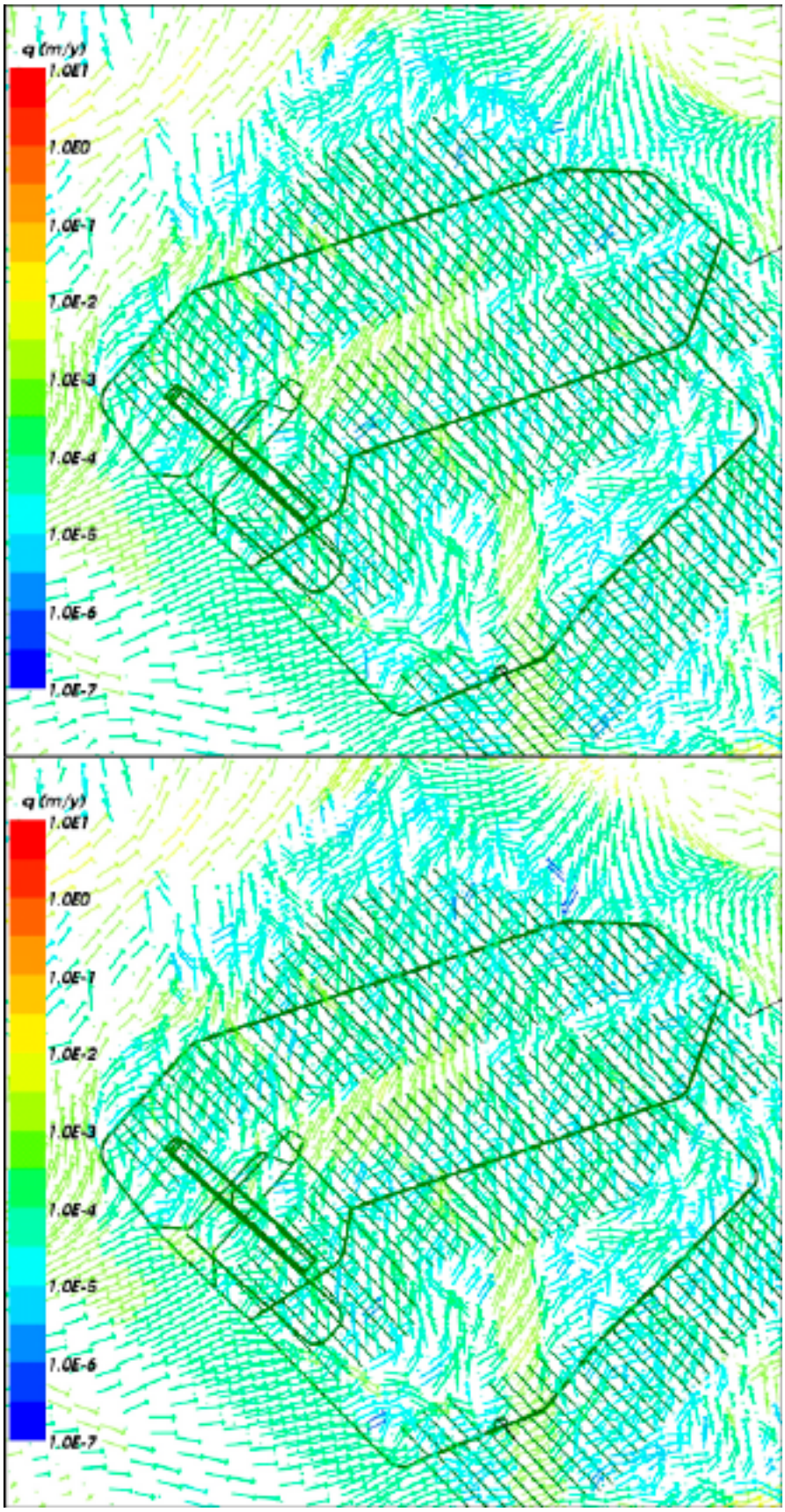

Figure 3-24. *Distribution of the Darcy velocity, q, in the ECPM reference case on a horizontalal slice through the repository (shown superimposed). One velocity arrow is drawn per finite-element, which means there is a greater density of arrows in the central region where there is more refinement. Top: 5,000 AD. Bottom: 9,000 AD. Arrows show the direction of velocity in 3D and the colour indicates the magnitude of the vector.*

3.2.4 Flow-paths

The results of the particle tracking calculations using the advective flow-field from three different snapshots in time are illustrated in several different ways. In Figure 3-25 the distributions of F-quotient ($\log_{10}$) at 6,824 particle starting locations in the repository for the ECPM reference case are presented. Results are shown for three selected release times; 2,020 AD (top), 3,000 AD (middle) and 9,000 AD (bottom). The blue colour indicates smaller values, F-quotient about 10^4 y/m, and red indicates higher values around 10^9 y/m. Figure 3-26 shows the distribution of F-quotient ($\log_{10}$) at particle exit locations for the same three selected release times. Figure 3-27 shows the exit locations for particles coloured by release time; 2,020 AD (red), 3,000 AD (green) and 9,000 AD (blue). Figure 3-28 shows the flow-paths and exit locations for particles from three different projections and colouring the particle tracks by release time to differentiate between them. In each case the repository is superimposed and other contextual information such as roads and buildings on the surface.

At 2,020 AD the flow in the repository is mainly upwards, even if a lot of particles start going downward for the first 100–200 m and then turn upwards again. The F-quotients are around 10^6 to 10^7 y/m. The highest F-quotients are found in the centre of the repository. In the northern part of the repository the particles have very short path-lengths of about 500–1,000 m, indicating a path from the repository straight up to the surface. The south-east part of the repository contains some particles with very high F-quotients and very long flow-paths. However, in this particular case the statistics indicate that the particles actually reach the surface after oscillating in the flow-field to the east in area around the edge of the tectonic lens at the coast. This represents less than 1% of the particles that are lost in this way at 2,020 AD in this way, and should be noted that the path-length of along these flow-paths is perhaps artificially long.

At 3,000 AD the flow pattern has changed significantly due to land-rise. In the northern part of the repository, the flow-paths are still upwards and very short. In the southern part of the repository area the predominant flow direction is downwards sending particles deeper into the model. The flow-paths are now more spread across the model. At 3,000 AD we have the highest concentration of stuck particles. This is seen particularly among the particles released in the southern part and in the north-west part of the repository where we have very long flow-paths. Almost 30% of the released particles are lost due to numerical problems in the particle tracking for this release time. The problems are thought to be due to a very narrow flow cell developing between the northern edge of the tectonic lens and the coast.

At 9,000 AD a more certain picture of the situation emerges. This release time shows almost no lost particles. It is clear that both the F-quotient and the path-lengths have now increased due to changes in the flow-field. There is also a correlation between particles with high F-quotients and long flow-paths. At this time we see that there are some areas in the repository with upward flow resulting in very short flow-paths. This of course has an impact on the performance measures showing lower values of median F-quotient and flow-paths. The area of short flow-paths is situated in the northern half of the repository. The rest of the repository, where the predominant flow direction is downward, is covered with starting locations resulting in long flow-paths and large F-quotients. There are lots of particles reaching all the way to the large fracture zone at the model boundary where the shoreline is at this time. A few particles exit through the large regional fracture zone half way to the boundary where a lake forms at this time.

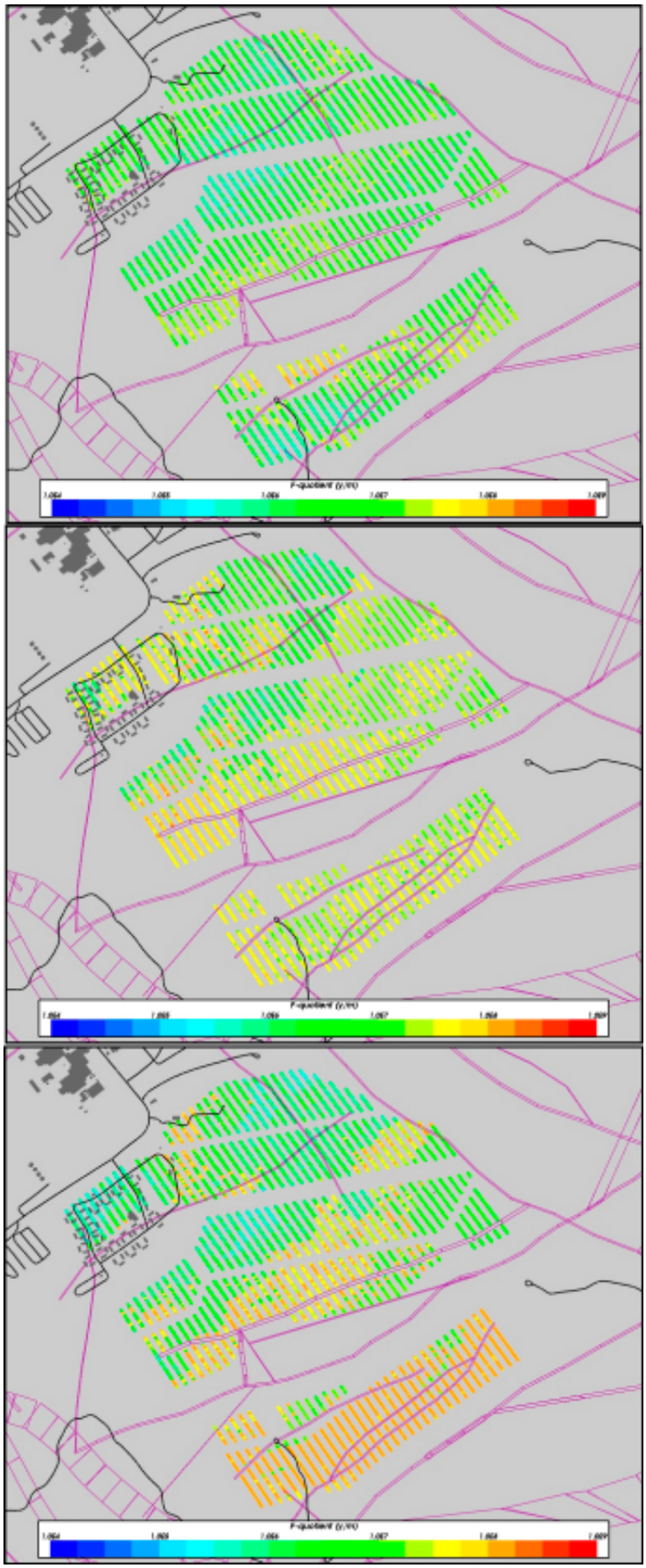

Figure 3-25. *Distribution of $\log_{10}(F_r)$ at 6,824 particle start locations for the ECPM reference case release times (from top to bottom) 2,020 AD, 3,000 AD and 9,000 AD. Also, the HCD model at z=–400 m (purple), roads and buildings (black).*

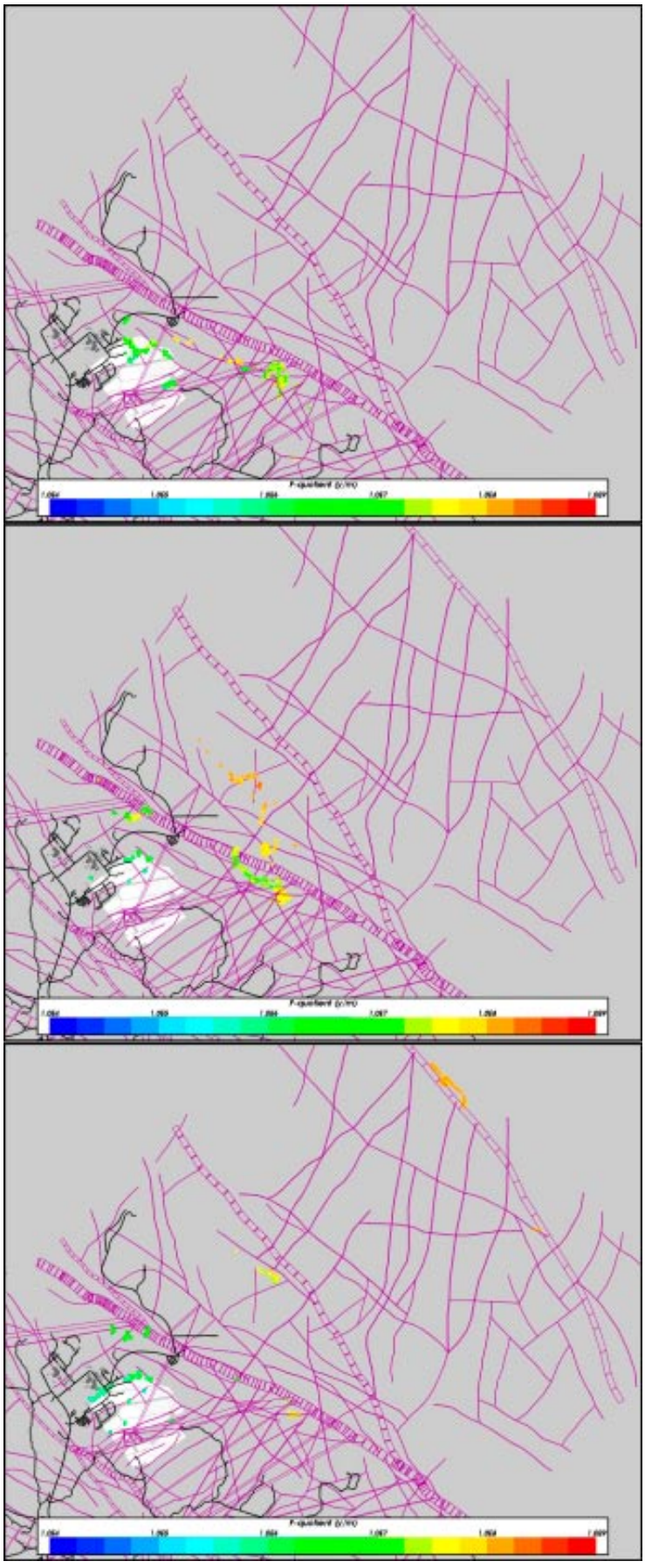

Figure 3-26. *Distribution of $\log_{10}(F_r)$ at 6,824 particle exit locations for the ECPM reference case release times (from top to bottom) 2,020 AD, 3,000 AD and 9,000 AD. Also, the HCD model at z=–400 m (purple), roads and buildings (black).*

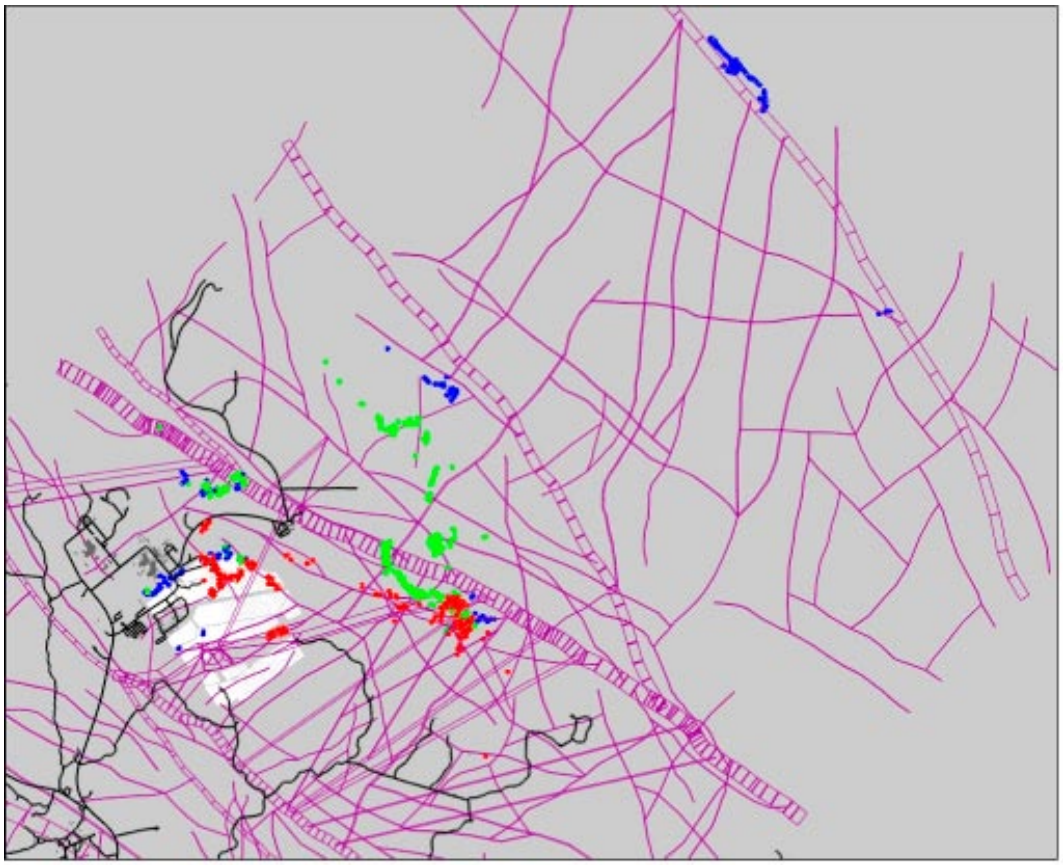

Figure 3-27. *Exit locations for particles coloured by release time; 2,020 AD (red), 3,000 AD (green) and 9,000 AD (blue) for the ECPM reference case. A section through the HCD model at z=–30 m is superimposed (purple). The repository is shown in white and roads are shown in black for context.*

For all release times one can find areas of low F-quotients side by side with areas of high F-quotients. These effects reflect the heterogeneity of the model and that the gently undulating surface topography leads to some localised flow cells.

In Figure 3-26 and Figure 3-27 it is seen that there is a localised discharge area in the north-west than persists for all times, while other particles discharge at the coast as it evolves in time, and by 9,000 AD become lakes that form as depressions in the seabed are exposed as the land-rises. This is also seen nicely in the particle trajectories shown in Figure 3-28.

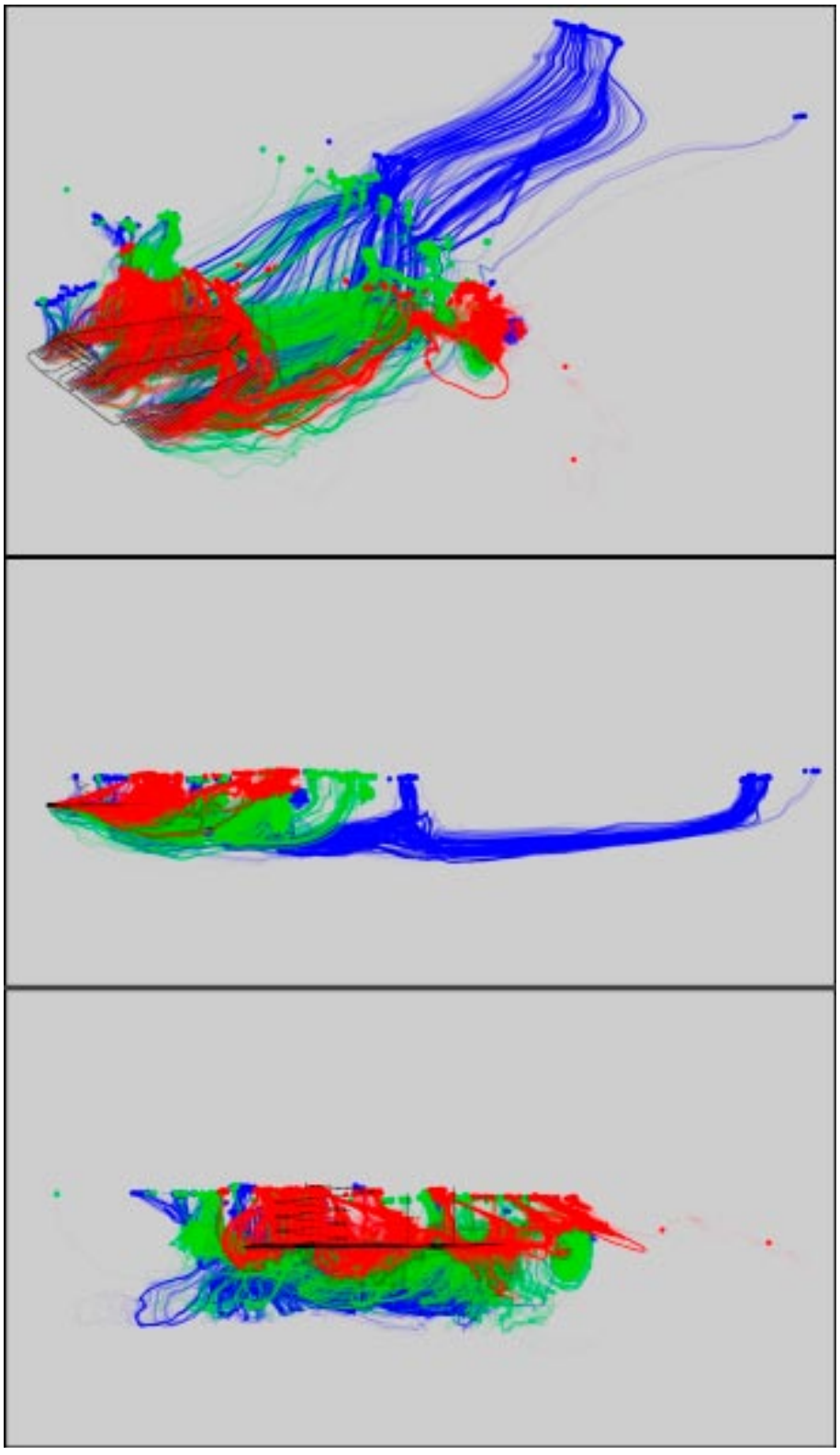

Figure 3-28. *Flow-paths and exit locations for particles coloured by release time; 2,020 AD (red), 3,000 AD (green) and 9,000 AD (blue) for the ECPM reference case. Top: oblique view. Middle: vertical section, SW-NE. Bottom: vertical section NW-SE. The repository is shown in shown in black for context.*

3.2.5 Performance measures

One of the main questions we wanted to address using this case was: what representative times should we use for quantifying PMs for PA calculations? It was achieved by calculating particle-tacks for release times every thousand years from 2,020 AD to 9,000 AD and calculating various PM statistics. The statistical results for the ECPM reference case are shown in Figure 3-29 as bar and whisker-plots for the key PMs: t_r, U_r, and F_r, respectively. The statistics are calculated in $\log_{10}$ space. There is a clear and general trend that at around 3,000 AD–4,000 AD the flow field around the repository area is subject to major changes. At this time the shoreline moves away from the vicinity of the repository and the head gradients are changed significantly. The flow pattern in the candidate area is quite complex due to the sharp changes in hydraulic properties between the very tight rock in RFM017 and RFM029 and the surrounding more conductive rock mass outside the candidate area. The flow tends to veer downward when leaving the candidate area and the shape of this deflection in the path is highly affected by the changing head gradients as the shoreline moves away. This is the probable explanation to the peaks in performance measure values that are seen in the statistical results. The travel times are quite stable over time with a peak at 3,000 AD to 4,000 AD. The inter quartile range does not change much in time. The same accounts for the initial Darcy velocity. The F-quotients however shows a different behaviour. The median F-quotients increases up to 4,000 AD and then drops while the 75th and 95th percentiles stay at a high level. The results tell us that for all times there are both very short and very long particles to be found. The decrease of the median value at later times is due to the flattening of the flow-paths compared to early times when particles initially went deeper into the model. The same effects can be observed for the F-quotient.

Based on these plots the following times were selected for use in the particle tracking and considering Figure 3-29 are representative of different stages in the future evolution of transport:

- **2,020 AD:** to represent approximately 2,020 AD–2,500 AD.
- **3,000 AD:** to represent approximately 2,500 AD–4,500 AD.
- **9,000 AD:** to represent approximately 4,500 AD–9,000 AD.

These times will be used for all the following transport calculations to quantify and compare cases.

Cumulative distribution plots of the PMs are shown in Figure 3-30 for the eight release times. There is large heterogeneity in all PMs, especially t_r and F_r. Velocity, U_r, shows the least sensitivity to the release time probably since it only depends on the magnitude of velocity and not on the direction and overall flow-path as with the other measures. Generally, the tails of the distributions in t_r and F_r get longer as the flow-path toward the sea gets longer and longer. The minimum value in F-quotient, F_r, seems to remain fairly constant around 5.5 in $\log_{10}$ space.

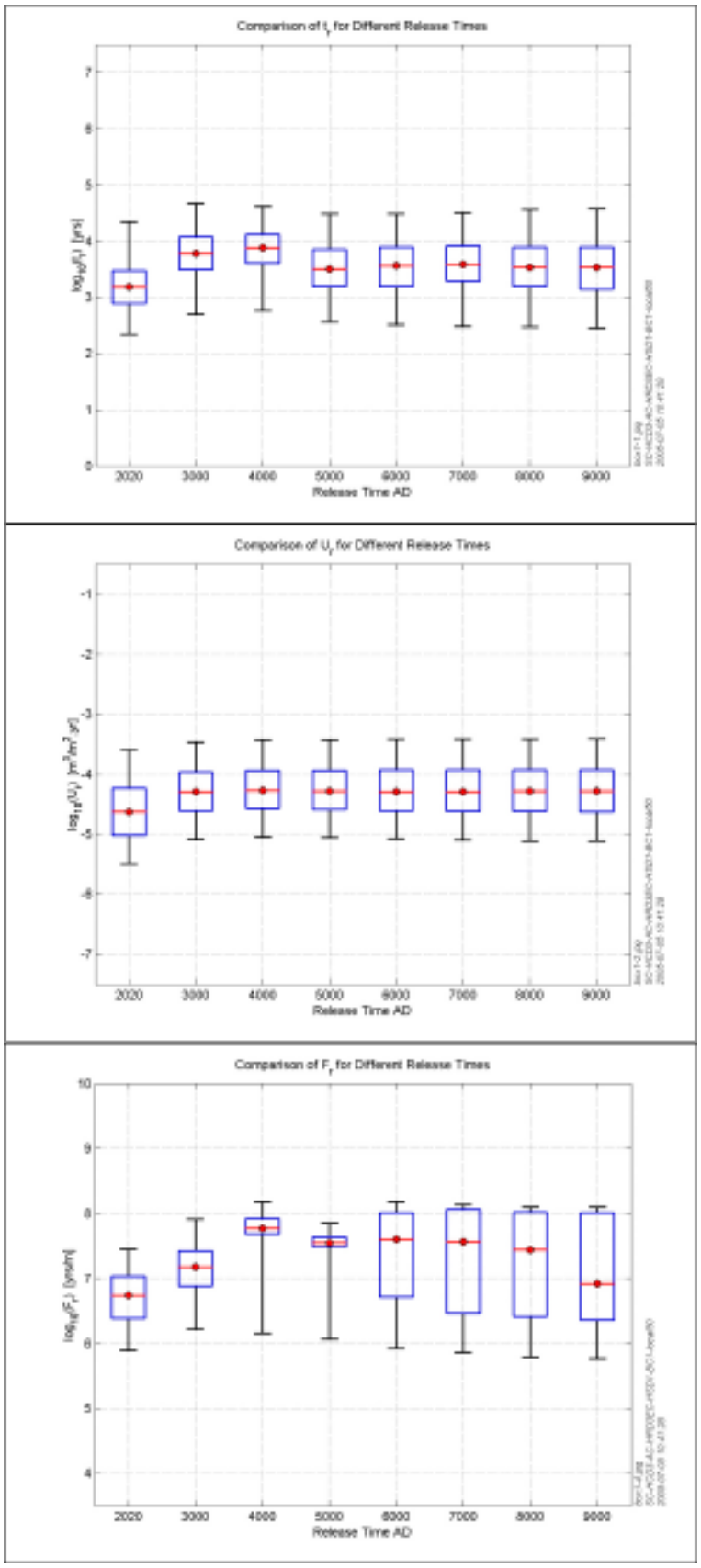

Figure 3-29. *Bar and whisker-plots for the ECPM reference case with 6,824 particles released every thousand years from 2,020 AD to 9,000 AD. From the top: t_r, U_r, and F_r. The statistical measures are the median (red), 25th and 75th percentile (blue bar) and the 5th and 95th percentile (black "whiskers").*

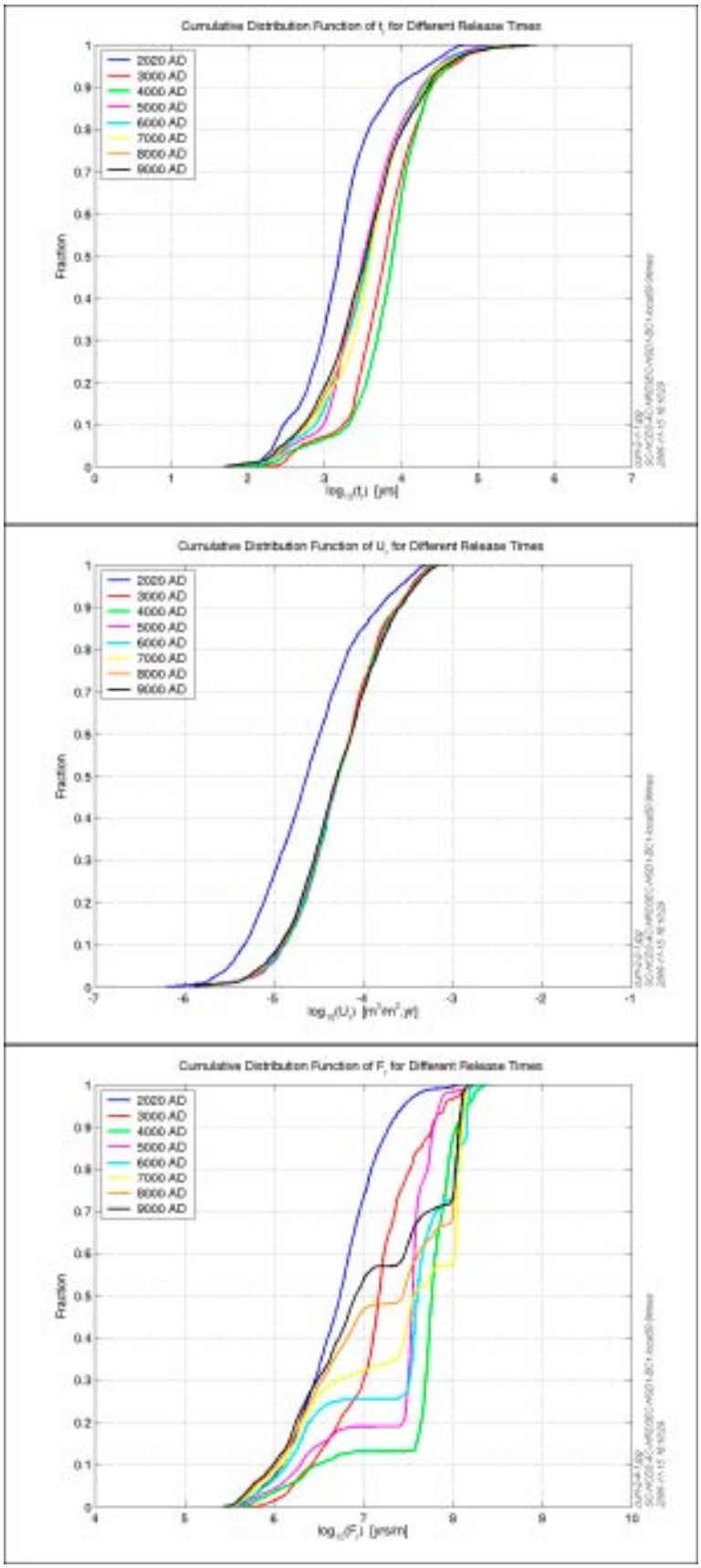

Figure 3-30. *Cumulative distribution plots for the ECPM reference case with 6,824 particles released at different times 2,020 AD–9,000 AD. From the top: t_r, U_r, and F_r.*

3.3 Sensitivities

Here a more comprehensive set of sensitivities are considered than was possible in the site-modelling of SDM F 1.2, and more emphasis is put on the sensitivity of PA performance measures rather than model calibration.

3.3.1 Summary of applied regional model cases

The main sensitivities addressed within this study are:

- Alternative conceptual models.
- Alternative geological models.
- Hydro-DFN parameters.
- HCD transport properties.
- HRD hydraulic properties.

The ECPM reference case has already been discussed thoroughly in the preceding sections. A summary of the main regional-scale variants considered about the ECPM reference case are listed in Table 3-4. The list uses a colour coding to highlight the key sensitivity they were designed to address. The corresponding DFN models used within these cases are listed in Table 3-5. Each of the key sensitivities and associated variants are discussed in the following sections.

For each of these variants, transient calculations were performed for groundwater flow and reference water transport from 8,000 BC until 9,000 AD, and the following results were collated:

1. Spatial distributions of groundwater chemistry (as mixing fractions (reference waters), constituents (major ions and environmental isotopes) and salinity) in boreholes.
2. Hydraulic conductivities in boreholes.
3. Darcy velocity distribution.
4. Pressure distribution.
5. Performance measure statistics (travel time (t_r), initial velocity (U_r), pathlength (L_r) and F-quotient (F_r)) for particles released from each of the canister locations.
6. Particle exit locations.

Using these results the variants are then ordered according to sensitivity of the PMs and group into three ranks of sensitivity: 1 (significant), 2 (moderate), 3 (negligible). For brevity only a selection of variants that have sensitivity of rank 1 are presented in this section. Results for three selected release times; 2,020 AD, 3,000 AD and 9,000 AD will be shown in terms of flow-paths (particle exit locations) and distribution of F-quotient (at particle starting and exit locations). The flow-path analysis provides two important results. Firstly, it provides a set of PMs for quantifying the groundwater flow situation that can be used to compare variants and quantify uncertainties. Secondly, it helps with the identification of discharge areas.

Table 3-4. Summary of the main regional-scale model cases performed. The cases are grouped by colour coding according to the sensitivities they quantify: Conceptual model (white); Geological model (yellow); DFN cases (green); HCD transport properties (blue); HRD hydraulic properties (purple).

Case description SR-Can Forsmark v1.2	Sensitivity	Properties	Description
SC_HCD3_AC_HRD3EC	Conceptual model	ECPM – Correlated T/L (Volume E DFN)	ECPM reference case (SDM F 1.2 CONNECTFLOW)
SC_HCD3_AC_HRDDT	Conceptual model	CPM	CPM base case (SDM F 1.2 DarcyTools)
SC_HCD3_BC_HRD3EC	Geological model	ECPM – Correlated T/L	Base Case (BC) Geological model to demonstrate differences
SC_HCD3_AC_HRD3A2_T	DFN	ECPM	Lower transmissivity (1/10) below ZFMNE00A2
SC_HCD3_AC_HRD3A2_P32	DFN	ECPM	Lower open P_{32} (1/2) below ZFMNE00A2
SC_HCD3_AC_HRD3ES	DFN	ECPM – Semi-correlated T/L	DFN – Semi-correlated T/L
SC_HCD3_AC_HRD3EU	DFN	ECPM – Uncorrelated T/L	DFN – Uncorrelated T/L
SC_HCD3_AC_HRD3SA2_T	DFN	ECPM – Semi-correlated T/L	Lower transmissivity (1/10) below ZFMNE00A2, DFN – Semi-correlated T/L
SC_HCD3_AC_HRD3UA2_T	DFN	ECPM – Uncorrelated T/L	Lower transmissivity (1/10) below ZFMNE00A2, DFN – Uncorrelated T/L
SC_HCD3_AC_HRD3EC2	DFN	ECPM	Stochastic DFN Realisation 2 of the ECPM reference case
SC_HCD3_AC_HRD3EC3	DFN	ECPM	Stochastic DFN Realisation 3 of the ECPM reference case
SC_HCD3_AC_HRD3EC_VG	DFN	ECPM	Variant Geo-DFN; fracture radius distribution (slope=2.75)
SC_HCD3N2_AC_HRD3EC	Transport properties	ECPM	HCD – lower kinematic porosity in FZs
SC_HCD3N3_AC_HRD3EC	Transport properties	ECPM	HCD – lower kinematic porosity in FZs, $n_e=10e_t/b$
SC_HCD3F3_AC_HRD3EC	Transport properties	ECPM	HCD – lower a_r = 4/width
SC_HCD3_AC_HRD3ECK2	Hydraulic properties	ECPM	HRD – higher hydraulic conductivity in top 100 m

Table 3-5. Summary of the main regional-scale DFN models generated.

Case description SR-Can Forsmark v1.2	Sensitivity	Properties	Grid	Length truncation
K_base_VolE_corr (for SC_HCD3_AC_HRDEC, etc.)	Reference case for ECPM	Volume E (KFM03A) Correlated *T/L*	Refined grid (50 m) for repository patch, and KFM02A and KFM03A patch. Tectonic lens has 100 m grid.	L_{min}=12.5 m local, 25 m regional
K_base_VolE_uncorr (for SC_HCD3_AC_HRD3EU)	*T* vs. *L* relationship	Volume E (KFM03A) Uncorrelated *T/L*	As above	As above
K_base_VolE_semicorr (for SC_HCD3_AC_HRD3ES)	*T* vs. *L* relationship	Volume E (KFM03A) Semi-correlated *T/L*	As above	As above
K_base_VolE_corr_variantGeoDFN (for SC_HCD3_AC_HRDEC_VG)	Power-law K_r	Volume E (KFM03A) Correlated *T/L*, variant GeoDFN	As above	As above
K_base_VolE_corr_A2_P32 (for SC_HCD3_AC_HRD3A2_P32)	Lower P_{32} under A2	Volume E (KFM03A) Correlated *T/L*, half lower P_{32} below ZFMNE00A2	As above	As above
K_base_VolE_corr_A2_T (for SC_HCD3_AC_HRD3A2_T)	Lower *T* under A2	Volume E (KFM03A) Correlated *T/L*, tenth lower *T* below ZFMNE00A2	As above	As above
K_base_VolE_corr2 (for SC_HCD3_AC_HRD3EC_2)	Reference case – Realisation 2	Volume E (KFM03A) Correlated *T/L*	As above	As above
K_base_VolE_corr3 (for SC_HCD3_AC_HRD3EC_3)	Reference case – Realisation 3	Volume E (KFM03A) Correlated *T/L*	As above	As above

3.3.2 Sensitivity to conceptual model

The first sensitivity we consider is to the choice of conceptual model, i.e. CPM versus ECPM.

CPM base case (SC_HCD3_AC_HRDDT)

A summary of the results for the CPM base case are given here to show the sensitivity of the groundwater flow and hydro-geochemistry to the alternative conceptual model.

Description of past evolution

Given the difference in conceptual model for the CPM case, the comparison with field-data is also given for this model.

Reference waters

Figure 3-31 to Figure 3-34 show the calibration of the CPM base case against the four interpreted reference water profiles for the cored boreholes KFM01A to KFM04A. The mixing fractions in both the fracture system and matrix are shown. Below the calibration is discussed for each of the cored boreholes separately. As in the ECPM model, a_r=0.25 m^2/m^3 which gives a lag between the concentration in the matrix to the fracture system. For this value of a_r it takes of the order of 5,000 years for diffusion into the matrix blocks for the fracture system, and hence there is a lag of about 5,000 years in the groundwater chemistry between pore-water chemistry and that in the fractures. For example, meteoric water than entered the top surface only after the site rose form the sea 1,000 to 2,000 years ago has infiltrated the top 200 m of rock, but the matrix still contains large amounts of Marine water from the Littorina phase. In SDM F 1.2, a larger flow wetted surface was used, a_r=1.0 m^2/m^3, which gives a much shorter lag of about 300 years and hence little difference between fracture and matrix pore-water chemistry.

KFM01A. Figure 3-31 shows that the calibration in the top 300 m is similar to the ECPM model. This is because the properties in Volume B in the CPM model are similar to those in the ECPM model based on Volume E. However, below 350 m depth the CPM model uses a lower hydraulic conductivity in Volume D which leads to less penetration of the Marine pulse with a transition from Marine to Glacial at about 500 m depth rather than 800 m in the ECPM model. However, there is no data yet to confirm whether this is more realistic.

KFM02A. In Figure 3-32 the CPM model predicts a shallower penetration of Marine water and less flushing of Glacial than in the ECPM model. Marine water is seen from about 300 m to 600 m depth, whereas it penetrated to 800 m in the ECPM model. Again this is due to the low hydraulic conductivity in Volume B below 500 m depth. Data also indicates a more gradual transition and faster transport of Rain 1960 and Marine down to 500 m depth while both models show a sharp transition around 250 m depth. Again, there are no data to confirm the deep profiles of Brine and Glacial waters.

KFM03A. Figure 3-33 shows that the CPM model gives a very similar prediction to the ECPM model for this borehole. This is because the hydraulic conductivity for Volume A in the CPM model is similar to that in Volume E in the ECPM model. The data suggest 50% Marine water close to the surface which could not be reproduced by the SDM F 1.2 model. In these models however, the FWS is relatively low and the effect is that even if the Marine fraction in the fracture system is still low, the matrix now shows a considerably higher fraction of Marine water close to the surface. That is, again the Marine fraction is more similar to the model prediction in the matrix than the fracture system. The Glacial water profile is predicted reasonably.

KFM04A. Figure 3-34 shows that the model reasonably predicts the data at 250–300 m depth, but can not reproduce the surface water composition with high fractions of Marine water. Compared to the ECPM model, the Marine water only penetrates to about 600 m rather than 800 m depth, as the borehole enters the low conductivity Volume D at about 500 m depth.

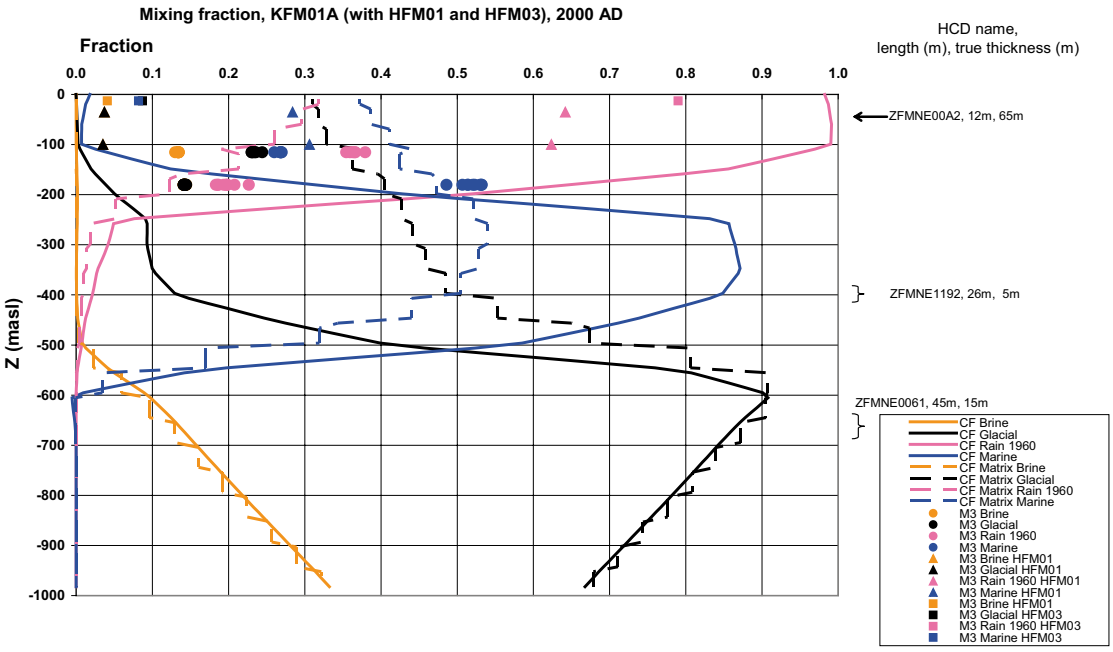

Figure 3-31. *Comparison of 4 reference water fractions in KFM01A for the CPM base case. The mixing fractions in the fracture system are shown by solid lines, in the matrix it is dashed, and the data by points.*

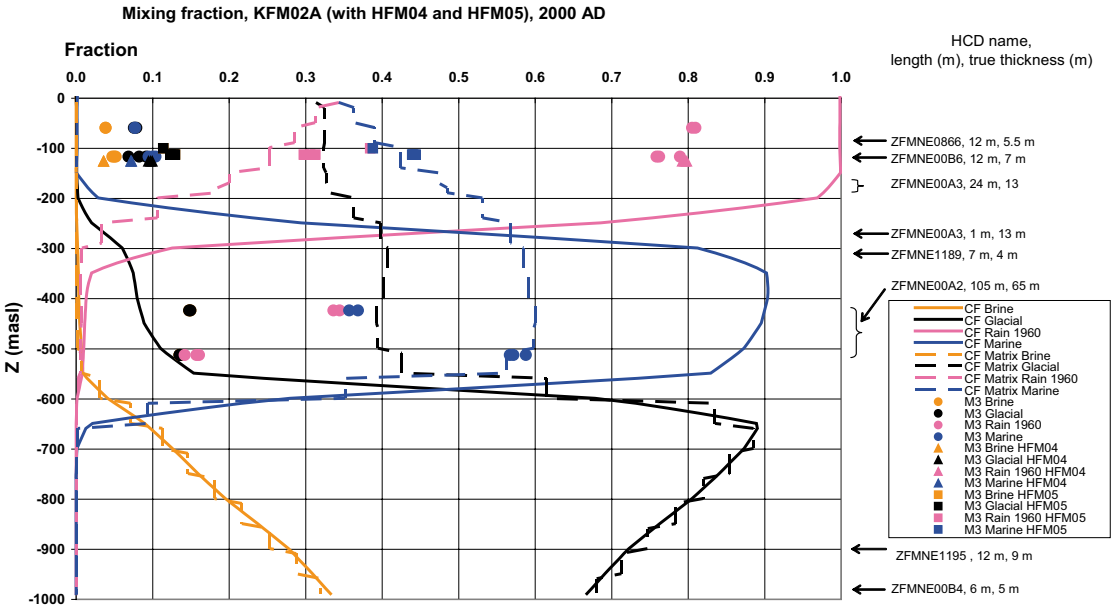

Figure 3-32. *Comparison of 4 reference water fractions in KFM02A for the CPM base case. The mixing fractions in the fracture system are shown by solid lines, in the matrix it is dashed, and the data by points.*

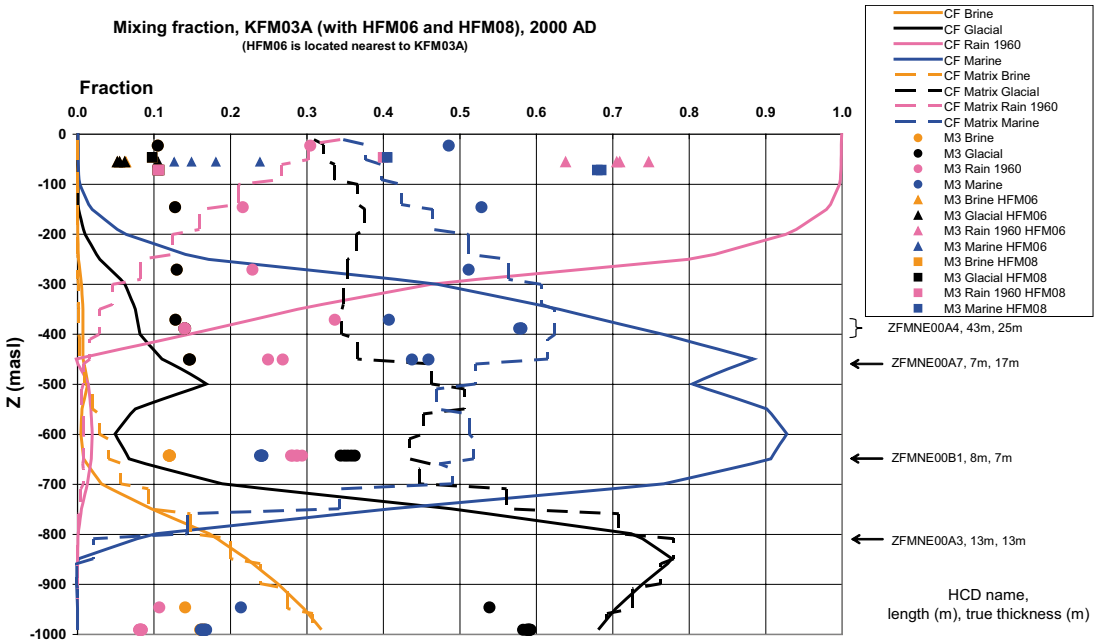

Figure 3-33. *Comparison of 4 reference water fractions in KFM03A for the CPM base case. The mixing fractions in the fracture system are shown by solid lines, in the matrix it is dashed, and the data by points.*

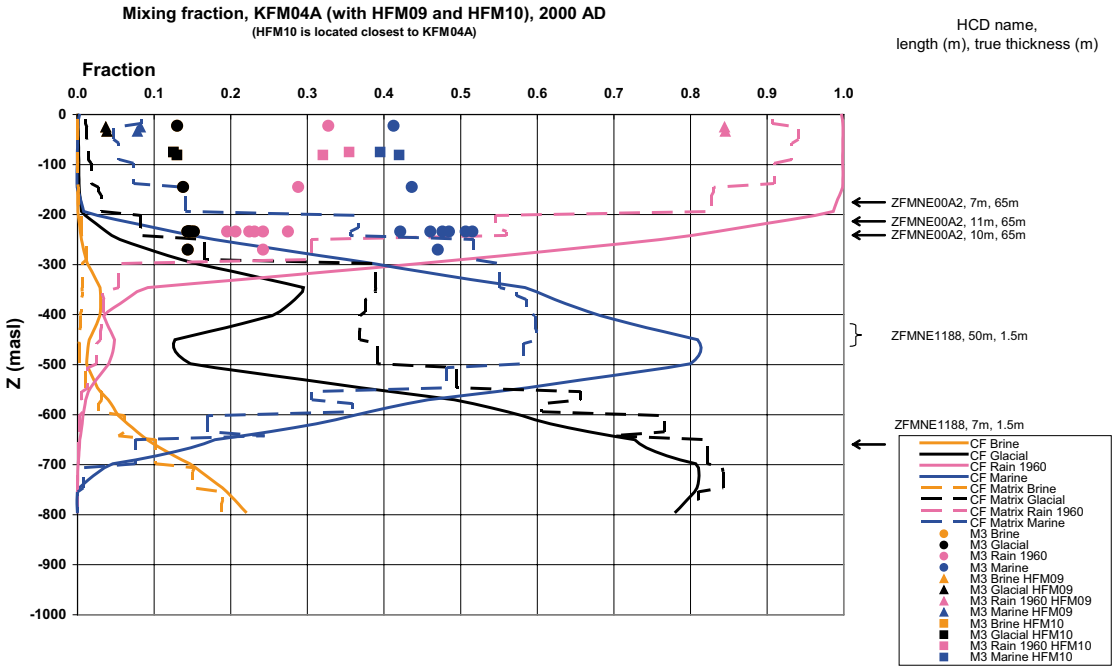

Figure 3-34. *Comparison of 4 reference water fractions in KFM04A for the CPM base case. The mixing fractions in the fracture system are shown by solid lines, in the matrix it is dashed, and the data by points.*

Salinity

Figure 3-35 shows the calculated salinity profiles in the fracture system compared to measured data in KFM01A–KFM04A for the CPM base case. Salinity closely follows the profile of Brine, although there is also a contribution from the Marine reference water. The results are similar to the SDM F 1.2 study, with a smooth trend of salinity with depth. Except for KFM02A, the model still under-predicts salinity above 200 m depth and is very similar to the ECPM model. It would be interesting to see how salinity in the matrix compares with the data also. The most significant effect being that the salinity temporarily decreases around 600 m depth in the CPM model due to the persistence of a pulse of Glacial water under the Marine. It suggests that salinity is not strongly dependent on the conceptual model for the range of hydraulic conductivities considered, and is probably more dependent on initial and boundary conditions.

Major ions and environmental isotopes

Figure 3-36 shows the profiles of the three constituents, $\delta^{18}O$, Cl and Mg in KFM01A–KFM04A for the CPM base case. The error bars only indicate the laboratory analysis uncertainty of about 5%. This comparison of relatively conservative ions complements the more uncertain interpretation derived from the M3 analysis.

$\delta^{18}O$ allows the identification of Glacial water by a large negative ratio and differentiates between Rain 1960 and Glacial freshwaters. The model predictions are generally good where there are corresponding data. The CPM model suggests Glacial spikes below 500 m depth where only data from KFM03A is provided. The spikes are somewhat more pronounced than in the ECPM base case, but it is not clear which is the more realistic.

Cl indicates the presence of either Brine or Marine water. Mg is then used to differentiate between saline Marine (high Mg) and Brine (low Mg). The Cl profiles correlate to salinity which was discussed previously.

Mg is then used in combination with the Cl profiles to distinguish between salinity originating from Brine and salinity originating from Marine water. Data suggests a rather sharp transition between these two water types at about 500 m depth. This is correctly modelled by the CPM model while the ECPM model suggests a transition 200 m deeper down. Mg data also gives evidence for Marine water in the near surface for KFM01A, KFM03A and KFM04A which is not reproduced in the modelled fracture system, only in the matrix.

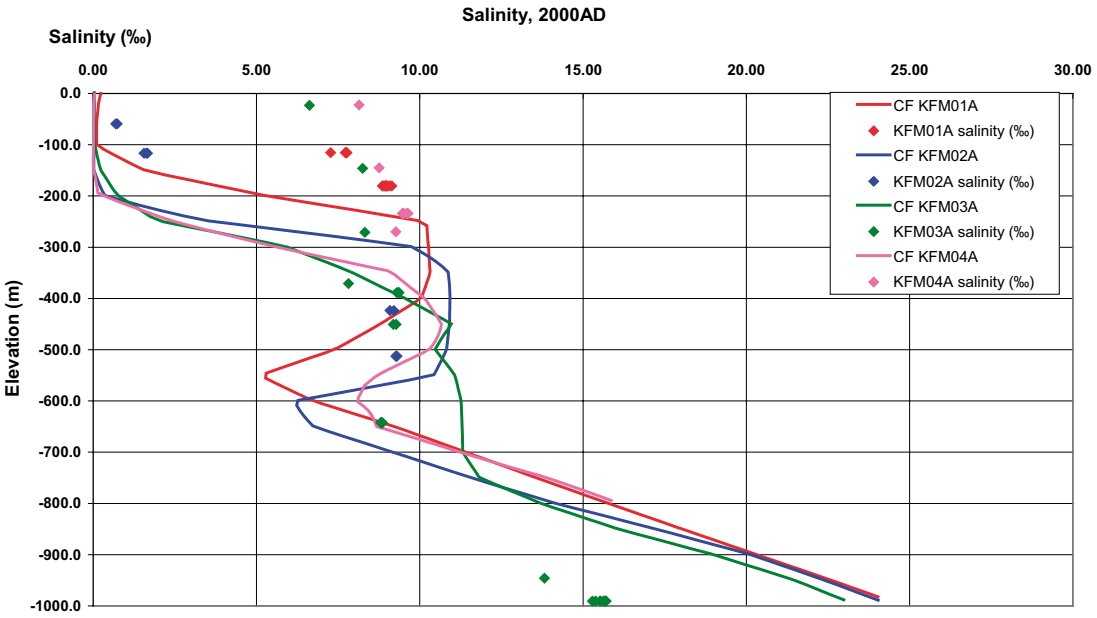

Figure 3-35. Comparison of salinity (TDS) in KFM01A–KFM04A for the CPM base case. The salinity in the fracture system is shown by solid lines and the data by points.

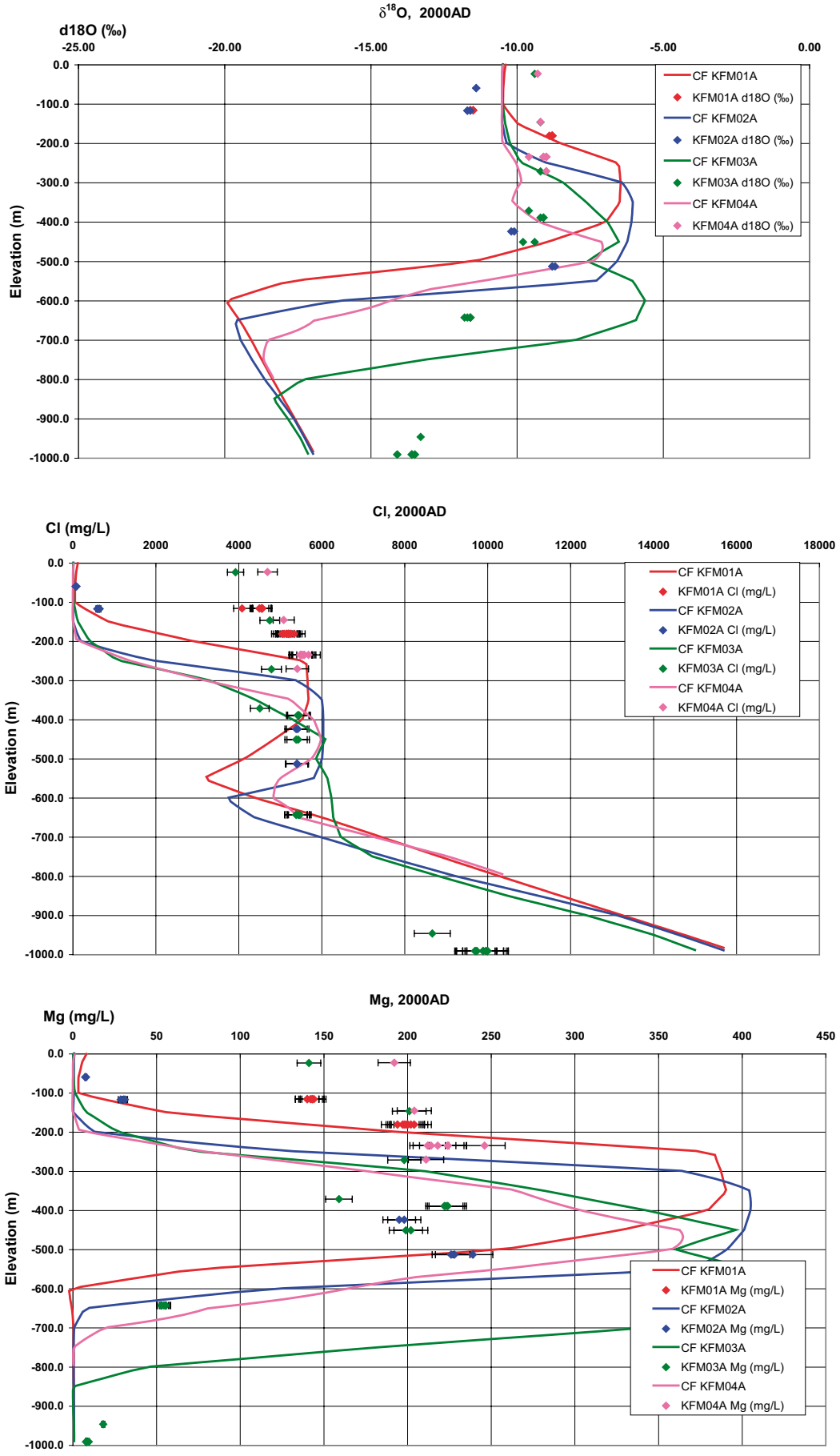

Figure 3-36. *Comparison of $\delta^{18}O$, Cl and Mg in KFM01A–KFM04A for the CPM base case. Values in the simulated fracture system are shown by solid lines and the data by points.*

Comparison of hydraulic conductivities in boreholes

Figure 3-37 to Figure 3-41 show the modelled and measured hydraulic conductivities in the CPM base case for boreholes KFM01A, KFM02A, KFM03A, KFM04A and KFM05A for the top 1,000 m of borehole. KFM01A, KFM02A and KFM03A are compared with the 100 m PSS data, while KFM04A and KFM05A are compared with the PFL anomaly data converted to an average conductivity over 100 m intervals. In the figures the depths and thickness of DZs in the geological model are indicated since they correlate strongly with the high conductivity intervals. The models use a 50 m grid refinement throughout the area characterised by boreholes.

The properties of the HCDs have been conditioned to 100 m PSS data, so the intervals with large hydraulic conductivity are reproduced reasonably well by the model. This is seen in all five boreholes. The main difference between the CPM and ECPM models can be found in the less conductive intervals. In the CPM model the background hydraulic conductivity is assigned explicitly to the model while the ECPM model uses an upscaled stochastic DFN model. Generally, the CPM model captures the low hydraulic conductivities (e.g. in KFM01A, bottom of KFM02A and KFM05A) better than the ECPM reference model which tends to over-predict the values. Clearly then the CPM model is more representative of the bulk properties in tight volumes of rock seen in the lower sections of boreholes in the candidate area. For this reasons some variants on the ECPM model with different fracture properties were constructed to be more consistent with the borehole hydraulic conductivity measurements. In Table 3-4 these are named SC_HCD3_AC_HRD3A2_T and SC_HCD3_AC_HRD3A2_P32. It has to be commented though that it would be optimistic to expect all rock encountered by the repository to be of such low hydraulic conductivity.

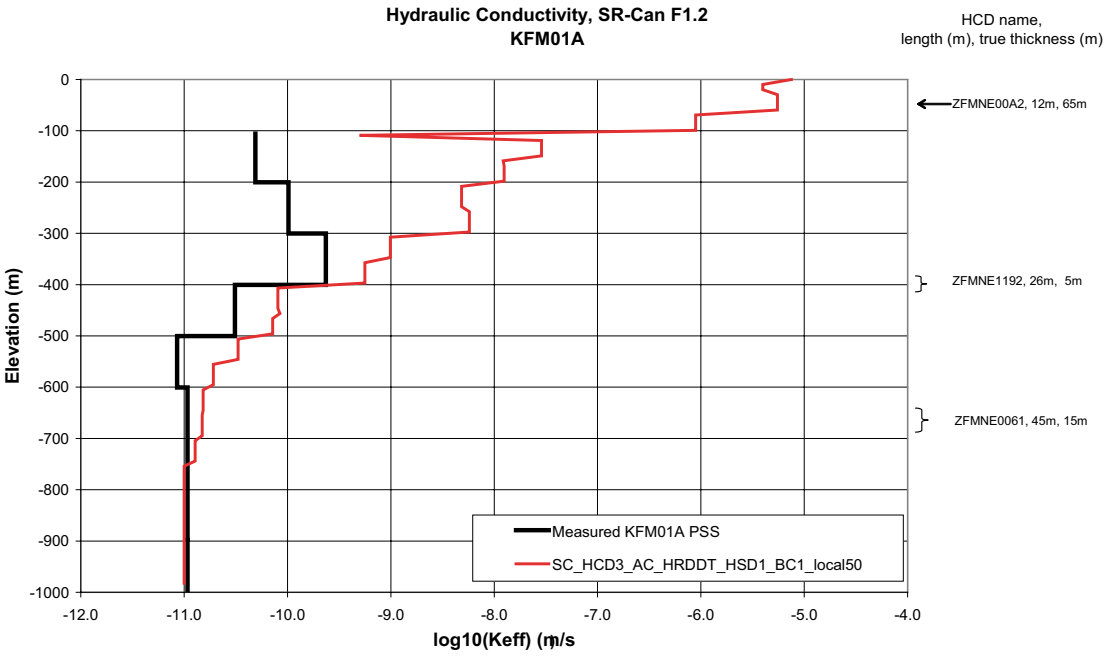

Figure 3-37. *Comparison of hydraulic conductivity in KFM01A for the CPM base case. Values simulated in the model are shown by red lines while the measured values in 100 m intervals are shown in black.*

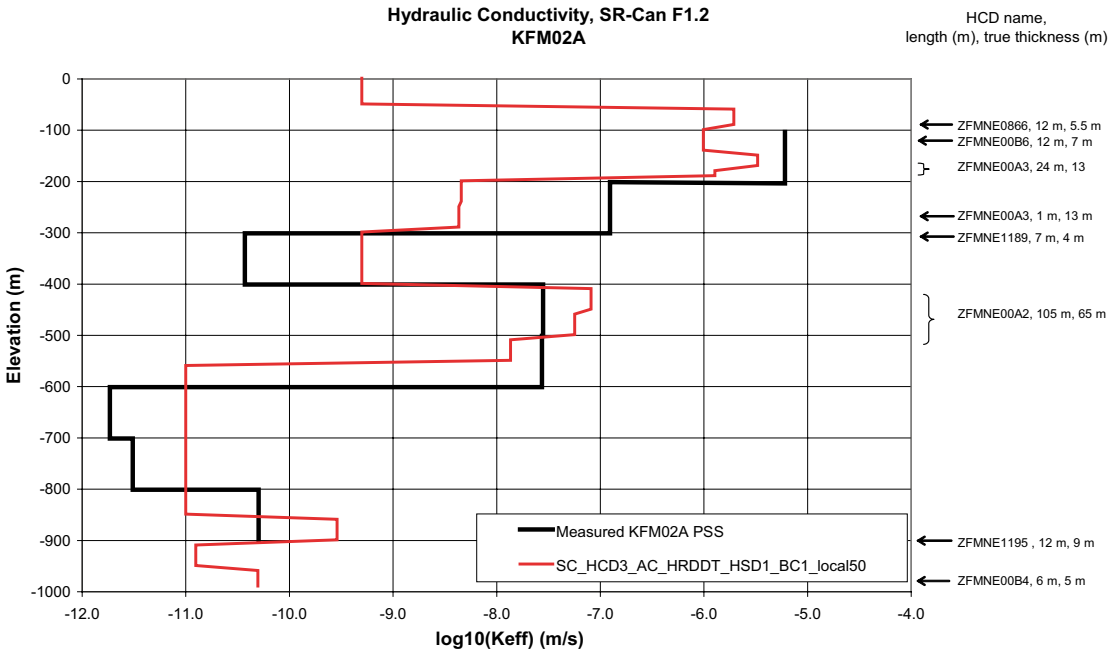

Figure 3-38. *Comparison of hydraulic conductivity in KFM02A for the CPM base case. Values simulated in the model are shown by red lines while the measured values in 100 m intervals are shown in black.*

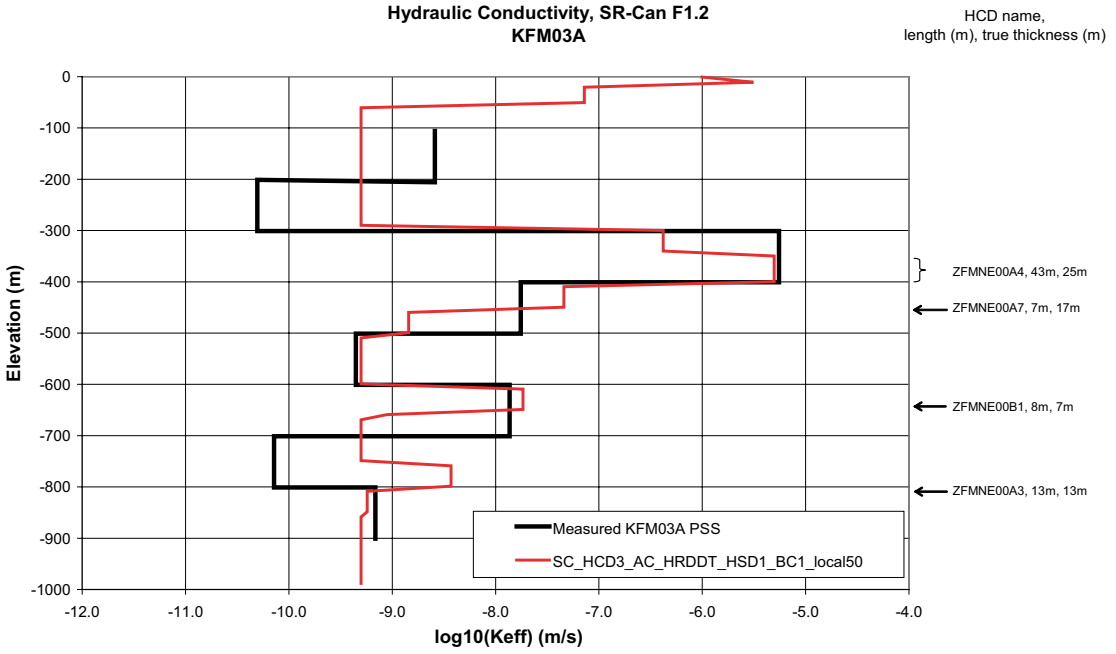

Figure 3-39. *Comparison of hydraulic conductivity in KFM03A for the CPM base case. Values simulated in the model are shown by red lines while the measured values in 100 m intervals are shown in black.*

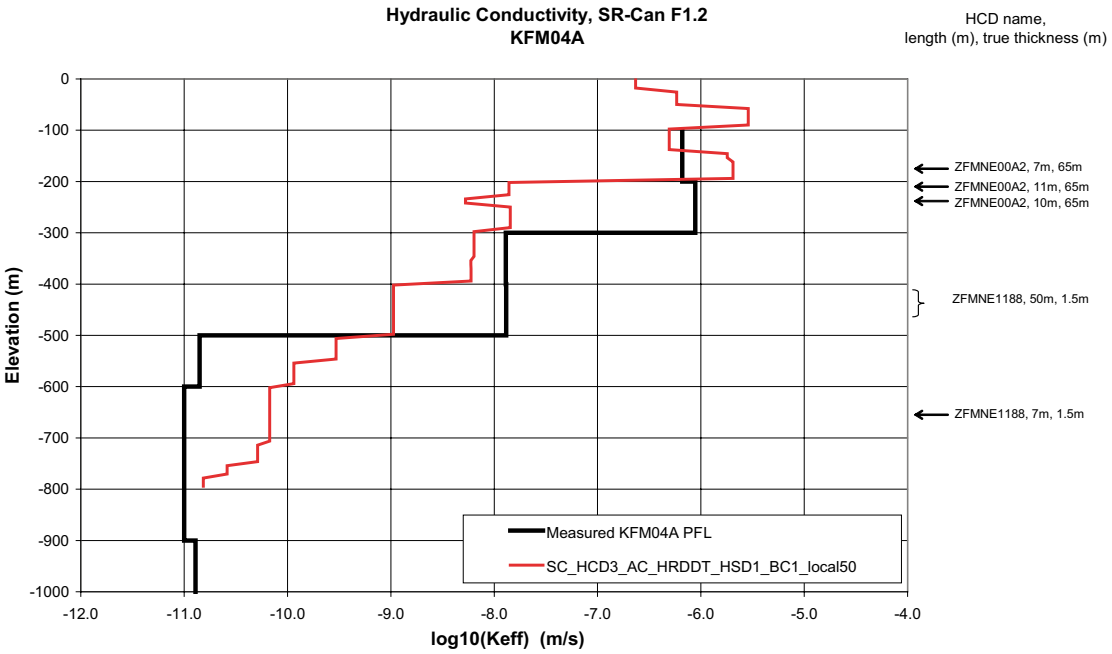

Figure 3-40. *Comparison of hydraulic conductivity in KFM04A for the CPM base case. Values simulated in the model are shown by red lines while the measured values in 100 m intervals are shown in black.*

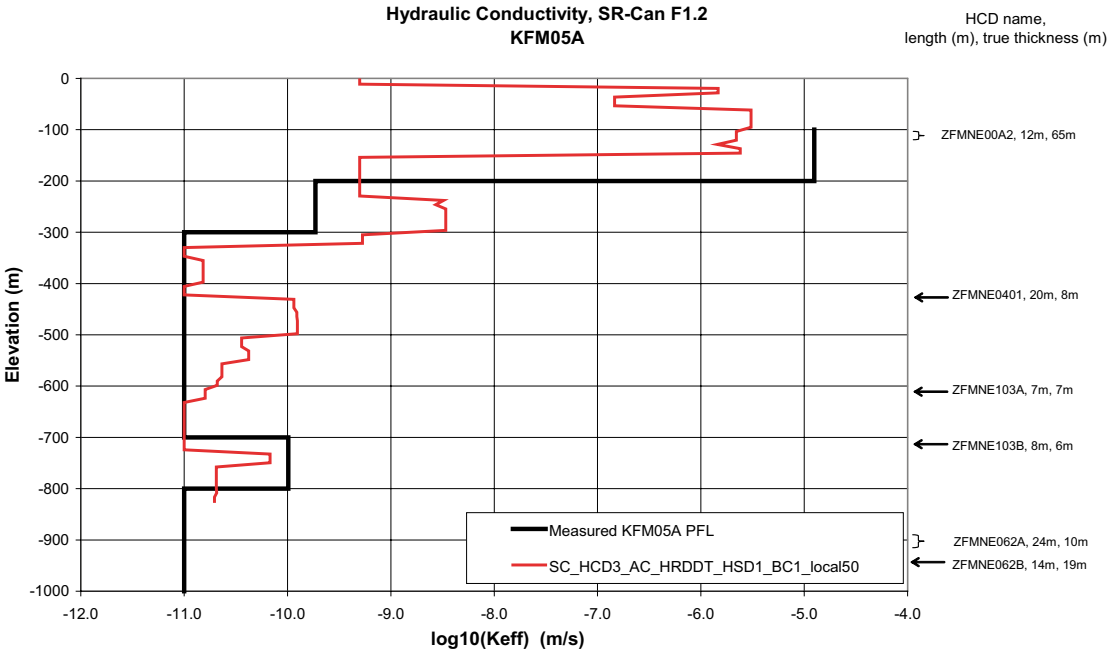

Figure 3-41. *Comparison of hydraulic conductivity in KFM05A for the CPM base case. Values simulated in the model are shown by red lines while the measured values in 100 m intervals are shown in black.*

Description of future evolution

The future evolution of the four reference waters Brine, Marine, Glacial and Rain 1960 for the CPM base case is shown in Figure 3-42 and Figure 3-43. The distributions of the different water types are presented in vertical slices at three times corresponding to: 2,020 AD, 3,000 AD and 9,000 AD. The fraction of each water type is calculated.

The CPM base case seemingly shows the same behaviour for the Brine as the ECPM reference case so the distribution is quite stable in time and only very slowly mixes with the infiltrating freshwater (Rain 1960).

Marine water penetrates less into the tighter CPM base case model compared to the ECPM reference case. The differences between the two models are restricted to the candidate area (local-scale area) where the less conductive rock of the CPM model effectively slows down the penetration of Marine water. Again it is clear how Marine water enters the system through the sloping sub-horizontal fracture zones. The differences between the cases are visible only at early times, and by 9,000 AD almost all Marine water has been replaced by infiltrating Rain 1960 in the system, as it did in the ECPM reference case.

Figure 3-43 again shows the effects of the less conductive local-scale area in the CPM base case. The Glacial water is left in the rock at substantially higher fractions even as late as 9,000 AD where there are still areas of around 100% Glacial water fractions.

At 2,020 AD there is little difference in the Rain 1960 distribution compared to the ECPM reference case. At 3,000 AD and 9,000 AD there is slightly less penetration in the CPM base case and so the Rain 1960 is found higher up in the rock of the local-scale area.

Recharge and discharge

In Figure 3-44 the distribution of Darcy velocity is shown on a vertical slice through the repository for three selected times: 2,020 AD, 3,000 AD and 9,000 AD. These times represent when the coast is at the site, when it has moved a few kilometres away, and at the end of temperate period when the coast is about 10 km away. The velocity is up around 1 to 100 m/y in the surface layers, but drops to about 10^{-7} to 10^{-5} m/y in rock domain RFM029/017. The pattern of flow for the simpler CPM case is more homogeneous than the ECPM model. It shows more clearly the evolution of velocity direction around the repository with time. At 2,020 AD flow is mainly upwards and then along the top of RFM029/017 discharging at the coast. At 3,000 AD flow is more horizontal and then dips down at the northern end of the tectonic lens where hydraulic conductivity increases. By 9,000 AD flow is downward to considerable depths. Hence, the period of highest flows and shortest paths is likely to correspond to early times around the present. In comparison with the ECPM case, this case has much lower flow velocities and paths tend to go deeper, so it can clearly be expected to give positive results for PA.

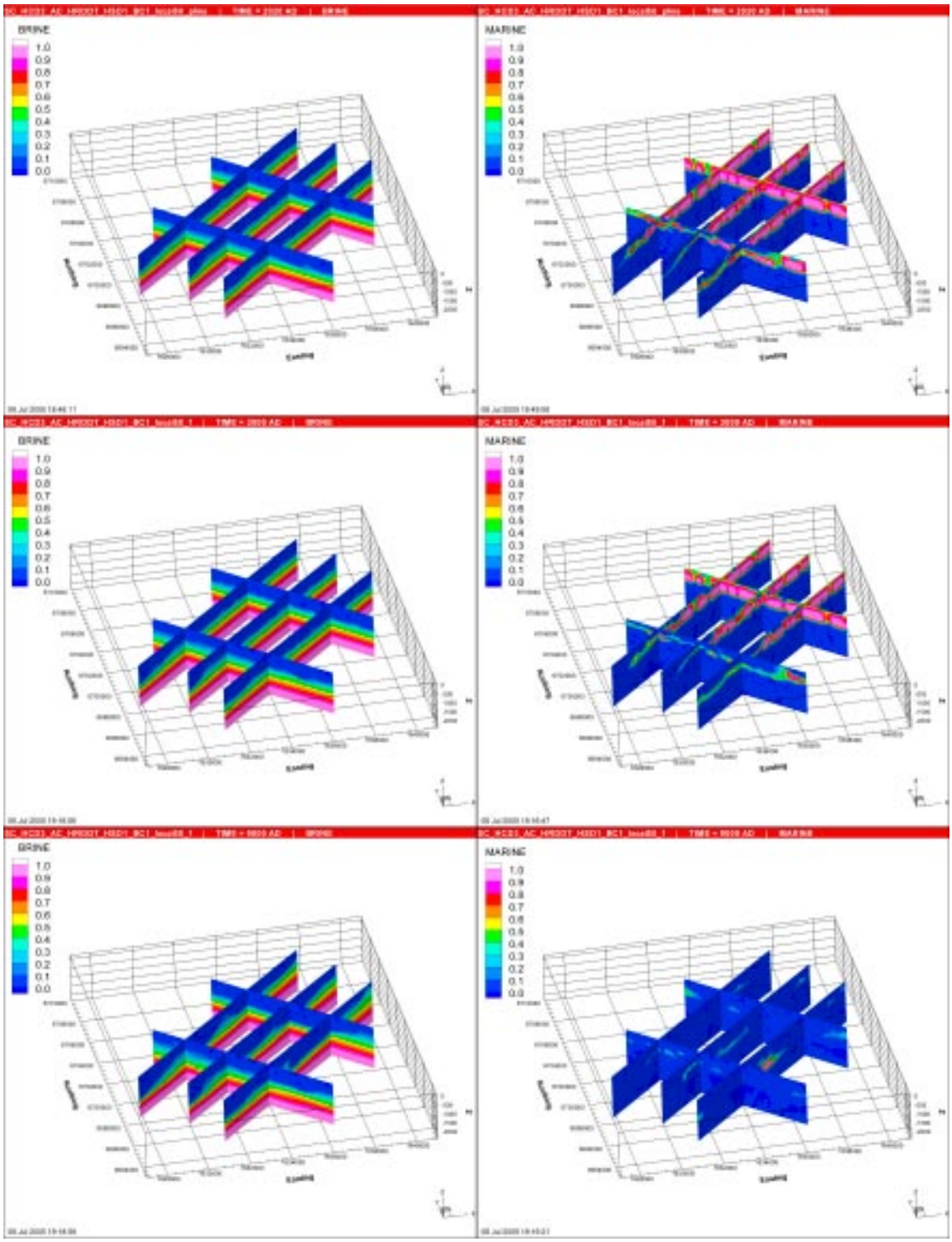

Figure 3-42. *Distribution of Brine (left) and Marine water (right) in vertical slices at times equal to (from top to bottom) 2,020 AD, 3,000 AD and 9,000 AD, for the CPM base case.*

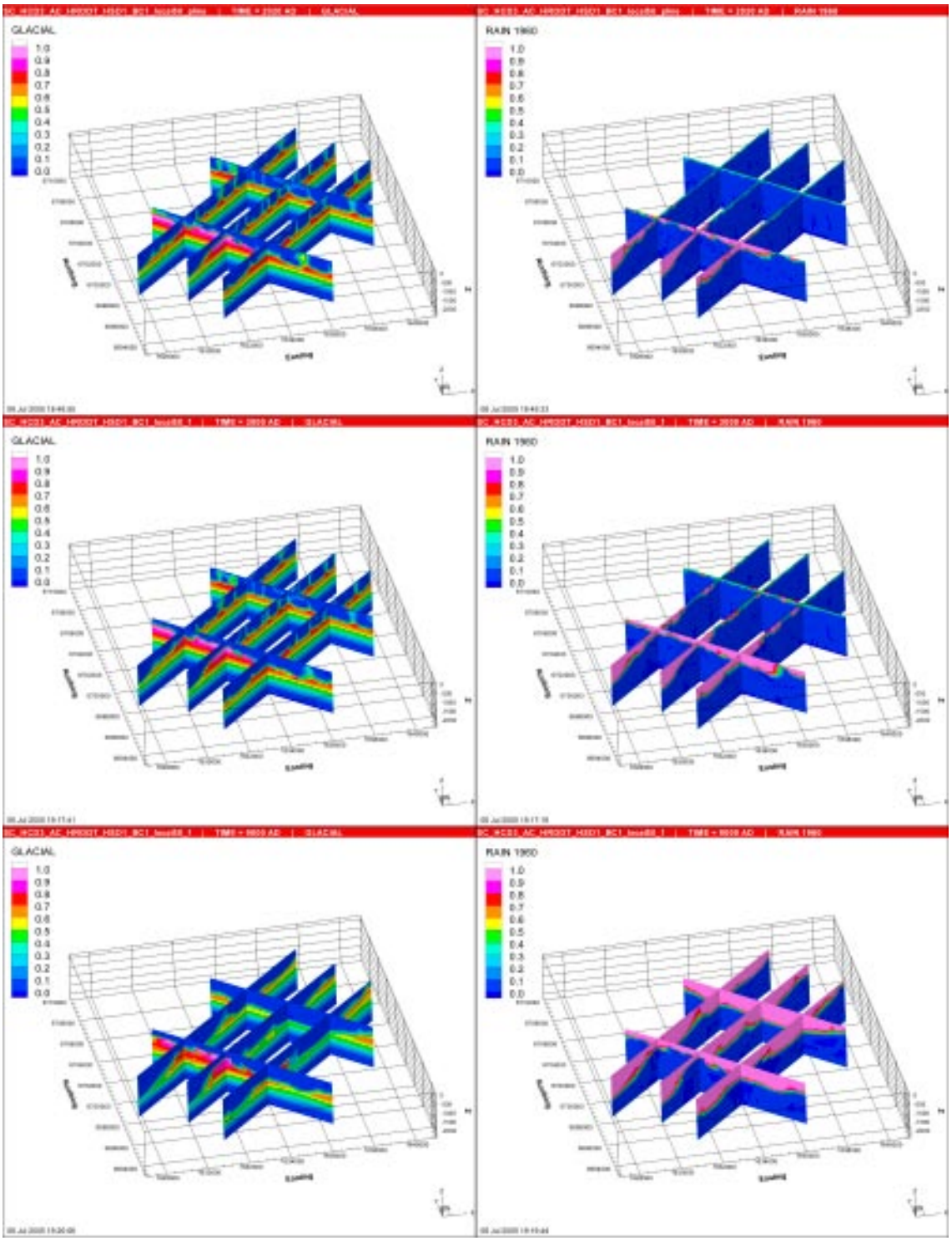

Figure 3-43. *Distribution of Glacial water (left) and Rain 1960 (right) in vertical slices at times equal to (from top to bottom) 2,020 AD, 3,000 AD and 9,000 AD, for the CPM base case.*

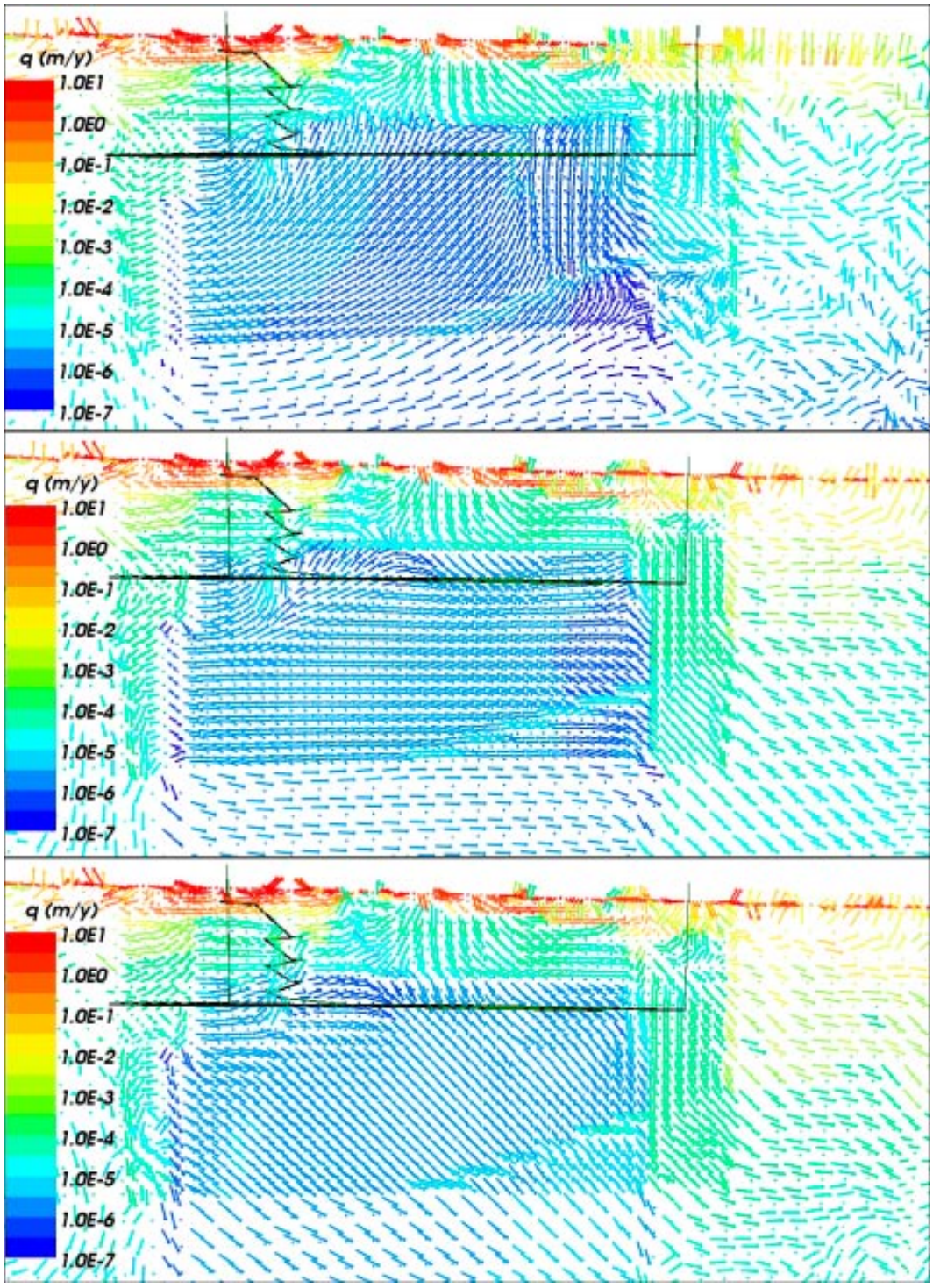

Figure 3-44. *Distribution of the Darcy velocity, q, in the CPM base case on a vertical slice from SW (left) to NE (right) through the repository. The repository is shown in black with the two vertical shafts and the ramp to the left. One velocity arrow is drawn per finite-element, which means there is a greater density of arrows in the central region where there is more refinement. From top to bottom: 2,020 AD, 3,000 AD and 9,000 AD. Arrows show the direction of velocity in 3D and the colour indicates the magnitude of the vector.*

Flow-paths

It is worth illustrating the flow-path calculations for the CPM model as the results are very different to the ECPM model. In Figure 3-45 the distributions of F-quotient ($\log_{10}$) at 6,824 particle starting locations in the repository for the CPM base case are presented. Results are shown for the three reference release times; 2,020 AD, 3,000 AD and 9,000 AD. The blue colour indicates smaller values (F-quotient about 10^4 y/m) and red indicates higher values (F-quotient about 10^9 y/m). Figure 3-46 shows the distribution of F-quotient ($\log_{10}$) at particle exit locations for the same three selected release times. Figure 3-47 shows the exit locations for particles coloured by release time; 2,020 AD, 3,000 AD and 9,000 AD. It has already been shown in Figure 3-44 that the Darcy velocities within the tectonic lens are generally about two orders of magnitude lower than in the surrounding rock at similar depths.

At 2,020 AD the flow in the repository is mainly upwards resulting in F-quotients of around 10^7 to 10^9 y/m. The highest F-quotients are found in the centre of the repository. The majority of the particles have short path-lengths of about 500–1,000 m, roughly corresponding to the shortest distance from the repository to the surface. In the south east part of the repository there are some particles with very high F-quotients and very long flow-paths. Caution should be paid to these particles since they are associated with numerical difficulties and become stuck just at the shoreline. No attempt is made to exclude failed particles from these pictures. Note: in the later statistical analysis below all stuck particles are removed to avoid skewing the results.

At 3,000 AD the shoreline has moved away a bit from the repository causing the flow pattern to change. In the northern part of the repository the flow is still directed upwards resulting in short flow-paths. But in the southern part of the repository area, the predominant flow direction is now downwards sending particles deeper into the model. At 3,000 AD we have the highest number of stuck particles. This is seen among the particles released in the southern part of the repository where we have very long flow-paths and high F-quotients. Almost 40% of the released particles are actually lost due to numerical problems in the particle tracking for this release time. Most of these particles are stuck out in a thin flow cell between the boundary of RFM029/17 and the shoreline.

At 9,000 AD a more reliable picture of what is going on is presented. This release time shows almost no lost particles. It is now very clear that the F-quotient, and also path-lengths, have increased due to changes in the flow-field. At this time we see that there are just a few spots in the repository with upward flow resulting in smaller F-quotient. The rest of the repository, where the predominant flow direction is downward, is covered with starting locations resulting in large F-quotients. There are a significant number of particles reaching all the way to the large fracture zone at the model boundary where the shoreline is at this time.

In general, the exit locations are associated with topographical low points and fracture zones. At early times, the released particles exit close to the repository similar to the ECPM model. Particles released later move deeper (down to 1,200–1,300 m depth) and further away. There is a clear correlation between long flow-paths and particles with high F-quotients for all release times and generally the longest flow-paths are found in the southern part of the repository. The longest flow-paths are not influenced greatly by the larger fracture zones, apart from the Singö fault zone at early times, as the flow direction is generally orthogonal to them. There may be other factors causing this result, such as a low contrast between fracture and bedrock properties at depth and the grid resolution in this area being only 100 m so that the high hydraulic conductivities in the zones get smeared out.

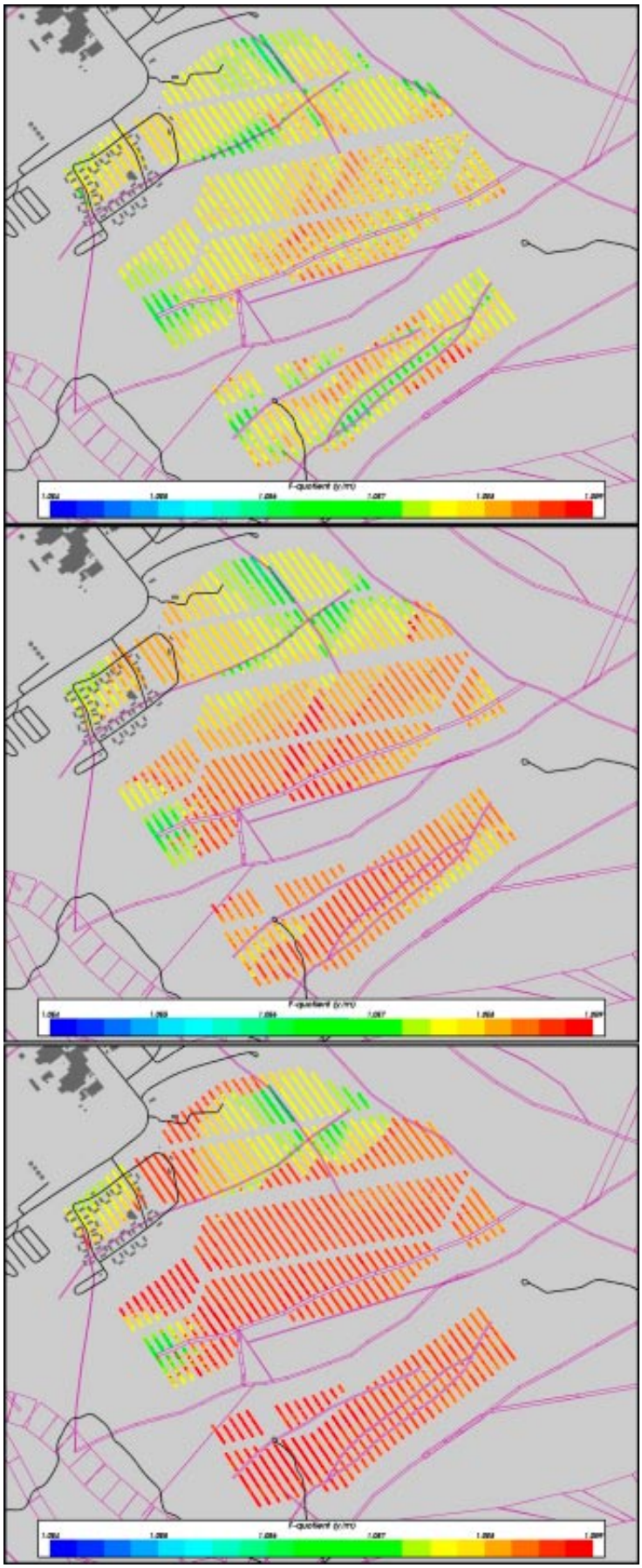

Figure 3-45. *Distribution of $\log_{10}(F_r)$ at 6,824 particle start locations for the CPM base case release times (from top to bottom) 2,020 AD, 3,000 AD and 9,000 AD. Also, the HCD model at z=–400 m (purple), roads and buildings (black).*

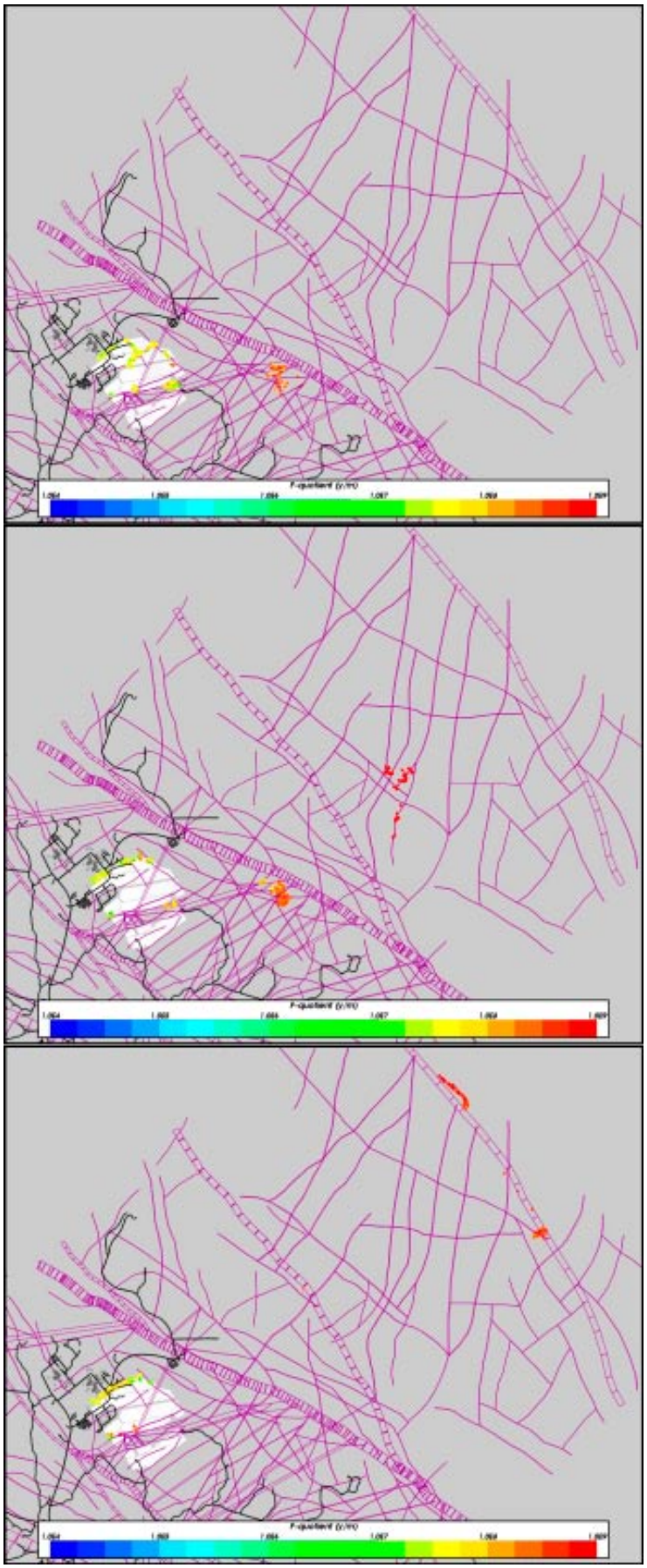

Figure 3-46. *Distribution of $\log_{10}(F_r)$ at 6,824 particle exit locations for the CPM base case release times (from top to bottom) 2,020 AD, 3,000 AD and 9,000 AD. Also, the HCD model at z=–400 m (purple), roads and buildings (black).*

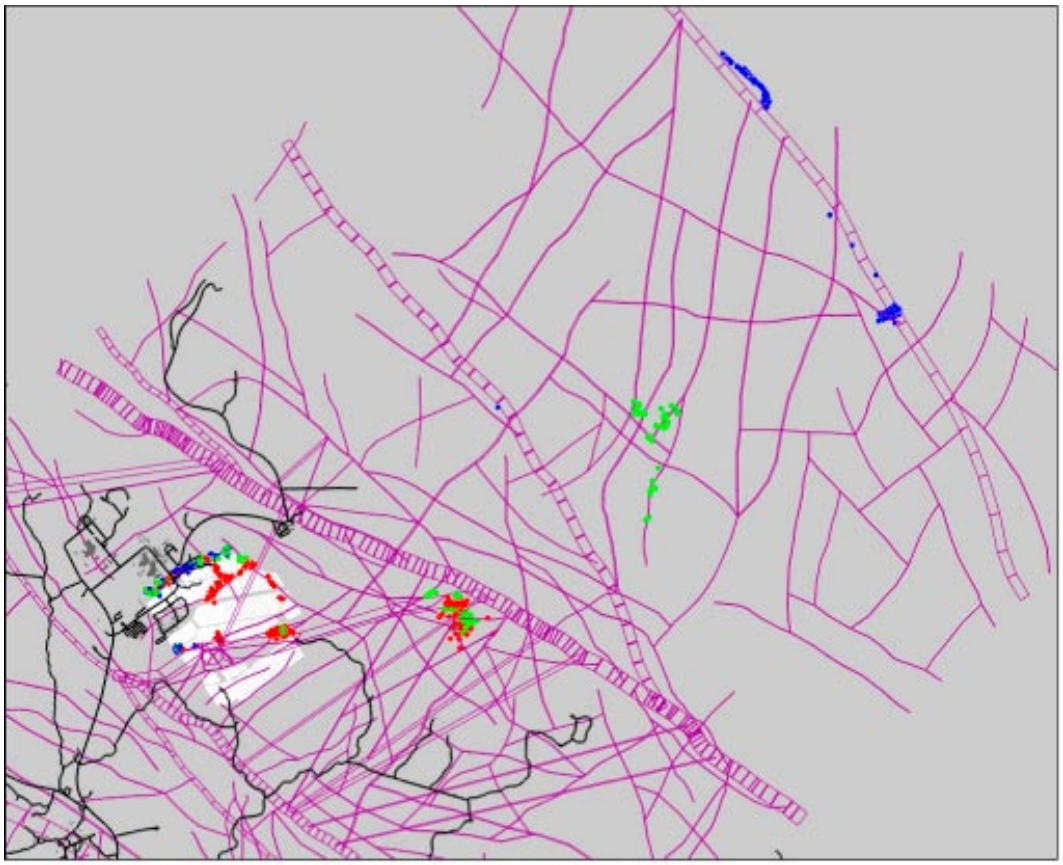

Figure 3-47. *Exit locations for particles coloured by release time; 2,020 AD (red), 3,000 AD (green) and 9,000 AD (blue) for the CPM base case. A section through the HCD model at z=–30 m is superimposed (purple). The repository is shown in white and roads are shown in black for context.*

Performance measures

A summary of the PMs for different release times is shown in Figure 3-48 and Figure 3-49. The bar and whisker plots confirm that the choice of reference release times is appropriate for this case also, and so we shall focus just on these three times from now on. It also shows that greatest risk is associated with a release at the present-day in terms both shorter travel times and smallest F-quotient. At 2,020 AD travel times are around 1,000 to 10,000 years, and then rises to around a 1,000,000 years at 3,000 AD and afterwards. This seemingly dramatic change is an artefact of altering the porosity in the model immediately after 2,020 AD to represent the introduction of a backfilled repository. The repository does not affect the retention properties in the rock, so the F-quotient changes a little more gradually, but still ranges from 10^7 y/m to over 10^8 y/m. The cumulative distribution plots in Figure 3-49 show a slight bi-modal behaviour in t_r and F_r, especially at later times, suggesting that the flow-paths are either very long, going through the homogeneous rock mass, or very short finding their ways through deformation zones present in the rock.

Compared to the ECPM model, F-quotients are about an order of magnitude higher and the distributions are much tighter due to the absence of heterogeneity. The initial Darcy velocity is about one and half orders of magnitude lower due to the lower hydraulic conductivities. It is interesting that the CPM model gives only slightly higher travel-times at 2,020 AD, but over two orders of magnitude afterwards. This suggests heterogeneity has some subtle effects on flow probably by creating significant spatial variability in the sign of vertical flow and therefore has to be considered in PA calculations.

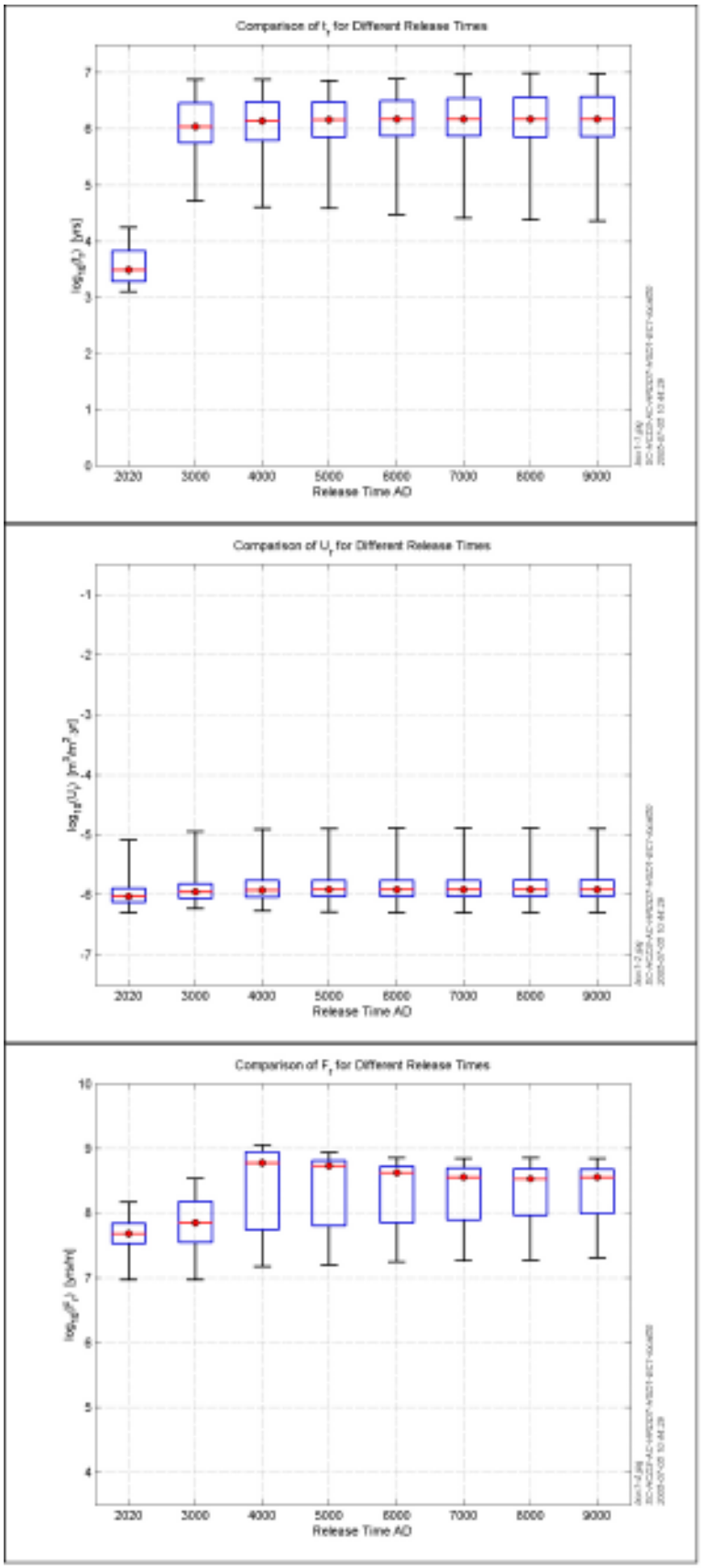

Figure 3-48. *Bar and whisker-plots for the CPM base case with 6,824 particles released every thousand years from 2,020 AD to 9,000 AD. From the top: t_r, U_r, and F_r. The statistical measures are the median (red), 25th and 75th percentile (blue bar) and the 5th and 95th percentile (black "whiskers").*

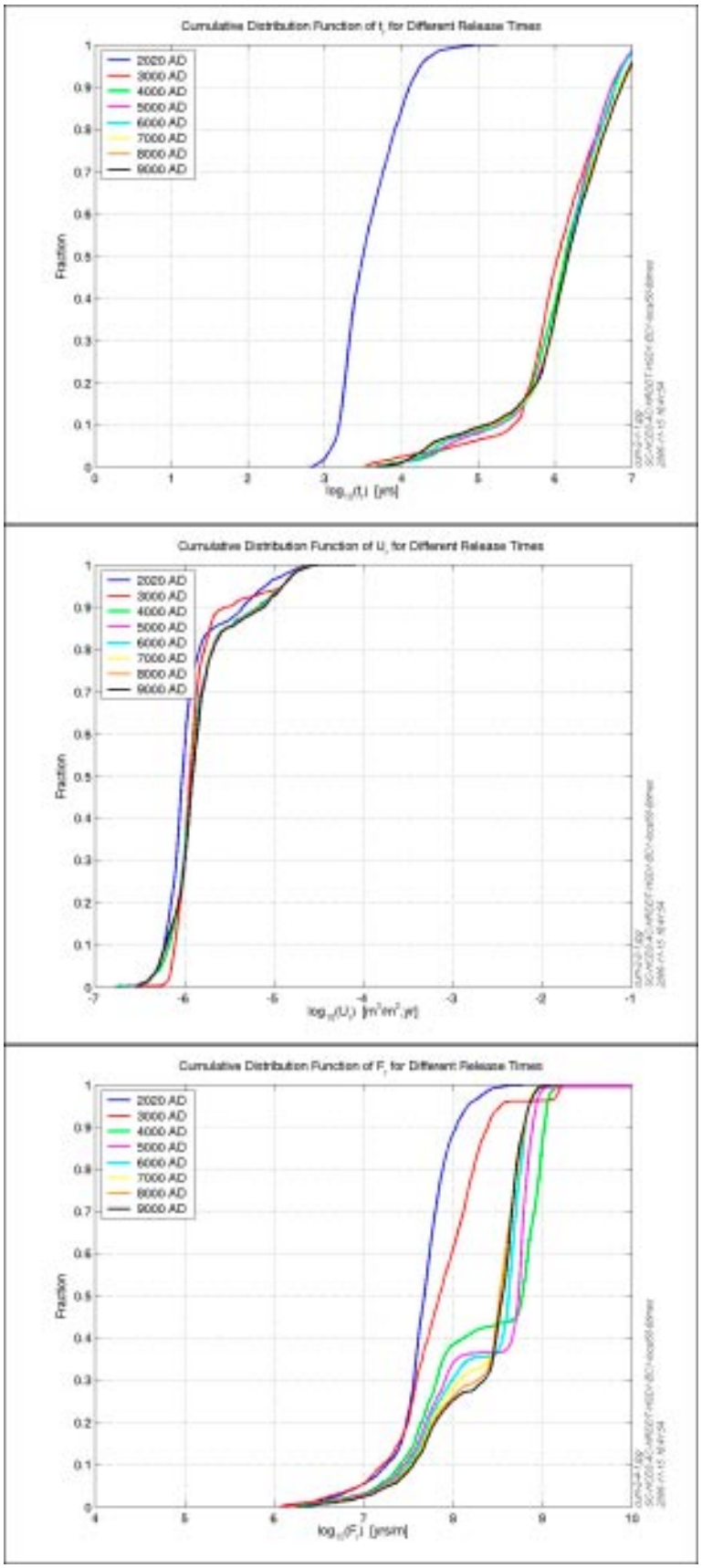

Figure 3-49. *Cumulative distribution plots for the CPM base case with 6,824 particles released at different times 2,020 AD–9,000 AD. From the top: t_r, U_r, and F_r.*

3.3.3 Sensitivity to geological model

The next major issue is the sensitivity to the choice of geological model. As was mentioned earlier, the Alternative Case (AC) geological model was selected for the central case in the SR-Can groundwater flow calculations for reasons of conservatism, despite many of the lineaments being of low identification confidence. This contrasts with SDM F 1.2 where models were centred on the Base Case (BC) geological model. The BC geological model has fewer deformations zones outside rock domains RFM029/017 compared to the AC geological model. The expected effect of reducing the number of structures is similar to decreasing the hydraulic conductivity.

BC geological model (SC_HCD3_BC_HRD3EC)

A variant was constructed based on the ECPM model using the BC geological model for comparison with the results in Section 3.2. Only a brief summary of the results in terms of PMs is given here.

In Figure 3-50 the distributions of F-quotient ($\log_{10}$) at 6,824 particle starting locations in the repository for the ECPM model using the BC geological model are presented at the 3 reference release times. Figure 3-51 shows the distribution of F-quotient ($\log_{10}$) at particle exit locations for the same three release times. A quick visual scan in comparison with Figure 3-25 of the F-quotient at start locations suggests the BC model contains areas with more start locations coloured red, i.e. high F-quotients around 10^8–10^9 y/m. At 2,020 AD the flow in the repository is similar to the ECPM reference case as was suggested in SDM F 1.2. A lot of particles start going downward for 100–200 m and then turn upwards. The F-quotient and the path-lengths are slightly larger compared to the ECPM reference case. In the northern part of the repository, the particles have very short path-lengths of about 500–1,000 m, indicating a path from the repository straight up to the surface. As with the ECPM reference case, the south east part of the repository contains some particles with very long flow-paths. About 3% of the particles are lost at 2,020 AD, so the absolute length of the very long flow-paths is slightly uncertain.

At 3,000 AD the differences in performance measures compared to the ECPM reference case are more pronounced. The BC geological model gives longer flow-paths and higher F-quotient. In a few spots of the northern part of the repository, the flow-paths are still upwards and very short. The F-quotient is noticeably higher in the northern and central section of the repository than for the reference case. In the southern part of the repository area, the predominant flow direction is downwards sending particles deeper into the model. Compared to the ECPM reference case, the flow-paths have a slightly different distribution across the model surface even if the major exit areas remain the same. The latter comment confirms it is the shoreline that controls the discharge areas in the main rather than the structural model. About 5% of the released particles are lost due to numerical problems in the particle tracking for this release time. At 9,000 AD the results resemble the ECPM reference case to a high degree. For the BC geological model, the flow-paths are slightly longer and the F-quotient slightly larger. Again this release time shows almost no lost particles. Some of the exit locations have moved further north in the middle of the model. Still there are a lot of particles reaching the model boundary.

Figure 3-52 and Figure 3-53 show the statistical results for the BC geological model as bar and whisker-plots, and as cumulative distribution plots for the calculated PMs t_r, U_r, L_r and F_r. The statistics are calculated in $\log_{10}$ space and results are presented for the three reference release times. The travel time and the initial Darcy velocity show behaviour very similar to the ECPM reference case. The F-quotient however shows slightly higher values especially at later times. There is generally less variability in this case also. This is an effect of the more homogeneous hydraulic conductivity, and in this aspect resembles the results in the CPM model. In general, the flow-paths show broadly the same qualitative behaviour as in the ECPM reference case. The main difference is the range of the performance measures where the ECPM reference case shows generally lower values. The penetration of the flow-paths to depth is of the same magnitude as in the ECPM reference case, reaching down to 800–900 m depth. The same tendency can be seen as for the CPM base case regarding the distribution of flow-paths and exit locations.

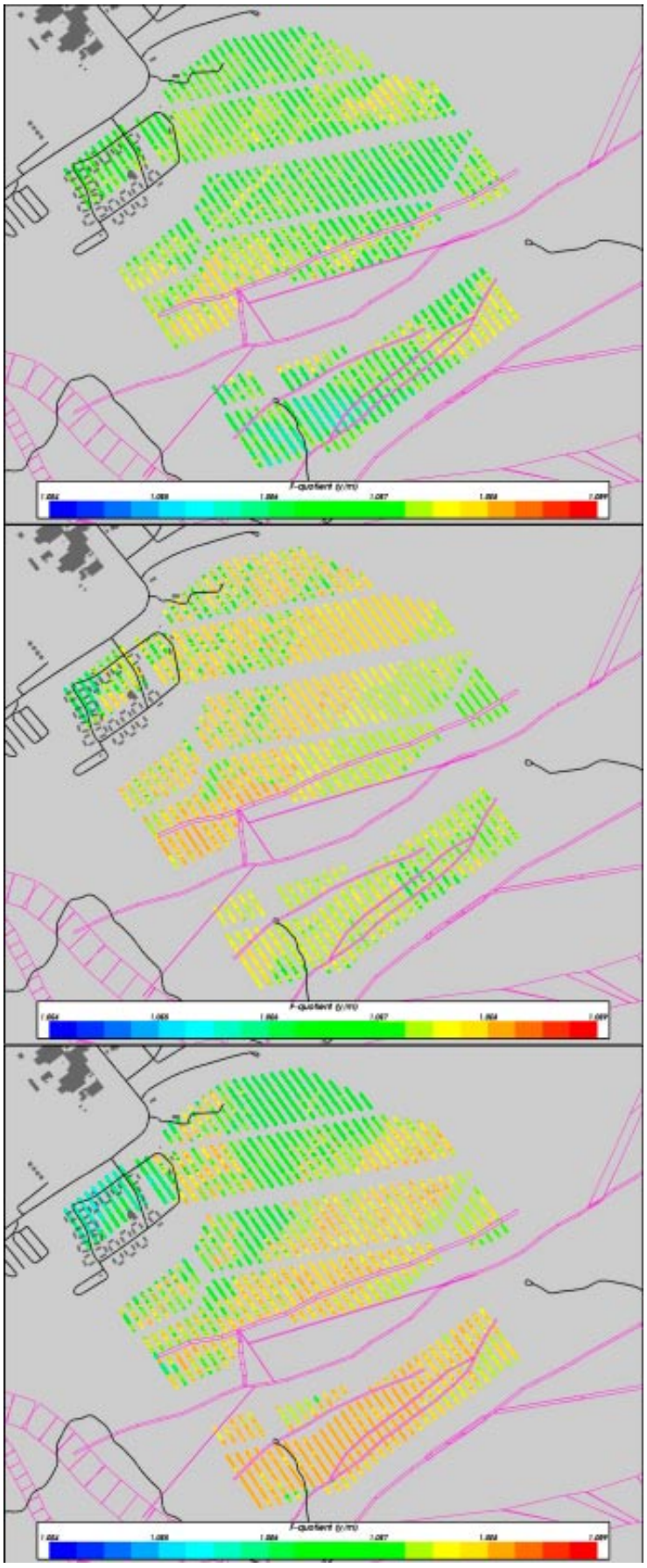

Figure 3-50. *Distribution of $\log_{10}(F_r)$ at 6,824 particle start locations for the BC geological model at release times (top to bottom) 2,020 AD, 3,000 AD and 9,000 AD. Also, the HCD model at z=–400 m (purple), roads and buildings (black).*

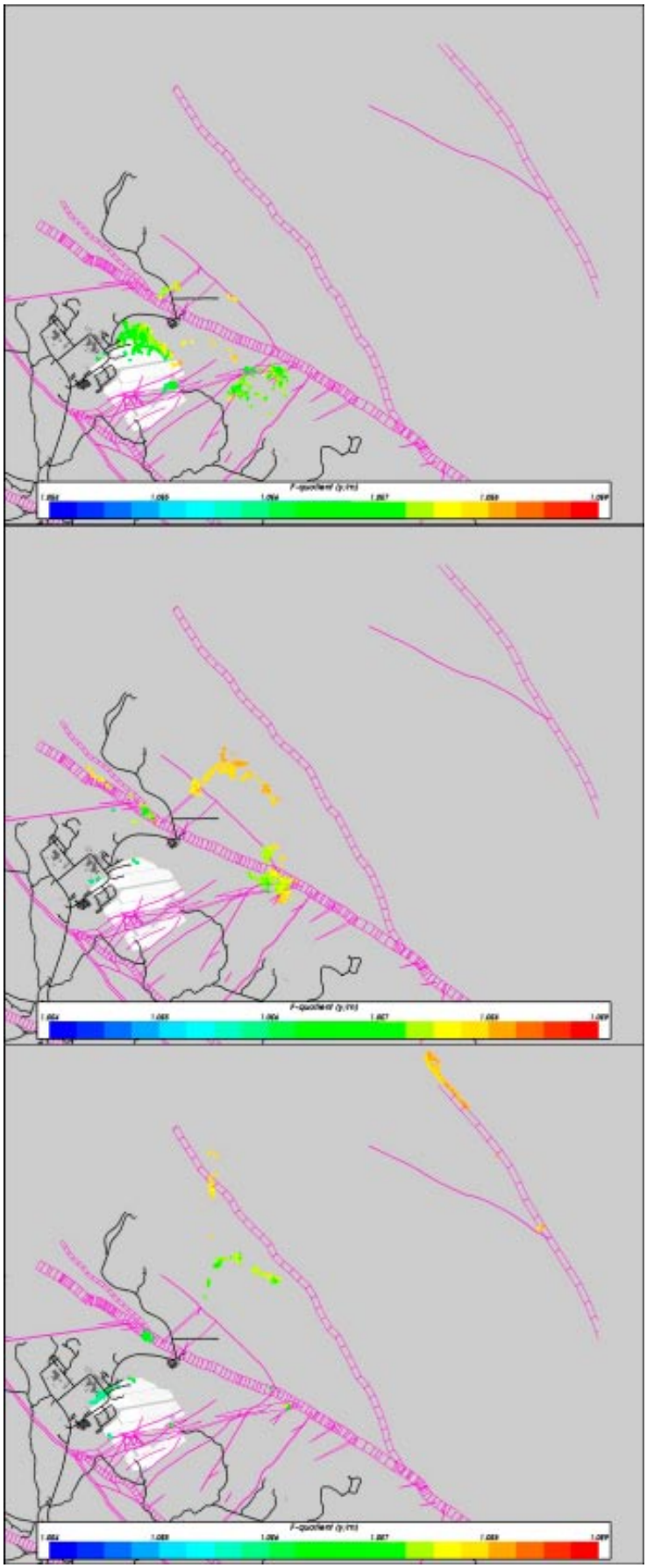

Figure 3-51. *Distribution of $\log_{10}(F_r)$ at 6,824 particle exit locations for the BC geological model at release times (top to bottom) 2,020 AD, 3,000 AD and 9,000 AD. Also, the HCD model at z=–400 m (purple), roads and buildings (black).*

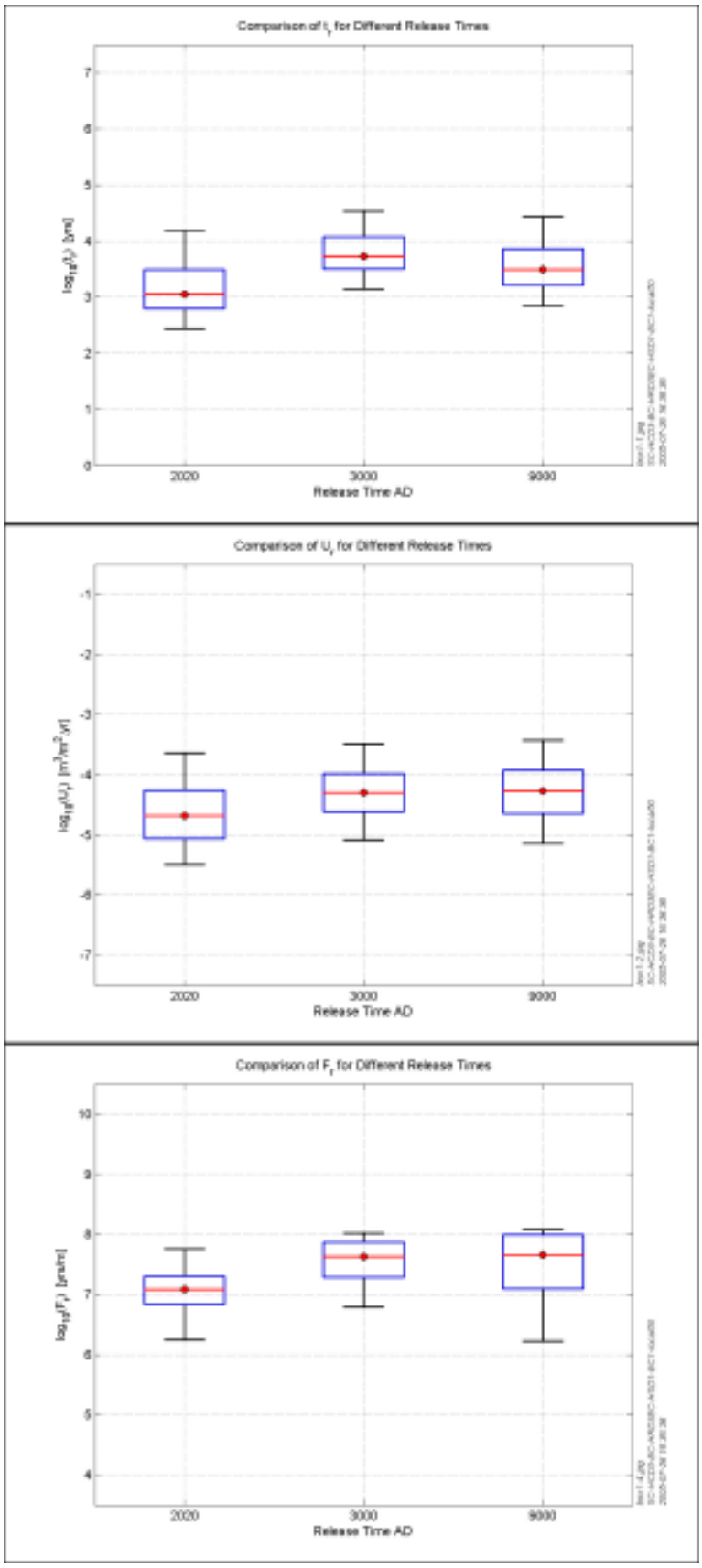

Figure 3-52. *Bar and whisker-plots for the BC geological model with 6,824 particles released at 2,020 AD, 3,000 AD and 9,000 AD. From the top: t_r, U_r, and F_r. The statistical measures are the median (red), 25th and 75th percentile (blue bar) and the 5th and 95th percentile (black "whiskers").*

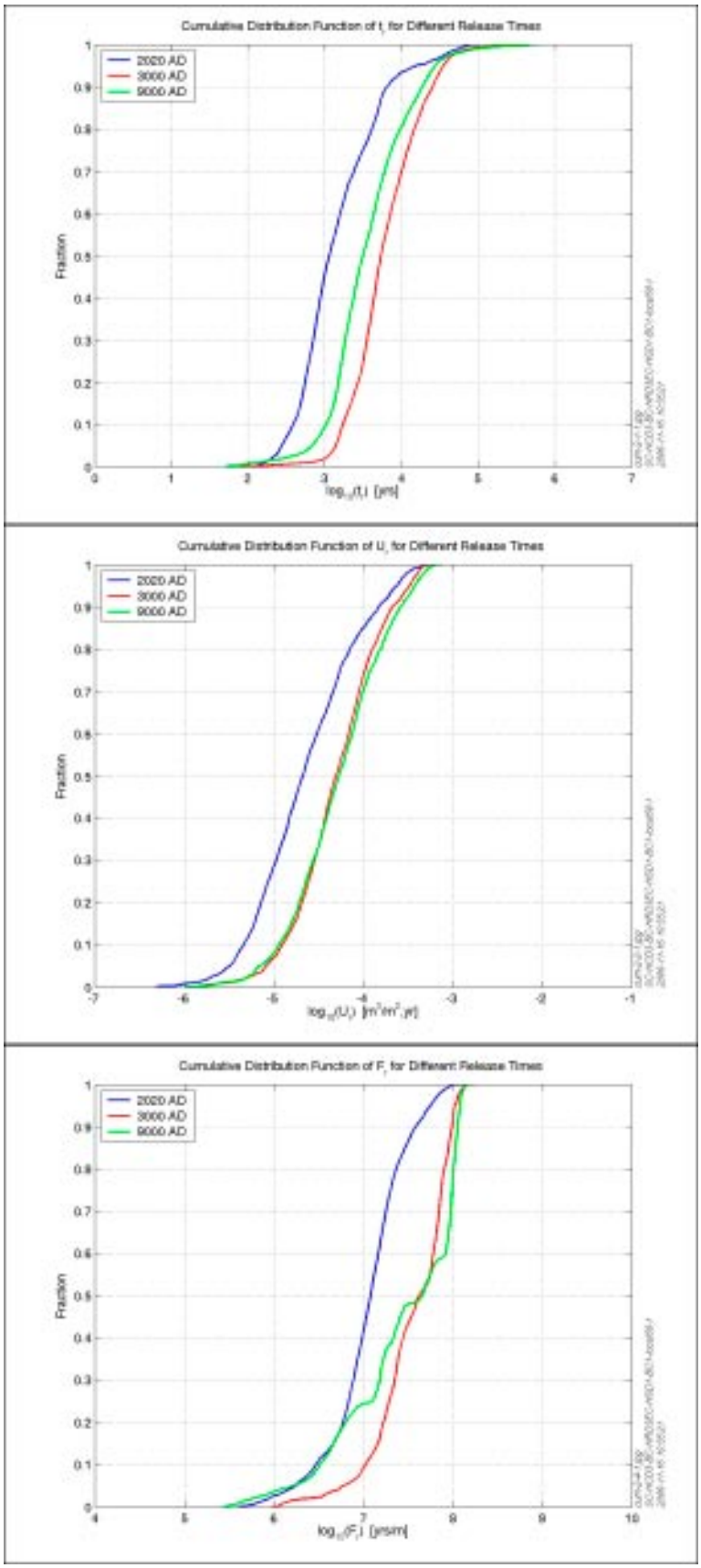

Figure 3-53. *Cumulative distribution plots for the ECPM case for the BC DZ model with 6,824 particles released at times 2,020 AD, 3,000 AD and 9,000 AD. From the top: t_r, U_r, and F_r.*

A somewhat wider pattern appears compared to the ECPM reference case. This can be expected when using a model with less deterministic fractures as the flow-paths are less focussed on their way through the rock.

3.3.4 Selection of conceptual and geological model for further analyses

The SDM F 1.2 hydrogeological study proposed two alternative conceptual models: an ECPM approach based on a DFN representation of rock domains RFM029 and RFM017, and a CPM approach throughout the entire model domain. These two model representations have been analysed further in the present SR-Can study. It was also decided to further analyze the effects of different geological models using the AC and BC geological models. The SDM F 1.2 study did not show much sensitivity to the choice of geological model. However, it is demonstrated here that this was due to only considering the present-day flow-field. When future shoreline movements are considered, particles released in the future often access parts of the model domain that were not reached previously and are affected by the presence of lineaments that are possible hydraulic features in the AC model. This suggests that the geological interpretation outside the candidate area might have an increased impact on the results for the future evolution of the site hydrogeology.

It was decided that the main sensitivity analyses should be performed using the most conservative combination of the given conceptual and geological models above. Here, the word conservative is used in the context that the case is likely to lead to a higher computed risk. The selection process, shown in a schematic view in Figure 3-54, is mainly based on statistical analysis of performance measures. Three models were assessed to guide this choice: ECPM reference case, CPM base case and BC geological model as presented in earlier sections. Comparing the results for the two conceptual models, it is evident that the ECPM model is the most conservative. The travel time, t_r, is 2.5 orders of magnitude lower for the ECPM reference case and the initial Darcy velocity, U_r, is about 1.5 orders of magnitude higher. Clearly this is an effect of the higher hydraulic conductivity used throughout rock domains RFM029/017 in the ECPM model based on the Hydro-DFN developed from KFM03A data, while the CPM reduced the hydraulic conductivity below ZFMNE00A2 and depth 350 m. The sensitivity to the geological model is smaller than it is to the conceptual model. However, the F-quotient is generally almost half a magnitude lower and the path-length is generally shorter for the AC geological model. The initial Darcy velocity is not affected since the differences between the models are restricted to the area outside of rock domains RFM029/017. The conclusion is that the AC geological model is the more conservative model.

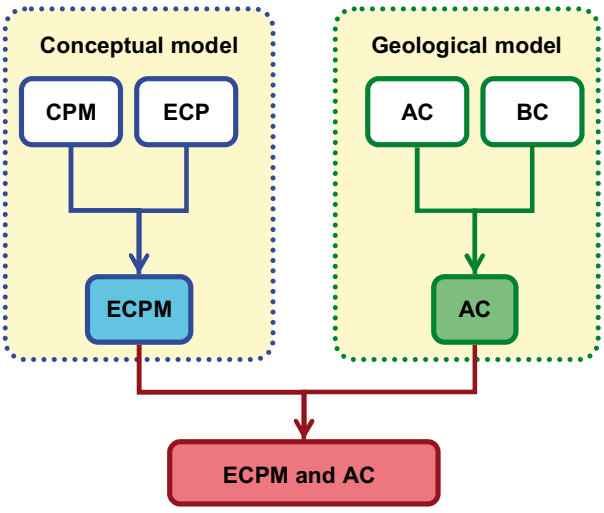

Figure 3-54. *A schematic view of the process of selecting a conservative regional-scale hydrogeological model. The selection is based on two conceptual models, CPM) and ECPM and two geological models, Alternative Case (AC) and Base Case (BC).*

Based on the results discussed above it was decided that the reference case used for further sensitivity analyses should be based on the ECPM model using the Alternative Case (AC) geological model.

3.3.5 Sensitivity to Hydro-DFN model

The other sensitivity that was found to have a significant impact on PMs was the Hydro-DFN parameters used in driving the ECPM properties. With reference to Section 2.3.2, a number of uncertainties are associated with the Hydro-DFN as follows:

1. Spatial variability in the Hydro-DFN parameters more consistent with the spatial variability seen in the site boreholes.
2. The fracture transmissivity versus length relationship.
3. The fracture radius distribution as a variant on the Geo-DFN.

Variants were constructed to address each of these issues by the quantification of sensitivities. It was found that the first two issues suggested significant sensitivities in the PMs and so we detail some of the results for these cases below. The length distribution was found to be less influential.

Lower transmissivity below ZFMNE00A2 (SC_HCD3_AC_HRD3A2_T)

Two variants were considered to address the spatial variability interpreted in the site Hydro-DFN that honours the division into sub-volumes suggested by Figure 2-21. As such, these two cases are more representative of the fracturing encountered at the site than the reference ECPM model. In Section 3.2, the distinction between Volumes E, F and G was not implemented in the ECPM reference case since properties from Volume E were used throughout. Hydraulic data suggests that flow is very limited within Volume G, but from a safety assessment point of view it is not clear whether it is appropriate to model potential flows of small magnitude mainly below the detection limit as a fracture network of very low transmissivity fractures or of very low intensity. Perhaps reality is a bit of both. The bulk flow through these systems would be of similar magnitude and very low, but the first would give small flows around a significant number of fractures while gives slightly higher flows but only around a few canisters. It is not clear which of these cases is likely to give the relatively higher risk, so we shall quantify performance measures for the two scenarios. Hence, the first variant has a reduced fracture transmissivity by a factor 10 in Volume G (corresponding to the lower sections of boreholes KFM01A, KFM04A and KFM05A). The second variant reduced the fracture intensity in Volume G, P32, to 0.4 m^2/m^3 as proposed in Table 2-6. It should be noted that only Hydro-DFN properties in Volume G were modified and this was defined as the volume within rock-domain RFM029/017, below zone ZFMNE00A2, and below an elevation of z=–350 m. Hydro-DFN properties in Volume F were the same as those in Volume E (see Table 2-3). As can be envisaged, implementing such a complicated spatial variability in a numerical DFN model starts to get quite intricate, and it will be one of the challenges for the ongoing site-modelling as more data becomes available.

The case we describe in this section is the one with a lower transmissivity in Volume G. Because of the change in transmissivity, it is interesting to see how much better the hydraulic properties are reproduced by the ECPM model in this variant. Figure 3-55 to Figure 3-59 show the modelled and measured hydraulic conductivities for boreholes KFM01A, KFM02A, KFM03A, KFM04A and KFM05A for the top 1,000 m of borehole. KFM01A, KFM02A and KFM03A are compared with the 100 m PSS data, while KFM04A and KFM05A are compared with the PFL anomaly data converted to an average conductivity over 100 m intervals. In the figures the depths and thickness of DZs in the geological model are indicated since they correlate strongly with the high conductivity intervals.

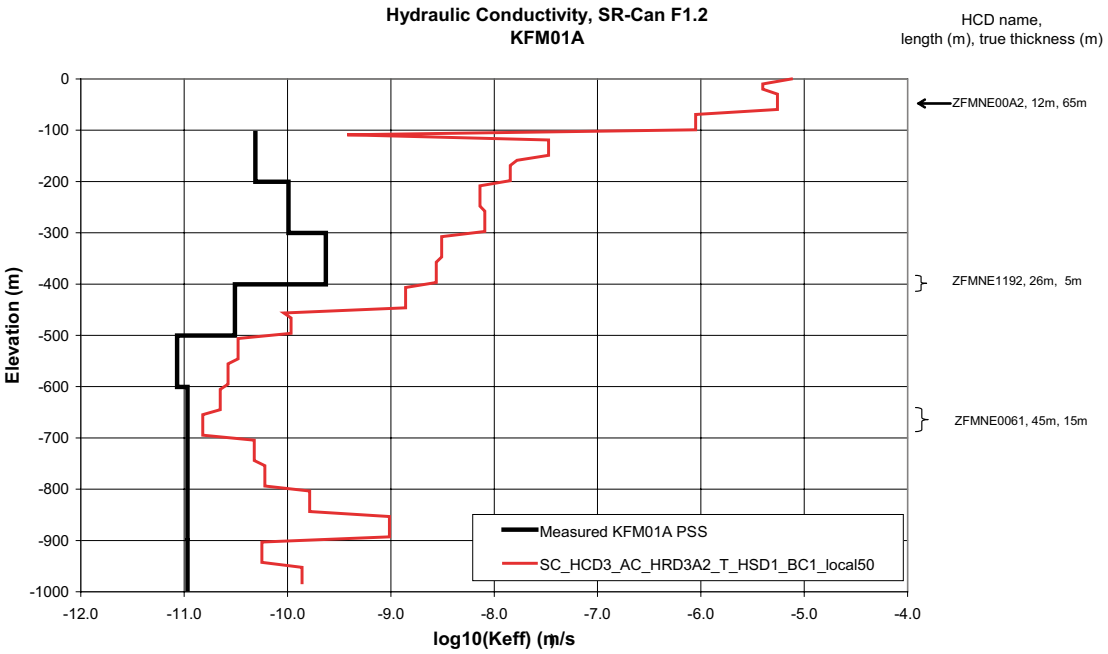

Figure 3-55. *Comparison of hydraulic conductivity in KFM01A for lower transmissivity below ZFMNE00A2. Values simulated in the model are shown by red lines while the measured values in 100 m intervals are shown in black.*

Compared to the ECPM reference case presented in Section 3.2, the hydraulic calibration of the bedrock properties has improved considerably. Significant improvements are seen in KFM01A below z=–400 m, in KFM02A below z=–600 m, and in KFM05A below z=–400 m. The modified model suggest a background hydraulic conductivity of around 10^{-11} m/s and occasional spikes around 10^{-10} m/s in Volume G, which is qualitatively consistent with field-data around the

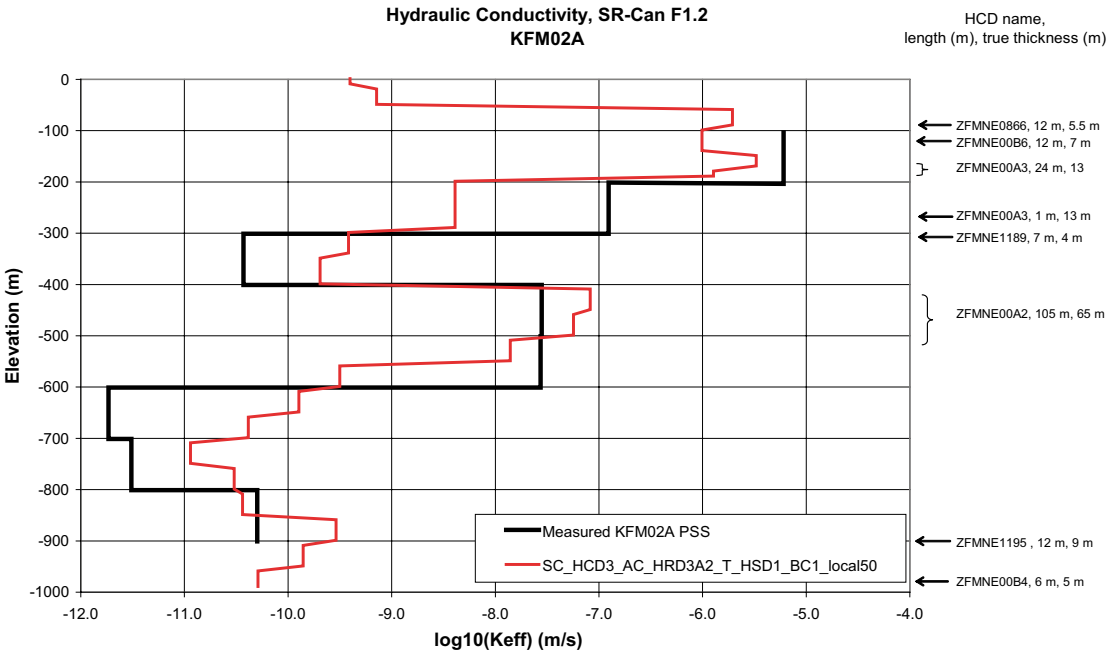

Figure 3-56. *Comparison of hydraulic conductivity in KFM02A for lower transmissivity below ZFMNE00A2. Values simulated in the model are shown by red lines while the measured values in 100 m intervals are shown in black.*

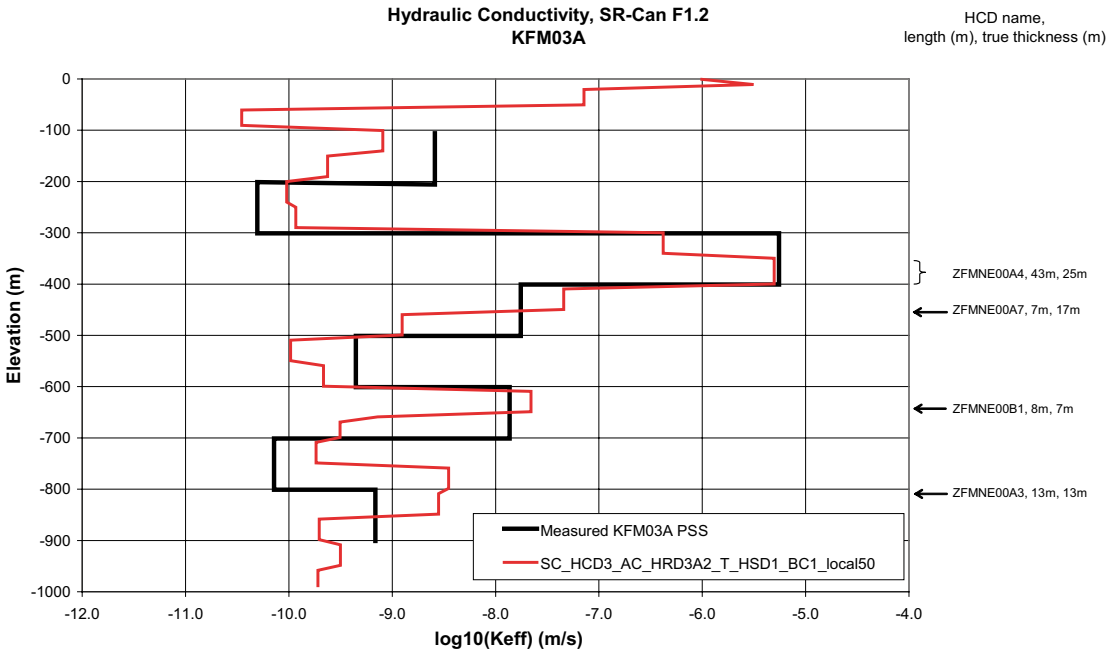

Figure 3-57. *Comparison of hydraulic conductivity in KFM03A for lower transmissivity below ZFMNE00A2. Values simulated in the model are shown by red lines while the measured values in 100 m intervals are shown in black.*

base of KFM02A and KFM05A, though no such spikes occur in KFM01A. It can be concluded that the changes made to the transmissivity of the DFN have improved the calibration on hydraulic conductivity in the model substantially. Again though we should urge some caution when comparing block properties in 50 m elements with the interpreted hydraulic conductivity seen in a 7.6 cm diameter borehole especially for such sparse fracture networks, since the upscaled block properties are likely to be an upper bound.

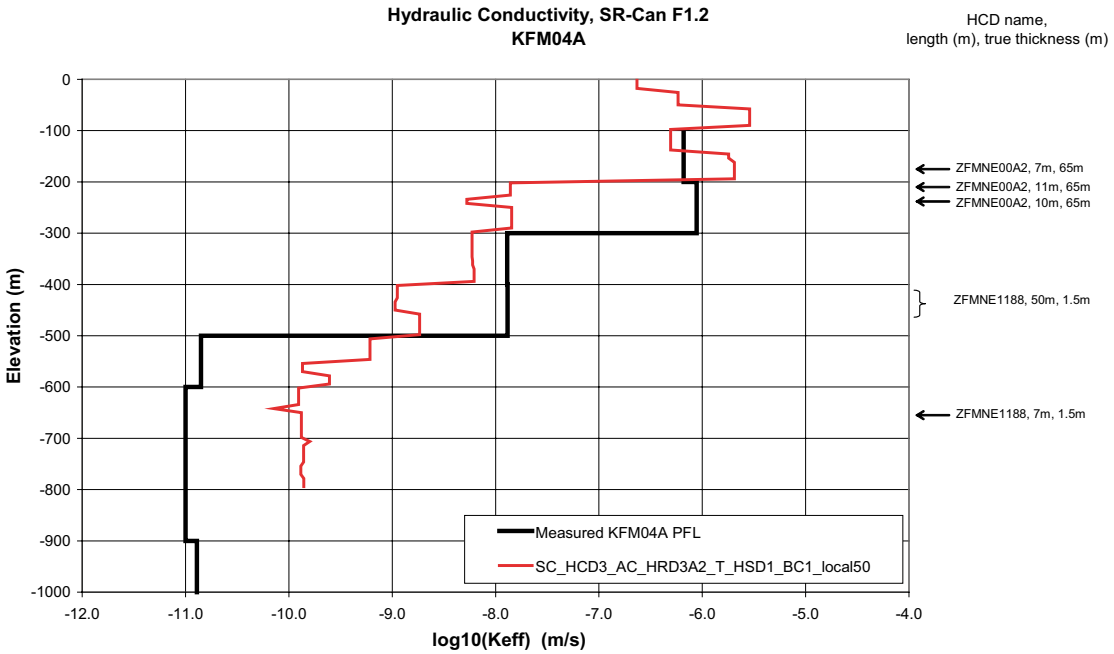

Figure 3-58. *Comparison of hydraulic conductivity in KFM04A for lower transmissivity below ZFMNE00A2. Values simulated in the model are shown by red lines while the measured values in 100 m intervals are shown in black.*

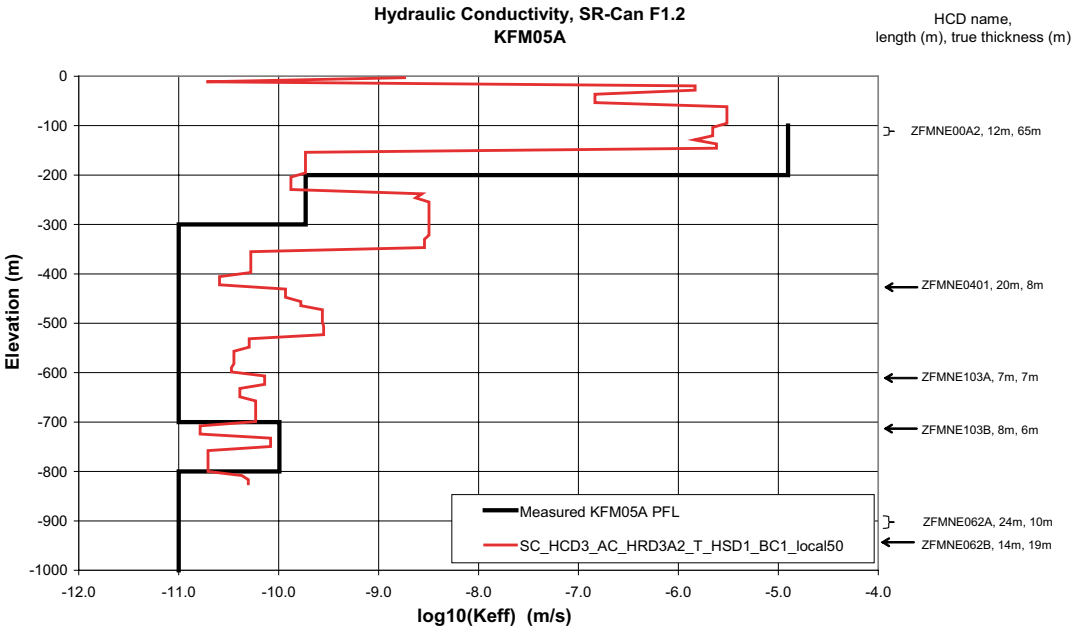

Figure 3-59. *Comparison of hydraulic conductivity in KFM05A for lower transmissivity below ZFMNE00A2. Values simulated in the model are shown by red lines while the measured values in 100 m intervals are shown in black.*

Figure 3-60 shows the profiles of the three constituents, $\delta^{18}O$, Cl and Mg in KFM01A–KFM04A for the ECPM case with lower transmissivity below ZFMNE00A2. The error bars only indicate the laboratory analysis uncertainty of about 5%. Generally the hydro-geochemical profiles are more like those in the CPM case (Figure 3-36) than in the ECPM reference case (Figure 3-11). The pulse of Marine water is narrower and shallower than for the ECPM reference case.

In Figure 3-61 the distributions of F-quotient ($\log_{10}$) at 6,824 particle starting locations in the repository for the case using a lower transmissivity below ZFMNE00A2 are presented for each of the 3 reference times. The blue colour indicates smaller values (F-quotient about 10^4 y/m) and red indicates higher values (F-quotient about 10^9 y/m). Figure 3-62 shows the distribution of F-quotient ($\log_{10}$) at particle exit locations for the same 3 release times. At all times there is a striking increase in the F-quotient compared to the ECPM reference case. At 2,020 AD flow is mainly upwards apart from a group of particles started within the southern part of the repository. The path-lengths are almost identical to the ECPM reference case, but the F-quotient increases almost half an order of magnitude. The exit locations are almost identical to the ECPM reference case. At 3,000 AD only 40% of the particles reach the surface. The values of the F-quotient have increased markedly compared to the ECPM reference case. Flow-paths are deeper in this case which is not unexpected considering the lower transmissivity below ZFMNE00A2 and is in line with the CPM case. The exit locations are broadly the same even if the distribution of the flow-paths is a little wider compared to the ECPM reference case. At 9,000 AD the picture is different compared to the ECPM reference case. The values of the performance measures are considerably higher everywhere apart from the south-west corner. The median F-quotient is almost one and a half order of magnitude higher and the path-lengths are more than half an order of magnitude longer for the median. Here, very few particles exit close to the surface. The major part of the released particles reaches all the way to the model boundary in the north. Also, at this time the flow-paths are deeper than for the ECPM reference case. Figure 3-63 and Figure 3-64 show the statistical results for this variant as bar and whisker plots and as cumulative distribution plots for the PMs: t_r, U_r, and F_r. The statistics are calculated in $\log_{10}$ space and results are presented for three reference release times. Travel-time is only slightly longer for 2,020 AD than the ECPM reference case, but about one order of magnitude higher for later times. Initial Darcy velocity is an order of magnitude lower at all times, as to be expected by an order of magnitude lowering in transmissivity. F-quotient rises by about one order of magnitude throughout.

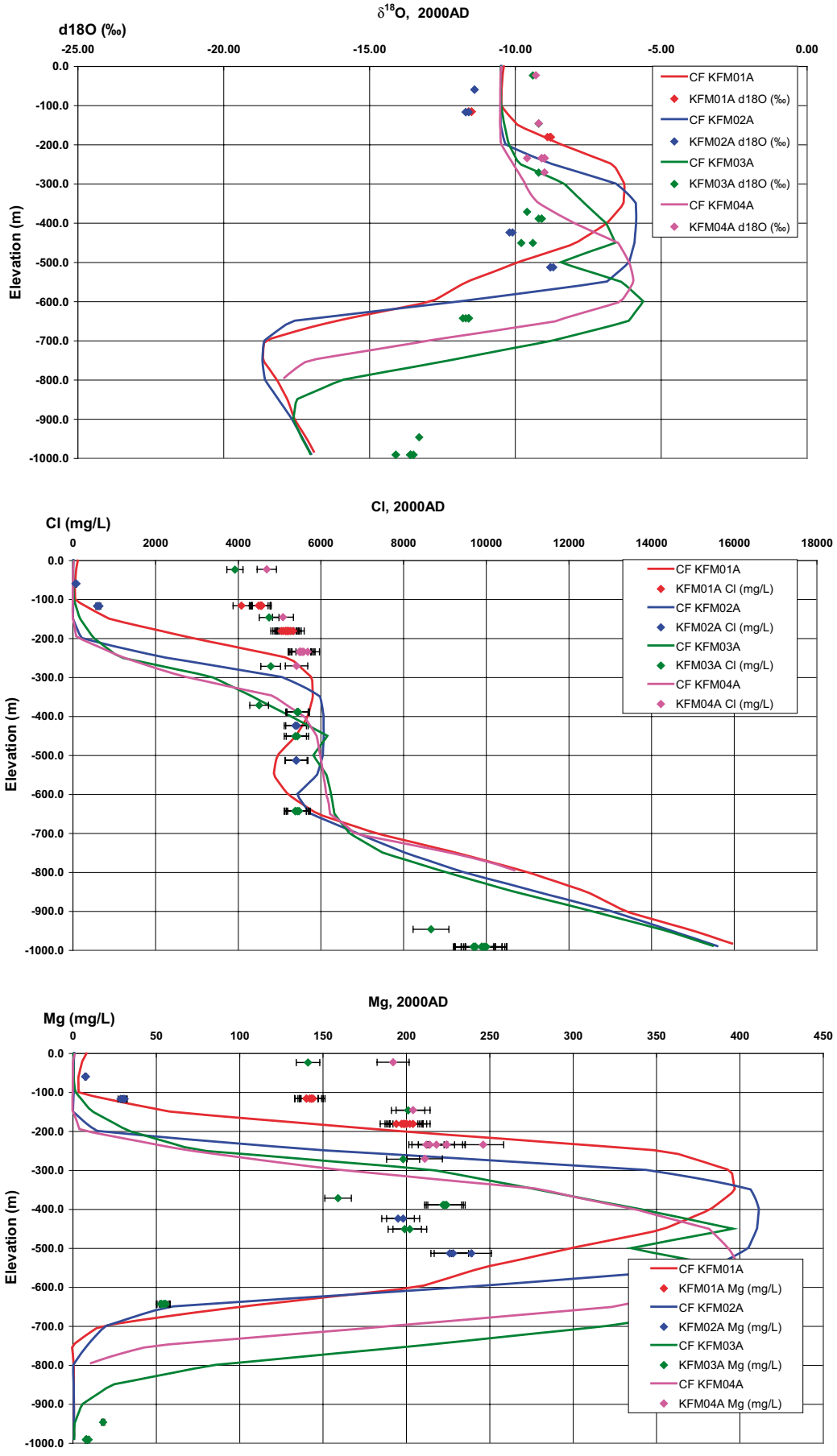

Figure 3-60. *Comparison of $\delta^{18}O$, Cl and Mg in KFM01A–KFM04A for lower transmissivity below ZFMNE00A2. Values in the simulated fracture system are shown by solid lines and the data by points.*

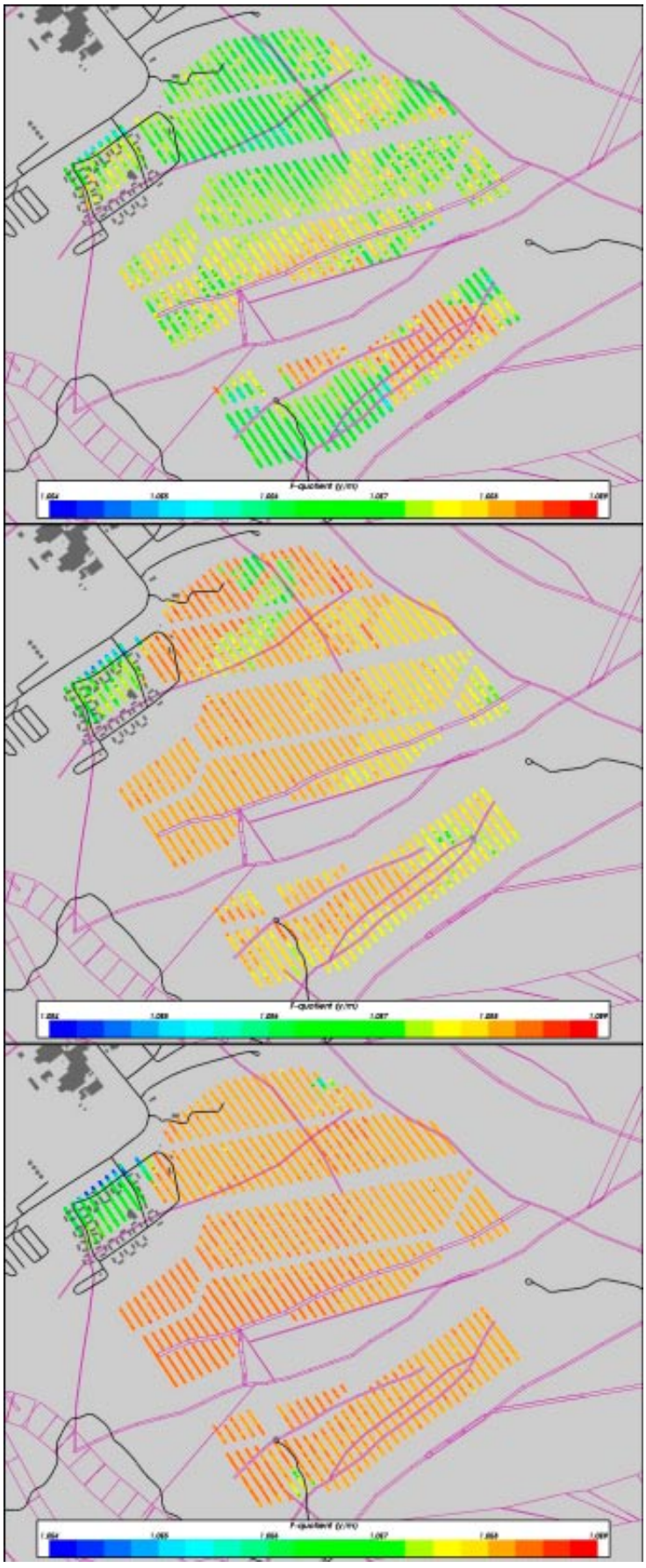

Figure 3-61. *Distribution of $\log_{10}(F_r)$ at 6,824 particle start locations for the lower transmissivity below ZFMNE00A2 at release times (top to bottom) 2,020 AD, 3,000 AD and 9,000 AD. Also, the HCD model at z=–400 m (purple), roads and buildings (black).*

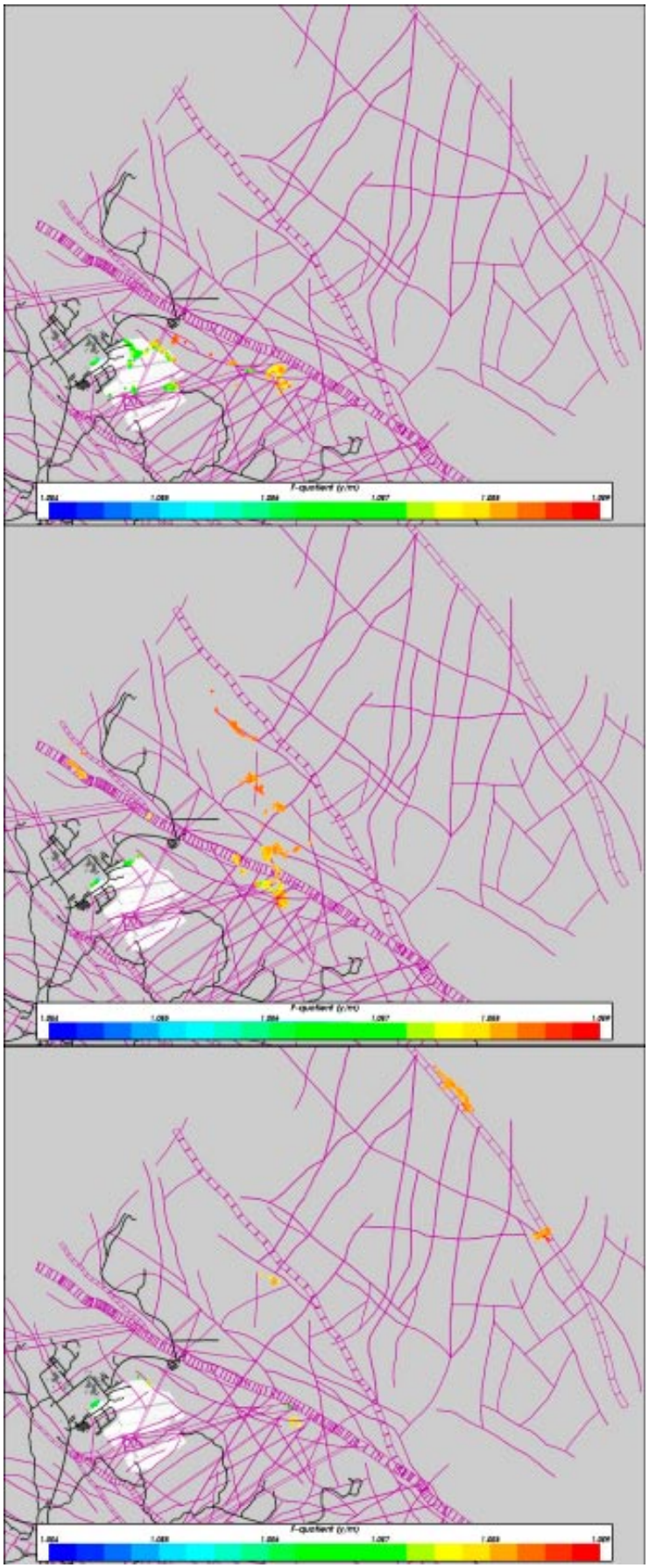

Figure 3-62. *Distribution of $\log_{10}(F_T)$ at 6,824 particle exit locations for the lower transmissivity below ZFMNE00A2 at release times (top to bottom) 2,020 AD, 3,000 AD and 9,000 AD. Also, the HCD model at z=–400 m (purple), roads and buildings (black).*

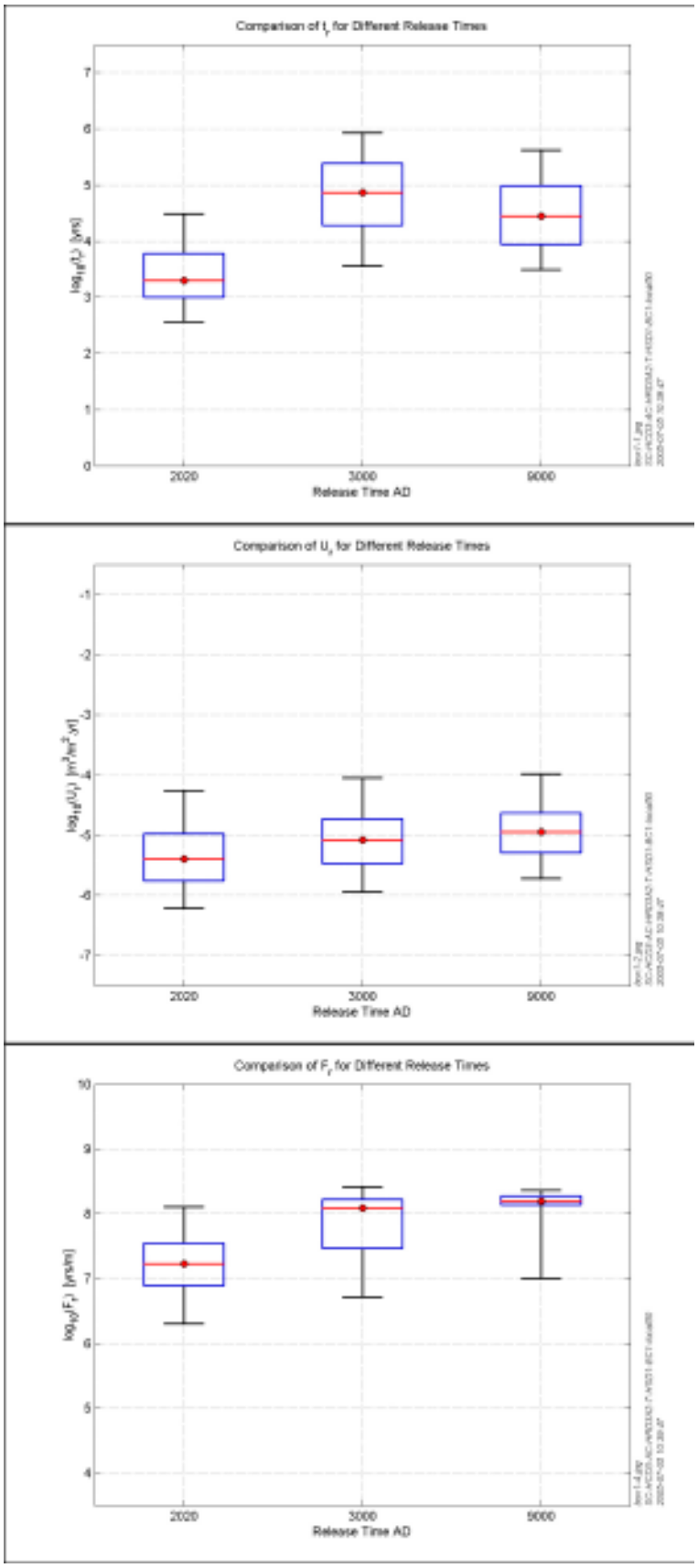

Figure 3-63. *Bar and whisker-plots for lower transmissivity below zone ZFMNE00A2 with 6,824 particles released at 2,020 AD, 3,000 AD and 9,000 AD. From the top: t_r, U_r and F_r. The statistical measures are the median (red), 25th and 75th percentile (blue bar) and the 5th and 95th percentile (black "whiskers").*

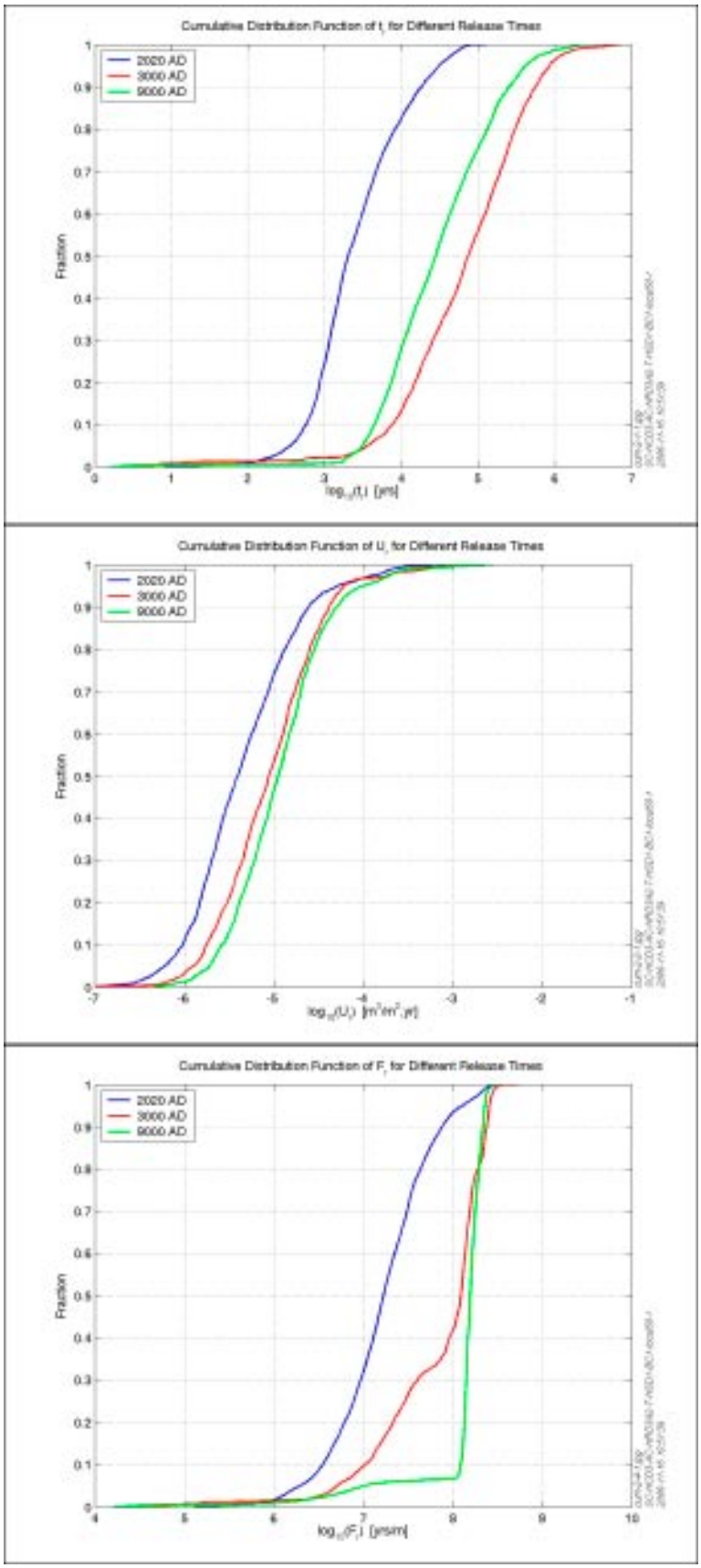

Figure 3-64. *Cumulative distributions for lower transmissivity below zone ZFMNE00A2 with 6,824 particles released at times 2,020 AD, 3,000 AD and 9,000 AD. From the top: t_r, U_r, and F_r.*

Lower open P32 below ZFMNE00A2 (SC_HCD3_AC_HRD3A2_P32)

The case we describe in this section is the one with lower fracture intensity, P32, in Volume G.

In Figure 3-65 the distributions of F-quotient ($\log_{10}$) at 6,824 particle starting locations in the repository for the case using a lower P32 below zone ZFMNE00A2 are presented for each of the 3 reference times. The blue colour indicates smaller values (F-quotient about 10^4 y/m) and red indicates higher values (F-quotient about 10^9 y/m). Figure 3-66 shows the distribution of F-quotient ($\log_{10}$) at particle exit locations for the same 3 release times. At each time there is a notable increase in the F-quotient, which is most significant at 3,000 AD and 9,000 AD.

At 2,020 AD the flow situation in the repository is very similar to the ECPM reference case, though the F-quotients are slightly higher mainly in parts of the southern and central repository sections. The exit locations are almost identical and the flow-paths are very much the same with very shallow flow-paths. Particles started within the northern part and the middle of the repository go more or less straight up to the surface. The particles started from the southern part of the repository exit in the sea close to the shoreline.

At 3,000 AD the flow has changed somewhat compared to the ECPM reference case. The F-quotient has increased in parts of the southern and central repository sections. The distribution of flow-paths is wider in this case compared to the ECPM reference case. The paths are a little deeper and the particles manage to find some new paths through the rock. Almost 30% of the particles become stuck in a narrow flow cell between the edge of the tectonic lens and the shoreline at this time, the same as for the ECPM reference case.

At 9,000 AD the median F-quotient and path-length are significantly higher than for the ECPM reference case. Here, more particles reach the large fracture zone at the model boundary and less particles exit close to the repository area. The flow-paths are more tightly grouped than at 3,000 AD. The only areas that remain with relatively low F-quotients are in the far north-west of the repository.

Figure 3-67 and Figure 3-68 show the statistical results for this variant as bar and whisker plots and as cumulative distribution plots for the PMs: t_r, U_r, and F_r. The statistics are calculated in $\log_{10}$ space and results are presented for three reference release times. The median travel-time is about half an order of magnitude higher for all release times. Initial Darcy velocity is about half an order of magnitude lower at all times. F-quotient has also risen by about half an order of magnitude throughout compared to the ECPM reference case. It is noticeable that travel-time and Darcy velocity are very similar at 3,000 AD and 9,000 AD suggesting the main changes in the flow-field occur in the first 1,000 years. The PM's for this case are very similar to those for the ECPM model with lower transmissivity below ZFMNE00A2.

In general, it can be concluded that the case using a lower P32 in Volume G initially shows similar results to the ECPM reference case. After that both F-quotient and travel-time increase significantly, though not quite as much as for the case with a lower transmissivity. On the other hand, this variant is perhaps more realistic in that it reflects the lower fracture intensity in Hydro-DFN for Volume G as proposed in the site-modelling.

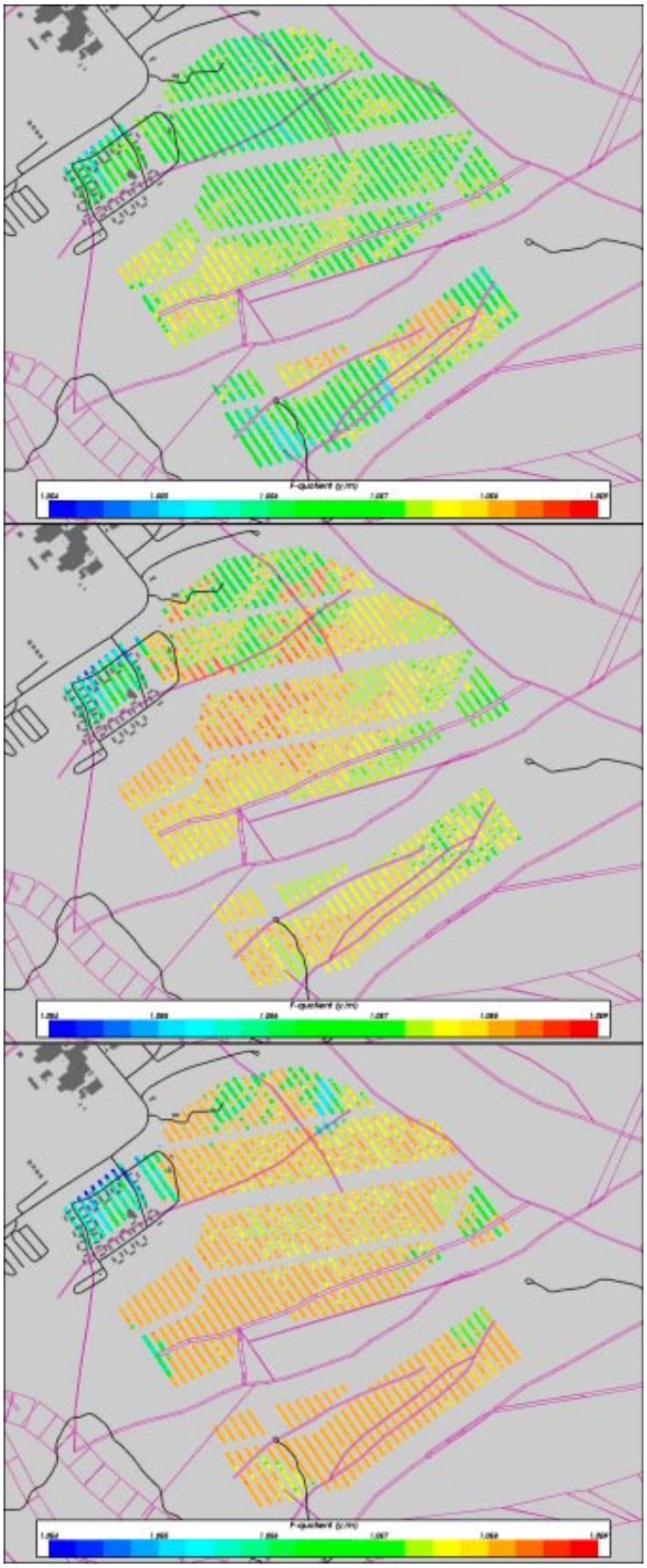

Figure 3-65. *Distribution of $\log_{10}(F_t)$ at 6,824 particle start locations for lower P32 below ZFMNE00A2 at release times (top to bottom) 2,020 AD, 3,000 AD and 9,000 AD. Also, the HCD model at z=–400 m (purple), roads and buildings (black).*

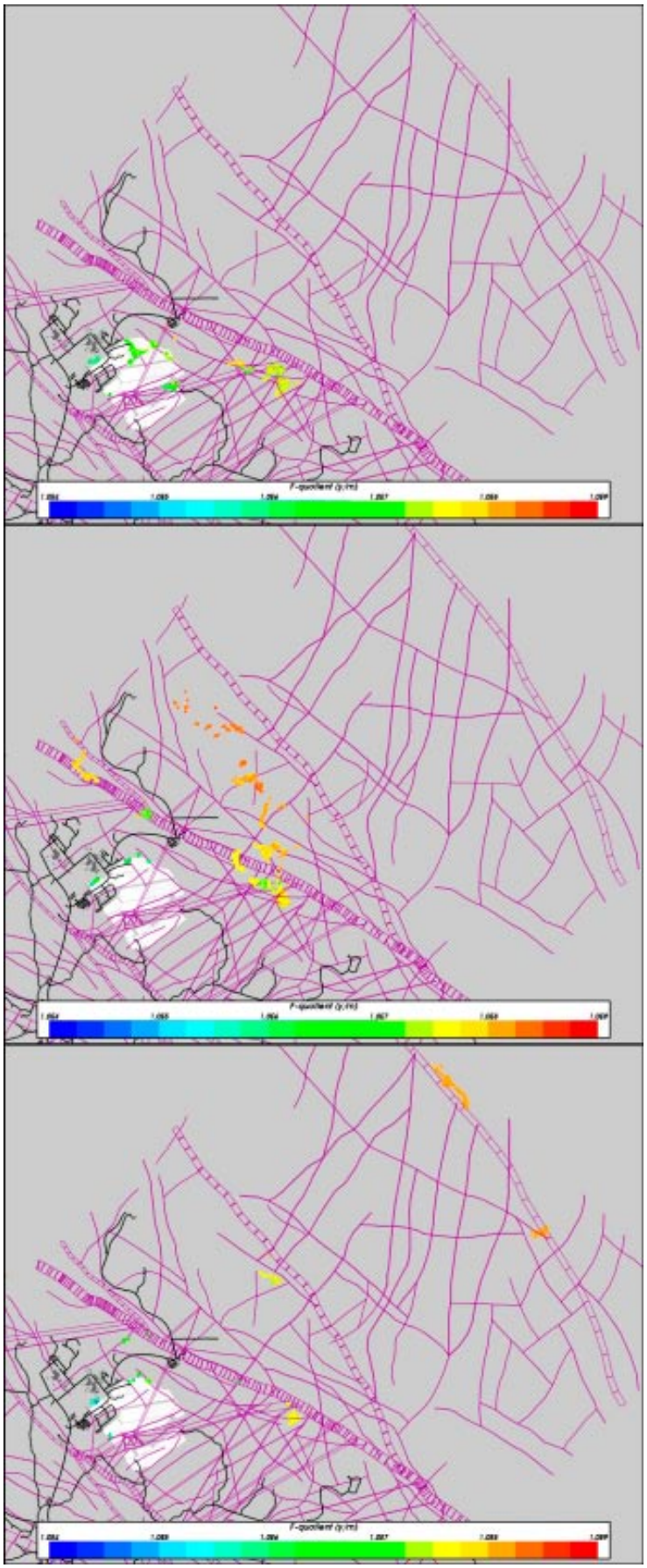

Figure 3-66. *Distribution of $\log_{10}(F_r)$ at 6,824 particle exit locations for lower P32 below ZFMNE00A2 at release times (top to bottom) 2,020 AD, 3,000 AD and 9,000 AD. Also, the HCD model at z=–400 m (purple), roads and buildings (black).*

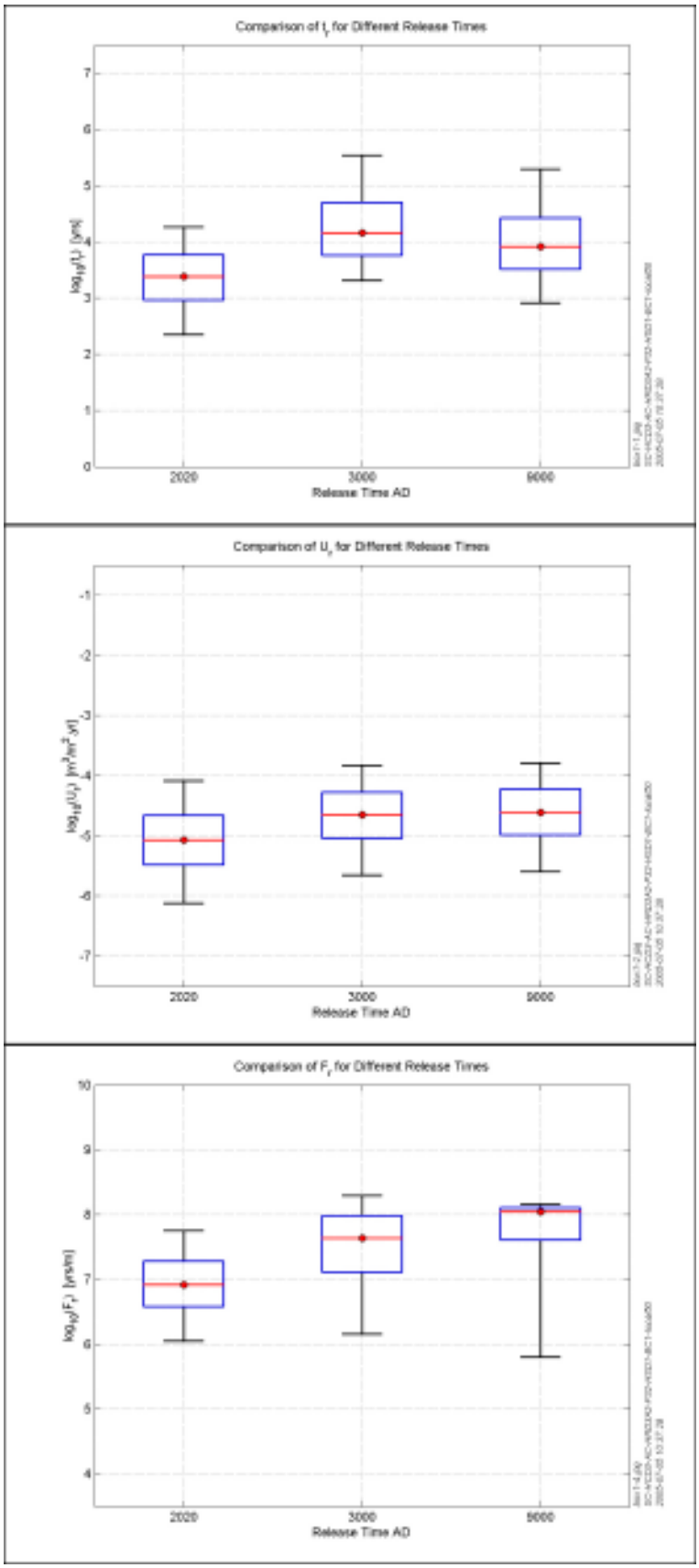

Figure 3-67. *Bar and whisker-plots for lower P32 below zone ZFMNE00A2 with 6,824 particles released at 2,020 AD, 3,000 AD and 9,000 AD. From the top: t_r, U_r, and F_r. The statistical measures are the median (red), 25th and 75th percentile (blue bar) and the 5th and 95th percentile (black "whiskers").*

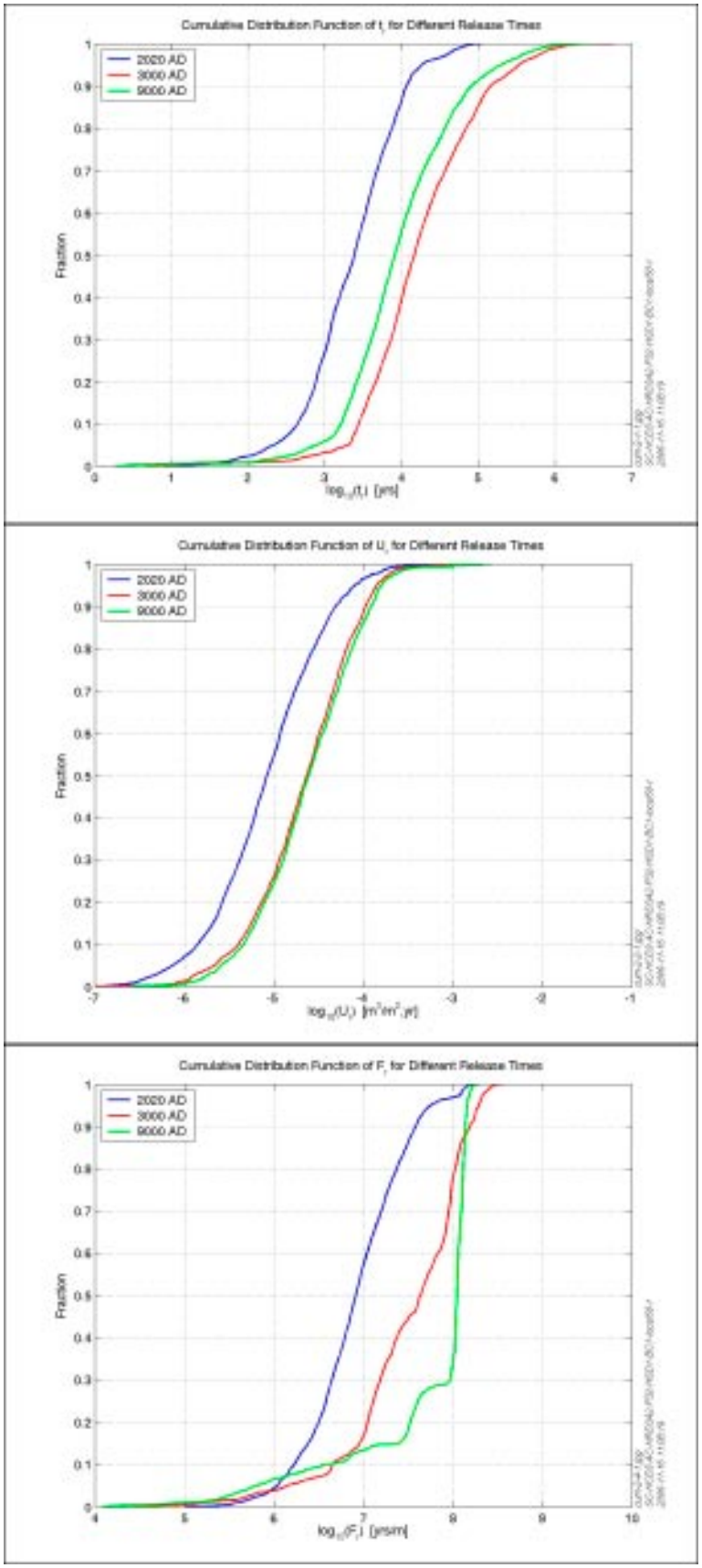

Figure 3-68. *Cumulative distributions for lower P32 below zone ZFMNE00A2 with 6,824 particles released at times 2,020 AD, 3,000 AD and 9,000 AD. From the top: t_r, U_r, and F_r.*

Semi-correlated transmissivity (SC_HCD3_AC_HRD3ES)

Another key parameter of the Hydro-DFN that was found to result in significant sensitivity was the relationship between fracture transmissivity and length. Hence, two variants that consider the semi-correlated and uncorrelated transmissivity models are include here and in the next section. The data for these cases comes from the suggested transmissivity settings given in Table 2-4. As for the reference case, this variant uses the homogeneous Hydro-DFN properties throughout RFM029/017 based on Volume E. Therefore, it should be noted that the model is likely to over-predict hydraulic conductivity within Volume G around KFM01A.

In Figure 3-69 the distributions of F-quotient ($\log_{10}$) at 6,824 particle starting locations in the repository for the case using a semi-correlated are presented for each of the 3 reference times. The blue colour indicates smaller values (F-quotient about 10^4 y/m) and red indicates higher values (F-quotient about 10^9 y/m). Figure 3-70 shows the distribution of F-quotient ($\log_{10}$) at particle exit locations for the same 3 release times. At each time there is a notable increase in the F-quotient, which is most significant at 3,000 AD and 9,000 AD.

At 2,020 AD the flow situation in the repository is slightly different to the ECPM reference case. The particles exit through the surface close to the repository. The flow-paths are slightly deeper compared to the ECPM reference case. However, the F-quotient is slightly lower than for the ECPM reference case while the median path-length stays the same. The shapes of the flow-paths are quite different to the other cases, in the sense that the paths are not as tightly grouped as before. Presumably because the direct correlation between transmissivity and length is relaxed here, then flow is less channelised into the large fractures and has to follow a more tortuous path to find a conduit to the surface. The lowest F-quotients are found in the central and southern parts of the repository, which is different to all other variants considered.

At 3,000 AD the flow pattern has changed considerably. The median F-quotient is now almost two orders of magnitude lower than for the ECPM reference case and the flow-paths are much shorter. The shortest flow-paths and the lowest F-quotients are found in the northern and central parts of the repository. The most striking difference is that the spread of paths and exit locations are considerably larger than seen before. This is thought to be due to a greater dispersion of flow-paths within RFM029/017.

At 9,000 AD the performance measures are of the same size as for 3,000 AD and the long flow-paths with high F-quotients are found in the same area of the repository. However, there are now a larger fraction of particles with long flow-paths, reaching all the way to the model boundary. As was seen at 3,000 AD, the large spread of flow-paths and exit locations remains to some extent. A group of particles go further east and exit much further to the north-east than has been seen in the other cases.

Figure 3-71 and Figure 3-72 show the statistical results for this variant as bar and whisker plots and as cumulative distribution plots for the PMs: t_r, U_r, and F_r. The statistics are calculated in $\log_{10}$ space and results are presented for three reference release times. The median travel-time is about the same as the ECPM reference case at 2,020 AD, but becomes near to 2 orders of magnitude lower than the reference case at 3,000 AD and 9,000 AD. Initial Darcy velocity is about an order of magnitude higher at all times. F-quotient also rises by about one order of magnitude at 2,020 AD, and two orders of magnitude afterwards. It should also be noted that the short path is more persistent in this case than for the reference case.

In general, it can be said that the semi-correlated transmissivity shows lower values for F-quotient and travel times and hence is a more pessimistic model. Part of the explanation for this comes from the hydraulic block properties given in /Hartley et al. 2005/ which show that the semi-correlated model gives a median hydraulic conductivity about half an order of magnitude higher than the correlated case. In the semi-correlated transmissivity model, large fractures have generally higher transmissivity, but there is also a spread superimposed on this trend.

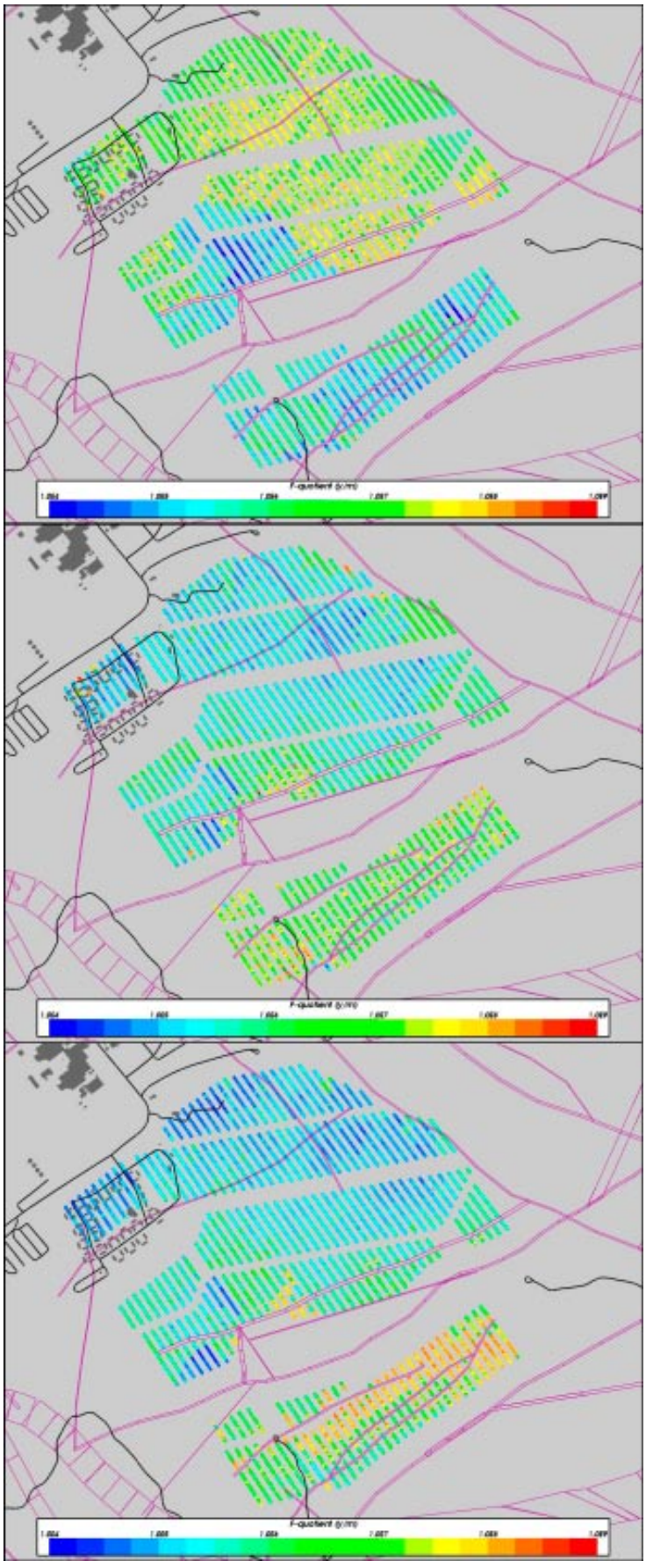

Figure 3-69. *Distribution of $\log_{10}(F_r)$ at 6,824 particle start locations for the semi-correlated transmissivity at release times (top to bottom) 2,020 AD, 3,000 AD and 9,000 AD. Also, the HCD model at z=–400 m (purple), roads and buildings (black).*

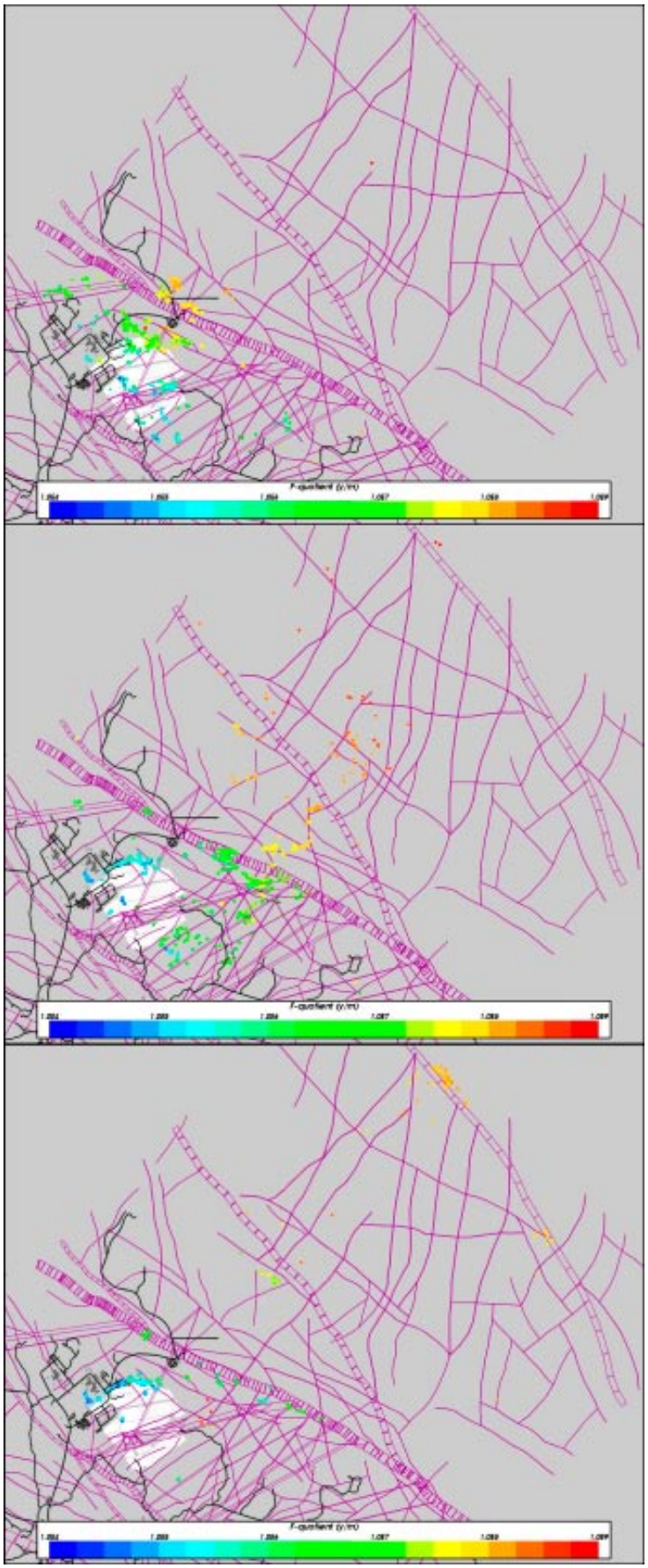

Figure 3-70. *Distribution of $\log_{10}(F_r)$ at 6,824 particle exit locations for the semi-correlated transmissivity at release times (top to bottom) 2,020 AD, 3,000 AD and 9,000 AD. Also, the HCD model at z=–400 m (purple), roads and buildings (black).*

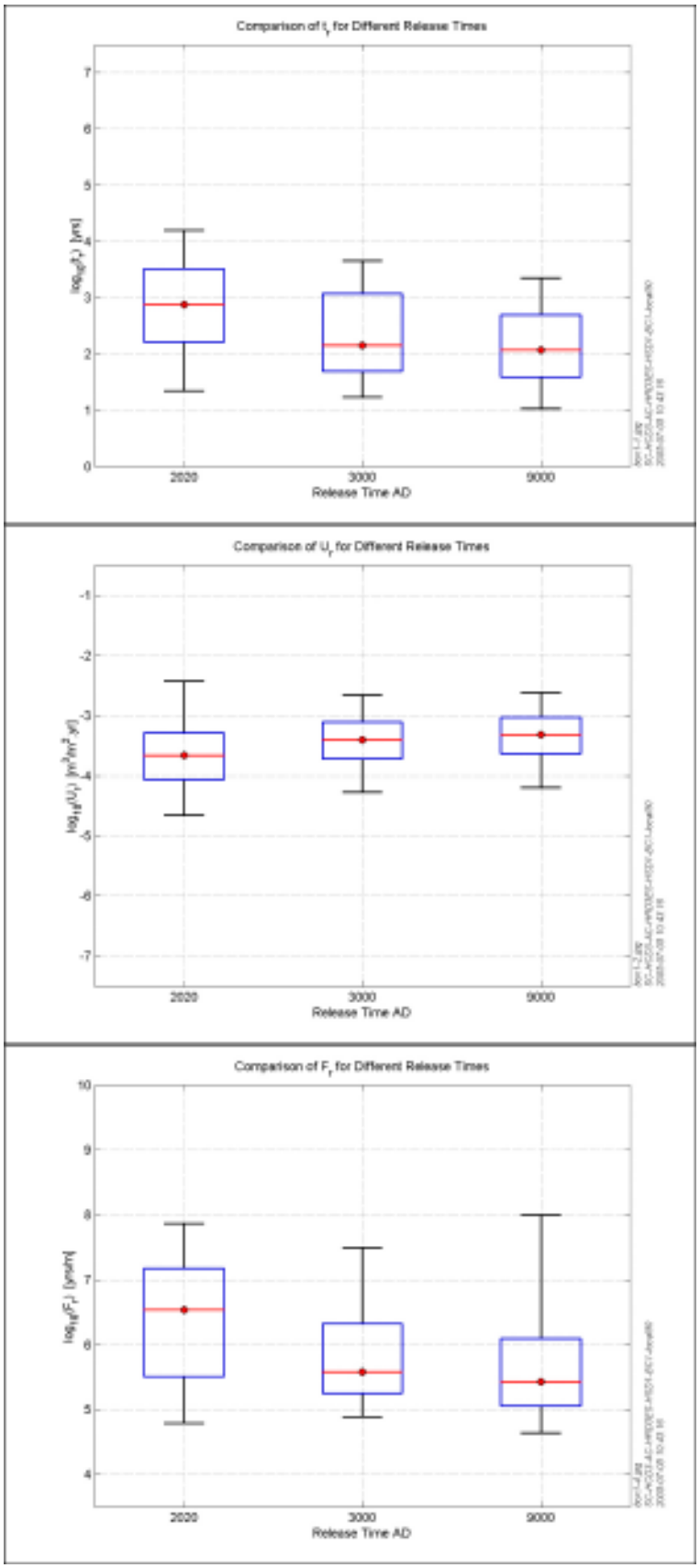

Figure 3-71. *Bar and whisker-plots for the semi-correlated transmissivity with 6,824 particles released at 2,020 AD, 3,000 AD and 9,000 AD. From the top: t_r, U_r, and F_r. The statistical measures are the median (red), 25th and 75th percentile (blue bar) and the 5th and 95th percentile (black "whiskers").*

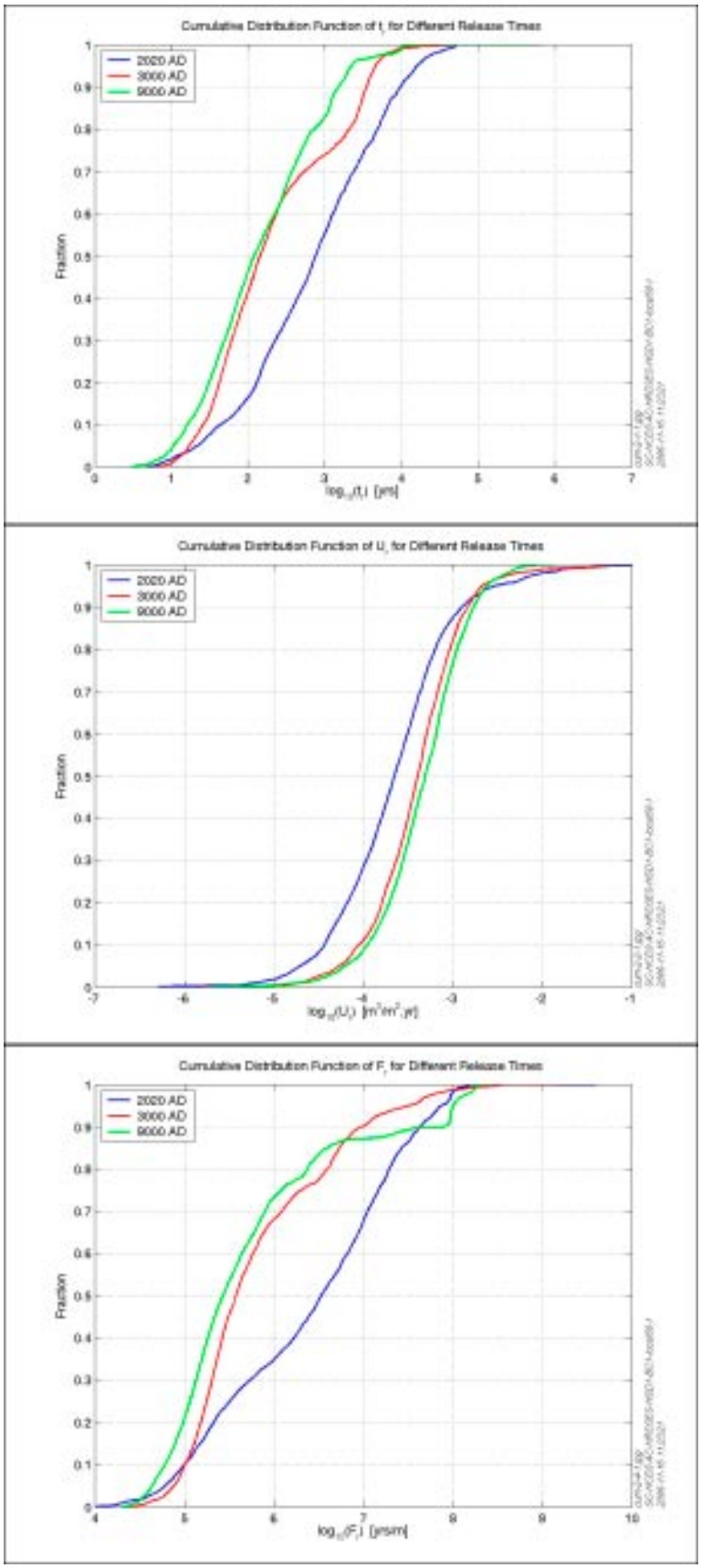

Figure 3-72. *Cumulative distributions for the semi-correlated transmissivity with 6,824 particles released at times 2,020 AD, 3,000 AD and 9,000 AD. From the top: t_r, U_r, and F_r.*

Hence, compared to the ECPM reference case, this model will tend to relegate some channels associated with large stochastic fractures, but exaggerate others when a random component is added to the transmissivity relationship. In part the new 'exaggerated' channels give rise to the low travel-time and F-quotient values. Another consequence is the flow channels will tend to be shorter, making connections to the surface easier than to the horizontal boundaries. The result is a more persistent short vertical flow-path.

Uncorrelated transmissivity (SC_HCD3_AC_HRD3EU)

In this section we look at the uncorrelated transmissivity model where there is no correlation at all between fracture transmissivity and length. The site-modelling suggested block-scale hydraulic conductivities similar to those for the uncorrelated case.

In Figure 3-73 the distributions of F-quotient ($\log_{10}$) at 6,824 particle starting locations in the repository for the case using a lower P32 below zone ZFMNE00A2 are presented for each of the 3 reference times. The blue colour indicates smaller values (F-quotient about 10^4 y/m) and red indicates higher values (F-quotient about 10^9 y/m). Figure 3-74 shows the distribution of F-quotient ($\log_{10}$) at particle exit locations for the same 3 release times. At each time there is a notable increase in the F-quotient, which is most significant at 3,000 AD and 9,000 AD.

At 2,020 AD the flow-field is significantly different from the ECPM reference case. The particles started in the middle and in the northern part of the repository are located in an upward flow causing most particles to exit very close to the repository area. In the southern part however, the flow is downward and the particles are sent deep down into the model, to a depth of about 1,600–1,700 m. The F-quotient is considerably lower than for the ECPM reference case, but the path-length is about the same. A similar wide spread of the flow-paths and exit points as was seen in semi-correlated case can be found here. Again, this is presumably due to removing the correlation length and transmissivity which makes the high flow channels through the network become more disperse and tortuous.

At 3,000 AD the performance measure results are slightly higher than the semi-correlated case, but still significantly lower than for the ECPM reference case. The exit locations are found in the same areas as for the semi-correlated case. However, the flow-paths are very much different. In this case the flow-paths do not go as much to the east as for the semi-correlated case. A wider spread across the model area, both sideways and in the length direction relative to the regional hydraulic gradient, can be observed. In fact, many of the flow-paths resemble the long paths usually seen for the later release time.

At 9,000 AD the performance measures are of the same magnitude as for 3,000 AD. Compared to the semi-correlated case there is a lower fraction of very long flow-paths. The exit locations are however still similar. The flow-paths are not nearly as deep as for the previous release times. Most flow-paths do not reach deeper than 500–600 m.

Figure 3-75 and Figure 3-76 show the statistical results for this variant as bar and whisker plots and as cumulative distribution plots for the PMs: t_r, U_r, and F_r. The statistics are calculated in $\log_{10}$ space and results are presented for three reference release times. The median travel-time is about the same as the ECPM reference case at 2,020 AD, but becomes one order of magnitude lower than the reference case at 3,000 AD and 9,000 AD. Initial Darcy velocity is about an order of magnitude higher at all times. F-quotient also rises by about half an order of magnitude at 2,020 AD, and one order of magnitude afterwards. The PMs are similar to the semi-correlated case suggesting that weakening the link between transmissivity and length leads to shorter paths and more flow percolating down into small fractures reducing retention.

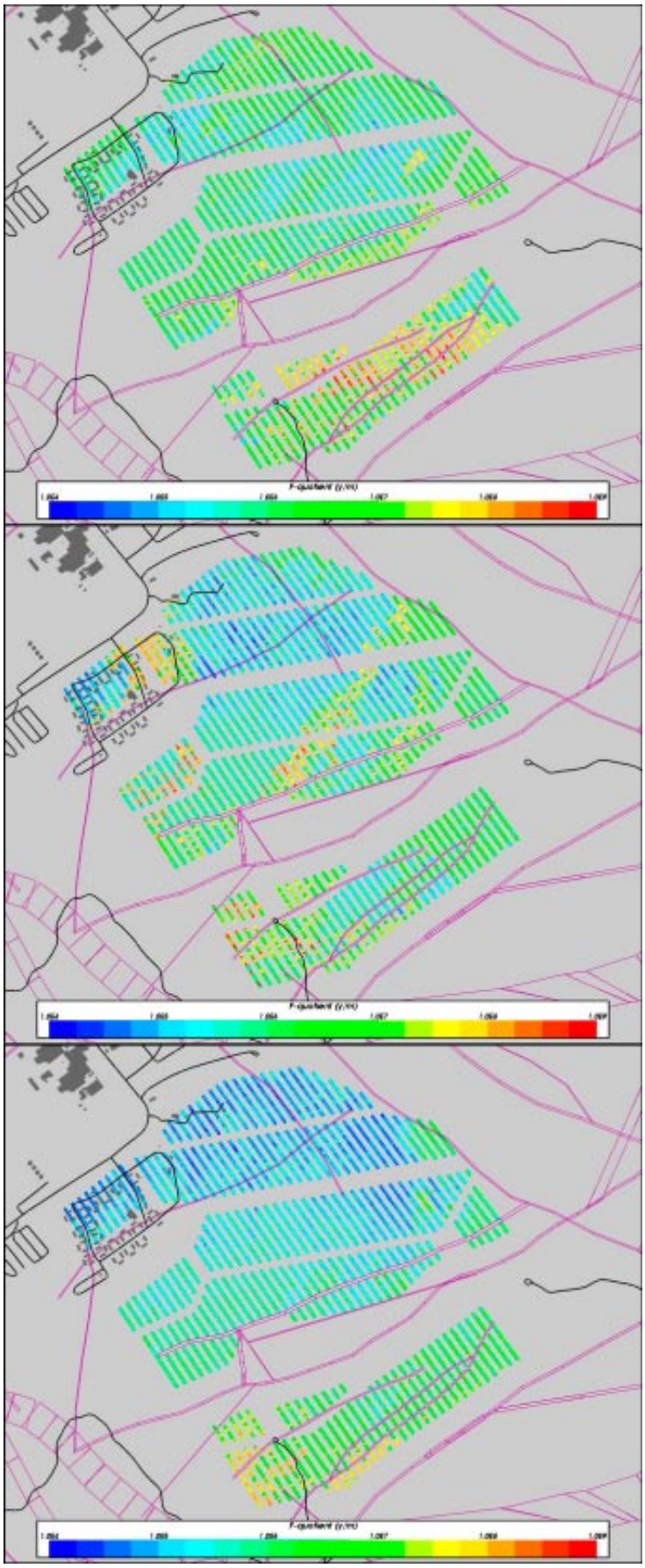

Figure 3-73. *Distribution of $\log_{10}(F_r)$ at 6,824 particle start locations for the uncorrelated transmissivity at release times (top to bottom) 2,020 AD, 3,000 AD and 9,000 AD. Also, the HCD model at z=–400 m (purple), roads and buildings (black).*

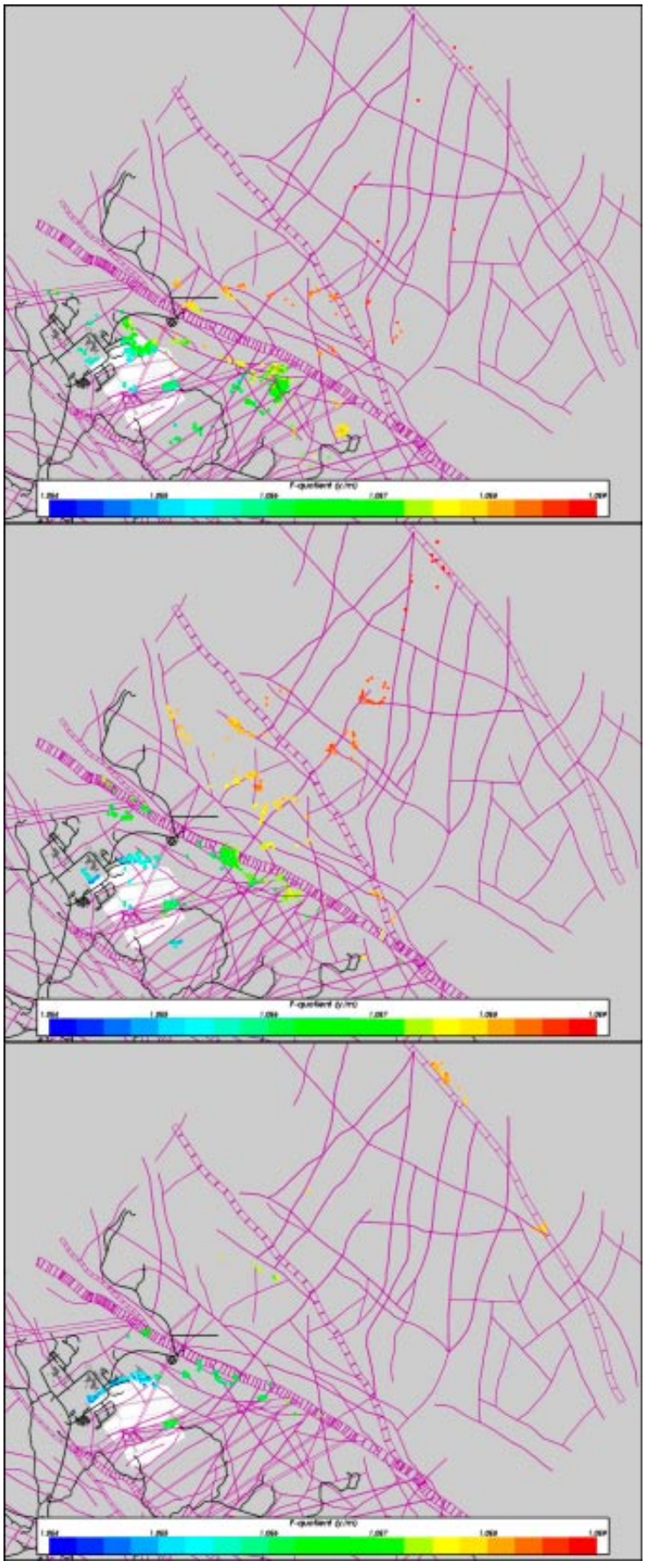

Figure 3-74. *Distribution of $\log_{10}(F_r)$ at 6,824 particle exit locations for the uncorrelated transmissivity at release times (top to bottom) 2,020 AD, 3,000 AD and 9,000 AD. Also, the HCD model at z=–400 m (purple), roads and buildings (black).*

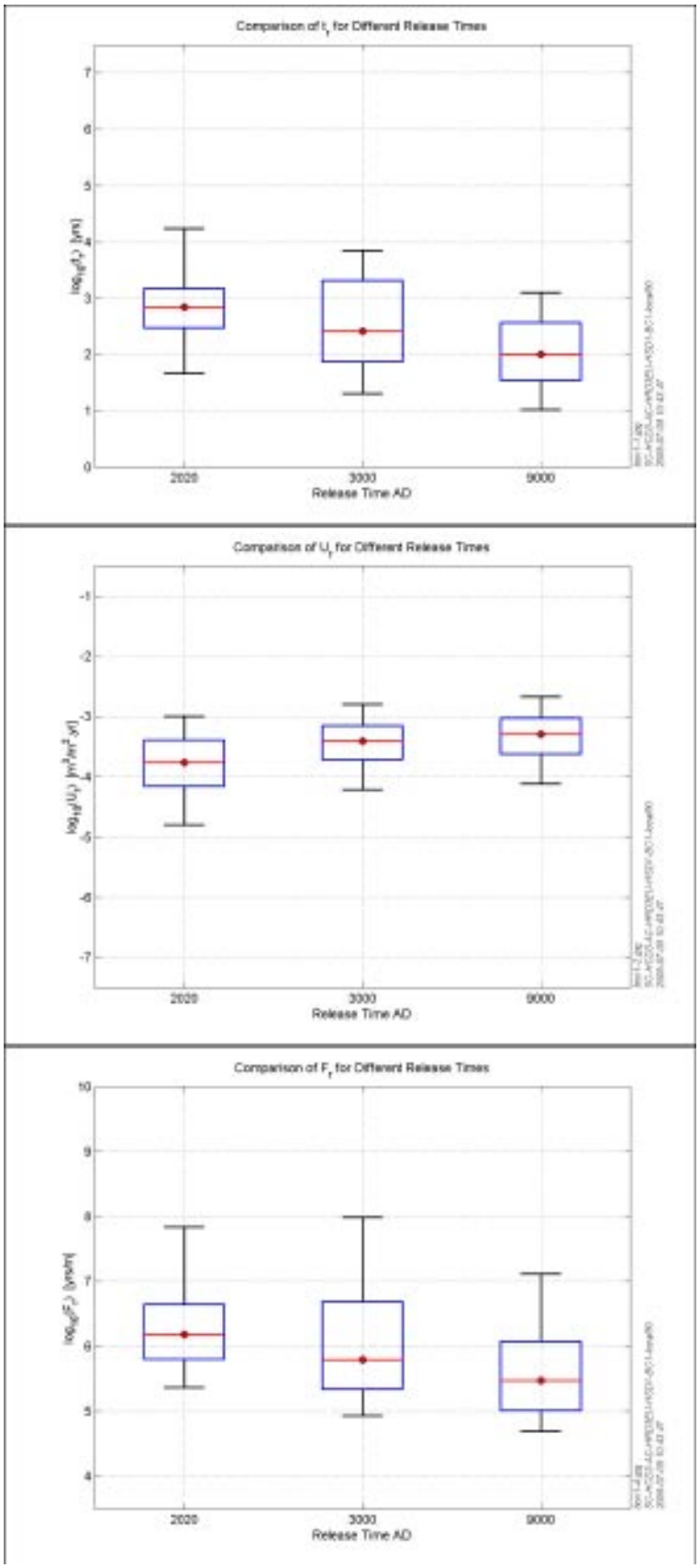

Figure 3-75. *Bar and whisker-plots for the uncorrelated transmissivity with 6,824 particles released at 2,020 AD, 3,000 AD and 9,000 AD. From the top: t_r, U_r, and F_r. The statistical measures are the median (red), 25th and 75th percentile (blue bar) and the 5th and 95th percentile (black "whiskers").*

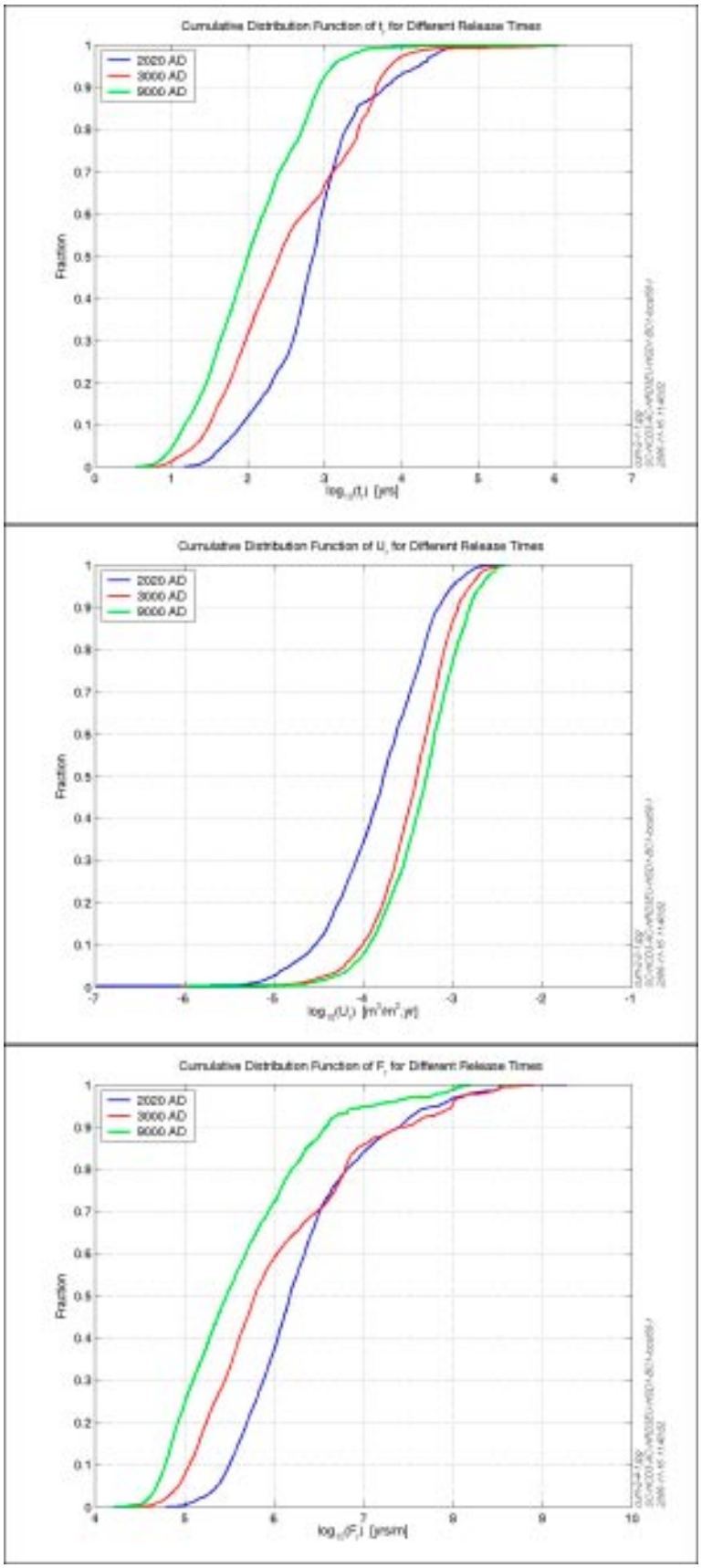

Figure 3-76. *Cumulative distributions for the uncorrelated transmissivity with 6,824 particles released at times 2,020 AD, 3,000 AD and 9,000 AD. From the top: t_r, U_r, and F_r.*

In general, it can be said that the uncorrelated transmissivity shows lower values for travel-time and F-quotient compared to the ECPM reference case. The explanation is much the same as for the semi-correlated case. These results are interesting since they suggest a poor correlation in the transmissivity to length relationship gives fewer long connections through the network and tends to make smaller flow cells, and hence reduces the sensitivity to the shoreline progression.

3.4 Discussion

A more comprehensive set of sensitivities have been considered in this study than was possible in the site-modelling study for F 1.2. A full list of the sensitivities considered and the variants used to quantify them is listed in Table 3-4. Sensitivities were quantified with regard to the effect on the key PA performance measures (PMs): travel-time, initial Darcy velocity, and F-quotient along flow-paths started from each canister position. Then, sensitivities were ranked according to the order of the effect on PMs to highlight those most important for further interpretation and to guide the choice of variants that need to be considered in the more detailed repository-scale modelling which is reported in the next section. Table 3-6 summarises the main conclusions from the cases performed. The cases are grouped by colour coding according to the assigned rank which denotes the degree of sensitivity found compared to the ECPM reference case. Cases with rank = 1 showed a sensitivity in the first significant figure for one or more performance measures. Cases with rank = 2 showed a sensitivity in the second significant figure for several performance measures, while rank = 3 cases showed sensitivity generally in the third significant figure. Only result for the group with rank = 1 have been discussed in any detail in the sections above. Many of the other variants show little or no difference compared to the ECPM reference case. Therefore there is not much to say about these results apart from the conclusion that the sensitivity studied had little effect. Out of fifteen cases performed, seven showed significant sensitivity compared to the ECPM reference case. These variants have already been discussed in the report. The remaining seven cases (rank 2 and 3) are of moderate or no interest since they showed no effects. For case with rank 1, PM statistics are tabulated in Appendix B.

The sensitivities that were found to be of rank 1 included:

- The choice between a multi-component CPM model and an ECPM model based an underlying DFN concept made a big difference to the PMs. Travel-times and F-quotient are about an order of magnitude higher for the CPM model. Part of the explanation for this was obvious from the fact that the CPM model took a more optimistic view of hydraulic conductivity in rock domains RFM029/017 by using the PSS measurement limit. However, there are also more subtle differences, such as flow is more channelised in the ECPM model due to heterogeneities, and flow tends to be shallower in the ECPM model. The F-quotient tends to be lower in the ECPM model since, a_r, is computed based on the connected fracture intensity in each element and flow-paths are often shorter.
- The choice of geological model has an effect mainly at future times, since the presence and properties of deformation zones outside the candidate area affect flow velocities downstream of the repository area. Flow-paths are generally longer for the BC geological model than the AC model. The location of discharge points is only moderately sensitive to the structural model, presumably because the shoreline position has a stronger effect.
- Using a multi-component DFN model that better captures the spatial variability within the candidate area improves the match against hydraulic conductivity. It also has a large positive effect on the PMs. The case with a lower transmissivity around the repository gave an F-quotient about half an order of magnitude higher for a release at 2,020 AD, one order of magnitude at 3,000 AD, and one and a half orders of magnitude at 9,000 AD.

- Another related case with lower fracture intensity around the repository gave a similar effect. For this case, both the block-scale hydraulic conductivity was in effect lowered as was the flow-wetted-surface. F-quotient was about half an order of magnitude for all release times in this case. These two variants are more realistic of site conditions around the repository based on F 1.2 borehole data and for this reason a multi-component DFN is considered in more detail in the next section.
- Alternatives were considered to the Hydro-DFN properties by using different relationships between fracture transmissivity and length. A case was considered with a semi-correlated model which specified that the mean transmissivity increases with length, but there is also a random variation about the mean. This gave travel-times and F-quotients that were two orders of magnitude lower for many paths, and a significantly larger spread in flow-paths and exit locations. Part of the reason is slightly higher block-scale hydraulic conductivities for this case. Another is thought to be that the heterogeneity in this model will tend to shorten flow channels making connections easier to the surface than to the horizontal boundaries, and so favour the vertical path straight up rather than the longer path to the shoreline.
- Similar results were observed for a case with no correlation between fracture transmissivity and length. The results are significant since they suggestion heterogeneity or a lack of correlation tends not only to disperse particles and exit locations, but also to shorten paths by making long horizontal flow-paths less likely.

The sensitivities that were found to be of rank 2 included:

- The sensitivity to the stochastic DFN in terms of considering different realisation did not have significant effect on the ensemble statistics of PMs over all 6,824 canisters. It suggests that the uncertainty in where the stochastic fractures are located and their properties can be captured to a large extent by considering the spatial variability in the fracture network in a single realisation over the repository volume by considering all canisters. Of course, we would need more realisations to obtain useful statistics for a particular canister or tunnel, but in terms of the overall performance of the repository, then a single realisation seems adequate to capture the general picture.
- Modifying the fracture radius distribution by use of the Variant Geo-DFN (power-law slope k_r=2.75) showed moderate sensitivity, and is probably of less importance than the transmissivity to length relationship. The reason is thought to be that both the reference case ECPM model and the Variant Geo-DFN were calibrated against the hydraulic data for KFM03A. This meant that the numbers and magnitudes of flowing features were adjusted in both cases to be about the same, and hence the connectivity and bulk flows in both cases are likely to be very similar. Hence, it is probably not necessary to consider the Variant Geo-DFN in the following detailed modelling.
- A lower kinematic porosity in the deformation zones was considered since it is possible that flow within them is limited to a small volume of the zone, e.g. a thin layer near the top. This gave only a moderate effect on the PMs. Presumably because much of the travel-time and F-quotient occurs in the background rock during the initial part of flow-paths between the release point and the first deterministic deformation zone.

The sensitivities that were found to be of rank 3 included:

- A layer of enhance hydraulic conductivity in the top 100 m was thought to be possible and needed to be considered since the cored boreholes are cased in the top 100 m. However, this was found to have almost no effect on results.
- Also, changing the transport properties (within the plausible range of values) of the HCD had little effect on the results.

Table 3-6. Summary of the main conclusions from the cases performed. The cases are grouped by colour coding according to the assigned rank which denotes the degree of shown sensitivity compared to the ECPM reference case: Highly sensitive or of general interest (red); Moderately sensitive (orange); Not sensitive (green).

Case description SR-Can Forsmark v1.2	Sensitivity	Rank	Conclusion
SC_HCD3_AC_HRD3EC	Conceptual model	1	The ECPM reference case. Model propagated from SDM F 1.2 and slightly modified for SR-Can.
SC_HCD3_AC_HRDDT	Conceptual model	1	The CPM base case as suggested by the DarcyTools team in SDM F 1.2. Shows great sensitivity to the choice of representation of hydraulic conductivity in the candidate area. Homogeneous properties result in less conservative performance measures compared to the ECPM reference case.
SC_HCD3_BC_HRD3EC	Geological model	1	The Base Case (BC) Geological model does not show very much sensitivity but is still of great importance since it affect the choice of structural model. Slightly less conservative performance measures compared to the ECPM reference case.
SC_HCD3_AC_HRD3A2_T	DFN	1	The lower transmissivity below ZFMNE00A2 has a great effect on the calibration of hydraulic conductivities and provides a significantly better match to data compared to the ECPM reference case. Higher F-quotients and longer flow-paths than the ECPM reference case.
SC_HCD3_AC_HRD3A2_P32	DFN	1	The lower P_{32} below ZFMNE00A2 has a great effect on results compared to the ECPM reference case even if they are slightly less pronounced than the lower transmissivity. Higher F-quotients and longer flow-paths than the ECPM reference case.
SC_HCD3_AC_HRD3ES	DFN	1	The semi-correlated transmissivity shows a great sensitivity and suggests much lower F-quotients and shorter flow-paths than for the ECPM reference case.
SC_HCD3_AC_HRD3EU	DFN	1	The uncorrelated transmissivity shows a great sensitivity and suggests much lower F-quotients and shorter flow-paths than for the ECPM reference case even if they are slightly higher than for the semi-correlated case.
SC_HCD3_AC_HRD3EC2	DFN	2	There is a moderate effect from the second realisation of the stochastic DFN. There are differences in the calculated statistical performance measures but the variation is not significant. And the median values are broadly the same as for the first realisation of the ECPM reference case.
SC_HCD3_AC_HRD3EC3	DFN	2	There is a moderate effect from the third realisation of the stochastic DFN. There are differences in the calculated statistical performance measures but the variation is not significant. And the median values are broadly the same as for the first realisation of the ECPM reference case.
SC_HCD3_AC_HRD3EC_VG	DFN	2	Moderate changes in the performance measure statistics compared to the ECPM reference case.
SC_HCD3N2_AC_HRD3EC	Transport properties	2	Moderate changes in the performance measure statistics compared to the ECPM reference case.
SC_HCD3N3_AC_HRD3EC	Transport properties	3	Little or no effect seen in the performance measure statistics compared to the ECPM reference case.
SC_HCD3F3_AC_HRD3EC	Transport properties	3	Little or no effect seen in the performance measure statistics compared to the ECPM reference case.
SC_HCD3_AC_HRD3ECK2	Hydraulic properties	3	Little or no effect seen in the performance measure statistics compared to the ECPM reference case.

Other general remarks:

- Flow-paths show that the flow-field changes considerably over time and that the flow-paths initially are short and localized but tend to become longer as the shoreline retreats. Although the shoreline has a very strong effect, there are always short paths to be found at all release times controlled by topography and the structural model just depending on where the particles are started in the repository. The western part of the repository tends to have the shortest paths; the eastern part has the longest.
- There are great differences in F_r and t_r for the released particles depending on which of these two generic paths are followed.
- Generally the discharge areas (particles exit locations) are limited to a few places in large deformation zones and low topographic areas or the shoreline. At 9,000 AD many particles follow the shoreline all the way to the northern model boundary.
- A specified infiltration boundary condition instead of a specified topographic head has already been considered in the site modelling /Hartley et al. 2005/ which found little effect on transport performance measures for the infiltration and properties of Quaternary deposits used. Given the very low topographic relief in the area it is not surprising that the assumption that the watertable is at ground surface is reasonable.

4 Detailed repository-scale modelling and input to PA

As described in Section 2.2.5, the PA methodology requires flow-paths to be calculated for three potential paths for radionuclides to leave the canister and enter the host rock: via a fracture adjacent to the deposition hole; through the EDZ around the base of the tunnel, or via the tunnel itself. To quantify each of these paths it is necessary to perform detailed flow and transport calculations down to the scale of a metre or less around the repository. Hence, fine-scale models have to be constructed, and must also be nested in some way to capture the larger scale flow and transport situation at a variety of times.

A methodology for how we approach this problem is outlined schematically in Figure 2-11. Generally, the approach is to retain two conceptual models for the bedrock: the DFN and CPM concepts. Firstly, we consider a combined model that represents the bedrock as a DFN which surrounds a CPM representation of the porous materials used to backfill the deposition holes (bentonite) and tunnel system (mixed bentonite and crushed rock). Secondly, we consider a multi-component CPM model with homogeneous properties within the various components of the bedrock, and a CPM representation of the tunnels in the same way as for the first model. In each of these two models, the repository is represented explicitly down to the resolution of a metre or less, and so the domain of these models has to be limited for practical reasons to cover just one main access tunnel, and associated deposition tunnels, at a time. Potentially this means that the individual repository-scale model domains to capture an entire flow-path, so pathlines may have to be continued in the corresponding regional-scale ECPM model once a particle reaches the boundary of the repository-scale. For the CPM representation this is not a major concern because the representation is consistent on both scales. However, for the DFN model it is less satisfactory if the calculation of flow-paths uses a DFN representation for the repository-scale transport and then switches to an ECPM representation to reach the surface. In practice this problem was avoided for the majority of paths by extending the DFN repository-scale model to almost the surface of the model, and because it turns out that flow tends to be focussed on the larger sub-vertical fractures giving flow-paths that are predominantly upwards once they reach such a fracture.

Another issue is that these models require that boundary conditions be defined on all external surfaces by importing the fluid density and pressure from the regional-scale models. In order to quantify how sensitive results are to nesting models in this way and to test the robustness of the approach, a third type of model is deployed that combines the entire regional-scale domain with a local-scale DFN model including a representation of the repository, but not down to the detail of individual deposition holes.

The repository-scale models provide a much better resolution of flow and transport than the regional-scale models, and hence are used to provide the performance measures required as input to PA calculations. The models constructed here represent a refinement of the regional-scale cases described in Section 3. Uncertainties need to be quantified for this series of models also, but we shall only consider some of the key variants ranked 1 in the previous section to cut-down the number of calculations. In addition, there is a need to measure the sensitivity to the backfill and EDZ properties.

4.1 Combined DFN/CPM repository-scale model

We shall start by describing the DFN/CPM combined model where a DFN sub-model is used for the bedrock and a CPM sub-model for the repository. This model is regarded as being conceptually more realistic than the pure CPM model since it is based on the assumption that flow occurs exclusively in fractures, which has been validated by the PFL data in boreholes KFM03A and KFM02A, for example. The stochastic nature of the model also exhibits heterogeneities in the occurrence and magnitude of flow which is consistent with field-tests, and are expected to be encountered around a repository.

For both this model, and the pure CPM model, it was necessary for practical reasons to split the repository into 3 blocks, one for each main access tunnel as shown in Figure 4-1. The overall repository has an area roughly 2 km by 2 km (see Figure 2-16), and it should be noted that it is non-coplanar since each deposition tunnel slopes down slightly toward its adjoining access tunnel. For the combined DFN/CPM model a relatively thick domain was use so that many particles could be tracked to the surface within the DFN sub-model, and hence avoids some of the approximations that have to be made if particles have to be restarted in an ECPM regional model to complete the flow-path to the surface. For these models a domain approximately 900 m by 2 km by 580 m thick was used. The vertical extent is from z=–600 m to z=–20 m elevation with the base of the deposition tunnels at around z=–410 m on average. For the pure CPM model, a continuum representation is used on both the repository- and regional-scales, and PMs such as F-quotient are calculated in the same way. Therefore, there is less of an issue in nesting the calculation of flow-paths for this model concept, and so a slightly thinner domain from z=–500 m to z=–250 m was used for the repository-scale CPM model to give quicker calculations.

As shown in Figure 4-1, the 3 blocks overlap to keep the grid topology relatively simple. To calculate flow and transport for the whole repository, flow simulations were performed for each of the three blocks separately. Although there is an overlap, flow-paths were only calculated once for each deposition tunnel by calculating the flow-path only in the block associated with the relevant main tunnel. For each block a nesting procedure was used that set boundary conditions on the external surfaces of the block by interpolation from the corresponding regional-scale ECPM model at a selected time. The model set-up and numerical procedure is the same for each block, so we shall largely focus on the western block as an example of the model set-up and results.

For the safety assessment calculations it was felt that the central case should reflect the current understand of the site, and hence a multi-component DFN model should be used consistent with the observed heterogeneity in fracture properties. Based on the DFN model sensitivities considered in Section 3.3.5 the model with a lower fracture transmissivity below ZFMNE00A2 was chosen as the central ‘Realistic’ case for repository-scale DFN model. This was used since it predicts flow, although very small, around a significant number of canisters. Using this as the central case, a number of variants as given in Table 4-1 were considered with different backfill, EDZ and fracture transmissivity parameters.

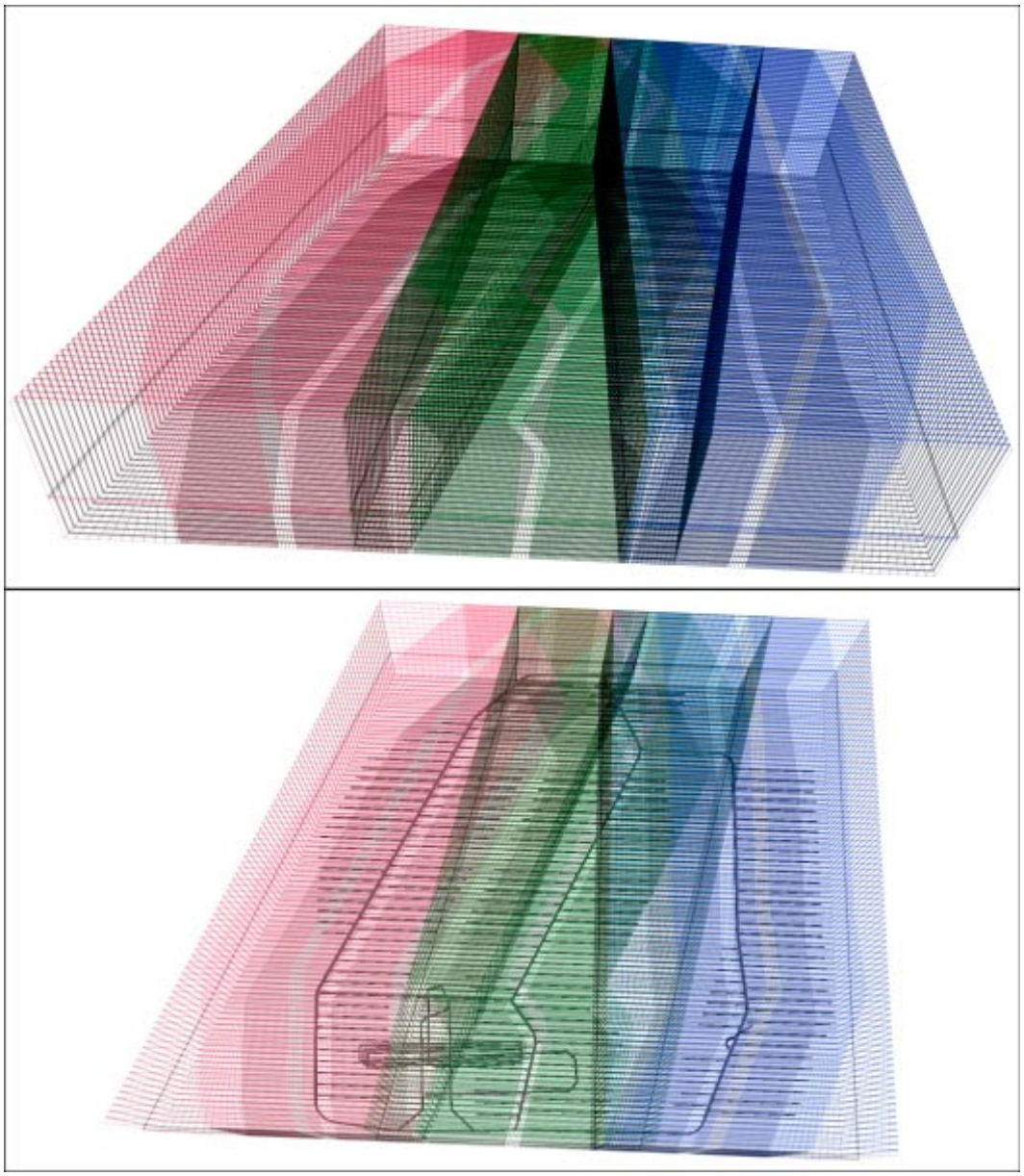

Figure 4-1. *Repository-scale model grids split into 3 blocks: western access tunnel (red), central access tunnel (green), and eastern access tunnel (blue). Top: oblique view with grid only. Bottom: map view with repository tunnels shown inside, but not the shafts or ramp.*

Table 4-1. List of cases modelled in the DFN/CPM repository-scale modelling.

Case description	Sensitivity	Properties	Description
HCD3_AC_HRD4A2_T	Realistic case	DFN – Correlated T/L	Lower open fracture T below ZFMNE00A2
HCD3_AC_HRD4	Reference case	DFN – Correlated T/L	CF Base Case (Volume E DFN)
HCD3_AC_HRD4A2_T_EDZ	Realistic case + EDZ	DFN – Correlated T/L	100 times high conductivity in EDZ
HCD3_AC_HRD4A2_T_T2	Realistic case + Tunnel	DFN – Correlated T/L	100 times higher conductivity in tunnel backfill (10^{-8} m/s)
HCD3_AC_HRD4SA2_T	Realistic case + DFN	DFN – Semi-correlated T/L	Semi-correlated T model
HCD3_AC_HRD4UA2_T	Realistic case + DFN	DFN – Uncorrelated T/L	Uncorrelated T model

4.1.1 Model set-up and specification

An illustration of the model domain for the western block is shown in Figure 4-2. Most of the domain, i.e. apart from the repository, is the DFN sub-model. The CPM sub-model is composed of just the transport tunnels, access tunnels, deposition tunnels and deposition holes as shown in Figure 4-3 with properties as given in Table 2-2. Figure 4-3 also shows the finite-element grid used to discretise the tunnels. As can be seen, all structures are represented, but refinement is essentially the minimum that could be used with the grid size varying from about 1 m for the cross-section of deposition holes to about 10 m for the spacing along the access tunnels. The ramp and shafts were added as a conductive two-dimensional element to provide a simplification to their geometry which would have been difficult to include explicitly in three-dimensions.

The DFN sub-model that surrounds the repository is shown in Figure 4-4. The fractures are derived from 3 sources: deterministic deformation zones imported from the geological model, stochastic fractures imported from the regional DFN model including fractures down to a radius of 7 m, additional stochastic fractures in the radius range 1.1–7 m. With reference to Table 2-9, the connected fracture intensity calculated for a truncation radius of 1.1 m (2 m length) is about 0.1 m^2/m^3, that suggests a connected fracture spacing of about 10 m for a fracture radius truncation of 1.1 m. Since the height of the deposition hole is about 7 m, then a truncation radius of about 1 m is an appropriate choice. However, because the network is heterogeneous, then it does not guarantee that every deposition hole will be intersected by a connected fracture. Reducing the minimum fracture radius further is not feasible due to the size of model. The additional stochastic fractures down to a radius scale of 3.3 m were added throughout the model domain, but

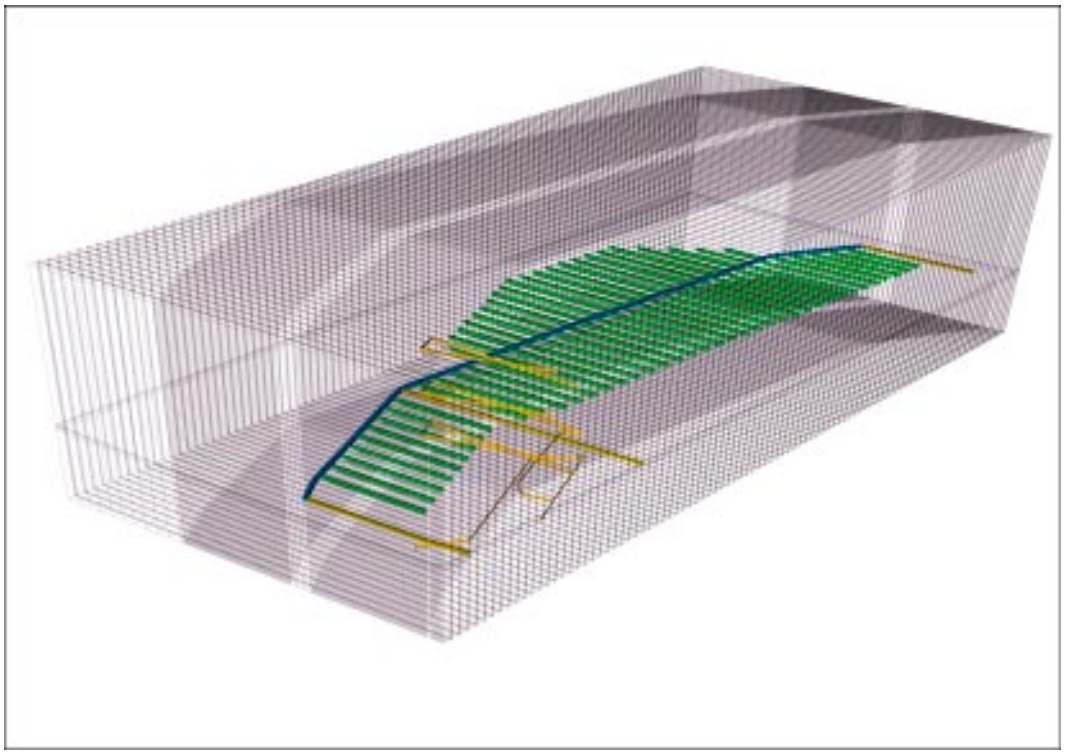

Figure 4-2. *Domain used for the combined DFN/CPM model for the western block. The outer grid shows the domain for the DFN sub-model. Inside of that, the repository structures are represented by a CPM sub-model (deposition tunnels are coloured light blue; access tunnels dark blue; transport tunnels yellow). The spiral ramp in the forefront (coloured yellow) is actually represented by equivalent fractures.*

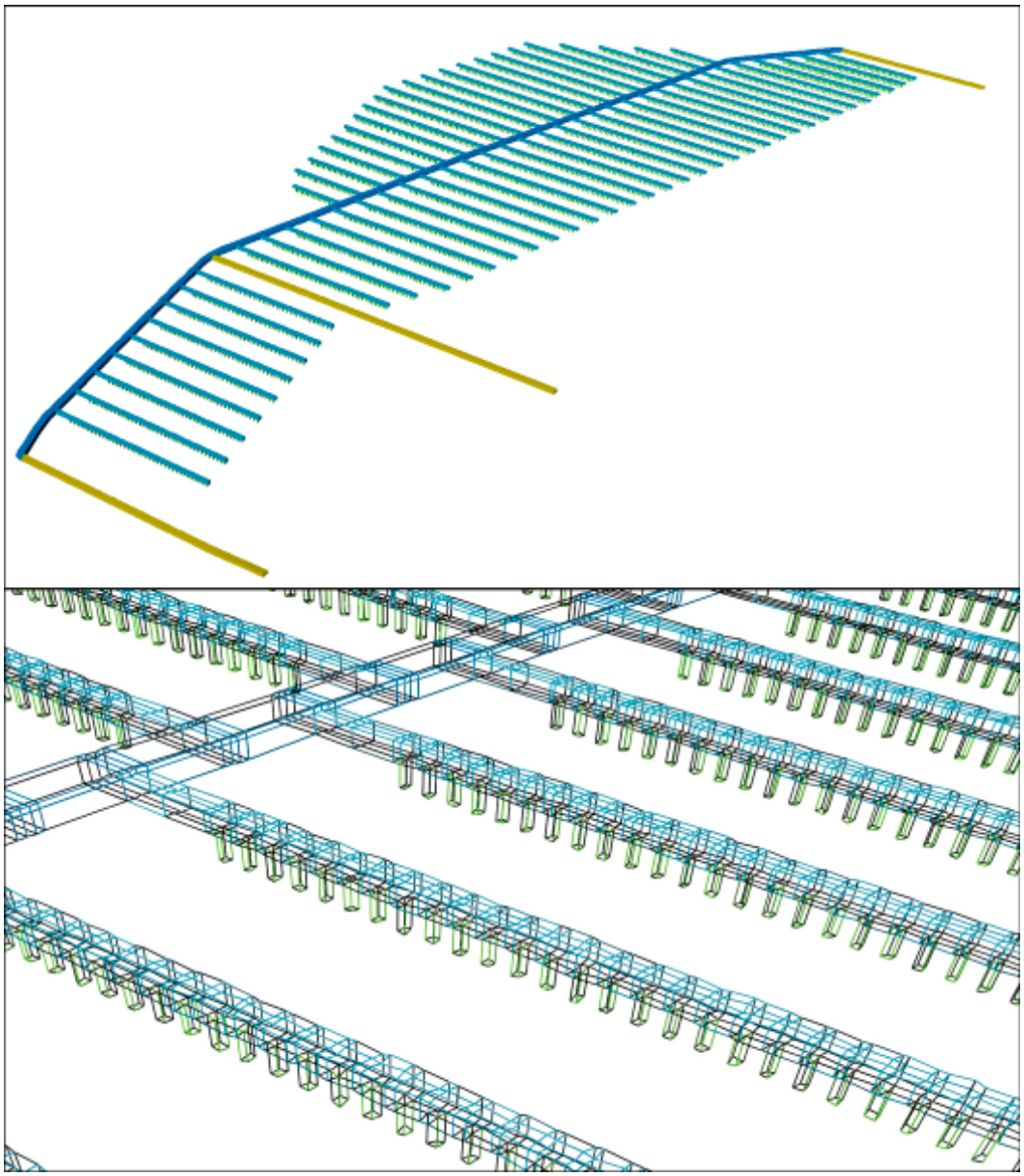

Figure 4-3. *Representation of repository structures as CPM sub-model within the combined DFN/CPM model for the western block. Deposition tunnels are coloured light blue; access tunnels dark blue; transport tunnels brown; and deposition holes green. Top: volumes coloured by properties. Bottom: close-up of finite-element grid.*

between lengths of 1.1 m to 3.3 m radius, the fractures were only generated between z=–425 m and z=–395 m, i.e. 15 m above and below the repository. The geometrical fracture properties for the stochastic network were based on the Hydro-DFN for Volume E, see Table 2-4. For the western block about 1.44 million fractures were generated in the model region. Some of these were subdivided to improve the discretisation of flow and transport giving a total of about 1.83 million fracture objects. Each fracture larger than 5.6 m radius (10 m length) is sub-divided into 5.6 m sub-fractures ('tessellated'). As part of the flow calculations, the first step was to remove isolated or dead-end fractures. Since the network is sparsely connected, as many as 1.2 million fractures are removed since they will not influence flow. The remaining connected network contains about 1.51 million degrees of freedom located at fracture intersections and in the CPM parts.

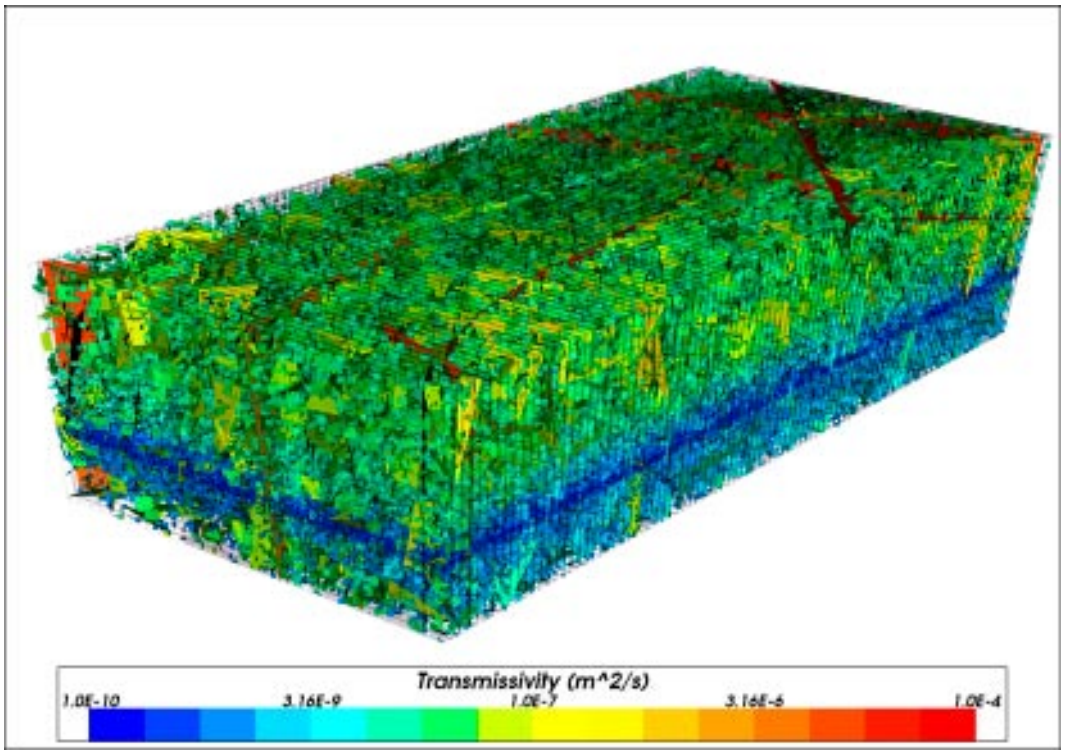

Figure 4-4. DFN sub-model for the combined DFN/CPM base case model of the western repository block. Fractures are coloured by transmissivity. The larger fractures correspond to deterministic deformation zones from the geological model. A lower transmissivity is used below –350 m which corresponds to Volume G.

The connectivity of the network is illustrated in Figure 4-5 by showing a slice through the network at repository depth before and after removing unconnected parts of the network. The effect is dramatic and consistent with the study made in Section 2.3.3. Observe that more fractures are removed away from the repository as the tunnels actually create extra hydraulic connections that would not otherwise exist. It is perhaps worth saying that the dead-end fractures removed are ones where a fracture has only one connection with another fracture. It is then removed, and the algorithm is recursive in order to remove any sequences of dead-ends. However, dead-ends can occur as closed loops of fractures each connected to two or more other fractures but with only one way in/out of the loop, and these are not removed. Such closed loops may be a side-shoot of the main network or may only be connected to a section of tunnel. These were found to occur in the DFN models of Forsmark and caused problems for particle tracking.

The boundary conditions for each combined model were obtained by interpolation of the residual pressure and groundwater density from the relevant regional-scale ECPM model (the ECPM reference case for the models shown here) at selected times. Again, the times selected were 2,020 AD, 3,000 AD and 9,000 AD. The residual pressure was held constant on the outer boundary of the DFN sub-model. At the interface between the two sub-models, extra internal conditions were enforced to ensure continuity of residual pressure and conservation of mass-flux across the interface between the CPM and DFN parts.

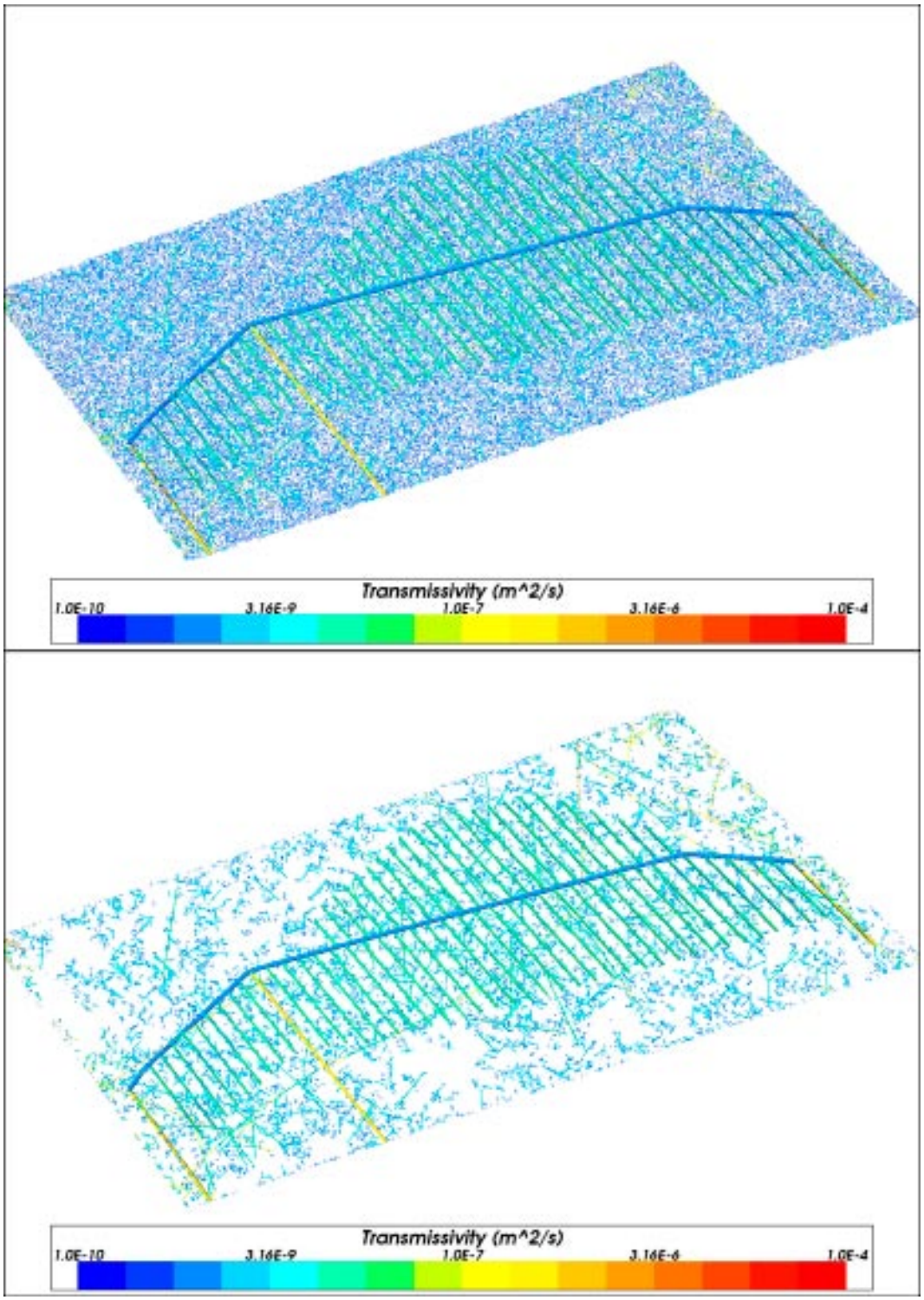

Figure 4-5. *A horizontal slice through the combined DFN/CPM base case model of the western repository block. Fractures are coloured by transmissivity. The CPM part is the fishbone like structure. Top: all fractures generated greater than 2 m length. Bottom: only connected fractures.*

4.1.2 Variable-density flow calculations

Steady-state calculations of groundwater flow in the combined DFN/CPM models were performed at selected instances in time. The effects of variable groundwater density were taken into account in both regions using some new developments in CONNECTFLOW. This allows a consistent flow-field to be calculated given a fixed spatial distribution of groundwater density. The distribution of density was obtained by interpolating the groundwater density calculated in the regional-scale ECPM model at a specified time on to each fracture intersection in the DFN sub-model, and on to each finite-element in the CPM sub-model. Figure 4-6 shows the density in the fracture system. Roughly speaking, density increases with depth and towards the coast. Likewise, the residual pressure was also interpolated from the regional-scale model. In the flow calculations, groundwater density was held fixed throughout the whole domain, while residual pressure was only fixed as a boundary condition at the external intersections of the DFN sub-model. The steady-state residual pressure consistent with the fluid density and fixed pressure boundary conditions was then calculated in the DFN model with the pressure degrees of freedom calculated at each fracture intersection. This methodology was verified in a simple situation using the Henry test case, see Appendix D. The distribution of residual pressure calculated at 2,020 AD is shown in Figure 4-7 with the fractures above the repository removed to show the continuity of residual pressure through the DFN and CPM sub-models. A residual pressure of 10^4 N/m^2 equates to a head of about 1 m. Note: the equations solved for variable-density are conservation of mass-flux (density multiplied by Darcy velocity) rather than just conservation of flow as with the constant-density case. Also, the Darcy velocity has two components coming from the gradient of residual pressure and a buoyancy term in the vertical direction.

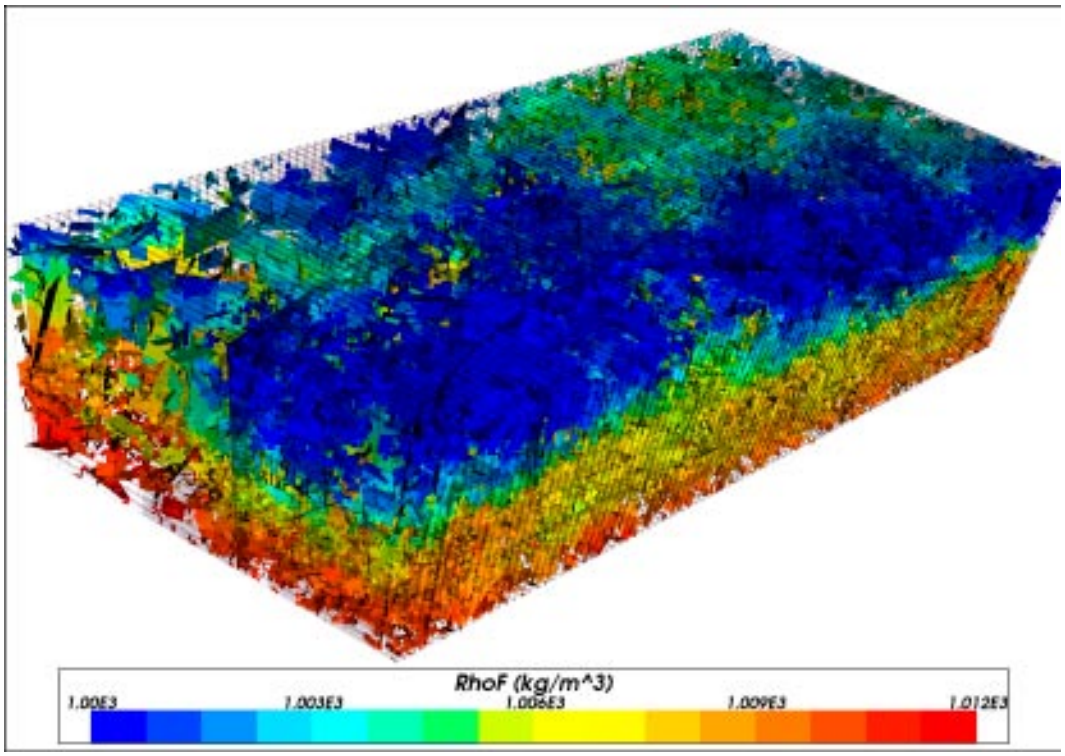

Figure 4-6. *Distribution of groundwater density used in the flow calculation at 2,020 AD in the western repository block for the combined DFN/CPM base case model. Only the connected fractures are shown and are coloured by fluid density (kg/m^3).*

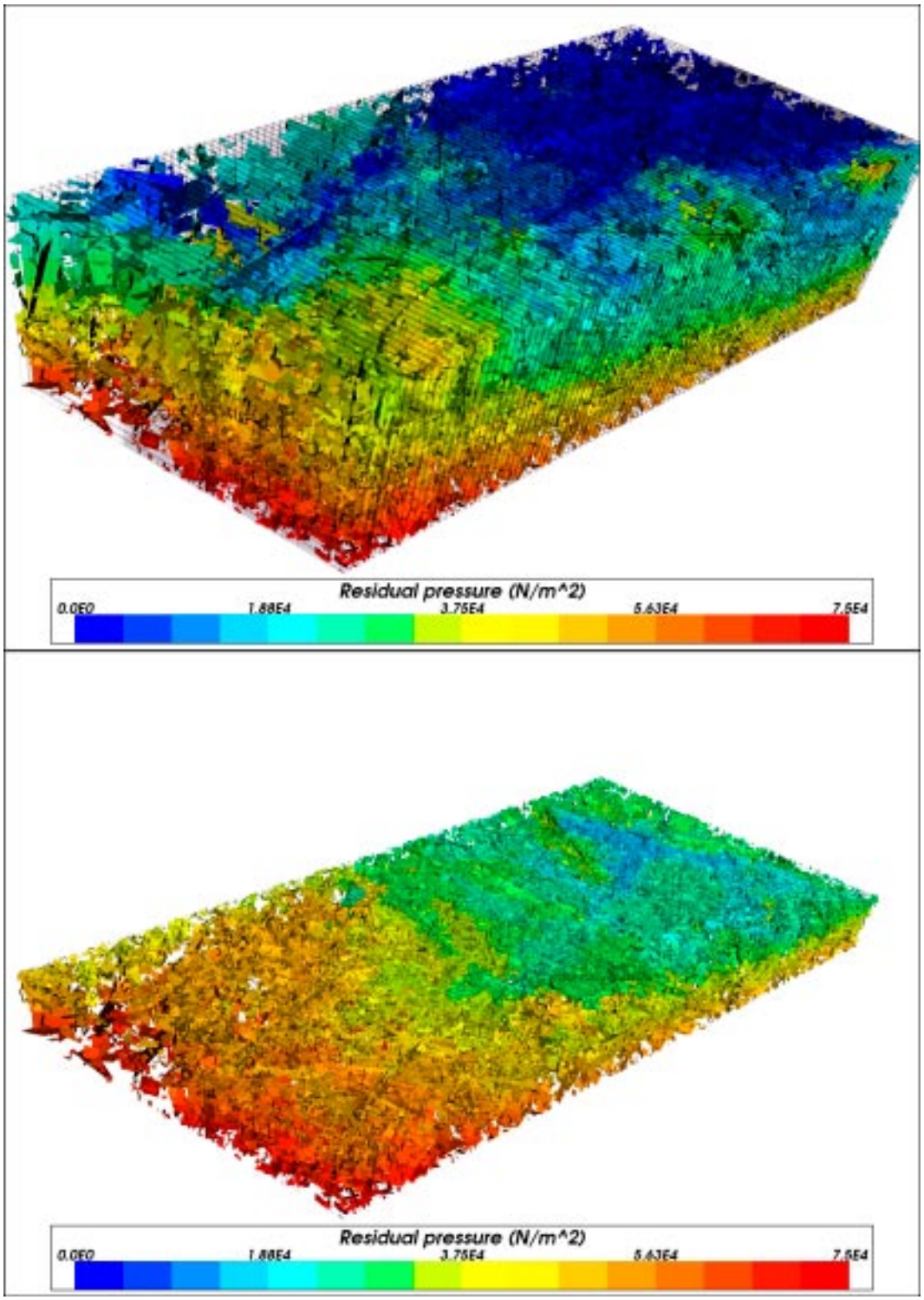

Figure 4-7. *Results of variable-density flow calculation at 2,020 AD in the western repository block for the combined DFN/CPM realistic case model. Only connected fractures are shown and are coloured by residual pressure. Top: all fractures and model boundary. Bottom: with fractures above the repository at z=–410 m removed to show residual pressure around and including the CPM sub-model.*

4.1.3 Flow-paths

The algorithm in CONNECTFLOW for calculating particle-tracking through a DFN model was enhanced to support variable-density flow-fields. The general approach remains that particles are moved between fracture intersections in a stochastic way with successive particle destinations being selected by a random process weighted according to the fluxes between pairs of intersections, but the fluxes are modified to account for buoyancy-driven flows.

As described in Section 2.2.5, three particles are released around each canister:

1. Path_Q1 in the fracture that intersects the deposition hole with the highest flux.
2. Path_Q2 in the EDZ fracture adjacent to the deposition hole.
3. Path_Q3 in the CPM tunnel 1 m directly above the deposition hole.

A total of 2,504 particles are released for each path in the western repository block. Particles are tracked until they reach the boundary of the repository-scale model. The approach allows particles to move from the DFN sub-model to the CPM sub-model, or vice versa, any number of times according to the flow-field, so particles may pass through one or more sections of tunnel (see Section 2.2.4). To compute a complete path from a canister to the surface, once the particle exits the repository-scale model, the particle is restarted in the regional-scale ECPM flow-field corresponding to the same release time. This introduces an approximation that the far-field flow can be handled adequately by an ECPM model. Hence, we shall consider how much of the retention or F-quotient is in the repository-scale DFN compared to the regional-scale ECPM model, and in Section 4.4 a different approach to nesting a DFN is considered to quantify the sensitivity to the choice of nesting method.

A major issue in the calculation of flow-paths was found to be the poor connectivity of the Hydro-DFN network which meant it was difficult to apply the methodology for providing input to PA as envisaged. The problem is that many of the deposition holes are not intersected by fractures that connect to the main flowing network, and also there are sections of tunnel with essentially stagnant flow where Darcy velocities are around 10^{-6} m/y or less. An illustration of the connected fracturing around some holes along 4–5 deposition tunnels is shown in Figure 4-8. A sizeable proportion of holes, around 60%, are either not intersected by a connected fracture or by a cluster that is only connected to the tunnel system but not the main connected network. There are two significant effects on the numerical methods used. Firstly, we use an iterative solver method, namely Generalised Minimum Residual (GMRES) with incomplete LU factorisation preconditioning, to obtain the solution to the groundwater flow problem, the size of the residual fluxes over the global system are reduced to a relative error of about 10^{-15} or less (net flux/gross flux), which is very accurate overall, but because flow velocities vary over a huge range, it does not guaranteed that the residual flux is small in fractures that have very low velocities relative to the small flow magnitudes. That is, the flow in fractures with large fluxes are resolved extremely accurately, while we are not guaranteed mass-balance in fractures that have fluxes that are very small, i.e. around 10^{-15} of the maximum flux. Then flow-paths can get stuck if we start particles in fractures or sections of tunnels with very small flows. Secondly, if we start particles in fracture connections that form closed loops, then particles will also tend to get stuck.

Figure 4-9 shows particles released in the western repository block at 2,020 AD. The particle-tracks are shown together with the exit locations on the top surface in this case. It is very noticeable how the particles congregate on a few large fractures, and hence in the lower plot we superimpose fractures greater than 50 m. This shows very clearly that if a particle can enter the connected network, then it tends to focus rapidly on the larger fractures, most notably the deterministic deformation zones, but also the large stochastic fractures greater than about 50 m in length. A very significant point is that particles tend to move vertically upwards in large fractures since there are too few long horizontal connections through the network, and this suggests a markedly different transport pathway to the ones we saw in the continuum

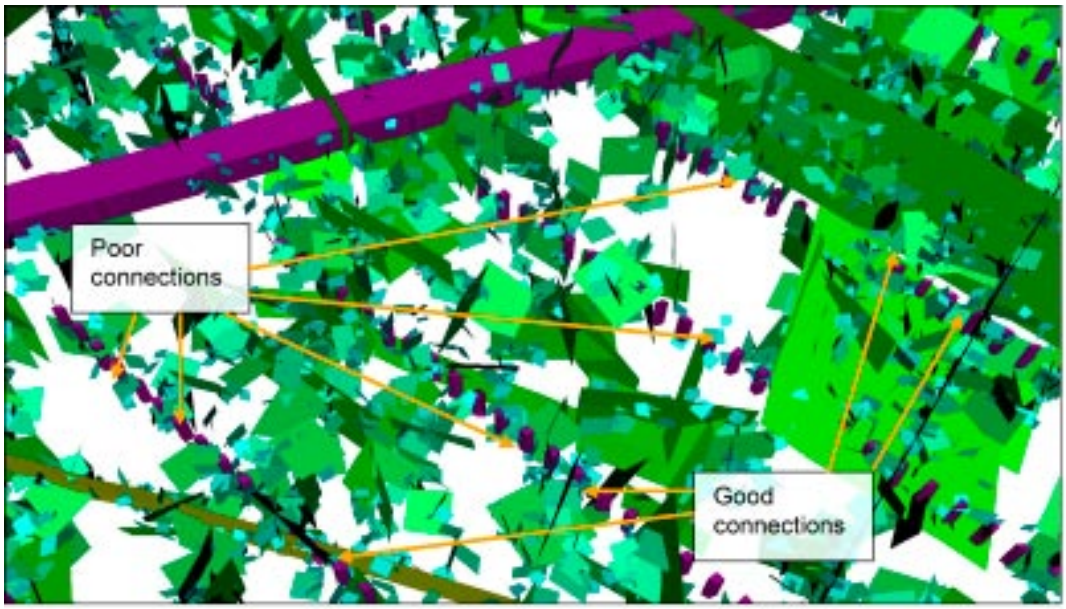

Figure 4-8. *Connected fracture network surrounding the canisters in the combined DFN/CPM realistic case model. The deposition holes and access tunnel are coloured purple, and the fractures are coloured by transmissivity. Only the connected fractures between z=–405 m and –440 m are shown.*

based models reported in Section 3. It implies quite different results and conclusions are to be expected compared to the continuum models even for the supposedly equivalent ECPM model, and reinforces the need to consider alternative concepts when the site is characterised by poor connectivity.

It is important to note that 40% of particles that are started near a canister tend to become stuck very close to their start location. This is because the flow around the repository is very heterogeneous even in the tunnel and there are areas of stagnant flow such when particles are started there they are either stationary or move around closed loops at very low velocity for numerical reasons. Table 4-2 summarises the situation for paths Q1, Q2 and Q3 at release time 2,020 AD. For Q1, particles are released in the fracture abutting the deposition hole with highest Darcy velocity. Although nearly all canisters are intersected by a fracture, many of these fractures are either unconnected and therefore have no flow, or are connected to a closed loop of fractures that has essentially no flow. Table 4-2 shows that about 27% of canisters are without an adjoining connected fracture, and a further 32% are in areas of stagnant flow with no connected path away from canister. Only about 1% of particles become stuck due to mass balance problems in the numerical solution. This leaves about 40% of canisters that have Q1 paths to the surface. Of these, only about 15% of canisters are intersected by a connected fracture above

Table 4-2. Summary of the particle tracking results for the combined DFN/CPM realistic case model released at 2,020 AD. For each of the 6,824 canister positions, paths Q1, Q2 and Q3 are computed.

Particles/canisters [%]	Q1	Q2	Q3
Fracture with $T>10^{-9}$ m^2/s	14.7%	N/A	N/A
No connected fracture	27.3%	N/A	N/A
Particles that reach surface	39.9%	58.4%	57.9%
Stagnant flow	31.8%	40.2%	40.9%
Mass balance problems	1.0%	1.4%	1.2%

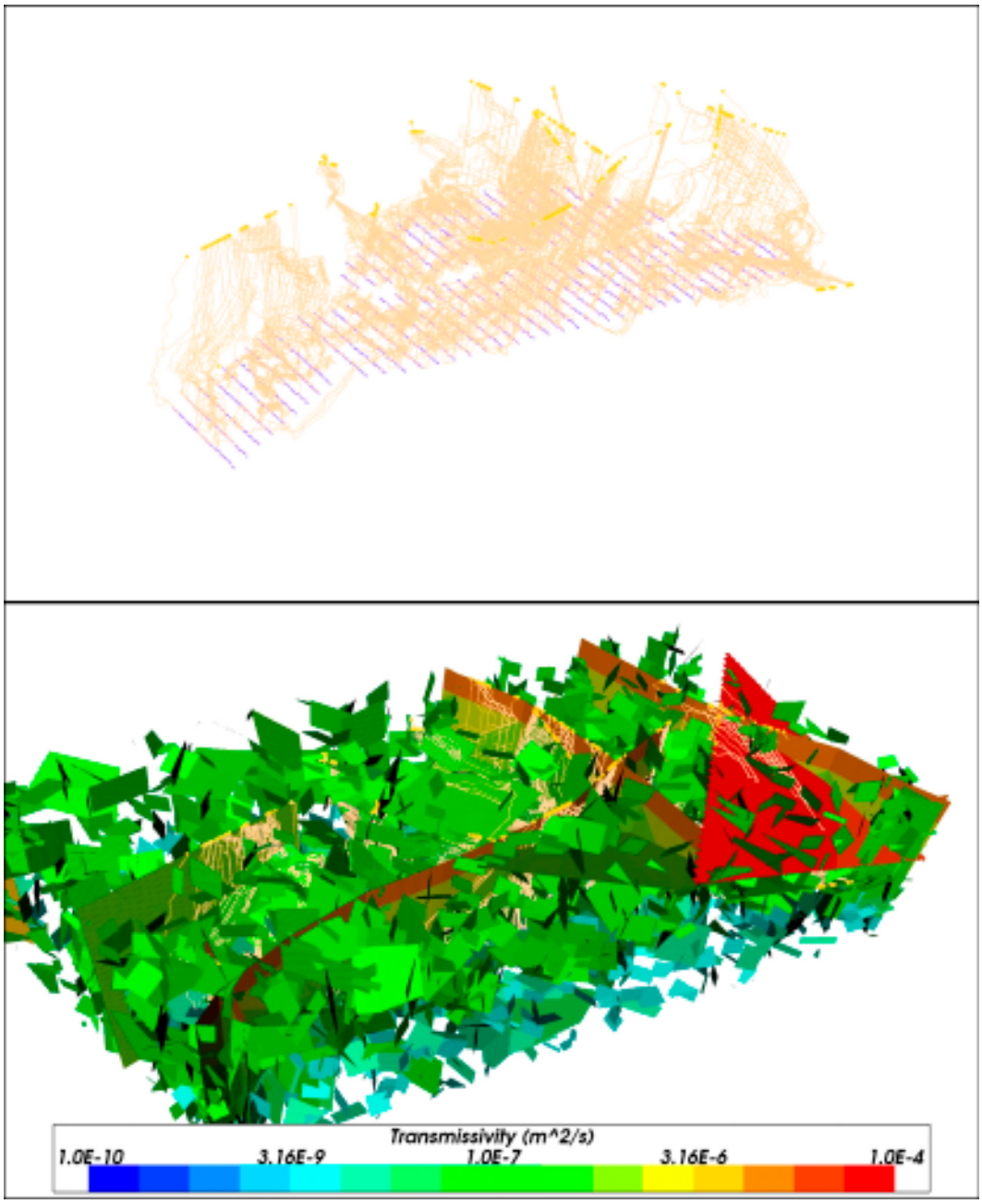

Figure 4-9. *Flow-paths in the variable-density flow through the combined DFN/CPM realistic case model of the western repository block for a release at 2,020 AD. Top: The start locations of particles are shown in purple with the exit locations as orange dots and the flow-paths also in orange. Bottom: as above but with fractures longer than 50 m superimposed.*

the PFL detection limit of around 10^{-9} m^2/s. For the releases in the EDZ and the tunnel, Q2 and Q3, about 40% of particles remain close to the repository due to stagnant flow, 58% make it to the surface of the model. The reason there are areas of stagnant flow in the tunnel and EDZ is that each deposition tunnel is essentially a dead-end, so to get advection along or out of the tunnel there must be a head gradient along it which requires that at least two moderate to large water-bearing fractures intersect the tunnel. The results suggest this occurs only for about 60% of the deposition length. Further, the general head gradient tends to be orthogonal to the axis of the deposition tunnels which also reduces advective velocities along tunnels.

In Figure 4-10 the distribution of F-quotient (log_{10}) at 6,824 Q1 starting locations in the repository are shown for the 40% particles that reach the surface of the model for the combined DFN/CPM realistic case model and at release times 2,020 AD, 3,000 AD and 9,000 AD. The blue colour indicates smaller values (F-quotient about 10^4 y/m) and red indicates higher values (F-quotient 10^9 y/m). Firstly, looking simply at the canister positions that are not shown because they don't have a path to the surface suggests that it is quite random and all tunnels seem to have some canister positions with a Q1 path. Also the pattern is largely the same at the different release times, as is to be expected since it is mainly a function of the geometry of fracture connections, though there will be some effect of boundary conditions also. The smallest F-quotients (blue colour) around 10^4 y/m to 10^5 y/m lie close to the deterministic deformation zones as shown in the figures. It is likely in these areas that the deformation zones give rise to areas of enhanced fracture connectivity locally that makes it easier for particles to find a route through the background fracture network to the deformation zone. Comparing this figure with the equivalent ECPM case in Figure 3-61 suggests the DFN model gives F-quotients one or two orders of magnitude lower. One of the main reasons is that flow-paths are shorter, predominantly vertically upwards rather than to the shoreline as in the ECPM model. Another factor is that paths tend to be more focussed towards channels through the larger fractures and deformation zones in the DFN model, whereas they are more diffuse in the continuum model.

Figure 4-11 shows the distribution of F-quotient (log_{10}) at particle exit locations for the same 3 releases times. Very evident here is that the discharge is heavily focussed on the deformation zones. Flow-paths are significantly shorter than the equivalent ECPM case and tend to be less sensitive to changes in the shoreline position. Note the slice through the deformation zones is at an elevation of –400 m rather than at the surface. Clearly, since the deformation zones have a dominant effect on transport, then the key sensitivities in the DFN model are going to be the geological structural model and the properties of deformation zones.

Some investigations were made towards the end of the project to consider some possible enhancements to the particle tracking algorithm that mainly focussed on removing dead-end clusters of fractures, improving the method for moving particles from the CPM to DFN sub-domains, and a more regular discretisation of the deformation zones. These enhancements lead to an increase in the number of particles reaching the surface for path Q1 to about 60% and about 83% for paths Q2 and Q3. This suggests these enhancements and others planned should address most of these numerical issues in time for the SR-Site assessment. There was insufficient time for these trial results to feed through into the SR-Can risk assessment calculations, but some results are included in Section 4.1.4 as an illustration of the possible impact on the performance measures.

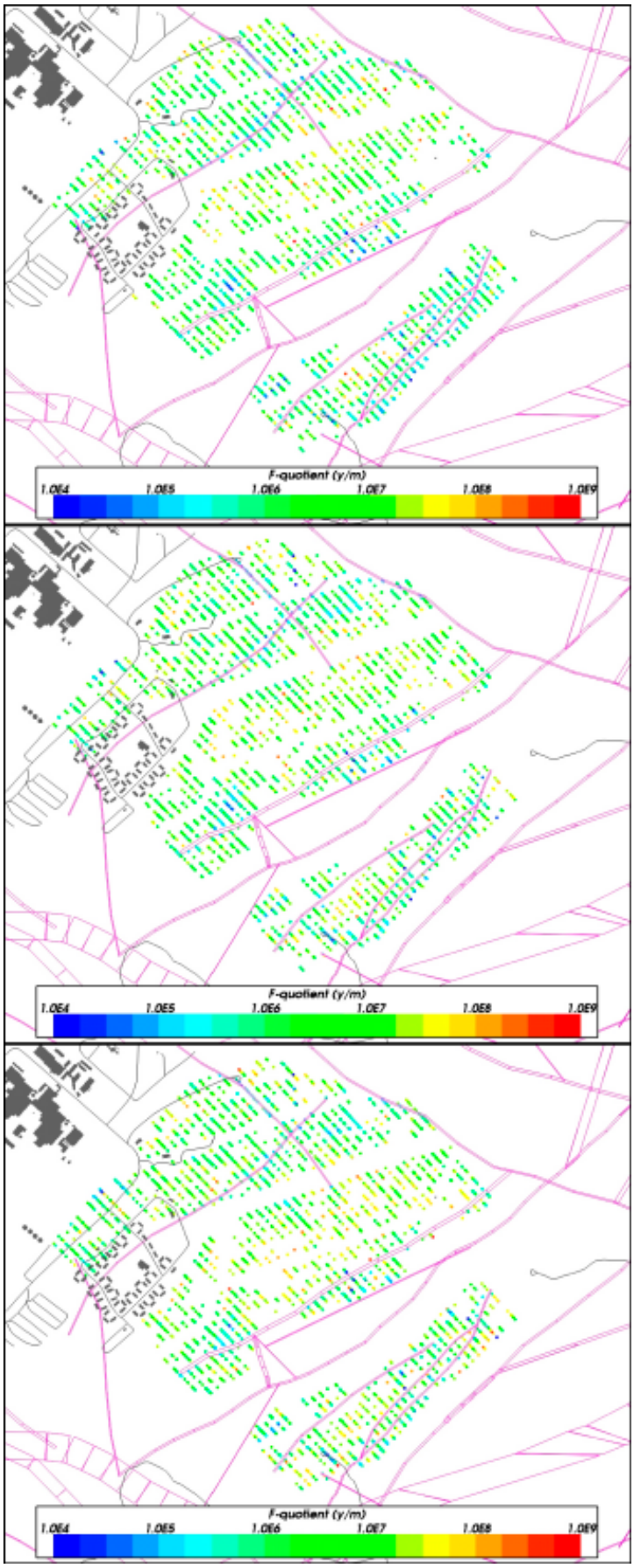

Figure 4-10. *Distribution of $\log_{10}(F_r)$ at 6,824 particle start locations in the combined DFN/CPM realistic case model for path Q1 at release times (top to bottom) 2,020 AD, 3,000 AD and 9,000 AD. Also, the HCD model at z=–400 m (purple), roads and buildings (black).*

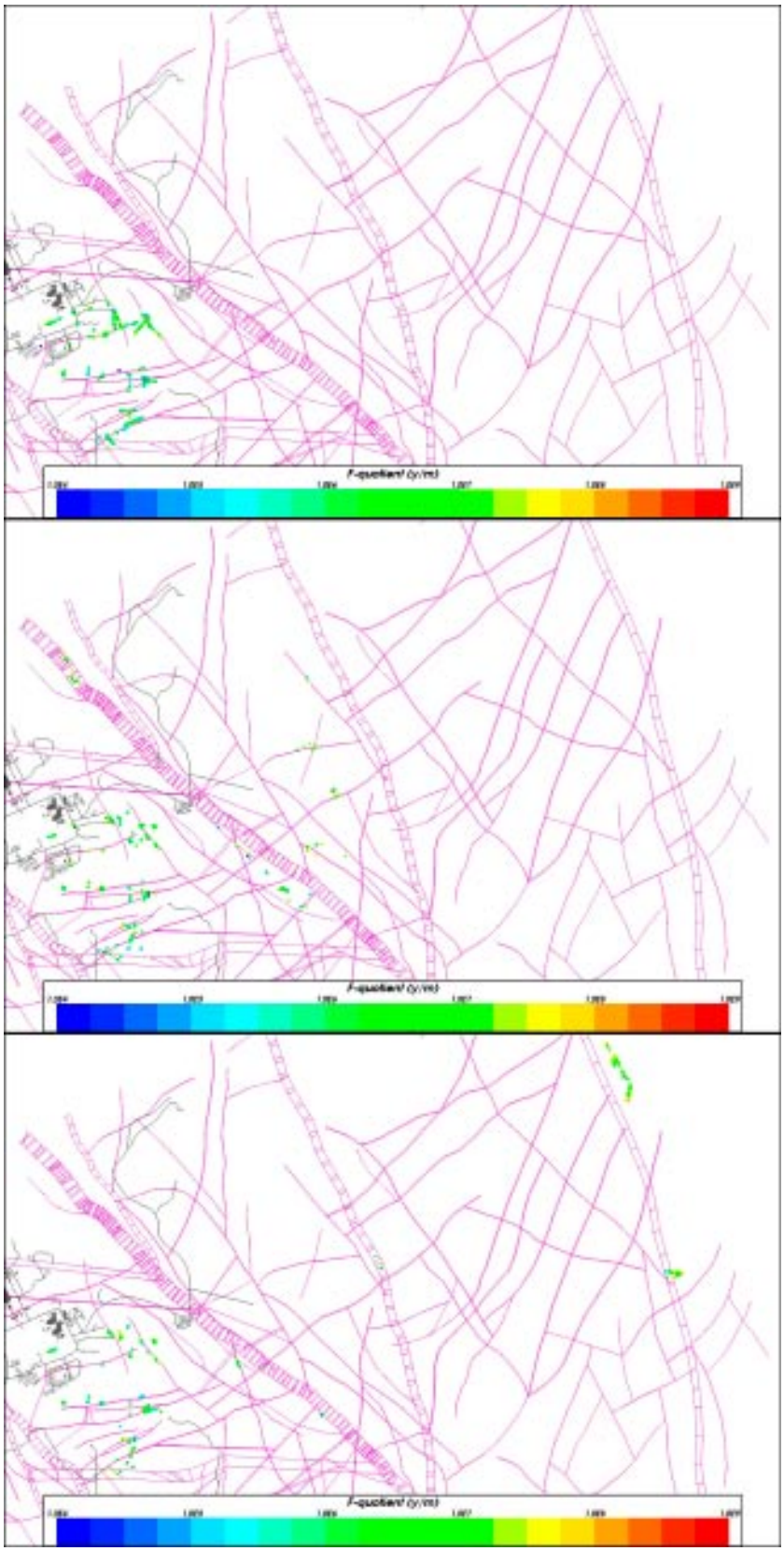

Figure 4-11. *Distribution of $\log_{10}(F_r)$ at 6,824 particle exit locations for the combined DFN/CPM realistic case model for path Q1 at release times (top to bottom) 2,020 AD, 3,000 AD and 9,000 AD. Also, the HCD model at z=–400 m (purple), roads and buildings (black).*

4.1.4 Performance measures

A summary of the PMs for releases for each of the paths Q1, Q2 and Q3 at 3 different release times is shown in Figure 4-12 to Figure 4-15. The main performance measures t_r, U_r and F_r are shown in Figure 4-12 as cumulative distributions with paths Q1, Q2 and Q3 side-by-side for release time 2,020 AD. Here, the plots are normalised with respect to the total number of deposition holes; the offset to the left corresponds to deposition holes with zero flow. The offset to the right indicates the fraction of flow paths which do not find a complete path through the geosphere. Thus, the curves represent the fraction of deposition holes which simultaneously have a flow greater than zero and have flow paths which exit the geosphere. For example, for Q1 27% of deposition holes are not intersected by a fracture bearing advective flow and 45% of particles that start from the deposition hole do not find a pathway to the surface. The offset on the left is a legitimate result of a low intensity of connected fractures around the deposition holes. The offset on the right is more of a numerical artefact of the difficulty in tracking particles through sparse heterogeneous networks. It is expected that these numerical effects will be largely resolved in time for SR-Site. Figure 4-16 shows the results of some preliminary efforts to improve the particle tracking algorithm giving about 16% of particles not making it to the surface. The travel-time and F-quotient in the rock, t_r, and F_r, are almost identical for each of the release points around the canister, which suggests that the flow-path is the same for each release point and that flow does not diverge down different flow conduits around the repository. Hence, in terms of the far-field modelling, only a single path need be considered. Only the initial velocities are moderately different for the three release points. All initial Darcy velocities have a median around 10^{-5} m/y, slightly higher in the tunnel and slightly lower in the EDZ. The initial velocity has a much greater variability in the rock with a 95th percentile of $8 \cdot 10^{-4}$ m/y and a 5th percentile of $4 \cdot 10^{-7}$ m/y. F-quotients in the rock are mostly in the range 10^5–10^8 y/m. A few values are as low as 10^4 y/m corresponding to particles starting very close to the additional lineaments present in the AC geological model that were not taken into account in the D1 Repository Layout. Figure 4-13 shows that release time also has little affect since transport is more strongly influenced by the presence of structures, i.e. large stochastic or deterministic fractures, than variations in boundary conditions. Travel times and F-quotients are slightly less, and initial velocities slightly higher, at a 2,020 AD than at later times.

Comparing results with the regional ECPM model in Figure 3-30, initial velocities and F-quotients are similar to the ECPM model for a release at 2,020 AD, but travel times are generally an order of magnitude less. The travel time is longer in the ECPM model due to the choice of kinematic porosity. In the DFN model, flow-paths tend to get focussed into larger fractures as they seek out a route to the surface meaning they only tend to see the fracture volume associated with the transport aperture of relatively few fractures. In the ECPM model, a kinematic porosity was calculated based on the total volume of connected fractures per volume of rock, which will include the smaller fractures not necessarily accessed by the principal advective flow channels. Hence the kinematic porosity, typically around 10^{-5}, used in the ECPM model and shown in Figure 3-2 is probably an over-estimate for advective flow-paths.

Figure 4-14 present histograms of the cumulative flow-path distances spent in the rock, tunnel and EDZ for each of the release positions path Q1, Q2 and Q3, at 2,020 AD. Again, the plots confirm that all three release points give very similar paths. The spread in L_r is between about 480 m and 2,000 m. For the realistic case backfill properties, the distance travelled in the tunnel, L_t, is about 0–80 m with a median around 17 m. In the EDZ, the distance, L_{EDZ}, is only about 0–40 m with a median of about 9 m. All PMs for this case are tabulated in Appendix C.

Bar and whisker plots for the PMs in the rock are shown in Figure 4-15. It confirms that the median travel-times, initial Darcy velocity and F-quotient vary in magnitude by no more than about 0.2 in log-space between the different release times. Comparing with the equivalent ECPM model results in Figure 3-63 demonstrates that the equivalent continuum porous medium model approach tends to give optimistic predictions of the performance measures.

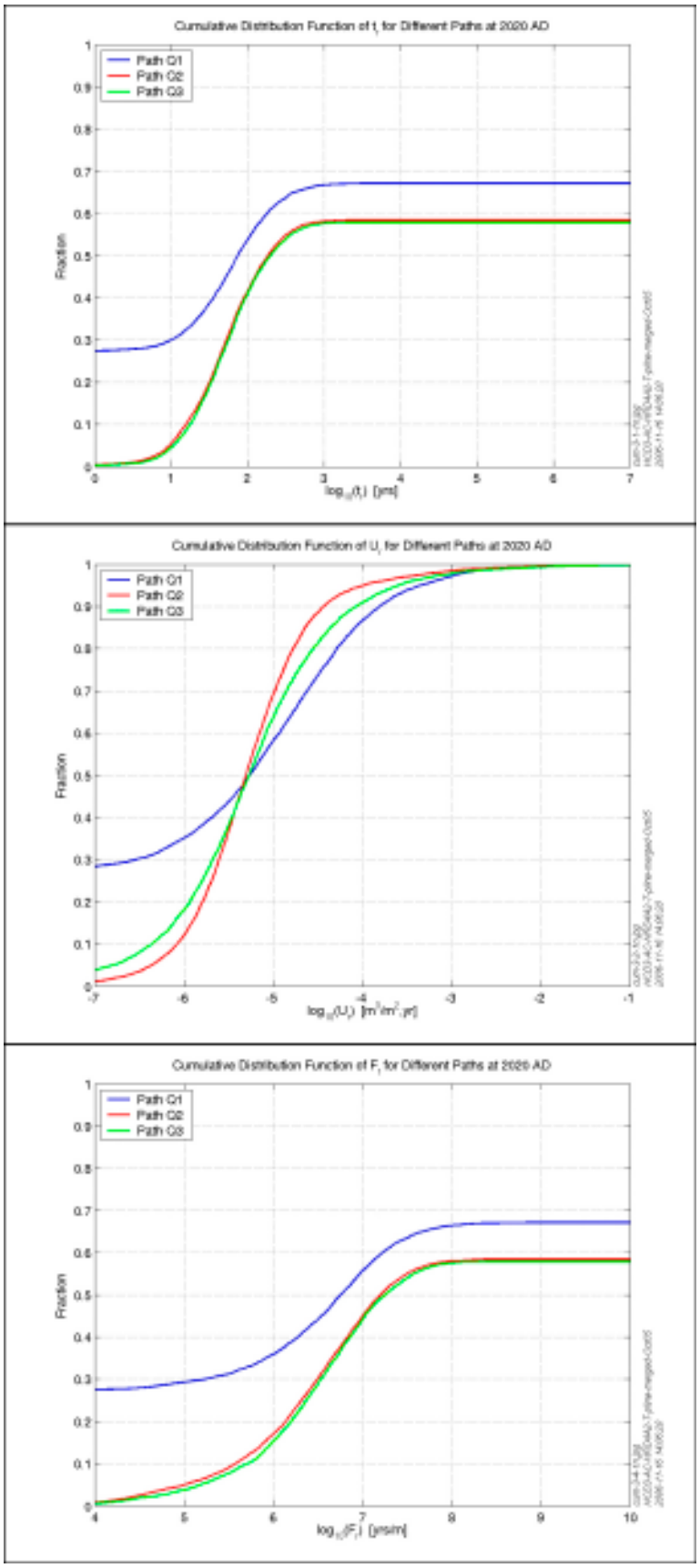

Figure 4-12. *Cumulative distributions for the combined DFN/CPM realistic case model with 6,824 particles released for paths Q1, Q2 and Q3 at 2,020 AD. From the top: t_r, U_r, and F_r.*

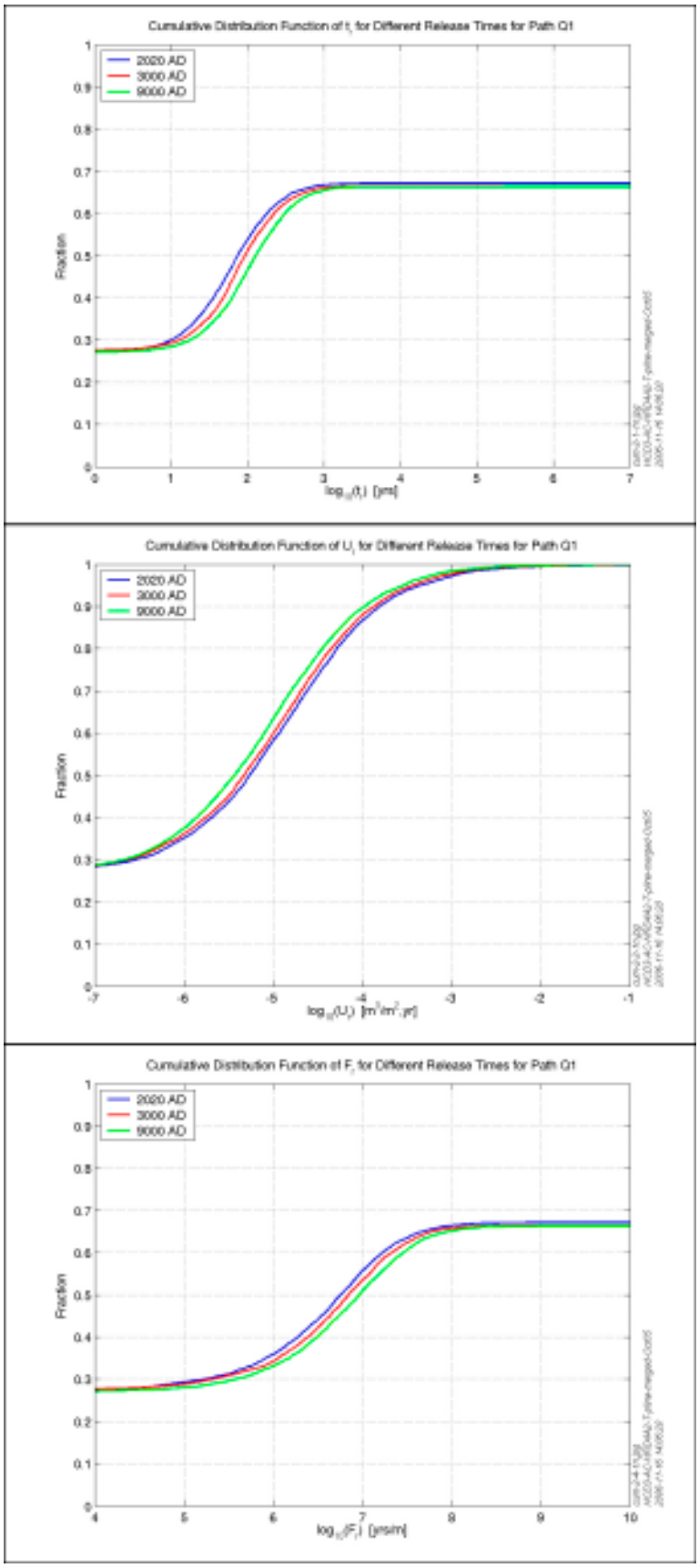

Figure 4-13. *Cumulative distributions for the combined DFN/CPM realistic case model with 6,824 path Q1 tracks released at 2,020 AD, 3,000 AD and 9,000 AD. From the top: t_r, U_r and F_r.*

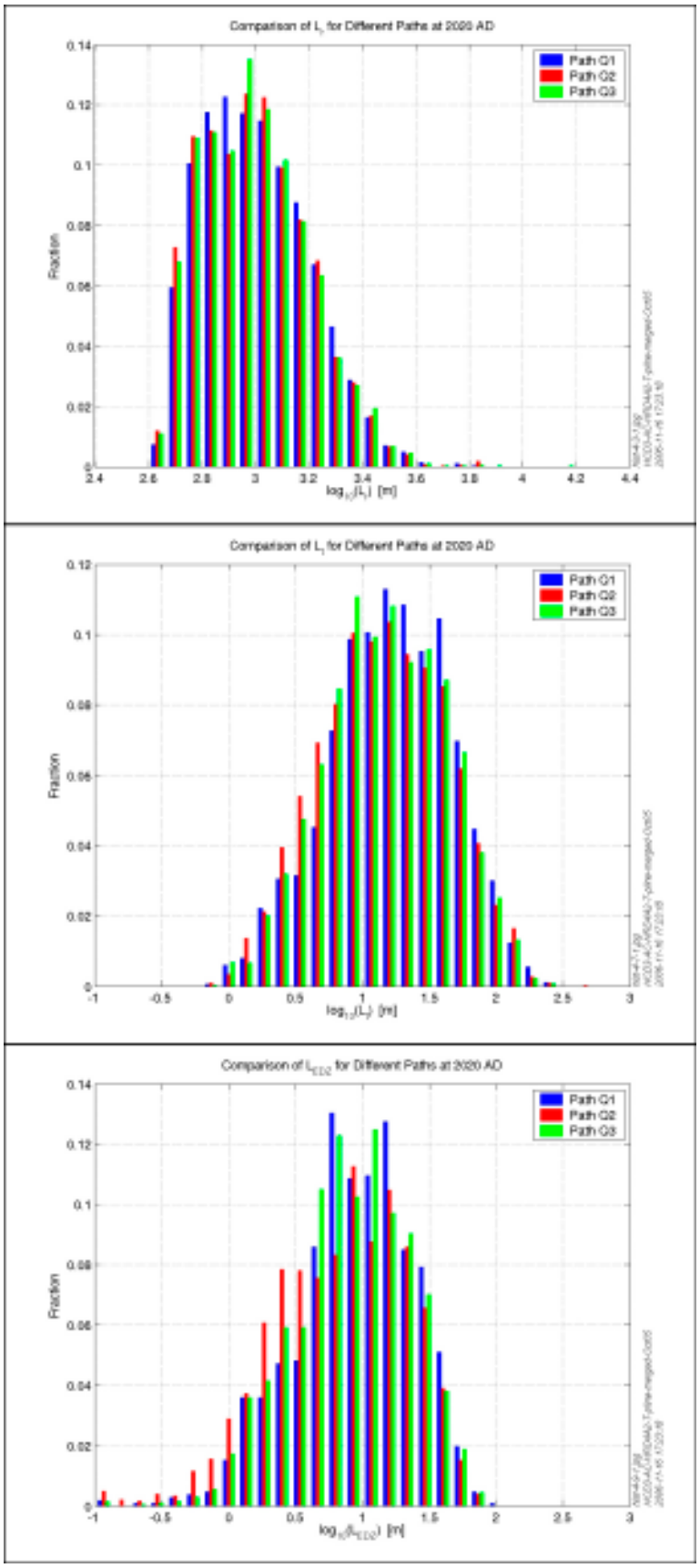

Figure 4-14. *Histograms for the combined DFN/CPM realistic case model with 6,824 particles released for paths Q1, Q2 and Q3 at 2,020 AD. From the top: L_p, L_t, and L_{EDZ}.*

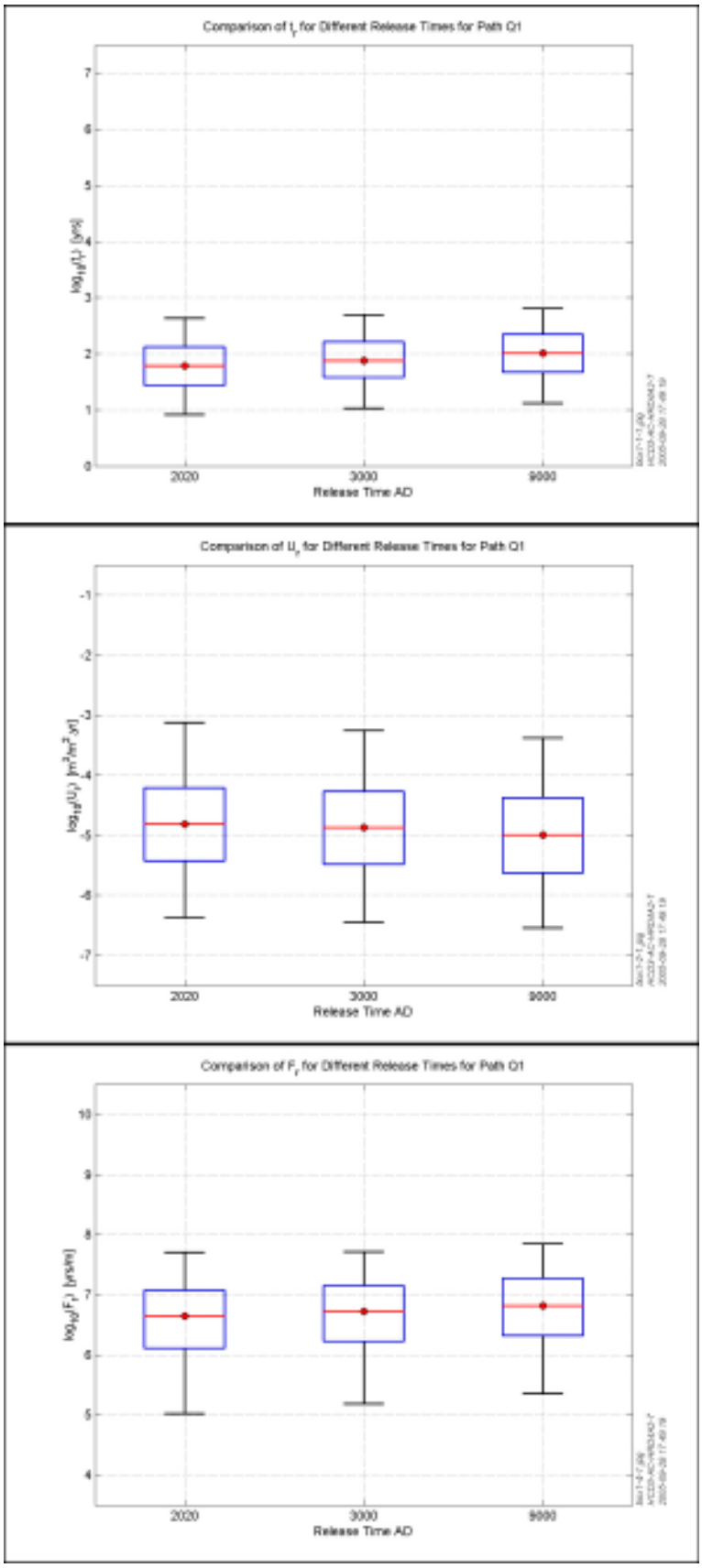

Figure 4-15. *Bar and whisker-plots for the combined DFN/CPM realistic case model with 6,824 particles released at 2,020 AD, 3,000 AD and 9,000 AD. From the top: t_r, U_r, and F_r. The statistical measures are the median (red), 25th and 75th percentile (blue bar) and the 5th and 95th percentile (black "whiskers").*

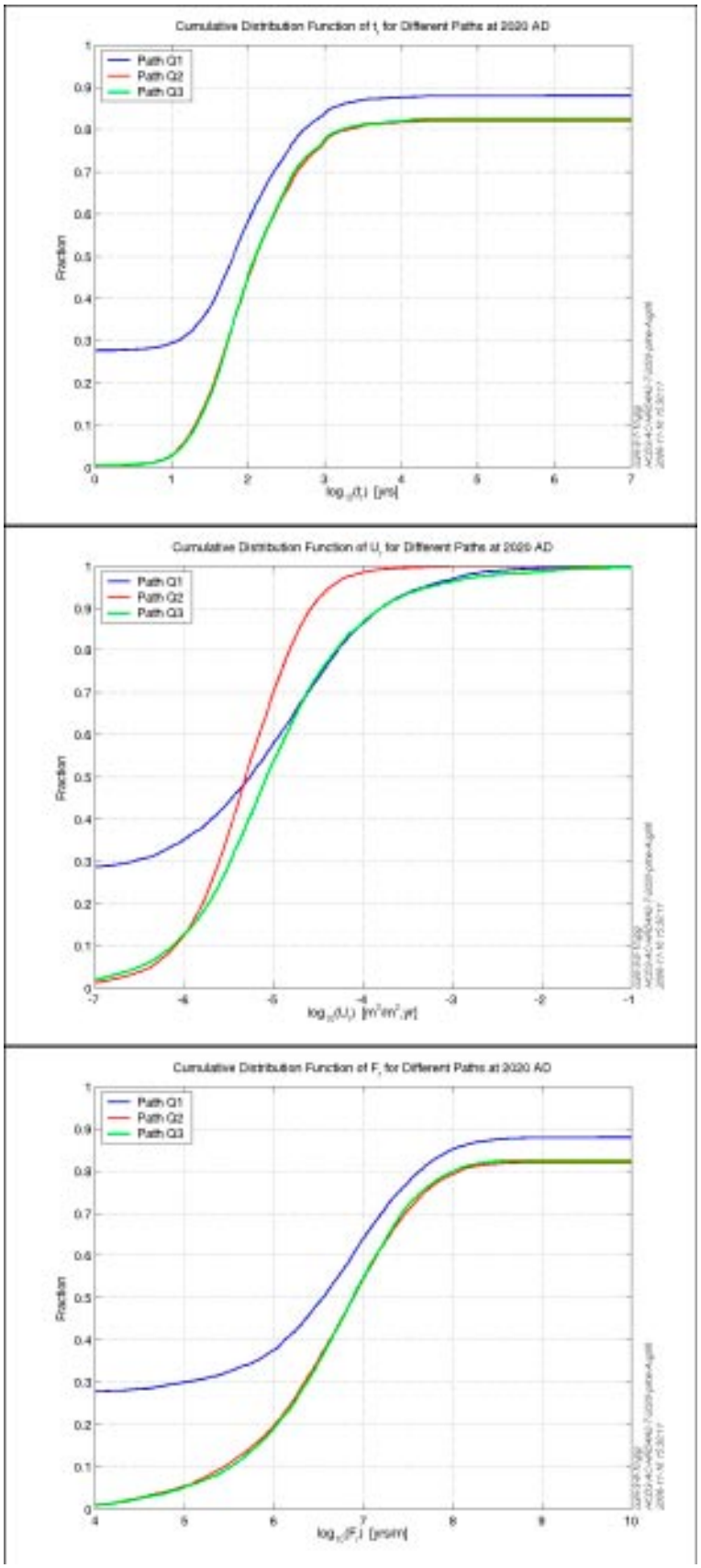

Figure 4-16. *Cumulative distributions for the combined DFN/CPM realistic case model with 6,824 particles released for paths Q1, Q2 and Q3 at times 2,020 AD based on an exnhancement of the particle tracking algorithms for comparison with Figure 4-12. From the top: t_i, U_i, and F_i.*

Median travel times are about one and a half orders of magnitude lower for the DFN case. Initial; Darcy velocity is about half an order of magnitude higher, and F-quotient is about an order of magnitude lower than the ECPM model. The explanation is thought to be that the ECPM model allows long horizontal flow-paths which are not possible through the sparse poorly connected fracture network where shorter vertical flow-paths predominate.

4.2 Parameter sensitivities

The sensitivity cases performed for the combined DFN/CPM model were:

- A variant with degraded backfill of relatively high hydraulic conductivity in the deposition tunnels.
- A variant with very poor EDZ that is continuous and of relatively high axial hydraulic conductivity.
- A variant which uses the semi-correlated transmissivity model in the DFN.
- A variant which uses the uncorrelated transmissivity model in the DFN.

Since the central realistic case model indicated that performance measures are relatively insensitive to the release time, then variant calculations were only performed at a release time of 2,020 AD.

4.2.1 Tunnel backfill and engineered damage zone properties (EDZ)

For the degraded backfill case the only change was to use a hydraulic conductivity of 10^{-8} m/s. The values chosen was based on identifying a value big enough for the tunnel to have a significant impact rather than based on a realistic assessment of backfill degradation. The impact on performance measures for this case is shown in Figure 4-17 and Figure 4-18. Comparing with the central realistic case, travel-times decrease slightly by about 0.2 for paths Q1 and Q2, and by about 0.35 for path Q3 in $\log_{10}$-space. Initial Darcy velocity increases significantly for the Q3 path by about one and a half orders of magnitude, as might be expected for an increase in backfill hydraulic conductivity of two orders of magnitude. F-quotient decreases slightly by 0.2 for paths Q1 and Q2, and by about half an order of magnitude for path Q3. The distance travelled in the tunnel increases to a range between 0 and about 160 m with a median around 25 m for path Q3.

A similar approach was used for the EDZ variant by choosing a hydraulic conductivity for the EDZ that was sufficiently high that it started to have an impact on flow-paths. The value used was $3 \cdot 10^{-9}$ m/s. The performance measures for this case are shown in Figure 4-19 and Figure 4-20. Changes are very slight for this case around 0.1 in $\log_{10}$-space for most performance measures. The most notable changes are an increase in the initial Darcy velocity for the Q2 path of over half an order of magnitude, and an increase in the distance travelled in the EDZ to a range of 0 to about 60 m with a median around 16 m.

In summary, the sensitivity to the backfill and EDZ properties is not great since the system of deposition tunnels is arranged orthogonal to the head gradients. Therefore flow tends to be limited by what the fracture system can supply and paths have to leave the tunnel or EDZ after relatively short distance to find a flow-path to the surface through the fracture network.

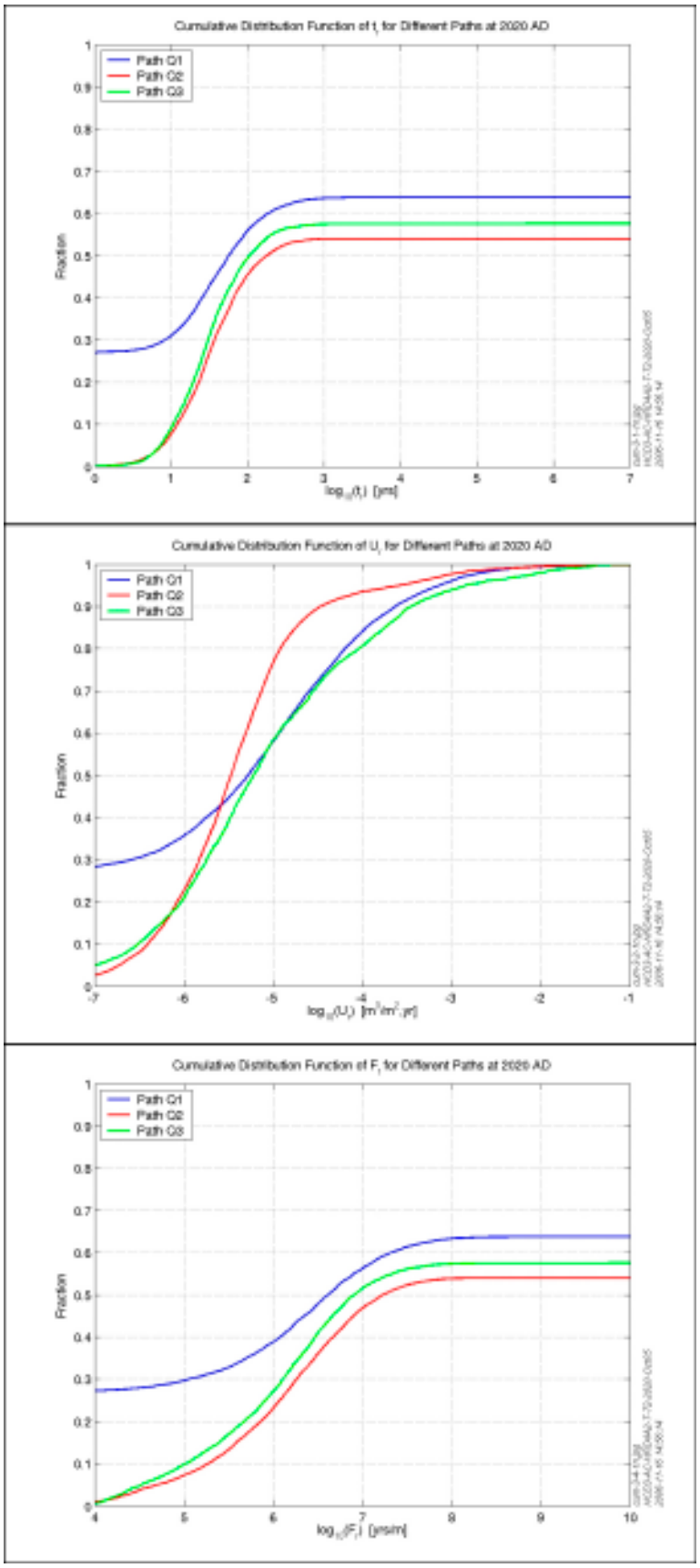

Figure 4-17. *Cumulative distributions for higher tunnel conductivity in the combined DFN/CPM realistic case model for paths Q1, Q2 and Q3 at time 2,020 AD. From the top: t_r, U_r, and F_r.*

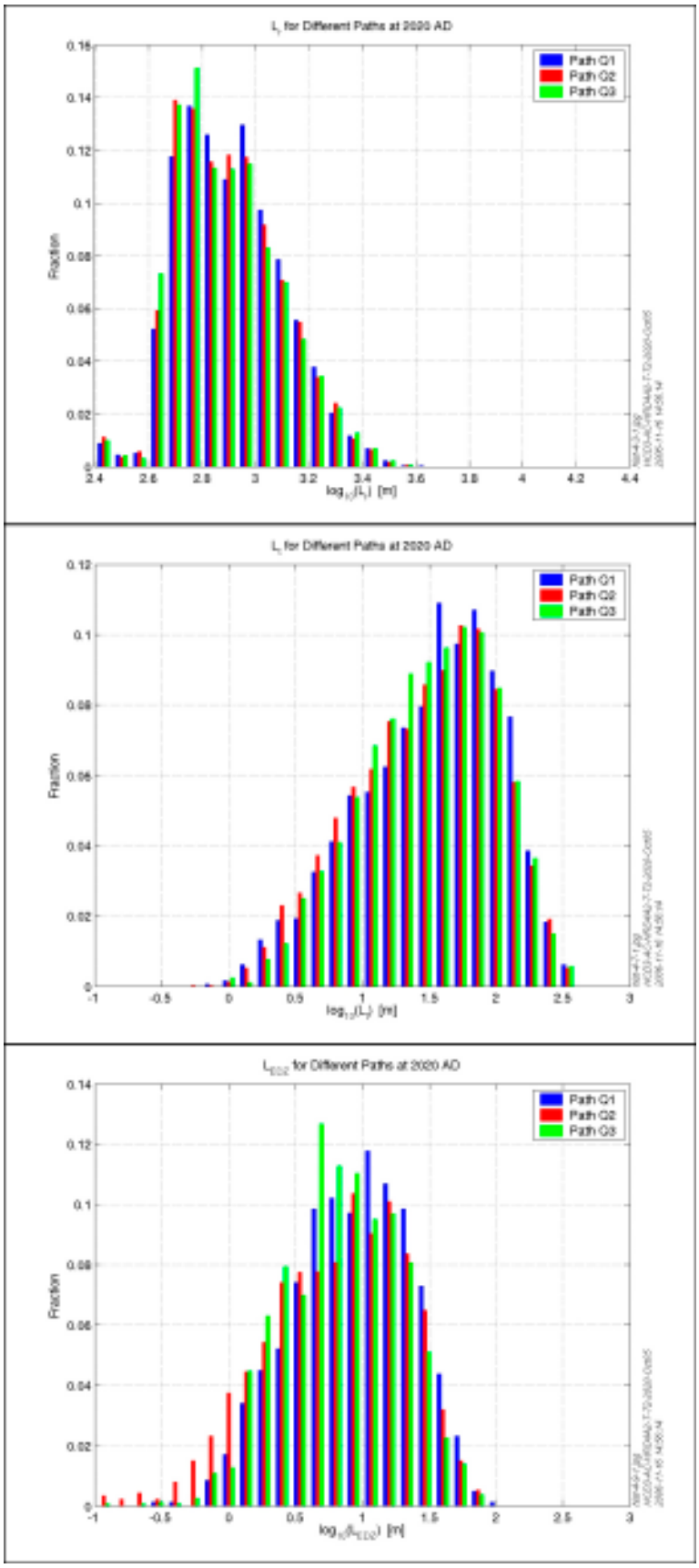

Figure 4-18. *Histograms for higher tunnel conductivity in the combined DFN/CPM realistic case model in paths Q1, Q2 and Q3 at 2,020 AD. From the top: L_p, L_b, and L_{EDZ}.*

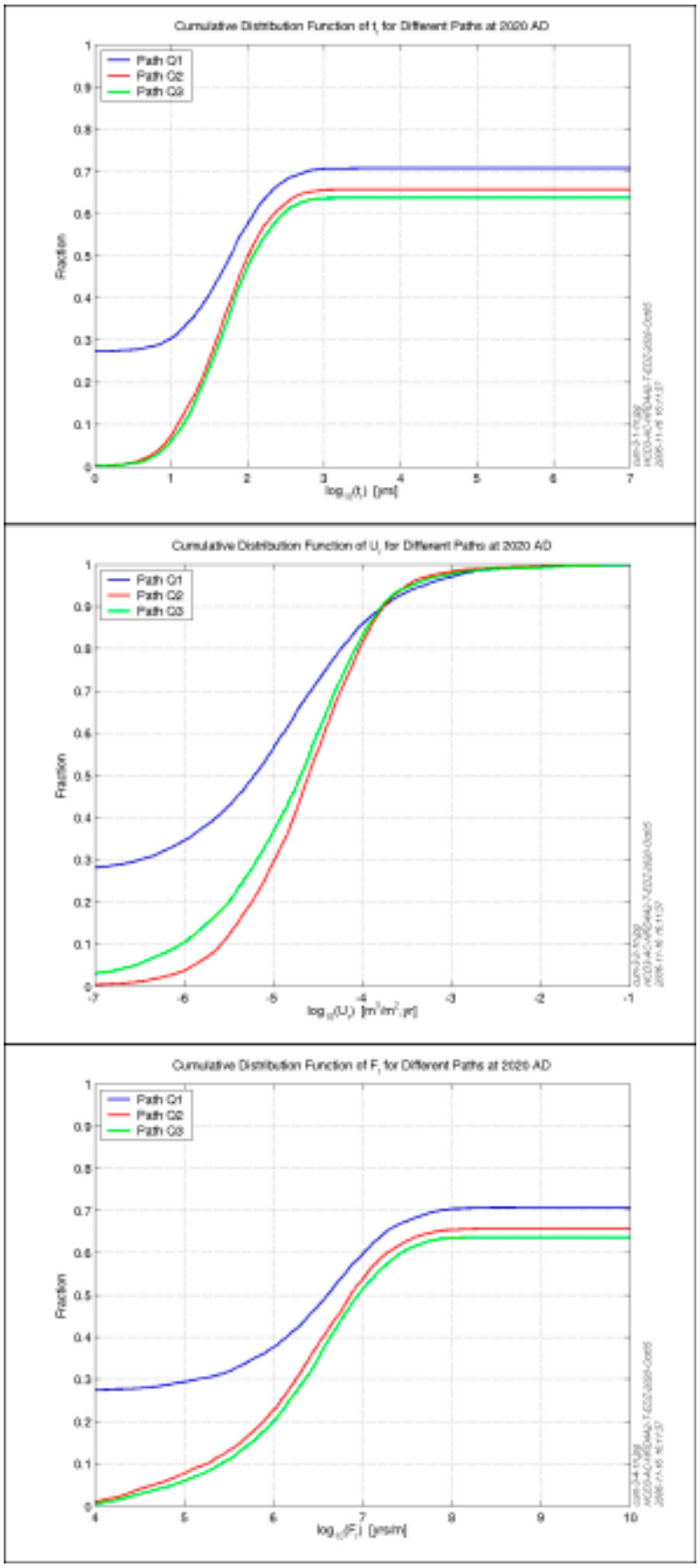

Figure 4-19. *Cumulative distributions for higher EDZ conductivity in the combined DFN/CPM realistic case model for paths Q1, Q2 and Q3 at 2,020 AD. From the top: t_r, U_r, and F_r.*

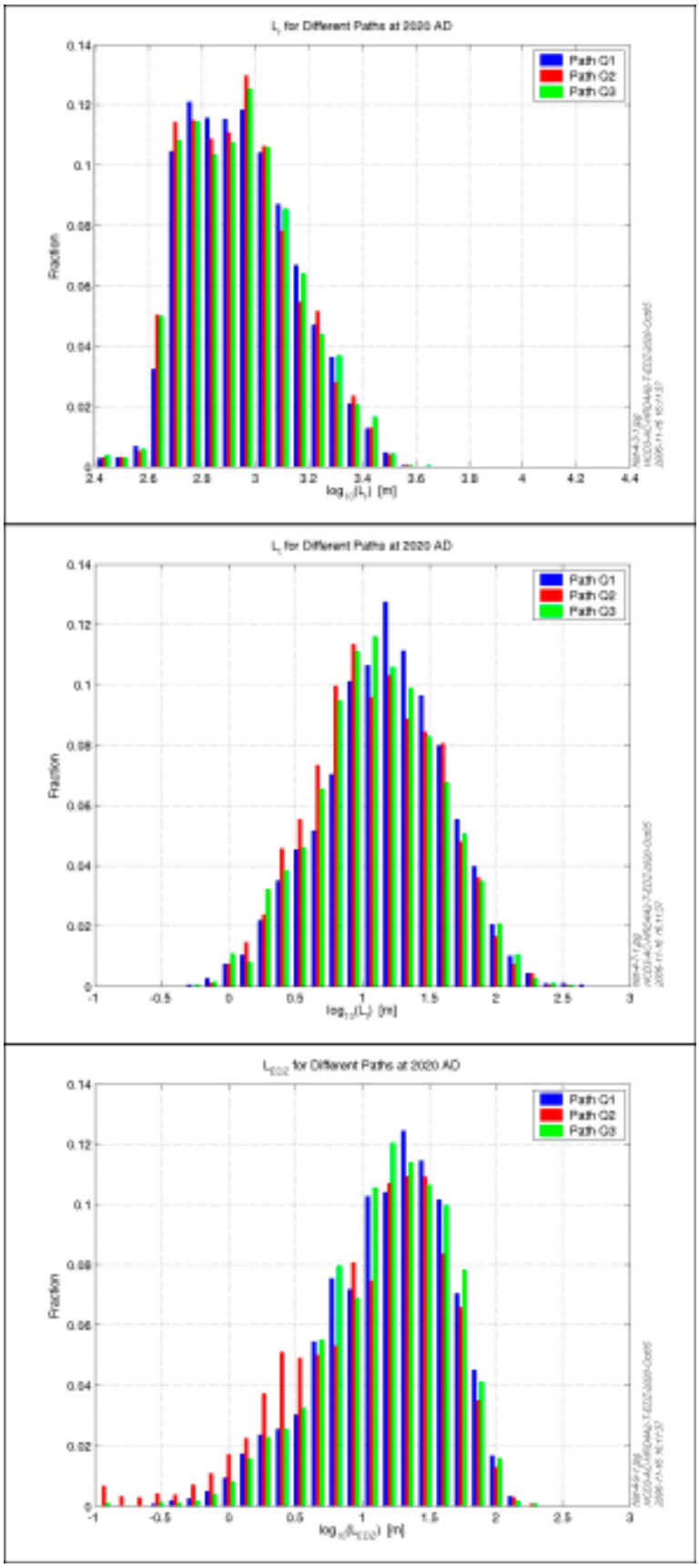

Figure 4-20. *Histograms for higher EDZ conductivity in the combined DFN/CPM realistic case model for paths Q1, Q2 and Q3 at 2,020 AD. From the top: L_p, L_t, and L_{EDZ}.*

4.2.2 Hydro-DFN properties

The sensitivity of performance measures to the Hydro-DFN properties considered was the transmissivity model since this was found to have a significant effect on the results in Section 3. Two variants of the combined DFN/CPM realistic cases model were run based on:

- A semi-correlated relationship between fracture radius and transmissivity.
- An uncorrelated relationship between fracture radius and transmissivity.

The parameters used for these variants are given in Table 2-4. In order to have regional distributions of fluid density and residual pressure for use in these models, two additional ECPM models consistent with the DFN parameterisation were constructed. These are the cases SC_HCD3_AC_HRD3SA2_T and SC_HCD3_AC_HRD3UA2_T in Table 3-4.

A summary of the particle tracking results for the two variants is given in Table 4-3. The percentage of canisters with no connected fracture intersecting the deposition hole is about 26–27% as for the correlated case since this is primarily a function of fracture geometry and the fracture radius truncation used. Interestingly, higher percentages of canisters have connected fractures of significant transmissivity intersecting the deposition holes, 18–20%, but this is to be expected with a reduced correlation between length and transmissivity as it is mostly small fractures that intersect the deposition holes. The percentage of particles starting in stagnant flow areas increases to 67–74% for the two variants compared to 40% for the correlated case. This is indicative of flow being more heterogeneous for the variants and there being fewer advective pathways through the model, as was found in the equivalent ECPM regional models. The distribution of performance measures t_r, U_r and F_r are given for the semi-correlated cases in Figure 4-21 and Figure 4-22, and are also tabulated in Appendix C. It should be noted that the tabulated statistics are taken only over the particles that make it the surface of the model. The median travel-time is 1.6 for the semi-correlated variant and 1.7 for the uncorrelated case compared to 1.8 for the correlated case in $\log_{10}$-space, and the standard deviation is also similar about 0.5–0.6 for all cases. Initial Darcy velocity is about –4.5 for the semi-correlated variant and –4.3 for the uncorrelated case compared to –4.8 for the correlated case in $\log_{10}$-space. Hence, these two variants tend to have slightly higher initial flow rates as was found with the ECPM regional-scale models. Notably, the initial velocities for each of the 3 paths, Q1, Q2 and Q3 are more similar for these two variants. F-quotient is about 5.7 for the semi-correlated variant and 5.7 for the uncorrelated case compared to 6.5 for the correlated case in $\log_{10}$-space, and the standard deviation is also similar about 0.7–0.8 for all cases. Therefore, the results are moderately sensitive to the relationship used for the transmissivity to length relationship, and the semi-correlated and uncorrelated models may give moderately worse results than the correlated model in terms of inputs to PA, although fewer particles escape to the surface for these cases.

Table 4-3. Summary of the particle tracking results for the combined DFN/CPM realistic case variants with semi-correlated and uncorrelated transmissivities released at 2,020 AD. For each of the 6,824 canister positions, paths Q1, Q2 and Q3 are computed.

Particles/canisters [%]	Semi-correlated SC_HCD3_AC_HRD3SA2_T			Uncorrelated SC_HCD3_AC_HRD3UA2_T		
	Q1	Q2	Q3	Q1	Q2	Q3
Fracture with T>10^{-9} m^2/s	20.3%	N/A	N/A	18.4%	N/A	N/A
No connected fracture	25.9%	N/A	N/A	26.9%	N/A	N/A
Particles that reach surface	22.8%	32.2%	31.3%	18.8%	24.9%	25.1%
Stagnant flow	50.4%	66.6%	67.2%	53.4%	74.0%	74.0%
Mass balance problems	0.8%	1.2%	1.5%	0.8%	1.1%	0.9%

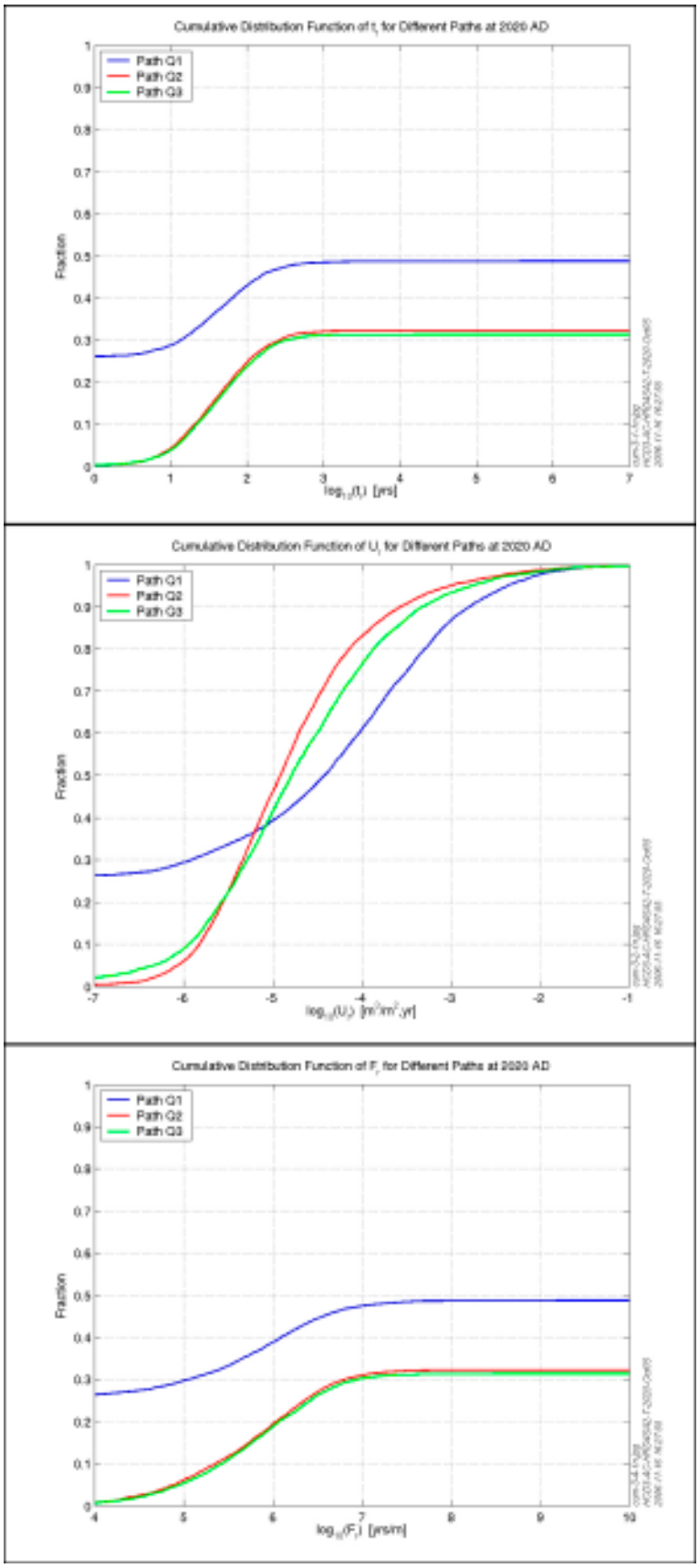

Figure 4-21. *Cumulative distributions for a semi-correlated fracture transmissivity in the combined DFN/CPM realistic case model for paths Q1, Q2 and Q3 at time 2,020 AD. From the top: t_r, U_r, and F_r.*

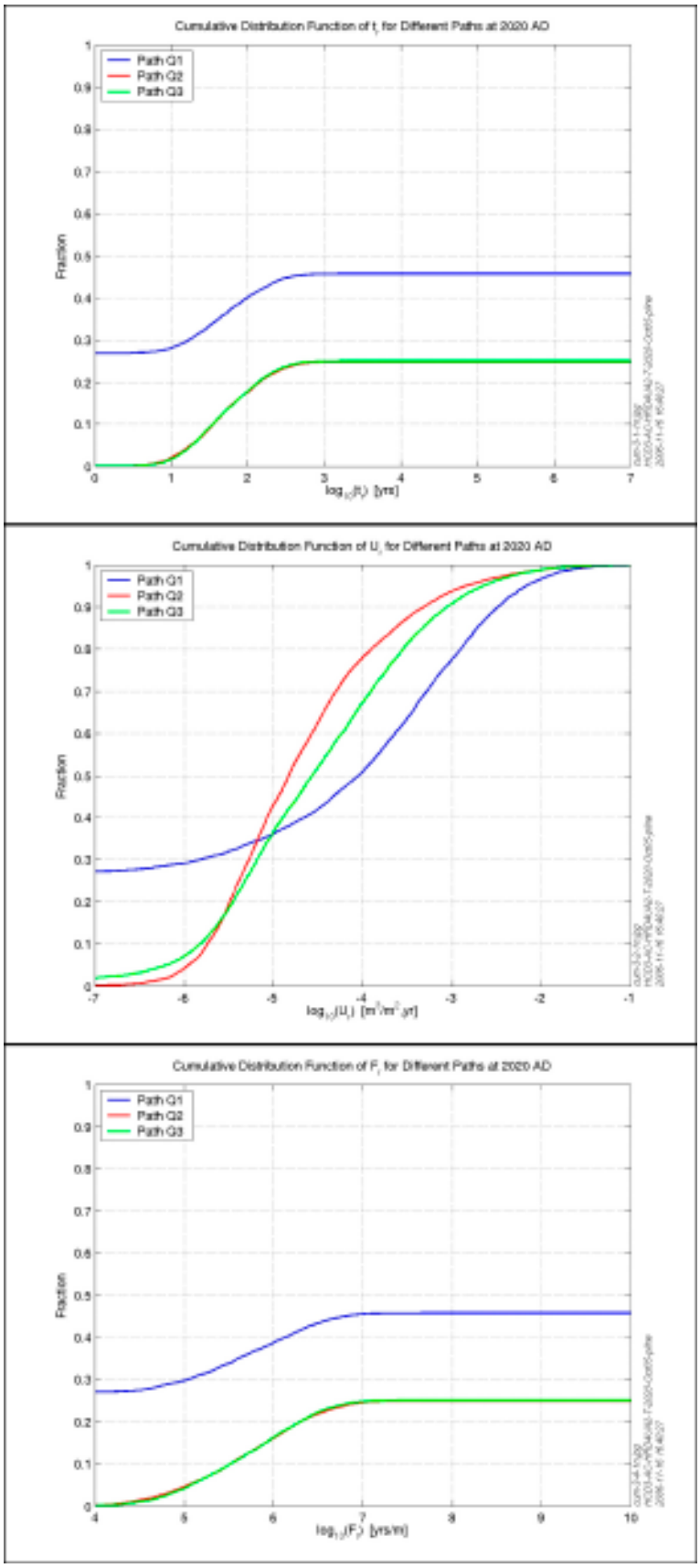

Figure 4-22. *Cumulative distributions for an uncorrelated fracture transmissivity in the combined DFN/CPM realistic case model for paths Q1, Q2 and Q3 at time 2,020 AD. From the top: t_r, U_r, and F_r.*

4.3 Alternative concept: nested CPM repository-scale model

Next we consider the alternative conceptual model of a tight porous medium. This is based on the CPM model described in Section 3.3.2, but with much higher resolution around the repository and a restricted domain. The model is used to consider the sensitivity of detailed PA input parameters to the conceptual model for flow.

4.3.1 Model set-up and specification

The repository-scale CPM model was also split into 3 blocks as for the combined DFN/CPM model. The finite-element grid for the western block is shown in Figure 4-23. The vertical extent of the blocks was from z=–510 m to 250 m and this was subdivided into finite-elements about 20 m thick away from the repository. Extra refinement is included around the tunnels and deposition holes in a similar way to Figure 4-3. Here, the EDZ was modelled explicitly as an extra layer of finite-elements beneath the tunnel, as shown in Figure 2-18. The hydraulic properties of the western block are shown in Figure 4-24. The area of lower hydraulic conductivity in the centre corresponds to rock domains RFM029/017 which is surrounded by a fringe of higher hydraulic conductivity outside the tectonic lens. The lens has an irregular boundary due to the interpolation of the rock domain from a coarse 100 m regular grid definition (Voxel file) aligned at an angle to the grid giving the artificial 'stair-step' boundary to the low conductivity lens. Unfortunately, this resulted in a few deposition holes being located incorrectly outside RFM029/017, but overall this is a very small proportion. Figure 4-24 also shows the presence of three small deterministic deformation zones from the AC geological model crossing this part of the repository that have not been taken into account by the Repository Design Team, so again some particles are likely to start in areas of high hydraulic conductivity.

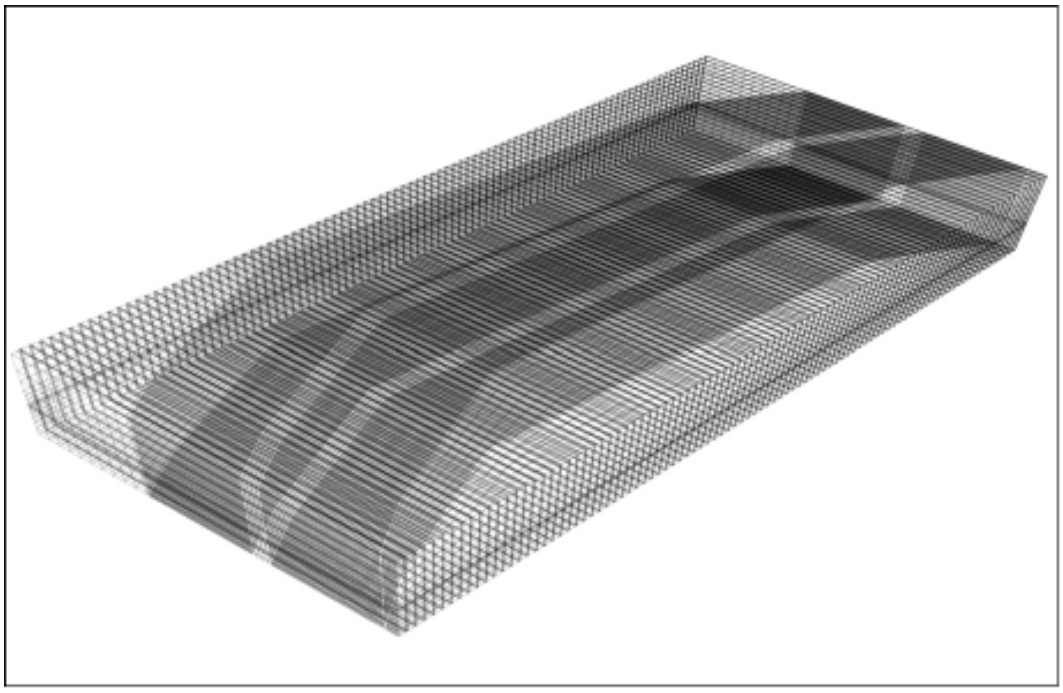

Figure 4-23. *Finite-element grid used in pure CPM repository-scale model of western repository block. Oblique view from south.*

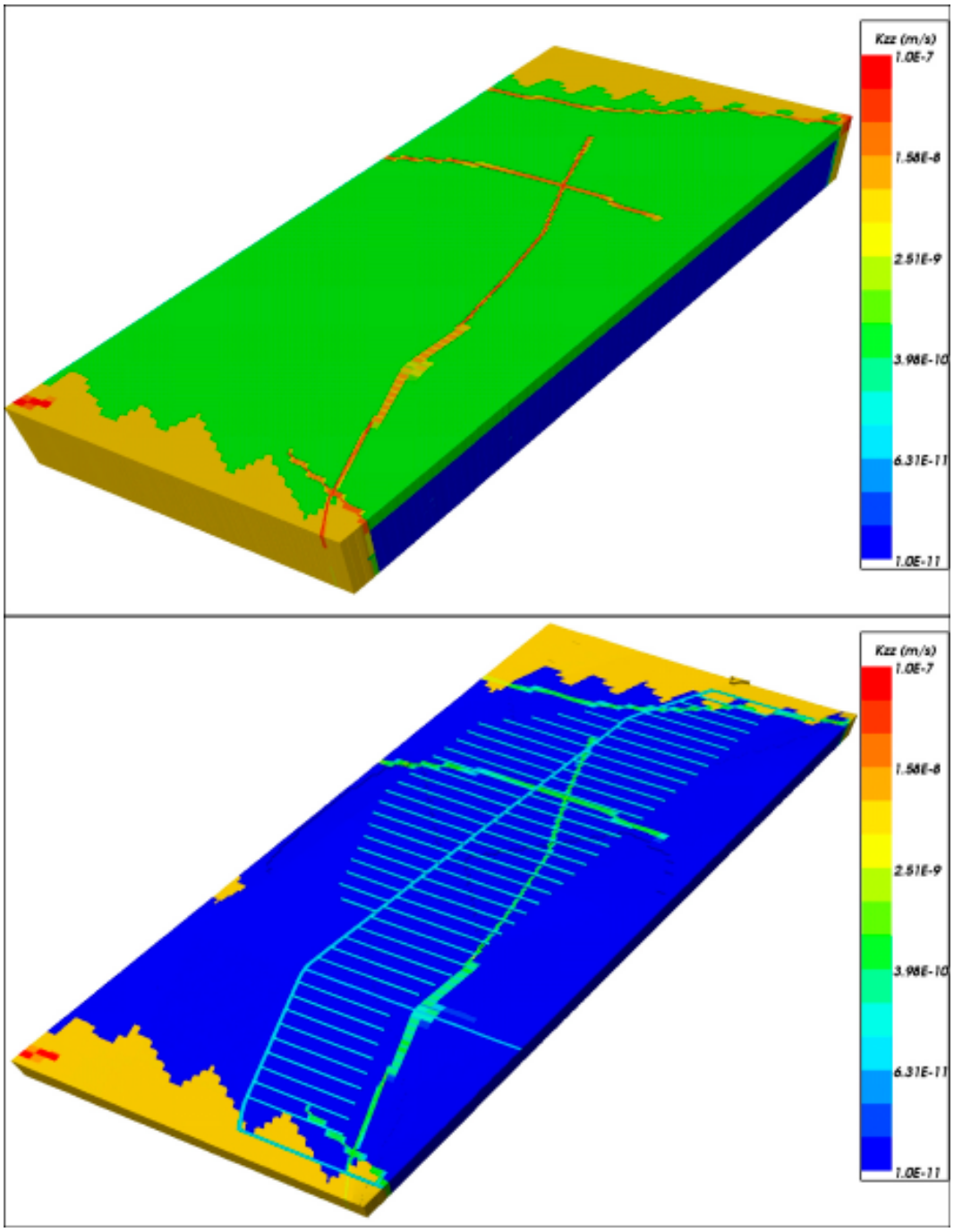

Figure 4-24. *Hydraulic conductivity in pure CPM model of the western repository block. Oblique view from south. Top: whole model showing higher conductivity above z=–350 m (green shade) and outside of RFM029/017 (orange shade) and deformation zones (red-yellow shade). Bottom: elements above z=–405 m showing repository tunnels.*

4.3.2 Variable-density flow calculations

Variable-density flow calculations were performed at snapshots in time at 2,020 AD, 3,000 AD and 9,000 AD using a methodology very similar to the combined DFN/CPM model. The residual pressure and fluid density fields were exported from the regional-scale CPM model at the required times and interpolated onto the regional-scale mesh. Holding fluid density fixed

throughout the domain and the residual pressure on the boundary, a self-consistent flow-field was calculated. For 2,020 AD this resulted in the residual pressure distribution as shown in Figure 4-25 for the whole domain of the western block. A residual pressure of 10^4 N/m^2 equates to a head of about 1 m. The equivalent distributions are shown at repository depth in Figure 4-26. Here, the distribution of density for the CPM regional model is quite different to that in the more conductive ECPM model as groundwater is actually less saline around the repository than above. It is caused by a lens of Glacial water lying between the Marine above and Brine below persisting in the CPM regional model, whereas the Marine penetrates down to repository depth in the ECPM regional model.

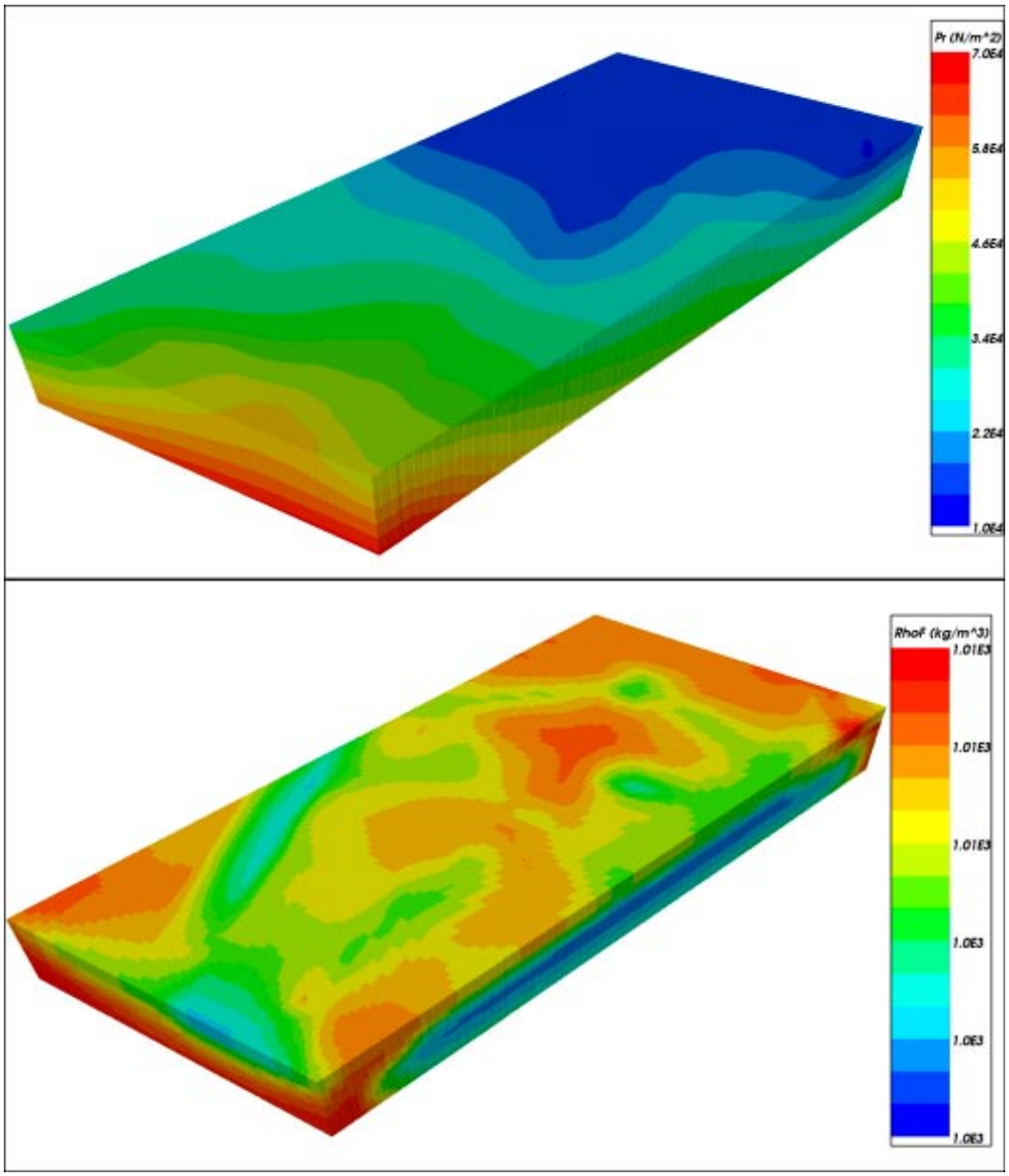

Figure 4-25. *Results of variable-density flow calculation at 2,020 AD in the western repository block for the CPM repository-scale model. Oblique view from south. Top: distribution of residual pressure from z=–250 m to z=–500 m. Bottom: distribution of fluid density.*

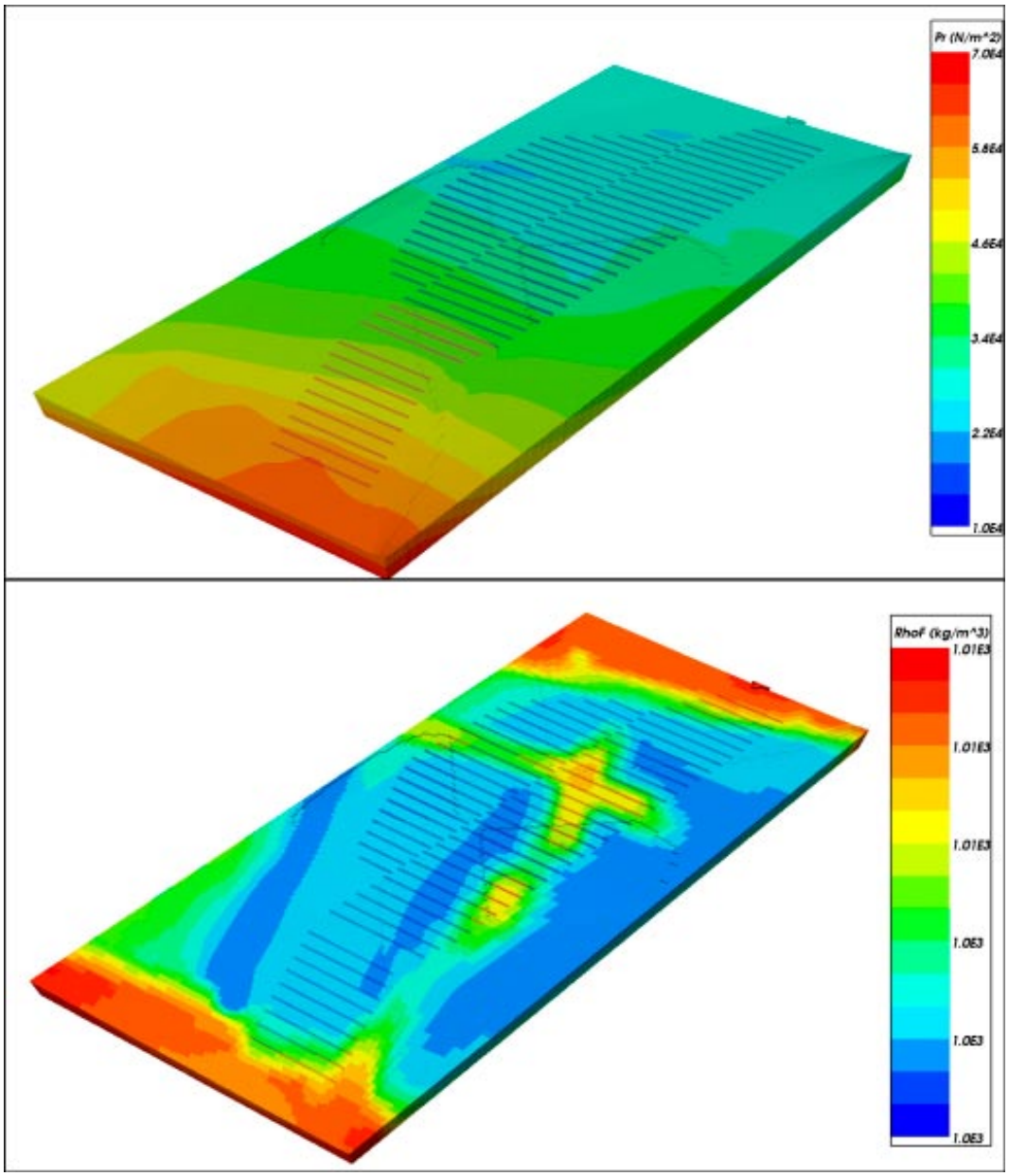

Figure 4-26. *Results of variable-density flow calculation at 2,020 AD in the western repository block for the CPM repository-scale model with elements below z=–405 m around the repository. Oblique view from south. Top: residual pressure. Bottom: distribution of fluid density.*

4.3.3 Flow-paths

Particles were released adjacent to the deposition hole, in the EDZ, and in the tunnel to yield PMs for Paths Q1, Q2 and Q3. For the release in deposition hole, Path Q1, Figure 4-27 shows the F-quotient at each of the 6,824 canister locations at release times 2,020 AD, 3,000 AD and 9,000 AD. This should be compared with the CPM regional model in Figure 3-45. The results are very similar although some of the higher F-quotients seen in the regional model are reduced slightly here. It isn't surprising since both models are homogeneous apart from near the deformation zones, so no extra heterogeneity is resolved on the repository-scale. Presumably the areas where F-quotient is reduced are due to the increases resolution of hydraulic conductivity around the zones. As before, F-quotients are moderate around 10^6–10^8 y/m at 2,020 AD and then generally lower afterwards apart from the north-western part of repository. Exit locations are also nearly identical to the regional-scale CPM model.

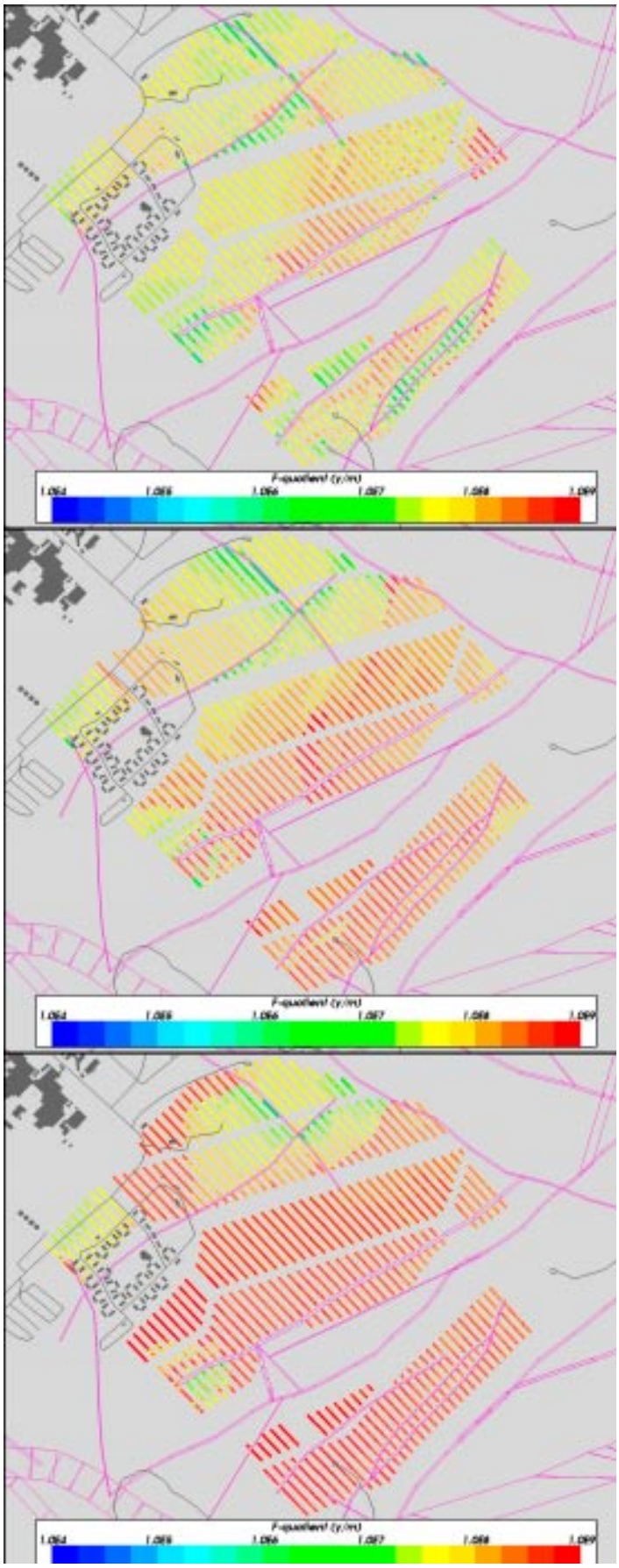

Figure 4-27. *Distribution of $\log_{10}(F_t)$ at 6,824 particle start locations for the nested CPM model for Path Q1 at release times (top to bottom): 2,020 AD, 3,000 AD and 9,000 AD. Also, the HCDs at z=–400 m (purple), large stochastic fractures (yellow), roads and buildings (black).*

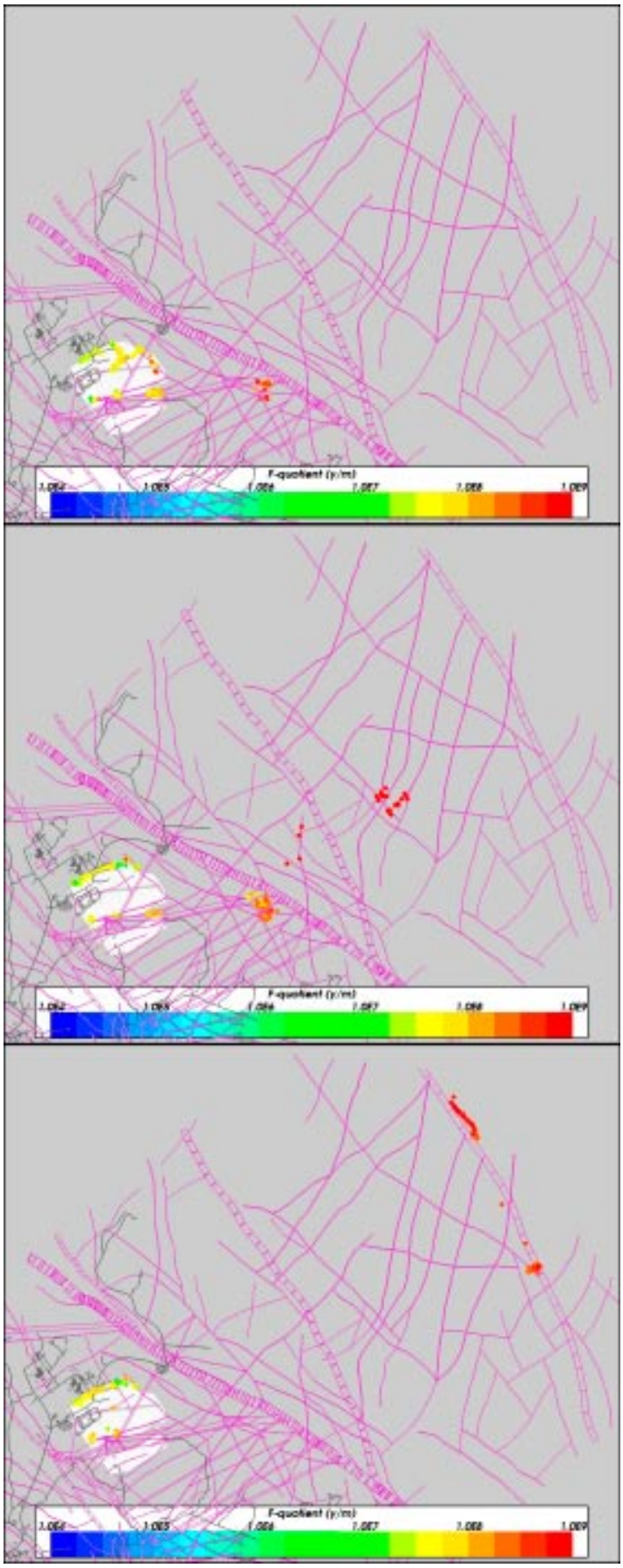

Figure 4-28. *Distribution of $\log_{10}(F_r)$ at 6,824 particle exit locations for the nested CPM model for Path Q1 at release times (top to bottom): 2,020 AD, 3,000 AD and 9,000 AD. Also, the HCDs at z=–400 m (purple), large stochastic fractures (yellow), roads and buildings (black).*

4.3.4 Performance measures

A summary of the PMs for releases for the paths Q1 at different release times is shown in Figure 4-29 to Figure 4-31. Results for the different release points Q1, Q2 and Q3 are almost identical with a difference only in the initial velocities due to different hydraulic conductivities at the 3 start locations. This suggests that the flow-path is the same for each release point and that flow does not diverge down different flow conduits around the repository. This would not be expected anyway given the properties in the rock are homogeneous. Hence, in terms of the far-field modelling, only a single path need be considered. In contrast, the initial velocities are different for the three release points as this is a function of hydraulic conductivity used in the material where the particle is released. The main performance measures t_r, U_r and F_r are shown in Figure 4-29 as cumulative distributions for path Q1 at release times 2,020 AD, 3,000 AD and 9,000 AD. Initial Darcy velocities are around 10^{-6} m/y in the rock and EDZ, and about 10^{-5} m/y in the tunnel. There are a small number of deposition holes with higher initial velocities that lie in either one of the additional deformation zones in the AC geological model or just outside of the tectonic lens in the coarse representation of its boundary. F-quotients are generally high greater around 10^7–10^8 y/m or higher at 9,000 AD. The offset on the right corresponds to particles that become stuck in the particle tracking. This appears to be more of an issue at 3,000 Ad than at all other release times. Comparing results with the regional CPM model in Figure 3-49, the PM distribution are very similar apart from the travel-times when particles are released at 3,000 AD and 9,000 AD. The repository-scale model gives travel times in the range 10^3 to 10^4 years whereas the regional-scale model gave around 10^6 years. The simple explanation is that in the regional model the kinematic porosity was modified for future times in the finite-elements intersected by the repository to represent the effect of the backfill resulting in effective porosities of order 10^{-1} compared with $5 \cdot 10^{-6}$ for the bedrock, and hence the very significantly higher travel times predicted in the regional model. In the repository-scale model, the backfill is modelled explicitly so that the properties of the rock and repository are kept distinct. Further, in the particle tracking any travel-time spent in the tunnel is recorded separately.

Figure 4-30 present histograms of the cumulative flow-path distances spent in the rock, tunnel and EDZ for the release positions and 3 release times. At 2,020 AD a large spread in L_r between about 500 m and 10,000 m is seen showing a mixture of short vertical paths and much longer deep paths. At 9,000 AD only about 20% of particles follow a short path vertically upwards. The remainder follow a path about 10 km long to the coast at the northern boundary. For the base case backfill properties, the distance travelled in the tunnel, L_t, is about 0–30 m with a mode around 10 m. In the EDZ, the distance, L_{EDZ}, is only about 0–10 m with a mode of only about 1 m. All PMs for this case are tabulated in Appendix C. Bar and whisker plots for the PMs in the rock are shown in Figure 4-31. It confirms that the median travel-times and initial Darcy velocity varies less than half an order of magnitude between different release times, only the F-quotient increases at 9,000 AD. Comparing with Figure 3-48 also demonstrates the consistency with the regional-scale PMs.

4.3.5 Parameter sensitivities

The sensitivity of PMs measures to a degraded tunnel backfill, or pessimistic EDZ scenario were considered by increasing the hydraulic conductivity of these components until a significant effect was seen on the route that flow-paths took. For the tunnel, a backfill hydraulic conductivity of 10^{-8} m/s was used as the smallest plausible value for which flow-paths consistently entered travelled along the tunnel. Figure 4-32 shows the PMs in the rock for this case. It shows that t_r and F_r are virtually unchanged, as is U_r for path Q1. Only the initial Darcy velocity is increased by about two orders of magnitude. In terms of path-length, Figure 4-33 shows there is little effect on L_r and L_{EDZ}, but L_t rises significantly with a mode of about 100 m. These results suggest that although particles can be diverted along the tunnel for a moderate distance with a very degrades backfill, they still have to travel through similar routes through the bedrock to reach the surface, and this because the tunnels are generally oriented perpendicular to the flow gradient.

A continuous EDZ of hydraulic conductivity of $3 \cdot 10^{-9}$ m/s began to make the EDZ a significant hydraulic feature. Again, the flow-paths only see a small influence with the velocity in the EDZ rising by two orders of magnitude, and the path-length in the EDZ rising to 10–100 m for about half the particles, as shown in Figure 4-34 and Figure 4-35.

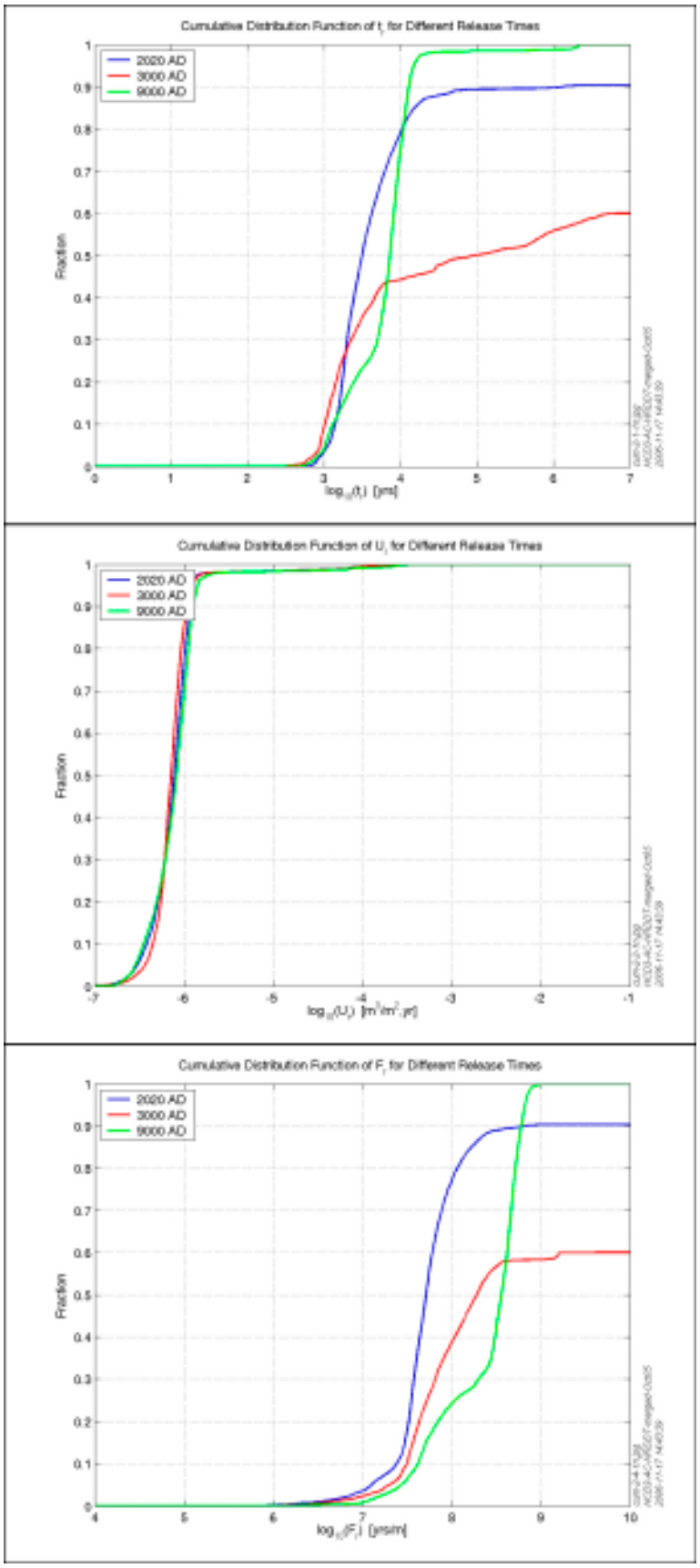

Figure 4-29. *Cumulative distributions for the nested CPM model with 6,824 particles released for pathQ1 at times 2,020 AD, 3,000 AD and 9,000 AD. From the top: t_r, U_r, and F_r.*

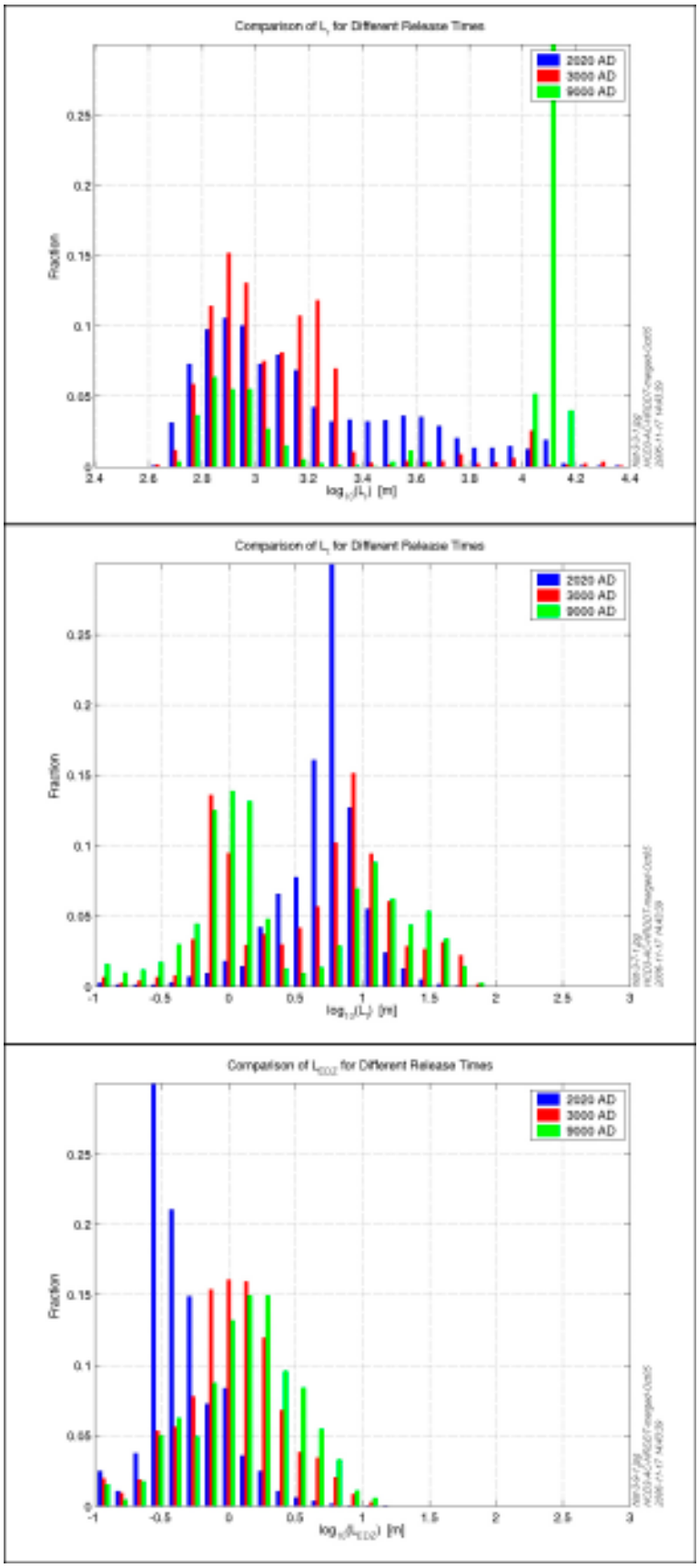

Figure 4-30. *Histograms for the nested CPM model with 6,824 particles released for path Q1 at times 2,020 AD, 3,000 AD and 9,000 AD. From the top: L_r, L_t, and L_{EDZ}.*

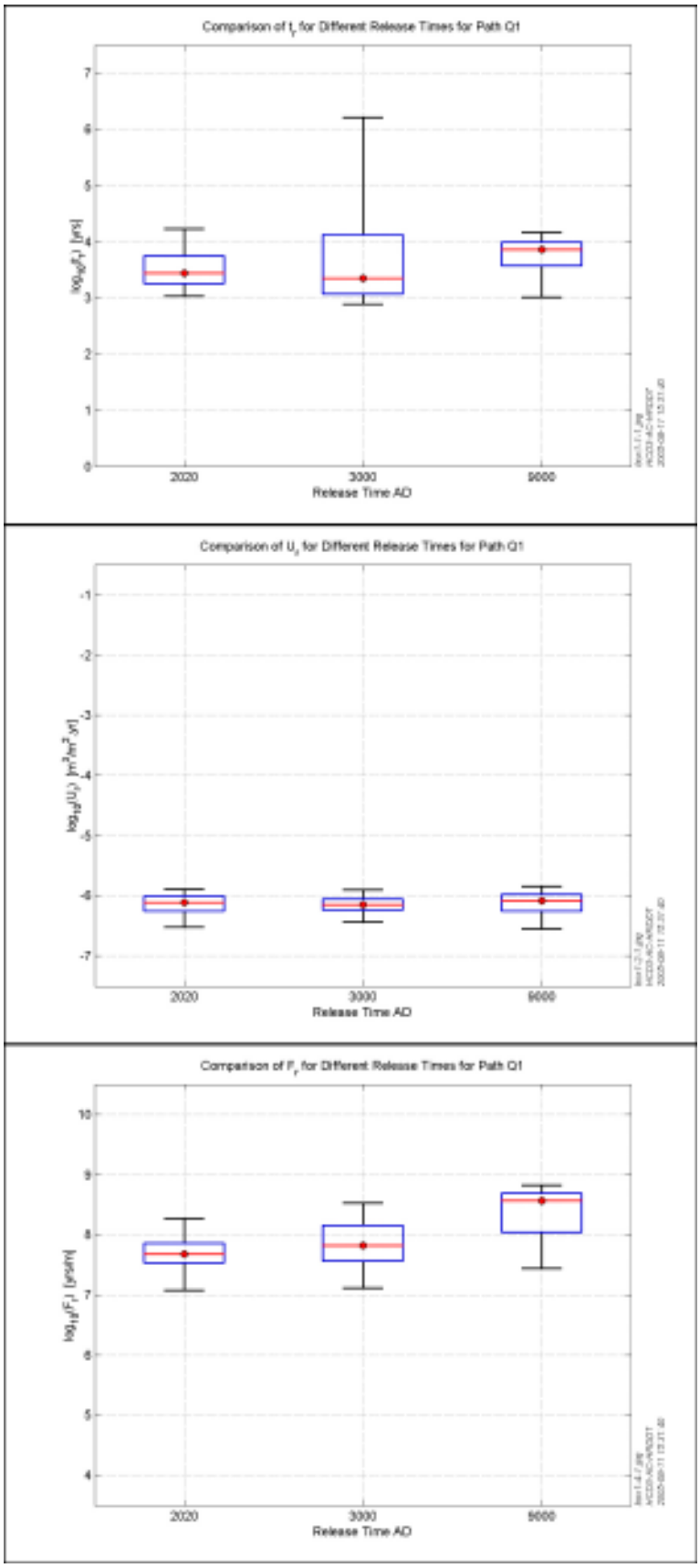

Figure 4-31. *Bar and whisker-plots for the nested CPM model with 6,824 particles released at 2,020 AD, 3,000 AD and 9,000 AD. From the top: t_r, U_r, and F_r. The statistical measures are the median (red), 25th and 75th percentile (blue bar) and the 5th and 95th percentile (black "whiskers").*

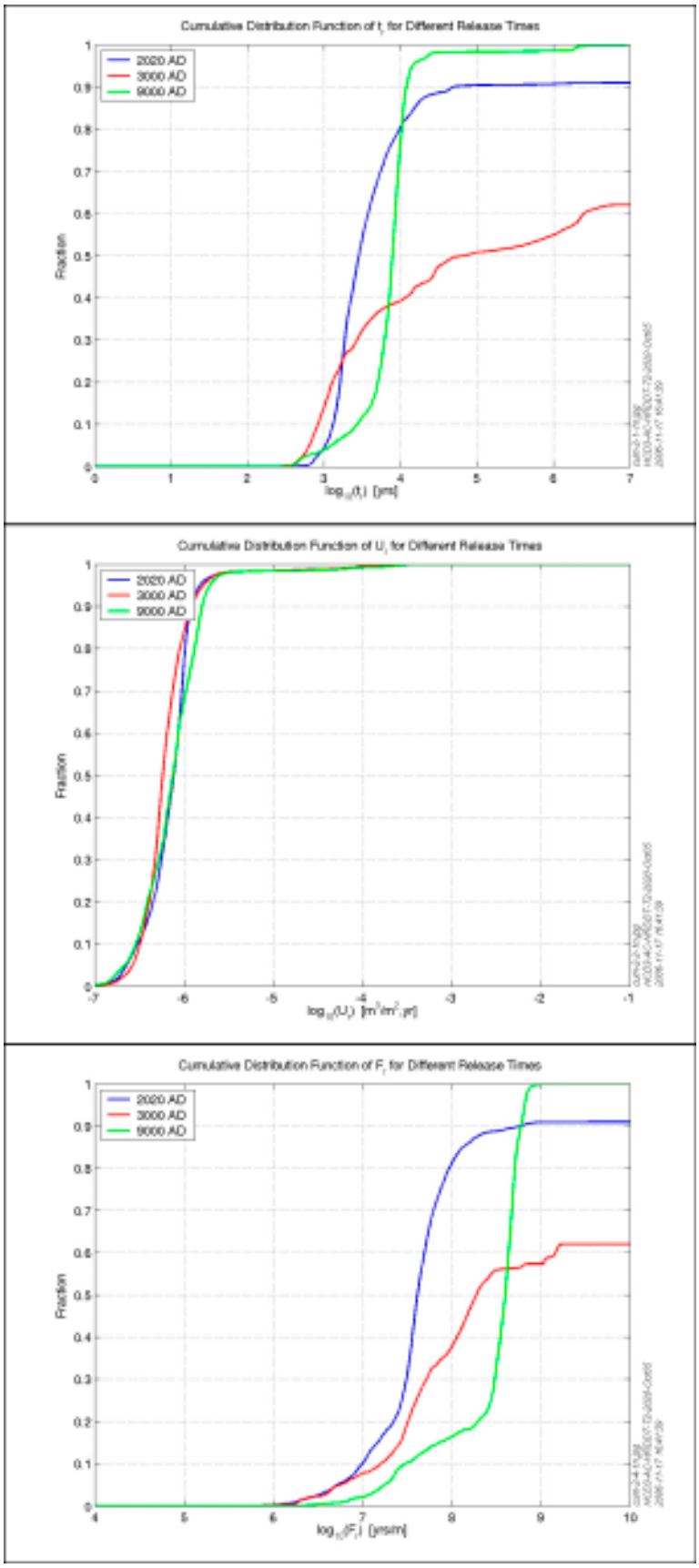

Figure 4-32. *Cumulative distributions for higher tunnel conductivity CPM with 6,824 particles released for paths Q1 at times 2,020 AD, 3,000 AD and 9,000 AD. From the top: t_r, U_r, and F_r.*

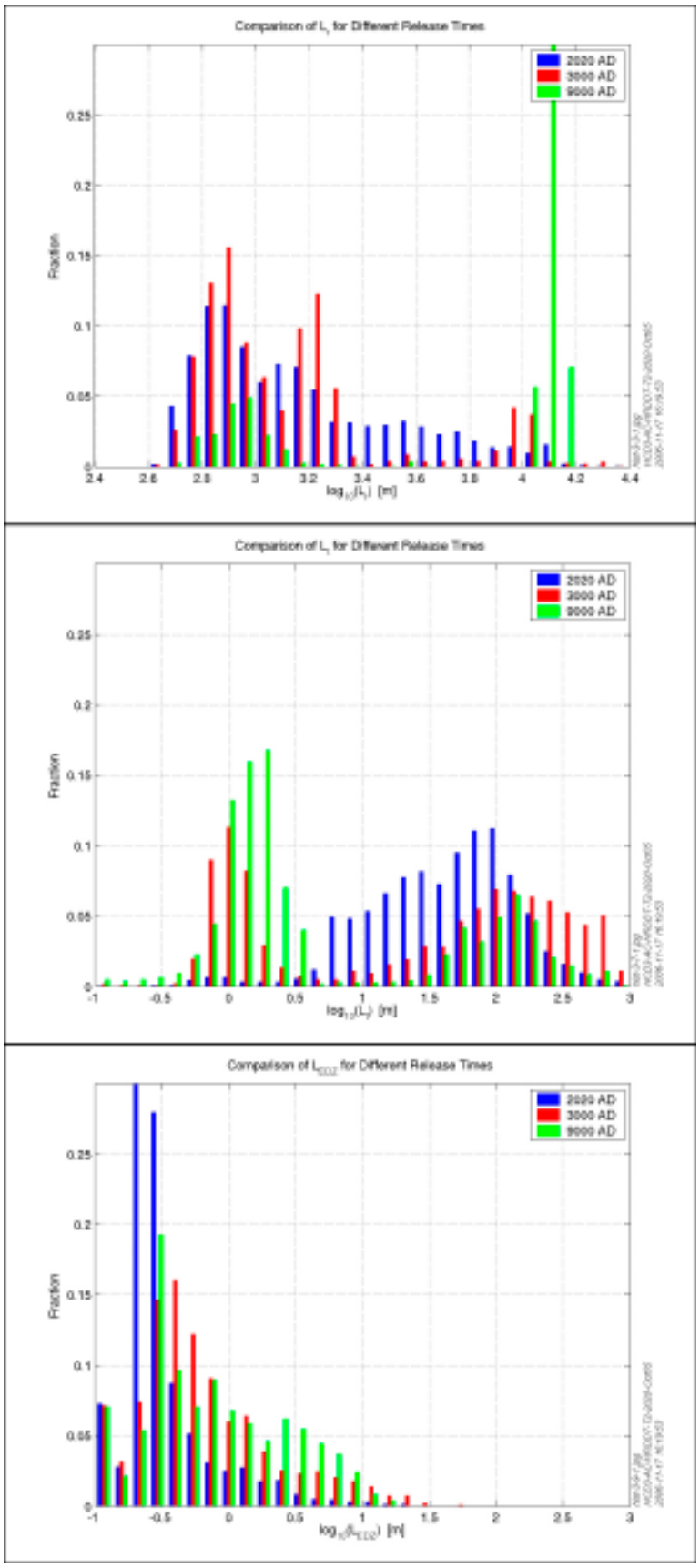

Figure 4-33. *Histograms for higher tunnel conductivity CPM with 6,824 particles released for paths Q1 at times 2,020 AD, 3,000 AD and 9,000 AD. From the top: L_r, L_t, and L_{EDZ}.*

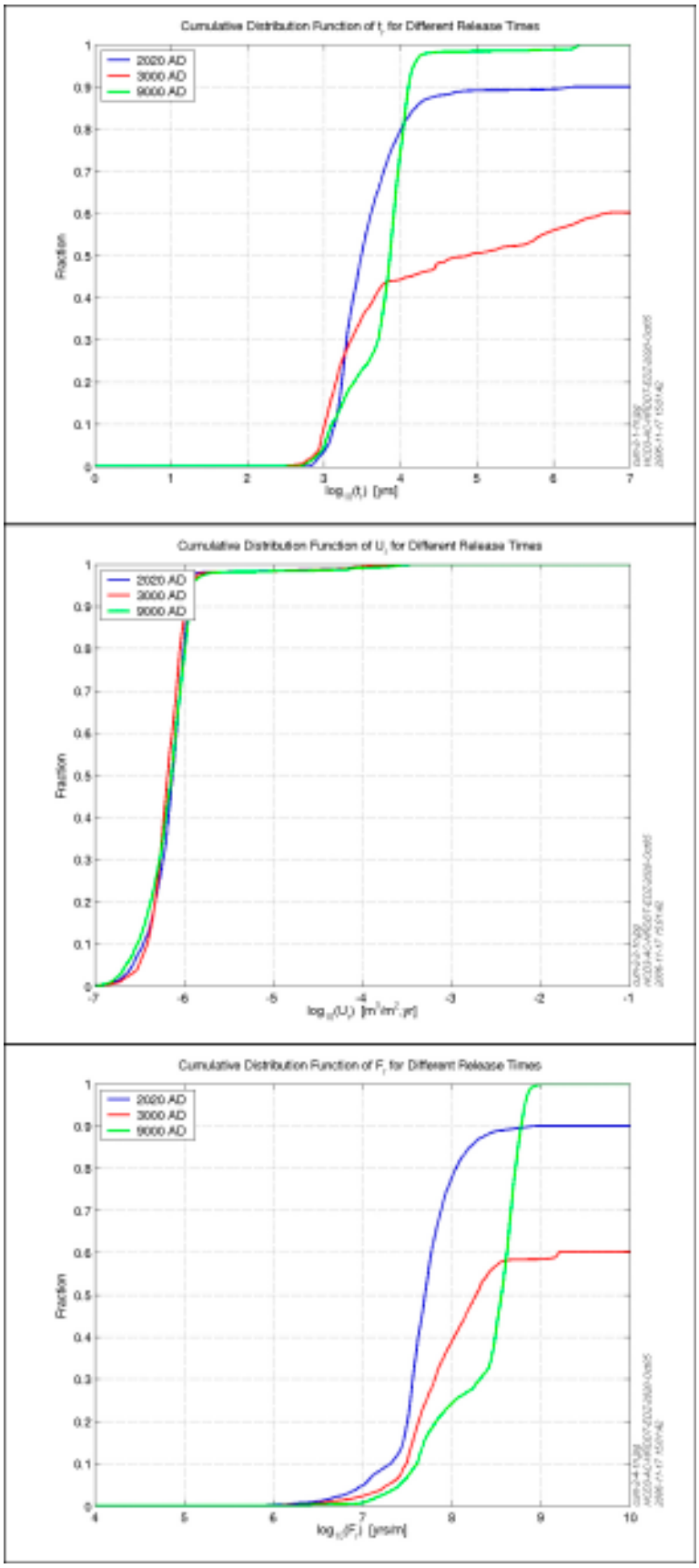

Figure 4-34. *Cumulative distributions for higher EDZ conductivity CPM with 6,824 particles released for path Q1 at times 2,020 AD, 3,000 AD and 9,000 AD. From the top: t_r, U_r, and F_r.*

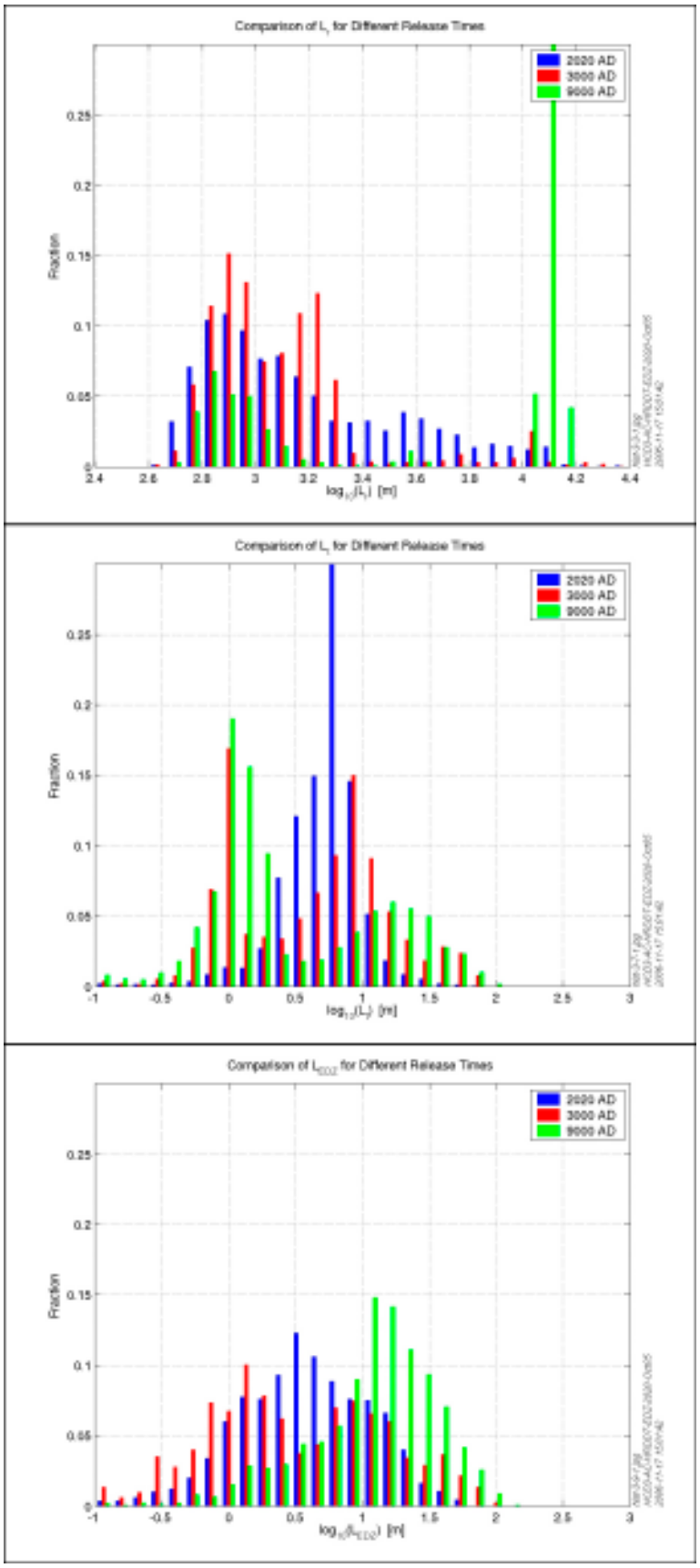

Figure 4-35. *Histograms for higher EDZ conductivity CPM with 6,824 particles released for paths Q1 at times 2,020 AD, 3,000 AD and 9,000 AD. From the top: L_p, L_p, and L_{EDZ}.*

4.4 Alternative nesting: combined regional-scale ECPM/DFN

An alternative configuration was considered for the combined model to quantify how sensitive flow and transport is to choices made in the nesting procedure. In this case, we take a top down approach of starting from the regional-scale realistic ECPM model, insert a local-scale DFN sub-model with the corresponding parameters, and include a slightly idealised representation of the repository. The objective is to construct a single model that can capture particle tracks starting in the repository-scale structures through a DFN sub-model that covers a large part of rock domain RFM029/017 and on through a regional-scale ECPM model. This was found to be tractable, though some compromises were necessary, mainly that the smallest fractures that could be included were 6 m in length and the repository had to be approximated by equivalent fractures rather than as explicit volumes.

4.4.1 Model set-up and specification

In the combined ECPM/DFN model, the continuum sub-model was identical to the realistic case with lower transmissivity below zone ZFMNE00A2 described in Section 3.3.5, and a local-scale DFN model was inserted within the tectonic lens around the repository, as shown in Figure 4-36. The DFN model was inserted below the HSD surface layers and has dimensions of 1,626×1,626×1,100 m, encompassing the entire repository footprint and spanning the tectonic lens from SW to NE. The fractures were imported firstly from the deterministic AC geological model, then from the regional-scale DFN that includes stochastic fractures from 1,000 m down to 12.5 m, and finally additional stochastic fractures were added down to 6 m in length. The stochastic fracture statistics were specified as in Section 3.3.5 and used the correlated transmissivity model, see Section 2.3.2. The fractures between length scales 6 m to 10 m were only generated between z=–510 m and –240 m in line with the repository-scale model to reduce the size of model. Figure 4-37 shows the nested ECPM/DFN model with the deterministic AC deformation zones superimposed. As can be seen, the red-coloured features in the ECPM model of high hydraulic conductivity all correspond to deterministic features. In the local-scale DFN model these zones are modelled explicitly as planar features, and as can be seen there is continuity in the representation across the interface between the two sub-models.

Looking at the model in a SW-NE vertical cross-section, Figure 4-38, shows the different scales modelled with the variety of fracture sizes shown in the DFN sub-model compared to the 50 m in the local-scale grid and 100 m regional-scale grid. The properties in the local-scale model of RFM029/017 to the NW, SE out of section and below the DFN are a heterogeneous upscaled DFN, while the properties outside RFM029/017 are generally homogeneous apart from in a deterministic deformation zone. This plot shows the slightly more intense band of smaller scale fractures that were only included between z=–510 m and –240 m around the repository.

Viewing the model as a horizontal cross-section in map view, Figure 4-39, shows the interface the DFN and ECPM sub-models and between RFM029/017 and the rest of the domain. In the top figure it can be seen how the broad sub-horizontal zone ZFMNE00A2 connects to a linear feature just cutting the SE corner of the DFN sub-model. The lower picture shows the detailed level of fracture incorporated around the repository and the large variation in fracture scales that result from the power-law length distribution. This figure also shows how the repository is represented by low transmissivity fracture. All tunnels, shafts and the ramps were represented in this way. Figure 4-40 (upper plot) shows in yet closer detail the individual fractures around some deposition tunnels. It can be estimated from this that only one or two large fractures cut across adjacent tunnels on average, and many of the smaller fractures may not connect to the network (although 3D connectivity can be under-represented on 2D slices). Figure 4-40 also shows how the repository tunnels were included in the DFN region as vertical fractures with an equivalent transmissivity to represent a backfilled tunnel of specified hydraulic conductivity and cross-sectional area. These ‘tunnel fractures’ will exchange flow with the surrounding fracture network. Similarly, the EDZ was represented as horizontal fractures at the base of the tunnel forming an inverted T-shape so as to ensure a connection between the tunnel and EDZ.

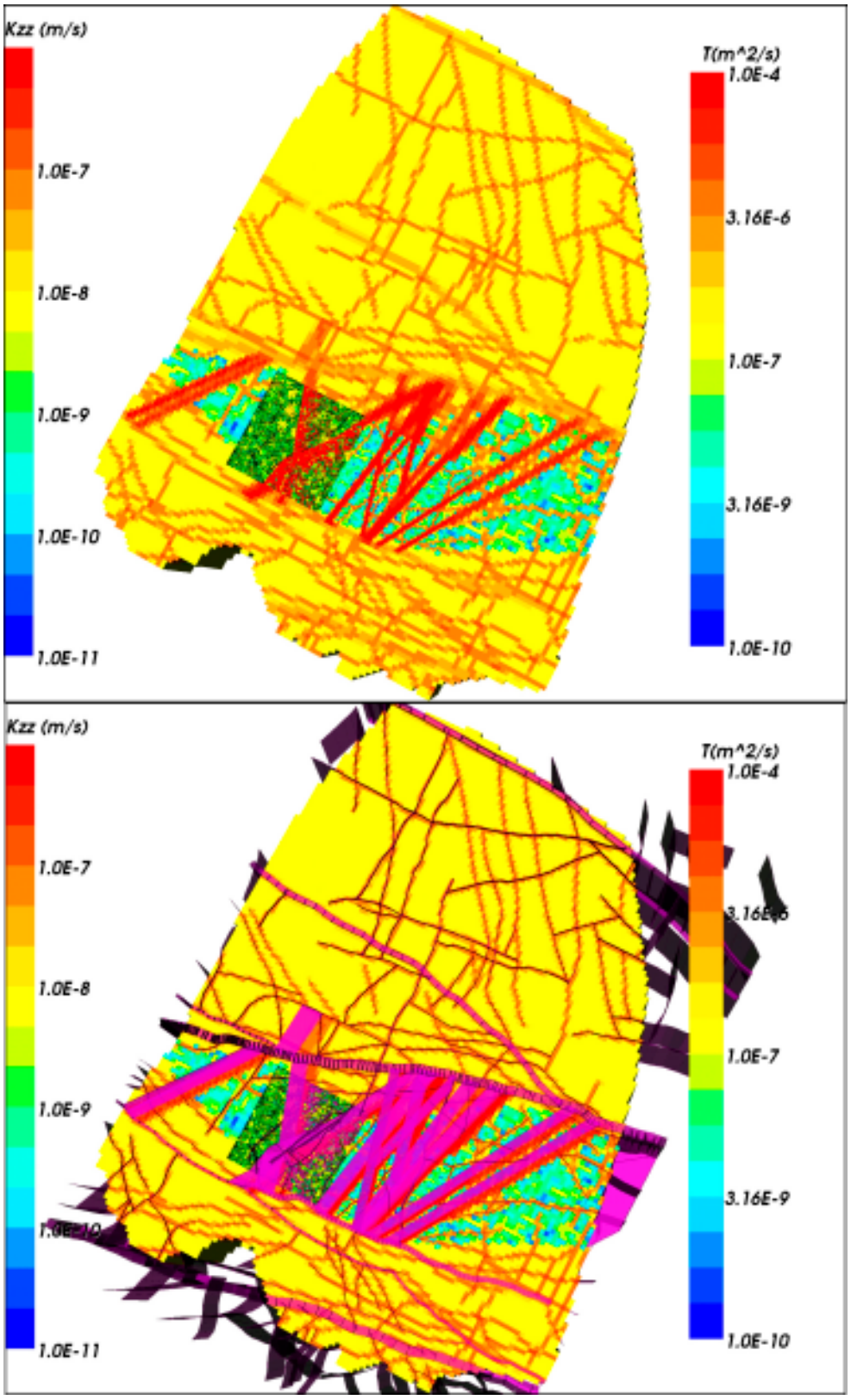

Figure 4-36. *Regional combined ECPM/DFN model with the surface 2 layers removed to show the central local-scale DFN sub-model. The CPM model is coloured by vertical hydraulic conductivity (Kzz), the DFN model is coloured by fractures transmissivity. Bottom: with AC geological model superimposed in purple.*

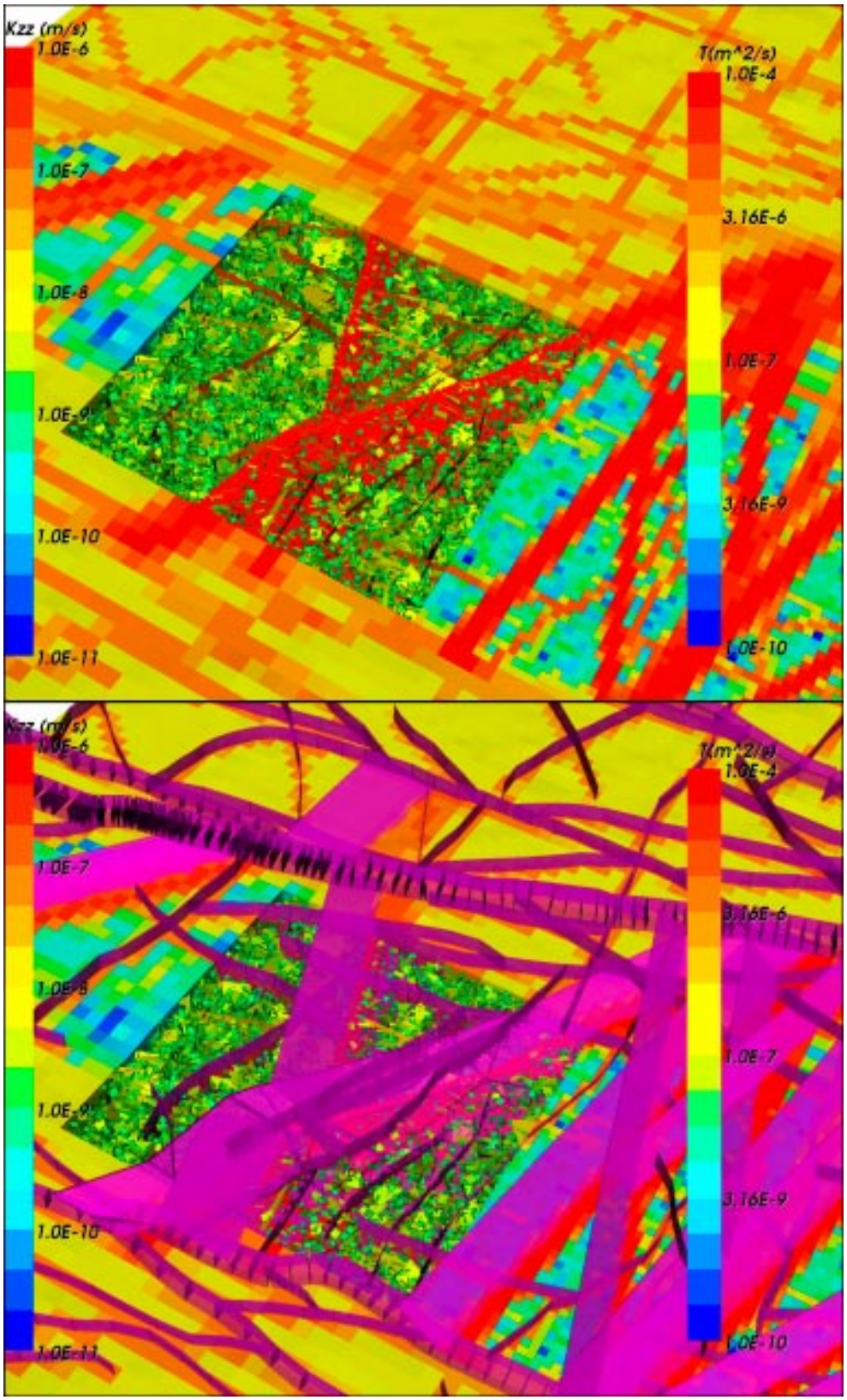

Figure 4-37. *Regional combined ECPM/DFN model showing how the deformation zones are represented in the DFN and their continuity into the surrounding ECPM. The ECPM model is coloured by vertical hydraulic conductivity (Kzz), the DFN model is coloured by fractures transmissivity. Bottom: with AC geological model superimposed in purple.*

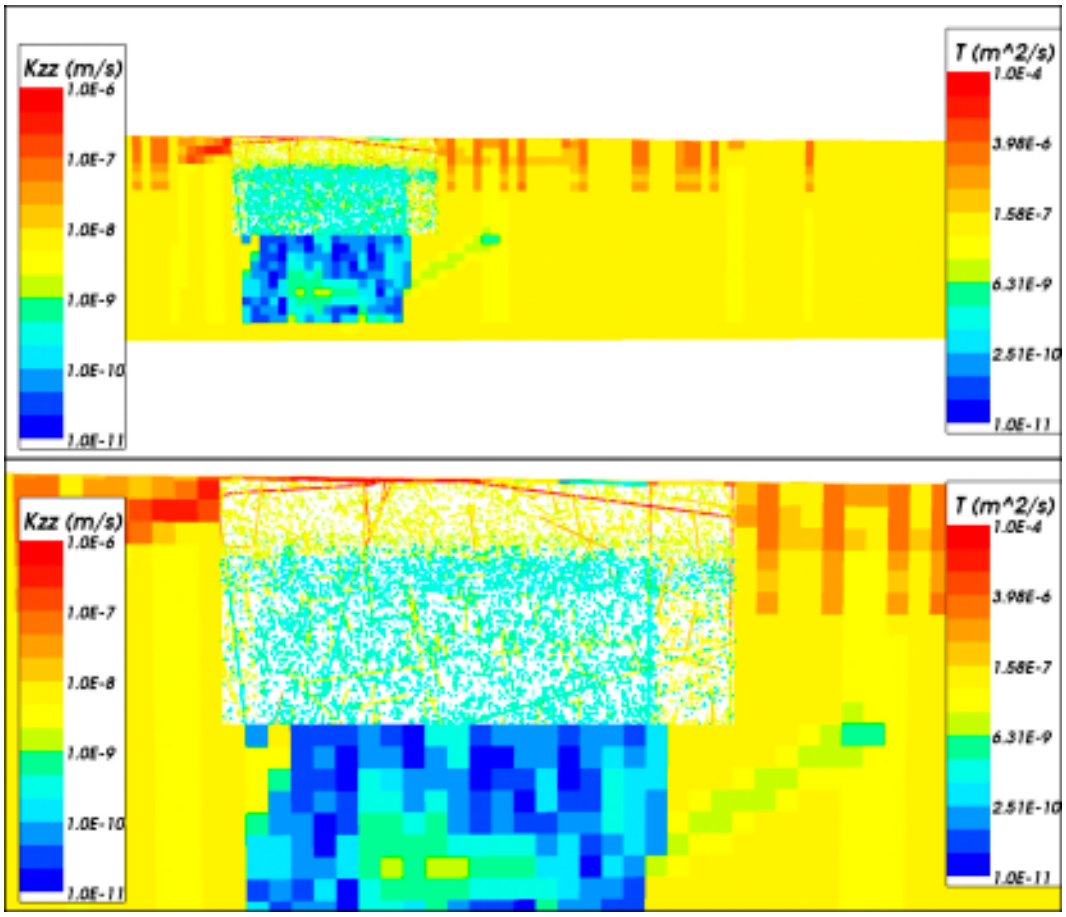

Figure 4-38. *A vertical slice through the combined ECPM/DFN regional model cutting through the repository from SW (left) to NE (right). Top: the whole ECPM and DFN model. Bottom: just around the DFN. The ECPM model is coloured by vertical hydraulic conductivity (Kzz), the DFN is coloured by transmissivity. Extra stochastic fractures are seen in a horizontal band about a third of the way down the DFN sub-model. The lower transmissivity of fractures within the tectonic lens below zone ZFMNE00A2 and z=–350 m can also be seen.*

Using this representation, it is possible to track particles released from the repository, initially through the fractures close to the repository and on through the ECPM sub-model. Also, if there is no connected pathway through the fracture system around a particle release point then the flow-path may enter the tunnel or EDZ, or both, where that carries more flow.

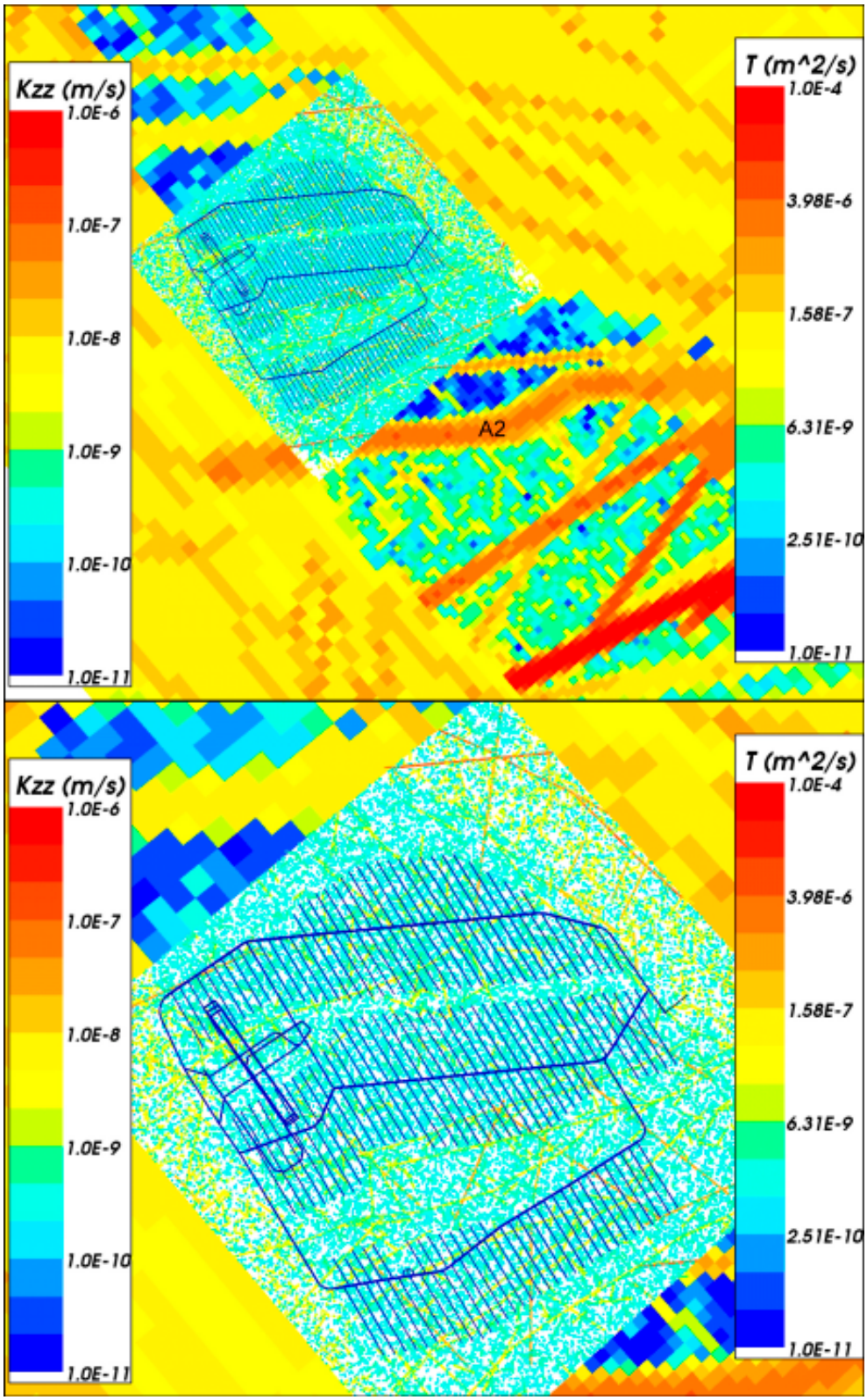

Figure 4-39. *A horizontal slice through the combined ECPM/DFN regional model at repository depth (z=–410 m). Showing the DFN area (top), and the repository area (bottom). The CPM model is coloured by vertical permeability (Kzz). For the DFN model, fractures are coloured by transmissivity.*

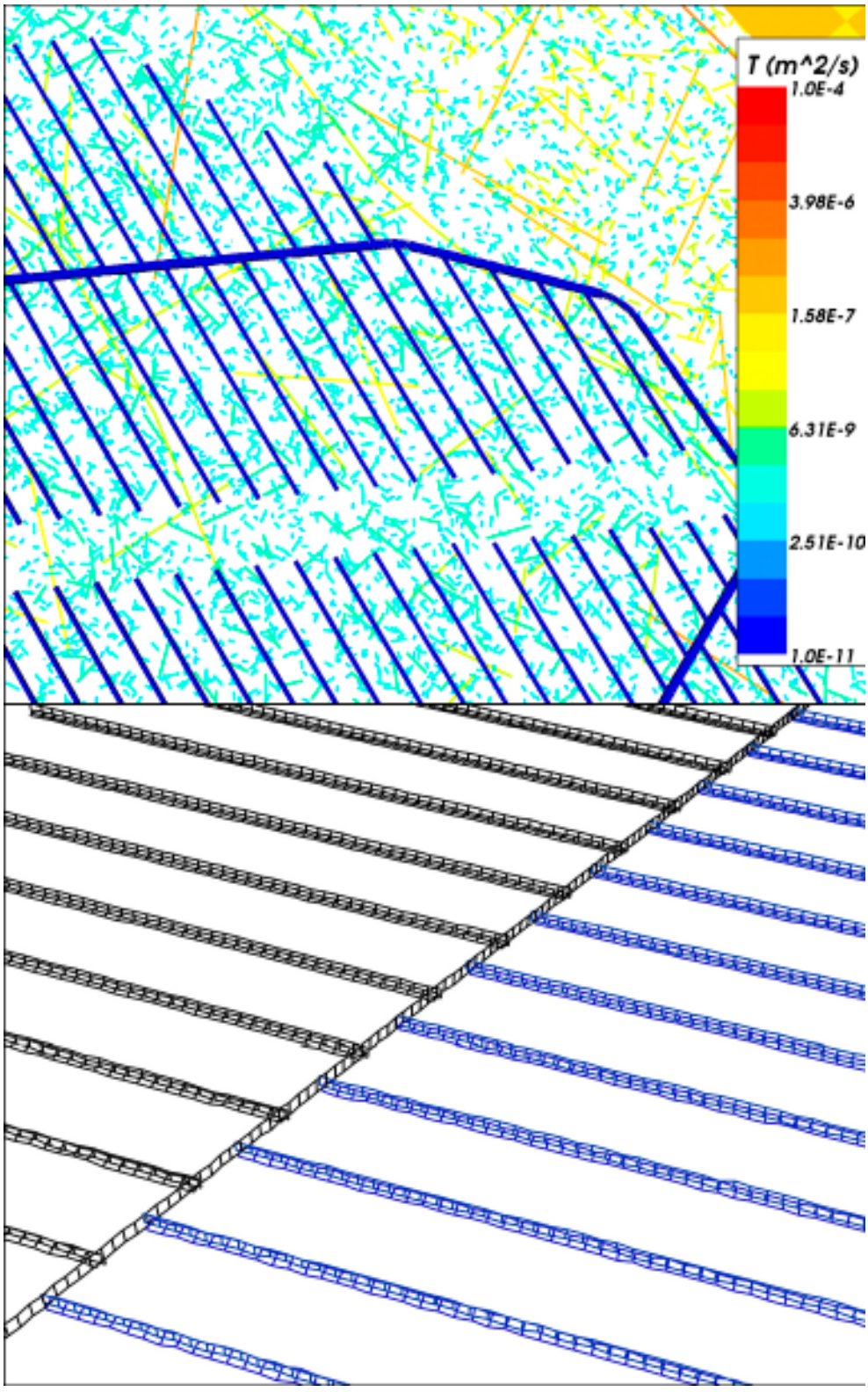

Figure 4-40. *More details of the DFN model around the repository. Top: the fracturing around some of the deposition tunnels. Fractures are coloured by transmissivity. Bottom: representation of tunnels and EDZ as equivalent fractures discretised into 6 m long fracture sections.*

4.4.2 Variable-density flow calculations

Using an identical approach to the repository-scale model, the fluid density was interpolated from the pure realistic case ECPM model at 2,020 AD on to both sub-models, and then a self-consistent distribution of residual pressure and flow-field was computed. Continuity of fluid density and residual pressure along with conservation of mass-flux was ensured at the interface between the two sub-models. Figure 4-41 shows the consistent pressure distribution calculated in the ECPM/DFN model just below the surface layers. The fracture network is shown with all fractures. Those coloured grey are not connected to the network. The continuity in pressure can be seen across the interface. It can be seen that the DFN sub-model includes a number of localised maxima corresponding to islands and small peninsulas. In Figure 4-42 the DFN sub-model is shown in greater focus and with the unconnected fractures removed to show the pressure continuity better. The figure also shows the distribution of fluid density near the surface which is mostly fresh with a few areas in the NW that are slightly denser due to the infiltration of Marine water from the Baltic. The equivalent plots for repository depth are presented in Figure 4-43. Generally the pressure is around $2 \cdot 10^4$ to $7 \cdot 10^4$ N/m^2 and the density is also higher. It should be noted that these plots are not horizontal slices, but are created by stripping off the features above, and hence in the DFN you can see through the network to deeper fractures with higher pressure and fluid density. By inspecting several horizontal slices through the combined model at different depths it was confirmed that the density and pressure are consistent at the interface.

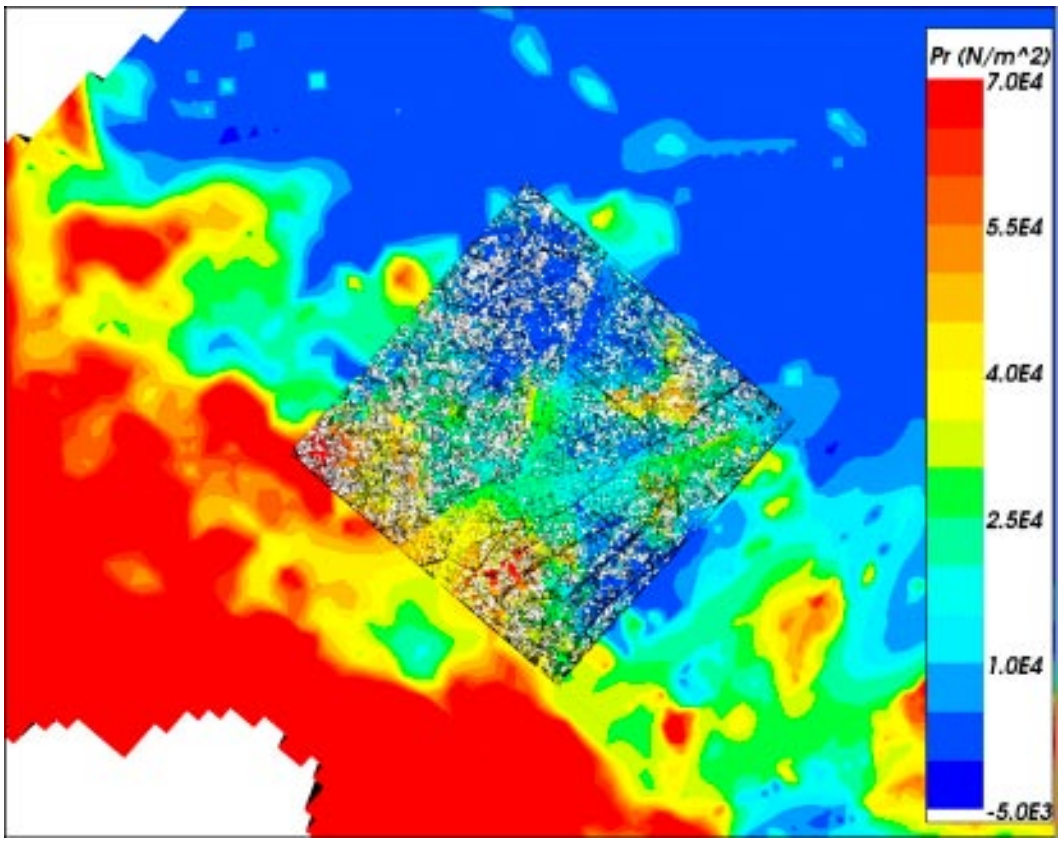

Figure 4-41. *Distribution of residual pressure in the combined regional ECPM/DFN model near the top of the model with the top surface HSD layers removed. In the DFN sub-model, fractures not connected to the network arte coloured grey.*

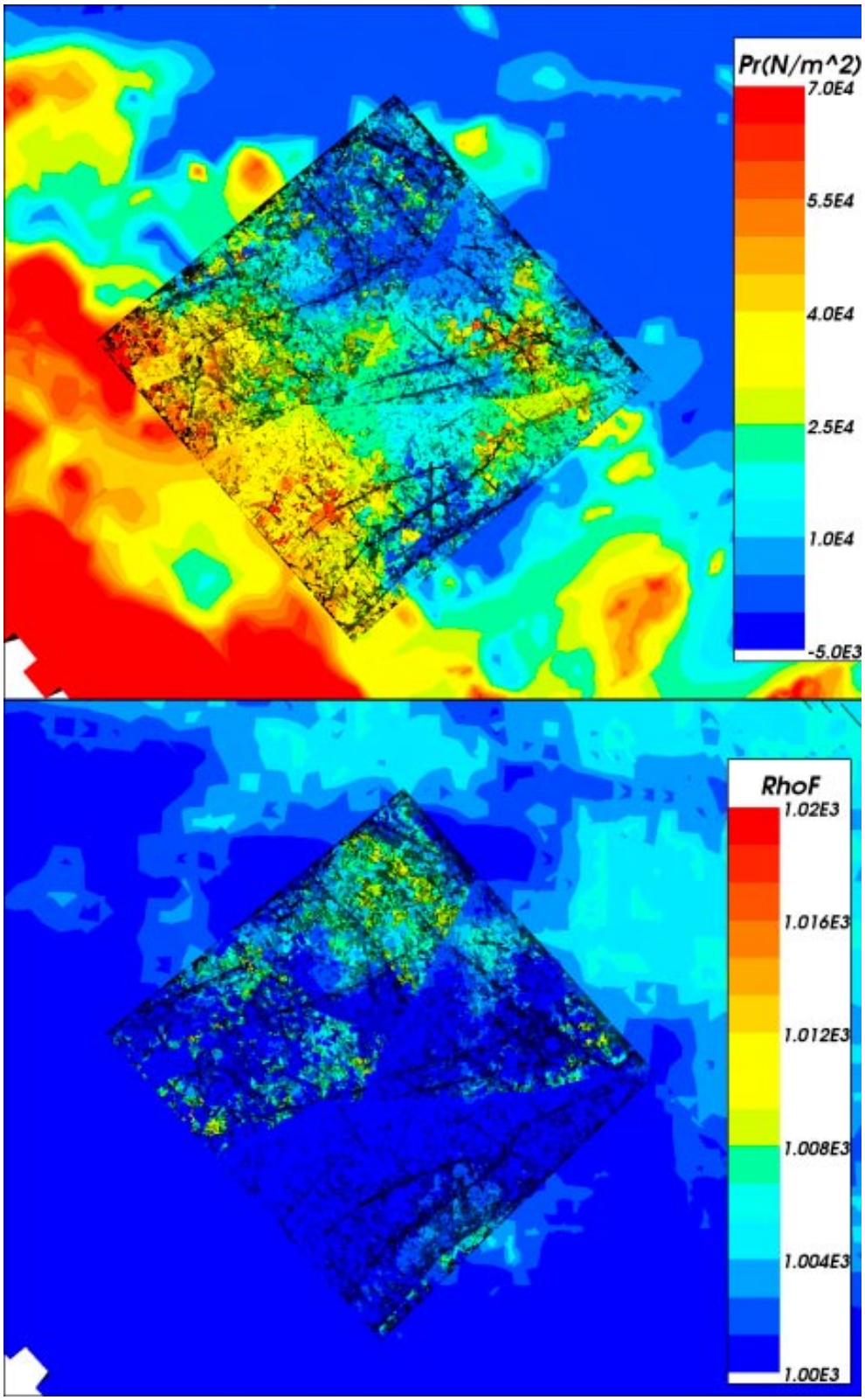

Figure 4-42. *Results of variable-density flow calculation at 2,020 AD for the combined ECPM/DFN model in close-up of DFN near top surface. Top: distribution of residual pressure. Bottom: distribution of fluid density.*

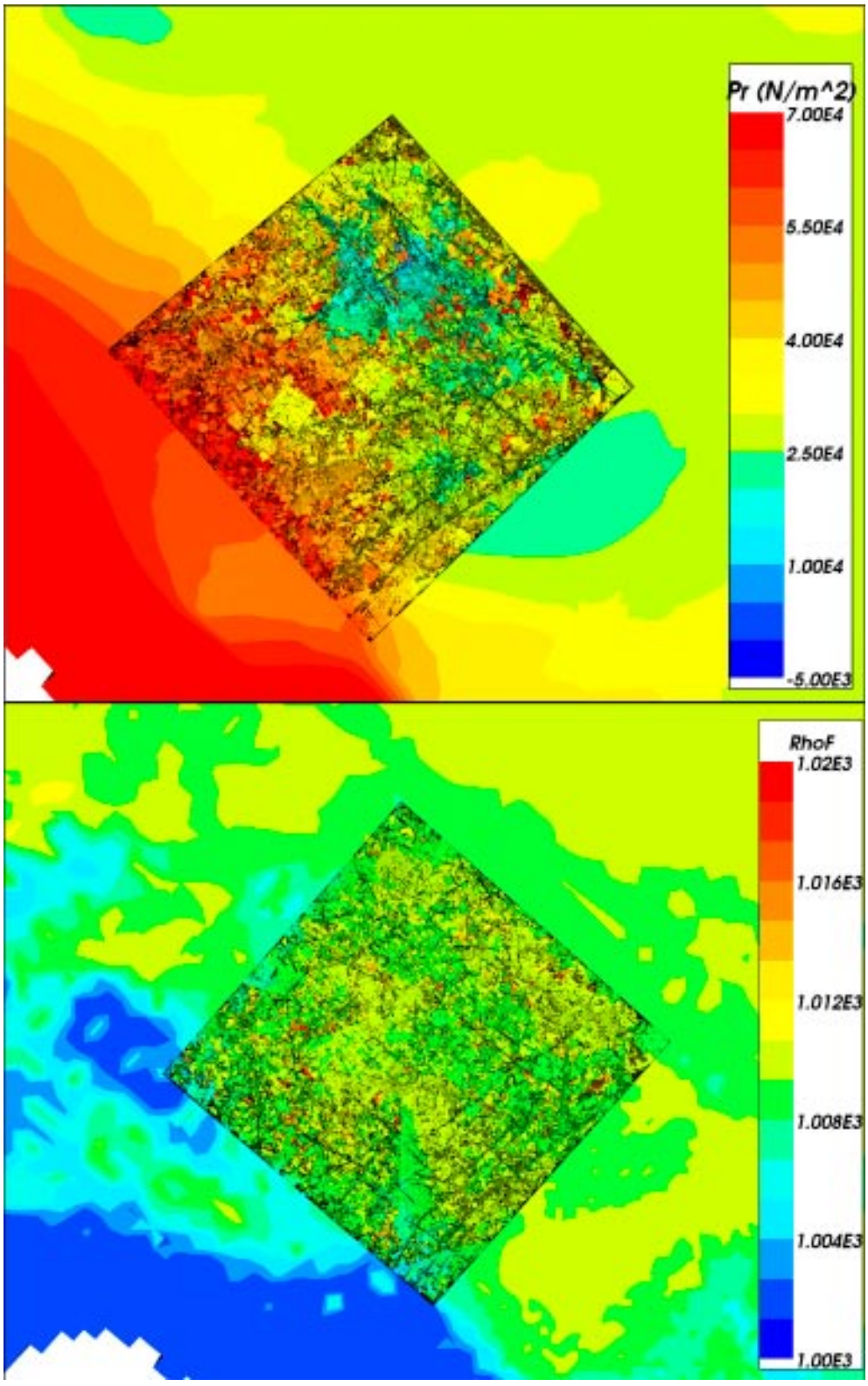

Figure 4-43. *Results of variable-density flow calculation at 2,020 AD for the combined ECPM/DFN model in close-up of DFN at z=–410 m. Top: distribution of residual pressure. Bottom: distribution of fluid density.*

4.4.3 Flow-paths

Flow-paths were calculated for all 6,824 canister positions, but since the deposition holes are not modelled explicitly and the minimum fracture size was 6 m, then it wasn't appropriate to try and differentiate between the three different particle release locations around each deposition hole. Instead, particles were released at the fracture intersection with the highest flux within a 3 m radius sphere around the canister centre, and if no such intersection could be found, then the nearest fracture intersection was used. This meant that sometimes particles were started in a nearby fracture, and sometimes in a fracture representing the tunnel or EDZ. Hence, the near-field release is a mixture of Q1, Q2 and Q3 paths compared to the more detailed repository-scale models. However, the aim is more to get an alternative calculation of the full far-field flow-path. After releasing particles, they are tracked through the local-scale DFN and ECPM model to the surface. As such, this model gives a good representation of transport and retention on all scales apart from the smallest canister-scale details. The same 3 reference times were considered at 2,020 AD, 3,000 AD and 9,000 AD. Again, some problems were encountered with particle tracking in the very sparse networks interpreted at Forsmark. Here, between 23% at 3,000 AD and 16% at 2,020 AD of particles become stuck in the network, mostly close to the repository. In this case because the local-scale is a pure DFN model, then the cause can only be due to starting particles in closed flow loops, i.e. a connected loop of fractures that have only one way in/out. The cycling around closed flow loops is essentially a numerical artefact as a consequence of the very low connectivity of the network and the iterative solution methods used. As for the repository-scale models, efforts were made to obtain good convergence in the numerical models. A relative mass balance fraction of 10^{-8} net flux divided by gross flux was achieved in the DFN sub-model, for example. The approximately 20% of canister locations associated with stuck particles is thought to reflect a realistic situation where there is no advective fracture network in close proximity to the canister. This figure perhaps sheds light on the greater percentage of stuck particles encountered in the repository-scale model. It suggests that for about 20% of particles there is no connected fracture network nearby, and for about a further 20% there is essentially stagnant flow in the tunnel also.

Figure 4-44 shows the distribution of F-quotients on the particle release locations at 2,020 AD, 3,000 AD and 9,000 AD. A clear observation is that the distributions are quite similar suggesting much less sensitivity to the position of the shoreline than in the regional-scale ECPM model. There are a number of F-quotients around 10^4–10^6 y/m mainly with a clear correlation to the proximity to either a deterministic deformation zone or a large stochastic fracture. Small F-quotients are more prevalent in the NW and central parts of the repository, but there are much localised variations just depending on the localised fracturing. It confirms that flow is very heterogeneous and mostly localised.

Figure 4-45 shows the equivalent plot of F-quotients, but this time at the release points on the top surface. Again, this is in stark contrast to the result of the regional-scale ECPM, see Figure 3-62, with much more localised release and few paths crossing the Singö deformation zone in this model. At 2,020 AD all particles appear almost vertically above the repository. At 3,000 AD and 9,000 AD some particles get as far as the Singö zone, but the very long paths to the future shoreline are not seen. This is shown by the 3D full particle tracks in Figure 4-46. This illustrates how flow is predominantly vertically upwards at 2,020 AD, but then goes more horizontal in some of the northern and eastern areas of the repository at later times. Few particles follow deep paths beyond about 500–600 m depth. There is possibly a slight progression toward deeper particles at future times, but only for some start locations.

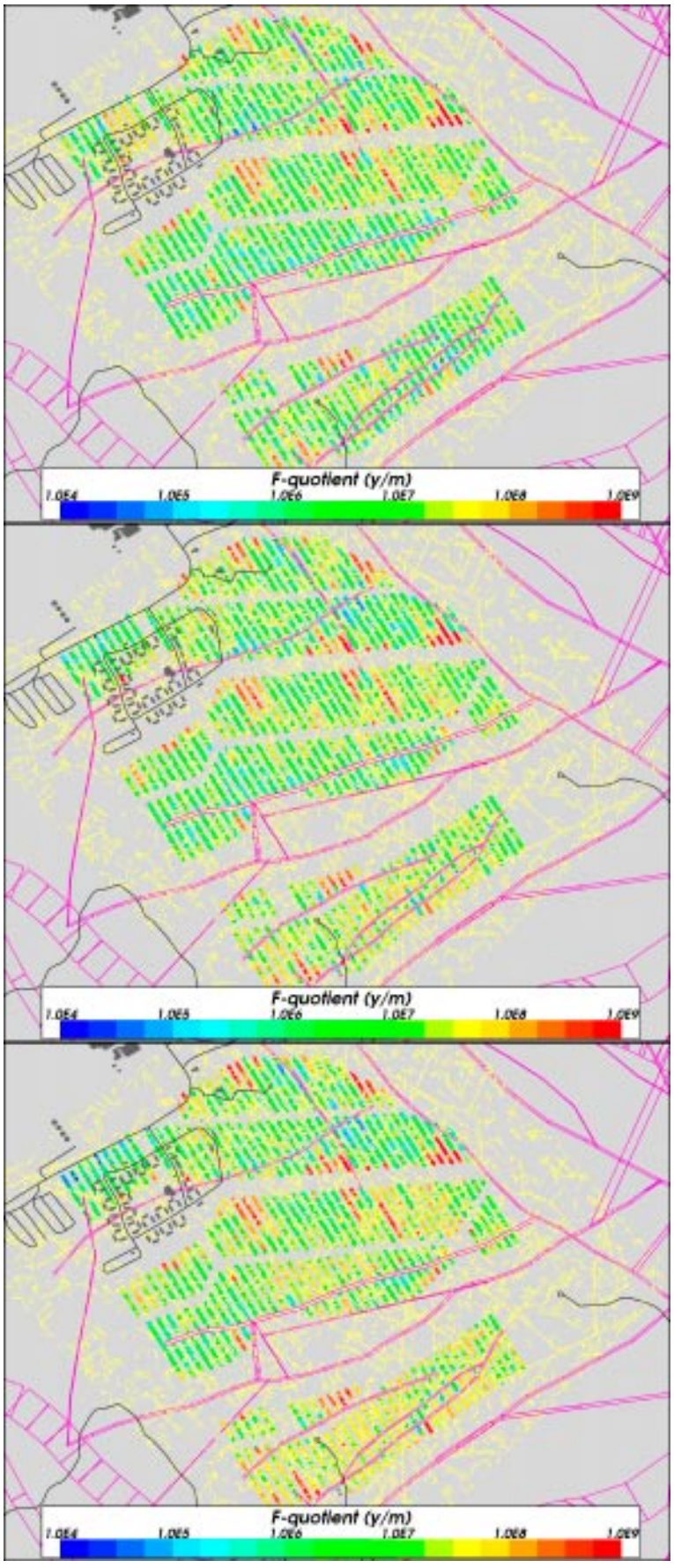

Figure 4-44. *Distribution of $\log_{10}(F_r)$ at 6,824 particle start locations for the combined ECPM/DFN model at release times (top to bottom): 2,020 AD, 3,000 AD and 9,000 AD. Also, the HCDs at z=–400 m (purple), large stochastic fractures (yellow), roads and buildings (black).*

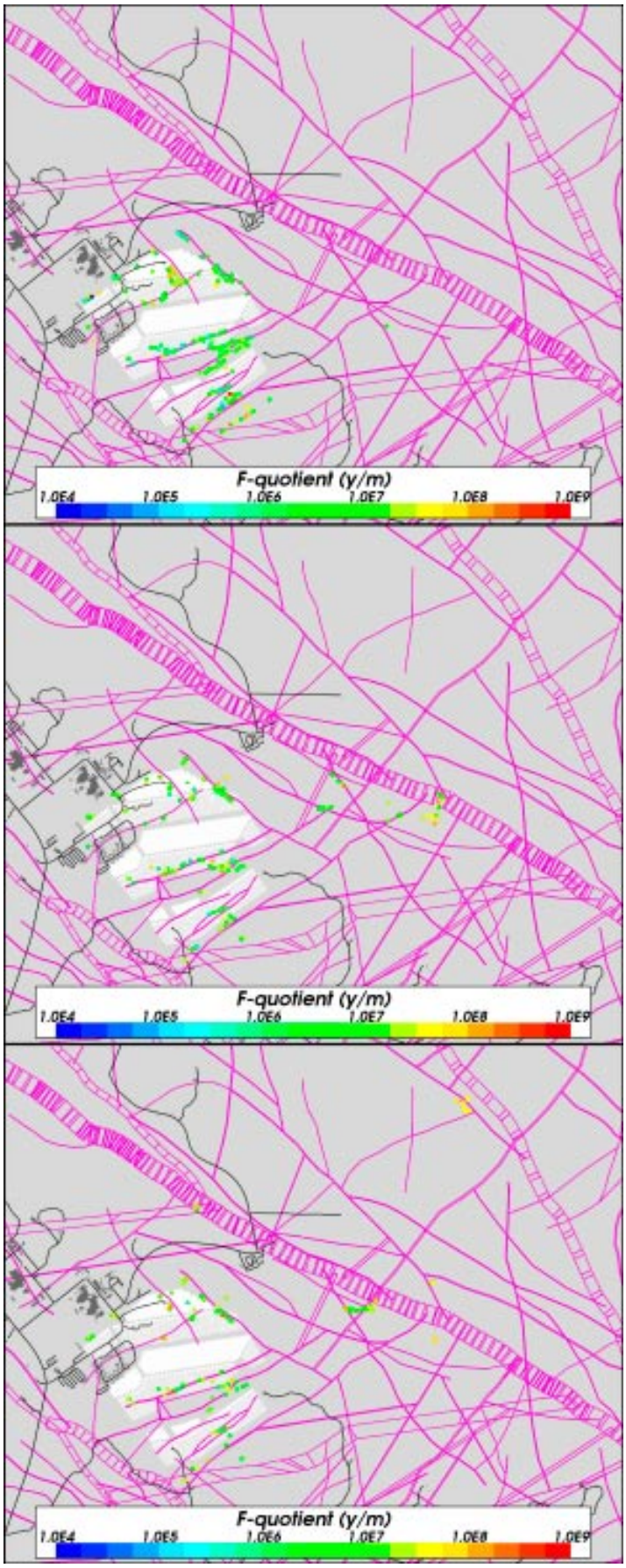

Figure 4-45. *Distribution of $\log_{10}(F_r)$ at 6,824 particle exit locations for the combined ECPM/DFN model at release times (top to bottom): 2,020 AD, 3,000 AD and 9,000 AD. Also, the HCDs at z=–400 m (purple), roads and buildings (black).*

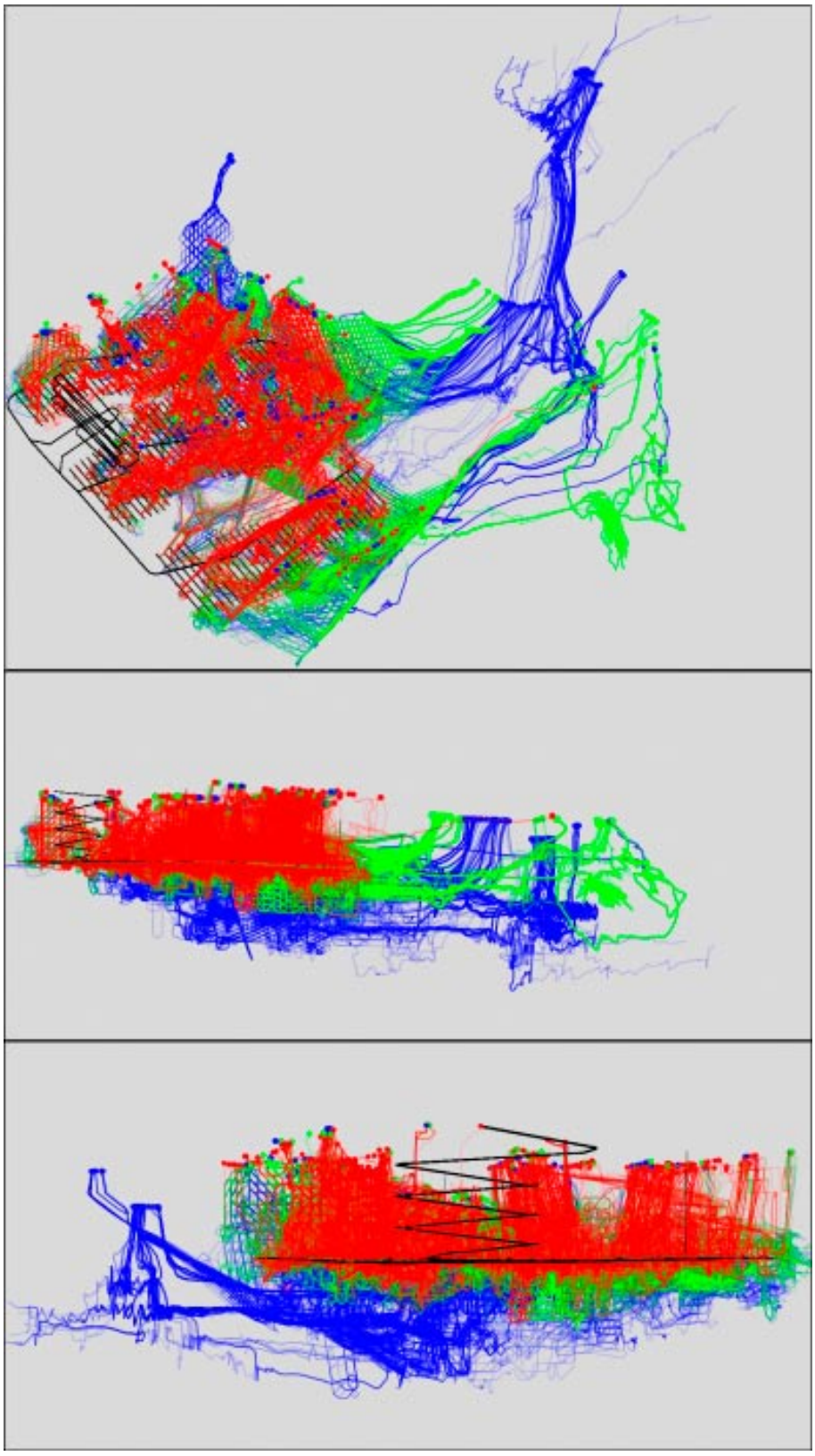

Figure 4-46. *Flow-paths and exit locations for the combined ECPM/DFN model coloured by release time; 2,020 AD (red), 3,000 AD (green) and 9,000 AD (blue) for the combined ECPM/DFN model. Top: oblique view. Middle: vertical section SW-NE. Bottom: vertical section NW-SE. The repository is shown in shown in black for context.*

4.4.4 Performance measures

The PMs for the rock t_r, U_r and F_r at all 3 reference times are shown as cumulative distributions in Figure 4-47. The travel-time varies hugely between about 10 years to over 10 million years with a bi-modal profiles. The mode values are around a few hundred years and 100,000 years. These distinct travel-times do not appear to correspond with radically different local-scale paths or areas of the repository. Rather short travel times, about 25%, correspond with well connected paths in the fracture network around deformation zones or large stochastic fractures. The remaining paths tend be more tortuous and include sections of path through one or more tunnels, although the travel-time presented is only that spent in the rock. For example, some particles drift from the tunnel in to a short fracture connection and then either back into the same tunnel or another, presumably very low velocities before eventually finding a much better connected part of the network. The overall median travel time is about 40,000 years. Travel times in the rock in the repository-scale model were less than 100 years which is consistent with the values calculated for the quick paths calculated here. It perhaps indicates that some of the time spent in the 'tunnel fractures' has been included in the travel-time in the rock for some paths. The initial Darcy velocity also has a very wide distribution, although more continuous, between about 10^{-7} to 10^{-4} m/y. The changes are slight at future release times. F-quotient varies between about 10^5 and 10^8 y/m with a median around $6 \cdot 10^6$ y/m. This statistics for F-quotient is very consistent with the repository-scale model.

The statistics for path-length in the rock, tunnel and EDZ, L_r, L_t and L_{EDZ} are presented as histograms in Figure 4-48. The variation in L_r is between about 500 m and 2,000 m with a mode around 1,000 m. The increase in path-length at 9,000 AD is just about discernible. For the base case backfill properties used here, the spread in path-lengths in the tunnel is about 10 m to 180 m with a mode about 50 m. This confirms that the sparsity of the network often forces particles to travel through the tunnel a considerable distance to find a connected fracture to enter an advective flow channel through the bedrock. Interestingly, the distance is higher than the repository-scale CPM model that supposedly has lower bulk hydraulic properties, and the distance in the tunnel is more similar to the CPM model with a high backfill hydraulic conductivity. The distance travelled in the EDZ, L_{EDZ}, is generally less, about 3 to 70 m, with mode around 16 m. All PMs for this case are tabulated in Appendix C.

The PMs demonstrate the variability in the travel-time which is far greater than for the realistic ECPM regional-scale model shown in Figure 3-64. The median is over an order of magnitude lower than in the realistic ECPM regional model, though there are almost 3 orders of magnitude between 5th and 95th percentile here compared to only half an order of magnitude fro the ECPM model. The initial Darcy velocity is also one order of magnitude lower than the regional ECPM model, while the F-quotient is about the same with a median about $3 \cdot 10^7$ y/m. This comparison illustrates the very significant differences between a sparse DFN and an upscaled ECPM model based on a relatively coarse grid. Travel-time and initial Darcy-velocity suffer the most inaccuracy in using the coarse ECPM regional-scale model mainly because they are very sensitive to not resolving the detailed flow in the scale of individual fractures. F-quotient seems the least sensitive which may be because the flow-wetted surface, a_r, was well estimated in the ECPM model.

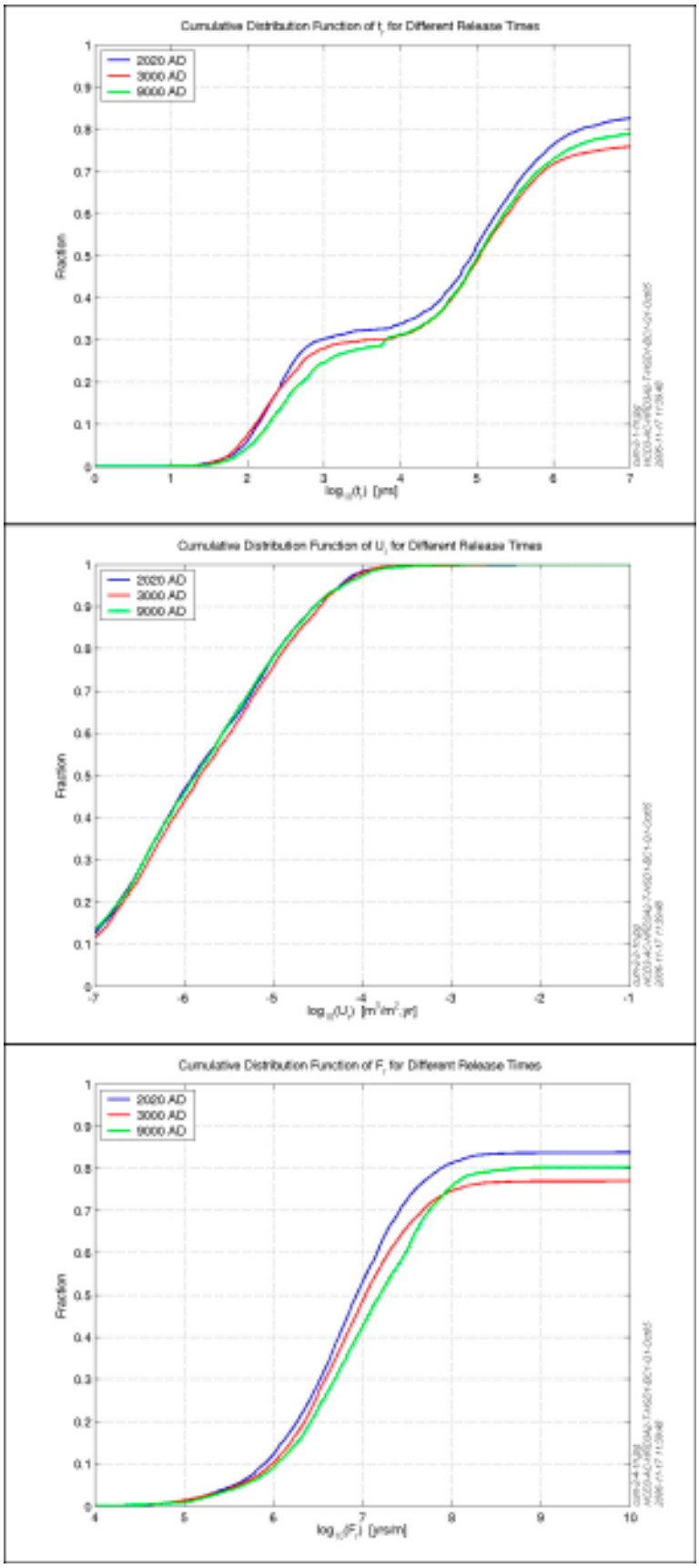

Figure 4-47. *Cumulative distributions for the combined ECPM/DFN model with 6,824 particles released at times 2,020 AD, 3,000 AD and 9,000 AD. From the top: t_r, U_r, and F_r.*

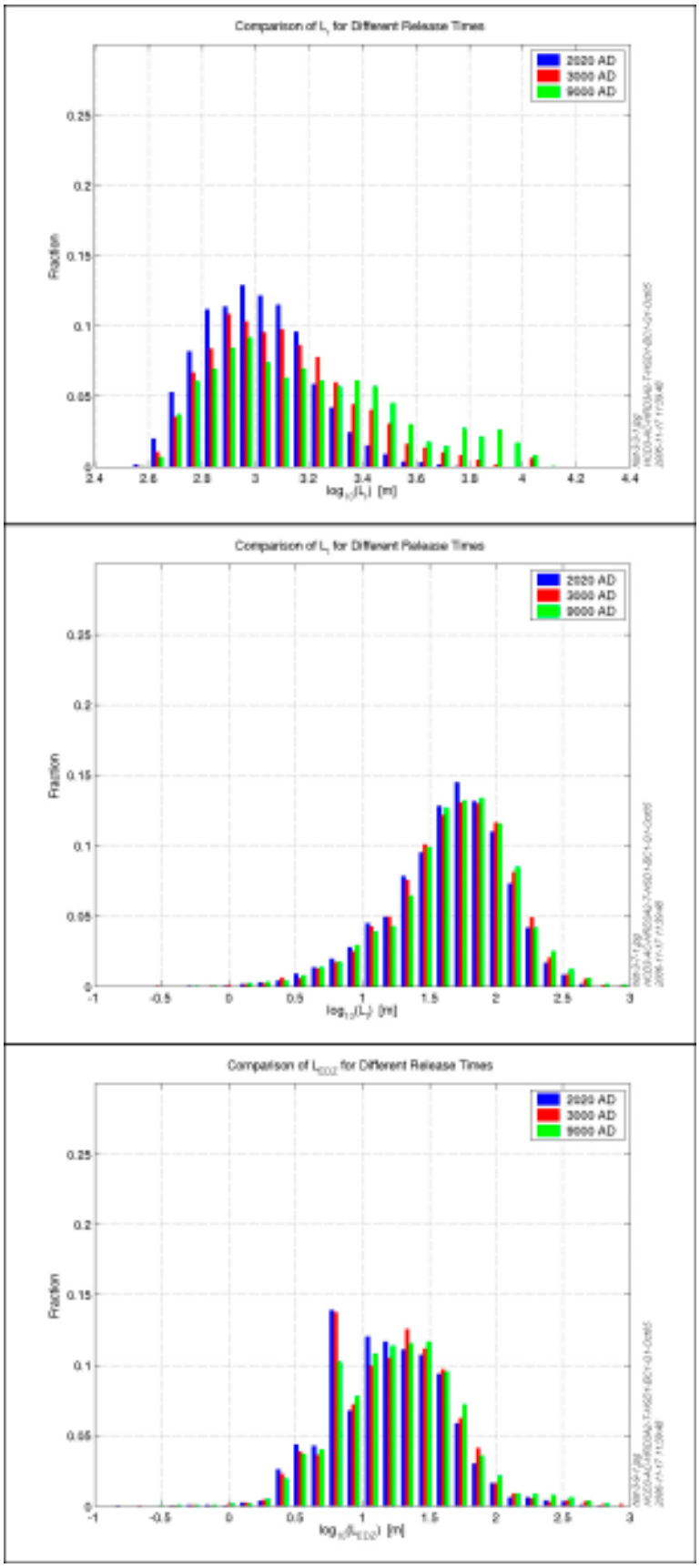

Figure 4-48. *Histograms for the combined ECPM/DFN model with 6,824 particles released at times 2,020 AD, 3,000 AD and 9,000 AD. From the top: L_r, L_t, and L_{EDZ}.*

4.5 Deposition hole rejection criteria

All the statistics given in the above sections are based on an ensemble over all 6,824 deposition hole locations. However, in practice some deposition holes will not be excavated to avoid areas that may have an adverse effect on repository performance. Such a decision will be based on two main criteria. The first is that a deposition hole will not be constructed directly beneath a fracture sufficiently large to cross-cut the full perimeter of the deposition tunnel face. This full perimeter intersection criterion (FPC) is to avoid large sub-vertical fractures that have a higher probability of carrying relatively large groundwater flows. If the location passes this first criterion, then a probe hole will be drilled to check whether there is a transmissive sub-horizontal fracture intersecting the trajectory of the deposition hole based on some type of hydraulic test in the probe hole. This deposition hole screening process is likely to eliminate many of the less favourable locations, and hence improve repository performance. The impact may be quantified by simulating this process using the repository-scale DFN models developed in this section.

An algorithm was used to post-process the DFN models and create three extra columns in the performance measures for each deposition hole location. The first column records whether a fracture that cuts the deposition hole also cross-cuts all four sides of the deposition tunnel above. The second column gives the linear side length of the largest fracture intersecting the deposition hole, and the final column gives the transmissivity of the most transmissive fractures intersecting the deposition hole. Here, the deposition tunnel is approximated as having a square cross-section.

In more detail, the algorithm is implemented as follows:

a) Loop over all the deposition holes.

b) For each deposition hole, firstly identify the corresponding deposition tunnel and second determine all the fractures that intersect the hole.

c) For each fracture that intersects the deposition hole determine:
   1) Is the fracture a deterministic deformation zone? If "Yes", write a "2" in the first column of the output file and "1,000.0" (a generic length) in the second column.
   2) Is the fracture associated with the EDZ? If "Yes", skip the fracture. In particular, do not include the fracture when determining the maximum fracture size for fractures that intersect the deposition hole.
   3) The fracture properties. Since the centre and edge vectors of the rectangular fracture plane are require to calculate whether the fracture intersects the full perimeter of the tunnel, and the length and transmissivity are also of interest.

d) Does the fracture cross-cut the deposition tunnel? If at least one of the fractures intersecting the deposition hole cross-cuts the deposition tunnel, then the deposition hole is marked as failing the full perimeter criterion (FPC).

e) Calculate the linear length of the largest fracture intersecting the deposition hole. This is set to zero if no fractures intersect the deposition hole.

f) Calculate the transmissivity of the most transmissive fracture intersecting the deposition hole.

The FPC, fracture length, and fracture transmissivity values derived for each deposition hole are used to with the performance assessment to simulate engineering criteria used to reject deposition holes and assess how this process impacts on risk. Two criteria were considered. The first is based on FPC only, and the second is based on both FPC and whether the transmissivity is greater than 10^{-6} m^2/s.

The results of applying the deposition hole rejection criteria are presented in Table 4-4 below in terms of remaining deposition hole positions.

Table 4-4. Calculated percentage of remaining deposition positions using various rejection criteria. The total number of deposition holes is 6,824.

Rejection criterion	Remaining percentage of deposition holes after rejection criteria [%]							
	Excluding only deposition holes intersected by low confidence zones	FPC	T > 10^{-6} m²/s	T > 10^{-7} m²/s	T > 10^{-8} m²/s	FPC and T > 10^{-6} m²/s	FPC and T > 10^{-7} m²/s	FPC and T > 10^{-8} m²/s
Base case DFN with correlated (*T* vs. *r*)	99.8	94	99.8	99.4	97	94	94	93
DFN with semi-correlated (*T* vs. *r*)	99.8	94	98.9	77	38	93	74	37

In the table it is seen that the FPC criterion for both correlation cases results in more deposition locations being removed than using the only the hydraulic condition $T > 10^{-6}$ m²/s criterion. A lower threshold of $T > 10^{-7}$ m²/s results in comparable or more locations being removed than using the FPC alone. Furthermore, combining the FPC and $T > 10^{-6}$ m²/s criterion has a minor effect relative to using the FPC criterion alone. If lower transmissivity thresholds are used, these dominate the screening and the FPC has a minor effect on the number of rejected deposition locations.

Applying the FPC criterion or combined FPC and $T > 10^{-6}$ m²/s criterion results in somewhat shifted Q_{eq} and F-factor distributions for the Q1 path as shown for Forsmark conditions in Figure 4-49 and Figure 4-50 below. Specifically, the Q_{eq} distribution shows that the highest flow rates are removed from the distribution, whereas the F distribution shows a shift to higher values by slightly less than half a unit in log space. The difference between applying the FPC criterion alone or in combination with the $T > 10^{-6}$ m²/s criterion has a minor effect as indicated already by Table 4-4. Hence, based on the current fracture model, the FPC criterion seems to be a sufficient test for screening out the worst deposition hole locations.

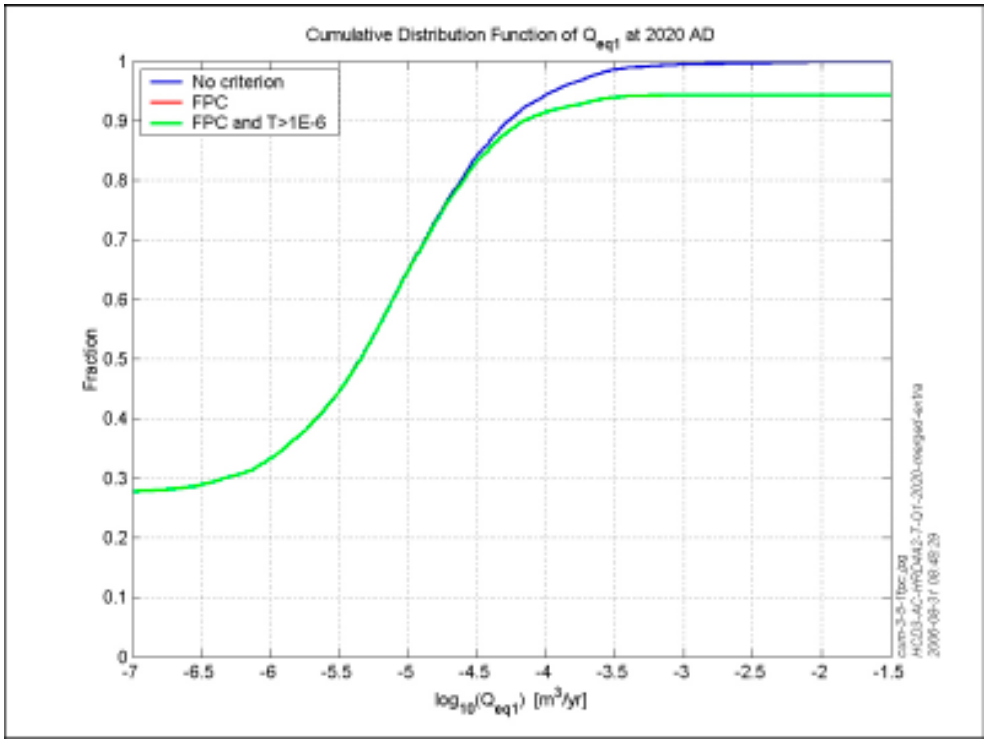

Figure 4-49. *Comparison of cumulative distribution plots of Qeq for path Q1 in the combined DFN/CPM realistic case model with 6,824 particles released at time 2,020 AD based on different deposition hole rejection criteria.*

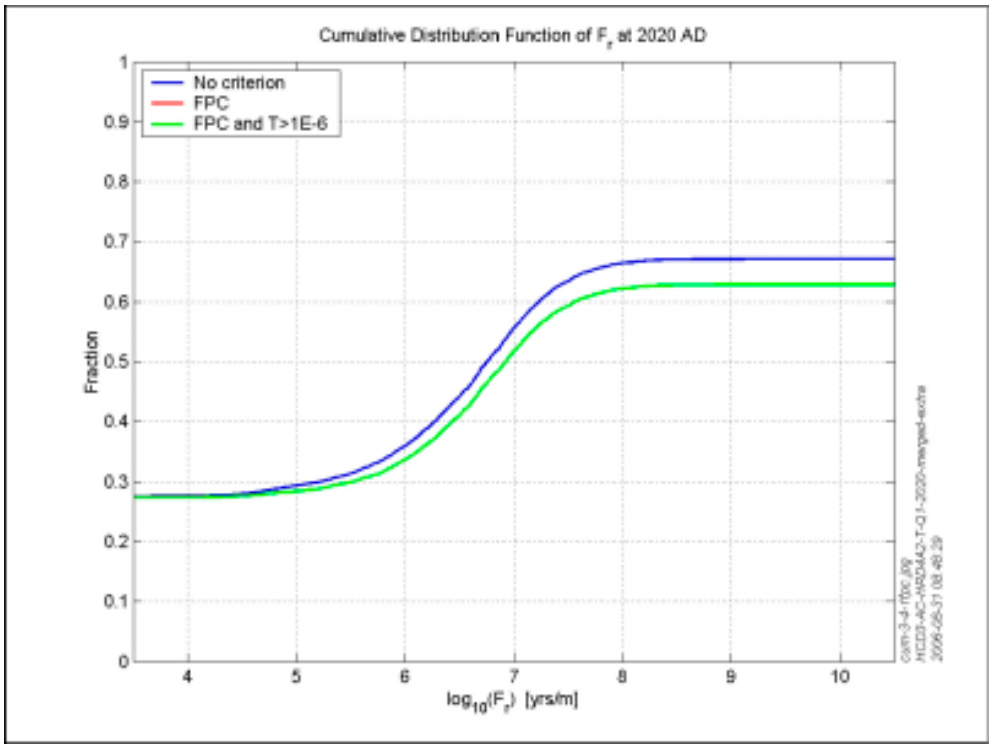

Figure 4-50. *Comparison of cumulative distribution plots of F_r for path Q1 in the combined DFN/CPM realistic case model with 6,824 particles released at time 2,020 AD based on different deposition hole rejection criteria.*

4.6 Discussion

Detailed repository-scale models have been used to derive near-field and far-field performance measures for input to PA calculations. Two main types of conceptual models, DFN and CPM, have been applied to model the entire repository and flow in the bedrock around each deposition hole down to the scale of a few metres or less. As an advance on the methodology used in the interim SR-Can assessment, variable-density flow calculations have been implemented in DFN models so that the effects of buoyancy-driven flow due to the presence of salinity are represented consistently in both DFN and CPM conceptual models. Since the PA calculations use a streamline concept for the far-field modelling in FARF31, groundwater flow and flow-paths are calculated at an appropriate series of representative times with boundary conditions and the salinity distribution being interpolated on to the steady-sate repository-scale models from transient regional-scale coupled groundwater flow and salt transport models. Properties of both the CPM and DFN models have been developed since the site modelling of SDM F 1.2 to incorporate a multi-domain definition of properties that is more realistic and better reflects the observed spatial variability in fracture and hydraulic properties at the site.

The use of different conceptual models has allowed us to quantify the sensitivity the choice of model. For Forsmark it is found that the two types of model yield quite different results. This stems from the fact that the bedrock within the repository candidate area is very sparsely fractured with generally poor connectivity. In consequence, a DFN model predicts a very disjoint flow system with poor connections, areas of stagnant flow, tortuous flow-paths such that significant flow and transport is restricted to the deterministic deformation zones and the larger stochastic fractures. The lack of connectivity horizontally over long distances restricts long flow-paths from forming, and hence flow tends to be much localised and discharge from the repository is mainly to the immediate surface above. Transport is mainly sensitive to the structural model and occurrence of large stochastic fractures, while transient processes such as

shoreline retreat are less influential. In contrast, a CPM model with isotropic hydraulic properties allows flow connections in all directions, and although the CPM bulk hydraulic properties are equivalent on a large-scale (100 m), the detailed flow and transport is very different. Generally in the CPM model flow is more homogeneous with flow around all deposition holes and longer flow-paths many of which reach the shoreline. In this case, results are sensitive to the position of the shoreline, and flow-paths less dominated by the geological structural model. An example of different behaviour of the two models is when a particle reaches a high transmissivity sub-vertical zone which lies orthogonal to the head gradient. In a CPM model the particle will tend to pass through the zone and continue in the low conductivity bedrock, while in the DFN model it will tend to travel vertically up through the zone even for a small head gradient. To implement a representation of a sparse fracture network in a porous medium model one would have to use a fine-scale heterogeneous ECPM model that captures the intact block between the water conducting fractures, and this may not be practicable. This intrinsic difference between the two types of model has possible implications for the site-modelling also as it may affect the interpretation of interference tests and tracer tests.

In terms of the performance measures, the CPM model predicts travels times with a median over 10^3 years, while the DFN model median is less than 10^2 years; Initial velocity has a median around 10^{-6} m/y in the CPM model with small variability, while the DFN predicts a median around 10^{-5} m/y but with a standard deviation nearly one order of magnitude; The F-quotient has a median just under 10^8 y/m for the CPM model, and under 10^7 y/m for the DFN model with a standard deviation of about 0.8 in $\log_{10}$-space. Generally, the DFN representation is a worse scenario, but it does have some positive aspects also. For example, the DFN model predicts there is advection away from the canister via a fracture that intersects the deposition hole for only about 40% of canisters, and of these only about 15% have a significant transmissivity (greater than 10^{-9} m^2/s). Similarly, there are stagnant flow conditions in parts of the EDZ and tunnel that amounts to about 40% of the canisters. Hence, for many canisters there are essentially no advective routes for radionuclides to escape.

A comparison of the alternative conceptual models, DFN versus CPM, is summarised in Figure 4-51 and Figure 4-52 in terms of the equivalent flow rates, Q_{eq}, for path Q1 and Q2 that are used as input to the near-field radionuclide transport models (see Section 2.2.6), and the F-factor. Sensitivities have been considered to the tunnel and EDZ properties as well as the relationship used between fracture transmissivity and length. The sensitivity to the backfill and EDZ properties is not great since the system of deposition tunnels is arranged orthogonal to the head gradients. Therefore flow tends to be limited by what the fracture system can supply and paths have to leave the tunnel or EDZ after relatively short distance to find a flow-path to the surface through the fracture network. For the semi-correlated and uncorrelated transmissivity DFN variants higher percentages of canisters have connected fractures of significant transmissivity (greater than 10^{-9} m^2/s) intersecting the deposition holes, 18–20%, giving higher equivalent flow-rates, although the percentage of particles starting in stagnant flow areas increases to 67–74% for the two variants. This is indicative of flow being more heterogeneous for the variants and there being fewer advective pathways through the model, as was found in the equivalent ECPM regional models. Therefore, the results are moderately sensitive to the relationship used for the transmissivity to length relationship, and the semi-correlated and uncorrelated models may give moderately worse results than the correlated model in terms of inputs to PA, although fewer particles escape to the surface for these cases.

The alternative nested model, local-scale DFN inside a regional-scale ECPM, confirms that the paths calculated in the repository-scale DFN/CPM model are representative, and that discharge areas are generally localised to vertically above the site for present and future times. It also confirms the repository-scale model gives a good estimate of F-quotient and path-length. Although it predicts slightly longer distances are travelled in the tunnel, this may be a consequence of having a higher truncation in fracture radius modelled, 3.3 m against 1.1 m for the repository-scale models.

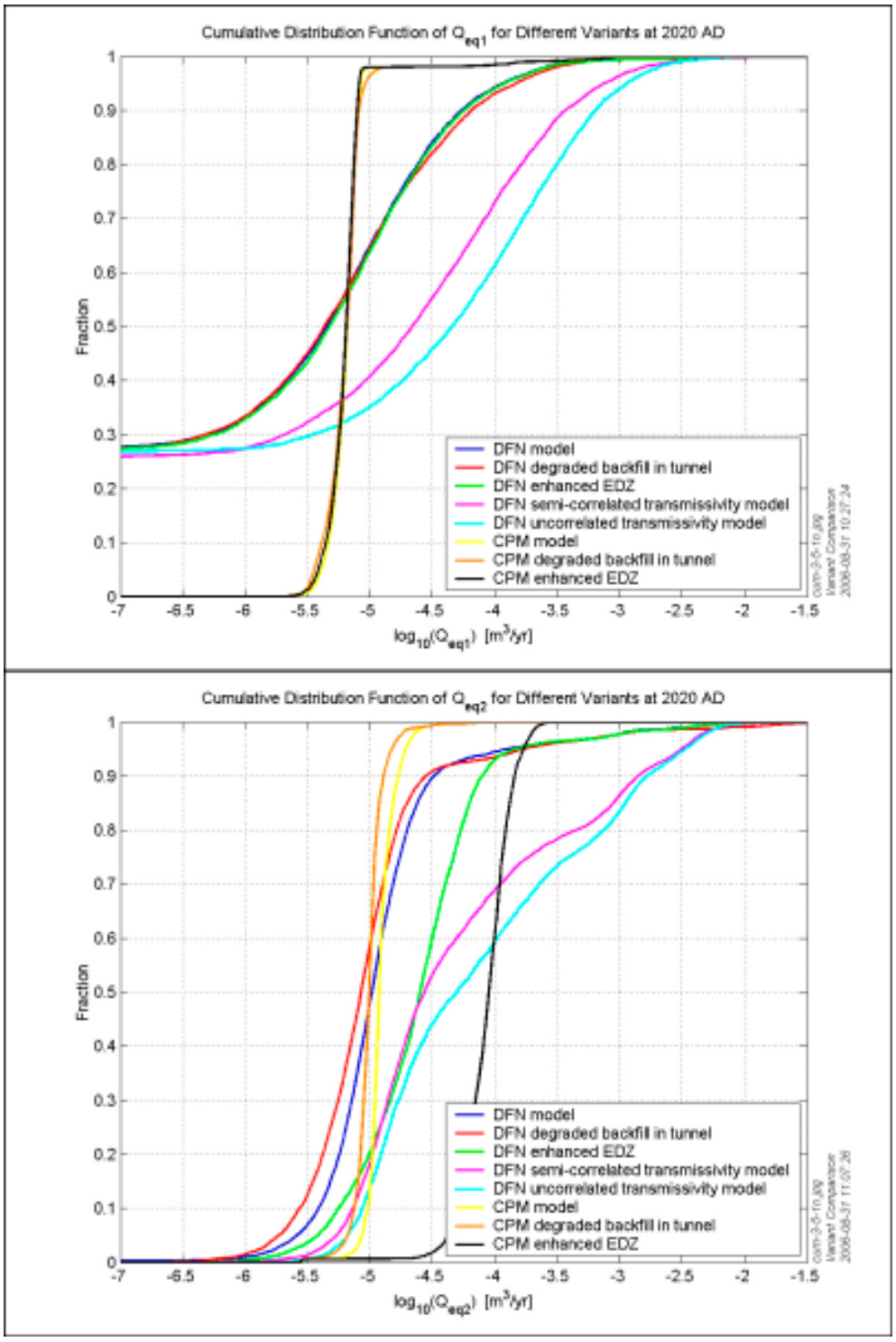

Figure 4-51. *Comparison of cumulative distribution plots of equivalent flow rates Q_{eq} for paths Q1 and Q2 at release time 2,020 AD for the alternative DFN and CPM models together with the various sensitivity cases considered.*

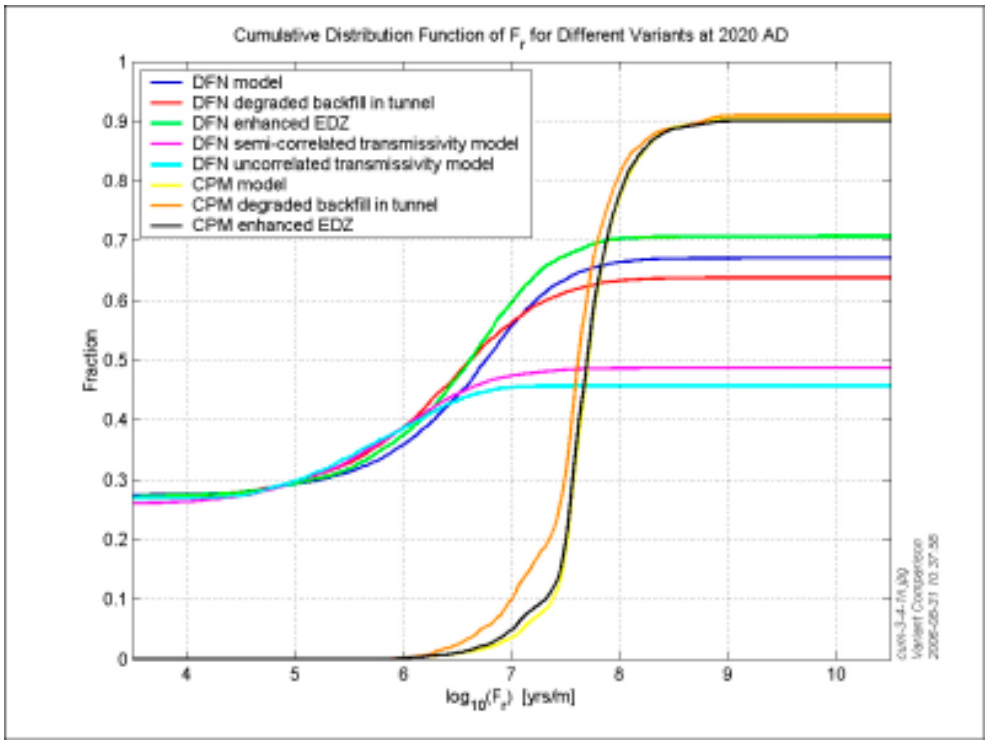

Figure 4-52. *Comparison of cumulative distribution plots of F-factor, F_r, for paths Q1 at release time 2,020 AD for the alternative DFN and CPM models together with the various sensitivity cases considered.*

For the current fracture model, avoiding locations where fractures intersect the full perimeter of a tunnel seems to be a sufficient test for screening out the worst deposition hole locations without having to perform flow tests of fracture transmissivity in deposition pilot holes.

Acknowledgement

We are grateful for the help of Rhys Gywnllyw, University of West Of England, toward the development of variable-density flow in DFN models.

5 Gas migration and its effects on groundwater flow

Gas is expected to be produced from corrosion of the iron insert in any copper canister that allows ingress of water through a breach in the copper shell as a result of damage or a manufacturing defect. To escape, the gas will need to pass through the bentonite buffer around the copper canister without damaging the properties of the buffer as a barrier to groundwater flow and the transport of radionuclides. Such damage might be caused by an excessive build up of gas pressure, but current expectations are that the gas will escape satisfactorily through the buffer.

Gas escaping from the buffer will then migrate through the geosphere. The potential gas migration through the geosphere, and any consequences it might have for a repository at Forsmark, are addressed in this section and contribute to the wider SR-Can assessment. As the work will be of a different nature to the geosphere groundwater flow and transport calculations, for example in not being so amenable to large-scale numerical modelling, this work is carried out as a more or less separate activity from the main groundwater flow and transport calculations, although it does draw on the data used in those calculations and on some of their results as described in Sections 3 to 4.

A comparable simple gas assessment was carried out for an earlier stage of the development of the SKB copper canister concept for the disposal of spent fuel. This work was reported in SKB TR 93-31 /Wikramaratna et al. 1993/ but is now more than a decade old. The intention of the current work is to update and extend this earlier work to bring it into line with current requirements and with data specific to Forsmark. In particular:

a) Understanding of gas flow has developed over the last ten years, and it is appropriate to consider how this might affect the performance safety assessment.

b) The data has improved over the last ten years. In particular, there are better measurements of the canister corrosion rates /Smart 2001/, there has been an improved canister assessment /Bond et al. 1997/, and there are now site-specific hydrogeological data which can be taken into account /SKB 2004b/. The current conceptual model of flow in DFN's used in SR-Can is also different from that used in /Wikramaratna et al. 1993/; the current concept is of flow through fracture planes, the previous model was of flow along fracture intersections.

c) Additional issues not discussed in SKB TR 93-31 /Wikramaratna et al. 1993/ have been identified for consideration in the SR-Can assessment. These are the possible effects of free gas in the geosphere on groundwater flow and radionuclide transport.

The following three sections address the following issues:

a) the sources and amounts of gas that might be generated or be present in the repository or host rock,

b) the characteristics of the flow and transport of gas through the geosphere,

c) assessment of any implications that geosphere gas transport might have for groundwater flow and the transport of dissolved radionuclides.

A summary of the conclusions reached is provided in Section 5.5.

5.1 Sources and amount of gas

Although the primary objective of the work described in this section, Section 5, is the characterisation of gas flow through the geosphere and its effects, a prerequisite for this is an understanding of the rates of gas production that could come from the wastes, and of any other sources of gas that might be present. Gas generation is expected to result predominantly from the anaerobic corrosion of the cast iron insert in the copper canister to release hydrogen. This requires the presence of a breach in the canister, but it also depends on the availability of water. The extent to which the rate of the corrosion process may be limited by the availability of water needs to be considered, and therefore is assessed here. It is possible that some gas will be trapped in the repository at repository closure and that sources of natural gas may exist. The potential volumes of such gases in relation to the volumes that might arise from corrosion in a canister are briefly reviewed, and any implications of their presence noted.

Other sources of gas from the spent fuel wastes have been previously assessed to be insignificant from the point of view of radiological hazard and the volume of gas involved (e.g. helium from radioactive decay and ^{14}C from the fuel itself and from the Zircaloy cladding), and are not reassessed here.

5.1.1 Gas production from corrosion in canisters

The scenario that will lead to generation of gas from a waste canister is envisaged to be one in which a small defect present in a canister allows ingress of groundwater into the canister, resulting in generation of hydrogen from the anaerobic corrosion of the cast iron insert in the canister. An upper limit to the rate of gas generation may be derived by assuming that water is freely available to the corroding iron surface, in which case the gas generation rate is determined by the iron surface area and the corrosion rate (which may in principle vary with time and groundwater chemistry). However, water availability may be limited by the rate at which it can be supplied by transport through the breach, the bentonite buffer, the host rock, and repository features such as the tunnel and engineering damaged zone (EDZ).

Availability of water is also likely to be affected in a complex way by the build up of gas pressure in the canister as a result of gas production (and possibly water ingress), and by the formation of corrosion product. Gas pressure build up will oppose the advective flow of water into the canister, which would cease once the gas pressure reached the local hydrostatic pressure. Thereafter, any water flow into the container would be gas phase diffusion of water vapour. The precise behaviour could be complex, with a number of factors affecting the evolution of the system:

a) any free water present may be forced from the hole in the copper shell by a build up of gas pressure, the extent to which this could occur depending on the position of the breach and whether any free water was present in the canister as a result of water ingress (significant quantities of free water should only be present if, for a time at least, the flow rate of water into the canister is greater than the rate of water consumption by the corrosion reaction),

b) the nature and position of any open connection between the inside (channels for the fuel assemblies) and the outside (annular space between the insert and the copper shell) of the iron insert will affect the access of water to the inside iron surfaces,

c) anaerobic corrosion of iron, to produce magnetite, results in an increase in the volume of solid, and this expansion could close up the space between the iron insert and the copper shell, particularly around the breach in the copper shell, restricting the movement of water or water vapour within the canister.

These issues were considered in detail in SKB TR 93-31 /Wikramaratna et al. 1993/ and in SKB TR 97-19 /Bond et al. 1997/, and the detailed analysis provided is not repeated here, but the overall conclusions are reviewed in relation to the current situation. Note that it is assumed that only a small proportion of the canisters in the repository are breached at any particular time,

so that the time scale for gas release only needs to be considered in relation to the particular canister not the repository as a whole (except for possible effects on radionuclide transport).

An upper bound to the gas generation rate per breached canister is obtained by assuming that water is freely available. The cast iron insert is cylindrical in external shape, and has the dimensions shown in Table 5-1 /SKB 2004d, SKB 1999/, where the dimensions of the channels for fuel assemblies are for BWR fuel (see Figure 5-1). Since canisters for BWR fuel are more numerous and have a larger iron/steel surface area than for containers for PWR fuel, only canisters for BWR fuel are considered here. The arguments are immediately transferable to canisters for PWR fuel, but the potential gas generation rates will be slightly reduced if controlled by the surface area of the cast iron insert (and water penetrates to the channels containing the fuel assemblies).

Table 5-1. Dimensions of iron insert in copper fuel canister for BWR Fuel.

Dimension	Value	Unit
External diameter	949	mm
External height	4,573	mm
Side of square channel for fuel assembly	160	mm
Length of channel for fuel assembly	4,470	mm
Number of channels for fuel assemblies	12	–

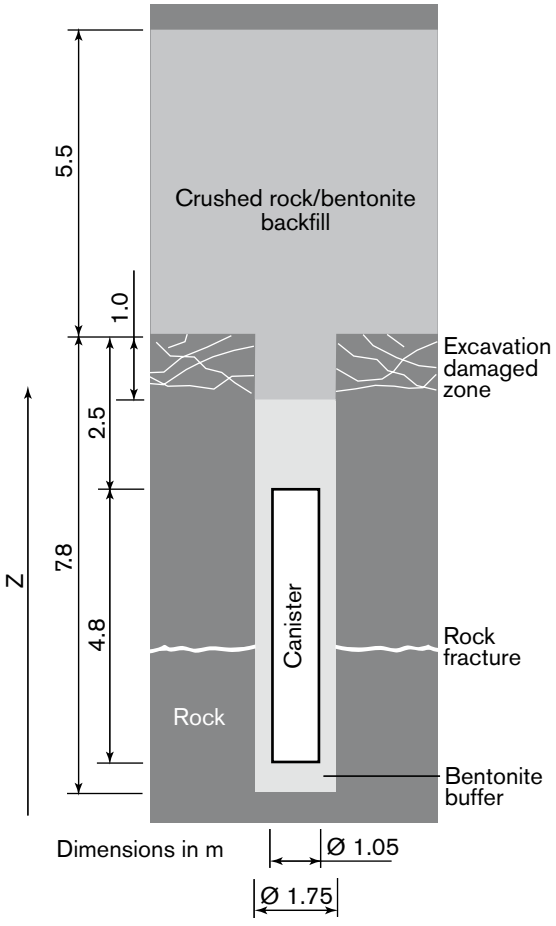

Figure 5-1. *A canister is shown in a deposition hole with surrounding bentonite buffer.*

From the figures shown in Table 5-1, it follows that the internal[2] and external areas of the cast iron insert are 35.7 and 15.1 m^2, giving a total surface area of 50.8 m^2. The best long-term estimate of the corrosion rate of mild steel is given in /Smart 2001/ as 0.1 µm y^{-1} (see also /SKB 2004a/), with a possible uncertainty of an order of magnitude in either direction. At 50°C, the corrosion rate for cast iron is somewhat lower than that of carbon steel[3]. Taking the density and molar mass of the iron insert to be those of pure iron, and taking the anaerobic corrosion of iron to occur as in the following equation:

$$3Fe + 4H_2O \rightarrow 4H_2 + Fe_3O_4 \qquad (5\text{-}1)$$

the gas generation rate from corrosion over the total surface area of the iron insert is $2.1 \cdot 10^{-2}$ m^3y^{-1} at STP[4]. The corresponding rate of consumption of water is $1.7 \cdot 10^{-5}$ m^3y^{-1}, taking the density of water to be 999.5 kg m^{-3} at 12°C /Lide 1994/, the ambient temperature given in /SKB 2004d/ for the repository depth and assumed throughout in this section. The assumption that water can reach the fuel assembly channels is consistent with the conservative assumptions made for water-borne radionuclide transport in the canister defect scenario, since unless water does reach the fuel assemblies, no such radionuclide transport can occur.

Whether or not corrosion can occur at the best estimate rate of 0.1 µm y^{-1} depends therefore on whether water can reach the iron and steel surfaces at a rate of $1.7 \cdot 10^{-5}$ m^3y^{-1}. This will depend on the rate at which water can pass through the bentonite buffer and be supplied by the fracture network connected to the outer surface of the buffer.

As discussed in /Wikramaratna et al. 1993/, advection of liquid water through the bentonite to a small hole or crack in the canister will be largely controlled by the size of the hole and the behaviour close to the orifice, where most of the pressure gradient driving the water flow will be concentrated. It is suggested in /SKB 1999/ that the maximum size of a defect that would escape detection during canister inspection would be 1 mm^2, although this could enlarge with time after disposal. The saturated bentonite buffer annulus between the canister and the rock wall of the deposition hole is 0.35 m thick. Following /Wikramaratna et al. 1993/, the water flow rate through the orifice is obtained by considering flow through a hemispherical shell with an inner radius equal to the radius of the defect (considered as a circular hole), and an outer radius equal to the thickness of the bentonite buffer (see Figure 5-2). The flow rate, Q_w [m^3s^{-1}] of water through the hole is given by:

$$Q_w = 2\pi K \frac{r_i}{1 - \frac{r_i}{r_o}} \frac{p_o - p_i}{\rho_w g} \qquad (5\text{-}2)$$

where

K is the hydraulic conductivity of the bentonite [m s^{-1}],
r_i is the inner radius of the hemispherical shell [m],
r_o is the outer radius of the hemispherical shell [m],
p_o is the water pressure on the outer boundary [Pa],
p_i is the water pressure on the inner boundary [Pa],
ρ_w is the density of the water [kg m^{-3}],
g is the acceleration due to gravity [m s^{-2}].

---

[2] In calculating the inner surface area, it is assumed that the whole of the bottom surface of the lid to the insert and the facing surface of the insert (minus the gaps for the channels) are accessible to water. This is consistent with the assumption that radionuclides can diffuse from the fuel when water access to the insert is achieved, although it is possible that corrosion product will seal the gaps between the lid and the body of the insert.

[3] Note that, although the insert is largely cast iron, the fuel assembly channels are lined with carbon steel as part of the fabrication process.

[4] Standard temperature and pressure of 0°C and 1 atmosphere (101,325 Pa) pressure.

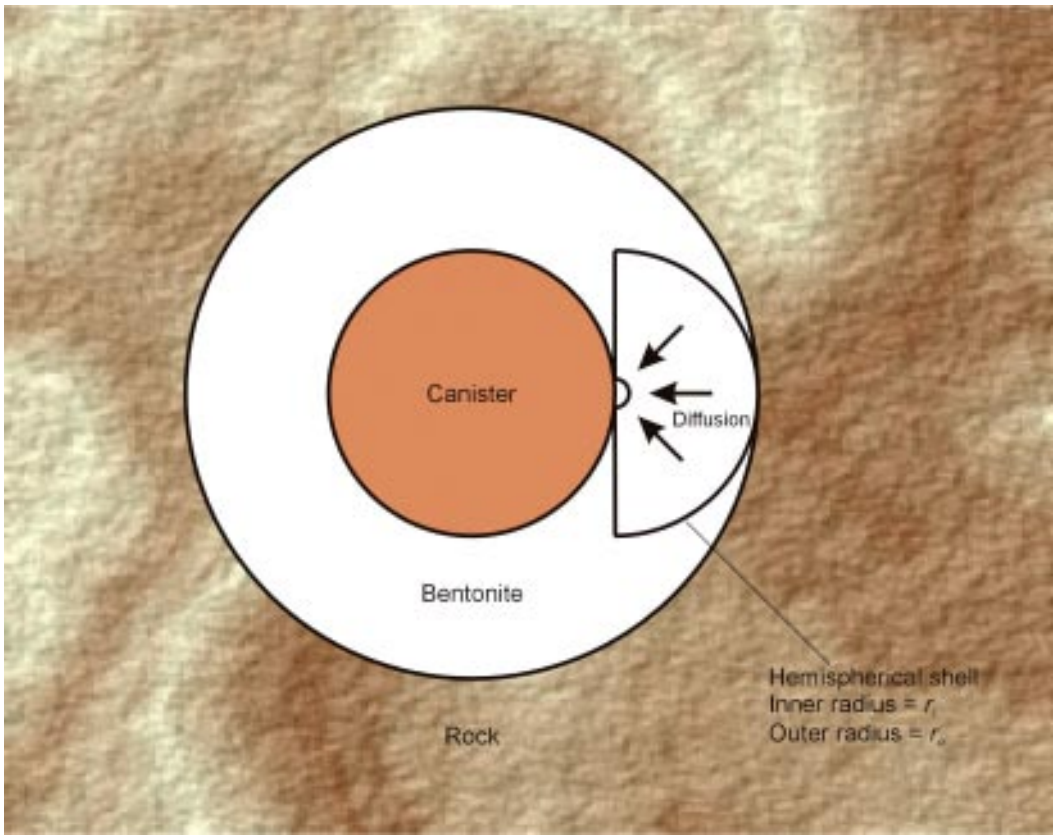

Figure 5-2. *A schematic diagram (in plan view) shows spherical diffusion through the bentonite buffer to a defect in the canister.*

The hydraulic conductivity for saturated bentonite at the reference dry density of 1.59 kg m^{-3} /SKB 2004d/ is less than 10^{-13} m s^{-1} /Börgesson et al. 1995, Börgesson et al. 1996/, and is consistent with the design requirement /SKB 2004c/ that the hydraulic conductivity be less than 10^{-12} m s^{-1}. The canisters are expected to be placed at a depth of about 400 m, at which depth the hydrostatic pressure would be about 3.9 MPa (this is calculated assuming the density of the groundwater is that of pure water at 12°C; in practice the density of the water and hence the hydrostatic pressure would be somewhat higher because of the salinity of the groundwater). Initially the gas pressure in the canister would be about 0.1 MPa (approximately atmospheric pressure). Taking the inner radius to be that of a circular hole of area 1 mm^2 (0.56 mm radius) and the external radius to be 0.35 m, the water flow rate through the defect would be $4.37 \cdot 10^{-6}$ $m^3 y^{-1}$, assuming a bentonite permeability of 10^{-13} m s^{-1}. This is about 26% of the inflow rate required to sustain corrosion at 0.1 µm y^{-1} over the whole surface area of the iron insert. It is possible that a defect in a canister could have an effective radius greater than 0.56 mm. Radii of 1 and 1.5 mm are considered in reference /SKB 2004a/, with the recognition that these are rather large values. Such an increase in radius would not be quite sufficient to provide enough water to support the corrosion rate over the whole surface of the metal insert. As indicated in the introduction to this section, there are other factors that will tend to reduce water ingress.

Water availability may be limited by the capacity of the host geology to supply water at a sufficiently high rate. The calculated capacity of the host geology to supply the required groundwater to support unconstrained corrosion depends somewhat on the computational model assumed.

Using the ECPM variant "lower transmissivity below ZFMNE00A2"[5], groundwater flow calculations for the Darcy velocities adjacent to the deposition holes give a geometric mean value of $1.0 \cdot 10^{-5}$ m y^{-1} (this is the value from the calculation at 9,000 AD, which gave the largest mean Darcy velocity, although the values at different times were similar). The Darcy velocity required to support corrosion at the experimentally observed rate over all the iron surfaces, assuming the groundwater flows through a circular area of radius 0.35 m, is $4.5 \cdot 10^{-5}$ m y^{-1}. The calculated mean Darcy velocity is 23% of this value. The variability of the Darcy velocities between different deposition holes is significant. The mean Darcy velocity plus two standard deviations (in logarithm space) is $1.7 \cdot 10^{-4}$ m y^{-1}, enough to support corrosion over all the iron surfaces without constraints from water supply. The Darcy velocities obtained from the ECPM variant model are sufficient to support unrestricted corrosion at the deposition holes for less than 14% of the deposition holes. However, more than 72% have Darcy velocities within an order of magnitude of that required to support unrestricted corrosion.

Using the CPM base case /Hartley et al. 2005/, groundwater flow calculations for the Darcy velocities adjacent to the deposition holes give a geometric mean value of $8.0 \cdot 10^{-7}$ m y^{-1} at 9,000 AD (the values at different times and for variant input data were very similar). This is more than an order of magnitude smaller than the ECPM variant, and is less than 2% of the water influx rate required to support corrosion at the experimentally observed rate over all the iron surfaces.

At long times, when any defect has enlarged or some other damage to the canister may have occurred, groundwater flow from a larger area than for a small defect may converge towards the aperture in the canister, in which case the groundwater flow rate may place less restriction on the gas generation rate.

Although these estimates based on calculated Darcy velocities only provide a rough measure of the effect of groundwater flow in the host rock on water availability, they do indicate that in general the geosphere would provide a further significant restriction on water availability. In practice, because groundwater flow at repository depth occurs through a fracture network of relatively low fracture density, there will be greater variation in groundwater availability between deposition holes. Some deposition holes are likely not to be intersected by a flowing fracture; for these, groundwater flow towards the canister defect is likely to be very small. Others will have a significant conducting feature intersecting the deposition hole close to the defect, and for some of these there may be an adequate supply of groundwater to support the corrosion. Others still may be intersected by a flowing feature but the intersection could be some distance from the defect in the canister; in these cases, groundwater would have to flow for a significant linear distance through the bentonite buffer, perhaps from the backfilled access tunnel or the damage zone surrounding this, and this would further restrict availability of water from the host rock. However, because of the likely variability in local groundwater flows, no reliance is placed on restricted groundwater flow through the geosphere in assessing the effects of water availability in controlling gas production from corrosion. The fact that the low groundwater flow is likely to be limiting in restricting corrosion gives additional robustness to upper bound estimates of the gas generation rate from a canister.

The conclusions of the above is that, while the defect in the canister is limited to a small hole, corrosion over the whole surface area of the iron insert cannot occur at a rate more than the best estimate value about 0.1 μm y^{-1} because of controls on the advective flux of water through the bentonite buffer. Additionally, constraints provided by the geosphere on groundwater flow are likely to restrict the effective corrosion rate (i.e. taken to occur over the whole surface of the iron insert) to a value less than this for the great majority of the deposition holes. In addition, the corrosion rate will slow as an opposing gas pressure builds up in the canister. An indication

[5] This variant is thought to give a more realistic description of flows near the repository than the ECPM base case. As compared to the CPM base case, the ECPM variant uses a higher permeability for the rock zone immediately above the repository. This higher permeability gives a more cautious (i.e. larger) estimate for the groundwater flows at depth.

of the time-scale over which the pressure builds up and the water influx rate reduces can be obtained if it is assumed that the gas production rate is limited by water supply (i.e. the gas generation rate is determined by the water inflow rate, all the inflowing water being converted to hydrogen).

Using Equations (5-1 to 5-2), the change of pressure in the canister is given by:

$$\frac{dp_i(t)}{dt} = 2\pi K \frac{r_i}{1-\frac{r_i}{r_o}} \frac{p_o - p_i(t)}{\rho_w g} \frac{R\Theta}{V} \zeta_w = \alpha\left[p_o - p_i(t)\right] \tag{5-3}$$

where

R is the Universal Gas Constant [8.3145 J mol^{-1}K^{-1}],
Θ is the absolute temperature in the canister [K],
V is the void volume in the canister when filled with fuel and sealed,
ζ_w is the molar density of water [mol m^{-3}],
$\alpha = 2\pi K \frac{r_i}{1-\frac{r_i}{r_o}} \frac{R\Theta}{\rho_w g V} \zeta_w$.

Integrating Equation (5-3) gives:

$$p_i(\mathrm{t}) = p_o - [p_o - p_i(t=0)]\, e^{-at} \tag{5-4}$$

and the gas production rate, Q_g [m^{3}s^{-1} at STP], as a function of time becomes:

$$Q_g = 2\pi K \frac{r_i}{1-\frac{r_i}{r_o}} \frac{p_o - p_i(t)}{\rho_w g} \zeta_w \frac{R\Theta_s}{p_s} \tag{5-5}$$

where

Θ_s is standard temperature (0°C),
p_s is standard pressure (101,325 Pa).

The void volume, V, in the canister is taken to be 1 m^3. This is as assumed in SKB TR-04-44 /SKB 2004c/. The volume calculated from the canister geometry without allowing for the presence of the fuel assemblies would be 1.39 m^3, so a void volume of 1 m^3 seems reasonable when account is taken of these.

Figure 5-3 shows the variation of canister pressure and gas generation rate calculated on the basis of the above assumptions.

The figure shows that the canister gas pressure would increase sufficiently to reduce the water ingress rate and hence the potential gas generation rate significantly after 1,000 years, reducing the latter by almost an order of magnitude after about 15,000 years. At some point the advective flux of water into the canister will have diminished to such an extent that the diffusion of water vapour into the canister will become the main water supply mechanism. This is discussed in some detail using numerical models in /Bond et al. 1997/ but it is possible to derive an upper bound to the potential diffusive flux by considering diffusion just through the defect in the copper canister. If this is modelled as a channel of uniform cross-section, then the diffusive flux, Q_v [mol s^{-1}] of water vapour can be estimated as

$$Q_v = AD_v \frac{1}{L} \frac{p_v}{R\Theta} \tag{5-6}$$

where

A is the area of the defect channel in the copper overpack [m^2],
D_v is the diffusion coefficient for water vapour in hydrogen [m^{2}s^{-1}],
L is the thickness of the copper overpack [m],
p_v is the saturated water vapour pressure under the ambient conditions [Pa].

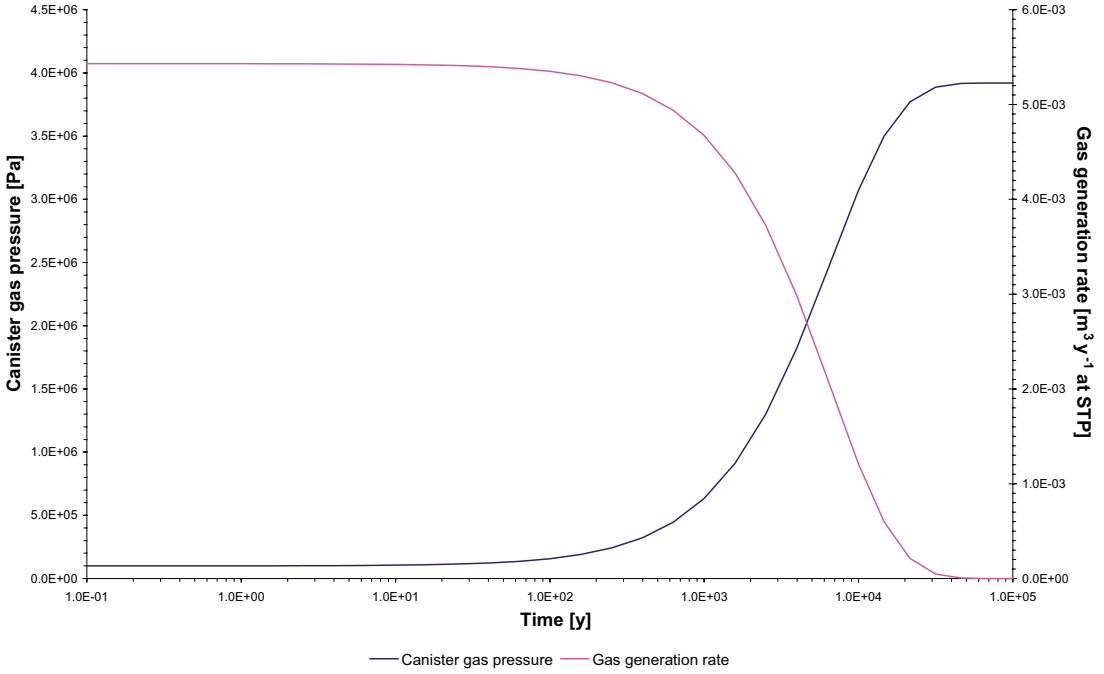

Figure 5-3. *Variation of canister gas pressure and gas generation rate as gas accumulates in canister.*

It is assumed that diffusion away from the inside end of the defect channel is much faster than diffusion through the channel itself so that the concentration of water vapour at the end of the channel can be taken as zero. This may not be the case, in particular because of the build up of magnetite corrosion product in the annulus between the iron insert and the copper overpack, especially close to the defect, but this assumption provides an upper bound to the diffusive flux /cf Bond et al. 1997/. As noted above, the area of the defect is taken to be 1 mm^2. The thickness of the copper canister is 50 mm, which gives the length of the path for diffusion. An upper bound to the diffusion coefficient at atmospheric pressure is estimated to be 10^{-4} m^{2}s^{-1}, on the basis of comparison with values for comparable binary gas mixtures (e.g. in /Lide 1994/). Since gas-phase diffusion coefficients are inversely proportional to pressure, the diffusion coefficient at hydrostatic pressure, when the gas pressure has built up to this value in the canister, would be $2.6 \cdot 10^{-6}$ m^{2}s^{-1}. The saturated vapour pressure for water at 12°C is 1.411 kPa /Lide 1994/.

The above assumptions and data values give a diffusive flux of water vapour through the defect channel of $1.7 \cdot 10^{-8}$ m^{3}y^{-1} of liquid water equivalent, which would produce $2.2 \cdot 10^{-5}$ m^{3}y^{-1} at STP of gas. This is about 0.1% of the rate of gas generation produced by corrosion at 0.1 µm y^{-1} over all the surfaces of the cast ion insert. From Figure 5-3 it can be seen that it would be more than 30,000 years before water availability became controlled by vapour diffusion through the defect rather than by advection through the bentonite buffer.

When the corrosion is controlled by vapour diffusion, the pressure would continue to rise, but at most at a rate of 2.3 Pa y^{-1}. What the effect would be depends on the properties of the bentonite buffer. The bentonite would not be expected to deform around the defect until the gas pressure reached the stress exerted by the bentonite. The swelling pressure of the saturated bentonite is estimated to be in the range 5.8–13 MPa /SKB 2004a/, so when the hydrostatic pressure of about 4 MPa is added to this the stress in the buffer will be in the approximate range of 10–17 MPa. To reach a pressure of, say, 15 MPa, at a rate of increase from hydrostatic of 2.3 Pa y^{-1} would take a further $4.8 \cdot 10^6$ years after the time at which the gas pressure reaches that of the ambient water pressure. Whether this would result in the gas creating a gas-filled gap between the canister and the buffer from which the gas could diffuse, or whether it deformed the bentonite around the defect, ultimately creating a gas pathway through the bentonite, depends on the behaviour of the bentonite buffer, which is beyond the scope of

this study. However, some comments on potential gas transport mechanisms through the bentonite are provided in Section 5.2 as background to discussion of gas transport through the geosphere. /Wikramaratna et al. 1993/ considered various scenarios for the diffusion of dissolved hydrogen through the buffer from the canister. Their results obtained indicated that diffusion of dissolved hydrogen from the defect itself through the bentonite would not be sufficient to remove hydrogen from the canister at the rate at which it is generated, but if the gas formed a gap between the bentonite and the canister then the much increased area over which diffusion would occur could allow the gas to diffuse through the bentonite at the rate at which it is generated once the generation rate is controlled by diffusion of water vapour into the canister. This depends on the groundwater being able to transport the dissolved gas away from the outer surface of the bentonite sufficiently quickly. These conclusions are further examined in Section 5.2.

Table 5-2 provides a summary of gas generation rates obtained when this is controlled by different processes, together with the corresponding water consumption rate.

Where comparisons are possible, these gas generation rates are similar to those presented in the SR 97 assessment /SKB 1999/, with some small differences due to differences in assumptions (for example, in the area of iron surface potentially subject to corrosion).

The constraints of water supply mean that the maximum potential rate of gas production from corrosion is unlikely to be realised. Corrosion is also likely to be constrained by issues such as the accessibility of the entire iron surface because of lack of connection between the inner and outer surfaces and because of the build up of corrosion product. Build up of gas pressure in the canister will further restrict water inflow and reduce the gas generation rate, so that in the medium term the rate of gas production will drop substantially, and only be sustained by water vapour diffusion. The value of the gas generation rate given for this regime in Table 5-2 is probably an over estimate because it neglects any impediments to diffusion of the water vapour within the canister.

Figure 5-4 shows the cumulative gas production corresponding to the gas generation rate shown in Figure 5-3. It also shows the growth of the metal surface due to the replacement of iron by less dense magnetite (density about 5,200 kg m^{-3}), assuming corrosion occurs uniformly across all iron surfaces (these two curves are clearly rescaled versions of each other). With this magnetite density, the iron undergoes an expansion by a factor of about 2.09 as a result of corrosion to produce magnetite. With corrosion controlled by advection of water through the buffer, the magnetite corrosion product is never sufficient to fill the 1 mm wide gap between the cast iron insert and the copper overpack (but water supply by diffusion would be expected eventually to allow corrosion to close the gap). In practice, corrosion is likely to occur more rapidly closer to the defect through which the water enters the canister than at more distant locations. Even here, if corrosion occurs at a rate of 0.1 μm y^{-1}, unrestricted by water availability, it would take 10,000 years to completely block the gap.

Table 5-2. Summary of gas generation and equivalent water consumption rates corresponding to different controlling processes.

Controlling process	Gas generation rate (m^3y^{-1} at STP)	Equivalent water consumption rate (m^3y^{-1})
Corrosion at 0.1 μm y^{-1} on all insert surfaces	$2.1 \cdot 10^{-2}$	$1.7 \cdot 10^{-5}$
Water advection through bentonite buffer	$5.4 \cdot 10^{-3}$	$4.4 \cdot 10^{-6}$
Water vapour diffusion through defect in copper	$2.2 \cdot 10^{-5}$	$1.7 \cdot 10^{-8}$
Mean groundwater flow at deposition hole†	$5.0 \cdot 10^{-3}$	$4.0 \cdot 10^{-6}$

† This is the mean groundwater flow from the ECPM variant “lower transmissivity below ZFMNE00A2”.

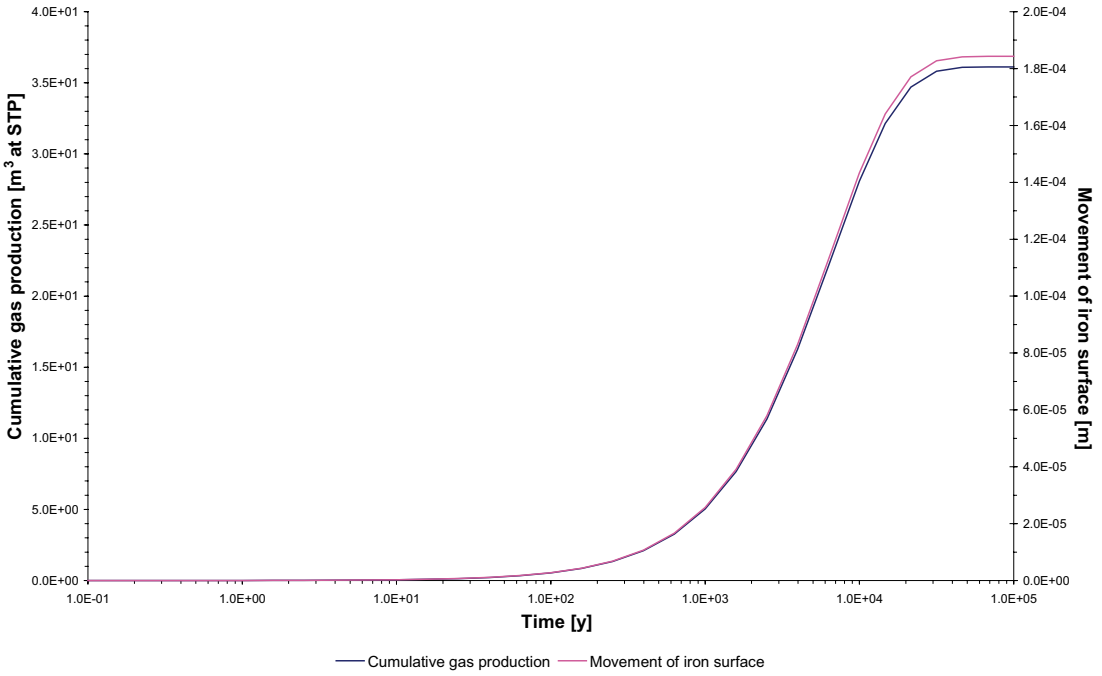

Figure 5-4. *Cumulative gas production and growth of corroding metal surface for corrosion controlled by liquid phase water supply.*

At the corrosion rate of 0.1 µm y^{-1}, the cast iron insert would be expected to last at least 250,000 years. Over this length of time, the possibility must be envisaged that any defect in the canister may have become enlarged or some copper overpacks may have failed in some other more drastic way, allowing less restricted access to the iron insert by groundwater. At this point corrosion may occur at a rate unrestricted by the engineered barriers, although the passivation of the metal by thick magnetite layers would tend to keep the corrosion rate at the lower end of the measured values, and restriction of water availability by the geosphere would remain.

The effect of corrosion of the iron insert caused by water ingress on canister integrity was examined in detail by /Bond et al. 1997/. They found that the build-up of corrosion product would initially be localised around the defect because of the effect of the build-up of corrosion product in restricting diffusion of water vapour in the annulus between the insert and the copper overpack. This localised corrosion would eventually, after ~ 200,000 years, lead to the failure of the copper canister around the defect producing a larger hole in the canister, estimated to have an area of 0.01 m^2. Beyond this time water availability is assumed not to limit the corrosion (much of the iron would still remain at this time because of the way corrosion was restricted prior to canister failure), although in practice there would usually be limitations imposed by the low groundwater flows through the host rock. Note that after 100,000 years the radiotoxicity of the fuel is estimated to have declined to about that of the uranium ore mined to produce the fuel, and remains at about that level thereafter /SKB 1999/. After ~ 400,000 years further corrosion would force the lid from the copper canister. For the transport of radionuclides from a defective canister in the groundwater, it is cautiously assumed that appearance of the larger hole (0.01 m^2) in the canister occurs after 20,000 years, and that after this the canister itself no longer contributes to the containment.

For the purpose of assessing gas migration through the geosphere, it would be reasonable to assume that an upper bound to the gas generation rate is that resulting from unrestricted corrosion ($2.1 \cdot 10^{-2}$ $m^3 y^{-1}$ at STP). The rate is likely to drop to a value at least an order of magnitude less than this over a period of 15,000 years, and remain low until greater disruption of the canister occurs to allow more water ingress, at which point, which is estimated to occur after ~ 200,000 years, the gas production rate is likely to be similar to that resulting from unrestricted corrosion.

Figure 5-5 provides an indication of the rate of gas production and the cumulative gas production for the extended period covered by these scenarios: corrosion limited by advected supply of water; followed by corrosion limited by diffusion of water vapour; and finally corrosion not limited by water availability. Two cases are shown: the first with the extensive canister failure at 20,000 years and the second with this failure at 200,000 years. The cumulative gas production is limited by the mass of cast iron present, so that the most gas that can be produced is $5.9 \cdot 10^3$ m^3 at STP. No account is taken of the change in the surface area of the iron as it corrodes in producing Figure 5-5.

5.1.2 Gas trapped in repository

Gas will be trapped in the repository when it is closed. This gas will be in the pore space of the unsaturated bentonite buffer blocks placed around the canisters; in the slots between the buffer and the rock walls of the deposition holes and the canister, and in the pore spaces and voids of the backfilled tunnel. Gas in these spaces may be regarded as "in communication" with the deposition holes in that there are no seals between these spaces and the deposition holes and they are in proximity to some holes. Gas will also be trapped in other repository spaces, such as the access ramp and shafts, transport and main tunnels, ventilation shafts, and central areas. However, there is insufficient information to consider the gas content of these spaces, and it is also reasonable to argue that these spaces are sufficiently isolated from the deposition holes that the gas content from them will not interfere with that from the waste canisters.

In the deposition holes, gas is trapped in the bentonite blocks and rings and in the spaces between the bentonite and the rock and the bentonite and the canister. The blocks are situated above and below the canister and the rings surround the canister along its length.

Table 5-3 shows the properties of the bentonite rings and blocks and the geometrical dimensions from which the gas-filled volume associated with the buffer-filled region of a deposition hole is obtained. The parameters shown are given in SKB R-04-35 /SKB 2004e/.

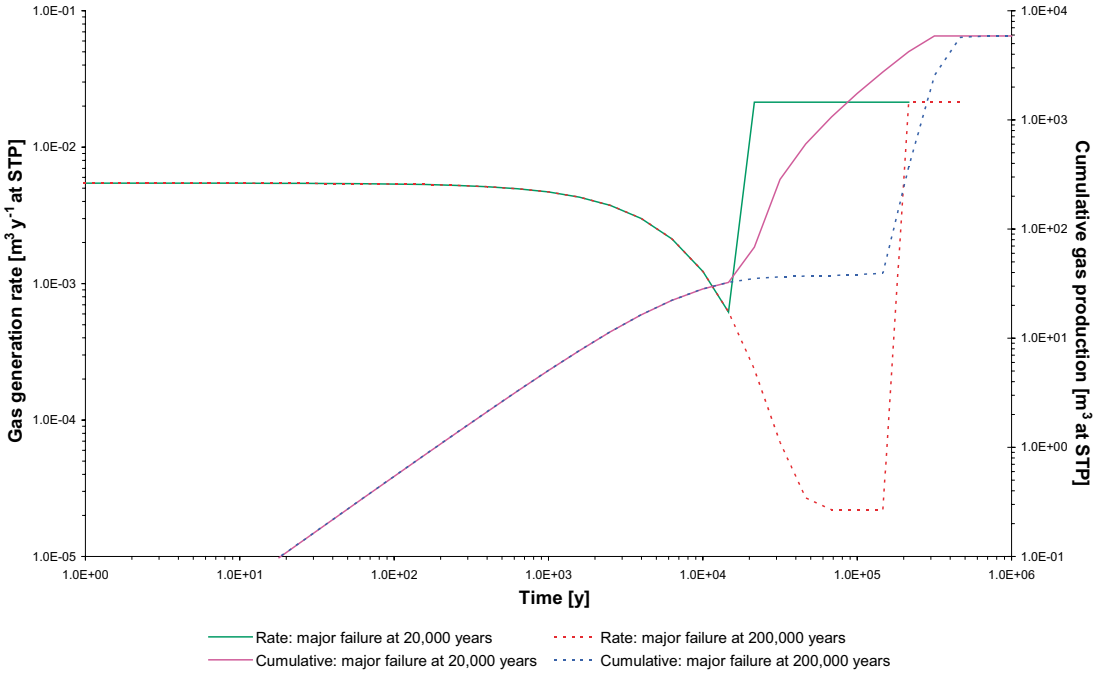

Figure 5-5. *Estimated rate of gas production and cumulative gas production over an extended time-scale, neglecting constraints from the geosphere on groundwater flow.*

Table 5-3. Properties and dimensions from which the gas-filled volume in bentonite-filled part of a deposition hole is obtained.

Shape	Inner diameter (m)	Outer diameter (m)	Void ratio	Water saturation	Canister diameter (m)	Hole diameter (m)	Length (m)
Block	–	1.690	0.680	0.70	1.050	1.750	2.5
Ring	1.060	1.690	0.585	0.81	1.050	1.750	4.833

Based on the figures in Table 5-3, the total gas-filled volume in the deposition hole (neglecting the short upper section filled with backfill) is 2.41 m^3 (Table 5-4). It is assumed that the gas initially trapped is at atmospheric pressure, and the ambient temperature. To the accuracy of the estimates of the trapped gas volume, this can be taken to be standard temperature and pressure.

Gas will also be trapped in the backfilled tunnels from which the deposition holes are drilled. Two options are being considered for the backfilling: a rock/bentonite mixture, and Friedland clay blocks /SKB 2004e/. The gas-filled void space would be larger if the Friedland clay were used mainly because of the spaces that would be present between the clay blocks on emplacement. The initial void fractions of the rock/bentonite mixture and the Friedland clay themselves are 0.59 and 0.33, and the initial water saturations are 0.54 and 0.27, respectively, but 20% of the tunnel volume is additionally assumed to consist of gas-filled voids in the case of the Friedland clay /SKB 2004e/. The fraction of the tunnel space initially occupied by gas is shown in Table 5-4. Also shown is the volume of gas in the tunnels that may be associated with each deposition hole. This is the gas filled volume in a 6 m length of tunnel, this being the spacing between the deposition holes, taking the tunnel cross-sectional area to be 25 m^2 (this is the cross-sectional area for a tunnel excavated by drilling and blasting; a larger area would result from tunnel boring, but the difference is ignored here). The gas-filled volume in the backfilling of the top of the deposition holes is included in this estimate of gas-filled volume per deposition hole.

Table 5-4. Gas-filled volumes (or volume fraction) initially present in deposition holes and backfilled tunnels.

Location	Gas-filled void volume (m^3) or volume fraction ($m^3 m^{-3}$)
Deposition hole (blocks, rings, and slots)	2.41
Backfilled tunnel – gas-filled volume fraction	
Rock/bentonite backfill	0.17
Friedland clay	0.35
Backfilled tunnel – gas-filled volume per deposition hole (i.e. per 6 m length of tunnel and assuming the cross-sectional area to be 25 m^2)	
Rock/bentonite backfill	25.8
Friedland clay	52.0

As the repository resaturates, the pressures will tend to the hydrostatic pressure of ~ 4 MPa, a 40-fold increase in pressure, which will cause a corresponding decrease in the gas-filled volume. Some of the gas initially present will also dissolve and may be transported from the tunnels in solution. From the data in Table 5-3, the water content of the backfill when it is resaturated can be calculated as a volume fraction of 0.46 and 0.87 for the rock/bentonite and Friedland clay backfill, respectively. The solubility in water of the main constituents of air, nitrogen (78.08%) and oxygen (20.95%), are rather similar, with nitrogen slightly less soluble /Lide 1994/. It can be shown that for the tunnel filled with rock and bentonite, enough water will be present after resaturation to dissolve all the trapped air at a pressure of 4 MPa. For the Friedland clay backfill, there is not quite enough water, and the pressure has to rise to about 4.5 MPa to dissolve all the air. These issues are discussed below in relation to geosphere gas transport.

The total trapped gas volume of around 25–50 m^3 per deposition hole corresponds to the amount of gas that would be generated in a defective canister over 1,200–2,400 years at the maximum rate considered likely. Since it is estimated that only 0.1% of the canisters could have a hole defect, the initial gas volume in the tunnel per *defective* canister would be $2.5 \cdot 10^4$–$5 \cdot 10^4$ m^3. This exceeds the $5.9 \cdot 10^3$ m^3 at STP of gas that could be produced by corrosion of the entire cast iron insert in a defective canister (Section 5.1.1).

5.1.3 Natural gases

Natural gases have been detected in groundwater samples from the Forsmark site /SKB 2005a/. The approximate concentrations of the more significant gases at the repository depth of about 400 m, estimated from the plots in reference /SKB 2005a/, are shown in Table 5-5. The solubilities are obtained from /Lide 1994/ assuming that the solubilities are proportional to the gas pressures.

It can be seen that the measured concentrations are all small compared with the solubilities of the gases at the repository depth. Only nitrogen, which has a concentration about 10% of its solubility at the repository hydrostatic pressure, is present in amounts that could be significant in terms of creating a free gas phase. The solubilities given in Table 5-5 are those in pure water. The presence of dissolved salts will lower the solubilities (the salting-out effect), but this effect is not expected to reduce the nitrogen solubility sufficiently to cause free nitrogen to appear. Free gas could appear as a result of pressure reduction as the groundwater and its dissolved gases moved towards the surface, but on the basis of the solubilities shown in Table 5-5, this would only occur when the groundwater had risen to within about 40 m of the surface.

If a free gas phase was formed as a result of hydrogen production from corrosion, dissolved natural gases could partition into this gas phase until their partial pressures in the gas phase were in equilibrium with the solution concentrations.

Table 5-5. Measured dissolved natural gas concentrations and expected solubilities at the repository depth (values of measured concentrations are estimates).

Gas	Measured concentration (mol m^3)	Approximate solubility at repository depth (mol m^3)
Nitrogen	2.5–3.5	$3.1 \cdot 10^1$
Helium	< 0.3	$1.5 \cdot 10^1$
Carbon dioxide	< 0.2	$1.9 \cdot 10^3$
Hydrogen	$< 1 \cdot 10^{-2}$	$3.3 \cdot 10^1$
Methane	$< 5 \cdot 10^{-3}$	$7.2 \cdot 10^1$

5.2 Flow and transport characteristics of gas

As discussed above, ingress of water into a canister through a defect, first mainly by advection, and then, when the gas pressure in the canister has risen to around the hydrostatic pressure, by vapour phase diffusion, will cause hydrogen generation from anaerobic steel corrosion. To demonstrate repository safety, it is necessary to develop an understanding of what will happen to this hydrogen in order, in particular, to show that the gas pressure will not build up in a way that will damage the near-field containment and that migration of the gas through the near and far fields will not have a deleterious effect on water-borne radionuclide transport.

The first barrier to gas migration from the canister is the saturated bentonite buffer. Examination of gas migration through the bentonite buffer is beyond the remit of this work, which is concerned with gas migration through the geosphere. However, it is appropriate to comment briefly on work that has been carried out on this leg of the gas migration pathway as background to the present consideration of gas migration through the geosphere.

As already noted in Section 5.1.1, /Wikramaratna et al. 1993/ have examined transport of dissolved gas by diffusion through the bentonite buffer. The flow rate of gas that can be achieved by this mechanism depends sensitively on the geometry of the diffusion pathway. If it is assumed that the gas diffuses from the area of the defect, the diffusion will, at least initially, follow a radial pathway through an approximate hemisphere centred on the defect (spherical diffusion). It is assumed in this model that gas emerging from the bentonite is transported away from the location sufficiently quickly that the concentration of dissolved hydrogen at the outer boundary of the bentonite can be taken to be zero. Following /Wikramaratna et al. 1993/, an effective diffusion coefficient of $2 \cdot 10^{-11}$ $m^2 s^{-1}$ is used in this calculation. /Tanai et al. 1999/ report measured values for this diffusion coefficient of 10^{-10}–10^{-11} $m^2 s^{-1}$, so the value used is consistent with this range. The value is also consistent with the values used for the diffusion of ions in bentonite in the SR 97 assessment /Lindgren and Lindström 1999/. Diffusion by this mechanism is found to be small. Updating the calculations to use current parameters gives a flow of $1.7 \cdot 10^{-6}$ $m^3 y^{-1}$ at STP, if the gas pressure is hydrostatic (at 400 m depth). The flow is proportional to the gas pressure, so if the pressure rises to 15 MPa, the flow would be $6.4 \cdot 10^{-6}$ $m^3 y^{-1}$ at STP.

These calculated flows are evidently much smaller than the upper bound to the potential gas generation rate of $2.1 \cdot 10^{-2}$ $m^3 y^{-1}$ at STP. They are also smaller than the estimate of $2.2 \cdot 10^{-5}$ $m^3 y^{-1}$ at STP for the rate of hydrogen production that would occur when the water supply is controlled by vapour diffusion, so that the gas pressure would continue to rise if this was the only gas escape mechanism.

If the gas pressure rises to a level comparable to the stress in the bentonite, it is possible that the gas could deform the bentonite creating a gas-filled gap between the bentonite and the canister (this could take a very long while unless the defect became enlarged – see Section 5.1.1). In these circumstances, gas could diffuse over a much larger surface area of the bentonite than for the case in which diffusion occurs just from the area of the defect. For this scenario, /Wikramaratna et al. 1993/ consider cylindrical diffusion across the thickness of the bentonite buffer, and vertical diffusion through the bentonite blocks at the top of the canister, in both cases assuming that the gas phase has spread across the whole surface of the copper canister. The dissolved hydrogen concentration at the outer surface of the bentonite is again taken to be zero. Given present understanding of the extent of fracturing of the host rock, the cylindrical diffusion scenario is probably optimistic, in that although the source of the gas for the diffusion may spread over the whole of the surface of the canister, the sink will be confined to the lines of around zero to two fracture intersections with the deposition hole.

Diffusion to a line sink, representing the fracture intersection with a deposition hole, may be modelled approximately as cylindrical diffusion in a half cylinder of length equal to the length of the line of intersection of the fracture with the deposition hole (see Figure 5-6). The diffusive flux, Q_{dg} [$m^3 s^{-1}$ at STP], is approximated as:

$$Q_{dg} = 2\pi^2 D_b \frac{r_d}{\log(2r_b/e_f)} H_H p_g \qquad (5\text{-}7)$$

where

D_b is the diffusion coefficient for dissolved hydrogen in buffer bentonite [m^2s^{-1}],

r_d is the radius of the deposition hole [m],

r_b is the distance over which the cylindrical diffusion occurs, taken to be the thickness of the bentonite buffer [m],

e_f is the aperture of the fracture intersecting the deposition hole [m],

H_H is a Henry's law constant for hydrogen dissolved in water [m^3 at STP $m^{-3}Pa^{-1}$],

p_g is the gas pressure in the canister [Pa].

It is assumed that the dissolved hydrogen concentration at the intersection of the fracture and the deposition hole is zero. The parameters relating to the bentonite buffer are shown in Table 5-6.

Table 5-6. Parameters for the saturated bentonite buffer.

Parameter	Value	Unit	Reference
Deposition hole radius	0.875	m	/SKB, 2004e/
Radial thickness of buffer	0.35	m	/SKB, 2004e/
Intrinsic diffusion coefficient	$2 \cdot 10^{-11}$	m^2s^{-1}	/Wikramaratna et al. 1993/ †

† This appears to be an estimated value based on comparison with values for other species. The diffusion coefficient for hydrogen in free water is $4.5 \cdot 10^{-9}$ m^2s^{-1} /Cussler 1984/, so the value quoted is considered reasonable for a compacted clay, and is consistent with measurements made in Japanese experiments. (See also discussion in main text.)

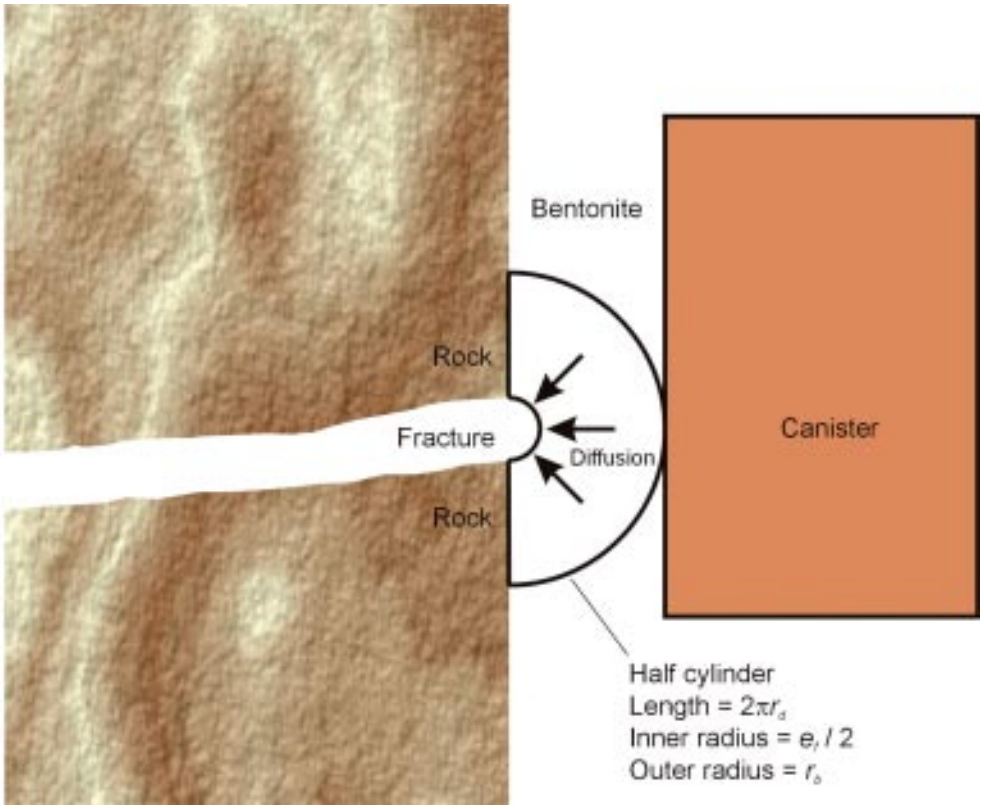

Figure 5-6. *A schematic diagram shows cylindrical diffusion through the bentonite buffer to a fracture intersection with a deposition hole.*

The Henry's law constant is set to $1.9 \cdot 10^{-7}$ m^3 at STP $m^{-3}Pa^{-1}$, to be consistent with the solubility data shown in Table 5-5. If the pressure in the gas phase is taken to 15 MPa (it must exceed the stress in the buffer to create a gap between the canister and the buffer), and the effective fracture transport aperture is taken to be 10^{-4} m, to provide an indicative measure of the diffusive flux, then the calculated flux into the fracture is $3.5 \cdot 10^{-3}$ m^3y^{-1} at STP. This diffusive flux does depend on the gas source being distributed over a larger area than simply that of the defect in the canister, but appears capable of supporting a hydrogen flow greater than the rate of generation of gas by diffusive supply of water vapour, and comparable to that if the gas generation rate is controlled by supply of water by advection through the bentonite. However, it is less than the rate required to disperse the gas at the upper bound gas generation rate assumed of $2.1 \cdot 10^{-2}$ m^3y^{-1} at STP.

Vertical diffusion through the bentonite and backfill to the tunnel may also offer a transport path for dissolved gas, particularly if significant groundwater flows are focused along the tunnel, thereby maintaining the dissolved gas concentration at the boundary between the tunnel and the deposition hole at a low value. Assuming that the dissolved gas diffuses from the area of the top of the canister over a distance of 2.5 m to the tunnel, and then the gas flow would be $6.2 \cdot 10^{-4}$ m^3y^{-1} at STP. This is again insufficient to remove gas at the maximum rate considered possible, but would be more than adequate to remove gas at the rate at which it could be generated if the process was controlled by vapour diffusion into the canister.

The above discussion indicates that diffusion of dissolved gas directly from the defect hole would be very small and would not prevent the gradual build up of pressure, but, in the very long term, after the gas pressure had built up and if the gas was able to spread out in a gap between the canister and the bentonite, then it is possible that the increased area from which diffusion could occur might allow the gas to escape at the rate at which it would be produced if controlled by water vapour diffusion. However, the time scale for this to occur is so long that it might be unreasonable to assume that further degradation to the copper canister has not occurred to allow freer access of water to the iron insert.

If the gas generated cannot pass through the bentonite by diffusion of dissolved gas, then free gas-phase transport through the bentonite is expected to occur once the pressure has reached a threshold value. The available experimental evidence suggests that this gas-phase transport will occur by fissuring of the buffer, and that the fissures will subsequently self seal, so that as far as the transport through the bentonite buffer is concerned this fissuring will provide a satisfactory method of relieving gas pressure build up in the canister, provided that the threshold pressure is not too high and that the gas can subsequently migrate through the geosphere without the geosphere contributing to a further build up of gas pressure. Note that the creation of gas-filled fissures in the bentonite may create an increased surface area from which dissolved gas can diffuse.

Once the gas has escaped from the buffer, it may directly enter the geosphere via a conducting fracture intersecting the deposition hole, or it may first enter the tunnel (including the EDZ around the tunnel), where it could reside for a time and may travel laterally, before escaping into the fracture network. As with transport through the buffer, gas transport through the geosphere may occur as a dissolved phase or as a free gas. These possibilities are considered in the next sections.

5.2.1 Dissolved gas

Aqueous phase diffusion of the gas produced through the sparse fracture network of the rock is not expected to make a significant contribution to gas migration through the geosphere. The capacity of gas to disperse in solution through the geosphere depends therefore on the flux of water that is available to carry the gas away and with which the gas makes contact (the latter may be an issue if the groundwater flow is concentrated along paths remote from the pathways followed by the gas). It might be imagined that groundwater flows would be concentrated

along excavated structures, in particular tunnels and access roads, including the EDZs, but the groundwater flow calculations do not show this occurring to an appreciable extent. This is because of the orientation of the tunnels to the head gradient and the fact that the permeabilities of the tunnels are comparable to those of the host rock.

Given that the solubility of hydrogen at repository depth is about 33 mol m^{-3} (Table 5-5) or 0.74 m^3 at STP m^{-3}, the flow of groundwater required to remove hydrogen at a rate of $2.1 \cdot 10^{-2}$ $m^3 y^{-1}$ at STP would be $2.8 \cdot 10^{-2}$ $m^3 y^{-1}$, assuming the groundwater was fully saturated with the hydrogen. Using the ECPM reference case (lower transmissivity below ZFMNE00A2), the geometric mean of the Darcy velocity close to 6,824 deposition holes, in the rock, EDZ, and the tunnels, from calculations at different times is $4.6 \cdot 10^{-6}$ m y^{-1}. This means that to remove the hydrogen generated in solution would require that the gas saturate the flowing groundwater over an area of $6.2 \cdot 10^3$ m^2. It is difficult to conceive that the extent of the contact between gas and flowing groundwater could be sufficient to saturate the flowing groundwater over such a cross-section of its flow-path.

It is possible that the gas could become trapped, for example in the tunnel, and this could provide an enhanced interface area between the trapped gas and the flowing groundwater from which gas could dissolve and diffuse into the water. It seems likely that, with the low density of fracturing predicted at the repository depth, intersections of fractures with the deposition holes will be non-existent or sparse, and in the latter case are likely to involve only low transmissivity fractures. It seems likely therefore that the gas will escape upwards into the deposition tunnel zone. Depending on the capillary pressure of the backfill in the tunnel, the gas may concentrate in the EDZ around the tunnel, but the available gas storage volume in the EDZ is expected to be small. If not prevented by the capillary entry pressure of the backfill, gas could also collect in the tunnel. The amount of gas that could collect in the tunnel would depend on the capillary entry pressure for the fractures (compared to the backfill), as discussed, for example by /Wikramaratna et al. 1993/, and on the spacing between intersections of fractures with the tunnel.

It will be assumed that the aperture that is relevant for gas migration is the fracture transport aperture, e_t [m], which has been correlated with the transmissivity, T [$m^2 s^{-1}$], according to /Hartley et al. 2004/:

$$e_t = 0.46 T^{0.5} \tag{5-8}$$

If the capillary pressure in the backfill is negligible compared with that in the fractures (which may not be the case once the backfill has resaturated), the thickness, h [m], of a gas cushion that could collect at the top of the tunnel as a consequence of the capillary pressure that would need to be overcome before gas could enter the fracture is given by:

$$h = \frac{1}{\rho_w g} \frac{2\sigma}{e_t} \tag{5-9}$$

where

σ is the surface tension of water [Pa m], which is 0.074 Pa m at 12°C /Lide 1994/.

Table 5-7 shows the estimated fracture transport aperture and gas cushion thickness for fractures with transmissivities in the range 10^{-6}–10^{-10} $m^2 s^{-1}$.

Table 5-7. Dependence of aperture-related properties of fractures on fracture transmissivity.

Transmissivity [$m^2 s^{-1}$]	$1 \cdot 10^{-6}$	$1 \cdot 10^{-7}$	$1 \cdot 10^{-8}$	$1 \cdot 10^{-9}$	$1 \cdot 10^{-10}$
Effective aperture [m]	$4.60 \cdot 10^{-4}$	$1.45 \cdot 10^{-4}$	$4.60 \cdot 10^{-5}$	$1.45 \cdot 10^{-5}$	$4.60 \cdot 10^{-6}$
Capillary pressure [Pa]	$3.21 \cdot 10^2$	$1.02 \cdot 10^3$	$3.21 \cdot 10^3$	$1.02 \cdot 10^4$	$3.21 \cdot 10^4$
Gas cushion thickness [m]	0.03	0.10	0.33	1.04	3.28

Gas from such a gas cushion may dissolve in water passing around the cushion. The general groundwater flow direction is, by design, orthogonal to the line of the tunnel, so groundwater flow across the tunnel could pass across the exposed lower surface of a gas cushion (the upper surface is neglected as there are presumed to be only a few discrete fracture intersections in contact with the gas cushion). Dissolved gas could diffuse into this flowing groundwater. The same general modelling approach could be used to estimate this as is used in estimating radionuclide diffusion into groundwater flowing around a deposition hole /Hartley et al. 2004/. In this approach, the advection-diffusion equation is solved in the boundary layer approximation (diffusion parallel to the groundwater flow is neglected). The flux, Q^t_{dg} [$m^3 s^{-1}$ at STP], of dissolved gas is given by:

$$Q^t_{dg} \approx c_s l_c \sqrt{\frac{4 D_e t_c}{\pi}} q_t = c_s l_c \sqrt{\frac{4 D_e w_t q_t}{\pi}} \qquad (5\text{-}10)$$

where

c_s is the saturation concentration of dissolved hydrogen at repository depth [m^3 at STP m^{-3}],

l_c is the length of the gas cushion along the tunnel [m],

D_e is the effective diffusion coefficient for dissolved hydrogen in the saturated backfill [$m^2 s^{-1}$] (the flow area is that of the rock and the dissolved concentration is in terms of pore water volumes),

t_c is the time that the groundwater is in contact with the gas cushion [s],

q_t is the Darcy velocity of the groundwater, which is assumed to be orthogonal to the axis of the tunnel [m s^{-1}],

w_t is the width of the tunnel [m].

The width of a gas cushion in a deposition tunnel would be about 6 m, determined by the tunnel geometry /SKB 2004e/. The mean value of the Darcy velocity at the repository depth at positions in the tunnels close to the deposition holes has been calculated in the ECPM variant "lower transmissivity below ZFMNE00A2" to be about $6.8 \cdot 10^{-6}$ m y^{-1}. The saturation concentration of hydrogen in water at the repository depth is 0.74 m^3 at STP m^{-3} (compare Table 5-5 and the above text). If the effective diffusion coefficient for hydrogen in the backfill is taken to be that of saturated bentonite, $2 \cdot 10^{-11}$ $m^2 s^{-1}$, and the length of the gas cushion along the tunnel was, say, 10 m, then the flow of dissolved gas from the cushion would be $1.3 \cdot 10^{-3}$ $m^3 y^{-1}$ at STP. This is insufficient to remove the gas generated by unrestricted corrosion at $2.1 \cdot 10^{-2}$ $m^3 y^{-1}$ at STP from a defective canister, but could contribute significantly to the removal of gas if the gas generation was significantly constrained by water availability (see Table 5-2). If the diffusion coefficient in the backfill was larger than in pure bentonite, then larger flows of dissolved gas could occur. The flow only depends on the square root of the diffusion coefficient (Equation (5-10)), so an increased diffusion coefficient is not likely to be sufficient to allow all the gas to be removed in solution at the upper bound gas generation rate, but it could result in the dissolution of all the gas produced at lower, more likely, rates.

Gas may dissolve in groundwater as it passes through the formations above the repository. If the horizontal Darcy velocity of the groundwater at depth z above the repository is $q_h(z)$ [m s^{-1}], the capacity of horizontally flowing groundwater to transport gas away from the region above the repository is given by:

$$\begin{aligned} Q^h_{dg} &= w_h \int_0^d q_h(z) H_H \rho_w g z dz \\ &\approx w_h \frac{H_H \rho_w g}{2} \sum_{i=1}^{n} q_{hi} \left(z_i^2 - z_{i-1}^2 \right) \end{aligned} \qquad (5\text{-}11)$$

where

Q_{dg}^{h} is the horizontal flow of dissolved gas between repository and the surface [m^3s^{-1} at STP],

w_h is the width orthogonal to the groundwater flow direction of the region of groundwater that is saturated with gas [m],

d is the repository depth [m],

q_{hi} approximates $q_h(z)$ as constant in the interval (z_i, z_{i-1}), $z_0=0$, $z_n=d$.

Average values of the horizontal groundwater flow velocity over the whole repository area have been abstracted from the ECPM reference case calculations at 50 m intervals. Taking these velocities as representative of each 50 m interval, the total flow of dissolved gas that can be transported away from the repository per unit distance orthogonal to the groundwater flow direction is $5.3 \cdot 10^{-1}$ m^3 at STP $y^{-1}m^{-1}$. The width of the region, w_h, that must become saturated with gas to remove in solution all the gas generated from a single defective canister at $2.1 \cdot 10^{-2}$ m^3y^{-1} at STP is only about 4 cm. Without details of the channels followed by the gas it is hard to prove that this amount of groundwater will become saturated with gas, but it is at least plausible that it would be, and certainly at lower gas generation rates it becomes more likely.

This estimate of the amount of gas that would dissolve in flowing groundwater above the repository is only crude, because the groundwater flow above the repository is quite complex, including vertical flows in cells bounded by geological features, as well as horizontal flows. The consideration of the dissolution of gas from a single defective canister also assumes that there are no interactions between canisters; that is, the groundwater does not already contain dissolved gas from another canister before it reaches the region of the canister being considered. Finally, the kinetics of the dissolution process have been neglected.

5.2.2 Gas phase

Gas transport as a free gas through an otherwise water-saturated sparse fracture network is likely to follow a complex behaviour that is difficult to represent. The variable aperture and orientation of fracture planes, and the geometry of fracture intersections will mean that gas will travel in channels of varying width, determined largely by the local capillary pressure variation, which depends on the local fracture aperture. In some places, constrictions in the flow-path, may cause greater filling of the fracture planes with gas upstream of the fracture, compared to places where there are no such constrictions and the gas can flow freely in a narrow channel. Instabilities may also occur in the gas-phase flow, with pathways collapsing and reforming, with some transport occurring as separated bubbles.

Such characteristics of gas transport through water-saturated fractures have been seen in a number of laboratory experiments, and have been explored in modelling studies (see, for example, /Hoch et al. 2001/ and /Rodwell et al. 1999/ and references therein), although the upscaling of these results to the field scale has proved elusive.

Some insight into the potential capacity of the fracture network at Forsmark to transport the gas generated from a defective waste canister through the geosphere can be obtained by considering the width of the channel required to support the flow in an idealised fracture network.

Stable gas channel

In a steady-state situation, it is reasonable to assume that the vertical component of the pressure gradient in the gas phase will be approximately equal to the hydrostatic gradient in the water phase. There will be local variations due to variations in capillary pressure (controlled by fracture aperture variations). Locally, the steady-state gas flow rate, $\mathbf{Q_g}$, in m^3s^{-1} at STP, is given by:

$$\mathbf{Q_g} = wT(w)\frac{\mu_w}{\mu_g}\left[\mathbf{e_z} + \frac{\nabla p_c(w)}{\rho_w g}\right]\frac{(\rho_w g z + p_s + p_c(w))}{p_s} \qquad (5\text{-}12)$$

where

w is the width of the gas filled channel in the fracture [m],

$T(w)$ is the transmissivity of the gas filled part of the fracture [m^2s^{-1}]. For a uniform, parallel-plate fracture, T would be independent of the gas channel width,

$\mathbf{e_z}$ is the unit vector in the vertical direction,

z is the depth below the surface [m],

p_s is the gas pressure at the surface [Pa],

$p_c(w)$ is the capillary pressure, which, in general, in a rough fracture will depend on the size of the gas channel in the fracture [Pa]. For a uniform fracture, the capillary pressure will be constant.

At the repository depth, the fracture transmissivities are expected to be 10^{-10}–10^{-8} m s^{-1}. This range corresponds to an effective fracture aperture range of ~ $5\cdot10^{-6}$–$5\cdot10^{-5}$ m, or a capillary pressure range of $3\cdot10^4$ – $3\cdot10^3$ Pa. The cushion of gas in saturated rock that could be supported by capillary pressures of this magnitude would have a thickness of 3.28–0.33 m. This suggests that, although locally the capillary pressure and hence the gas pressure gradient may show considerable variation, when averaged over a length scale of a few metres, and probably a few centimetres, the gas pressure gradient will be close to the hydrostatic pressure gradient. If there is a well connected set of sub-vertical fractures, and if it is assumed that the fractures each have constant aperture (the approximation in the DFN groundwater flow modelling, although it may be better justified there than here), then Equation (5-12) for vertical gas flow becomes:

$$Q_g = wT\,\frac{\mu_w}{\mu_g}\,\frac{\left(\rho_w g d + p_s + p_c\right)}{p_s} \qquad (5\text{-}13)$$

Assuming the gas flow rate is equal to the upper bound gas generation rate of $2.1\cdot10^{-2}$ m^3y^{-1} at STP, the gas occupied channel widths in sub-vertical fractures of different transmissivities as a function of depth are shown in Figure 5-7. Note that the width of the channel does not necessarily have to comprise a single channel; the channel may well be branched, flowing round asperities and fracture infill, and indeed at any particular depth may be divided between a number of fractures. The division of flow between a number of fractures may occur if the gas spreads out laterally below some region of restricted vertical flow in the fracture network.

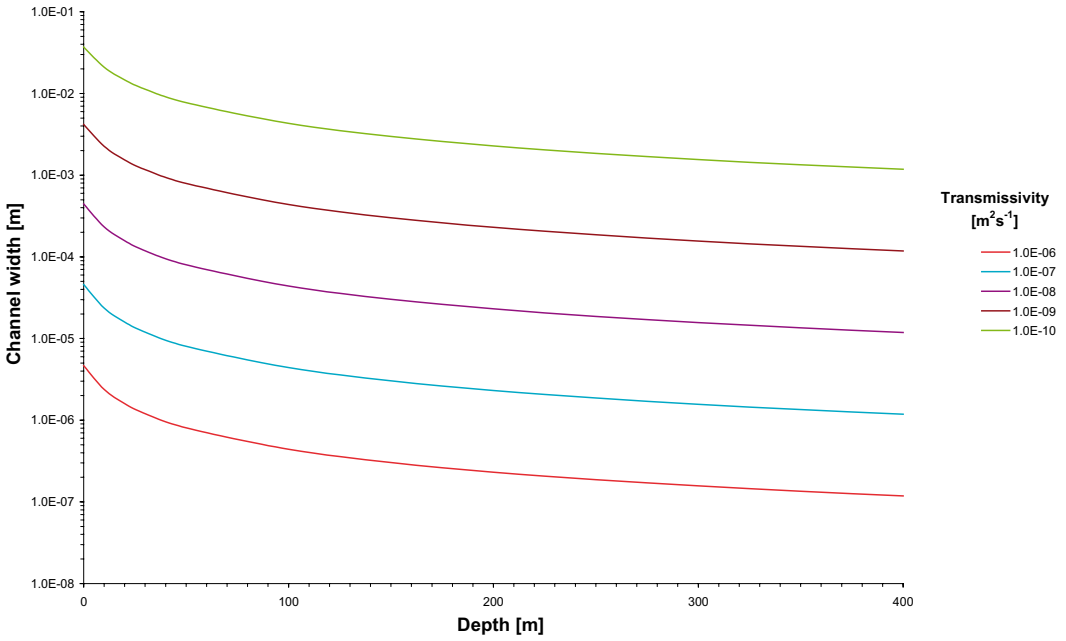

Figure 5-7. *Gas-filled channel width in idealised sub-vertical fractures as a function of depth and fracture transmissivity.*

Figure 5-7 shows that below 100 m a channel width of only about 1–5 mm, depending on depth, is needed to support the maximum required gas flow rate, even for fractures with the lowest transmissivity of 10^{-10} m^2s^{-1}. For more transmissive fractures, the channel width required becomes even less. Towards the surface the incidence of more transmissive fractures is expected to increase, offsetting to some extent the effect of gas expansion in increasing the gas channel width.

The travel time, t_t [s], for gas to move from repository to the surface using this model is given by:

$$t_t = d \frac{e_t}{T\left(\frac{\mu_w}{\mu_g}\right)} \qquad (5\text{-}14)$$

where

d is the repository depth [m];
e_t is the fracture transport aperture (see Equation (5-8)).

The travel times obtained for a continuous gas pathway using this model are given in Table 5-8.

These travel times are very short, probably unrealistically so. The concept of a continuous gas channel is invoked to give some feeling for the flow capacity of the rock to transport the gas. As already suggested, it is expected that the gas flow will be broken up by constrictions and intersections in the fracture network, and if the gas flow breaks up into bubbles then the travel time will be longer.

Instability

There have been few experiments on the stability of gas channels in fractured rock. The experimental data that do exist are often for artificial analogues of real fractures /e.g. Hoch et al. 2001/.

However, studies on gas flowing into Hele-Shaw cells[6] (see Figure 5-8) filled with viscous fluid, assuming an initially planar interface, suggest that:

a) at small inclinations of the Hele-Shaw cell, the interface between the two fluids stays a straight line,

b) at intermediate inclinations of the Hele-Shaw cell, a perturbation to the interface grows to form a stable finger whose width is a calculable fraction of the width of the Hele-Shaw cell,

c) at large inclinations of the Hele-Shaw cell, an apparently chaotic behaviour is observed in which fingers are formed that may branch or split. This is due to a viscous instability, and has been discussed elsewhere, for example /Saffman and Taylor 1958, Chuoke et al. 1959/.

Table 5-8. Travel time as a function of fracture transmissivity for gas to move along a continuous gas-filled channel from the repository to the surface.

Transmissivity [m^2s^{-1}]	$1.00\cdot10^{-6}$	$1.00\cdot10^{-7}$	$1.00\cdot10^{-8}$	$1.00\cdot10^{-9}$	$1.00\cdot10^{-10}$
Transport aperture [m]	$4.60\cdot10^{-4}$	$1.45\cdot10^{-4}$	$4.60\cdot10^{-5}$	$1.45\cdot10^{-5}$	$4.60\cdot10^{-6}$
Travel time [d]	$1.48\cdot10^{-2}$	$4.68\cdot10^{-2}$	$1.48\cdot10^{-1}$	$4.68\cdot10^{-1}$	1.48

[6] In a Hele-Shaw cell, the fluid is confined between two closely spaced, parallel, planar surfaces.

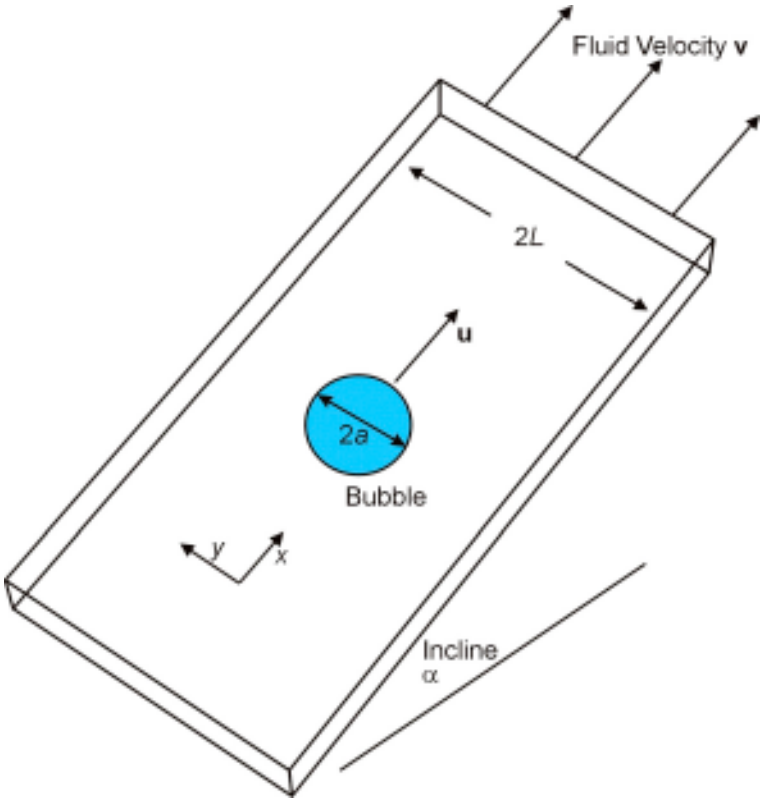

Figure 5-8. *A schematic diagram shows a gas bubble rising in a Hele-Shaw cell.*

Other relevant experimental work is concerned with the instability of a cylindrical gas jet injected into a liquid phase. At low injection velocities, bubbles form directly at the nozzle, and the forces acting on the forming bubble control their size. However, at higher injection velocities, a jet of gas issues from the nozzle and then breaks up into bubbles in a regular pattern /e.g. Meister and Scheele 1967, Tomotika 1934/.

These observations suggest that a gas channel in a fracture network may well be unstable.

Effects that could help to stabilise a gas channel include the variability in the capillary pressure due to variations in the fracture aperture, and interactions between the gas channel and the fracture walls.

The first effect has been observed in experiments with artificial rough fractures, for example /Hoch et al. 2001/.

The second effect has been observed in experiments with a Hele-Shaw cell /Hoch et al. 2001/. When the water in the Hele-Shaw cell was dyed with silicone oil, gas flows through the Hele-Shaw cell were consistent with standard models for such flows (i.e. the gas migrated as bubbles, at speeds consistent with Equation (5-16) given below). However, when the water was dyed with fluorescein, which is a surfactant, it became possible to form a narrow gas channel that persisted for up to a day. The difference between the two experiments is thought to be due to non-wetting of the Hele-Shaw cell surfaces by the water dyed with fluorescein. The gas was able to contact the Hele-Shaw cell surfaces, which stabilised the gas channel, and also led to trapping of gas and caused bubbles to migrate more slowly than expected. A repository for low-level and intermediate-level radioactive waste could contain organics and NAPLs, which might allow the gas that is generated to contact fracture surfaces, thereby stabilising a gas channel. However, the SKB repository for high-level radioactive waste will not contain organics and NAPLs, and it is expected that the geological history of the host rock (i.e. always in contact with water) will ensure that the fracture surfaces are wetted by the water rather than the gas.

On the basis of these considerations, it seems likely, although not proven, that a gas channel will break up into bubbles.

Flow of micro-bubbles

It has been suggested that the gas could flow as 'micro-bubbles', understood to be bubbles whose diameter is smaller than the fracture aperture, possibly in the range 10^{-6}–10^{-4} m.

Two arguments can be brought forward against gas migrating in the form of micro-bubbles:

a) It is difficult to form micro-bubbles by conventional snap-off methods /Hoch et al. 2001/.

b) Micro-bubbles dissolve rapidly into the surrounding water /Hoch et al. 2001/ unless the aqueous phase is sufficiently over-saturated with gas.

A simple model has been developed /Epstein and Plesset 1950, Hoch et al. 2001/ for the change in radius R_m [m] of a spherical gas bubble placed in water in which the dissolved gas concentration is c_0 [m^3 at STP m^{-3}]. The derivation assumes that the rate at which mass flows into or out of the bubble can be determined by solving the diffusion equation (with neglect of the motion of the bubble boundary), and that the ideal gas law applies to the gas in the bubble. The differential equation describing the change in radius of the bubble with time is:

$$\frac{dR_m}{dt} = p_s \frac{1}{\left(p_w + \frac{4}{3}\frac{\sigma}{R_m}\right)} D_w \left[c_0 - H_H\left(p_w + \frac{2\sigma}{R_m}\right)\right]\left(\frac{1}{R_m} + \frac{1}{\sqrt{\pi D_w t}}\right) \qquad (5\text{-}15)$$

where

p_s is standard pressure (101,325 Pa),
p_w is the ambient water pressure [Pa],
σ is the surface tension of water [Pa m];
D_w is the diffusion coefficient for dissolved hydrogen in water [$m^2 s^{-1}$],
H_H is a Henry's law constant for hydrogen dissolved in water [m^3 at STP $m^{-3} Pa^{-1}$].

This model was used to calculate the approximate lifetimes of micro-bubbles of various sizes present in water. Two saturation conditions, unsaturated and saturated, and two ambient pressure conditions, near surface and deep, were considered. The gas bubbles are unstable unless the surrounding water is sufficiently over-saturated, and in the case of micro-bubbles lifetimes are short (see Table 5.9).

Table 5-9. The lifetime of a gas bubble as a function of its initial radius, R_0, its depth below the surface, z, and the saturation state of the groundwater.

Near surface bubble, z = 0 m			
Saturation state	**Bubble lifetime [s]**		
	R_0 = 10^{-6} m	**R_0 = 10^{-5} m**	**R_0 = 10^{-4} m**
unsaturated	$7.7 \cdot 10^{-3}$	$9.6 \cdot 10^{-1}$	$10.3 \cdot 10^{1}$
saturated	$12.0 \cdot 10^{-2}$	$6.3 \cdot 10^{0}$	$5.9 \cdot 10^{3}$
Bubble at depth, *z* = –400 m			
Saturation state	**Bubble lifetime [s]**		
	R_0 = 10^{-6} m	**R_0 = 10^{-5} m**	**R_0 = 10^{-4} m**
unsaturated	$10.1 \cdot 10^{-3}$	$10.4 \cdot 10^{-1}$	$10.4 \cdot 10^{1}$
saturated	$2.3 \cdot 10^{-1}$	$2.3 \cdot 10^{2}$	$2.4 \cdot 10^{5}$

This leads to a conceptual model in which any small bubbles formed at depth might grow in size because of local over-saturation of the groundwater (if smaller than a critical size for the given over-saturation and pressure they will dissolve, otherwise they will grow). The bubbles continue to grow unless they migrate to a region of lower gas saturation, in which case they will start to re-dissolve. This process just helps to propagate the dissolved gas saturation front.

The above arguments suggest it is unlikely that micro-bubbles (i.e. bubbles whose diameters are less than 10^{-4} m) will contribute significantly to gas migration.

Flow of Hele-Shaw bubbles

It therefore seems that the most likely mechanism by which gas will migrate through a fracture network is as a stream of Hele-Shaw bubbles (i.e. bubbles whose diameters are larger than the fracture aperture). By assuming this mechanism, it is possible to develop an understanding of gas and induced groundwater flows in planar, constant aperture fractures, which then can be used as a guide to the flows in a fracture network.

The speed at which a Hele-Shaw bubble rises is taken to be /Hoch et al. 2001/:

$$u = -\frac{e_f^2}{12\mu_w}(\rho_w - \rho_g)\mathbf{g}\cdot\mathbf{e_X} \qquad (5\text{-}16)$$

where

e_f is the aperture of the Hele-Shaw cell (an analogue for a planar, constant aperture fracture) [m];

ρ_g is the density of the gas [kg m^{-3}];

$\mathbf{g}\cdot\mathbf{e_X}$ is the magnitude of the acceleration due to gravity in the plane of the Hele-Shaw cell [m s^{-2}].

This expression is reasonably accurate provided that:

a) the Hele-Shaw cell is sufficiently wide compared to bubble size that the side walls do not cause the bubble to distort, and

b) the water wets the surfaces of the Hele-Shaw cell.

The bubble speed depends mainly on the fracture aperture. In particular, an aperture of 10^{-5} m implies a speed in a vertical fracture of $8.2\cdot10^{-5}$ m s^{-1} or $2.6\cdot10^{3}$ m y^{-1}, and so the travel time to the surface would be 57 days. The bubble speed increases (and the travel time decreases) by a factor of 100 if the fracture aperture is 10^{-4} m.

These travel times, which have been derived for an idealised model of the fracture network, are unrealistically short. It is expected that constrictions and intersections in the fracture network will break up the gas flow; in some places gas will be trapped, thereby delaying the migration of the gas back to the surface.

It is also of interest to know the largest radius of Hele-Shaw bubble that is stable. To the best of our knowledge, this issue has not been studied rigorously. However, it may be acceptable to adapt models for the break-up of three-dimensional bubbles in viscous fluids /Grace et al. 1978/ to this case. In such models, a disturbance to the surface of a bubble grows in two stages:

a) In the first, the amplitude is small with respect to the wavelength of the disturbance λ, and a characteristic growth time can be predicted using the theory of unstable interfacial waves incorporating effects of viscosity and surface tension /Plesset and Whipple 1974/. The indentation grows exponentially and moves along the interface at (approximately) the local velocity in the undisturbed system.

b) In the second, the indentation grows at a nearly constant rate, and its motion along the interface is greatly inhibited.

Break-up of the bubble occurs if the first (exponential) growth stage is complete before the disturbance has reached the side of the bubble.

Now, the interface is unstable only for disturbances with wavelengths λ greater than λ_c, where /Plesset and Whipple 1974/:

$$\lambda_c = 2\pi\sqrt{\frac{\sigma\frac{\pi}{4}}{(\rho_w - \rho_g)|\mathbf{g}\cdot\mathbf{e_x}|}} \tag{5-17}$$

If the aperture of the Hele-Shaw cell, e_f, is small enough, a bubble will move so slowly that any disturbance can not be expelled from the region of instability before it has time to grow. In this case, the stable bubble radius, R_h, is actually determined by λ_c, i.e.

$$R_h = \frac{\lambda_c}{\pi} \tag{5-18}$$

Equation (5-18) applies to planar, constant aperture fractures with apertures less than about 10^{-4} m, and for these fractures the critical, or maximum, Hele-Shaw bubble radius is about $5\cdot10^{-3}$ m.

Finally, for a stream of Hele-Shaw bubbles the total gas flow rate is given by:

$$Q_g = 2\alpha_g u R_h e_f \tag{5-19}$$

where α_g is the gas volume fraction, defined to be the volume fraction that contains gas in the region where bubbles are flowing.

Combining Equations (5-16) to (5-19), for a single stream of Hele-Shaw bubbles which are rising vertically and just touching (i.e. $\alpha_g = \pi / 4$), it can be shown that the minimum fracture aperture required to support the upper bound gas generation rate of $2.1\cdot10^{-2}$ m^3y^{-1} at STP is about $15\cdot10^{-6}$ m at the depth of the repository and about $50\cdot10^{-6}$ m at the surface.

How does this minimum fracture aperture compare to the apertures predicted by the DFN model for those fractures that intersect the deposition tunnels? Considering only stochastic fractures with sizes greater than 10 m, P10 for the orientation of the deposition tunnels[7] is 0.0287 m^{-1}. In other words, on average about 9 fractures from the stochastic fracture network will intersect the axis of a typical deposition tunnel, which is about 300 m long. This number increases to about 18 if the deposition tunnel is modelled as a cylinder 3 m in radius and 300 m long. However, a percolation study[8] suggests that just 50% of these fractures are connected to the surface. A typical deposition tunnel is therefore intersected by about 9 fractures that belong to the fracture network connecting the tunnel to the surface. Figure 5-9 shows the distribution of transport apertures (see Equation (5-8)) for the fractures that intersect the deposition tunnel. The minimum transport aperture is $46\cdot10^{-6}$ m.

These observations suggest that at Forsmark, there are sufficient fractures with large enough apertures to transport the gas generated from a defective waste canister through the geosphere. Even for the upper bound gas generation rate, the discrete fracture network should have the capacity to carry the gas from a defective canister to the surface.

---

[7] The stochastic fractures are generated by a Poisson process. Hence, the separation of fracture intersections, x, is given by the cumulative density function $D(x) = 1 - \exp[-\lambda x]$, where $\lambda = 0.0287$ m^{-1}, and the number of fracture intersections, n, per deposition tunnel (assumed to be 300 m long) is given by the probability density function $P(n) = \frac{(300\,\lambda)^n \exp[-300\,\lambda]}{n!}$. It follows that it is extremely unlikely that a deposition tunnel will have no intersections.

[8] The study was for a single tunnel. The presence of other deposition tunnels will increase the connectivity.

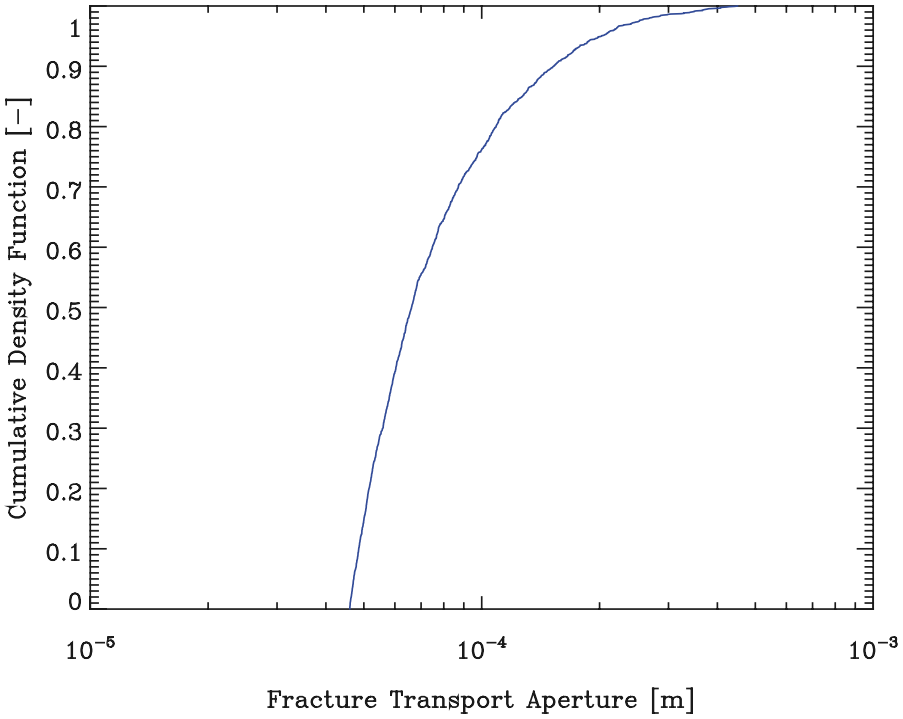

Figure 5-9. *Cumulative density function for the transport apertures of stochastic fractures greater than 10 m in size that intersect a 300 m long deposition tunnel.*

5.3 Implications for groundwater flow modelling

In this section, previously derived results for single Hele-Shaw bubbles will be used to estimate the effects of a stream of Hele-Shaw bubbles on the entrainment of water in a vertical, planar, constant aperture fracture (this model was originally developed in /Nash et al. 1997/).

For a circular gas bubble rising in a fracture, the radial and tangential components of the velocity of the surrounding groundwater are given by:

$$u_{w,r} = u\frac{R_h^2}{r^2}\cos(\theta)$$
$$u_{w,\theta} = u\frac{R_h^2}{r^2}\sin(\theta) \qquad (5\text{-}20)$$

where u is the terminal velocity of the bubble (see Equation (5-16)). Therefore, the vertical component of the velocity of the groundwater is:

$$u_{w,z} = u\frac{R_h^2}{r^2}\cos(2\theta) \qquad (5\text{-}21)$$

This result can be used to estimate the effects of a stream of bubbles on the entrainment of liquid. The assumption will be made that the velocity field surrounding a stream of bubbles can be calculated by linear superposition of the solution for a single bubble. This assumption is accurate only for a disperse system of bubbles, where the distance between the bubbles is large enough for bubble-bubble interactions to be negligible.

Consider an infinite stream of Hele-Shaw bubbles, with centres separated by distance s and with radii R_h, rising in a line. The vertical component of the velocity at a point with co-ordinates (x,z) in the liquid is given by:

$$\overline{u}_{w,z}(x,z) = \sum_{j=-\infty}^{\infty} u \frac{R_h^2}{r_j^2} \cos(2\theta_j) \tag{5-22}$$

where

$$r_j^2 = x^2 + (z - js)^2$$
$$\sin(\theta_j) = \frac{x}{r_j} \tag{5-23}$$

Symmetry of the bubble stream implies that the liquid velocity between each adjacent pair of bubbles must be similar. Hence, by integrating over the region of symmetry, it is possible to calculate an average vertical flow rate:

$$Q_{w,z} = \frac{1}{s} \int_{-\infty}^{\infty} dx \int_{0}^{s} dz \; e_f \delta(x,z) \, \overline{u}_{w,v}(x,z) \tag{5-24}$$

where δ (x,z) is an indicator function, which equals one if the point (x,z) is in the liquid surrounding the gas bubbles, and equals zero if the point is inside the gas bubbles.

This integral can be simplified to give (cf Equation (2.3.6) in /Nash et al. 1997/):

$$\frac{Q_{w,z}}{2uR_h e_f} = \frac{8}{\pi} \alpha_g^2 \int_0^1 d\eta \, \mathrm{Im}\left\{ \coth\left[2\alpha_g \left(\eta - i\sqrt{1-\eta^2} \right) \right] \right\} \tag{5-25}$$

where

α_g is the gas volume fraction, that is the fraction of the bubble region, $x < R_h$, containing gas, i.e. $\alpha_g = \frac{\pi R_h}{2s}$. Note that $0 \le \alpha_g < \frac{\pi}{4}$.

The model predicts that there is no contribution to the average liquid flow rate from liquid movement outside the bubble region. This does not imply that the liquid particles outside the bubble region are stationary, but that they move on a circulatory path such that there is no net liquid displacement from each rising bubble.

The right-hand side in Equation (5-25) can be evaluated using standard numerical methods.

A first approximation to the effects of bubble-bubble interactions on the gas phase may be calculated by assuming that each bubble feels the influence of the other bubbles due to the velocity they induce in the surrounding groundwater. The velocity of an individual bubble is assumed to increase by an amount equal to the sum of the liquid velocities from adjacent bubbles, calculated at the origin of the bubble under consideration. Thus the increased bubble velocity is:

$$u^* = u\left(1 + \frac{4}{3}\alpha_g^2 \right) \tag{5-26}$$

and the total gas flow rate becomes:

$$\frac{Q_g^*}{2uR_h e_f} = \alpha_g \left(1 + \frac{4}{3}\alpha_g^2 \right) \tag{5-27}$$

The non-dimensional gas flow rate and the non-dimensional induced groundwater flow are plotted as a function of the gas volume fraction in Figure 5-10.

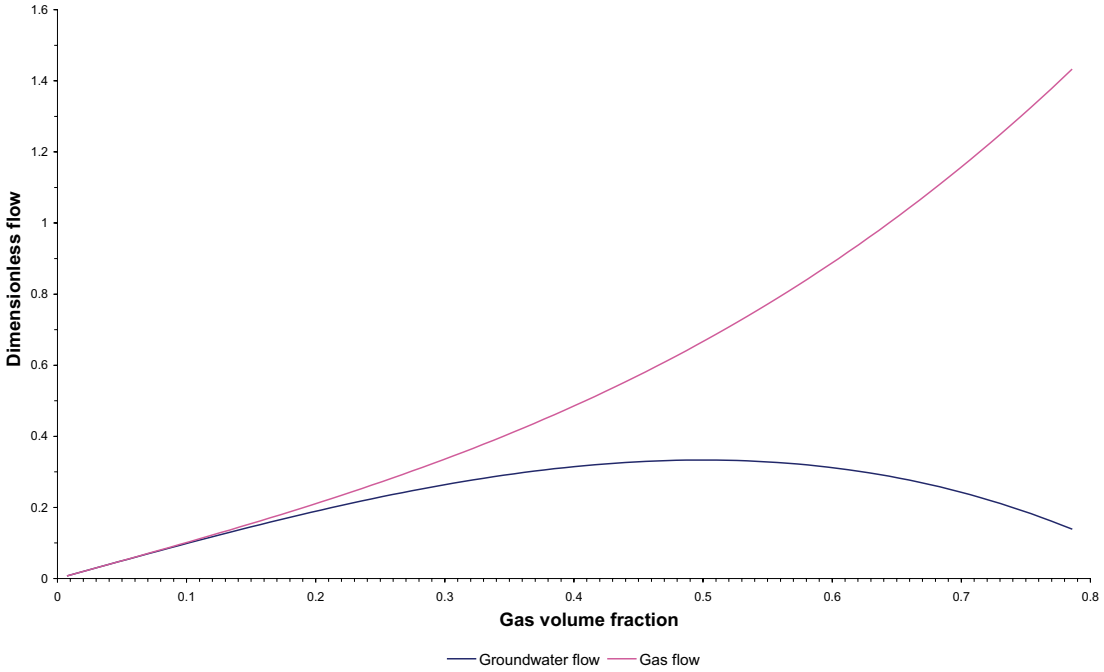

Figure 5-10. *The non-dimensional induced groundwater flow, $Q_{w,z}/2uR_h e_f$, and the non-dimensional gas flow rate, $Q_g^*/2uR_h e_f$, as a function of gas volume fraction.*

It follows that, in this simple model, the induced groundwater flow is always less than the corresponding gas flow rate, and that becomes more so as the gas volume fraction increases. The maximum induced groundwater flow occurs when the bubbles are very far apart, and then is equal to the gas flow rate[9].

To summarise, the model suggests:

a) A stream of gas bubbles will entrain groundwater.

b) The net flow of groundwater will be confined mainly to the bubble region.

c) It can be assumed, conservatively, that the induced groundwater flow is equal to the gas flow rate.

The conceptual model does not imply that groundwater will be transported rapidly to the surface. Rather, because of the inclination of the fractures, and constrictions and intersections in the fracture network, gas will be trapped in some places and that will disrupt any induced groundwater flow back to the surface. Groundwater possibly may flow quite quickly between pockets of trapped gas, but will be unable to cross those gas pockets.

At the depth of the repository the upper bound gas generation rate, and hence by implication the maximum induced groundwater flow, will be $5.4 \cdot 10^{-4}$ m^{3}y^{-1}.

A rising stream of gas bubbles will perturb the pre-existing groundwater flow near the repository over an area that is large enough to supply the induced groundwater flow. The mean value of the Darcy velocity at the repository depth at positions in the tunnels close to the deposition holes has been calculated in the ECPM variant "lower transmissivity below ZFMNE00A2" to be about $6.8 \cdot 10^{-6}$ m y^{-1}. The area through which this flow occurs that is required to supply the maximum possible induced groundwater flow (i.e. $5.4 \cdot 10^{-4}$ m^{3}y^{-1}) is just 79 m^2. Since the width

[9] This is just a consequence of Darwin's Theorem /Darwin 1953/, which states that "the added mass for a body translating uniformly in an infinite expanse of perfect fluid equals the drift-volume times the density of the fluid".

of a deposition tunnel is 5.5 m, the length of the tunnel that might be affected by the induced groundwater flow is 14.4 m. The part of the tunnel affected will be longer if the local Darcy velocity is smaller.

5.4 Implications for radionuclide transport

Should a separate gas phase flow appear then there are three mechanisms by which this might affect radionuclide transport:

a) the gas phase may transport volatile radionuclides;

b) as discussed in Section 5.3, the migrating gas may modify the groundwater flow with a corresponding effect on the transport of water-borne radionuclides.

c) it is known that colloids or other species may concentrate at the gas-water interface, and so may be transported along with any migrating gas bubbles that are formed.

The only volatile radionuclides that have been considered as potentially important for a copper canister spent fuel repository are ^{14}C in the form of carbon dioxide or methane and ^{222}Rn. The first has been assessed as radiologically insignificant even if it is released directly from a canister to the biosphere with no delay or dispersion in the geosphere /SKB 1999/.

Substantial quantities of ^{222}Rn may build up in a canister from in-growth of its parent ^{226}Ra from uranium decay, although this takes time. A canister is estimated to contain around 10^{11} Bq of ^{222}Rn after a few hundred thousand years /SKB 1999/. This corresponds to a generation rate of 6.6 TBq y^{-1}. What proportion of this release rate could be propagated to the surface would depend on the travel time to the surface, and the consequences would depend on the exposure pathway (accumulation in an occupied building is likely to be the most significant scenario). Some of the repository derived ^{222}Rn may dissolve in groundwater during transport as well as decaying. ^{222}Rn could also be released from fracture surfaces into a flowing gas stream, but this source is insignificant compared with the spent fuel.

Migrating gas may also affect the movement of groundwater and hence the transport of dissolved radionuclides. The potential consequences of such interactions will be mitigated by the following observations:

- With a small defect, it is not possible to get release of dissolved radionuclides and gas at the same time. The situation may be different if a large hole develops.
- Gas migration can only affect transport of dissolved radionuclides released from a different canister.
- Migrating gas is only likely to affect groundwater flows in the neighbourhood of a small number of canisters local to the canister generating gas, and there is a low probability that one of these also may be defective and releasing radionuclides.

A model study has been carried out to ascertain the importance of radionuclide transport on colloids attached to gas bubbles /Neretnieks and Ernstson 1997/. In the study it was assumed that all gas from a damaged canister is released in the form of small bubbles covered with montmorillonite particles from the bentonite buffer. The clay was further assumed to have sorbed radionuclides from the leaching of the fuel. The particles were assumed to remain irreversibly bound to the bubbles, while all gas was assumed to reach the ground surface. The actinides remained irreversibly bound to the clay particles, while caesium and strontium desorbed from the bentonite clay and underwent matrix diffusion combined with sorption during transport through the rock. The results of the calculations showed that the releases to the biosphere were very limited for all nuclides even with these very pessimistic assumptions.

5.5 Summary of issues relating to far field gas migration at Forsmark

In this section (Section 5), aspects are addressed of the consequences of the production of gas from iron corrosion in the small proportion of canisters (< 0.1%) that it is considered may have manufacturing defects that will allow water ingress. The main issues considered are:

a) The potential rate of gas generation from a defective canister (necessary in order to assess the effects of this gas generation).

b) The fate of gas in the geosphere (gas migration through bentonite buffer is part of buffer performance assessment and is considered elsewhere).

c) The transport of volatile radionuclides by migrating gas.

d) The effect of migrating gas on groundwater flow and the transport of dissolved radionuclides.

Gas is generated in defective canisters by anaerobic corrosion of the cast iron insert as a result of water ingress through the defect. The rate of gas generation is determined by the iron corrosion rate, the iron surface area exposed to water, and the availability of water. The corrosion rate of cast iron, once a passivating layer has formed, has been measured at 0.1 μm y^{-1}. At this corrosion rate and assuming that the whole surface of the iron insert is exposed to an unlimited supply of water, the rate of hydrogen production would be $2.1 \cdot 10^{-2}$ $m^3 y^{-1}$ at STP. This is an upper bound to the rate of gas production from a canister as in practice there are a number of factors which will limit the production of gas.

Water availability from ingress through the defect in the canister will be limited by the flow capacity of the bentonite, the build up of gas pressure in the canister opposing water ingress through the defect, and the capacity of the geosphere to supply groundwater:

a) The constraint on water flow through the bentonite is estimated to limit gas production to about $5.4 \cdot 10^{-3}$ $m^3 y^{-1}$ at STP.

b) The build up of gas pressure will limit liquid water ingress through the defect, reducing the influx by an order of magnitude over an estimated 15,000 years after the bentonite buffer has become resaturated and water ingress into the canister has begun. Eventually the influx of liquid water will become so low that the diffusion of water vapour through the defect will become the main mode of water ingress into the canister. The maximum gas generation rate that can be supported by water vapour diffusion through the defect is estimated to be $2.2 \cdot 10^{-5}$ $m^3 y^{-1}$ at STP.

c) The capacity of the geosphere to supply groundwater to support corrosion in a defective canister will vary substantially between deposition holes because it depends on the nature and number of flowing fractures intersecting the deposition hole. For a very small proportion of the deposition holes, the available local groundwater flow may be sufficient to support corrosion at the measured unconstrained rate. For most deposition holes this will not be the case, and, on average, constraints on groundwater supply to the deposition hole would limit gas production to $5.0 \cdot 10^{-3}$ $m^3 y^{-1}$ at STP.

Gas generation may also be limited by restrictions on movement of water within a canister, in particularly, in the long term, from the build up of corrosion product.

The net result of the above considerations is that the upper bound gas generation rate of $2.1 \cdot 10^{-2}$ $m^3 y^{-1}$ at STP is unlikely to be realised in most defective canisters whilst these contain only a single small hole. The generation rate for these is unlikely to exceed ~10^{-3} $m^3 y^{-1}$ at STP, and the build of gas pressure is likely to reduce the rate to less than ~10^{-4} $m^3 y^{-1}$ at STP. Bear in mind that no gas escapes from the defective canister until the gas pressure has reached at least hydrostatic. Gas generation will continue, but possibly only at these very low rates, for at least 250,000 years.

Should the build up of corrosion product, or some other event, produce a larger hole in a canister, some of the above constraints would have less effect; in particular, the build up of gas pressure may not limit water ingress so effectively. It has been estimated that it would take 200,000 years before the build up of corrosion product would start to disrupt a canister. Even if an enlarged defect were formed, water supply from the geosphere would still limit water supply to most defective canisters so that the gas generation rate would generally be less than $\sim 10^{-3}$ $m^3 y^{-1}$ at STP.

The amount of gas that would be trapped in backfilled tunnels on repository closure is significant, on a repository scale, compared with that produced from corrosion in a defective canister. $2.5 \cdot 10^4$–$5 \cdot 10^4$ m^3 of air at surface conditions would be trapped per *defective* canister in tunnels. This is more than the $5.9 \cdot 10^3$ m^3 of gas at STP that could be produced from each defective canister. However, the gas from a defective canister may not enter a tunnel or disperse along a tunnel very far from the location of the canister, and the volume of gas produced in a defective canister is substantially more than that trapped in the segment of the tunnel local to that borehole. The gas trapped in a tunnel will largely dissolve as the tunnel resaturates and the pressure is restored to hydrostatic.

The quantities of natural gases dissolved in the groundwater at Forsmark are assessed as unlikely to have a significant effect on repository performance.

Gas released from a defective canister needs to pass through the bentonite buffer if it is to escape from the vicinity of the canister. Even at the constrained gas generation rates discussed above, gas transport through the bentonite by diffusion in solution from the small defect will be inadequate to remove all the gas generated. However, if the gas pressure opens a gap between the canister and the buffer into which the gas can spread, the contribution of diffusion of dissolved gas to gas transport through the buffer may become more significant. In any event, is expected that, if the gas pressure rises sufficiently, movement of a free gas phase through the bentonite buffer will occur.

Once the gas has passed through the bentonite, it might collect in the tunnel and the EDZ associated with the tunnel, and it might enter the fracture network either from the tunnel or directly from the deposition hole. Some of the gas will dissolve in the groundwater and be transported away by the groundwater flow. However, the groundwater flow at the repository depth is very slow, and it is unlikely that gas generated at the upper bound generation rate of $2.1 \cdot 10^{-2}$ $m^3 y^{-1}$ at STP could all dissolve and be transported away in groundwater flowing through the neighbourhood of the repository. If, as seems quite probable for most defective canisters, the gas release rate is 1–2 orders of magnitude less than the upper bound, it is possible that much if not all of the gas could be transported away in solution. A difficulty in demonstrating how much gas might dissolve is in establishing the degree of contact between the gas and water phases, particularly in a fracture network.

Depending on the degree of contact between the migrating gas and the groundwater, and on the groundwater flow rates in the rock between the repository and the surface, more gas might disperse into solution during its migration to the surface. If flowing groundwater to a width of 4 cm normal to the horizontal component of the groundwater flow direction becomes saturated with gas, then the gas from a single canister produced at $2.1 \cdot 10^{-2}$ $m^3 y^{-1}$ at STP could all dissolve before it reaches the surface.

Should the gas not all dissolve, simple estimates show that the gas transport capacity of the fracture network, assuming that it is sufficiently connected between the location of the defective canister and the surface, should be more than adequate to easily transport the gas to the surface without any significant increase in gas pressure in the neighbourhood of the repository.

Should free gas phase migration be sustained between the repository and the surface, this would be capable of transporting volatile radionuclides relatively rapidly from the repository to the surface. The only significant such radionuclides identified in the waste canisters are ^{14}C and ^{222}Rn. Direct release of the volatile ^{14}C in defective canisters to the surface has been previously

assessed as not causing a significant radiological hazard and so the capacity of migrating gas to transport this radionuclide is immaterial. Similar conclusions were reached for ^{222}Rn release, although it may be desirable to assess the consequences of ^{222}Rn release into an occupied dwelling.

Migrating gas may also affect the movement of groundwater and hence the transport of dissolved radionuclides. Such transport is mitigated by the following observations:

- With a small defect, it is not possible to get release of dissolved radionuclides and gas at the same time. The situation may be different if a large hole develops.
- Gas migration can only affect transport of dissolved radionuclides released from a nearby different canister, and the probability of two defective canisters being present close together must be quite small..
- Migrating gas is only likely to affect groundwater flows in the neighbourhood of a small number of canisters local to the canister generating gas, and there is a low probability that one of these also may be defective and releasing radionuclides.

6 Thermal effects on groundwater flow and transport

6.1 Background

Spent Fuel disposed in a repository generates heat because of radioactive decay (see Figure 6-1). Although the rate of heat generation initially falls off quite rapidly, the rate remains potentially significant for hundreds of years. The heat will raise the temperature of the rocks and groundwater in the vicinity of the repository. This leads to buoyancy forces that tend to create convection cells with flow up through the repository and down as the water cools at some distance from the repository. This flow will be combined (not linearly) with the flow that would otherwise occur. The modification of the flow would alter the migration paths of radionuclides which leaked from the repository during the period when the buoyancy forces are significant (although leakage during this period is very unlikely). Further, the thermal-buoyancy-driven flow could, in principle, lead to upcoming of salinity beneath the repository, which might affect chemical conditions within the repository. In addition, the increased temperature in the vicinity of the repository will alter the groundwater density and viscosity there, which will also affect the flow.

Thermal effects on groundwater flow and transport were not taken into account in the main calculations for SR-Can, because the effects are expected to be small and to occur predominantly at early times when leakage of radionuclides from the repository is unlikely. However, scoping calculations of the effects were undertaken, and are reported in this section.

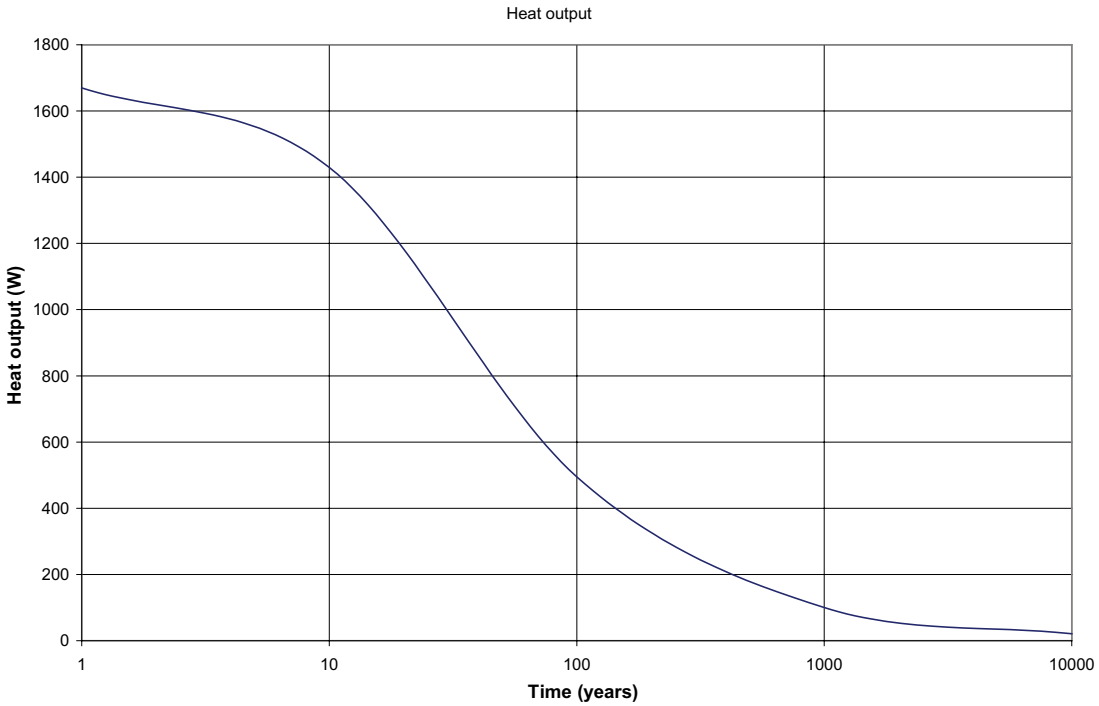

Figure 6-1. *The heat output from a canister as a function of time.*

6.2 Model

The scoping calculations of thermal effects on groundwater flow and transport were undertaken with a slightly refined version of the continuum model used for regional-scale groundwater flow calculations in SR-Can. The refined region of the regional model in the vicinity of the repository was further refined by subdividing vertically, by a factor of 4 to 12.5 m, in each of the two layers of elements (with thickness about 50 m) at depths between 450 m and 350 m (see Figure 6-2). This refinement was made in order to better represent the temperature and groundwater flow in the immediate vicinity of the repository.

The initial conditions for the calculations were obtained from the results of the regional CPM calculations for 2,020 AD. Calculations of coupled groundwater flow and heat transport were made until 6,020 AD. The calculations were carried out for two different conceptual models: CPM and ECPM.

The calculations used the same boundary conditions on flow as the regional calculations. The boundary conditions for heat transport were taken to be a temperature of 6°C on the top surface of the model, a heat flux of $3.4 \cdot 10^{-2}$ Wm^{-2} on the bottom of the model (corresponding to the observed geothermal gradient) and no flux of heat through the vertical sides of the model. The heat output from the Spent Fuel was modelled as a uniform heat source corresponding to the total heat output from the 6,824 canisters in the repository distributed over a rectangular region 1,800 m × 1,500 m × 12.5 m, corresponding approximately to the repository. This was considered to be an appropriate approximation for the scoping calculations, which gives the overall temperature and flow distributions on the scale of the repository, although it does not give accurate representations at early times on the scale of individual canisters.

The calculations represented flow of the four reference waters (Brine, Glacial, Marine and Rain 1960 waters), coupled to heat transport by conduction, which is the main mechanism for heat transport in the rocks of interests. Convection of heat is less important because the flow velocities are low since the rocks are not very permeable. In order to carry out these calculations, the option for modelling transport of reference waters was enhanced appropriately. The development was tested using several test cases, as described in Appendix F.

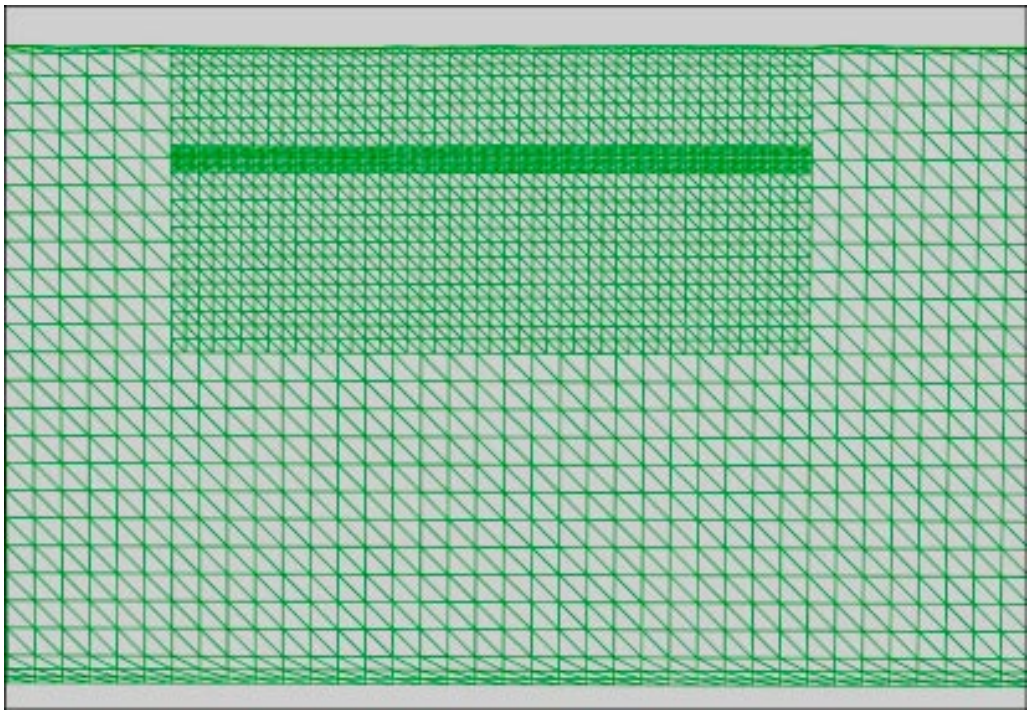

Figure 6-2. *A cross section through the grid on a vertical plane parallel to the N-S axis at Easting 1631850 showing the region of additional vertical refinement (The triangles are an artefact of the program used to plot the grid).*

6.3 Results of calculations

Here, the impact of thermally driven flows is illustrated for both the ECPM reference and CPM base case models. The discussion starts with the CPM model since the homogeneous properties it uses makes it slightly easier to interpret the results.

6.3.1 CPM base case model (SC_HCD3_AC_HRDDT)

The distribution of hydraulic conductivity for the CPM model was illustrated in Figure 3-3. The evolution of the calculated temperature on a vertical plane through the repository are shown in Figure 6-3 and Figure 6-4; and Figure 6-5 shows the temperature evolution on a vertical line through the middle of the repository.

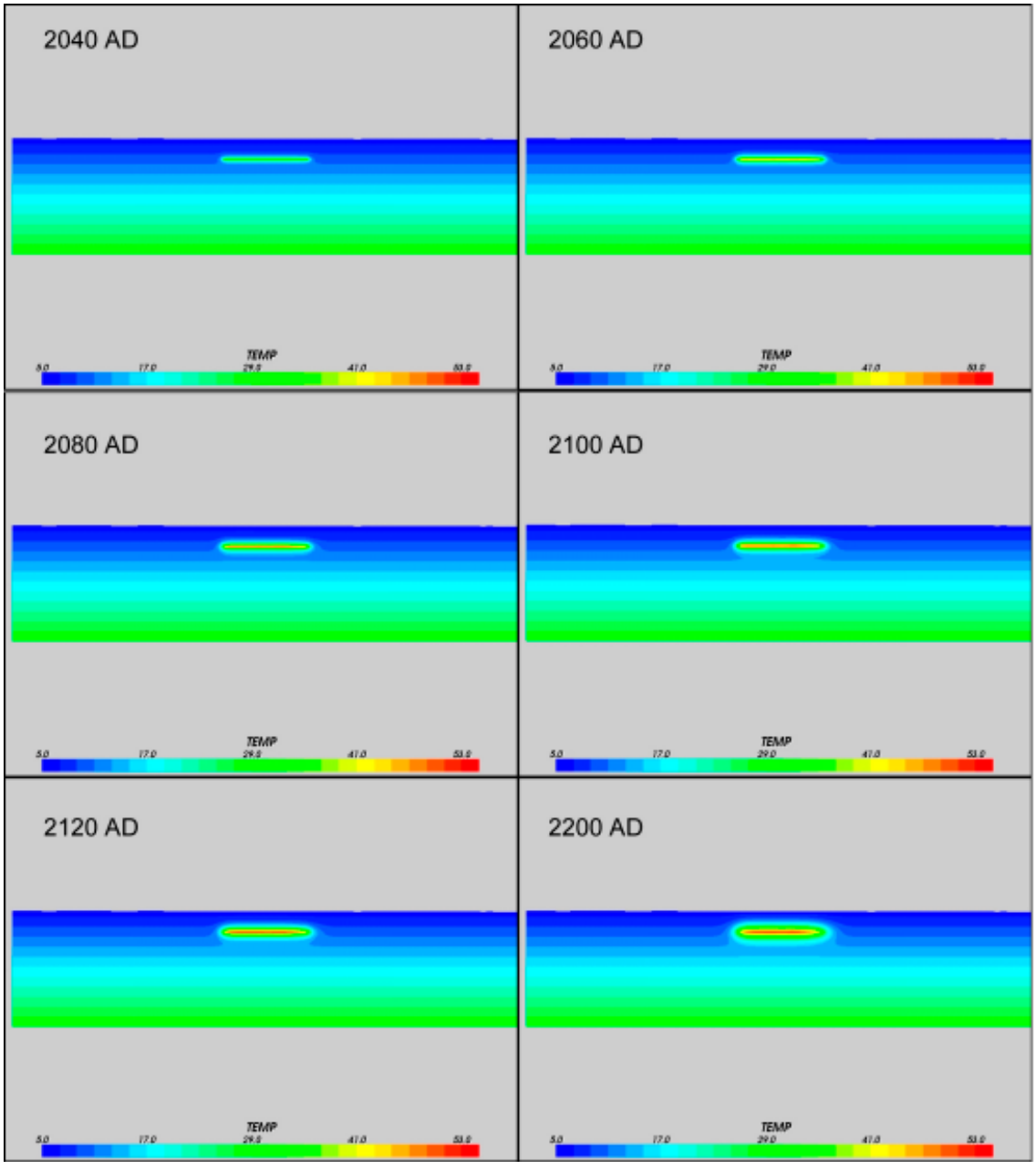

Figure 6-3. *Evolution of the temperature for the CPM model on a vertical plane parallel to the N-S axis at Easting 1631850.*

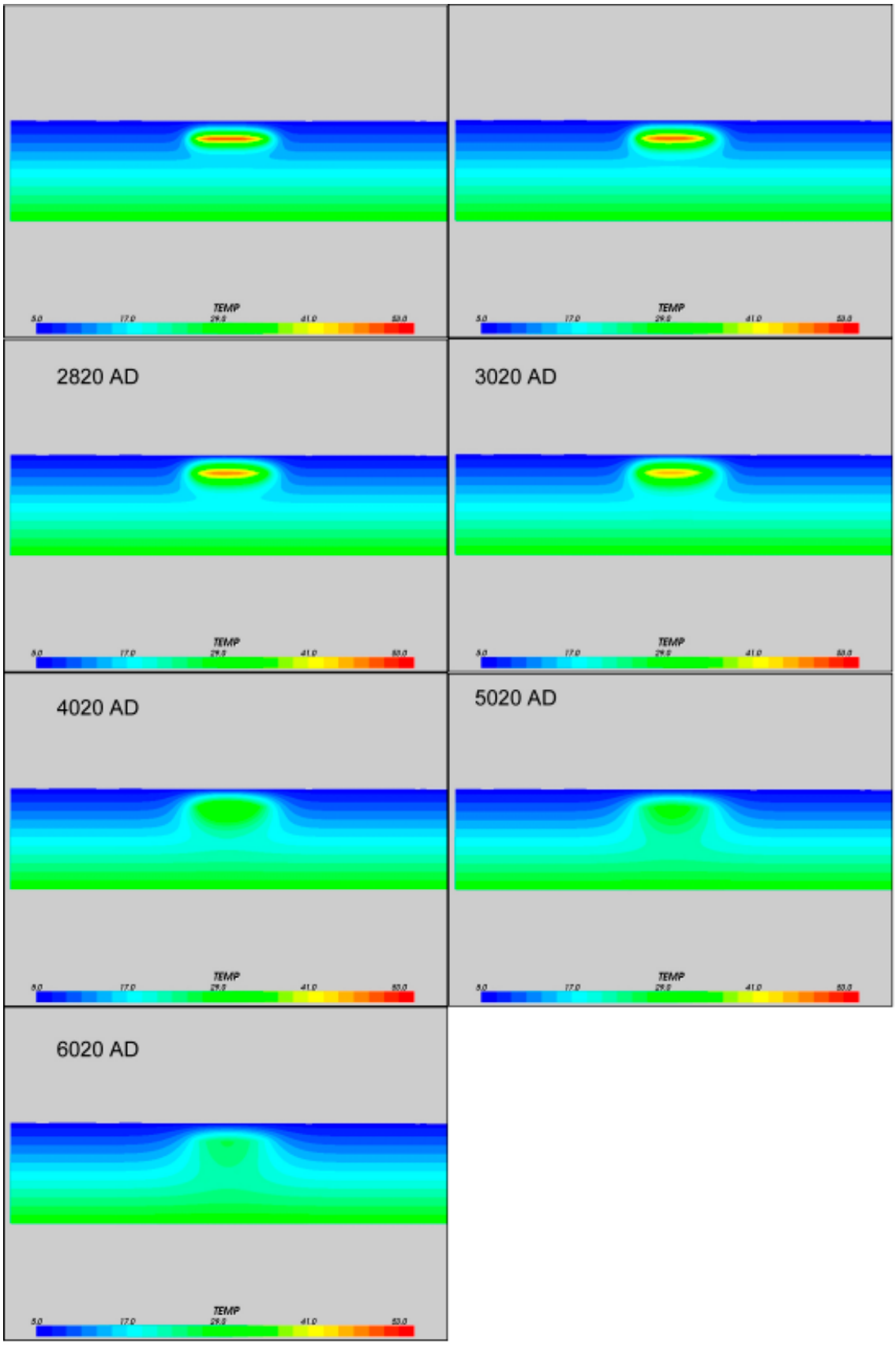

Figure 6-4. *Evolution of the temperature for the CPM model on a vertical plane parallel to the N-S axis at Easting 1631850.*

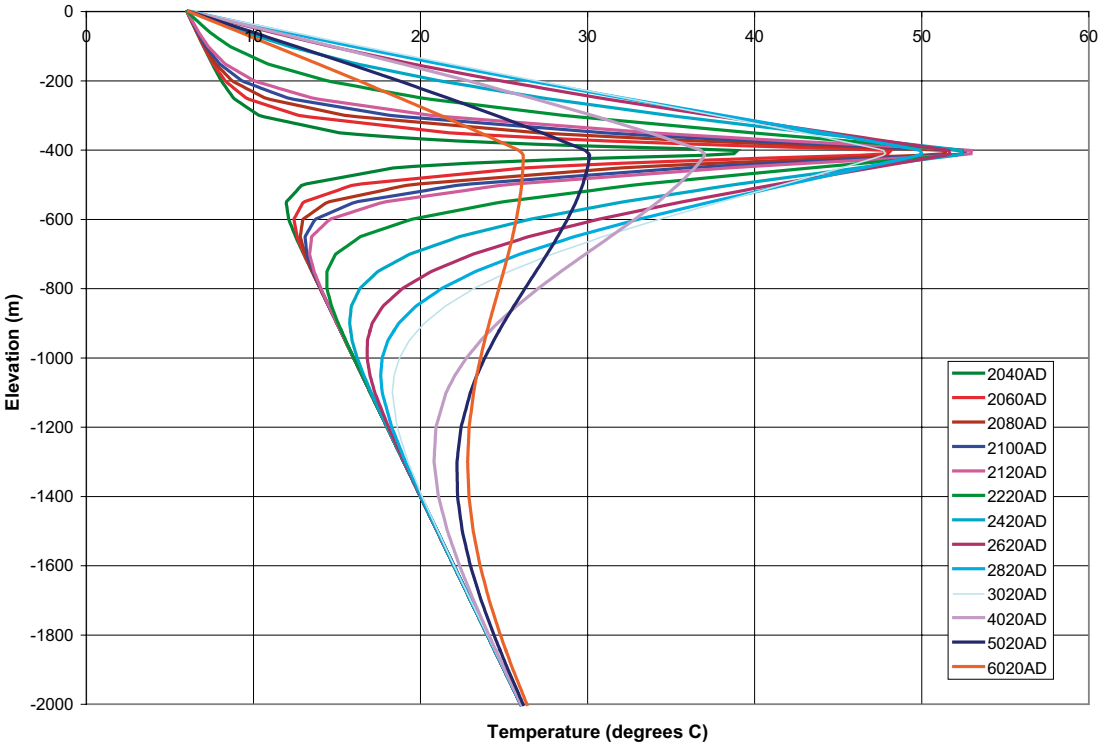

Figure 6-5. *Evolution of the temperature for the CPM model on a vertical line through the middle of the repository.*

Figure 6-6 to Figure 6-9 show the evolution of the flow-field on a vertical plane through the repository. This flow combines the flow driven by thermal buoyancy effects with the flow that would occur in the absence of the heat from the repository. The evolution of the flow-field is further illustrated by Figure 6-10. One potentially important aspect of the flow is the extent to which thermal buoyancy effects lead to an upward component to the flow in the vicinity of the repository. This is shown in Figure 6-10, which presents the evolution of the average vertical component of the flow calculated for 11×11 grids of points at several levels above and below the repository.

As can be seen from Figure 6-10, thermal effects have a significant impact on the flow in the immediate vicinity of the repository, which persists for hundreds of years, although the resulting flow is of a similar magnitude to the flow calculated without taking thermal effects into consideration. Further, as can be seen from Figure 6-6 to Figure 6-10, there are, in a sense, two contributions to the flow resulting from thermal effects. As well as the upward buoyancy-driven flow, there is also a downward contribution to the flow below the repository at early times. It is considered that this is due to thermal expansion of the water within the repository pore space. This leads to a flow directed upwards above the repository and downwards below the repository. The thermal expansion flow is sufficiently strong that the overall flow immediately beneath the repository is directed downwards for about 100 years after repository closure, although it might naively have been expected that thermal effects would lead to an upward flow in the vicinity of the repository. (Similar behaviour is shown by the HYDROCOIN test case discussed in Appendix F, which has an analytic solution.) Although, on average, the downward flow is about an order of magnitude smaller than the upward flow, at particular locations, the downward flow has comparable magnitude to the upward flow. The thermal expansion flow may be particularly significant because the repository is much more porous than the surrounding rocks, and so the expansion of the water within the repository pore space may lead to relatively high flow velocities in the surrounding rock.

It should also be noted that the main impact of thermal effects on the flow may not be the buoyancy forces, but rather the changes to the groundwater density and, particularly, the viscosity. As can be seen from Figure 6-3 to Figure 6-4, elevated temperatures persist in the vicinity of the repository for several thousand years. Even after 4,000 years, the increased temperature is sufficient that the viscosity is reduced by a factor of about two.

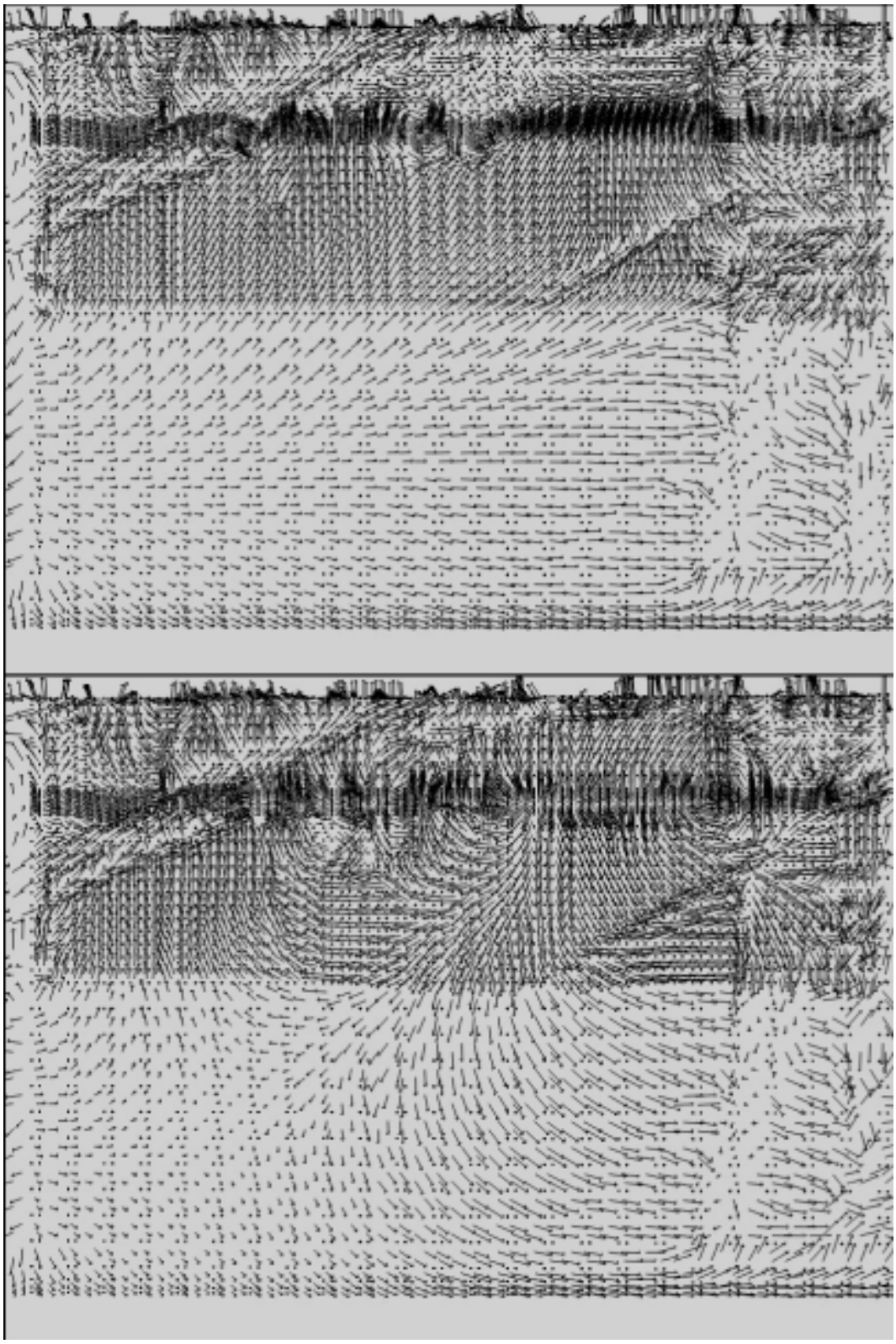

Figure 6-6. *Evolution of the flow-field for the CPM model on a vertical plane parallel to the N-S axis at Easting 1631850 (only the flow direction is shown). Top: 2,040 AD. Bottom: 2,060 AD. One velocity arrow is drawn per finite-element, which means there is a greater density of arrows in the central region where there is more refinement.*

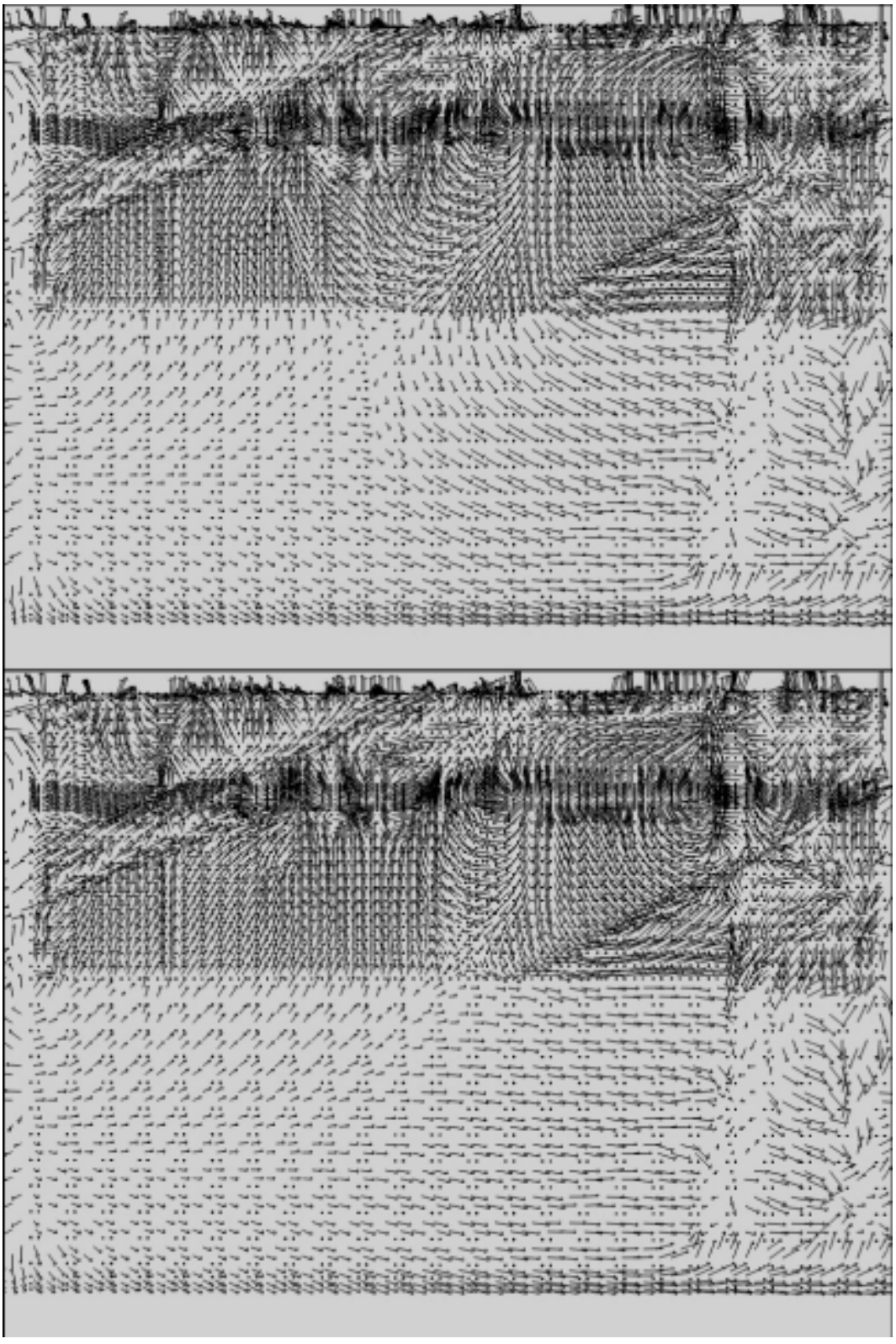

Figure 6-7. *Evolution of the flow-field for the CPM model on a vertical plane parallel to the N-S axis at Easting 1631850 (only the flow direction is shown). Top: 2,080 AD. Bottom: 2,100 AD. One velocity arrow is drawn per finite-element, which means there is a greater density of arrows in the central region where there is more refinement.*

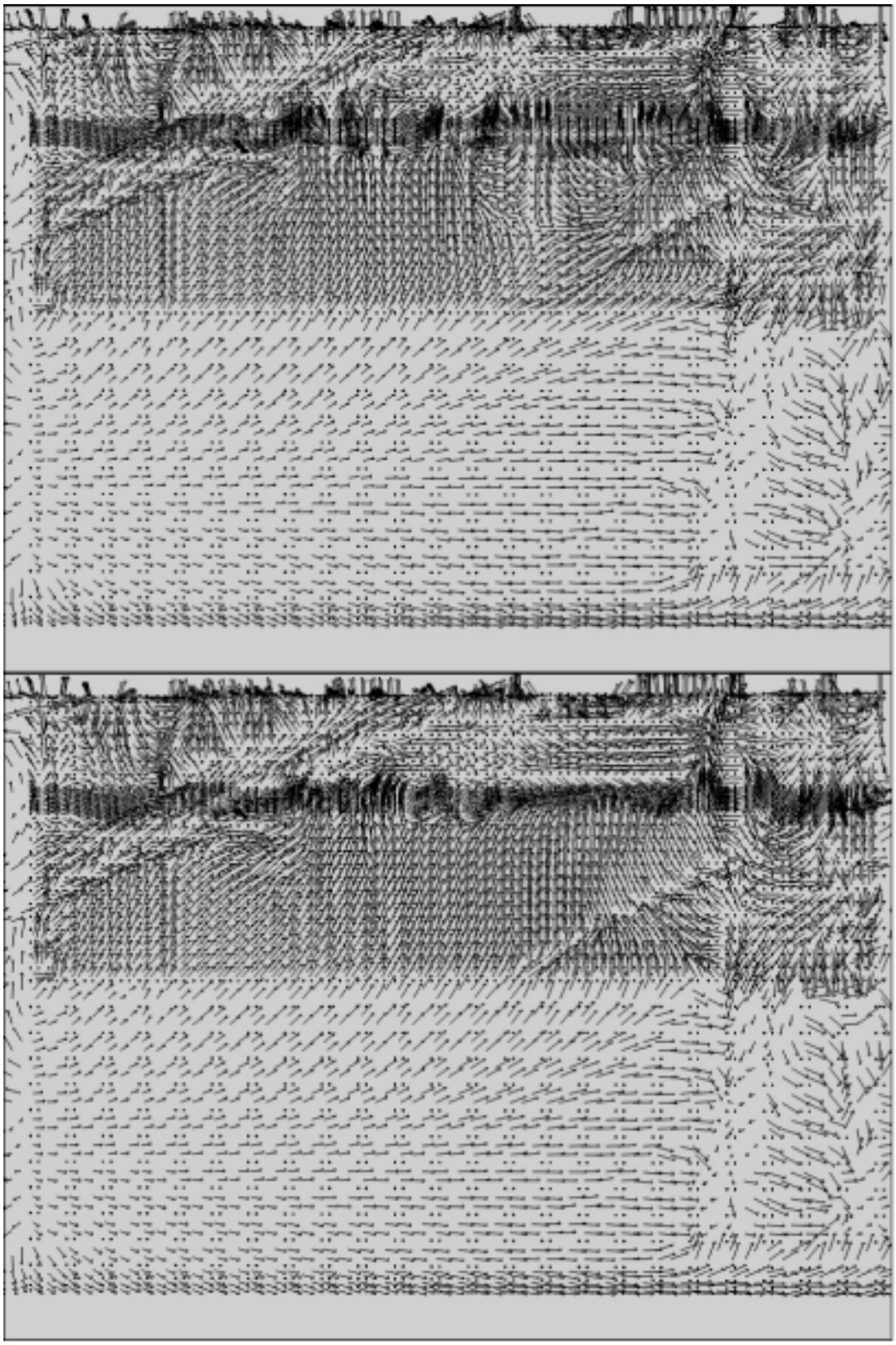

Figure 6-8. *Evolution of the flow-field for the CPM model on a vertical plane parallel to the N-S axis at Easting 1631850 (only the flow direction is shown). Top: 2,120 AD. Bottom: 2,220 AD. One velocity arrow is drawn per finite-element, which means there is a greater density of arrows in the central region where there is more refinement.*

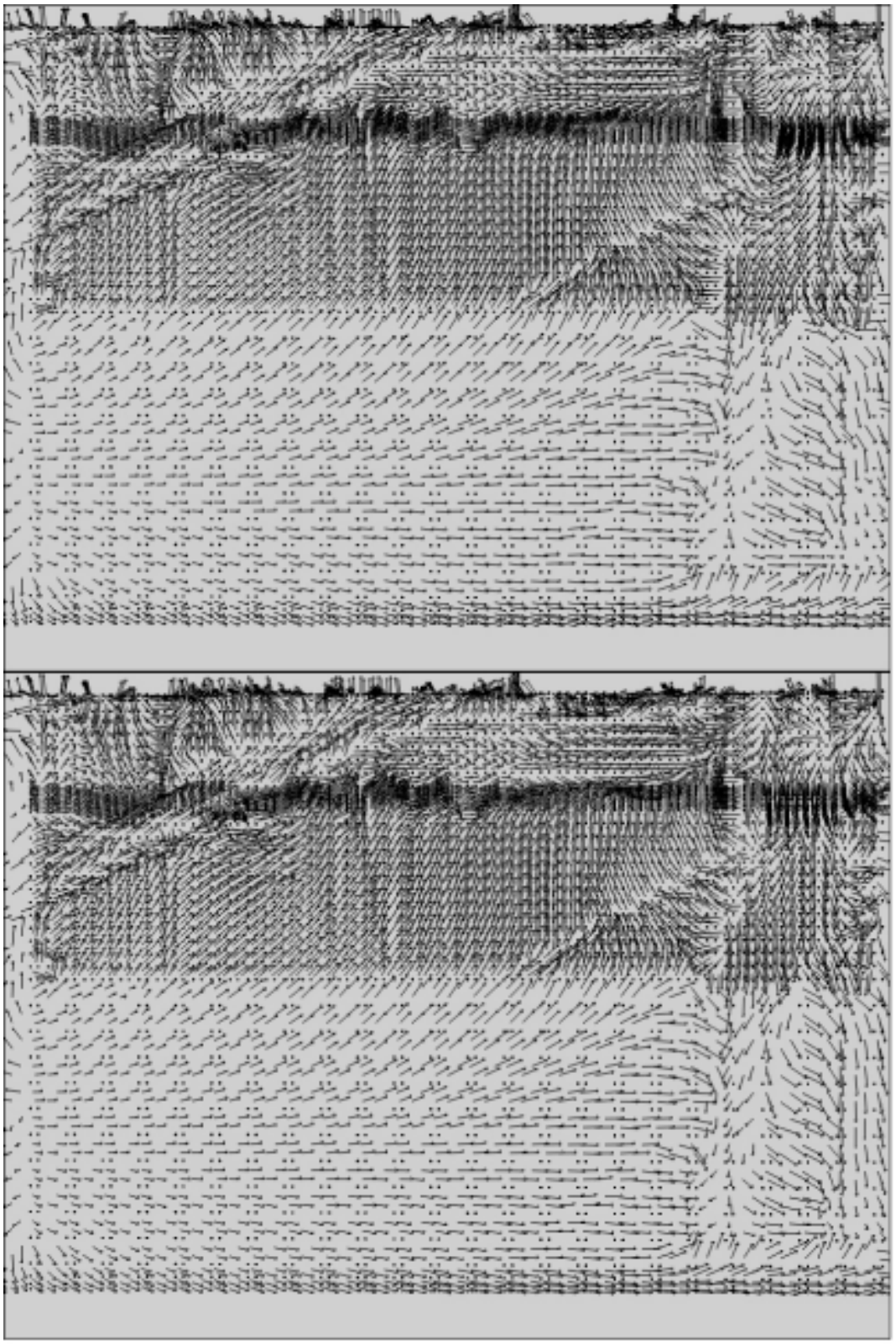

Figure 6-9. *Evolution of the flow field for the CPM model on a vertical plane parallel to the N-S axis at Easting 1631850 (only the flow direction is shown). Top: 2,420 AD. Bottom: 2,620 AD. One velocity arrow is drawn per finite-element, which means there is a greater density of arrows in the central region where there is more refinement.*

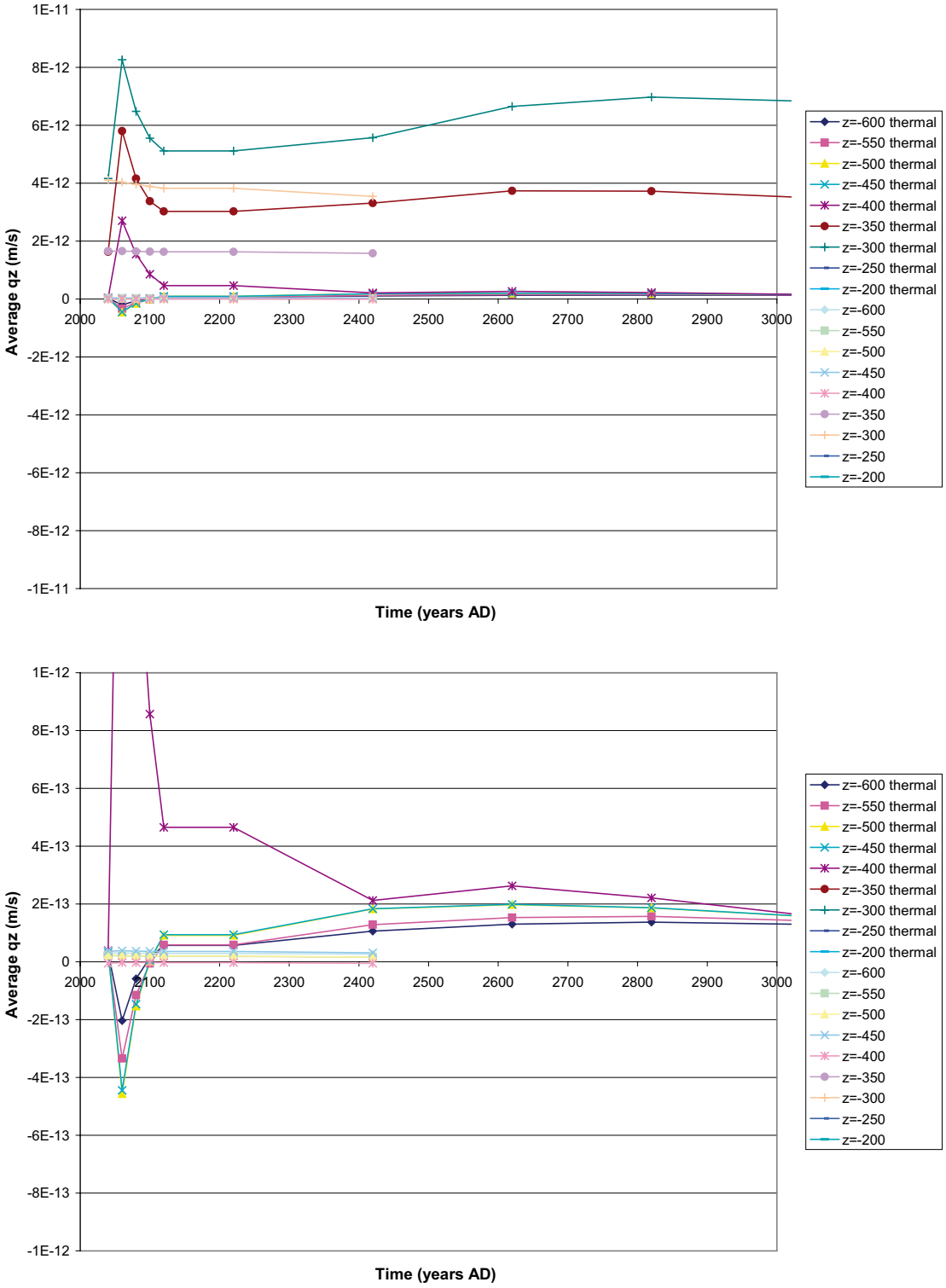

Figure 6-10. *Evolution of the average vertical Darcy velocity for the CPM model on 11×11 grids of points at several horizontal levels above and below the repository. Top: variations on a scale from* -10^{-11} *to* 10^{-11} *m/s. Bottom: variations on a scale from* -10^{-12} *to* 10^{-12} *m/s.*

Figure 6-11 shows the evolution of the salinity (strictly the fraction of the Brine reference water) on a vertical plane through the repository, and Figure 6-12 shows the evolution of the salinity on the vertical line through the middle of the repository. The graph is very uneventful, but the key point is that the profiles of Brine do not change discernibly in time, and hence there is negligible upcoming of the deep brine. This is probably because the increasing salinity with depth effectively provides a stabilising force that counteracts the upward force due to thermal effects.

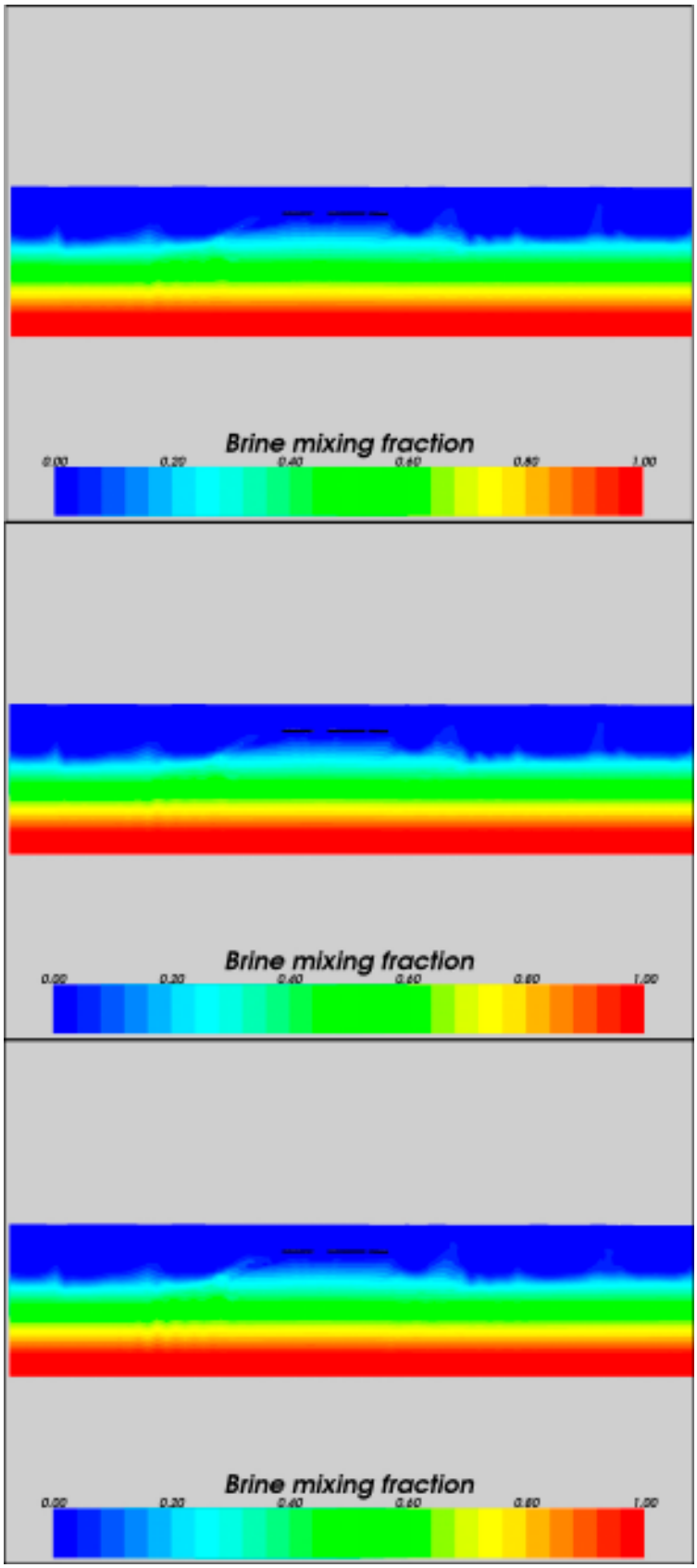

Figure 6-11. *Evolution of the fraction of Brine reference water for the CPM model on a vertical plane parallel to the N-S axis at Easting 1631850. From top to bottom: 2,040 AD, 2,120 AD and 3,020 AD. The repository is in black.*

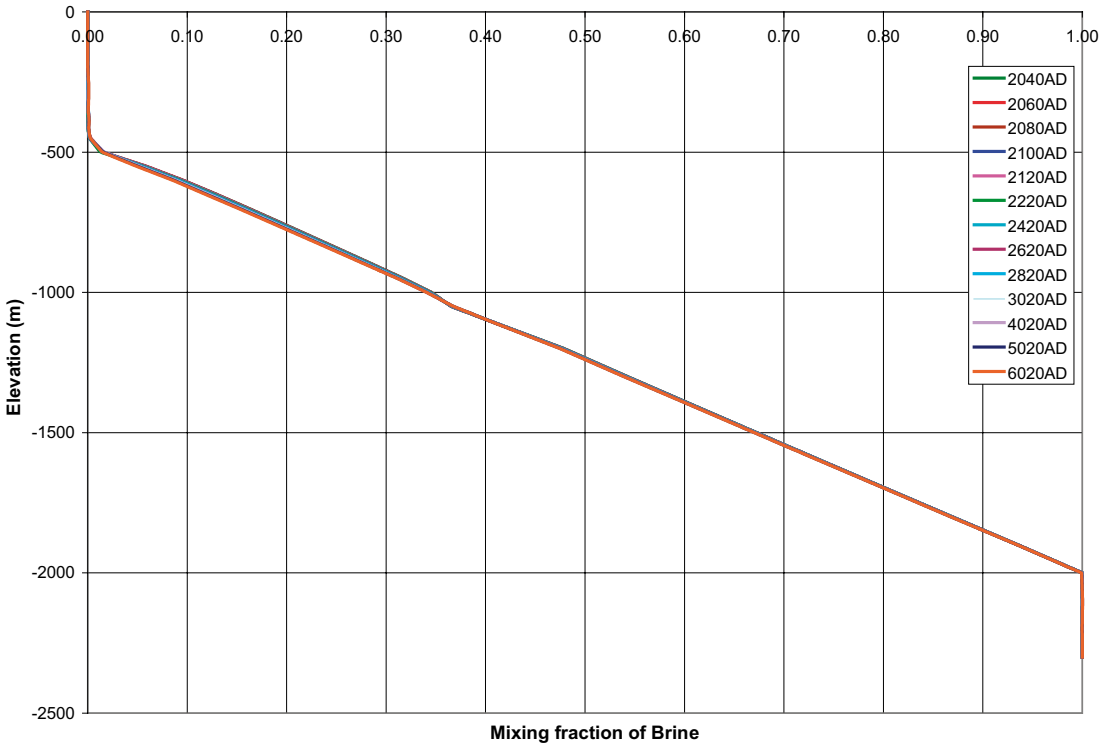

Figure 6-12. *Evolution of the fraction of Brine reference water for the CPM model on a vertical line through the middle of the repository.*

Figure 6-13 and Figure 6-14 show the pathlines calculated for various cases. The pathline calculations for the regional flow model were carried out for constant flow fields at selected times. This was done partly to aid understanding of the results, and partly because calculations for a constant flow field require significantly less computational time than pathline calculations for a transient flow field for the current version of the program CONNECTFLOW used for the calculations. It should also be noted that the pathlines for transient flow fields would be different for different radionuclides, with differing retardations due to sorption. Addressing this would also lead to would also increase the computational time.

Thermal effects lead to flow that changes on a time scale of hundreds of years, which is potentially comparable to pathline travel times. Therefore, most of the pathline calculations for flows affected by thermal effects took the transient nature of the flow field into account. In order to reduce the overall computational time for the calculations, pathlines were only calculated starting from 10% of the canister locations. Further, calculations were only carried out for un-retarded particles and no account was taken of matrix diffusion.

The following point should also be noted. The model uses the ‘Implicit Fracture Zone’ option within CONNECTFLOW to represent transmissive features, which may be much thinner than the dimensions of the elements within the model. In particular, this option is used to represent the repository. The option leads to modified values of the hydraulic conductivity and kinematic porosity for elements crossed by transmissive features. The modified value of the porosity, which will be higher than the porosity of the rock, will lead to longer travel times. These will be more appropriate to transport in the repository tunnels.

In order to illustrate clearly the potential impact of thermal effects on the pathlines, the effect of transmissive features on the porosity of the deep rocks was not taken into account in the pathline calculations. Rather, the calculations used the unmodified porosity. If this were not done, then the porosity for an element crossed by a transmissive feature (such as a repository tunnel) would be much higher. In consequence, if a pathline entered such an element, it would take a long time

to cross it, during which time the thermal effects on the flow would greatly decrease. Although this would give a good representation for a pathline that moved into the transmissive feature itself, it would be less realistic for a nearby pathline in the element that did not move into the transmissive feature.

Because the flow field is changing (on time scales of hundreds of years), the pathlines depend on the starting time. Therefore, pathlines were calculated starting at 2,020 AD, 2,500 AD and 3,000 AD. For comparison, pathlines were also calculated in the constant flow field equal to the flow at 2,020 AD. The results of the pathline calculations are illustrated by Figure 6-13 and Figure 6-14. As can be seen, in the immediate vicinity of the repository, pathlines starting shortly after repository closure are significantly affected by thermal effects. These lead to the pathlines following somewhat different routes in the vicinity of the repository. However, at some distance from the repository, the routes followed are broadly the same. In general, the discharge locations are similar. This is as expected, because the discharge locations are effectively determined by the locations of the surface water bodies at the time of discharge, and these are primarily determined by the surface topography and the sea level.

Figure 6-15 summarises the impact of thermal effects on the travel times. The greatest impact is for pathlines starting shortly after repository closure. The median travel time for such pathlines is reduced by a factor of more than an order of magnitude. However for pathlines starting a few hundred years later, the median travel time is in fact slightly increased by thermal effects.

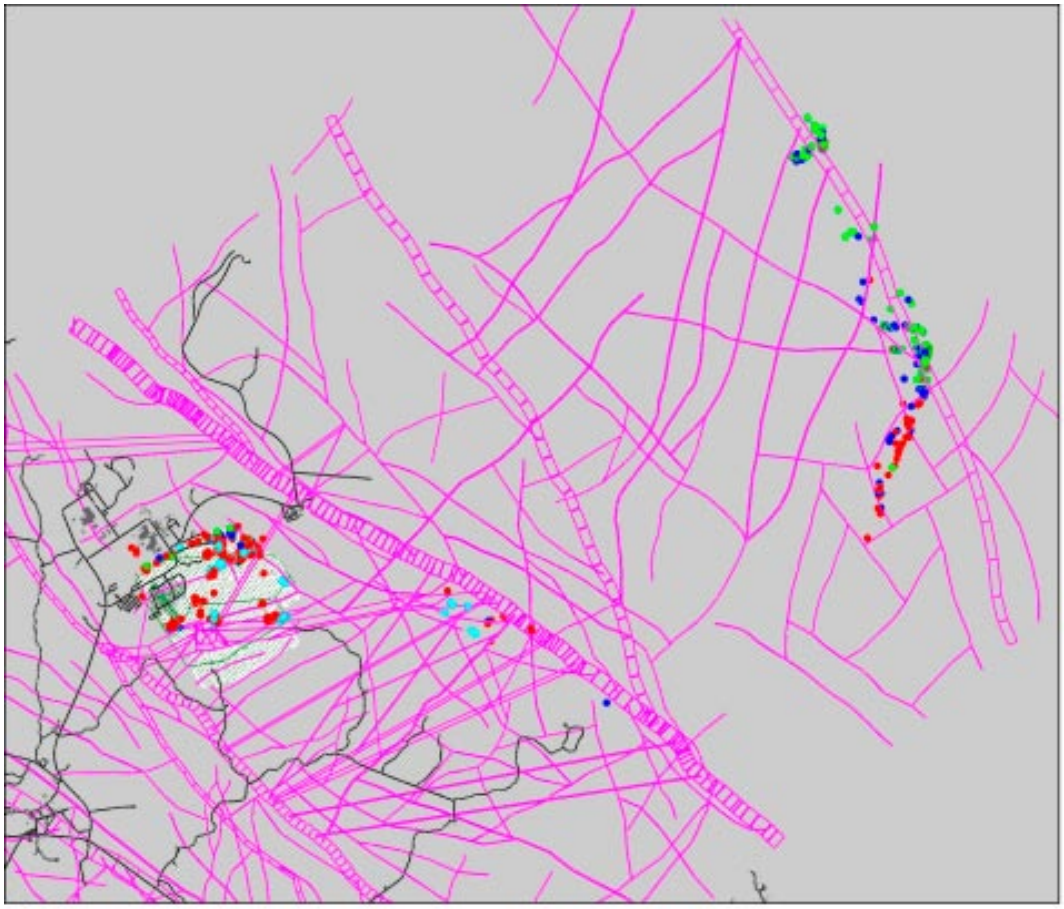

Figure 6-13. *Exit locations for particles for the CPM base case. Light blue – particles in the constant flow-field at 2,020 AD; red – particles starting at 2,020 AD in the flow affected by thermal effects; green – particles starting at 2,500 AD in the flow field affected by thermal effects; dark blue – particles starting at 3,000 AD in the flow field affected by thermal effects. The repository is shown in white and roads are shown in black for context.*

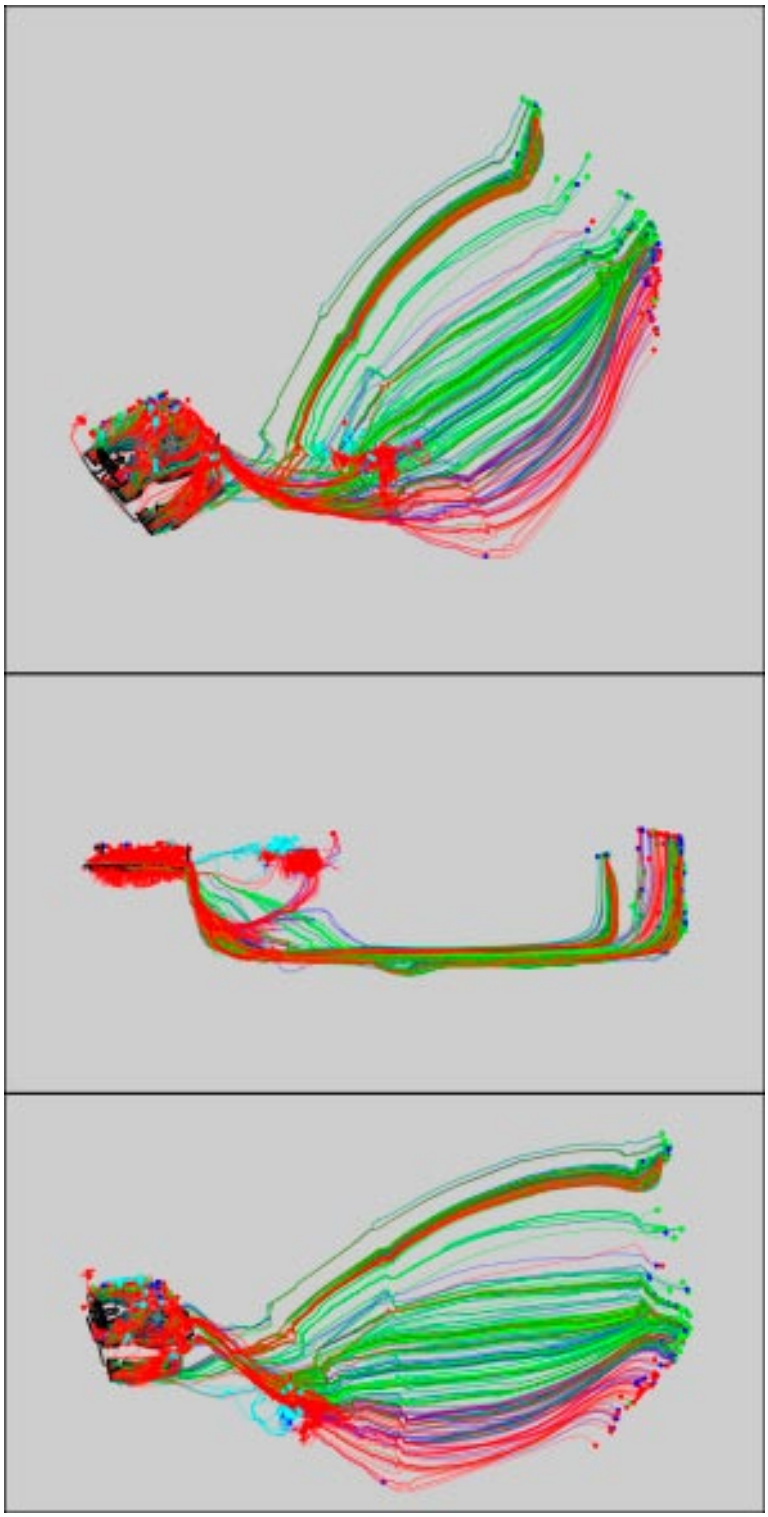

Figure 6-14. *Flow-paths and exit locations for particles for the CPM model. Light blue – particles in the constant flow field at 2,020 AD; red – particles starting at 2,020 AD in the flow affected by thermal effects; green – particles starting at 2,500 AD in the flow field affected by thermal effects; dark blue – particles starting at 3,000 AD in the flow field affected by thermal effects. Top – oblique view; middle – side view; bottom – plan view. The repository is shown in black for context.*

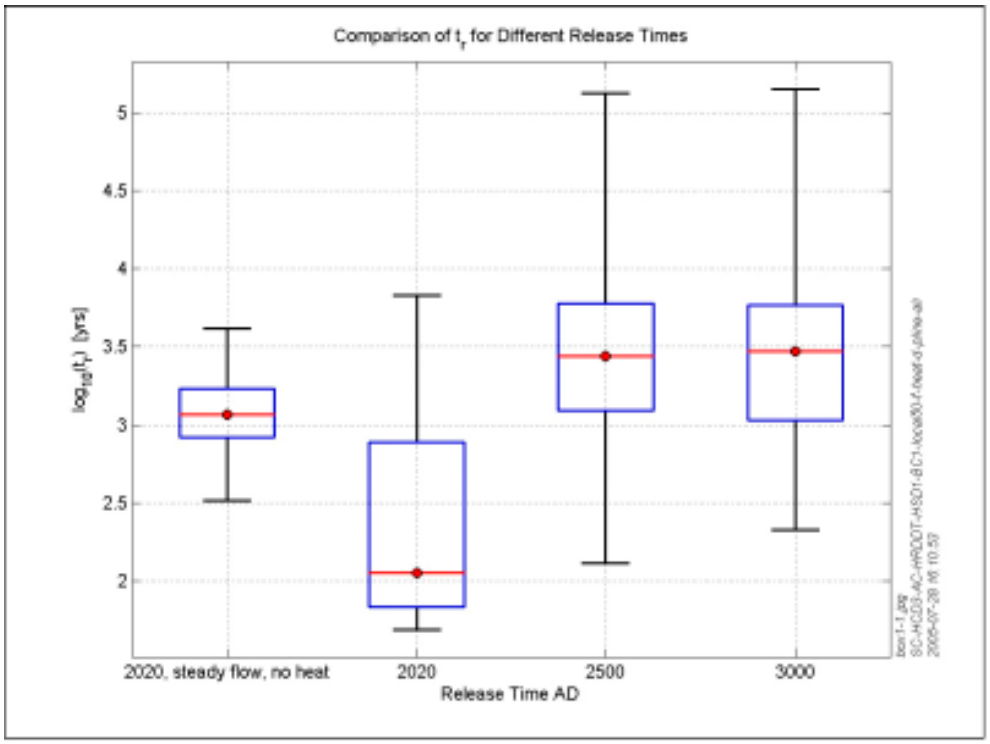

Figure 6-15. *Comparison of the distributions of travel time for the various cases for the CPM model.*

6.3.2 ECPM reference case model (SC_HCD3_AC_HRD3EC)

The distribution of hydraulic conductivity for the ECPM model was illustrated in Figure 3-1. The evolution of the distribution of temperature for this case is, of course, the same as that for the CPM model (shown in Figure 6-3 and Figure 6-4), because only heat transport by conduction is modelled and the thermal properties of the rocks are the same for both cases. The evolution of the flow-field for this model is shown in Figure 6-16 to Figure 6-19, and the evolution of the average flow on 11×11 grids of points at various levels in the vicinity of the repository is shown in Figure 6-20. Interestingly, Figure 6-20 does not show the downward velocities immediately below the repository at early times. It is considered that this is probably because the rock is much more permeable for this case, and as a result the flows are larger, and the early time period in which the thermal expansion flow would be apparent is shorter than the time step used.

The results of the pathline calculations are illustrated by Figure 6-21 and Figure 6-22. Again, in the immediate vicinity of the repository, pathlines starting shortly after repository closure are significantly affected by thermal effects. These lead to the pathlines following somewhat different routes in the vicinity of the repository. However, at some distance from the repository, the routes followed are broadly the same. In general, the discharge locations are similar.

Figure 6-23 summarises the impact of thermal effects on the travel times. Again, the median travel time for pathlines starting shortly after repository closure is reduced compared to that for pathlines in the constant flow field at 2,020 AD. However, the greatest impact in this case appears to be for pathlines starting at 2,500 AD.

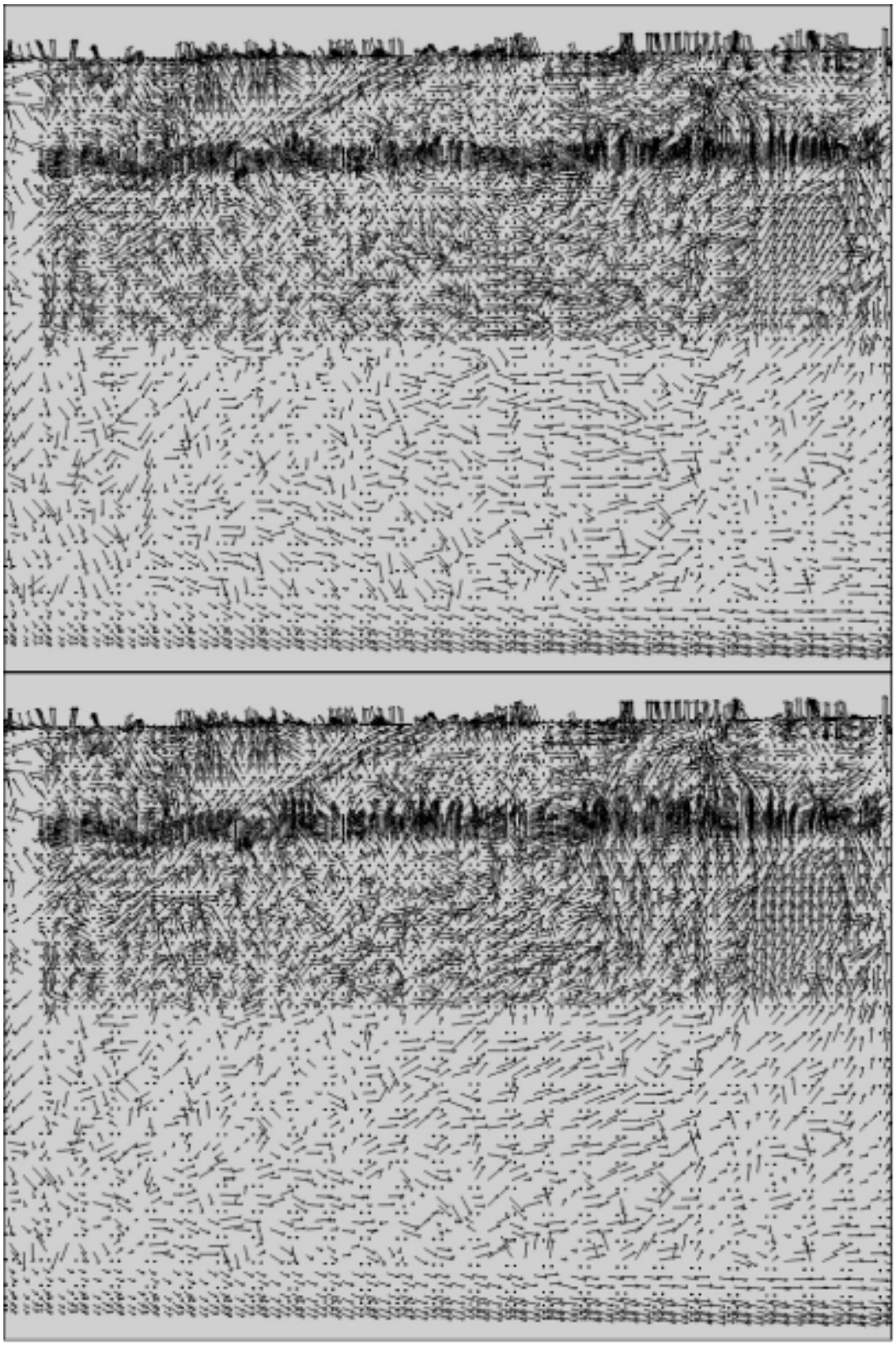

Figure 6-16. *Evolution of the flow-field for the ECPM model on a vertical plane parallel to the y-axis at an x-coordinate of 1631850 (only the flow direction is shown). Top: 2,040 AD. Bottom: 2,060 AD. One velocity arrow is drawn per finite-element, which means there is a greater density of arrows in the central region where there is more refinement.*

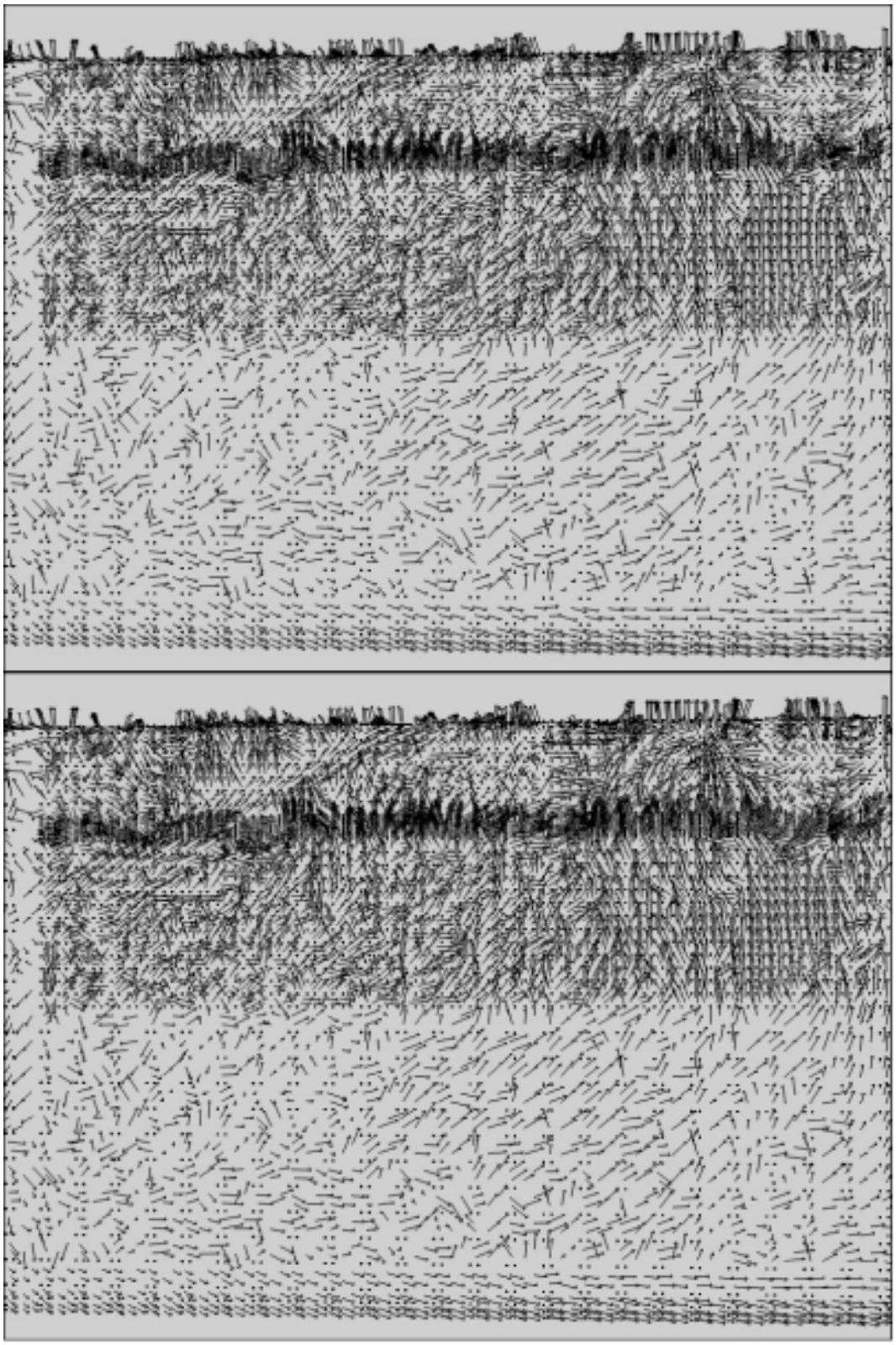

Figure 6-17. *Evolution of the flow-field for the ECPM model on a vertical plane parallel to the y-axis at an x-coordinate of 1631850 (only the flow direction is shown). Top: 2,080 AD. Bottom: 2,100 AD. One velocity arrow is drawn per finite-element, which means there is a greater density of arrows in the central region where there is more refinement.*

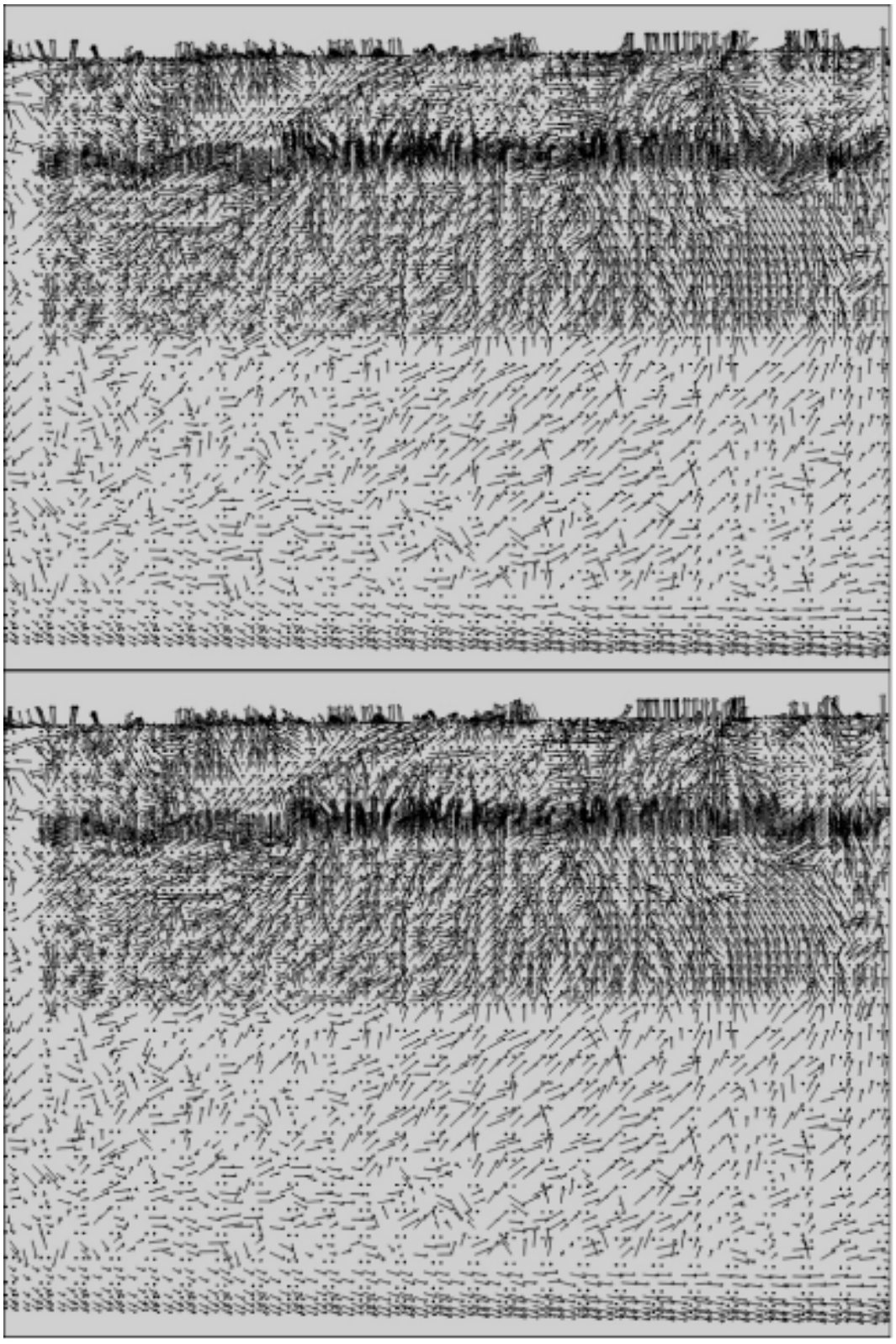

Figure 6-18. *Evolution of the flow-field for the ECPM model on a vertical plane parallel to the y-axis at an x-coordinate of 1631850 (only the flow direction is shown). Top: 2,120 AD. Bottom: 2,220 AD. One velocity arrow is drawn per finite-element, which means there is a greater density of arrows in the central region where there is more refinement.*

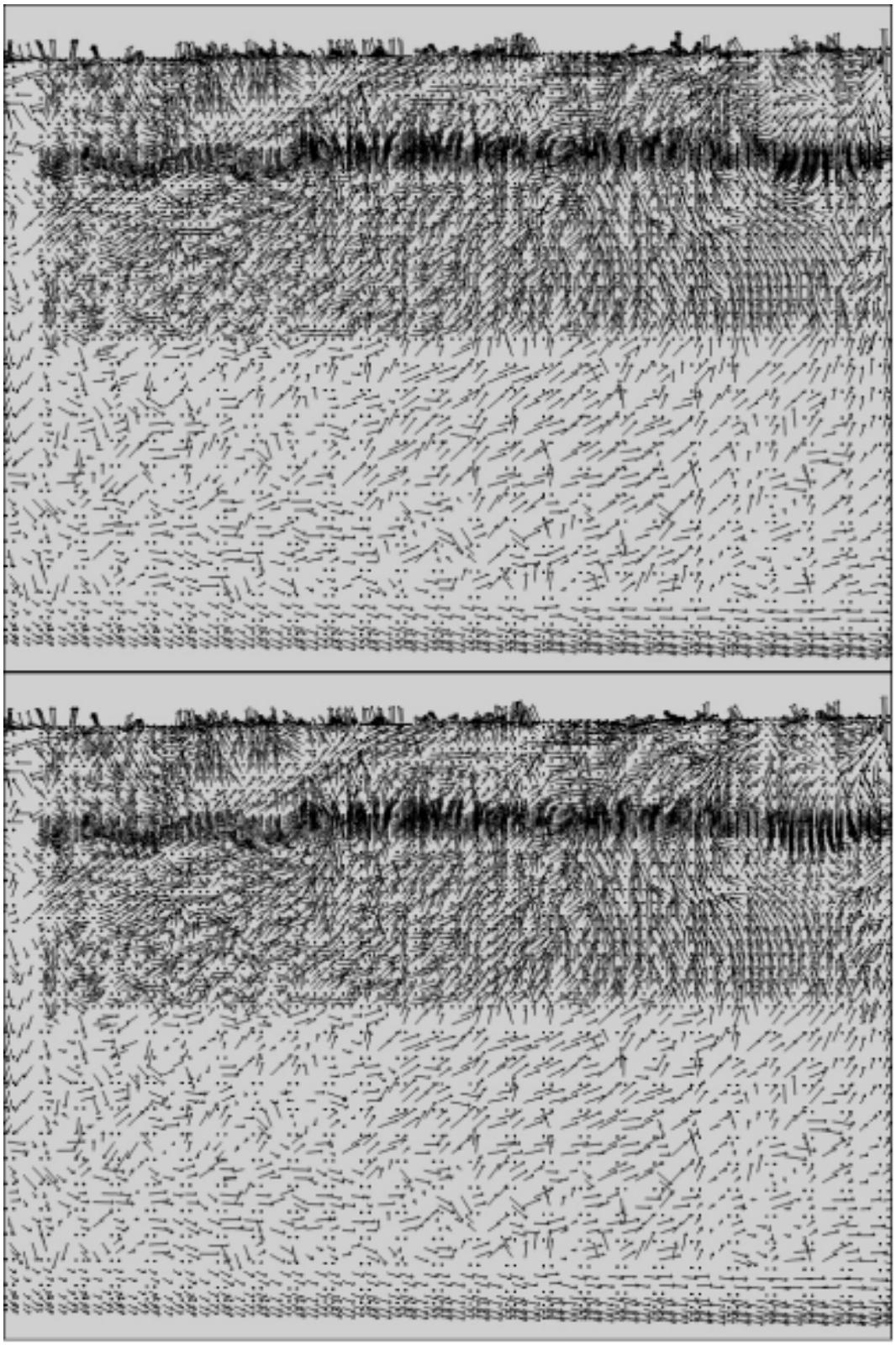

Figure 6-19. *Evolution of the flow-field for the ECPM model on a vertical plane parallel to the y-axis at an x-coordinate of 1631850 (only the flow direction is shown). Top: 2,420 AD. Bottom: 2,620 AD. One velocity arrow is drawn per finite-element, which means there is a greater density of arrows in the central region where there is more refinement.*

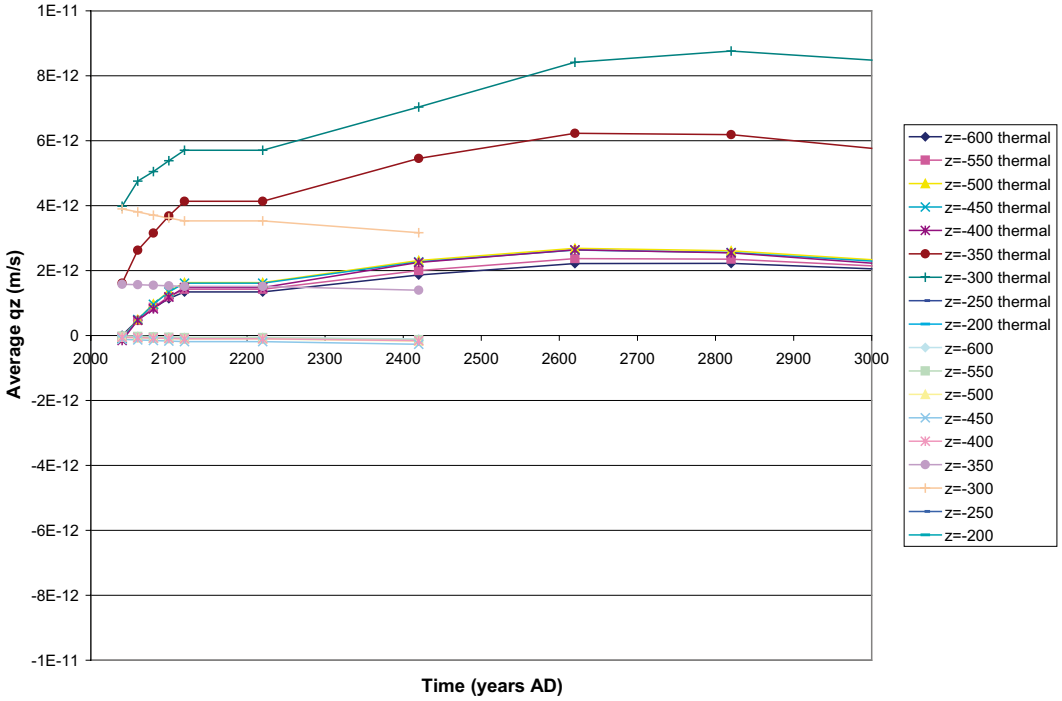

Figure 6-20. *Evolution of the average vertical Darcy velocity for the ECPM model on 11×11 grids of points at several horizontal levels above and below the repository.*

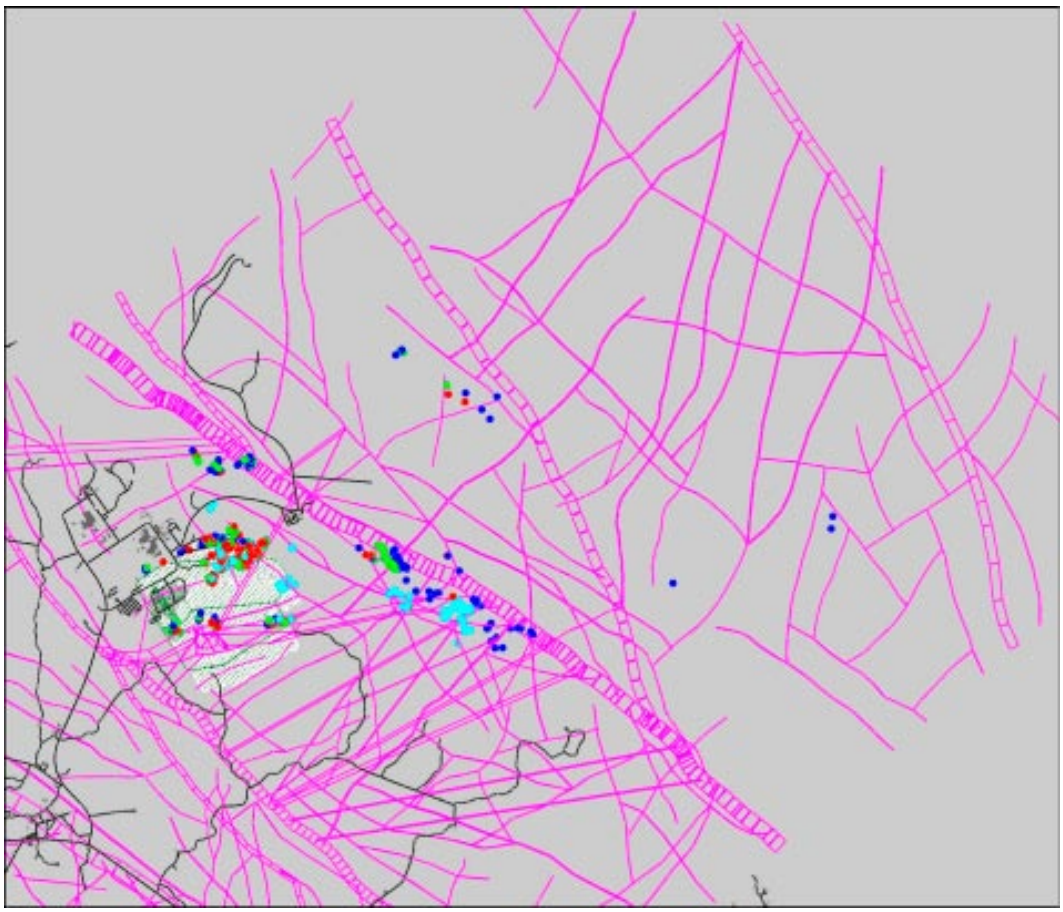

Figure 6-21. *Exit locations for particles for the ECPM model. Light blue – particles in the constant flow-field at 2,020 AD; red – particles released at 2,020 AD in the flow-field affected by thermal effects; green – particles released at 2,500 AD in the flow-field affected by thermal effects; dark blue – particles released at 3,000 AD in the flow-field affected by thermal effects. The repository is shown in white and roads are shown in black for context.*

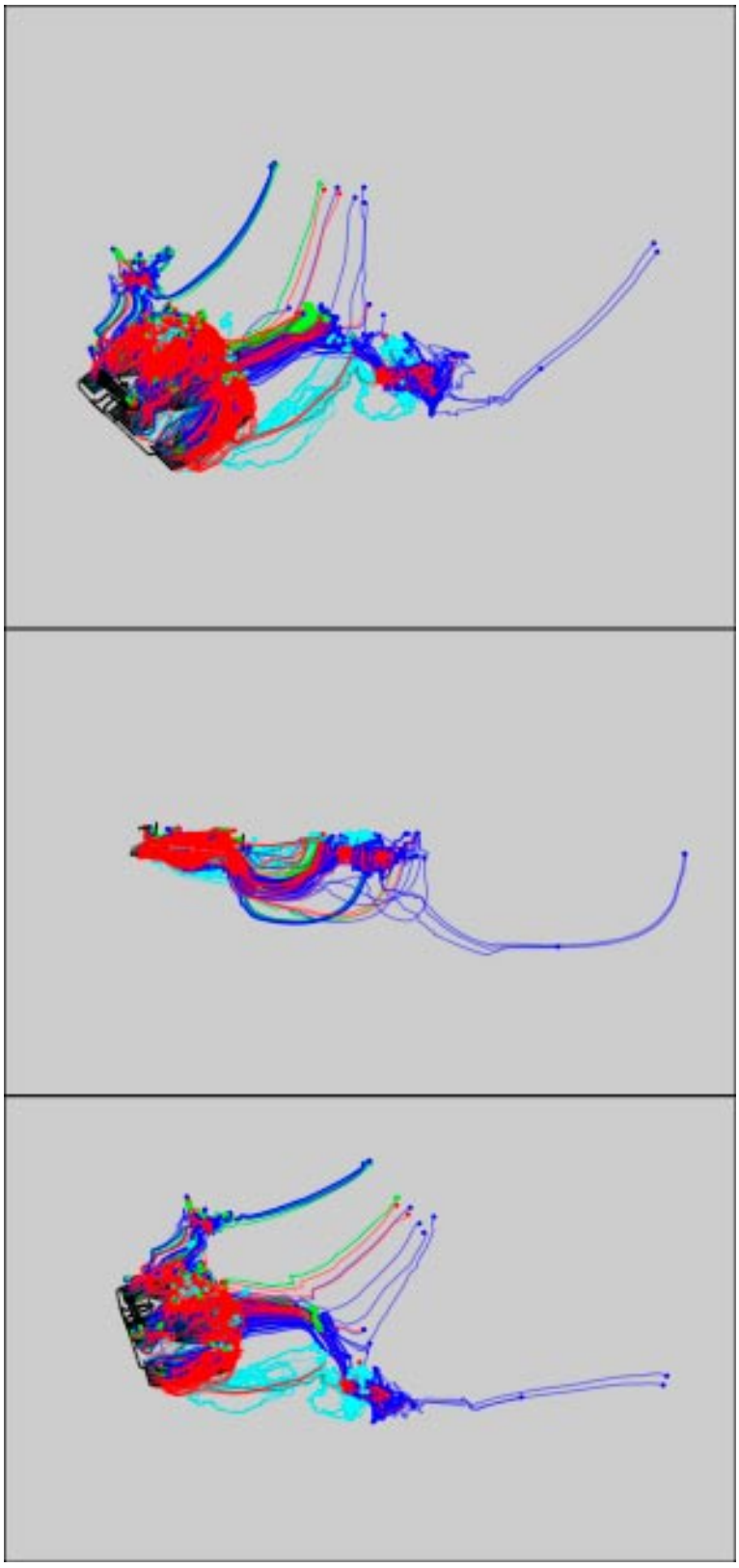

Figure 6-22. *Flow-paths and exit locations for particles for the ECPM reference case. Light blue – particles in the constant flow field at 2,020 AD; red – particles released at 2,020 AD in the flow-field affected by thermal effects; green – particles released at 2,500 AD in the flow-field affected by thermal effects; dark blue – particles released at 3,000 AD in the flow-field affected by thermal effects. Top – oblique view; middle – side view; bottom – plan view. The repository is shown in black for context.*

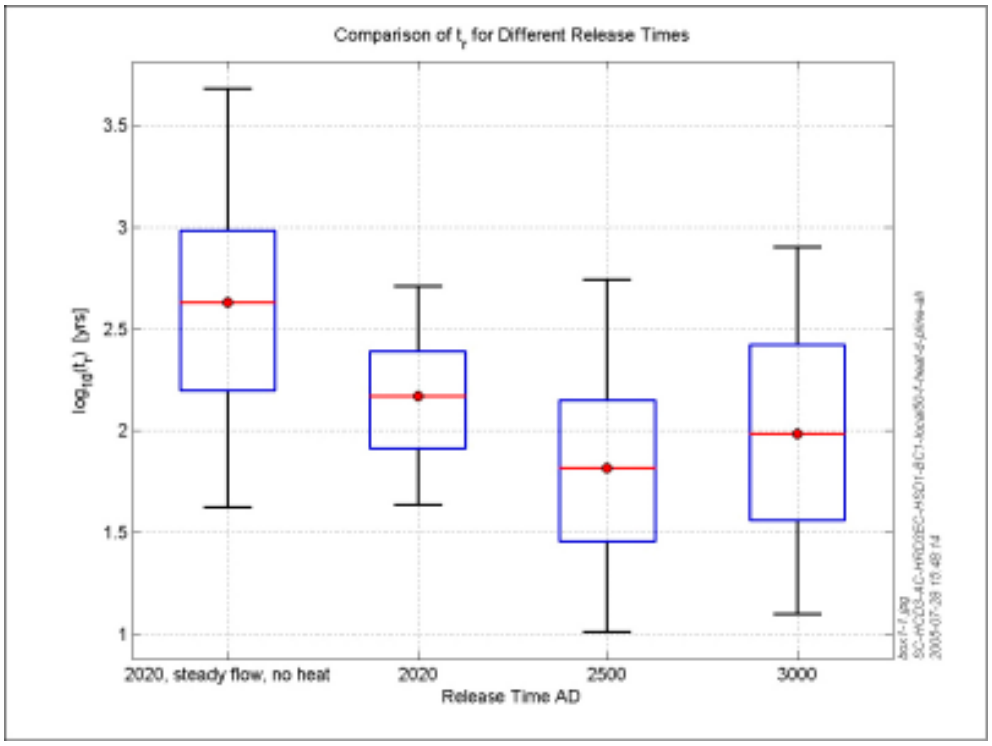

Figure 6-23. *Bar and whisker-plots to compare distributions of travel time for the different release times in the ECPM model.*

6.4 Discussion

The results presented here show that thermal effects can potentially have a moderate impact on groundwater flow and transport from a repository. The flow-paths can be significantly modified in the immediate vicinity of the repository. The potential effects are greatest for radionuclides released from the repository shortly after repository closure, but such releases are very unlikely. However, the discharge locations are not greatly effected, because these are determined by the location of surface water bodies, which are determined by lows in the surface topography and by sea level. Possibly the most important impact of thermal effects might be due to their effect on the groundwater viscosity, which might be reduced by a about a factor of two in a region around the repository for many thousands of years. This effect possibly ought to be taken into account in the PA transport calculations.

However, the results presented here potentially over-estimate the impact of thermal effects for several reasons. The calculations have not taken into account the long times spent in the repository tunnels. During such times, the impact of thermal effects would be reduced, because of the decay of the heat source (although the temperature remains elevated for long times). Similarly, the calculations have not taken retardation due to sorption or to rock-matrix diffusion into account. Again, the impact of thermal effects would be reduced if these effects were taken into account.

7 Conclusions

This hydrogeological study of F 1.2 within the SR-Can project has considered three main issues:

1. Groundwater flow and transport from a repository to the surface to provide input to PA calculations.
2. An assessment of gas generation, migration and its potential effect on groundwater flow.
3. An assessment of the potential effects of heat generation on groundwater flow and hydro-geochemistry.

The findings are summarised below.

7.1 Conclusions for groundwater flow

As part of the assessment of the groundwater pathway models on two different scales were constructed: regional-scale transient porous medium models, and more detailed repository-scale steady-state models using both DFN and CPM representations. The regional-scale was used to assess the effects of transient processes such as land-rise and the evolution of hydro-geochemistry coupled to groundwater flow, as well as to perform a sensitivity study of transport performance measures (PMs) to conceptual and parameter uncertainties. The repository-scale modelling was performed with much more detail to resolve the flow around individual deposition holes and calculate flow-paths to the surface for input to PA calculations. For all models, transport was characterised by four main PMs for each canister position in terms of travel-time, initial Darcy velocity, path-length and F-quotient along flow-paths started from each canister position. Additional PMs were derived for the repository-scale models such as distances and travel-times in the EDZ and tunnels. In terms of some basic transport parameters, the Posiva Flow Log (PFL) data and the Hydro-DFN derived in SDM F 1.2 consistently predict a flow-wetted surface a_r=0.2–0.3 m^2/m^3 in the bedrock above and East of deformation zone ZFMNE00A2, and a_r=0.03–0.05 m^2/m^3 in the bedrock below and West of ZFMNE00A2. The spacing of water-bearing fracture along a vertical borehole in the same volumes is about 28 m and 174 m, respectively.

The regional-scale modelling was a natural continuation of the site-modelling study for F 1.2. However, several small but significant changes were made to the model used there to ensure it honoured observed site conditions more realistically. The two key changes were to use a lower flow-wetted surface, a_r=0.25 m^2/m^3 and a multi-component Hydro-DFN model that had modified fracture properties to give lower groundwater below deformations zone ZFMNE00A2 and an elevation of –350 m. Another important decision made in this study was to use the alternative case (AC) geological structural model as the central case for the deterministic deformation zones since this case tends to give shorter flow-paths at future times once the shoreline retreats, and hence its use is conservative. A key aspect of the study was to analyse two alternative conceptual models for hydraulic property assignment based on either an equivalent continuum porous medium model (ECPM) using stochastic Hydro-DFN properties within specified hydrogeological domains, or a simpler continuum porous medium (CPM) model using homogeneous hydraulic properties within specified hydrogeological domains. Transient simulations of coupled groundwater flow and reference water transport with rock matrix diffusion were performed from 8,000 BC until the 2,020 AD at which time a representation of the repository was introduced instantaneous, and then simulations carried on until 9,000 AD. The most significant transient changes were found to take place between 2,020 AD and 3,000 AD as the shoreline retreats from very close to the site to a few kilometres away. Some discharge points at the coast follow the retreat of the shoreline, though a significant number of shorter paths to the immediate surface remain. More moderate changes occur later on as the shoreline retreats further to

several kilometres from the site. Representative times were selected at 2,020 AD, 3,000 AD and 9,000 AD to quantify PMs for use in the streamline based far-field (FARF31) PA transport calculations.

For the homogeneous CPM model the median travel-time is about 4,000 years, initial Darcy velocity is about $1.3 \cdot 10^{-6}$ m/y, and a F-quotient of about $5 \cdot 10^{7}$ y/m for a release at 2,020 AD. For the realistic case ECPM model with a lower fracture transmissivity beneath ZFMNE00A2, the median travel-time is about 2,500 years, an initial velocity of about $5 \cdot 10^{-6}$ m/y, and a F-quotient of about $1.6 \cdot 10^{7}$ y/m for a release at 2,020 AD. For this case, at later times, median travel-time increases by about an order of magnitude, initial velocity increases slightly, while path-length and F-quotient both rise by about an order of magnitude. Hence, the present time is likely to give the highest risk based on a porous medium model since all discharge areas are close to the site at this time. Both of these cases are consistent with the hydraulic data and predict PMs that are similar, though risk is likely to be slightly higher for the ECPM case based on an underlying DFN. There are some other differences between the models, such as flow is more channelised in the ECPM model due to heterogeneities, and flow tends to be shallower in the ECPM model.

A more comprehensive set of sensitivities have been considered in this study than was possible in the site-modelling study for F 1.2. For example, variants in the geological model have shown that deformation zones outside the candidate area affect flow velocities downstream of the repository area with the flow-paths being generally shorter for the AC model than the BC model. Another uncertainty is whether the lower hydraulic conductivity seen in the candidate area is due to a lower fracture transmissivity or fracture intensity. Based on two variants, one on fracture intensity and one on fracture transmissivity, which both match the observed hydraulic data, the case with lower fracture intensity gives slightly higher initial Darcy velocity and lower F-quotient, but has very poor fracture connectivity. Alternatives were considered to the Hydro-DFN properties by using different relationships between fracture transmissivity and length. A case was considered with a semi-correlated model. This gave travel-times and F-quotients that were two orders of magnitude lower for many paths, and a significantly larger spread in flow-paths and exit locations. Part of the reason is slightly higher block-scale hydraulic conductivities for this case. Another is thought to be that the heterogeneity in this model will tend to shorten flow channels making connections easier to the surface than to the horizontal boundaries, and so favour the vertical path straight up rather than the longer path to the shoreline. Similar results were observed for a case with no correlation between fracture transmissivity and length. The results are significant since they suggestion heterogeneity or a lack of correlation tends not only to disperse particles and exit locations, but also to shorten paths by making long horizontal flow-paths less likely.

Sensitivities found to be of only moderate importance were the particular realisation of the Hydro-DFN used, modifying the fracture radius distribution by use of the Variant Geo-DFN (power-law slope k_r=2.75), and a lower kinematic porosity in the deformations zones. The weakest sensitivities of the PMs of those explored were to have a layer of enhance hydraulic conductivity in the top 100 m and changing the transport properties (within the plausible range of values) of the HCD. A specified infiltration boundary condition instead of a specified topographic head has already been considered in the site modelling /Hartley et al. 2005/ which found little effect on transport performance measures for the infiltration and properties of Quaternary deposits used. Given the very low topographic relief in the area it is not surprising that the assumption that the watertable is at ground surface is reasonable.

Detailed repository-scale models have been used to derive near-field and far-field performance measures for input to PA calculations. Two main types of conceptual models, DFN and CPM, have been applied to model the entire repository and flow in the bedrock around each deposition hole down to the scale of a few metres or less. As an advance on the methodology used in the interim SR-Can assessment, variable-density flow calculations have been implemented in DFN models so that the effects of buoyancy-driven flow due to the presence of salinity are represented consistently in both DFN and CPM conceptual models. Since the PA calculations use a streamline concept for the far-field modelling in FARF31, groundwater flow and flow-

paths are calculated at an appropriate series of representative times with boundary conditions and the salinity distribution being interpolated on to the steady-sate repository-scale models from transient regional-scale coupled groundwater flow and salt transport models. Properties of both the CPM and DFN models have been developed since the site modelling of SDM F 1.2 to incorporate a multi-domain definition of properties that is more realistic and better reflects the observed spatial variability in fracture and hydraulic properties at the site.

The use of different conceptual models has allowed us to quantify the sensitivity to the choice of model. For Forsmark it is found that the two types of model yield quite different results. This stems from the fact that the bedrock within the repository candidate area is very sparsely fractured with generally poor connectivity. In consequence, a DFN model predicts a very disjoint flow system with poor connections, areas of stagnant flow, tortuous flow-paths such that significant flow and transport is restricted to the deterministic deformation zones and the larger stochastic fractures. The lack of connectivity horizontally over long distances restricts long flow-paths from forming, and hence flow tends to be much localised and discharge from the repository is mainly to the immediate surface above. Transport is mainly sensitive to the structural model and occurrence of large stochastic fractures, while transient processes such as shoreline retreat are less influential. In contrast, a CPM model with isotropic hydraulic properties allows flow connections in all directions, and although the CPM bulk hydraulic properties are equivalent on a large-scale (100 m), the detailed flow and transport is very different. Generally in the CPM model flow is more homogeneous with flow around all deposition holes and longer flow-paths many of which reach the shoreline. In this case, results are sensitive to the position of the shoreline, and flow-paths less dominated by the geological structural model. To implement a representation of a sparse fracture network in a porous medium model one would have to use a fine-scale heterogeneous ECPM model that captures the intact block between the water conducting fractures, and this may not be practicable. This intrinsic difference between the two types of model has possible implications for the site-modelling also as it may affect the interpretation of interference tests and tracer tests.

In terms of the performance measures, the CPM model predicts travels times with a median over 10^3 years, while the DFN model median is less than 10^2 years; Initial velocity has a median around 10^{-6} m/y in the CPM model with small variability, while the DFN predicts a median around 10^{-5} m/y but with a standard deviation nearly one order of magnitude; The F-quotient has a median just under 10^8 y/m for the CPM model, and under 10^7 y/m for the DFN model with a standard deviation of about 0.8 in $\log_{10}$-space. Generally, the DFN representation is a worse scenario, but it does have some positive aspects also. For example, the DFN model predicts there is advection away from the canister via a fracture that intersects the deposition hole for only about 40% of canisters, and of these only about 15% have a significant transmissivity (greater than 10^{-9} m^2/s). Similarly, there are stagnant flow conditions in parts of the EDZ and tunnel that amounts to about 40% of the canisters. Hence, for many canisters there are essentially no advective routes for radionuclides to escape.

Sensitivities have been considered to the tunnel and EDZ properties as well as the relationship used between fracture transmissivity and length. The sensitivity to the backfill and EDZ properties is not great since the system of deposition tunnels is arranged orthogonal to the head gradients. Therefore flow tends to be limited by what the fracture system can supply and paths have to leave the tunnel or EDZ after relatively short distance to find a flow-path to the surface through the fracture network. For the semi-correlated and uncorrelated transmissivity DFN variants higher percentages of canisters have connected fractures of significant transmissivity (greater than 10^{-9} m^2/s) intersecting the deposition holes, 18–20%. The percentage of particles starting in stagnant flow areas increases to 67–74% for the two variants. This is indicative of flow being more heterogeneous for the variants and there being fewer advective pathways through the model, as was found in the equivalent ECPM regional models. Therefore, the results are moderately sensitive to the relationship used for the transmissivity to length relationship, and the semi-correlated and uncorrelated models may give moderately worse results than the correlated model in terms of inputs to PA, although fewer particles escape to the surface for these cases.

For the current fracture model, avoiding locations where fractures intersect the full perimeter of a tunnel seems to be a sufficient test for screening out the worst deposition hole locations without having to perform flow tests of fracture transmissivity in deposition pilot holes.

7.2 Conclusions for gas migration and its effects on groundwater flow

The consequences of gas production from iron corrosion in the small proportion of canisters (< 0.1%) that it is considered may have manufacturing defects that will allow water ingress were addressed.

Gas is generated in defective canisters by anaerobic corrosion of the cast iron insert as a result of water ingress through the defect. The rate of gas generation is determined by the iron corrosion rate, the iron surface area exposed to water, and the availability of water. Assuming that the whole surface of the iron insert is exposed to an unlimited supply of water, the rate of hydrogen production would be $2.1 \cdot 10^{-2}$ m^3y^{-1} at STP. This is an upper bound to the rate of gas production from a canister as in practice water availability will be limited by the flow capacity of the bentonite, the build up of gas pressure in the canister opposing water ingress through the defect, and the capacity of the geosphere to supply groundwater. The generation rate is unlikely to exceed $\sim 10^{-3}$ m^3y^{-1} at STP, and the build of gas pressure is likely to reduce the rate to less than $\sim 10^{-4}$ m^3y^{-1} at STP. Bear in mind that no gas escapes from the defective canister until the gas pressure has reached at least hydrostatic. Gas generation will continue, but possibly only at these very low rates, for at least 250,000 years.

Gas released from a defective canister needs to pass through the bentonite buffer if it is to escape from the vicinity of the canister. Even at the constrained gas generation rates discussed above, gas transport through the bentonite by diffusion in solution from the small defect will be inadequate to remove all the gas generated. However, if the gas pressure opens a gap between the canister and the buffer into which the gas can spread, the contribution of diffusion of dissolved gas to gas transport through the buffer may become more significant. In any event, is expected that, if the gas pressure rises sufficiently, movement of a free gas phase through the bentonite buffer will occur.

Once the gas has passed through the bentonite, it might collect in the tunnel and the EDZ associated with the tunnel, and it might enter the fracture network either from the tunnel or directly from the deposition hole. Some of the gas will dissolve in the groundwater and be transported away by the groundwater flow. However, the groundwater flow at the repository depth is very slow, and it is unlikely that gas generated at the upper bound generation rate of $2.1 \cdot 10^{-2}$ m^3y^{-1} at STP could all dissolve and be transported away in groundwater flowing through the neighbourhood of the repository. If, as seems quite probable for most defective canisters, the gas release rate is 1–2 orders of magnitude less than the upper bound, it is possible that much if not all of the gas could be transported away in solution.

Should the gas not all dissolve, simple estimates show that the gas transport capacity of the fracture network, assuming that it is sufficiently connected between the location of the defective canister and the surface, should be more than adequate to easily transport the gas to the surface without any significant increase in gas pressure in the neighbourhood of the repository.

Should free gas phase migration be sustained between the repository and the surface, this would be capable of transporting volatile radionuclides relatively rapidly from the repository to the surface. The only significant such radionuclides identified in the waste canisters are ^{14}C and ^{222}Rn. Direct release of the volatile ^{14}C in defective canisters to the surface has been previously assessed as not causing a significant radiological hazard and so the capacity of migrating gas to transport this radionuclide is immaterial. Similar conclusions were reached for ^{222}Rn release, although it may be desirable to assess the consequences of ^{222}Rn release into an occupied dwelling.

Migrating gas may also affect the movement of groundwater and hence the transport of dissolved radionuclides. Such transport is mitigated by the following observations:

- With a small defect, it is not possible to get release of dissolved radionuclides and gas at the same time. The situation may be different if a large hole develops.
- Gas migration can only affect transport of dissolved radionuclides released from a nearby different canister, and the probability of two defective canisters being present close together must be quite small.
- Migrating gas is only likely to affect groundwater flows in the neighbourhood of a small number of canisters local to the canister generating gas, and there is a low probability that one of these also may be defective and releasing radionuclides.

7.3 Conclusions for heat generation

Based on porous medium calculations it is concluded that thermal effects can potentially have a moderate impact on groundwater flow and transport from a repository. The flow-paths can be significantly modified in the immediate vicinity of the repository. The potential effects are greatest for radionuclides released from the repository shortly after repository closure though such releases are very unlikely. However, the discharge locations are not greatly effected, because these are determined by the location of surface water bodies, which are determined by lows in the surface topography and the shoreline. Possibly the most important impact of thermal effects might be due to their effect on the groundwater viscosity, which might be reduced by a about a factor of two in a region around the repository for many thousands of years, and in consequence Darcy velocity might be increased by a factor of two. This effect possibly ought to be taken into account in the PA transport calculations.

However, the results presented here potentially over-estimate the impact of thermal effects for several reasons. The calculations have not taken into account the long times spent in repository tunnels. During such times, the impact of thermal effects would be reduced, because of the decay of the heat source (although the temperature remains elevated for long times). Similarly, the calculations have not taken retardation due to sorption or to rock-matrix diffusion into account. Again, the impact of thermal effects would be reduced if these effects were taken into account.

References

Bear J, 1972. Dynamics of Fluids in Porous Media, American Elsevier Publishing Company.

Bond A E, Hoch A R, Jones G D, Tomczyk A E, Wiggin R M, Worraker W J, 1997. Assessment of a spent fuel disposal canister: assessment studies for a copper canister with cast steel inner component, SKB TR 97-19, Svensk Kärnbränslehantering AB.

Börgesson L, Johannesson L-E, Sandén T, Hernelind J, 1995. Modelling of the physical behaviour of water saturated clay barriers: laboratory tests, material models, and finite element application, SKB R-95-20, Svensk Kärnbränslehantering AB.

Börgesson L, Karnland O, Johannesson L-E, 1996. Modelling of the physical behaviour of clay barriers close to water saturation, Eng. Geol, 41, 127–144.

Carrera J, Sanchez-Vila X, Benet I, Medina A, Galarza G, Guimera J, 1998. On Matrix Diffusion: Formulations, Solution Methods and Quantitative Effects, Hydrogeology Journal, 6, No. 1, 178–190.

Carslaw H S, Jaeger J C, 1959. Conduction of Heat in Solids, Oxford University Press.

Chuoke R L, van Meurs P, van der Poel C, 1959. The instability of slow, immiscible, viscous liquid-liquid displacements in permeable media, Pet. Trans. AIME, 216, 188–194.

Cussler E L, 1984. Diffusion: mass transfer in fluid systems, Cambridge University Press.

Darwin C, 1953. Note on hydrodynamics, Proc. Camb. Phil. Soc., 49, 342–354.

de Marsily G, 1986. Quantitative Hydrogeology, Academic Press.

Dershowitz W, Winberg A, Hermanson J, Byegård J, Tullborg E-L, Andersson P, Mazurek M, 2003. Äspö Hard Rock Laboratory. Äspö Task Force on modelling of groundwater flow and transport of solutes – Task 6C – A semi-synthetic model of block scale conductive structures at the Äspö HRL, SKB Report IPR-03-13, Svensk Kärnbränslehantering AB.

Epstein P S, Plesset M S, 1950. On the stability of gas bubbles in liquid-gas solutions, J. Chem. Phys. 18, 1505–1509.

Follin S, Stigsson M, 2005. Regional Hydrogeological Simulations for Forsmark – Numerical Modelling Using DarcyTools, SKB R-05-60, Svensk Kärnbränslehantering AB.

Grace J R, Wairegi T, Brophy J, 1978. Break-up of drops and bubbles in stagnant media, Can. J. Chem. Eng., 56, 3–8.

Gustafsson B G, 2004a. Millenial changes of the Baltic Sea salinity. Studies of the sensitivity of the salinity to climate change, SKB TR 04-12, Svensk Kärnbränslehantering AB.

Gustafsson B G, 2004b. Sensitivity of Baltic Sea salinity to large perturbations in climate, Climate Research 27, 237–251, 2.

Hartley L, Cox I C S, Holton D, Hunter F M I, Joyce S, Gylling B, Lindgren M, 2004. Groundwater flow and transport modelling using CONNECTFLOW in support of the SR-Can assessment, SKB R-04-61, Svensk Kärnbränslehantering AB.

Hartley L, Cox I, Hunter F, Jackson P, Joyce S, Swift B, Marsic N, 2005. Regional Hydrogeological Simulations for Forsmark – Numerical Modelling Using CONNECTFLOW, SKB R-05-32, Svensk Kärnbränslehantering AB.

Henry H R, 1964. Effects of dispersion on salt encroachment in coastal aquifers, in Sea Water in Coastal Aquifers, U.S. Geol. Surv. Supply Pap., 1613-C, 70–84.

Hoch A R, Swanton S W, Manning M C, Rodwell W R, Swift B T, Duddridge G A, 2001. Gas migration in low-permeability fractured rock: theoretical and experimental studies, AEA Technology Report AEAT/ERRA-0323.

Hoch A R, Jackson C P, 2004. Rock-matrix Diffusion in Transport of Salinity. Implementation in CONNECTFLOW, SKB R-04-78, Svensk Kärnbränslehantering AB.

Hodgkinson D, 1985. Specification of a Test Problem for HYDROCOIN Level 1 Case 4: Transient Thermal Convection in a Saturated Permeable Medium, AERE R-11566, U K Atomic Energy Authority.

International HYDROCOIN Project, 1988. Groundwater Hydrology Modelling Studies for Performance Assessment of Nuclear Waste Disposal. Level 1: Code Verification, OECD Nuclear Energy Agency.

Jackson C P, Hoch A R, Todman S J, 2000. Self-consistency of a Heterogeneous Continuum Porous Medium Representation of a Fractured Medium, Water Resources Research, 36, No. 1, 189–202.

Kestin J, Khalifa H E, Correia R J, 1981. Tables of the Dynamic and Kinematic Viscosity of Aqueous NaCl Solutions in the Temperature Range 20–150°C and the Pressure Range 0.1–35 MPa, J. Phys. Chem. Ref. Data, 10, 71–87.

La Pointe P R, Wallmann P, Follin S, 1995. Estimation of Effective Block Conductivities Based on Discrete Network Analyses Using Data from the Äspö Site, SKB TR 95-15, Svensk Kärnbränslehantering AB.

Lide D (ed), 1994. CRC handbook of chemistry and physics, CRC Press.

Lindgren M, Lindström F, 1999. SR 97: radionuclide transport calculations, SKB TR-99-23, Svensk Kärnbränslehantering AB.

Marsic N, Hartley L J, Jackson C P, Poole M J, Morvik A, 2001. Development of Hydrogeological Modelling Tools Based on NAMMU, SKB R-01-49, Svensk Kärnbränslehantering AB.

Meister B J, Scheele G F, 1967. Generalized solution of the Tomotika stability analysis for a cylindrical jet, AIChE Journal, 13, 682–688.

Moreno L, Gylling B, 1998. Equivalent flow rate concept used in near field transport model COMP23 – Proposed values for SR 97, SKB R-98-53, Svensk Kärnbränslehantering AB.

Munier R, 2004. Statistical analysis of fracture data, adapted for modelling Discrete Fracture Networks-Version 2, SKB R-04-66, Svensk Kärnbränslehantering AB.

Nash P J, Cox I C S, Rodwell W R, 1997. Gas-water interactions in gas migration from a deep repository in fractured hard rock, UK Nirex Report NSS/R251.

Neretnieks I, 1979. Transport Mechanism and Rates of Transport of Radionuclides in the Geosphere as Related to the Swedish KBS-Concept, Proc. Symp. Underground Disposal of Radioactive Wastes, Otaniemi, Finland, July 2–6, 1979, Vol II. p 108, International Atomic Energy Agency.

Neretnieks I, Ernstson M-L, 1997. A note on radionuclide transport by gas bubbles. In: W J Gray and I R Triay (eds.), MRS symposium proceedings 465, Scientific basis for nuclear waste management XX, 855–862, MRS, Pittsburgh, Pennsylvania, USA.

Neretnieks I, 2006. A Note on flow and transport in a damaged zone due to spalling. Department of Chemical Engineering and Technology, Royal Institute of Technology, KTH, Stockholm, Sweden.

Plesset M S, Whipple C G, 1974. Viscous effects in Rayleigh-Taylor instability, Phys. Fluids, 17, 1–7.

Påsse T, 1997. A mathematical model of past, present and future shore level displacement in Fennoscandia, SKB TR 97-28, Svensk Kärnbränslehantering AB.

Rodwell W R, Harris A W, Horseman S T, Lalieux Ph, Müller W, Ortiz Amaya L, Pruess K, 1999. Gas migration through engineered and geological barriers for a deep repository for radioactive waste. A joint EC/NEA status report published by the European Commission, European Commission Report EUR 19122 EN.

Rowe A M, Chou J C S, 1970. Pressure-volume-temperature Concentration Relation of Aqueous NaCl Solutions, J. Chem. Eng. Data, 15, 61–66.

Saffman P G, Taylor G, 1958. The penetration of a fluid into a porous medium or Hele-Shaw cell containing a more viscous liquid, Proc. R. Soc. Lond., A245, 312–329.

Serco Assurance, 2005a. CONNECTFLOW Release 9.0 Technical Summary Document, Serco Assurance Report SA/ENV/CONNECTFLOW/15.

Serco Assurance, 2005b. NAMMU Release 9.0 Technical Summary Document, Serco Assurance Report SA/ENV/CONNECTFLOW/8.

Serco Assurance, 2005c. NAPSAC Release 9.0 Technical Summary Document, Serco Assurance Report SA/ENV/CONNECTFLOW/12.

SKB, 1997. ZEDEX – A study of damage and distrurbance from tunnel excavation and tunnel boring. SKB TR-97-30, Svensk Kärnbränslehantering AB.

SKB, 1999. Deep repository for spent nuclear fuel. SR 97: post-closure safety (main report Summary, main report Volume 1, and main report Volume 2), SKB TR-99-06, Svensk Kärnbränslehantering AB.

SKB, 2004a. Interim main report of the safety assessment SR-Can, SKB TR-04-11, Svensk Kärnbränslehantering AB.

SKB, 2004b. Preliminary site description of the Forsmark area (Version 1.1), SKB R-04-15, Svensk Kärnbränslehantering AB.

SKB, 2004c. Interim process report for the safety assessment SR-Can, SKB R-04-33, Svensk Kärnbränslehantering AB.

SKB, 2004d. Interim data report for the safety assessment SR-Can, SKB R-04-34, Svensk Kärnbränslehantering AB.

SKB, 2004e. Interim initial state report for the safety assessment SR-Can, SKB R-04-35, Svensk Kärnbränslehantering AB.

SKB, 2005a. Hydrogeochemical evaluation of the Forsmark site (Version 1.2), SKB R-05-17, Svensk Kärnbränslehantering AB.

SKB, 2005b. Preliminary site description Forsmark area – version 1.2, SKB R-05-18, Svensk Kärnbränslehantering AB.

Smart N R, 2001. The anaerobic corrosion of carbon steel and cast iron in artificial ground-waters, SKB TR-01-22, Svensk Kärnbränslehantering AB.

Svenson U, 2005. ‘Open repository’, SKB R-05-??, Svensk Kärnbränslehantering AB.

Tanai et al. 1999. Measurements of diffusion coefficients for hydrogen in bentonite, communicated by P Sellin.

Tomotika S, 1934. On the instability of a cylindrical thread of a viscous liquid surrounded by another viscous liquid, Proc. R. Soc. Lond., **A150**, 322–337.

Wikramaratna R S, Goodfield M, Rodwell W R, Nash P J, Agg P J, 1993.
A preliminary assessment of gas migration from the copper/steel canister, SKB TR 93-31, Svensk Kärnbränslehantering AB.

Appendix A

Glossary of abbreviations and symbols

For clarity, the SKB advised terminology for referring to fracture size is as follows.

r	Equivalent fracture radius (m) Fractures are modelled as squares. However, an equivalent fracture radius, $r = \sqrt{\frac{A}{\pi}}$, where A is fracture area, is used to describe fracture size throughout this report.
k	The shape parameter for a general power-law distribution
k_r	The shape parameter for the power-law distribution for fracture radii
x_0	The location parameter of a general power-law distribution (m)
r_0	The location parameter of the power-law distribution for fracture radii (m)

Other abbreviations and notation used are:

AC	Alternative case deformation zone model
a_r	Fracture surface area per unit volume (2×P32) (m^2m^{-3})
BC	Base case deformation zone model
CF	CONNECTFLOW
CPM	Continuum porous medium
DFN	Discrete fracture network
DZ	Deformation zone
DT	DarcyTools
ECPM	Equivalent continuum porous medium
e_t	Fracture transport aperture (m)
F	F-quotient (y/m)
F 1.2	Forsmark version 1.2
FWS	Flow-wetted surface, same as a_r
GWF	Groundwater flow
HCD	Hydraulic conductor domains
HRD	Hydraulic rock domains
HSD	Hydraulic surface domains
IC	Initial condition
IFZ	Implicit fracture zone
K	Hydraulic conductivity (ms^{-1})
K_{eff}	Effective isotropic hydraulic conductivity (m/s)
K_{hmax}	Maximum horizontal hydraulic conductivity (m/s)
K_{hmin}	Minimum horizontal hydraulic conductivity (m/s)
K_x	Hydraulic conductivity in the E-W direction (m/s)
K_y	Hydraulic conductivity in the N-S direction (m/s)
K_z	Hydraulic conductivity in the vertical direction (m/s)
KFM	Cored borehole at Forsmark
L_{EDZ}	Path-length in the EDZ (m)

L_r	Path-length in the rock (m)
L_T	Path-length in the tunnel (m)
M3	Mixing and mass-balance modelling
n_e	Kinematic porosity (–)
n_{et}	Kinematic porosity of HCD based on averaging the transport aperture over the zone thickness (–)
n_{etb}	Bulk kinematic porosity of HRD based on averaging the sum of connected fracture transport aperture over a block volume (–)
n_m	Matrix porosity (–)
P10	Linear fracture intensity: number of fractures per metre along a borehole (m^{-1})
$P10_c$	Linear fracture intensity of connected fractures: number of connected fractures per metre along a borehole (m^{-1})
$P10_{corr}$	Terzaghi corrected linear fracture intensity: 'true' number of fractures per metre along a borehole corrected for the bias introduced by the angle of the borehole made with fractures (m^{-1})
$P10_{PFL}$	Linear fracture intensity of PFL-anomalies: number of PFL anomalies per metre along a borehole (m^{-1})
P21	Area fracture intensity: total fracture trace lengths per square metre of outcrop (m m^{-2})
P32	Volumetric fracture intensity: total fracture surface area per cubic metre of rock (m^2 m^{-3})
$P32_c$	Volumetric fracture intensity of connected fractures: total connected fracture surface area per cubic metre of rock (m^2 m^{-3})
PDF	Probability distribution function
PFL	Posiva flow-log
PM	Performance measure
PA	Performance assessment
PSS	Pipe-string system
Q	Groundwater flux (m^3s^{-1})
Qeq	Equivalent flow rate (m^3s^{-1})
q	Darcy velocity (m s^{-1})
RD	Rock domain
RMD	Rock matrix diffusion
r_{min}	Minimum fracture radius used in DFN simulations (m)
SDM	Site descriptive modelling
STP	Standard temperature and pressure
T	Transmissivity (m^2s^{-1})
t_{EDZ}	Travel-time in the EDZ (year)
t_r	Travel-time in the rock (year)
t_T	Travel-time in the tunnel (year)
Θ	Temperature (K)
T_V	Transmissivity model for steeply dipping DZs (m^2s^{-1})
T_H	Transmissivity model for gently dipping DZs (m^2s^{-1})
T_O	Transmissivity model for lineaments outside the tectonic lens (m^2s^{-1})
TDS	Total dissolved solids

Appendix B

Regional-scale modelling PM statistics

A general approach to characterising transport properties is to track particles advected by the fixed flow-field at several selected release times and record the travel time (t_r), initial Darcy velocity (U_r), path length (L_r) and F-quotient (F_r). The subscript "r" indicates that the performance measure is calculated in the rock. This additional information may be obsolete at this point but is used in order to distinguish these performance measures calculated in the CPM/ECPM regional model from performance measures that will be calculated and presented in other parts of the report.

6,824 particles, one for each canister position in the repository, are released at –400 m elevation. Statistics are given as percentiles (5th, 10th, 25th, 50th, 75th, 90th and 95th) and the first two moments (Mean and Variance) to measure the shape of the distributions. Also the fraction of released particles that reach the model surface is calculated (Fraction OK) as an indication of the level of numerical problems in the particle tracking. The statistics are calculated in $\log_{10}$ space and results are presented for three selected release times; 2,020 AD, 3,000 AD and 9,000 AD.

As has already been concluded many of the cases give results very similar to the ECPM Base Case. However, it was felt that at least the statistical results could still be of some interest even if the cases were rejected for further analyses. Therefore a number of cases that were modelled but yet not discussed thoroughly in the report will be presented in this Appendix.

The order of which the cases are listed in this section corresponds to the order of which they were presented and discussed in the report. Then follow the cases that were not presented in the report.

B.1 ECPM base case (SC_HCD3_AC_HRD3EC)

Table B-1 to Table B-4 summarise the performance measure statistics for t_r, U_r, L_r and F_r respectively, for the ECPM Base Case. The statistics are calculated in $\log_{10}$ space and results are presented for three selected release times; 2,020 AD, 3,000 AD and 9,000 AD.

Table B-1. Performance statistics: Distribution of $\log_{10}(t_r)$ at different release times for the ECPM Base Case (SC_HCD3_AC_HRD3EC).

$\log_{10}(t_r)$ [y]	2,020 AD	3,000 AD	9,000 AD
Mean	3.213	3.785	3.531
Median	3.186	3.783	3.532
5th percentile	2.339	2.695	2.452
10th percentile	2.468	3.244	2.732
25th percentile	2.886	3.498	3.148
75th percentile	3.471	4.077	3.894
90th percentile	3.921	4.390	4.344
95th percentile	4.339	4.670	4.580
Std deviation	0.547	0.521	0.630
Variance	0.300	0.271	0.397
Max value	5.115	5.691	5.760
Min value	2.032	2.143	1.690
Fraction OK	0.992	0.728	0.995

Table B-2. Performance statistics: Distribution of $\log_{10}(U_r)$ at different release times for the ECPM Base Case (SC_HCD3_AC_HRD3EC).

$\log_{10}(U_r)$ [m/yr]	2,020 AD	3,000 AD	9,000 AD
Mean	–4.608	–4.292	–4.274
Median	–4.626	–4.299	–4.288
5th percentile	–5.499	–5.085	–5.118
10th percentile	–5.316	–4.883	–4.927
25th percentile	–5.018	–4.610	–4.628
75th percentile	–4.241	–3.962	–3.922
90th percentile	–3.813	–3.668	–3.581
95th percentile	–3.585	–3.470	–3.412
Std deviation	0.562	0.476	0.509
Variance	0.316	0.227	0.259
Max value	–3.271	–3.113	–3.057
Min value	–6.197	–5.883	–5.902
Fraction OK	1.000	1.000	1.000

Table B-3. Performance statistics: Distribution of $\log_{10}(L_r)$ at different release times for the ECPM Base Case (SC_HCD3_AC_HRD3EC).

$\log_{10}(L_r)$ [m]	2,020 AD	3,000 AD	9,000 AD
Mean	3.175	3.458	3.523
Median	3.155	3.483	3.454
5th percentile	2.745	2.940	2.821
10th percentile	2.798	3.062	2.889
25th percentile	2.932	3.312	3.087
75th percentile	3.325	3.612	4.069
90th percentile	3.551	3.750	4.096
95th percentile	3.842	3.833	4.106
Std deviation	0.324	0.271	0.463
Variance	0.105	0.074	0.215
Max value	4.388	4.350	4.377
Min value	2.625	2.796	2.663
Fraction OK	0.992	0.728	0.995

Table B-4. Performance statistics: Distribution of $\log_{10}(F_r)$ at different release times for the ECPM Base Case (SC_HCD3_AC_HRD3EC).

$\log_{10}(F_r)$ [y/m]	2,020 AD	3,000 AD	9,000 AD
Mean	6.710	7.139	7.056
Median	6.742	7.175	6.916
5th percentile	5.891	6.215	5.765
10th percentile	6.106	6.423	6.000
25th percentile	6.383	6.887	6.361
75th percentile	7.031	7.421	8.013
90th percentile	7.290	7.770	8.069
95th percentile	7.453	7.910	8.095
Std deviation	0.465	0.486	0.806
Variance	0.216	0.236	0.650
Max value	8.117	8.370	8.226
Min value	5.459	5.651	5.426
Fraction OK	0.992	0.728	0.995

B.2 CPM base case (SC_HCD3_AC_HRDDT)

Table B-5 to Table B-8 summarise the performance measure statistics for t_r, U_r, L_r and F_r respectively, for the CPM Base Case. The statistics are calculated in $\log_{10}$ space and results are presented for three selected release times; 2,020 AD, 3,000 AD and 9,000 AD.

Table B-5. Performance statistics: Distribution of $\log_{10}(t_r)$ at different release times for the CPM Base Case (SC_HCD3_AC_HRDDT).

$\text{Log}_{10}(t_r)$ [y]	2,020 AD	3,000 AD	9,000 AD
Mean	3.580	6.032	6.090
Median	3.498	6.044	6.177
5th percentile	3.102	4.724	4.368
10th percentile	3.186	5.475	5.134
25th percentile	3.289	5.757	5.864
75th percentile	3.836	6.464	6.572
90th percentile	4.099	6.783	6.871
95th percentile	4.249	6.879	6.984
Std deviation	0.372	0.642	0.704
Variance	0.139	0.412	0.495
Max value	5.255	7.201	7.366
Min value	2.808	3.504	3.652
Fraction OK	0.899	0.639	0.999

Table B-6. Performance statistics: Distribution of $\log_{10}(U_r)$ at different release times for the CPM Base Case (SC_HCD3_AC_HRDDT).

$\text{Log}_{10}(U_r)$ [m/y]	2,020 AD	3,000 AD	9,000 AD
Mean	–5.926	–5.850	–5.817
Median	–6.025	–5.944	–5.909
5th percentile	–6.296	–6.222	–6.289
10th percentile	–6.233	–6.142	–6.209
25th percentile	–6.122	–6.051	–6.022
75th percentile	–5.891	–5.813	–5.750
90th percentile	–5.327	–5.254	–5.110
95th percentile	–5.087	–4.946	–4.894
Std deviation	0.359	0.363	0.389
Variance	0.129	0.132	0.151
Max value	–4.146	–4.189	–4.087
Min value	–6.746	–6.982	–6.553
Fraction OK	1.000	1.000	1.000

Table B-7. Performance statistics: Distribution of $\log_{10}(L_r)$ at different release times for the CPM Base Case (SC_HCD3_AC_HRDDT).

$\log_{10}(L_r)$ [m]	2,020 AD	3,000 AD	9,000 AD
Mean	3.169	3.091	3.772
Median	3.083	3.031	4.091
5th percentile	2.758	2.770	2.817
10th percentile	2.800	2.814	2.867
25th percentile	2.895	2.894	3.077
75th percentile	3.381	3.206	4.109
90th percentile	3.698	3.303	4.126
95th percentile	3.891	3.873	4.134
Std deviation	0.349	0.291	0.528
Variance	0.122	0.085	0.279
Max value	4.369	4.329	4.178
Min value	2.650	2.636	2.677
Fraction OK	0.899	0.639	0.999

Table B-8. Performance statistics: Distribution of $\log_{10}(F_r)$ at different release times for the CPM Base Case (SC_HCD3_AC_HRDDT).

$\log_{10}(F_r)$ [y/m]	2,020 AD	3,000 AD	9,000 AD
Mean	7.658	7.844	8.345
Median	7.683	7.851	8.559
5th percentile	6.975	6.968	7.305
10th percentile	7.261	7.224	7.559
25th percentile	7.533	7.549	7.989
75th percentile	7.843	8.177	8.688
90th percentile	8.035	8.395	8.797
95th percentile	8.170	8.540	8.855
Std deviation	0.355	0.522	0.521
Variance	0.126	0.273	0.271
Max value	9.193	9.282	9.227
Min value	6.070	6.071	6.249
Fraction OK	0.899	0.639	0.999

B.3 BC geological model (SC_HCD3_BC_HRD3EC)

Table B-9 to Table B-12 summarise the performance measure statistics for t_r, U_r, L_r and F_r respectively, for the BC Geological model. The statistics are calculated in $\log_{10}$ space and results are presented for three selected release times; 2,020 AD, 3,000 AD and 9,000 AD.

Table B-9. Performance statistics: Distribution of $\log_{10}(t_r)$ at different release times for the BC Geological model (SC_HCD3_BC_HRD3EC).

$\log_{10}(t_r)$ [y]	2,020 AD	3,000 AD	9,000 AD
Mean	3.166	3.786	3.561
Median	3.057	3.730	3.496
5th percentile	2.441	3.145	2.846
10th percentile	2.592	3.236	3.017
25th percentile	2.796	3.502	3.221
75th percentile	3.497	4.077	3.866
90th percentile	3.814	4.401	4.273
95th percentile	4.188	4.541	4.438
Std deviation	0.527	0.448	0.525
Variance	0.278	0.201	0.276
Max value	5.007	5.562	5.777
Min value	2.016	1.904	1.693
Fraction OK	0.978	0.947	1.000

Table B-10. Performance statistics: Distribution of $\log_{10}(U_r)$ at different release times for the BC Geological model (SC_HCD3_BC_HRD3EC).

$\log_{10}(U_r)$ [m/y]	2,020 AD	3,000 AD	9,000 AD
Mean	–4.640	–4.297	–4.274
Median	–4.679	–4.301	–4.270
5th percentile	–5.487	–5.078	–5.138
10th percentile	–5.333	–4.905	–4.937
25th percentile	–5.062	–4.612	–4.637
75th percentile	–4.262	–3.977	–3.923
90th percentile	–3.831	–3.677	–3.586
95th percentile	–3.633	–3.486	–3.426
Std deviation	0.563	0.472	0.510
Variance	0.317	0.223	0.260
Max value	–3.277	–3.188	–3.119
Min value	–6.322	–5.869	–5.986
Fraction OK	1.000	1.000	1.000

Table B-11. Performance statistics: Distribution of $\log_{10}(L_r)$ at different release times for BC Geological model (SC_HCD3_BC_HRD3EC).

$\log_{10}(L_r)$ [m]	2,020 AD	3,000 AD	9,000 AD
Mean	3.297	3.688	3.769
Median	3.247	3.672	3.803
5th percentile	2.820	3.374	3.132
10th percentile	2.922	3.436	3.300
25th percentile	3.083	3.551	3.628
75th percentile	3.508	3.815	4.075
90th percentile	3.696	4.002	4.098
95th percentile	3.828	4.091	4.109
Std deviation	0.305	0.229	0.340
Variance	0.093	0.053	0.116
Max value	4.407	4.360	4.259
Min value	2.668	2.801	2.729
Fraction OK	0.978	0.947	1.000

Table B-12. Performance statistics: Distribution of $\log_{10}(F_r)$ at different release times for the BC Geological model (SC_HCD3_BC_HRD3EC).

$\log_{10}(F_r)$ [y/m]	2,020 AD	3,000 AD	9,000 AD
Mean	7.052	7.548	7.435
Median	7.083	7.631	7.660
5th percentile	6.250	6.787	6.225
10th percentile	6.477	7.027	6.522
25th percentile	6.839	7.290	7.099
75th percentile	7.307	7.873	7.992
90th percentile	7.583	7.990	8.055
95th percentile	7.751	8.022	8.078
Std deviation	0.426	0.412	0.639
Variance	0.182	0.169	0.408
Max value	8.163	8.249	8.202
Min value	5.613	5.986	5.436
Fraction OK	0.978	0.947	1.000

B.4 Lower transmissivity below ZFMNE00A2 (SC_HCD3_AC_HRD3A2_T)

Table B-13 to Table B-16 summarise the performance measure statistics for t_r, U_r, L_r and F_r respectively, for the lower transmissivity below ZFMNE00A2. The statistics are calculated in $\log_{10}$ space and results are presented for three selected release times; 2,020 AD, 3,000 AD and 9,000 AD.

Table B-13. Performance statistics: Distribution of $\log_{10}(t_r)$ at different release times for the lower transmissivity below ZFMNE00A2 (SC_HCD3_AC_HRD3A2_T).

$\log_{10}(t_r)$ [y]	2,020 AD	3,000 AD	9,000 AD
Mean	3.401	4.801	4.469
Median	3.303	4.869	4.442
5th percentile	2.561	3.557	3.495
10th percentile	2.756	3.882	3.647
25th percentile	3.005	4.279	3.945
75th percentile	3.777	5.386	4.990
90th percentile	4.262	5.750	5.404
95th percentile	4.485	5.933	5.626
Std deviation	0.594	0.838	0.725
Variance	0.353	0.702	0.526
Max value	5.097	6.859	6.505
Min value	0.905	0.490	0.205
Fraction OK	0.964	0.395	0.998

Table B-14. Performance statistics: Distribution of $\log_{10}(U_r)$ at different release times for the lower transmissivity below ZFMNE00A2 (SC_HCD3_AC_HRD3A2_T).

$\log_{10}(U_r)$ [m/y]	2,020 AD	3,000 AD	9,000 AD
Mean	–5.338	–5.062	–4.928
Median	–5.394	–5.076	–4.949
5th percentile	–6.216	–5.934	–5.718
10th percentile	–6.018	–5.783	–5.572
25th percentile	–5.758	–5.470	–5.289
75th percentile	–4.974	–4.726	–4.629
90th percentile	–4.606	–4.377	–4.294
95th percentile	–4.261	–4.047	–3.985
Std deviation	0.599	0.577	0.531
Variance	0.358	0.333	0.282
Max value	–3.087	–2.836	–2.539
Min value	–7.171	–7.195	–6.346
Fraction OK	1.000	1.000	1.000

Table B-15. Performance statistics: Distribution of $\log_{10}(L_r)$ at different release times for the lower transmissivity below ZFMNE00A2 (SC_HCD3_AC_HRD3A2_T).

$\log_{10}(L_r)$ [m]	2,020 AD	3,000 AD	9,000 AD
Mean	3.170	3.539	4.018
Median	3.101	3.715	4.082
5th percentile	2.745	2.835	3.144
10th percentile	2.797	2.926	4.046
25th percentile	2.931	3.141	4.063
75th percentile	3.326	3.783	4.100
90th percentile	3.662	3.843	4.116
95th percentile	3.844	3.965	4.128
Std deviation	0.333	0.376	0.276
Variance	0.111	0.141	0.076
Max value	4.376	4.312	4.362
Min value	2.627	2.658	2.645
Fraction OK	0.964	0.395	0.998

Table B-16. Performance statistics: Distribution of $\log_{10}(F_r)$ at different release times for the lower transmissivity below ZFMNE00A2 (SC_HCD3_AC_HRD3A2_T).

$\log_{10}(F_r)$ [y/m]	2,020 AD	3,000 AD	9,000 AD
Mean	7.217	7.833	8.113
Median	7.228	8.090	8.200
5th percentile	6.306	6.713	7.010
10th percentile	6.553	7.026	8.088
25th percentile	6.894	7.469	8.140
75th percentile	7.547	8.224	8.278
90th percentile	7.877	8.384	8.343
95th percentile	8.108	8.415	8.364
Std deviation	0.528	0.606	0.451
Variance	0.279	0.367	0.204
Max value	8.640	8.730	8.529
Min value	5.115	4.579	4.214
Fraction OK	0.964	0.395	0.998

B.5 Lower open P32 below ZFMNE00A2 (SC_HCD3_AC_HRD3A2_P32)

Table B-17 to Table B-20 summarise the performance measure statistics for t_r, U_r, L_r and F_r respectively, for the open P_{32} below ZFMNE00A2. The statistics are calculated in $\log_{10}$ space and results are presented for three selected release times; 2,020 AD, 3,000 AD and 9,000 AD.

Table B-17. Performance statistics: Distribution of $\log_{10}(t_r)$ at different release times for the lower open P32 below ZFMNE00A2 (SC_HCD3_AC_HRD3A2_P32).

$\log_{10}(t_r)$ [y]	2,020 AD	3,000 AD	9,000 AD
Mean	3.354	4.230	3.972
Median	3.385	4.164	3.909
5th percentile	2.347	3.312	2.908
10th percentile	2.648	3.442	3.214
25th percentile	2.961	3.759	3.512
75th percentile	3.767	4.697	4.425
90th percentile	4.062	5.166	4.917
95th percentile	4.258	5.539	5.299
Std deviation	0.605	0.748	0.751
Variance	0.366	0.560	0.563
Max value	5.033	6.757	6.534
Min value	0.891	0.667	0.266
Fraction OK	0.987	0.738	0.991

Table B-18. Performance statistics: Distribution of $\log_{10}(U_r)$ at different release times for the lower open P32 below ZFMNE00A2 (SC_HCD3_AC_HRD3A2_P32).

$\log_{10}(U_r)$ [m/y]	2,020 AD	3,000 AD	9,000 AD
Mean	–5.075	–4.676	–4.614
Median	–5.073	–4.653	–4.612
5th percentile	–6.122	–5.654	–5.592
10th percentile	–5.849	–5.393	–5.335
25th percentile	–5.479	–5.039	–4.983
75th percentile	–4.658	–4.275	–4.215
90th percentile	–4.313	–3.976	–3.907
95th percentile	–4.090	–3.831	–3.789
Std deviation	0.608	0.562	0.557
Variance	0.369	0.316	0.310
Max value	–3.114	–2.884	–2.572
Min value	–6.898	–7.195	–6.605
Fraction OK	1.000	1.000	1.000

Table B-19. Performance statistics: Distribution of $\log_{10}(L_r)$ at different release times for the lower open P32 below ZFMNE00A2 (SC_HCD3_AC_HRD3A2_P32).

$\text{Log}_{10}(L_r)$ [m]	2,020 AD	3,000 AD	9,000 AD
Mean	3.186	3.590	3.884
Median	3.157	3.640	4.063
5th percentile	2.742	2.940	2.858
10th percentile	2.799	3.235	3.022
25th percentile	2.963	3.430	3.835
75th percentile	3.384	3.786	4.089
90th percentile	3.556	3.878	4.104
95th percentile	3.704	4.117	4.112
Std deviation	0.309	0.306	0.387
Variance	0.095	0.094	0.150
Max value	4.366	4.350	4.352
Min value	2.639	2.674	2.662
Fraction OK	0.987	0.738	0.991

Table B-20. Performance statistics: Distribution of $\log_{10}(F_r)$ at different release times for the lower open P32 below ZFMNE00A2 (SC_HCD3_AC_HRD3A2_P32).

$\text{Log}_{10}(F_r)$ [y/m]	2,020 AD	3,000 AD	9,000 AD
Mean	6.919	7.492	7.722
Median	6.917	7.637	8.043
5th percentile	6.045	6.159	5.803
10th percentile	6.234	6.666	6.613
25th percentile	6.584	7.113	7.611
75th percentile	7.280	7.982	8.106
90th percentile	7.582	8.194	8.140
95th percentile	7.752	8.295	8.163
Std deviation	0.529	0.662	0.732
Variance	0.279	0.438	0.535
Max value	8.258	8.558	8.317
Min value	4.997	4.416	4.088
Fraction OK	0.987	0.738	0.991

B.6 Semi-correlated transmissivity (SC_HCD3_AC_HRD3ES)

Table B-21 to Table B-24 summarise the performance measure statistics for t_r, U_r, L_r and F_r respectively, for the semi-correlated transmissivity. The statistics are calculated in $\log_{10}$ space and results are presented for three selected release times; 2,020 AD, 3,000 AD and 9,000 AD.

Table B-21. Performance statistics: Distribution of $\log_{10}(t_r)$ at different release times for the semi-correlated transmissivity (SC_HCD3_AC_HRD3ES).

$\log_{10}(t_r)$ [y]	2,020 AD	3,000 AD	9,000 AD
Mean	2.854	2.342	2.165
Median	2.880	2.158	2.075
5th percentile	1.344	1.230	1.027
10th percentile	1.646	1.414	1.206
25th percentile	2.218	1.698	1.587
75th percentile	3.515	3.074	2.697
90th percentile	3.987	3.541	3.175
95th percentile	4.204	3.661	3.347
Std deviation	0.869	0.808	0.754
Variance	0.755	0.654	0.569
Max value	4.802	5.808	5.746
Min value	0.674	0.806	0.462
Fraction OK	0.885	0.963	0.996

Table B-22. Performance statistics: Distribution of $\log_{10}(U_r)$ at different release times for the semi-correlated transmissivity (SC_HCD3_AC_HRD3ES).

$\log_{10}(U_r)$ [m/y]	2,020 AD	3,000 AD	9,000 AD
Mean	–3.637	–3.409	–3.341
Median	–3.652	–3.395	–3.308
5th percentile	–4.662	–4.279	–4.198
10th percentile	–4.429	–4.044	–3.954
25th percentile	–4.055	–3.711	–3.624
75th percentile	–3.286	–3.106	–3.027
90th percentile	–2.882	–2.831	–2.761
95th percentile	–2.424	–2.658	–2.612
Std deviation	0.672	0.519	0.484
Variance	0.452	0.269	0.234
Max value	–0.897	–1.219	–1.854
Min value	–6.288	–5.778	–5.700
Fraction OK	1.000	1.000	1.000

Table B-23. Performance statistics: Distribution of $\log_{10}(L_r)$ at different release times for the semi-correlated transmissivity (SC_HCD3_AC_HRD3ES).

$\log_{10}(L_r)$ [m]	2,020 AD	3,000 AD	9,000 AD
Mean	3.242	3.235	3.219
Median	3.158	3.059	3.067
5th percentile	2.796	2.810	2.762
10th percentile	2.863	2.846	2.792
25th percentile	2.970	2.916	2.883
75th percentile	3.520	3.537	3.446
90th percentile	3.725	3.920	4.071
95th percentile	3.839	4.044	4.155
Std deviation	0.336	0.413	0.440
Variance	0.113	0.170	0.194
Max value	4.235	4.302	4.278
Min value	2.671	2.671	2.631
Fraction OK	0.885	0.963	0.996

Table B-24. Performance statistics: Distribution of $\log_{10}(F_r)$ at different release times for the semi-correlated transmissivity (SC_HCD3_AC_HRD3ES).

$\log_{10}(F_r)$ [y/m]	2,020 AD	3,000 AD	9,000 AD
Mean	6.393	5.826	5.739
Median	6.534	5.581	5.431
5th percentile	4.788	4.888	4.643
10th percentile	5.001	5.007	4.785
25th percentile	5.509	5.247	5.060
75th percentile	7.172	6.323	6.094
90th percentile	7.631	6.989	7.878
95th percentile	7.871	7.492	8.004
Std deviation	0.985	0.803	0.987
Variance	0.971	0.644	0.975
Max value	9.596	9.158	8.458
Min value	3.738	4.380	4.300
Fraction OK	0.885	0.963	0.996

B.7 Uncorrelated transmissivity (SC_HCD3_AC_HRD3EU)

Table B-25 to Table B-28 summarise the performance measure statistics for t_r, U_r, L_r and F_r respectively, for the uncorrelated transmissivity. The statistics are calculated in $\log_{10}$ space and results are presented for three selected release times; 2,020 AD, 3,000 AD and 9,000 AD.

Table B-25. Performance statistics: Distribution of $\log_{10}(t_r)$ at different release times for the uncorrelated transmissivity (SC_HCD3_AC_HRD3EU).

$\log_{10}(t_r)$ [y]	2,020 AD	3,000 AD	9,000 AD
Mean	2.851	2.550	2.058
Median	2.850	2.413	2.003
5th percentile	1.663	1.303	1.021
10th percentile	1.923	1.496	1.173
25th percentile	2.470	1.865	1.543
75th percentile	3.181	3.317	2.562
90th percentile	3.785	3.672	2.925
95th percentile	4.239	3.856	3.109
Std deviation	0.686	0.873	0.692
Variance	0.471	0.762	0.478
Max value	5.264	6.158	6.116
Min value	1.157	0.628	0.524
Fraction OK	0.928	0.976	1.000

Table B-26. Performance statistics: Distribution of $\log_{10}(U_r)$ at different release times for the uncorrelated transmissivity (SC_HCD3_AC_HRD3EU).

$\log_{10}(U_r)$ [m/y]	2,020 AD	3,000 AD	9,000 AD
Mean	–3.801	–3.450	–3.343
Median	–3.764	–3.405	–3.295
5th percentile	–4.793	–4.208	–4.118
10th percentile	–4.512	–4.007	–3.932
25th percentile	–4.157	–3.709	–3.617
75th percentile	–3.390	–3.152	–3.027
90th percentile	–3.149	–2.940	–2.803
95th percentile	–2.993	–2.797	–2.672
Std deviation	0.552	0.439	0.451
Variance	0.305	0.193	0.204
Max value	–2.361	–2.353	–2.371
Min value	–7.015	–6.044	–6.003
Fraction OK	1.000	1.000	1.000

Table B-27. Performance statistics: Distribution of $log_{10}(L_r)$ at different release times for the uncorrelated transmissivity (SC_HCD3_AC_HRD3EU).

$Log_{10}(L_r)$ [m]	2,020 AD	3,000 AD	9,000 AD
Mean	3.198	3.267	3.167
Median	3.132	3.248	3.117
5th percentile	2.813	2.834	2.781
10th percentile	2.863	2.880	2.813
25th percentile	2.964	2.988	2.908
75th percentile	3.315	3.451	3.353
90th percentile	3.750	3.740	3.547
95th percentile	3.917	3.897	3.799
Std deviation	0.328	0.328	0.315
Variance	0.108	0.107	0.099
Max value	4.336	4.323	4.249
Min value	2.670	2.696	2.654
Fraction OK	0.928	0.976	1.000

Table B-28. Performance statistics: Distribution of $log_{10}(F_r)$ at different release times for the uncorrelated transmissivity (SC_HCD3_AC_HRD3EU).

$Log_{10}(F_r)$ [y/m]	2,020 AD	3,000 AD	9,000 AD
Mean	6.313	6.051	5.619
Median	6.183	5.793	5.472
5th percentile	5.371	4.937	4.695
10th percentile	5.505	5.057	4.787
25th percentile	5.804	5.342	5.010
75th percentile	6.647	6.690	6.078
90th percentile	7.410	7.468	6.587
95th percentile	7.845	7.991	7.113
Std deviation	0.727	0.918	0.764
Variance	0.528	0.842	0.584
Max value	9.283	8.999	8.719
Min value	4.798	4.415	4.218
Fraction OK	0.928	0.976	1.000

Appendix C

Repository-scale modelling PM statistics

C.1 Combined DFN/CPM repository-scale model realistic case with lower transmissivity below ZFMNE00A2 (HCD3_AC_HRD4A2_T)

Table C-1. Performance statistics: distribution of $log_{10}(t_r)$ for each path Q1, Q2 and Q3 at different release times for the combined DFN/CPM repository scale model with lower transmissivity below ZFMNE00A2.

$Log_{10}(t_r)$ [y]	2,020 AD			3,000 AD			9,000 AD		
Path	Q1	Q2	Q3	Q1	Q2	Q3	Q1	Q2	Q3
Mean	1.784	1.704	1.724	1.871	1.810	1.825	1.993	1.923	1.949
Median	1.789	1.703	1.718	1.874	1.814	1.826	2.006	1.943	1.968
5th percentile	0.920	0.857	0.899	1.036	1.025	1.037	1.126	1.064	1.086
10th percentile	1.128	1.026	1.077	1.241	1.209	1.195	1.354	1.276	1.290
25th percentile	1.440	1.357	1.379	1.583	1.493	1.498	1.673	1.589	1.616
75th percentile	2.128	2.067	2.069	2.207	2.141	2.164	2.348	2.273	2.296
90th percentile	2.455	2.384	2.396	2.504	2.452	2.456	2.630	2.582	2.609
95th percentile	2.638	2.560	2.573	2.688	2.631	2.612	2.806	2.760	2.784
Std deviation	0.526	0.527	0.512	0.506	0.499	0.490	0.516	0.521	0.521
Variance	0.277	0.278	0.262	0.256	0.249	0.240	0.267	0.271	0.271
Max value	3.896	3.444	3.289	3.521	3.793	3.776	3.679	3.554	3.688
Min value	–0.374	–0.421	–0.430	–0.520	–0.615	–0.588	–0.578	–0.716	–0.736
Fraction OK	0.398	0.581	0.577	0.389	0.572	0.551	0.392	0.567	0.568

Table C-2. Performance statistics: distribution of $log_{10}(U_r)$ for each path Q1, Q2 and Q3 at different release times for the combined DFN/CPM repository scale model with lower transmissivity below ZFMNE00A2.

$Log_{10}(U_r)$ [m/y]	2,020 AD			3,000 AD			9,000 AD		
Path	Q1	Q2	Q3	Q1	Q2	Q3	Q1	Q2	Q3
Mean	–4.807	–5.244	–4.884	–4.873	–5.320	–4.938	–4.985	–5.320	–5.007
Median	–4.814	–5.300	–4.855	–4.873	–5.380	–4.915	–4.988	–5.380	–4.999
5th percentile	–6.367	–6.338	–5.781	–6.445	–6.396	–5.774	–6.541	–6.396	–5.886
10th percentile	–6.039	–6.068	–5.537	–6.091	–6.133	–5.565	–6.203	–6.133	–5.659
25th percentile	–5.423	–5.687	–5.193	–5.476	–5.781	–5.248	–5.620	–5.781	–5.316
75th percentile	–4.210	–4.882	–4.546	–4.269	–4.946	–4.612	–4.373	–4.946	–4.673
90th percentile	–3.606	–4.424	–4.265	–3.675	–4.478	–4.334	–3.778	–4.478	–4.356
95th percentile	–3.121	–3.984	–4.083	–3.255	–4.050	–4.161	–3.379	–4.050	–4.179
Std deviation	0.995	0.769	0.520	0.977	0.764	0.499	0.980	0.764	0.519
Variance	0.990	0.592	0.271	0.955	0.584	0.249	0.959	0.584	0.269
Max value	–0.428	–0.285	–2.930	–0.632	–0.558	–3.149	–0.901	–0.558	–3.143
Min value	–9.147	–8.280	–7.653	–9.001	–8.577	–7.549	–8.926	–8.577	–7.516
Fraction OK	0.727	1.000	1.000	0.734	1.000	1.000	0.732	1.000	1.000

Table C-3. Performance statistics: distribution of $\log_{10}(L_r)$ for each path Q1, Q2 and Q3 at different release times for the combined DFN/CPM repository scale model with lower transmissivity below ZFMNE00A2.

$\log_{10}(L_r)$ [m]	2,020 AD			3,000 AD			9,000 AD		
Path	Q1	Q2	Q3	Q1	Q2	Q3	Q1	Q2	Q3
Mean	3.005	2.996	2.996	3.096	3.094	3.095	3.318	3.311	3.311
Median	2.988	2.984	2.982	3.038	3.041	3.035	3.076	3.074	3.076
5th percentile	2.723	2.707	2.714	2.776	2.758	2.757	2.766	2.753	2.755
10th percentile	2.755	2.745	2.746	2.819	2.807	2.808	2.813	2.808	2.808
25th percentile	2.847	2.835	2.839	2.919	2.908	2.909	2.924	2.914	2.913
75th percentile	3.139	3.128	3.124	3.215	3.226	3.228	4.070	4.070	4.067
90th percentile	3.274	3.260	3.260	3.436	3.442	3.445	4.102	4.100	4.100
95th percentile	3.351	3.350	3.359	3.736	3.737	3.750	4.118	4.113	4.113
Std deviation	0.198	0.200	0.198	0.259	0.263	0.268	0.517	0.516	0.517
Variance	0.039	0.040	0.039	0.067	0.069	0.072	0.268	0.267	0.267
Max value	3.823	3.857	4.195	4.075	4.096	4.169	4.348	4.324	4.390
Min value	2.621	2.620	2.617	2.670	2.657	2.657	2.648	2.663	2.651
Fraction OK	0.398	0.581	0.577	0.389	0.572	0.551	0.392	0.567	0.568

Table C-4. Performance statistics: distribution of $\log_{10}(F_r)$ for each path Q1, Q2 and Q3 at different release times for the combined DFN/CPM repository scale model with lower transmissivity below ZFMNE00A2.

$\log_{10}(F_r)$ [y/m]	2,020 AD			3,000 AD			9,000 AD		
Path	Q1	Q2	Q3	Q1	Q2	Q3	Q1	Q2	Q3
Mean	6.549	6.359	6.414	6.632	6.482	6.515	6.747	6.601	6.657
Median	6.647	6.475	6.506	6.722	6.575	6.623	6.819	6.682	6.738
5th percentile	5.025	4.649	4.853	5.188	4.940	4.997	5.386	5.162	5.283
10th percentile	5.522	5.182	5.305	5.607	5.443	5.485	5.759	5.590	5.684
25th percentile	6.112	5.893	5.975	6.219	6.045	6.083	6.326	6.162	6.215
75th percentile	7.077	6.968	6.978	7.146	7.023	7.063	7.268	7.142	7.173
90th percentile	7.465	7.340	7.374	7.523	7.420	7.419	7.619	7.521	7.555
95th percentile	7.707	7.551	7.573	7.710	7.615	7.599	7.845	7.726	7.754
Std deviation	0.794	0.856	0.813	0.767	0.794	0.780	0.750	0.776	0.758
Variance	0.631	0.733	0.662	0.588	0.631	0.608	0.563	0.603	0.575
Max value	9.371	8.719	8.451	8.686	9.055	9.045	8.971	8.660	8.976
Min value	3.372	3.218	3.041	3.427	3.024	3.051	3.658	2.923	2.903
Fraction OK	0.398	0.581	0.577	0.389	0.572	0.551	0.392	0.567	0.568

Table C-5. Performance statistics: distribution of $\log_{10}(t_T)$ for each path Q1, Q2 and Q3 at different release times for the combined DFN/CPM repository scale model with lower transmissivity below ZFMNE00A2.

$\log_{10}(t_T)$ [y]	2,020 AD			3,000 AD			9,000 AD		
Path	Q1	Q2	Q3	Q1	Q2	Q3	Q1	Q2	Q3
Mean	5.621	5.514	5.602	5.665	5.565	5.662	5.748	5.655	5.769
Median	5.714	5.627	5.656	5.755	5.676	5.713	5.842	5.754	5.806
5th percentile	4.313	4.068	4.433	4.295	4.144	4.527	4.328	4.245	4.597
10th percentile	4.634	4.442	4.720	4.728	4.492	4.791	4.735	4.647	4.903
25th percentile	5.199	5.075	5.173	5.286	5.137	5.252	5.304	5.177	5.344
75th percentile	6.130	6.042	6.080	6.163	6.100	6.112	6.286	6.200	6.246
90th percentile	6.501	6.390	6.410	6.470	6.436	6.459	6.629	6.533	6.569
95th percentile	6.667	6.564	6.592	6.688	6.607	6.678	6.799	6.715	6.745
Std deviation	0.737	0.768	0.670	0.725	0.760	0.657	0.753	0.753	0.658
Variance	0.544	0.590	0.449	0.526	0.577	0.432	0.568	0.567	0.433
Max value	7.682	8.057	8.063	7.440	7.534	7.819	7.828	7.759	8.090
Min value	2.508	2.387	3.123	2.611	2.208	3.168	2.953	2.077	3.187
Fraction OK	0.298	0.483	0.577	0.286	0.474	0.551	0.287	0.469	0.568

Table C-6. Performance statistics: distribution of $\log_{10}(L_T)$ for each path Q1, Q2 and Q3 at different release times for the combined DFN/CPM repository scale model with lower transmissivity below ZFMNE00A2.

$\log_{10}(L_T)$ [m]	2,020 AD			3,000 AD			9,000 AD		
Path	Q1	Q2	Q3	Q1	Q2	Q3	Q1	Q2	Q3
Mean	1.216	1.153	1.168	1.206	1.151	1.160	1.188	1.139	1.163
Median	1.229	1.157	1.165	1.233	1.176	1.160	1.217	1.145	1.163
5th percentile	0.404	0.383	0.425	0.368	0.321	0.391	0.361	0.315	0.375
10th percentile	0.603	0.525	0.572	0.550	0.457	0.540	0.512	0.485	0.558
25th percentile	0.918	0.813	0.853	0.908	0.800	0.826	0.847	0.793	0.842
75th percentile	1.552	1.506	1.511	1.540	1.518	1.510	1.548	1.502	1.497
90th percentile	1.785	1.765	1.748	1.793	1.786	1.778	1.806	1.781	1.776
95th percentile	1.921	1.906	1.895	1.933	1.929	1.904	1.937	1.909	1.897
Std deviation	0.453	0.468	0.452	0.463	0.491	0.467	0.478	0.486	0.458
Variance	0.205	0.219	0.205	0.214	0.241	0.218	0.228	0.236	0.209
Max value	2.398	2.636	2.346	2.323	2.480	2.355	2.593	2.883	2.704
Min value	–0.067	–0.128	–0.079	–0.197	–0.224	–0.193	–0.161	–0.277	–0.068
Fraction OK	0.298	0.483	0.577	0.286	0.474	0.551	0.287	0.469	0.568

Table C-7. Performance statistics: Distribution of $log_{10}(t_{EDZ})$ for each path Q1, Q2 and Q3 at different release times for the combined DFN/CPM repository scale model with lower transmissivity below ZFMNE00A2.

$Log_{10}(t_{EDZ})$ [y]	2,020 AD			3,000 AD			9,000 AD		
Path	Q1	Q2	Q3	Q1	Q2	Q3	Q1	Q2	Q3
Mean	1.272	1.125	1.292	1.306	1.178	1.340	1.393	1.291	1.435
Median	1.326	1.242	1.343	1.370	1.300	1.395	1.478	1.418	1.515
5th percentile	0.044	–0.401	0.121	0.142	–0.334	0.148	0.182	–0.192	0.209
10th percentile	0.364	–0.018	0.412	0.399	0.070	0.454	0.481	0.223	0.500
25th percentile	0.863	0.633	0.866	0.890	0.684	0.930	0.937	0.818	1.013
75th percentile	1.750	1.702	1.756	1.773	1.762	1.811	1.871	1.872	1.938
90th percentile	2.084	2.088	2.100	2.110	2.119	2.153	2.227	2.211	2.225
95th percentile	2.266	2.293	2.312	2.325	2.328	2.333	2.382	2.386	2.405
Std deviation	0.670	0.818	0.675	0.663	0.813	0.658	0.684	0.807	0.673
Variance	0.449	0.669	0.456	0.440	0.661	0.433	0.467	0.651	0.453
Max value	3.013	3.261	3.289	2.822	3.400	3.059	2.952	3.233	3.168
Min value	–2.164	–2.837	–2.164	–1.017	–1.928	–0.945	–1.212	–2.109	–1.689
Fraction OK	0.155	0.522	0.297	0.150	0.513	0.291	0.151	0.510	0.308

Table C-8. Performance statistics: distribution of $log_{10}(L_{EDZ})$ at different release times for the combined DFN/CPM repository scale model with lower transmissivity below ZFMNE00A2.

$Log_{10}(L_{EDZ})$ [m]	2,020 AD			3,000 AD			9,000 AD		
Path	Q1	Q2	Q3	Q1	Q2	Q3	Q1	Q2	Q3
Mean	0.943	0.825	0.906	0.924	0.807	0.919	0.944	0.833	0.932
Median	0.973	0.886	0.916	0.949	0.863	0.949	0.974	0.901	0.974
5th percentile	0.141	–0.039	0.161	0.158	–0.026	0.172	0.174	–0.064	0.163
10th percentile	0.325	0.166	0.310	0.301	0.171	0.296	0.372	0.174	0.346
25th percentile	0.696	0.469	0.646	0.632	0.434	0.648	0.685	0.477	0.662
75th percentile	1.259	1.206	1.226	1.249	1.192	1.241	1.271	1.206	1.242
90th percentile	1.493	1.442	1.457	1.475	1.433	1.460	1.488	1.447	1.477
95th percentile	1.604	1.559	1.578	1.584	1.539	1.580	1.619	1.575	1.604
Std deviation	0.445	0.503	0.434	0.434	0.507	0.431	0.442	0.513	0.433
Variance	0.198	0.253	0.188	0.188	0.257	0.186	0.195	0.263	0.187
Max value	1.951	1.908	1.900	1.855	2.062	1.973	1.914	1.980	1.906
Min value	–1.077	–1.223	–1.077	–0.422	–2.960	–0.629	–1.034	–1.460	–1.077
Fraction OK	0.155	0.522	0.297	0.150	0.513	0.291	0.151	0.510	0.308

C.2 Combined DFN/CPM repository-scale model realistic case with higher tunnel backfill conductivity (HCD3_AC_HRD4A2_T_T2)

Table C-9. Performance statistics: Distribution of $log_{10}(U_r)$ and $log_{10}(F_r)$ for each path Q1, Q2 and Q3 at release time 2,020 AD for the combined DFN/CPM repository scale model with higher tunnel backfill conductivity.

Path	Log10(U_r) [m/y]			Log10(F_r) [y/m]		
	Q1	Q2	Q3	Q1	Q2	Q3
Mean	–4.776	–5.413	–3.427	6.322	6.055	5.951
Median	–4.818	–5.474	–3.328	6.376	6.156	6.075
5th percentile	–6.471	–6.719	–4.641	4.835	4.383	4.316
10th percentile	–6.100	–6.406	–4.257	5.191	4.776	4.606
25th percentile	–5.470	–5.940	–3.764	5.812	5.511	5.357
75th percentile	–4.109	–5.033	–2.966	6.888	6.696	6.590
90th percentile	–3.393	–4.467	–2.693	7.346	7.136	7.021
95th percentile	–2.959	–3.589	–2.575	7.616	7.365	7.293
Std deviation	1.068	0.914	0.674	0.836	0.890	0.899
Variance	1.142	0.835	0.454	0.699	0.792	0.808
Max value	–0.413	–0.286	–1.686	9.588	8.371	9.504
Min value	–8.472	–9.378	–6.749	3.423	3.213	3.205
Fraction OK	0.729	1.000	1.000	0.368	0.540	0.576

Table C-10. Performance statistics: Distribution of $log_{10}(t_r)$, $log_{10}(t_T)$ and $log_{10}(t_{EDZ})$ for each path Q1, Q2 and Q3 at release time 2,020 AD for the combined DFN/CPM repository scale model with higher tunnel backfill conductivity.

Path	Log10(t_r) [y]			Log10(t_T) [y]			Log10(t_{EDZ}) [y]		
	Q1	Q2	Q3	Q1	Q2	Q3	Q1	Q2	Q3
Mean	1.613	1.515	1.478	5.075	5.055	4.884	1.478	1.286	1.417
Median	1.589	1.498	1.459	5.115	5.202	4.893	1.536	1.437	1.451
5th percentile	0.796	0.729	0.746	3.275	3.099	3.199	0.236	–0.446	0.170
10th percentile	0.982	0.907	0.888	3.720	3.649	3.549	0.486	–0.045	0.427
25th percentile	1.271	1.188	1.152	4.298	4.308	4.121	1.034	0.729	0.955
75th percentile	1.951	1.833	1.785	5.905	5.885	5.713	1.974	1.959	1.946
90th percentile	2.289	2.157	2.118	6.406	6.312	6.191	2.365	2.354	2.307
95th percentile	2.506	2.355	2.293	6.649	6.551	6.447	2.584	2.571	2.502
Std deviation	0.520	0.493	0.479	1.050	1.079	1.021	0.730	0.928	0.722
Variance	0.271	0.243	0.229	1.102	1.165	1.043	0.533	0.862	0.521
Max value	4.335	3.160	4.268	7.831	7.559	7.983	3.209	3.433	3.455
Min value	–0.244	–0.426	–0.434	1.796	0.931	1.889	–2.156	–2.872	–2.156
Fraction OK	0.368	0.540	0.576	0.289	0.453	0.576	0.121	0.481	0.233

Table C-11. Performance statistics: Distribution of log10(L_r), log10(L_T) and $\log_{10}(L_{EDZ})$ for each path Q1, Q2 and Q3 at release time 2,020 AD for the combined DFN/CPM repository scale model with higher tunnel backfill conductivity.

Path	Log10(L_r) [m]			Log10(L_T) [m]			Log10(L_{EDZ}) [m]		
	Q1	Q2	Q3	Q1	Q2	Q3	Q1	Q2	Q3
Mean	2.911	2.901	2.894	1.508	1.461	1.488	0.923	0.795	0.834
Median	2.895	2.885	2.872	1.588	1.527	1.532	0.942	0.861	0.831
5th percentile	2.651	2.646	2.638	0.546	0.510	0.610	0.158	–0.097	0.145
10th percentile	2.688	2.681	2.673	0.772	0.722	0.787	0.313	0.081	0.256
25th percentile	2.762	2.750	2.743	1.149	1.090	1.147	0.630	0.422	0.528
75th percentile	3.039	3.033	3.025	1.905	1.865	1.858	1.254	1.199	1.162
90th percentile	3.173	3.167	3.166	2.124	2.102	2.098	1.458	1.431	1.385
95th percentile	3.248	3.250	3.253	2.227	2.231	2.220	1.597	1.541	1.501
Std deviation	0.193	0.195	0.198	0.522	0.525	0.493	0.437	0.521	0.427
Variance	0.037	0.038	0.039	0.272	0.275	0.243	0.191	0.272	0.182
Max value	3.644	3.574	3.562	2.595	2.577	2.563	2.036	1.917	1.933
Min value	2.179	2.206	2.193	–0.123	–0.267	–0.066	–0.491	–1.365	–0.923
Fraction OK	0.368	0.540	0.576	0.289	0.453	0.576	0.121	0.481	0.233

C.3 Combined DFN/CPM repository-scale model realistic case with higher EDZ conductivity (HCD3_AC_HRD4A2_T_EDZ)

Table C-12. Performance statistics: Distribution of $\log_{10}(U_r)$ and $\log_{10}(F_r)$ for each path Q1, Q2 and Q3 at release time 2,020 AD for the combined DFN/CPM repository scale model with higher EDZ conductivity.

Path	Log10(U_r) [m/y]			Log10(F_r) [y/m]		
	Q1	Q2	Q3	Q1	Q2	Q3
Mean	–4.766	–4.624	–4.848	6.479	6.212	6.285
Median	–4.770	–4.598	–4.821	6.573	6.343	6.424
5th percentile	–6.346	–5.886	–5.763	4.998	4.422	4.577
10th percentile	–6.002	–5.587	–5.502	5.459	4.882	5.051
25th percentile	–5.381	–5.096	–5.147	6.045	5.714	5.816
75th percentile	–4.161	–4.133	–4.508	7.013	6.849	6.876
90th percentile	–3.568	–3.759	–4.213	7.381	7.233	7.275
95th percentile	–3.117	–3.496	–4.057	7.642	7.468	7.483
Std deviation	0.986	0.772	0.520	0.783	0.895	0.851
Variance	0.972	0.596	0.271	0.613	0.802	0.724
Max value	–0.423	–0.285	–2.939	9.156	8.500	8.713
Min value	–8.931	–8.019	–7.967	3.401	3.224	3.093
Fraction OK	0.728	1.000	1.000	0.436	0.657	0.637

Table C-13. Performance statistics: Distribution of log10(t_r), log10(t_T) and $\log_{10}(t_{EDZ})$ for each path Q1, Q2 and Q3 at release time 2,020 AD for the combined DFN/CPM repository scale model with higher EDZ conductivity.

Path	Log10(t_r) [y]			Log10(t_T) [y]			Log10(t_{EDZ}) [y]		
	Q1	Q2	Q3	Q1	Q2	Q3	Q1	Q2	Q3
Mean	1.735	1.638	1.671	5.612	5.490	5.593	0.648	0.610	0.697
Median	1.746	1.647	1.676	5.719	5.594	5.638	0.717	0.679	0.737
5th percentile	0.891	0.783	0.835	4.158	3.999	4.322	–0.582	–0.707	–0.447
10th percentile	1.083	0.966	1.012	4.587	4.413	4.667	–0.230	–0.335	–0.139
25th percentile	1.396	1.283	1.323	5.193	5.026	5.145	0.232	0.201	0.290
75th percentile	2.081	1.992	2.015	6.123	6.045	6.089	1.112	1.111	1.160
90th percentile	2.385	2.313	2.339	6.493	6.396	6.447	1.438	1.440	1.503
95th percentile	2.575	2.504	2.504	6.672	6.603	6.676	1.635	1.633	1.680
Std deviation	0.517	0.522	0.507	0.750	0.784	0.700	0.660	0.711	0.653
Variance	0.267	0.272	0.257	0.563	0.614	0.489	0.436	0.506	0.426
Max value	3.833	3.255	3.349	7.580	7.507	7.638	2.622	2.810	2.347
Min value	–0.182	–0.414	–0.384	2.027	2.645	3.127	–1.691	–2.679	–2.127
Fraction OK	0.436	0.657	0.637	0.336	0.543	0.637	0.237	0.602	0.431

Table C-14. Performance statistics: Distribution of $\log_{10}(L_r)$, log10(L_T) and $\log_{10}(L_{EDZ})$ for each path Q1, Q2 and Q3 at release time 2,020 AD for the combined DFN/CPM repository scale model with higher EDZ conductivity.

Path	Log10(L_r) [m]			Log10(L_T) [m]			Log10(L_{EDZ}) [m]		
	Q1	Q2	Q3	Q1	Q2	Q3	Q1	Q2	Q3
Mean	2.949	2.939	2.945	1.163	1.098	1.109	1.174	1.053	1.171
Median	2.933	2.927	2.935	1.181	1.084	1.106	1.239	1.165	1.227
5th percentile	2.671	2.658	2.659	0.371	0.344	0.326	0.288	0.035	0.305
10th percentile	2.706	2.695	2.692	0.535	0.485	0.493	0.539	0.285	0.549
25th percentile	2.790	2.776	2.779	0.876	0.774	0.807	0.877	0.696	0.872
75th percentile	3.085	3.068	3.079	1.480	1.446	1.434	1.513	1.473	1.517
90th percentile	3.230	3.223	3.229	1.752	1.697	1.712	1.734	1.698	1.723
95th percentile	3.309	3.305	3.316	1.880	1.846	1.874	1.829	1.802	1.825
Std deviation	0.200	0.202	0.205	0.455	0.460	0.459	0.466	0.569	0.460
Variance	0.040	0.041	0.042	0.207	0.212	0.211	0.217	0.323	0.212
Max value	3.539	3.594	3.618	2.609	2.531	2.558	2.130	2.226	2.287
Min value	2.248	2.289	2.244	–0.202	–0.126	–0.261	–0.528	–1.243	–1.067
Fraction OK	0.436	0.657	0.637	0.336	0.543	0.637	0.237	0.602	0.431

C.4 Combined DFN/CPM repository-scale model realistic case with semi-correlated transmissivity (HCD3_AC_HRD4SA2_T)

Table C-15. Performance statistics: Distribution of $log_{10}(U_r)$ and $log_{10}(F_r)$ for each path Q1, Q2 and Q3 at release time 2,020 AD for the combined DFN/CPM repository scale model with semi-correlated transmissivity.

Path	Log10(U_r) [m/y]			Log10(F_r) [y/m]		
	Q1	Q2	Q3	Q1	Q2	Q3
Mean	–3.985	–4.791	–4.663	5.810	5.725	5.748
Median	–3.918	–4.912	–4.651	5.888	5.802	5.807
5th percentile	–5.953	–6.061	–5.391	4.375	4.325	4.400
10th percentile	–5.537	–5.823	–5.203	4.728	4.670	4.707
25th percentile	–4.691	–5.442	–4.930	5.316	5.186	5.263
75th percentile	–3.228	–4.317	–4.392	6.357	6.304	6.325
90th percentile	–2.582	–3.569	–4.135	6.774	6.680	6.687
95th percentile	–2.187	–3.003	–3.959	7.069	6.919	6.922
Std deviation	1.125	0.956	0.434	0.828	0.827	0.801
Variance	1.265	0.915	0.188	0.686	0.685	0.641
Max value	0.531	0.702	–2.072	8.347	8.143	8.624
Min value	–7.916	–8.493	–6.846	2.038	1.966	2.001
Fraction OK	0.741	1.000	1.000	0.228	0.322	0.313

Table C-16. Performance statistics: Distribution of $log_{10}(t_r)$, $log_{10}(t_T)$ and $log_{10}(t_{EDZ})$ for each path Q1, Q2 and Q3 at release time 2,020 AD for the combined DFN/CPM repository scale model with semi-correlated transmissivity.

Path	Log10(t_r) [y]			Log10(t_T) [y]			Log10(t_{EDZ}) [y]		
	Q1	Q2	Q3	Q1	Q2	Q3	Q1	Q2	Q3
Mean	1.627	1.589	1.600	5.433	5.316	5.412	1.087	0.920	1.135
Median	1.640	1.597	1.610	5.533	5.435	5.440	1.154	1.029	1.199
5th percentile	0.698	0.714	0.706	3.949	3.925	4.276	–0.117	–0.480	0.023
10th percentile	0.931	0.904	0.936	4.353	4.248	4.538	0.218	–0.143	0.287
25th percentile	1.266	1.215	1.237	4.975	4.830	4.969	0.702	0.495	0.747
75th percentile	2.012	1.972	1.987	5.996	5.871	5.887	1.507	1.471	1.536
90th percentile	2.329	2.302	2.285	6.312	6.204	6.244	1.828	1.813	1.849
95th percentile	2.545	2.499	2.468	6.524	6.408	6.422	1.984	2.027	2.051
Std deviation	0.588	0.575	0.570	0.775	0.767	0.669	0.632	0.778	0.607
Variance	0.345	0.330	0.325	0.600	0.589	0.448	0.399	0.605	0.368
Max value	4.129	3.775	4.218	7.516	7.525	7.280	2.663	3.261	2.692
Min value	–0.894	–0.921	–0.965	2.627	2.447	2.634	–0.937	–2.329	–0.937
Fraction OK	0.228	0.322	0.313	0.160	0.267	0.313	0.067	0.231	0.141

Table C-17. Performance statistics: Distribution of $log_{10}(L_r)$, $log_{10}(L_T)$ and $log_{10}(L_{EDZ})$ for each path Q1, Q2 and Q3 at release time 2,020 AD for the combined DFN/CPM repository scale model with semi-correlated transmissivity.

Path	Log10(L_r) [m]			Log10(L_T) [m]			Log10(L_{EDZ}) [m]		
	Q1	Q2	Q3	Q1	Q2	Q3	Q1	Q2	Q3
Mean	3.052	3.056	3.057	1.119	1.100	1.116	0.866	0.740	0.866
Median	3.012	3.014	3.013	1.133	1.097	1.100	0.891	0.777	0.866
5th percentile	2.695	2.693	2.696	0.315	0.346	0.403	0.092	–0.038	0.139
10th percentile	2.743	2.736	2.735	0.493	0.517	0.554	0.246	0.134	0.289
25th percentile	2.839	2.832	2.838	0.810	0.778	0.823	0.602	0.421	0.635
75th percentile	3.209	3.235	3.234	1.452	1.420	1.413	1.148	1.092	1.156
90th percentile	3.455	3.476	3.464	1.706	1.698	1.681	1.375	1.341	1.379
95th percentile	3.568	3.574	3.585	1.856	1.854	1.815	1.498	1.469	1.484
Std deviation	0.264	0.271	0.270	0.465	0.461	0.430	0.420	0.482	0.401
Variance	0.070	0.073	0.073	0.217	0.213	0.185	0.176	0.232	0.161
Max value	3.820	3.790	3.784	2.409	2.512	2.788	1.992	1.992	1.967
Min value	2.615	2.603	2.583	–0.222	–0.228	–0.043	–0.350	–1.097	–0.149
Fraction OK	0.228	0.322	0.313	0.160	0.267	0.313	0.067	0.231	0.141

C.5 Combined DFN/CPM repository-scale model realistic case with uncorrelated transmissivity (HCD3_AC_HRD4UA2_T)

Table C-18. Performance statistics: Distribution of $log_{10}(U_r)$ and $log_{10}(F_r)$ for each path Q1, Q2 and Q3 at release time 2,020 AD for the combined DFN/CPM repository scale model with uncorrelated transmissivity.

Path	Log10(U_r) [m/y]			Log10(F_r) [y/m]		
	Q1	Q2	Q3	Q1	Q2	Q3
Mean	–3.637	–4.669	–4.591	5.743	5.682	5.699
Median	–3.507	–4.826	–4.587	5.759	5.718	5.724
5th percentile	–5.714	–5.951	–5.271	4.636	4.482	4.579
10th percentile	–5.218	–5.747	–5.097	4.819	4.720	4.798
25th percentile	–4.311	–5.382	–4.838	5.269	5.184	5.197
75th percentile	–2.841	–4.129	–4.341	6.244	6.207	6.211
90th percentile	–2.329	–3.314	–4.095	6.580	6.585	6.551
95th percentile	–2.028	–2.845	–3.928	6.776	6.783	6.744
Std deviation	1.107	0.968	0.406	0.668	0.695	0.672
Variance	1.226	0.937	0.165	0.447	0.484	0.451
Max value	–0.330	–0.551	–2.966	7.948	7.543	7.934
Min value	–8.248	–9.001	–6.534	3.419	3.485	3.545
Fraction OK	0.731	1.000	1.000	0.188	0.249	0.251

Table C-19. Performance statistics: Distribution of $log_{10}(t_r)$, $log_{10}(t_T)$ and $log10(t_{EDZ})$ for each path Q1, Q2 and Q3 at release time 2,020 AD for the combined DFN/CPM repository scale model with uncorrelated transmissivity.

Path	Log10(t_r) [y]			Log10(t_T) [y]			Log10(t_{EDZ}) [y]		
	Q1	Q2	Q3	Q1	Q2	Q3	Q1	Q2	Q3
Mean	1.729	1.697	1.704	5.347	5.219	5.327	1.001	0.829	1.049
Median	1.723	1.673	1.675	5.431	5.269	5.367	1.065	0.928	1.118
5th percentile	0.963	0.915	0.942	3.899	3.790	4.119	–0.180	–0.617	–0.051
10th percentile	1.092	1.042	1.087	4.236	4.116	4.369	0.120	–0.219	0.195
25th percentile	1.368	1.344	1.347	4.840	4.725	4.858	0.520	0.376	0.614
75th percentile	2.089	2.069	2.061	5.913	5.792	5.820	1.451	1.410	1.490
90th percentile	2.369	2.372	2.349	6.275	6.184	6.203	1.839	1.767	1.820
95th percentile	2.534	2.536	2.514	6.515	6.415	6.408	2.029	2.017	2.033
Std deviation	0.495	0.498	0.487	0.800	0.790	0.702	0.659	0.823	0.639
Variance	0.245	0.248	0.238	0.639	0.624	0.493	0.434	0.677	0.409
Max value	4.459	3.127	3.570	7.999	7.366	7.802	2.616	3.203	2.725
Min value	0.292	0.036	0.309	2.801	2.724	3.113	–0.923	–2.664	–1.036
Fraction OK	0.188	0.249	0.251	0.139	0.211	0.251	0.054	0.167	0.106

Table C-20. Performance statistics: Distribution of $log_{10}(L_r)$, $log_{10}(L_T)$ and $log_{10}(L_{EDZ})$ for each path Q1, Q2 and Q3 at release time 2,020 AD for the combined DFN/CPM repository scale model with uncorrelated transmissivity.

Path	Log10(L_r) [m]			Log10(L_T) [m]			Log10(L_{EDZ}) [m]		
	Q1	Q2	Q3	Q1	Q2	Q3	Q1	Q2	Q3
Mean	3.128	3.136	3.128	1.118	1.098	1.127	0.832	0.696	0.810
Median	3.080	3.070	3.080	1.119	1.077	1.101	0.858	0.740	0.834
5th percentile	2.725	2.720	2.722	0.243	0.347	0.417	0.139	–0.103	0.085
10th percentile	2.771	2.766	2.770	0.419	0.503	0.579	0.233	0.085	0.239
25th percentile	2.884	2.881	2.888	0.767	0.764	0.828	0.527	0.411	0.549
75th percentile	3.362	3.378	3.340	1.451	1.405	1.421	1.139	1.030	1.097
90th percentile	3.573	3.598	3.588	1.753	1.728	1.703	1.328	1.289	1.295
95th percentile	3.665	3.694	3.657	1.931	1.903	1.875	1.439	1.385	1.421
Std deviation	0.299	0.310	0.295	0.518	0.475	0.442	0.406	0.477	0.400
Variance	0.090	0.096	0.087	0.268	0.225	0.195	0.165	0.227	0.160
Max value	3.905	3.883	3.879	3.280	2.775	2.894	2.269	1.776	1.767
Min value	2.194	2.389	2.572	–0.181	–0.199	–0.062	–0.142	–1.457	–0.501
Fraction OK	0.188	0.249	0.251	0.139	0.211	0.251	0.054	0.167	0.106

C.6 Nested CPM repository-scale base case model (HCD3_AC_HRDDT)

Table C-21. Performance statistics: Distribution of $\log_{10}(t_r)$ for each path Q1, Q2 and Q3 at different release times for the nested CPM repository scale base case model.

$\log_{10}(t_r)$ [y]	2,020 AD			3,000 AD			9,000 AD		
Path	Q1	Q2	Q3	Q1	Q2	Q3	Q1	Q2	Q3
Mean	3.540	3.535	3.535	3.800	3.779	3.779	3.775	3.763	3.756
Median	3.445	3.436	3.437	3.354	3.336	3.332	3.859	3.857	3.855
5th percentile	3.033	3.032	3.035	2.888	2.862	2.864	3.015	2.992	2.990
10th percentile	3.128	3.121	3.129	2.956	2.947	2.946	3.115	3.091	3.087
25th percentile	3.255	3.249	3.249	3.080	3.061	3.061	3.575	3.540	3.519
75th percentile	3.749	3.745	3.745	4.145	4.086	4.092	3.996	3.993	3.992
90th percentile	4.054	4.039	4.047	5.809	5.793	5.806	4.106	4.101	4.100
95th percentile	4.226	4.221	4.228	6.211	6.188	6.229	4.171	4.166	4.164
Std deviation	0.435	0.442	0.441	1.060	1.060	1.063	0.466	0.472	0.468
Variance	0.189	0.195	0.195	1.123	1.123	1.129	0.217	0.223	0.219
Max value	6.305	6.292	6.285	6.849	6.961	6.772	6.838	6.895	6.530
Min value	2.749	2.679	2.695	2.474	2.444	2.446	2.640	2.489	2.485
Fraction OK	0.903	0.900	0.897	0.600	0.602	0.601	1.000	1.000	1.000

Table C-22. Performance statistics: Distribution of $\log_{10}(U_r)$ for each path Q1, Q2 and Q3 at different release times for the nested CPM repository scale base case model.

$\log_{10}(U_r)$ [m/y]	2,020 AD			3,000 AD			9,000 AD		
Path	Q1	Q2	Q3	Q1	Q2	Q3	Q1	Q2	Q3
Mean	–6.118	–6.068	–5.501	–6.125	–5.837	–5.316	–6.097	–5.837	–5.301
Median	–6.111	–6.102	–5.517	–6.144	–5.816	–5.298	–6.085	–5.816	–5.270
5th percentile	–6.524	–6.364	–5.802	–6.436	–6.244	–5.693	–6.545	–6.244	–5.777
10th percentile	–6.417	–6.277	–5.714	–6.350	–6.131	–5.585	–6.451	–6.131	–5.682
25th percentile	–6.252	–6.184	–5.600	–6.236	–5.934	–5.411	–6.251	–5.934	–5.460
75th percentile	–6.010	–5.979	–5.424	–6.054	–5.713	–5.196	–5.975	–5.713	–5.120
90th percentile	–5.931	–5.798	–5.248	–5.969	–5.592	–5.079	–5.901	–5.592	–5.003
95th percentile	–5.895	–5.678	–5.153	–5.904	–5.551	–5.036	–5.848	–5.551	–4.933
Std deviation	0.322	0.220	0.199	0.311	0.220	0.206	0.353	0.220	0.257
Variance	0.103	0.048	0.040	0.097	0.048	0.042	0.125	0.048	0.066
Max value	–3.440	–4.149	–3.741	–3.397	–4.163	–3.751	–3.259	–4.163	–3.716
Min value	–7.186	–7.206	–6.719	–7.075	–6.900	–6.388	–6.860	–6.900	–6.086
Fraction OK	1.000	1.000	1.000	1.000	1.000	1.000	1.000	1.000	1.000

Table C-23. Performance statistics: Distribution of $\log_{10}(L_r)$ for each path Q1, Q2 and Q3 at different release times for the nested CPM repository scale base case model.

$\log_{10}(L_r)$ [m]	2,020 AD			3,000 AD			9,000 AD		
Path	Q1	Q2	Q3	Q1	Q2	Q3	Q1	Q2	Q3
Mean	3.181	3.178	3.174	3.088	3.082	3.082	3.777	3.764	3.759
Median	3.081	3.077	3.073	3.031	3.020	3.020	4.091	4.090	4.089
5th percentile	2.755	2.752	2.752	2.783	2.779	2.777	2.813	2.805	2.805
10th percentile	2.795	2.794	2.795	2.820	2.817	2.814	2.862	2.854	2.852
25th percentile	2.897	2.893	2.890	2.897	2.893	2.893	3.104	3.062	3.047
75th percentile	3.426	3.420	3.416	3.210	3.209	3.207	4.109	4.108	4.108
90th percentile	3.728	3.728	3.727	3.302	3.299	3.299	4.124	4.123	4.123
95th percentile	3.932	3.939	3.912	3.758	3.755	3.738	4.130	4.130	4.129
Std deviation	0.363	0.365	0.361	0.283	0.279	0.279	0.526	0.533	0.536
Variance	0.132	0.133	0.131	0.080	0.078	0.078	0.277	0.284	0.287
Max value	4.394	4.347	4.384	4.385	4.351	4.337	4.182	4.189	4.181
Min value	2.649	2.647	2.665	2.641	2.638	2.638	2.681	2.676	2.643
Fraction OK	0.903	0.900	0.897	0.600	0.602	0.601	1.000	1.000	1.000

Table C-24. Performance statistics: Distribution of $\log_{10}(F_r)$ for each path Q1, Q2 and Q3 at different release times for the nested CPM repository scale base case model.

$\log_{10}(F_r)$ [y/m]	2,020 AD			3,000 AD			9,000 AD		
Path	Q1	Q2	Q3	Q1	Q2	Q3	Q1	Q2	Q3
Mean	7.686	7.667	7.671	7.850	7.828	7.827	8.362	8.347	8.341
Median	7.681	7.668	7.668	7.818	7.796	7.792	8.562	8.556	8.550
5th percentile	7.079	7.016	7.012	7.114	7.029	7.035	7.439	7.406	7.403
10th percentile	7.353	7.322	7.330	7.381	7.346	7.343	7.625	7.599	7.601
25th percentile	7.535	7.522	7.525	7.568	7.548	7.546	8.037	8.002	7.976
75th percentile	7.859	7.847	7.848	8.158	8.157	8.155	8.693	8.690	8.689
90th percentile	8.096	8.086	8.092	8.392	8.387	8.391	8.785	8.779	8.778
95th percentile	8.267	8.250	8.258	8.528	8.523	8.520	8.825	8.822	8.821
Std deviation	0.358	0.372	0.373	0.470	0.486	0.485	0.476	0.492	0.495
Variance	0.128	0.138	0.139	0.221	0.236	0.235	0.227	0.242	0.245
Max value	8.999	8.960	9.170	9.215	9.214	9.242	9.098	9.158	9.119
Min value	5.804	5.668	5.771	6.073	5.536	5.540	6.097	5.702	5.616
Fraction OK	0.903	0.900	0.897	0.600	0.602	0.601	1.000	1.000	1.000

Table C-25. Performance statistics: Distribution of $\log_{10}(t_T)$ for each path Q1, Q2 and Q3 at different release times for the nested CPM repository scale base case model.

$\log_{10}(t_T)$ [y]	2,020 AD			3,000 AD			9,000 AD		
Path	Q1	Q2	Q3	Q1	Q2	Q3	Q1	Q2	Q3
Mean	5.823	5.809	5.815	5.755	5.691	5.631	5.780	5.866	5.565
Median	5.842	5.811	5.816	5.734	5.677	5.616	5.698	5.870	5.606
5th percentile	5.229	5.395	5.422	5.033	5.186	4.716	5.141	5.193	4.556
10th percentile	5.396	5.504	5.528	5.371	5.320	4.885	5.383	5.436	4.650
25th percentile	5.676	5.708	5.719	5.548	5.466	5.451	5.526	5.660	5.193
75th percentile	6.052	5.927	5.929	6.020	5.855	5.895	6.054	6.117	5.993
90th percentile	6.206	6.067	6.067	6.249	6.189	6.225	6.341	6.346	6.314
95th percentile	6.286	6.220	6.218	6.440	6.354	6.403	6.476	6.470	6.462
Std deviation	0.337	0.254	0.247	0.425	0.370	0.456	0.417	0.391	0.583
Variance	0.114	0.065	0.061	0.180	0.137	0.208	0.174	0.153	0.339
Max value	7.002	6.884	6.880	6.873	6.815	6.809	7.012	7.026	7.120
Min value	3.035	2.775	3.603	3.540	3.383	4.367	3.646	2.570	3.362
Fraction OK	0.852	0.892	0.897	0.478	0.577	0.601	0.672	0.734	1.000

Table C-26. Performance statistics: Distribution of $\log_{10}(L_T)$ for each path Q1, Q2 and Q3 at different release times for the nested CPM repository scale base case model.

$\log_{10}(L_T)$ [m]	2,020 AD			3,000 AD			9,000 AD		
Path	Q1	Q2	Q3	Q1	Q2	Q3	Q1	Q2	Q3
Mean	0.704	0.780	0.790	0.602	0.742	0.794	0.441	0.641	0.531
Median	0.755	0.763	0.763	0.765	0.766	0.815	0.175	0.549	0.315
5th percentile	0.163	0.518	0.553	–0.220	0.043	–0.116	–0.495	–0.166	–0.129
10th percentile	0.336	0.573	0.600	–0.147	0.136	0.086	–0.282	–0.019	–0.086
25th percentile	0.612	0.672	0.694	–0.014	0.545	0.622	–0.069	0.223	0.041
75th percentile	0.848	0.856	0.863	1.021	0.954	1.012	1.067	1.077	0.999
90th percentile	0.998	1.019	1.028	1.304	1.294	1.336	1.412	1.419	1.369
95th percentile	1.095	1.169	1.178	1.552	1.513	1.553	1.534	1.565	1.558
Std deviation	0.304	0.203	0.200	0.588	0.424	0.429	0.682	0.551	0.566
Variance	0.092	0.041	0.040	0.346	0.180	0.184	0.465	0.304	0.320
Max value	1.716	1.731	1.674	1.906	1.911	1.918	1.894	1.912	1.946
Min value	–1.988	–0.814	–0.143	–1.831	–1.534	–0.152	–2.026	–1.683	–0.336
Fraction OK	0.852	0.892	0.897	0.478	0.577	0.601	0.672	0.734	1.000

Table C-27. Performance statistics: Distribution of $\log_{10}(t_{EDZ})$ for each path Q1, Q2 and Q3 at different release times for the nested CPM repository scale base case model.

$\log_{10}(t_{EDZ})$ [y]	2,020 AD			3,000 AD			9,000 AD		
Path	Q1	Q2	Q3	Q1	Q2	Q3	Q1	Q2	Q3
Mean	1.746	1.535	2.255	1.843	1.761	2.035	1.932	1.793	1.867
Median	1.712	1.484	2.359	1.873	1.676	2.054	1.935	1.748	1.893
5th percentile	1.349	1.222	1.370	1.150	1.261	1.583	0.849	1.149	1.080
10th percentile	1.503	1.271	1.512	1.350	1.327	1.682	1.269	1.227	1.340
25th percentile	1.597	1.366	1.942	1.673	1.453	1.865	1.742	1.451	1.673
75th percentile	1.896	1.622	2.590	2.074	2.052	2.194	2.251	2.144	2.135
90th percentile	2.091	1.875	2.831	2.312	2.363	2.446	2.537	2.433	2.312
95th percentile	2.242	2.157	3.006	2.505	2.515	2.581	2.643	2.571	2.510
Std deviation	0.294	0.324	0.547	0.422	0.423	0.328	0.496	0.470	0.425
Variance	0.086	0.105	0.299	0.178	0.179	0.108	0.246	0.220	0.180
Max value	3.150	3.392	3.485	2.981	3.305	3.589	3.177	3.216	2.986
Min value	–0.385	–0.214	–0.095	–0.212	–0.025	0.030	–0.271	0.091	–0.326
Fraction OK	0.706	0.895	0.028	0.211	0.602	0.147	0.134	0.993	0.372

Table C-28. Performance statistics: Distribution of $\log_{10}(L_{EDZ})$ at different release times for the nested CPM repository scale base case model.

$\log_{10}(L_{EDZ})$ [m]	2,020 AD			3,000 AD			9,000 AD		
Path	Q1	Q2	Q3	Q1	Q2	Q3	Q1	Q2	Q3
Mean	–0.351	–0.525	0.261	0.014	–0.030	0.268	0.111	–0.027	0.105
Median	–0.408	–0.595	0.256	0.028	–0.090	0.303	0.155	–0.125	0.156
5th percentile	–0.624	–0.850	–0.519	–0.591	–0.568	–0.172	–0.551	–0.599	–0.616
10th percentile	–0.589	–0.815	–0.289	–0.470	–0.513	–0.089	–0.436	–0.568	–0.419
25th percentile	–0.537	–0.708	–0.030	–0.185	–0.407	0.076	–0.119	–0.449	–0.097
75th percentile	–0.216	–0.455	0.554	0.239	0.277	0.438	0.373	0.368	0.365
90th percentile	0.035	–0.135	0.836	0.471	0.611	0.670	0.608	0.641	0.563
95th percentile	0.178	0.123	1.049	0.651	0.759	0.773	0.725	0.789	0.665
Std deviation	0.286	0.307	0.446	0.381	0.430	0.333	0.402	0.469	0.407
Variance	0.082	0.094	0.199	0.145	0.185	0.111	0.162	0.220	0.166
Max value	1.234	1.382	1.467	1.100	1.384	1.160	1.128	1.235	1.262
Min value	–2.286	–1.118	–1.163	–2.141	–1.048	–1.952	–2.018	–0.991	–1.921
Fraction OK	0.706	0.895	0.028	0.211	0.602	0.147	0.134	0.993	0.372

C.7 Nested CPM repository scale model with modified tunnel backfill (HCD3_AC_HRDDT_T2)

Table C-29. Performance statistics: Distribution of $\log_{10}(t_r)$ for each path Q1, Q2 and Q3 at different release times for the nested CPM repository scale model with modified backfill.

$\log_{10}(t_r)$ [y]	2,020 AD			3,000 AD			9,000 AD		
Path	Q1	Q2	Q3	Q1	Q2	Q3	Q1	Q2	Q3
Mean	3.505	3.498	3.498	3.920	3.896	3.724	3.853	3.847	3.777
Median	3.411	3.409	3.405	3.460	3.442	3.277	3.896	3.894	3.870
5th percentile	3.003	2.992	2.989	2.747	2.674	2.660	3.098	3.059	2.712
10th percentile	3.105	3.099	3.093	2.840	2.789	2.784	3.432	3.371	3.031
25th percentile	3.227	3.220	3.219	3.028	2.993	2.937	3.753	3.749	3.692
75th percentile	3.705	3.695	3.694	4.457	4.449	4.229	3.989	3.986	3.984
90th percentile	4.041	4.042	4.048	6.102	6.094	5.762	4.076	4.074	4.092
95th percentile	4.240	4.240	4.255	6.352	6.356	6.314	4.156	4.165	4.196
Std deviation	0.418	0.421	0.425	1.163	1.171	1.093	0.447	0.463	0.525
Variance	0.175	0.177	0.181	1.352	1.372	1.195	0.200	0.214	0.275
Max value	6.263	6.249	6.270	6.847	6.976	6.800	7.226	7.232	7.234
Min value	2.652	2.641	2.642	2.429	2.417	2.420	2.486	2.514	2.513
Fraction OK	0.909	0.909	0.916	0.620	0.624	0.624	1.000	1.000	1.000

Table C-30. Performance statistics: Distribution of $\log_{10}(U_r)$ for each path Q1, Q2 and Q3 at different release times for the nested CPM repository scale model with modified backfill.

$\log_{10}(U_r)$ [m/y]	2,020 AD			3,000 AD			9,000 AD		
Path	Q1	Q2	Q3	Q1	Q2	Q3	Q1	Q2	Q3
Mean	–6.138	–6.256	–4.195	–6.194	–6.105	–3.714	–6.121	–6.105	–3.733
Median	–6.115	–6.259	–4.104	–6.238	–6.064	–3.640	–6.124	–6.064	–3.634
5th percentile	–6.643	–6.591	–5.155	–6.577	–6.584	–4.372	–6.658	–6.584	–4.541
10th percentile	–6.521	–6.492	–4.920	–6.493	–6.467	–4.162	–6.538	–6.467	–4.362
25th percentile	–6.290	–6.371	–4.499	–6.352	–6.236	–3.874	–6.342	–6.236	–3.964
75th percentile	–6.007	–6.170	–3.831	–6.090	–5.952	–3.471	–5.930	–5.952	–3.413
90th percentile	–5.926	–6.029	–3.643	–5.917	–5.841	–3.347	–5.799	–5.841	–3.266
95th percentile	–5.820	–5.899	–3.542	–5.784	–5.768	–3.269	–5.710	–5.768	–3.203
Std deviation	0.350	0.234	0.485	0.341	0.260	0.373	0.394	0.260	0.439
Variance	0.122	0.055	0.236	0.116	0.068	0.139	0.155	0.068	0.193
Max value	–3.548	–4.474	–3.059	–3.538	–4.672	–2.975	–3.348	–4.672	–2.902
Min value	–7.164	–7.287	–5.971	–7.156	–7.199	–5.709	–7.081	–7.199	–5.960
Fraction OK	1.000	1.000	1.000	1.000	1.000	1.000	1.000	1.000	1.000

Table C-31. Performance statistics: Distribution of $\log_{10}(L_r)$ for each path Q1, Q2 and Q3 at different release times for the nested CPM repository scale model with modified backfill.

$\log_{10}(L_r)$ [m]	2,020 AD			3,000 AD			9,000 AD		
Path	Q1	Q2	Q3	Q1	Q2	Q3	Q1	Q2	Q3
Mean	3.160	3.159	3.163	3.125	3.123	3.093	3.891	3.880	3.825
Median	3.070	3.062	3.066	3.025	3.010	2.997	4.097	4.097	4.094
5th percentile	2.739	2.736	2.735	2.762	2.749	2.723	2.871	2.859	2.794
10th percentile	2.785	2.784	2.783	2.795	2.781	2.755	2.939	2.926	2.862
25th percentile	2.873	2.874	2.876	2.874	2.856	2.831	4.068	4.067	4.058
75th percentile	3.382	3.391	3.397	3.235	3.234	3.213	4.117	4.117	4.112
90th percentile	3.731	3.714	3.732	3.877	3.911	3.727	4.129	4.129	4.126
95th percentile	3.901	3.909	3.916	3.997	4.008	3.991	4.134	4.134	4.133
Std deviation	0.361	0.364	0.367	0.357	0.370	0.357	0.453	0.463	0.508
Variance	0.130	0.132	0.134	0.127	0.137	0.128	0.205	0.214	0.258
Max value	4.371	4.337	4.376	4.334	4.326	4.324	4.182	4.179	4.172
Min value	2.651	2.653	2.652	2.640	2.637	2.637	2.691	2.684	2.654
Fraction OK	0.909	0.909	0.916	0.620	0.624	0.624	1.000	1.000	1.000

Table C-32. Performance statistics: Distribution of $\log_{10}(F_r)$ for each path Q1, Q2 and Q3 at different release times for the nested CPM repository scale model with modified backfill.

$\log_{10}(F_r)$ [y/m]	2,020 AD			3,000 AD			9,000 AD		
Path	Q1	Q2	Q3	Q1	Q2	Q3	Q1	Q2	Q3
Mean	7.555	7.518	7.514	7.786	7.726	7.611	8.415	8.388	8.302
Median	7.591	7.571	7.570	7.743	7.714	7.596	8.607	8.602	8.566
5th percentile	6.686	6.607	6.588	6.622	6.442	6.380	7.254	7.171	6.860
10th percentile	6.964	6.865	6.837	6.865	6.621	6.581	7.487	7.423	7.257
25th percentile	7.411	7.370	7.365	7.439	7.330	7.268	8.443	8.440	8.296
75th percentile	7.772	7.760	7.758	8.207	8.214	8.069	8.696	8.694	8.674
90th percentile	8.017	8.008	8.011	8.499	8.575	8.413	8.781	8.775	8.756
95th percentile	8.219	8.210	8.205	9.112	9.141	9.062	8.823	8.822	8.817
Std deviation	0.445	0.474	0.480	0.665	0.750	0.741	0.495	0.551	0.623
Variance	0.198	0.225	0.230	0.443	0.562	0.549	0.246	0.304	0.389
Max value	9.058	9.663	8.989	9.262	9.269	9.500	9.169	9.141	9.192
Min value	5.669	5.688	5.688	5.718	5.430	5.425	6.142	5.928	6.114
Fraction OK	0.909	0.909	0.916	0.620	0.624	0.624	1.000	1.000	1.000

Table C-33. Performance statistics: Distribution of $\log_{10}(t_T)$ for each path Q1, Q2 and Q3 at different release times for the nested CPM repository scale model with modified backfill.

$\log_{10}(t_T)$ [y]	2,020 AD			3,000 AD			9,000 AD		
Path	Q1	Q2	Q3	Q1	Q2	Q3	Q1	Q2	Q3
Mean	5.533	5.429	5.400	5.548	5.688	5.336	5.682	5.892	5.201
Median	5.583	5.531	5.508	5.629	5.707	5.379	5.680	5.975	5.276
5th percentile	4.662	4.543	4.528	4.713	4.791	4.413	5.047	5.067	3.967
10th percentile	4.944	4.829	4.835	4.995	5.068	4.626	5.275	5.300	4.052
25th percentile	5.299	5.230	5.209	5.380	5.378	5.127	5.536	5.684	4.687
75th percentile	5.793	5.663	5.649	5.787	6.119	5.635	5.871	6.128	5.783
90th percentile	6.122	5.796	5.755	6.007	6.240	5.875	6.112	6.400	6.109
95th percentile	6.216	5.959	5.866	6.134	6.353	6.053	6.258	6.509	6.278
Std deviation	0.473	0.449	0.425	0.440	0.501	0.469	0.370	0.435	0.744
Variance	0.224	0.201	0.181	0.193	0.251	0.220	0.137	0.189	0.553
Max value	7.074	7.096	7.035	7.046	6.868	6.873	6.975	7.181	6.957
Min value	2.869	3.247	2.924	2.118	3.244	3.191	3.080	3.037	2.559
Fraction OK	0.901	0.907	0.916	0.559	0.599	0.624	0.632	0.733	1.000

Table C-34. Performance statistics: Distribution of $\log_{10}(L_T)$ for each path Q1, Q2 and Q3 at different release times for the nested CPM repository scale model with modified backfill.

$\log_{10}(L_T)$ [m]	2,020 AD			3,000 AD			9,000 AD		
Path	Q1	Q2	Q3	Q1	Q2	Q3	Q1	Q2	Q3
Mean	1.600	1.646	1.662	1.344	1.530	2.004	0.762	0.969	1.463
Median	1.680	1.710	1.717	1.732	1.829	2.050	0.277	0.618	1.514
5th percentile	0.748	0.786	0.826	–0.145	0.228	1.116	–0.202	0.049	0.179
10th percentile	0.888	0.934	0.971	–0.087	0.321	1.297	–0.060	0.185	0.439
25th percentile	1.243	1.294	1.312	0.094	0.475	1.594	0.081	0.445	0.922
75th percentile	1.994	2.018	2.015	2.278	2.338	2.428	1.784	1.789	2.064
90th percentile	2.220	2.240	2.237	2.619	2.677	2.749	2.201	2.207	2.365
95th percentile	2.359	2.388	2.389	2.768	2.792	2.820	2.350	2.364	2.581
Std deviation	0.549	0.507	0.484	1.074	0.935	0.556	0.941	0.810	0.732
Variance	0.302	0.257	0.234	1.154	0.874	0.309	0.885	0.655	0.536
Max value	2.922	2.929	2.944	2.952	2.958	3.039	2.876	2.880	2.885
Min value	–1.282	–0.150	–0.090	–1.615	–1.218	–0.105	–1.759	–1.279	–0.268
Fraction OK	0.901	0.907	0.916	0.559	0.599	0.624	0.632	0.733	1.000

Table C-35. Performance statistics: Distribution of $\log_{10}(t_{EDZ})$ for each path Q1, Q2 and Q3 at different release times for the nested CPM repository scale model with modified backfill.

$\log_{10}(t_{EDZ})$ [y]	2,020 AD			3,000 AD			9,000 AD		
Path	Q1	Q2	Q3	Q1	Q2	Q3	Q1	Q2	Q3
Mean	1.751	1.666	1.906	1.812	1.804	1.687	1.854	1.762	1.730
Median	1.661	1.565	1.845	1.736	1.694	1.733	1.838	1.659	1.671
5th percentile	1.141	1.213	0.713	0.986	1.240	0.382	0.432	1.119	0.811
10th percentile	1.345	1.310	1.095	1.225	1.365	0.675	0.718	1.229	1.079
25th percentile	1.557	1.414	1.497	1.480	1.470	1.264	1.412	1.351	1.476
75th percentile	1.901	1.806	2.377	2.132	2.049	2.049	2.420	2.104	1.995
90th percentile	2.339	2.225	2.903	2.636	2.534	2.617	2.854	2.562	2.425
95th percentile	2.651	2.539	3.114	2.870	2.726	2.825	3.151	2.774	2.723
Std deviation	0.459	0.439	0.716	0.584	0.488	0.697	0.777	0.542	0.530
Variance	0.210	0.193	0.513	0.342	0.238	0.486	0.603	0.294	0.281
Max value	3.745	3.718	3.647	3.738	3.775	3.794	3.706	3.777	3.730
Min value	–0.602	–0.418	–0.605	–0.741	–0.220	–0.266	–0.463	–0.167	0.071
Fraction OK	0.695	0.904	0.152	0.288	0.623	0.181	0.182	0.993	0.557

Table C-36. Performance statistics: Distribution of $\log_{10}(L_{EDZ})$ at different release times for the nested CPM repository scale model with modified backfill.

$\log_{10}(L_{EDZ})$ [m]	2,020 AD			3,000 AD			9,000 AD		
Path	Q1	Q2	Q3	Q1	Q2	Q3	Q1	Q2	Q3
Mean	–0.516	–0.595	–0.471	–0.225	–0.241	–0.205	–0.147	–0.316	–0.322
Median	–0.582	–0.712	–0.521	–0.318	–0.435	–0.292	–0.205	–0.514	–0.391
5th percentile	–1.036	–0.891	–1.616	–0.997	–0.798	–1.023	–1.022	–0.850	–1.105
10th percentile	–0.736	–0.882	–1.117	–0.746	–0.731	–0.730	–0.685	–0.793	–0.588
25th percentile	–0.681	–0.808	–0.901	–0.531	–0.598	–0.542	–0.545	–0.678	–0.520
75th percentile	–0.435	–0.525	–0.046	0.052	0.044	0.056	0.283	–0.057	–0.154
90th percentile	–0.012	–0.181	0.390	0.567	0.616	0.613	0.649	0.462	0.268
95th percentile	0.260	0.159	0.639	0.845	0.804	0.876	0.822	0.635	0.519
Std deviation	0.395	0.339	0.662	0.547	0.509	0.560	0.569	0.477	0.429
Variance	0.156	0.115	0.438	0.299	0.259	0.314	0.324	0.228	0.184
Max value	1.388	1.427	1.478	1.725	1.808	1.826	1.266	1.424	1.380
Min value	–2.751	–0.946	–2.631	–2.463	–0.940	–2.415	–2.434	–1.035	–1.867
Fraction OK	0.695	0.904	0.152	0.288	0.623	0.181	0.182	0.993	0.557

C.8 Nested CPM repository scale model with modified EDZ (HCD3_AC_HRDDT_EDZ)

Table C-37. Performance statistics: Distribution of $\log_{10}(t_r)$ for each path Q1, Q2 and Q3 at different release times for the nested CPM repository scale model with modified EDZ.

$\log_{10}(t_r)$ [y]	2,020 AD			3,000 AD			9,000 AD		
Path	Q1	Q2	Q3	Q1	Q2	Q3	Q1	Q2	Q3
Mean	3.531	3.527	3.529	3.797	3.768	3.760	3.775	3.750	3.735
Median	3.438	3.429	3.437	3.355	3.342	3.323	3.861	3.855	3.850
5th percentile	3.034	3.020	3.015	2.888	2.860	2.860	3.005	2.979	2.962
10th percentile	3.123	3.119	3.118	2.957	2.947	2.945	3.102	3.069	3.055
25th percentile	3.249	3.243	3.241	3.082	3.063	3.060	3.588	3.514	3.470
75th percentile	3.741	3.740	3.743	4.151	4.008	3.896	4.000	3.989	3.985
90th percentile	4.031	4.046	4.040	5.783	5.788	5.801	4.101	4.098	4.093
95th percentile	4.217	4.229	4.215	6.228	6.207	6.227	4.168	4.165	4.164
Std deviation	0.435	0.438	0.441	1.053	1.049	1.056	0.471	0.473	0.465
Variance	0.189	0.192	0.194	1.109	1.100	1.114	0.222	0.223	0.216
Max value	6.284	6.284	6.339	6.782	6.786	6.782	6.685	6.939	6.728
Min value	2.677	2.711	2.719	2.474	2.444	2.446	2.649	2.498	2.484
Fraction OK	0.900	0.903	0.901	0.602	0.604	0.604	1.000	1.000	1.000

Table C-38. Performance statistics: Distribution of $\log_{10}(U_r)$ for each path Q1, Q2 and Q3 at different release times for the nested CPM repository scale model with modified EDZ.

$\log_{10}(U_r)$ [m/y]	2,020 AD			3,000 AD			9,000 AD		
Path	Q1	Q2	Q3	Q1	Q2	Q3	Q1	Q2	Q3
Mean	–6.140	–4.386	–5.505	–6.161	–4.667	–5.309	–6.155	–4.667	–5.295
Median	–6.128	–4.357	–5.508	–6.182	–4.237	–5.274	–6.139	–4.237	–5.241
5th percentile	–6.576	–5.000	–5.849	–6.505	–5.900	–5.773	–6.649	–5.900	–5.891
10th percentile	–6.456	–4.833	–5.736	–6.410	–5.821	–5.628	–6.522	–5.821	–5.767
25th percentile	–6.275	–4.634	–5.618	–6.293	–5.673	–5.407	–6.319	–5.673	–5.473
75th percentile	–6.022	–4.144	–5.410	–6.065	–3.922	–5.173	–6.018	–3.922	–5.067
90th percentile	–5.952	–3.945	–5.245	–5.979	–3.803	–5.064	–5.940	–3.803	–4.949
95th percentile	–5.917	–3.797	–5.115	–5.917	–3.712	–5.010	–5.907	–3.712	–4.879
Std deviation	0.331	0.380	0.226	0.324	0.864	0.229	0.368	0.864	0.312
Variance	0.110	0.145	0.051	0.105	0.746	0.053	0.136	0.746	0.098
Max value	–3.432	–2.295	–3.766	–3.399	–2.307	–3.778	–3.269	–2.307	–3.744
Min value	–7.191	–6.073	–6.709	–7.152	–6.537	–6.519	–7.011	–6.537	–6.327
Fraction OK	1.000	1.000	1.000	1.000	1.000	1.000	1.000	1.000	1.000

Table C-39. Performance statistics: Distribution of $\log_{10}(L_r)$ for each path Q1, Q2 and Q3 at different release times for the nested CPM repository scale model with modified EDZ.

$\log_{10}(L_r)$ [m]	2,020 AD			3,000 AD			9,000 AD		
Path	Q1	Q2	Q3	Q1	Q2	Q3	Q1	Q2	Q3
Mean	3.173	3.175	3.176	3.089	3.081	3.075	3.780	3.759	3.746
Median	3.077	3.076	3.076	3.029	3.020	3.015	4.092	4.090	4.089
5th percentile	2.754	2.752	2.753	2.784	2.780	2.778	2.810	2.799	2.799
10th percentile	2.797	2.793	2.794	2.820	2.817	2.814	2.856	2.842	2.841
25th percentile	2.892	2.889	2.892	2.897	2.893	2.892	3.122	3.047	3.032
75th percentile	3.406	3.415	3.415	3.209	3.206	3.201	4.110	4.109	4.108
90th percentile	3.721	3.720	3.729	3.301	3.296	3.292	4.123	4.123	4.122
95th percentile	3.901	3.899	3.917	3.761	3.734	3.623	4.130	4.130	4.129
Std deviation	0.359	0.361	0.363	0.283	0.277	0.269	0.526	0.538	0.544
Variance	0.129	0.131	0.132	0.080	0.077	0.072	0.276	0.290	0.296
Max value	4.385	4.299	4.367	4.336	4.346	4.332	4.182	4.178	4.179
Min value	2.653	2.648	2.649	2.641	2.638	2.638	2.682	2.677	2.642
Fraction OK	0.900	0.903	0.901	0.602	0.604	0.604	1.000	1.000	1.000

Table C-40. Performance statistics: Distribution of $\log_{10}(F_r)$ for each path Q1, Q2 and Q3 at different release times for the nested CPM repository scale model with modified EDZ.

$\log_{10}(F_r)$ [y/m]	2,020 AD			3,000 AD			9,000 AD		
Path	Q1	Q2	Q3	Q1	Q2	Q3	Q1	Q2	Q3
Mean	7.662	7.648	7.659	7.847	7.818	7.809	8.360	8.329	8.315
Median	7.667	7.655	7.658	7.815	7.789	7.783	8.564	8.551	8.541
5th percentile	6.972	6.906	6.983	7.110	7.011	7.005	7.419	7.355	7.355
10th percentile	7.253	7.261	7.306	7.374	7.330	7.320	7.613	7.564	7.561
25th percentile	7.524	7.516	7.518	7.562	7.545	7.537	8.039	7.942	7.894
75th percentile	7.850	7.832	7.838	8.160	8.142	8.128	8.693	8.687	8.685
90th percentile	8.070	8.073	8.087	8.388	8.365	8.357	8.783	8.775	8.769
95th percentile	8.243	8.248	8.263	8.520	8.490	8.492	8.824	8.820	8.814
Std deviation	0.373	0.390	0.380	0.473	0.480	0.478	0.482	0.512	0.520
Variance	0.139	0.152	0.144	0.224	0.231	0.229	0.233	0.262	0.270
Max value	9.060	9.010	9.139	9.215	9.215	9.279	9.130	9.107	9.080
Min value	5.795	5.658	5.771	6.073	5.536	5.540	6.098	5.789	5.588
Fraction OK	0.900	0.903	0.901	0.602	0.604	0.604	1.000	1.000	1.000

Table C-41. Performance statistics: Distribution of $\log_{10}(t_T)$ for each path Q1, Q2 and Q3 at different release times for the nested CPM repository scale model with modified EDZ.

$\log_{10}(t_T)$ [y]	2,020 AD			3,000 AD			9,000 AD		
Path	Q1	Q2	Q3	Q1	Q2	Q3	Q1	Q2	Q3
Mean	5.850	5.776	5.883	5.782	5.527	5.676	5.848	5.365	5.548
Median	5.866	5.827	5.866	5.751	5.536	5.663	5.755	5.196	5.635
5th percentile	5.316	5.230	5.568	5.107	4.605	4.684	5.275	4.462	4.591
10th percentile	5.422	5.366	5.662	5.421	4.696	4.928	5.473	4.597	4.676
25th percentile	5.675	5.677	5.761	5.589	5.307	5.469	5.604	4.800	4.876
75th percentile	6.080	5.941	6.006	6.035	5.811	5.940	6.101	5.995	6.151
90th percentile	6.213	6.074	6.145	6.271	6.182	6.295	6.419	6.359	6.443
95th percentile	6.324	6.222	6.285	6.448	6.380	6.469	6.582	6.514	6.597
Std deviation	0.336	0.324	0.241	0.414	0.525	0.480	0.406	0.701	0.689
Variance	0.113	0.105	0.058	0.172	0.276	0.231	0.165	0.492	0.475
Max value	7.646	7.046	7.031	6.946	6.947	6.904	7.194	7.130	7.106
Min value	3.128	2.796	3.784	3.540	2.862	3.807	3.744	2.614	3.755
Fraction OK	0.854	0.884	0.901	0.478	0.577	0.604	0.666	0.847	1.000

Table C-42. Performance statistics: Distribution of $\log_{10}(L_T)$ for each path Q1, Q2 and Q3 at different release times for the nested CPM repository scale model with modified EDZ.

$\log_{10}(L_T)$ [m]	2,020 AD			3,000 AD			9,000 AD		
Path	Q1	Q2	Q3	Q1	Q2	Q3	Q1	Q2	Q3
Mean	0.707	0.745	0.852	0.612	0.676	0.832	0.465	0.427	0.595
Median	0.752	0.761	0.793	0.725	0.759	0.841	0.199	0.184	0.447
5th percentile	0.220	0.335	0.684	–0.189	–0.153	–0.127	–0.311	–0.286	–0.136
10th percentile	0.392	0.452	0.725	–0.089	–0.123	0.162	–0.169	–0.152	–0.125
25th percentile	0.579	0.651	0.748	0.028	0.420	0.676	0.003	–0.069	–0.071
75th percentile	0.858	0.860	0.922	1.005	0.936	1.068	1.085	1.012	1.164
90th percentile	0.978	1.017	1.099	1.301	1.287	1.397	1.432	1.414	1.490
95th percentile	1.089	1.127	1.237	1.563	1.513	1.585	1.592	1.576	1.651
Std deviation	0.284	0.257	0.191	0.565	0.506	0.438	0.649	0.645	0.644
Variance	0.081	0.066	0.036	0.319	0.256	0.192	0.421	0.416	0.415
Max value	1.806	1.801	1.818	1.925	1.974	1.987	1.962	1.994	2.097
Min value	–1.559	–1.244	–0.160	–1.831	–1.995	–0.195	–1.883	–2.023	–0.326
Fraction OK	0.854	0.884	0.901	0.478	0.577	0.604	0.666	0.847	1.000

Table C-43. Performance statistics: Distribution of $\log_{10}(t_{EDZ})$ for each path Q1, Q2 and Q3 at different release times for the nested CPM repository scale model with modified EDZ.

$\log_{10}(t_{EDZ})$ [y]	2,020 AD			3,000 AD			9,000 AD		
Path	Q1	Q2	Q3	Q1	Q2	Q3	Q1	Q2	Q3
Mean	0.972	0.896	1.105	1.363	1.451	1.271	1.002	0.946	0.964
Median	1.019	0.914	1.188	1.326	1.421	1.071	1.071	0.921	0.919
5th percentile	0.383	0.377	0.267	0.580	0.811	0.762	–0.048	0.545	0.458
10th percentile	0.639	0.597	0.545	0.803	0.882	0.863	0.340	0.628	0.625
25th percentile	0.862	0.758	0.900	1.020	1.019	0.981	0.823	0.746	0.783
75th percentile	1.147	1.062	1.439	1.777	1.767	1.540	1.298	1.128	1.164
90th percentile	1.292	1.208	1.576	1.975	2.162	2.068	1.513	1.385	1.386
95th percentile	1.354	1.355	1.643	2.099	2.345	2.241	1.649	1.598	1.539
Std deviation	0.333	0.306	0.478	0.489	0.492	0.487	0.480	0.346	0.333
Variance	0.111	0.094	0.229	0.240	0.242	0.237	0.230	0.120	0.111
Max value	2.151	2.415	1.944	2.799	2.947	2.704	2.188	2.146	2.112
Min value	–1.799	–1.225	–1.145	–0.585	–0.649	–1.126	–1.373	–1.247	–1.239
Fraction OK	0.837	0.897	0.044	0.240	0.604	0.158	0.251	0.993	0.663

Table C-44. Performance statistics: Distribution of $\log_{10}(L_{EDZ})$ at different release times for the nested CPM repository scale model with modified EDZ.

$\log_{10}(L_{EDZ})$ [m]	2,020 AD			3,000 AD			9,000 AD		
Path	Q1	Q2	Q3	Q1	Q2	Q3	Q1	Q2	Q3
Mean	0.574	0.522	0.904	0.512	0.467	1.017	1.063	0.981	0.988
Median	0.585	0.558	1.025	0.432	0.464	1.146	1.128	1.009	1.009
5th percentile	–0.234	–0.334	–0.334	–0.546	–0.539	–0.004	0.146	0.295	0.240
10th percentile	–0.047	–0.139	–0.086	–0.291	–0.460	0.257	0.366	0.428	0.438
25th percentile	0.244	0.223	0.671	0.026	–0.047	0.811	0.835	0.729	0.738
75th percentile	0.936	0.853	1.293	1.030	0.967	1.293	1.385	1.255	1.257
90th percentile	1.199	1.091	1.498	1.407	1.288	1.574	1.611	1.459	1.515
95th percentile	1.321	1.260	1.554	1.610	1.591	1.689	1.745	1.640	1.697
Std deviation	0.486	0.470	0.567	0.660	0.660	0.506	0.484	0.421	0.438
Variance	0.236	0.221	0.322	0.435	0.435	0.256	0.234	0.177	0.192
Max value	1.797	1.897	1.816	1.974	2.155	2.153	2.085	2.166	2.185
Min value	–1.644	–0.800	–1.242	–1.686	–0.891	–1.952	–1.426	–0.793	–1.762
Fraction OK	0.837	0.897	0.044	0.240	0.604	0.158	0.251	0.993	0.663

C.9 Combined ECPM/DFN regional-scale base case model (HCD3_AC_HRD3A2_T)

Table C-45 to Table C-47 summarise the performance measure statistics for t_r, L_r and F_r respectively, for the combined ECPM/DFN base case model. The statistics are calculated in $\log_{10}$ space and results are presented for three selected release times; 2,020 AD, 3,000 AD and 9,000 AD. Statistics for the initial velocity are not given since particles start at the nearest node in the model to the location of each deposition hole, but this includes a mixture of fractures, tunnels and the EDZ. This model represents transport in the tunnels and EDZ, so include extra performance measures t_T, L_T for parts of the path in the tunnel are given in Table C-48 and Table C-49, respectively. For the EDZ, t_{EDZ}, L_{EDZ} for parts of the path in the EDZ are given in Table C-50and Table C-51, respectively.

Table C-45. Performance statistics: Distribution of $\log_{10}(t_r)$ at different release times for the combined ECPM/DFN base case model.

$\log_{10}(t_r)$ [y]	2,020 AD	3,000 AD	9,000 AD
Mean	4.134	4.090	4.249
Median	4.627	4.606	4.662
5th percentile	1.895	1.831	1.973
10th percentile	2.079	2.004	2.193
25th percentile	2.477	2.458	2.720
75th percentile	5.364	5.314	5.364
90th percentile	5.938	5.825	5.963
95th percentile	6.310	6.170	6.348
Std deviation	1.559	1.550	1.490
Variance	2.431	2.401	2.221
Max value	9.246	8.352	8.528
Min value	0.947	0.796	0.598
Fraction OK	0.837	0.770	0.803

Table C-46. Performance statistics: Distribution of $\log_{10}(L_r)$ at different release times for the combined ECPM/DFN base case model.

$\log_{10}(L_r)$ [m]	2,020 AD	3,000 AD	9,000 AD
Mean	3.006	3.096	3.195
Median	2.996	3.065	3.143
5th percentile	2.708	2.739	2.743
10th percentile	2.756	2.787	2.795
25th percentile	2.855	2.900	2.926
75th percentile	3.134	3.253	3.412
90th percentile	3.265	3.446	3.733
95th percentile	3.348	3.571	3.869
Std deviation	0.196	0.259	0.336
Variance	0.039	0.067	0.113
Max value	3.763	4.061	4.079
Min value	2.579	2.581	2.600
Fraction OK	0.837	0.770	0.803

Table C-47. Performance statistics: Distribution of $\log_{10}(F_r)$ at different release times for the combined ECPM/DFN base case model.

$\log_{10}(F_r)$ [y/m]	2,020 AD	3,000 AD	9,000 AD
Mean	6.740	6.753	6.912
Median	6.772	6.781	6.940
5th percentile	5.470	5.483	5.564
10th percentile	5.820	5.864	5.950
25th percentile	6.297	6.335	6.431
75th percentile	7.223	7.228	7.493
90th percentile	7.611	7.646	7.839
95th percentile	7.854	7.858	8.025
Std deviation	0.712	0.713	0.759
Variance	0.507	0.508	0.577
Max value	9.676	9.727	9.263
Min value	4.017	3.965	4.173
Fraction OK	0.837	0.770	0.803

Table C-48. Performance statistics: Distribution of $\log_{10}(t_T)$ at different release times for the combined ECPM/DFN base case model.

$\log_{10}(t_T)$ [y]	2,020 AD	3,000 AD	9,000 AD
Mean	5.350	5.428	5.527
Median	5.909	5.917	5.988
5th percentile	0.436	0.542	0.692
10th percentile	0.991	1.318	1.568
25th percentile	5.223	5.292	5.329
75th percentile	6.493	6.450	6.530
90th percentile	6.951	6.876	7.037
95th percentile	7.326	7.215	7.402
Std deviation	2.004	1.892	1.877
Variance	4.017	3.580	3.524
Max value	10.386	10.422	9.591
Min value	–1.757	–2.081	–2.106
Fraction OK	0.720	0.657	0.677

Table C-49. Performance statistics: Distribution of $\log_{10}(L_T)$ at different release times for the combined ECPM/DFN base case model.

$\log_{10}(L_T)$ [m]	2,020 AD	3,000 AD	9,000 AD
Mean	1.644	1.669	1.679
Median	1.693	1.707	1.719
5th percentile	0.865	0.905	0.887
10th percentile	1.080	1.100	1.088
25th percentile	1.401	1.423	1.443
75th percentile	1.934	1.967	1.975
90th percentile	2.134	2.173	2.176
95th percentile	2.250	2.282	2.302
Std deviation	0.417	0.425	0.430
Variance	0.174	0.180	0.185
Max value	2.714	3.097	3.111
Min value	–0.268	–0.556	–0.268
Fraction OK	0.720	0.657	0.677

Table C-50. Performance statistics: Distribution of $\log_{10}(t_{EDZ})$ at different release times for the combined ECPM/DFN base case model.

$\log_{10}(t_{EDZ})$ [y]	2,020 AD	3,000 AD	9,000 AD
Mean	4.473	4.363	4.311
Median	5.068	5.017	5.027
5th percentile	0.661	0.650	0.600
10th percentile	1.228	1.111	1.137
25th percentile	2.941	2.513	2.263
75th percentile	5.687	5.652	5.732
90th percentile	6.487	6.300	6.508
95th percentile	7.041	7.087	7.326
Std deviation	2.009	2.048	2.143
Variance	4.036	4.196	4.592
Max value	9.954	9.958	10.270
Min value	–1.742	–1.342	–1.386
Fraction OK	0.588	0.529	0.543

Table C-51. Performance statistics: Distribution of $\log_{10}(L_{EDZ})$ at different release times for the combined ECPM/DFN base case model.

$\log_{10}(L_{EDZ})$ [m]	2,020 AD	3,000 AD	9,000 AD
Mean	1.196	1.227	1.257
Median	1.196	1.247	1.258
5th percentile	0.531	0.533	0.543
10th percentile	0.669	0.711	0.714
25th percentile	0.850	0.884	0.941
75th percentile	1.491	1.520	1.547
90th percentile	1.716	1.746	1.779
95th percentile	1.862	1.900	1.983
Std deviation	0.421	0.433	0.445
Variance	0.177	0.188	0.198
Max value	2.776	2.895	2.862
Min value	–0.866	–0.625	–0.507
Fraction OK	0.588	0.529	0.543

Appendix D

Verification of variable-density flow in discrete fracture networks

A simple test case was used to verify the implementation of variable-density flow in DFN models. The case chosen was the Henry test case /Henry 1964/. The Henry saltwater intrusion problem concerns a vertical slice through an isotropic, homogeneous, confined aquifer. A constant flux of freshwater is applied to the inland boundary, while the seaward boundary is exposed to a stationary body of higher density seawater. Saltwater intrudes from the sea boundary until equilibrium between the heavier intruded fluid and the lighter recharging fluid is reached. Figure D-1 illustrates the domain and boundary conditions.

Currently the implementation of variable-density flow in DFN models within CONNECTFLOW only allows a spatial distribution of fluid density to be imported into a DFN model and then the consistent residual pressure to be calculated within the fracture system based on conservation of mass and Darcy's Law. It does not as yet allow fully coupled groundwater flow and salt transport to be calculated. Therefore, the approach to the Henry test case followed the steps:

1. Calculate the coupled groundwater flow and salt transport in a pure CPM model.
2. Construct a DFN model as a single sub-divided fracture with the same domain and equivalent hydraulic properties (transmissivity) and transport properties (transport aperture).
3. Interpolate the fluid density from the CPM model on to the DFN model. This was done by interpolating the fluid density at each of the fracture intersections.
4. Calculate the consistent residual pressure in the DFN model. This is calculated as a field of pressure values at each fracture intersection.
5. Calculate flow-paths through the CPM and DFN models for a 4 by 4 array of start positions.
6. Test the results of the DFN model for various levels of refinement. In effect different sizes of fracture sub-divisions.

A similar series of steps was followed in the combined modelling, DFN/CPM and ECPM/DFN, of groundwater calculations reported in the main body of this report.

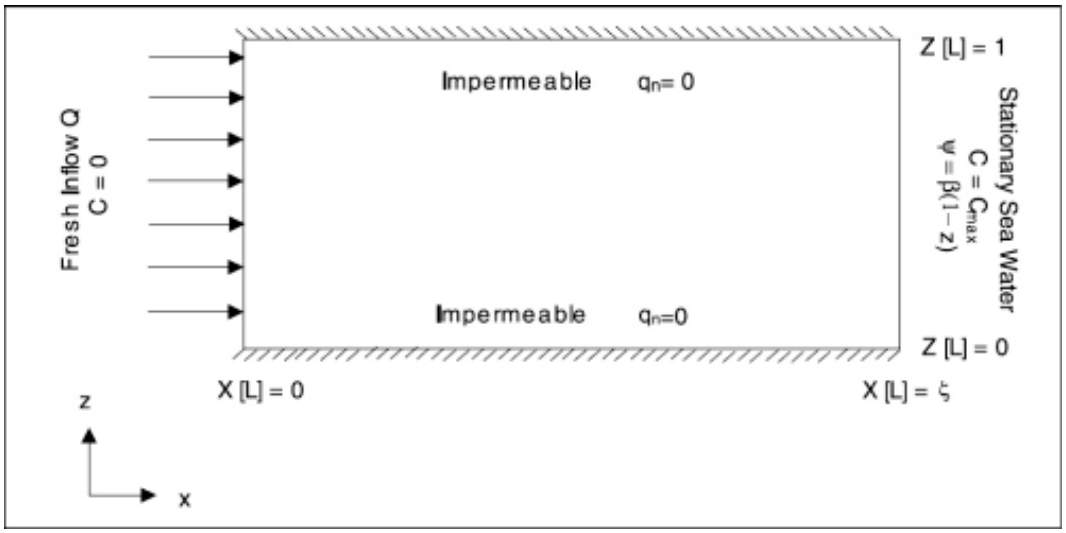

Figure D-1. *Domain and boundary conditions for the Henry saltwater intrusion problem. Here, ψ is the residual pressure.*

For the CPM calculations, the domain was divided into a grid of 40 by 20 finite-elements using a quadratic interpolation for pressure and linear for salinity. Steady-state coupled groundwater flow and salt transport calculations were performed using Newton-Raphson iterations to obtain a converged solution. The calculated distribution of fluid density and residual pressure are shown at the top of Figure D-2 and Figure D-3, respectively.

For the DFN calculations, a single fracture was generated and then sub-divided into many smaller fractures (tessellated) with intersections along their edges. Two different levels of refinement were considered. The first split the fracture into 40 by 20 sub-fractures as a coarse representation. The second used a much finer 200 by 100 grid of sub-fractures to test for convergence with respect to refinement. Figure D-2 shows the interpolation of fluid density on to the coarse and fine fracture networks. Here, each sub-fracture is coloured by the average fluid density within the fracture, although internally the fluid density is stored at the centre of each fracture intersection. Figure D-3 shows the distribution of residual pressure calculated in the coarse and fine DFN models. Comparing with the results of the CPM model, the residual pressure is in good agreement for both levels of refinement, but clearly is smoother for the fine DFN model.

Perhaps more interesting is how well the DFN model calculates particle tracking in a variable-density flow-field. Figure D-4 shows particle tracks starting at an array of 4 by 4 positions and advecting toward the top right of the domain. In the CPM model flow-paths are deterministic and very smooth. In the DFN model flow-paths are more discrete since the particle-tracking algorithm moves particles between fracture intersections in a stochastic way by a weighted random selection of the next destination depending on the flux between pairs of intersections. Only one realisation is shown here for each particle start location rather than the ‘mean’ path. It shows the flow-paths are broadly consistent for the coarse DFN model though subject to some dispersion due to the particle-tracking algorithm, while the finer sub-divided DFN gives much smoother flow-paths.

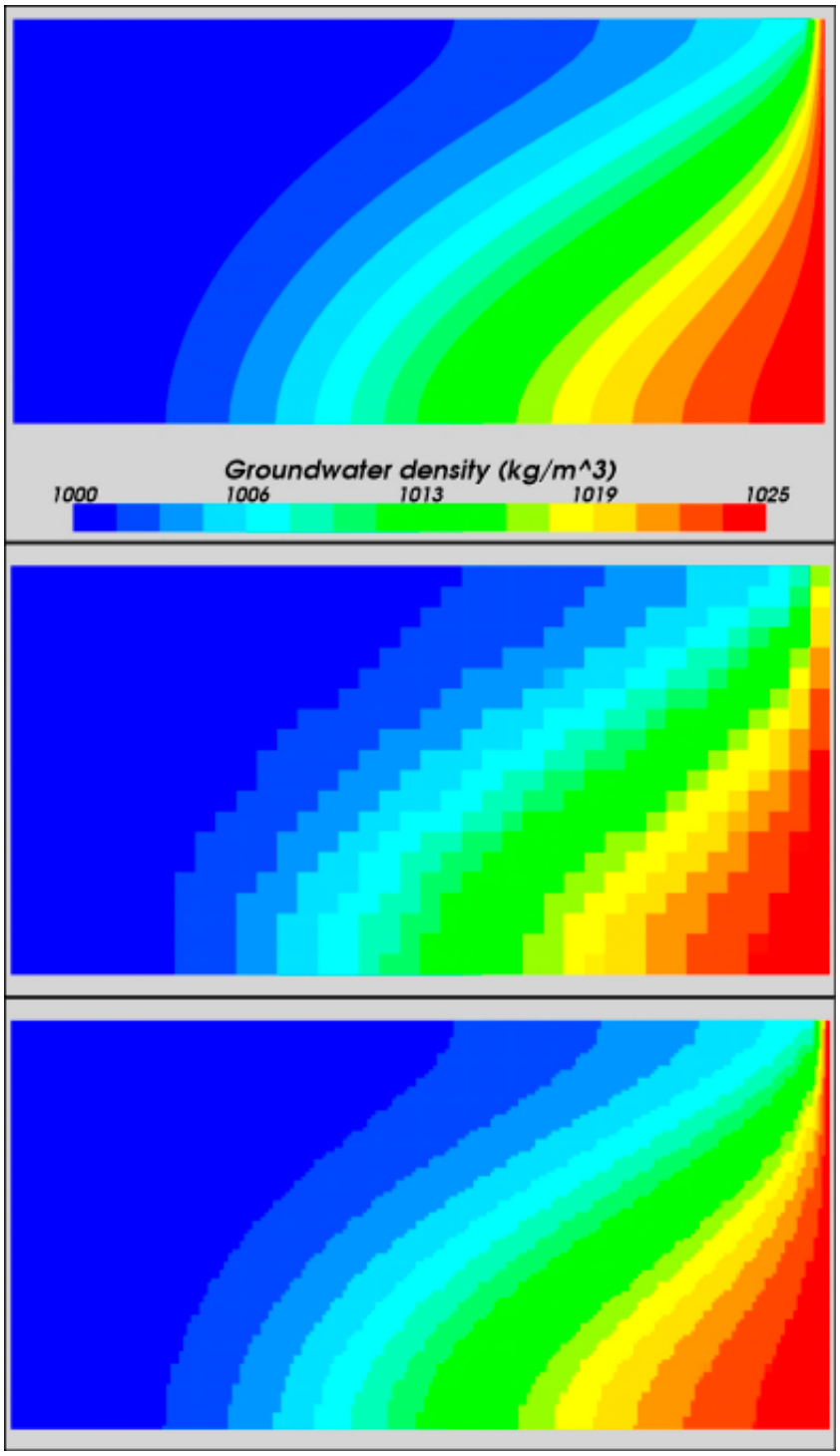

Figure D-2. *Distribution of fluid density in the Henry test case. Top: calculated steady-state density from pure CPM test case. Middle: fluid density interpolated on to a coarse DFN model with each sub-divided fracture coloured by the average density in the fracture. Bottom: fluid density interpolated on to a fine DFN model with each sub-divided fracture coloured by the average density in the fracture.*

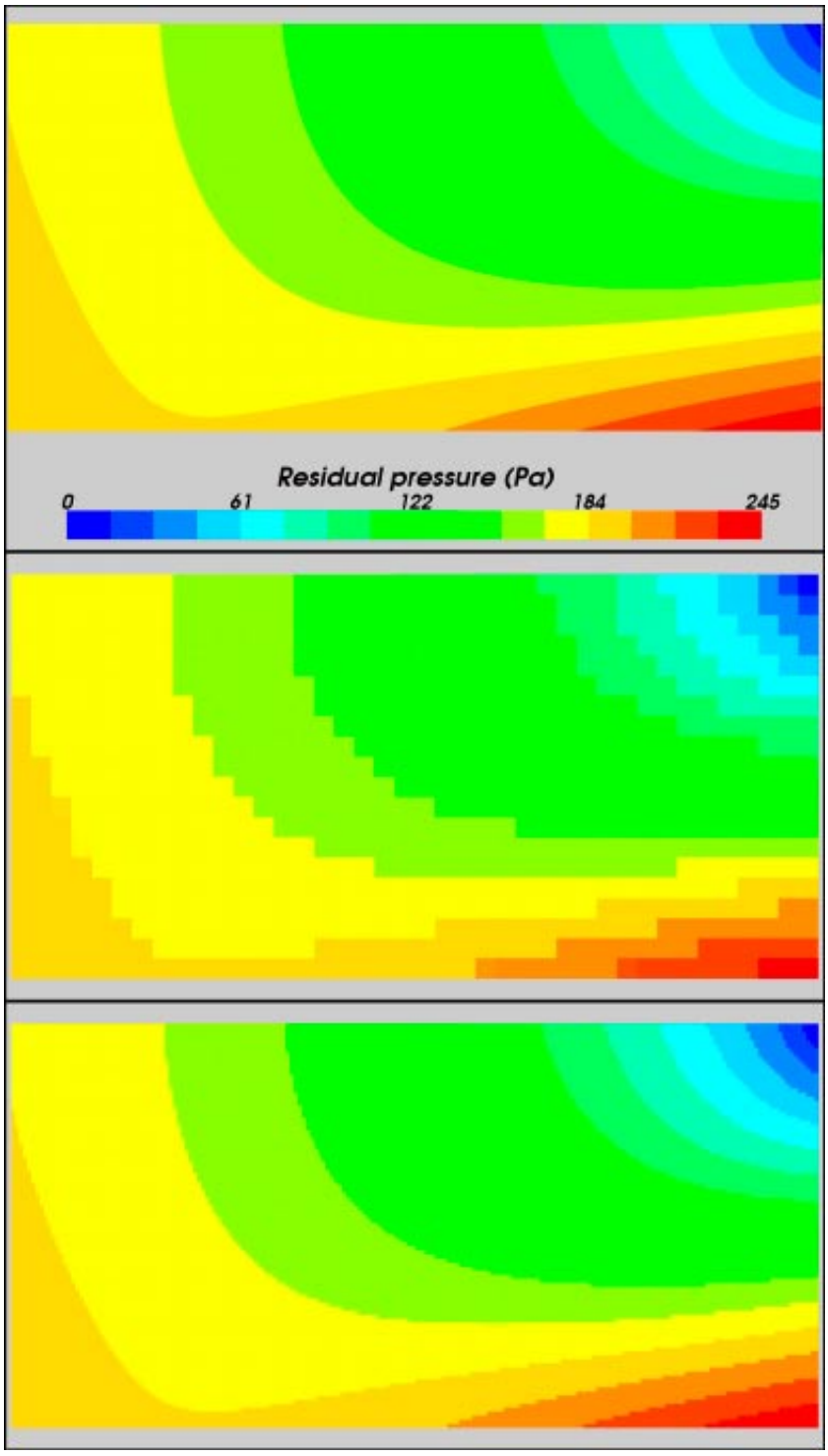

Figure D-3. *Distribution of residual pressure in the Henry test case. Top: calculated steady-state residual pressure from pure CPM test case. Middle: residual pressure calculated on a coarse DFN model with each sub-divided fracture coloured by the average pressure in the fracture. Bottom: residual pressure calculated on a fine DFN model with each sub-divided fracture coloured by the average pressure in the fracture.*

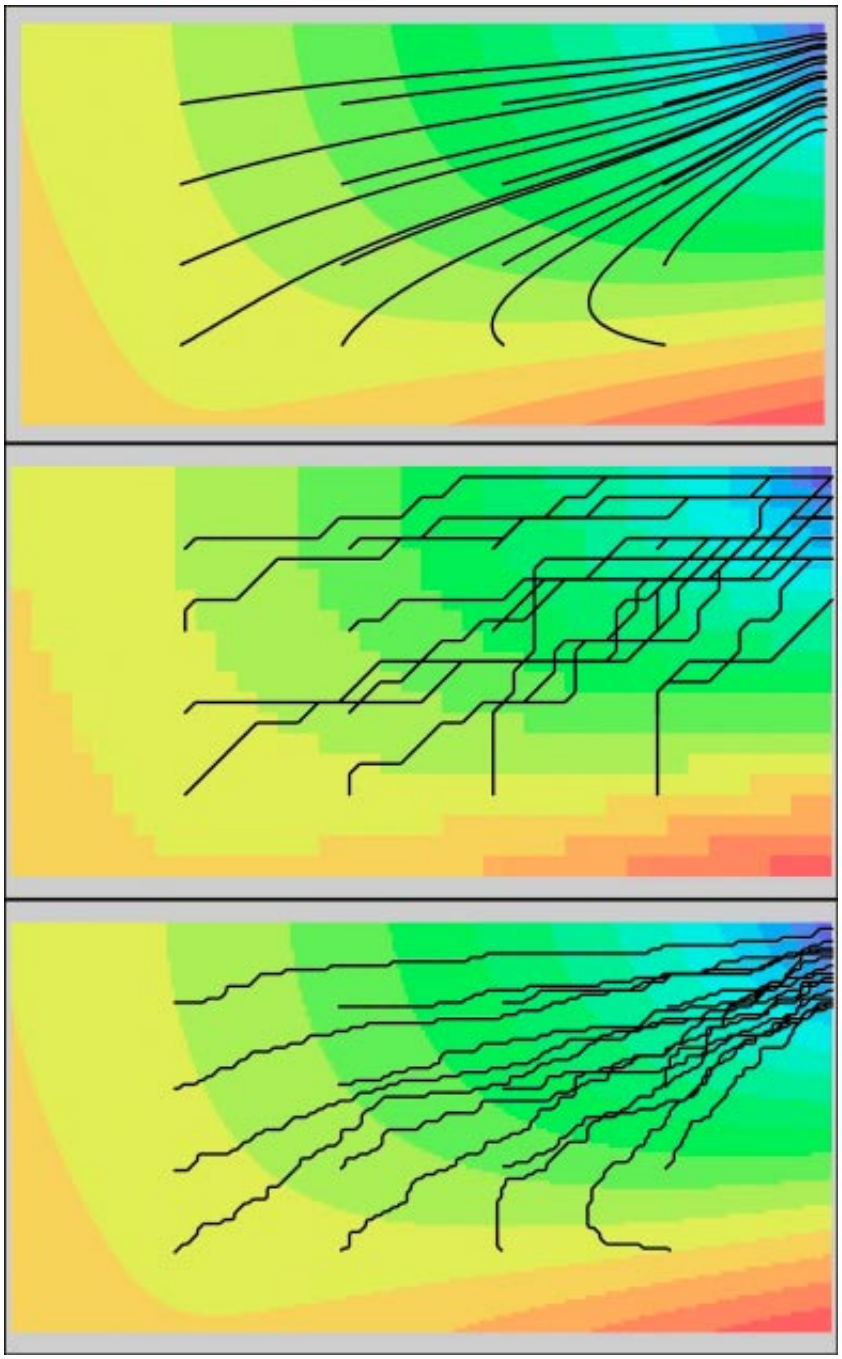

Figure D-4. *Flow-paths in variable-density flow in the Henry test case. Top: flow-paths starting on a 4 by 4 array of points in a pure CPM test case superimposed on residual pressure contours. Middle: flow-paths starting on a 4 by 4 array of points in a coarse DFN model with each sub-divided fracture coloured by the average residual pressure in the fracture. Bottom: flow-paths starting on a 4 by 4 array of points in a fine DFN model with each sub-divided fracture coloured by the average residual pressure in the fracture.*

Appendix E

Modifications to equivalent flow-rates for spalling

An effect that may potentially lead to higher equivalent flow-rates (Qeq) arises from mechanical effects of spalling in deposition holes induced by the waste heat. The effects of spalling change conditions for mass exchange between the buffer and the fractures intersecting the deposition hole, in the form of an altered Q_{eq} for the Q1 path. This section summarises the definitions and data used for the calculations of the increase in water flow rate in the damaged zone due to spalling. Spalling occurs when the rock nearest to the surface of the deposition hole for the waste canisters is damaged due to natural stress distribution in the rock and due to stresses induced due to heating by the waste in the canister /Neretnieks 2006/.

A wedge formed region of fractured rock on both sides of the deposition hole may form. The damaged zone is envisaged to extend some 10 cm into the rock and be 15 to 20 cm wide. The zone will contain several small fractures that form a connected network for flow. The porosity and hydraulic transmissivity of the damaged zone is assumed to be higher than that of the surrounding rock. A water conducting fracture that intersects the deposition hole will also intersect the zone with the damaged rock and allow water to flow through it. Water that enters the zone from the upstream side of a fracture will spread out in the zone both upward and downward before it again leaves at the downstream side. Because the hydraulic conductivity of the damaged zone is higher than the undamaged rock it may allow more water to be drawn in from the flowing fracture. The water in the porous damaged rock will have a longer residence time in contact with the buffer and may therefore have more time to equilibrate with pore water of the backfill /Neretnieks 2006/.

The flow rate of water will increase due to the presence of the damaged zone. However, only a fraction of that water will exchange solutes with the buffer. Nevertheless, the equivalent flow rate Q_{eqDZ} due to the presence of a damaged zone could be considerably larger than when there is no damage. Scoping calculations indicate that the increase can be on the order of up to ten times depending on the angle at which the deposition hole is intersected. For every canister position the flow rate q in the fracture that intersects the deposition hole has been determined from hydraulic calculations. To the Q_{eq} for a deposition hole without spalling should be added a Q_{eqDZ} caused by the presence of the damage /Neretnieks 2006/.

$$Q_{eq,tot} = Q_{eq} + Q_{eqDZ}$$

Q_{eqDZ} is defined slightly different depending on what type of hydrogeological model, CPM or DFN, that was used, see below. A more detailed description of the spalling phenomenon is presented in /Neretnieks 2006/.

CPM model

For a CPM model Q_{eqDZ} is defined as,

$$Q_{eqDZ} = 1.13\sqrt{\frac{D_p \cdot q \cdot W_{zone} \cdot L_{zone} \cdot \varepsilon_{zone}}{d_{zone}}}$$

where all parameter values and definitions are given in Table E-1 except for the flow rate q which is calculated from

$$q = U_{r0} \cdot A$$

where U_{r0} is the Darcy velocity and A the capture area. The Darcy velocity, and hence q, is determined from hydraulic calculations.

DFN model

For a DFN model Q_{eqDZ} is defined as,

$$Q_{eqDZ} = 1.13\sqrt{\frac{D_p \cdot q \cdot W_{zone} \cdot L_{zone} \cdot \varepsilon_{zone} \cdot f}{d_{zone}}}$$

where all parameter values and definitions are given in Table E-1 except for the flow-rate q which is calculated from

$$q = U_{r1} \cdot w_c \cdot \min[2L_{zone}, L_{fracture}]$$

where $L_{fracture}$ is the length of the fracture intersecting the spalled zone. The minimum value of $2 \cdot L_{zone}$ and $L_{fracture}$ is used. $L_{fracture}$ is obtained from the hydrogeological model used for the calculations. U_{r1} is the Darcy velocity for path Q1 and is determined from hydraulic calculations.

Figure E-1 present the cumulative distribution function of Q_{eq1} at 2,020 AD with and without spalling included for the different conceptual models and some variants used in F 1.2.

Table E-1. Definitions and data as used in the spalling calculations /Neretnieks 2006/.

Entity	Description	Value	Unit
Q_{eqDZ}	Equivalent flow rate in zone	–	m^3/s
q	Flow rate	–	m^3/s
D_p	Pore diffusion coefficient	10^{-10}	m^2/s
W_{zone}	Width of damaged zone	0.2	m
L_{zone}	Length of damaged zone	8	m
ε_{zone}	Porosity of damaged zone	0.01	–
d_{zone}	Thickness of damaged zone	0.1	m
f	Fraction of zone where water effectively flows	0.5	–
U_{r0}	Darcy velocity in a CPM model	Determined from hydraulic calculations	m/s
U_{r1}	Darcy velocity in a DFN model	Determined from hydraulic calculations	m/s
A	Capture area	12.8	m^2
w_c	Canister height	5	m
$L_{fracture}$	Length of the fracture intersecting the spalled zone		m

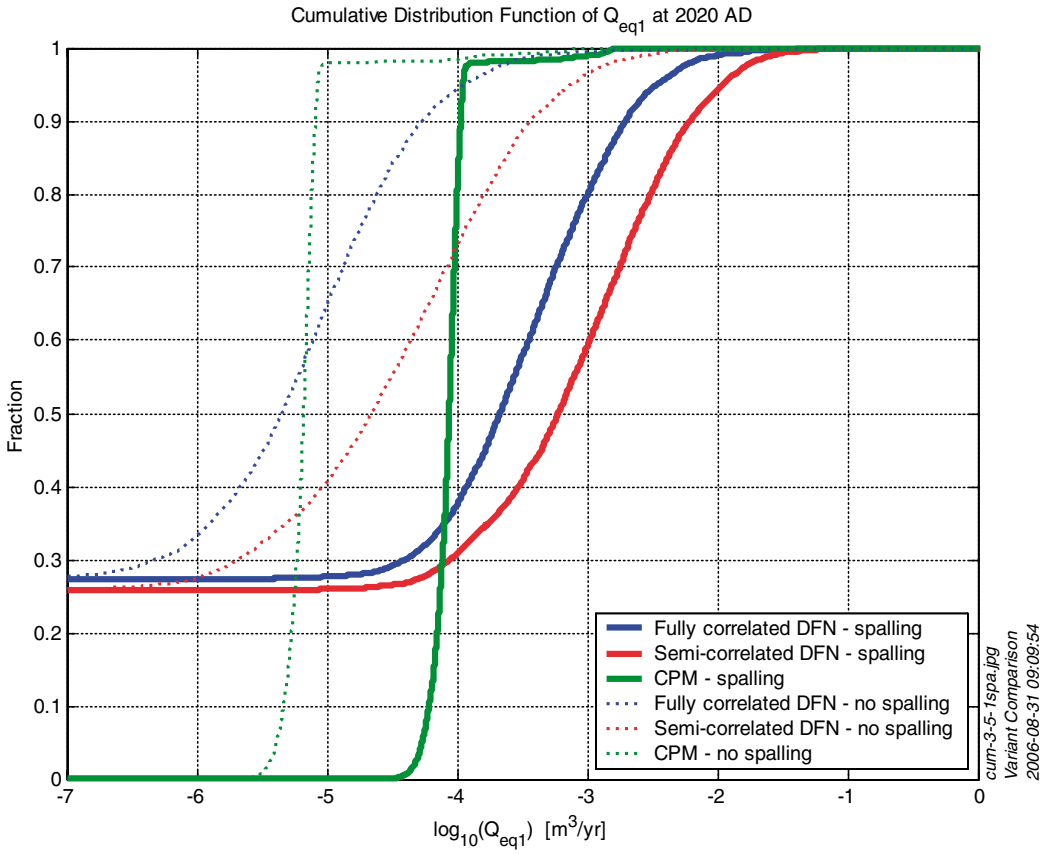

Figure E-1. *Cumulative distribution function of Qeq1 at 2,020 AD with and without spalling included for the correlated and semi-correlated DFN models and the alternative CPM conceptual model.*

Appendix F

Implementation of heat transport in CONNECTFLOW

F.1 Equations

In order to carry out the calculations of thermal effects on flow and transport for SR-Can, the option in CONNECTFLOW for modelling the flow of multiple reference waters, with possible diffusion into the rock matrix was extended to include coupling to heat transport calculations.

This is modelled using Darcy's law,

$$\mathbf{q} = -\frac{\mathbf{k}}{\mu}\cdot\left(\nabla P^R - (\rho_l - \rho_0)g\right) \tag{F-1}$$

the continuity equation,

$$\frac{\partial}{\partial t}(\phi\rho_l) + \nabla\cdot(\rho_l\mathbf{q}) = 0 \tag{F-2}$$

the advection-dispersion equation,

$$\frac{\partial}{\partial t}(\phi\rho_l f_i) + \nabla\cdot(\rho_l\mathbf{q}f_i) = \nabla\cdot(\phi\rho_l\mathbf{D}_c\nabla f_i) + \rho\sigma D_{e,i}\left.\frac{\partial f_i'}{\partial w}\right|_{w=0} \tag{F-3}$$

the equation for diffusion into the rock matrix (if this is modelled)

$$\alpha_i\frac{\partial f_i'}{\partial t} = D_{e,i}\frac{\partial^2 f_i'}{\partial w^2} \tag{F-4}$$

and the heat transport equation /Bear 1972/,

$$(\rho c)_a\frac{\partial\Theta}{\partial t} + \zeta\rho_l c_l\mathbf{q}\cdot\nabla\Theta = \nabla\cdot(\mathbf{D}_\Theta\nabla\Theta) + H \tag{F-5}$$

where

- $\mathbf{q}$ is the specific discharge (or Darcy velocity) [m s^{-1}],
- $\mathbf{k}$ is the rock permeability tensor [m^2],
- μ is the fluid viscosity [Pa s], which is determined by an appropriate equation of state /Kestin et al. 1981/,
- P^R is the residual fluid pressure [Pa],
- ρ_l is the fluid density [kg m^{-3}], which is determined by an appropriate equation of state /Rowe and Chou 1970, Kestin et al. 1981/,
- ρ_0 is the reference fluid density [kg m^{-3}],
- g is the magnitude of gravitational acceleration [m s^{-2}],
- t is the time [s],
- φ is the porosity [–],
- f_i is the fraction of reference water i in the fluid [–],
- $\mathbf{D}_c$ is the dispersion tensor for solute [m^2s^{-1}],
- f_i' is the fraction of reference water i in the rock matrix [kg $m^{-3}s^{-1}$],
- σ is the specific surface area of the fractures [m^{-1}],
- $D_{e,i}$ is the effective (or intrinsic) diffusion coefficient for reference water i in the rock matrix [m^2s^{-1}],
- α_i is the capacity factor for reference water i in the rock matrix [–],
- w is a coordinate in the rock matrix [m],

$(\rho c)_a$ is the average heat capacity of the rock and fluid [J m^{-3}K^{-1}],

Θ is the temperature [K],

ζ is a user-specified flag, which is set to 0 if convection of heat should not be considered and to 1 otherwise,

c_l is the specific heat capacity of the fluid [J kg^{-1}K^{-1}],

$\mathbf{D}_\Theta$ is the dispersion tensor for heat [W m^{-1}K^{-1}], and

H is the heat source [W m^{-3}].

The additional parameters that are required to model the transport of heat are as follows:

- The average heat capacity of the rock and fluid, which can be calculated from $(\rho c)_a = \varphi\rho_l c_l + (1-\varphi)\rho_s c_s$, where
  - ρ_s is the density of the rock solids [kg m^{-3}], which is assumed to be constant for a given rock type, and
  - c_s is the specific heat capacity of the rock solids [J kg^{-1}K^{-1}], which is assumed to be constant for a given rock type.
- The specific heat capacity of the fluid, c_l, which is assumed to be constant.
- The dispersion tensor for heat, which is given by /de Marsily 1986/

  $(\mathbf{D}_T)_{ij} = \Gamma_a\delta_{ij} + \zeta\,\phi\rho_l c_l\left[\alpha_T v\,\delta_{ij} + (\alpha_L - \alpha_T)\frac{v_i v_j}{v}\right]$, where
  - Γ_a is the average thermal conductivity of the rock and fluid [W m^{-1}K^{-1}], that is $\Gamma_a = \varphi\Gamma_l + (1-\varphi)\Gamma_s$, which is assumed to be constant for a given rock type,
  - α_T is the transverse dispersion length for heat [m],
  - α_L is the longitudinal dispersion length for heat [m],
  - v is the magnitude of the porewater velocity [m s^{-1}], which is given by $\boldsymbol{v} = \mathbf{q}/\varphi$, and
  - v_i is the i^{th}-component of the porewater velocity [m s^{-1}].

F.2 Verification

The development was verified by checking firstly that the existing test cases for CONNECTFLOW gave the same results as before, and then carrying out calculations for three additional test cases:

- 1D heat conduction with a time-varying temperature boundary condition (Test Case 1);
- 1D heat conduction with a specified heat flux boundary condition (Test Case 2).
- The HYDROCOIN Level 1 Test Case 5 for transient thermal convection in a saturated permeable medium containing a heat source with decaying power output (Test Case 3).

The new CONNECTFLOW test cases are described below.

Test Case 1: Heat conduction problem with a time-varying temperature boundary condition

The test case involves transient heat conduction /Carslaw and Jaeger 1959/ in 1D with a time-varying temperature at one boundary ($x = l$), and a zero heat flux boundary condition at the other ($x = 0$).

The equation to be solved is:

$$(\rho c)_a \frac{\partial\Theta}{\partial t} = \nabla\cdot(\Gamma_a\nabla\Theta) \qquad \text{(F-6)}$$

where

$(\rho c)_a$ is the average heat capacity of the rock and fluid [J m^{-3}K^{-1}];

Θ is the temperature [K];

t is the time [s]; and

Γ_a is the average thermal conductivity of the rock and fluid [W m^{-1}K^{-1}].

The input parameters for the test case are given in the following table:

Table F-1. Input parameters for Test Case 1.

Parameter	Symbol	Value
Thermal conductivity of rock and fluid	Γ_a	2.51 W m^{-1}K^{-1}
Density of rock and fluid	ρ	$2.6 \cdot 10^3$ kg m^{-3}
Specific heat of rock and fluid	c	$8.79 \cdot 10^2$ J kg^{-1}K^{-1}

The domain extends to a length of 1,000 m.

The 3D mesh comprises 100 equally spaced *CB81* finite elements, arranged in a line between x = 0 m and 1,000 m.

The boundary conditions imposed are $\Theta(x = 1{,}000\text{ m}) = 1.098 \cdot 10^{-7}$ t and and $\frac{\partial \Theta}{\partial t}(x = 0\,\text{m}) = 0$.

The required outputs are:

- The temperature as a function of time between 10^9 and 10^{12}s at points x = 0 m and 800 m.
- The temperature as a function of distance between points x = 0 m and x = 1,000 m at times of 10^{10} and 10^{11}s.

Good agreement was obtained with an analytical solution /Carslaw and Jaeger 1959/, building confidence that CONNECTFLOW models heat conduction correctly. For example, Figure F-1 and Figure F-2 show the temperature rise as a function of time compared with the analytical solution. (It should be noted that the analytical solution is expressed as a series that converges rapidly only for large times.)

Test Case 2: Heat conduction problem with a specified heat flux boundary condition

The test case involves transient heat conduction /Carslaw and Jaeger 1959/ in 1D with a specified heat flux at one boundary ($x = l$), and a zero heat flux boundary condition at the other ($x = 0$).

This test case differs from Test Case 1 only in the boundary conditions imposed, which here are $-\Gamma_a \frac{\partial \Theta}{\partial t}(x = 1{,}000\,\text{m}) = 1$ and $\frac{\partial \Theta}{\partial t}(x = 0\,\text{m}) = 0$.

Again good agreement was obtained with the analytical solution /Carslaw and Jaeger 1959/. For example, Figure F-3 and Figure F-4 show the temperature rise as a function of time compared with the analytical solution.

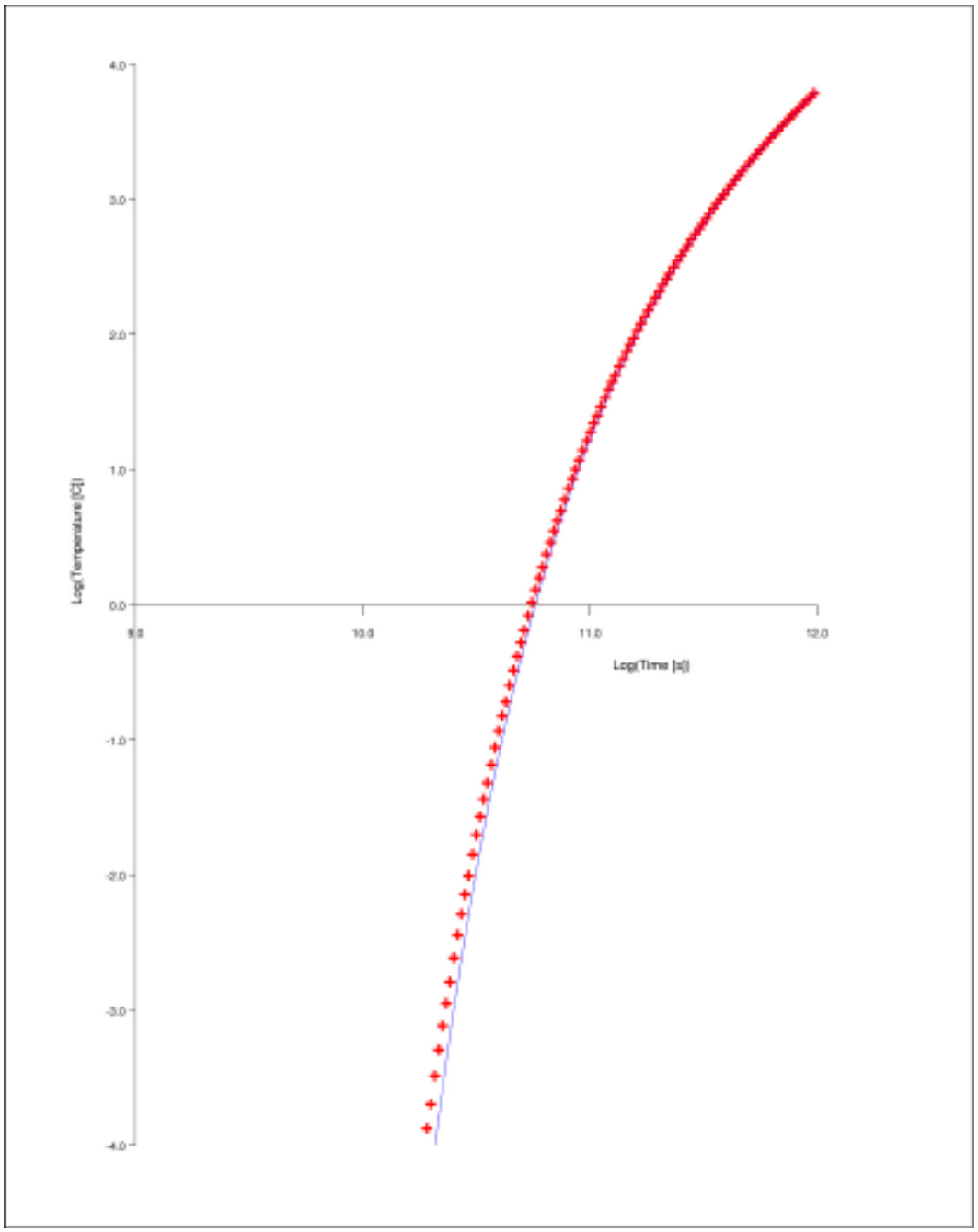

Figure F-1. *Test Case 1: the CONNECTFLOW prediction of the evolution of temperature at x = 0 m is compared against a semi-analytical solution. The semi-analytical solution is expressed as a series that converges rapidly only for large times.*

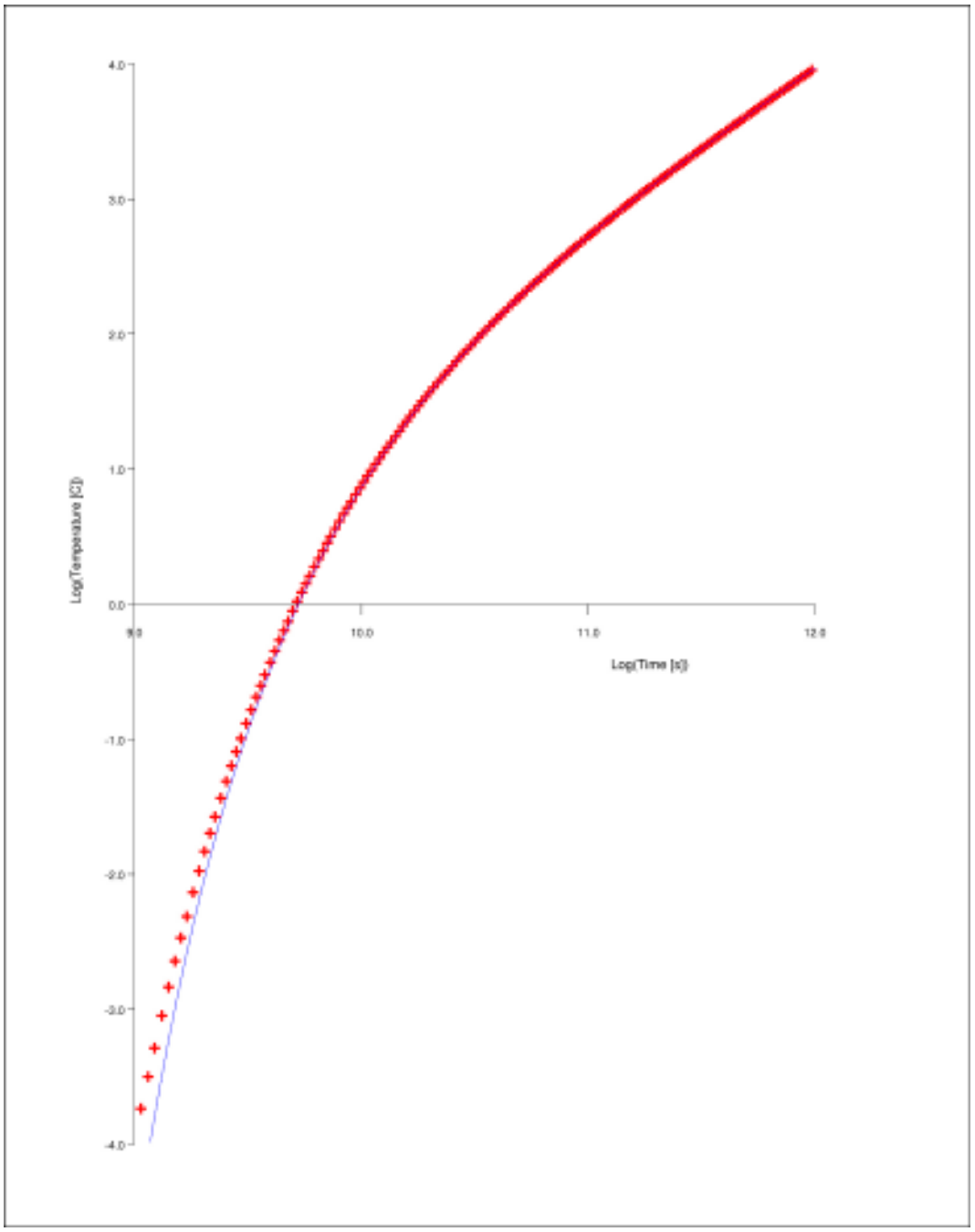

Figure F-2. *Test Case 1: the CONNECTFLOW prediction of the evolution of temperature at x = 800 m is compared against a semi-analytical solution. The semi-analytical solution is expressed as a series that converges rapidly only for large times.*

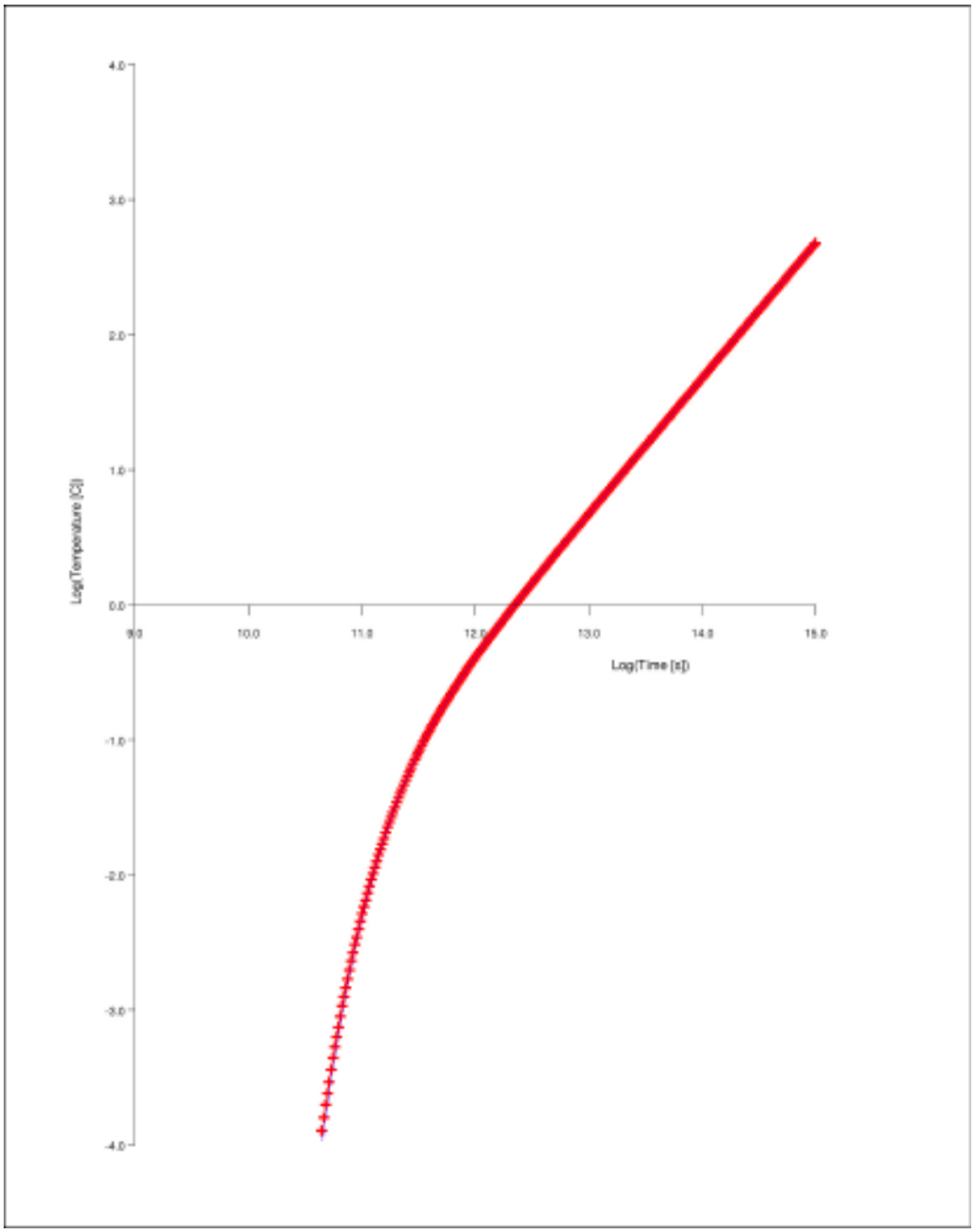

Figure F-3. *Test Case 2: the CONNECTFLOW prediction of the evolution of temperature at x = 0 m is compared against a semi-analytical solution. The semi-analytical solution is expressed as a series that converges rapidly for all times.*

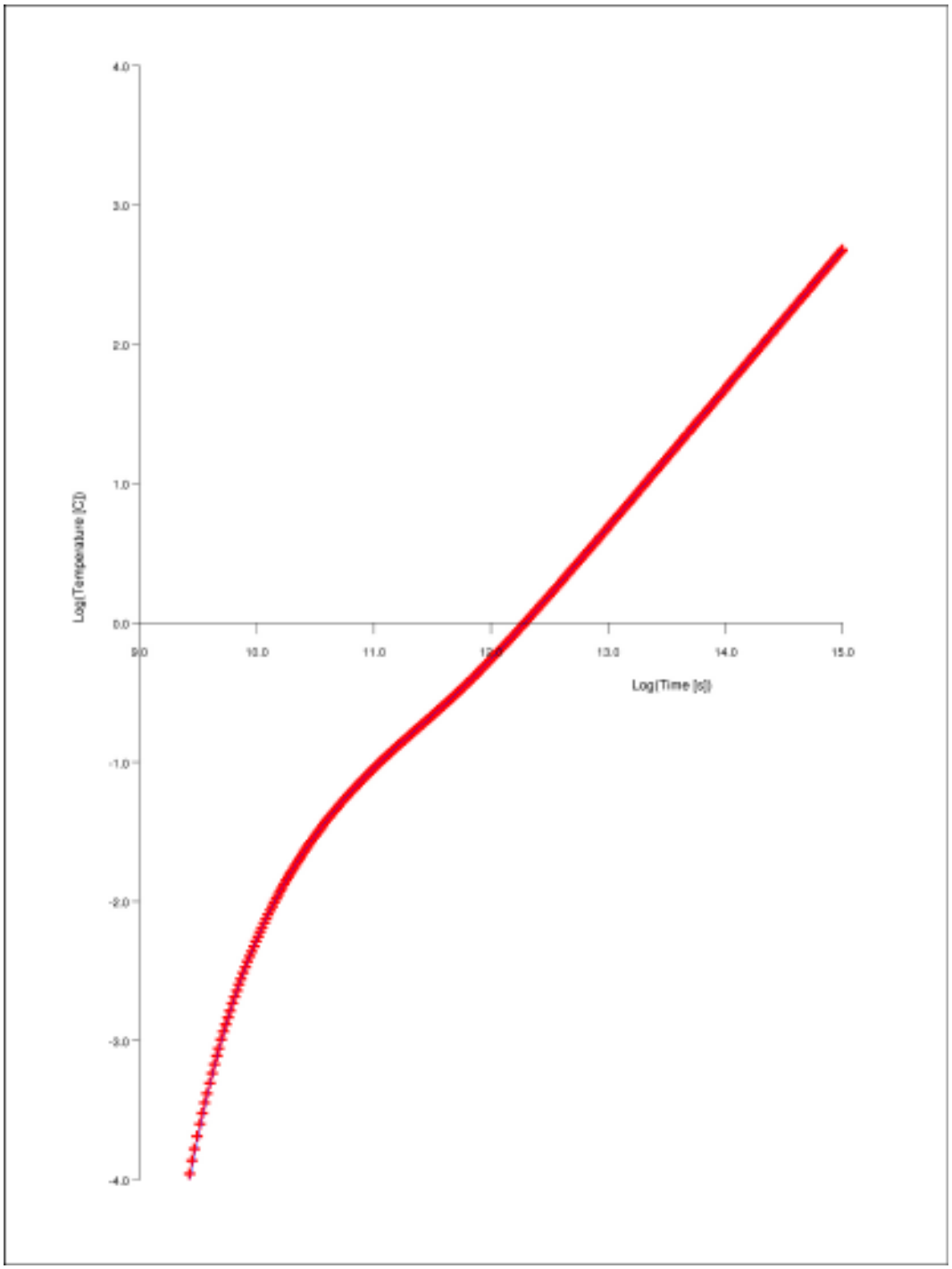

Figure F-4. *Test Case 2: the CONNECTFLOW prediction of the evolution of temperature at x = 800 m is compared against a semi-analytical solution. The semi-analytical solution is expressed as a series that converges rapidly for all times.*

Test Case 3: HYDROCOIN test problem for transient thermal convection in a saturated permeable medium

The test case involves transient thermal convection in a saturated permeable medium containing a heat source with decaying power output /Hodgkinson 1985, International HYDROCOIN Project 1988/. The test case examines buoyancy driven flows.

The host rock is assumed to be a homogeneous isotropic permeable medium of infinite extent with constant physical properties. The repository is idealised as a uniform spherical heat source with the same physical properties as the surrounding rock, and a power output that decays exponentially with time.

The model assumes that:

- Flow transients arising from compressibility of the groundwater can be neglected, since they occur on a time-scale that is short compared to the time-scale over which the regional temperature field evolves.
- The dominant heat transfer mechanism is conduction through the rock, rather than convection due to the flow of groundwater[10].
- The density of the groundwater varies linearly with temperature and is independent of pressure. The viscosity and volumetric thermal expansion coefficient of the groundwater are independent of temperature and pressure.

Thus, the equations to be solved are:

$$\nabla \cdot (\rho_l \mathbf{q}) = 0 \tag{F-7}$$

$$\mathbf{q} = -\frac{\mathbf{k}}{\mu} \cdot \left(\nabla P^R - (\rho_l - \rho_0) g \right) \tag{F-8}$$

and

$$(\rho c)_a \frac{\partial \Theta}{\partial t} = \nabla \cdot (\Gamma_a \nabla \Theta) + \frac{Q}{\frac{4}{3}\pi a^3} \exp(-\lambda t)\theta(r - a) \tag{F-9}$$

where

ρ_l is the fluid density [kg m^{-3}], which is given by $\rho_l = \rho_0 (1 + \beta\Theta)$, where the thermal expansion coefficient, β, is constant [K^{-1}],

$\mathbf{q}$ is the specific discharge (or Darcy velocity) [m s^{-1}],

$\mathbf{k}$ is the rock permeability tensor [m^2],

μ is the fluid viscosity [Pa s], which is constant,

P^R is the residual fluid pressure [Pa],

ρ_0 is the reference fluid density [kg m^{-3}],

g is the magnitude of gravitational acceleration [m s^{-2}],

$(\rho c)_a$ is the average heat capacity of the rock and fluid [J m^{-3}K^{-1}],

Θ is the temperature [K],

t is the time [s],

Γ_a is the average thermal conductivity of the rock and fluid [W m^{-1}K^{-1}],

Q is the total power output by the heat source at $t = 0$ [W],

a is the radius of the repository [m],

[10] This is the most likely situation for the low permeability rocks envisaged for geological disposal.

λ is the decay constant for the heat source [s^{-1}],

θ is the Heaviside step function ($\theta(x) = 0$ for $x < 0$, and $\theta(x) = 1$ for $x > 0$), and

r is the radial co-ordinate in spherical polar co-ordinates [m].

In fact, the original specification of the test case differs from the above because it makes the Boussinesq approximation, which amounts to keeping variations of the groundwater density only in the buoyancy term. Equation (F-7) is replaced by

$$\nabla \cdot \mathbf{q} = 0 \tag{F-10}$$

The difference between this equation and the one used in CONNECTFLOW is

$$\mathbf{q} \cdot \frac{\nabla \rho_l}{\rho_l} = \mathbf{q} \cdot \frac{\beta \nabla \Theta}{1 + \beta \Theta} \tag{F-11}$$

which will lead to a discrepancy of a few percent between the simulation and the specified pressure.

The input parameters for the test case are given in Table F-2[11].

The required outputs are:

- The temperature and residual pressure rises as a function of time between 10^0 and 10^4 years at points $z = 0$ m, 125 m, 250 m and 375 m vertically above the centre of the repository.
- The temperature and residual pressure rises as a function of distance between points $z = 0$ m and $z = 750$ m at times of 50, 100, 500 and 1,000 years.
- Pathlines from the mid-plane of the repository with radial starting positions $r = 0$ m, 125 m and 350 m, which should be calculated for starting times $t = 10^2$, 10^3 and 10^4 years. The performance assessment measures are the travel times and radial co-ordinates for the pathline to reach the plane z = 1,000 m. The pathlines are defined by $\frac{d\mathbf{r}}{dt} = \frac{1}{\phi}\mathbf{q}$.

The finite-element mesh is shown in Figure F-5. The domain extends to a radius of 3,000 m, which is twelve times the radius of the repository.

Table F-2. Input parameters for Test Case 3.

Parameter	Symbol	Value
Radius of repository	a	250 m
Initial power output	Q	10^7 W
Decay constant	λ	$7.3215 \cdot 10^{-10}$ s^{-1}
Thermal conductivity of rock and fluid	Γ_a	2.51 W $m^{-1}K^{-1}$
Density of rock and fluid	ρ	$2.6 \cdot 10^3$ kg m^{-3}
Specific heat of rock and fluid	c	$8.79 \cdot 10^2$ J $kg^{-1}K^{-1}$
Permeability of rock	k	10^{-16} m^2
Reference density of fluid	ρ_0	$9.922 \cdot 10^2$ kg m^{-3}
Expansion coefficient of fluid	β	$3.85 \cdot 10^{-4}$ K^{-1}
Viscosity of fluid	μ	$6.529 \cdot 10^{-4}$ Pa s
Flowing porosity	φ	10^{-4}
Acceleration due to gravity	g	9.8064 m s^{-2}

[11] These parameters are typical of a repository containing high-level waste, decaying with a half-life of thirty years, situated in a fractured hard rock.

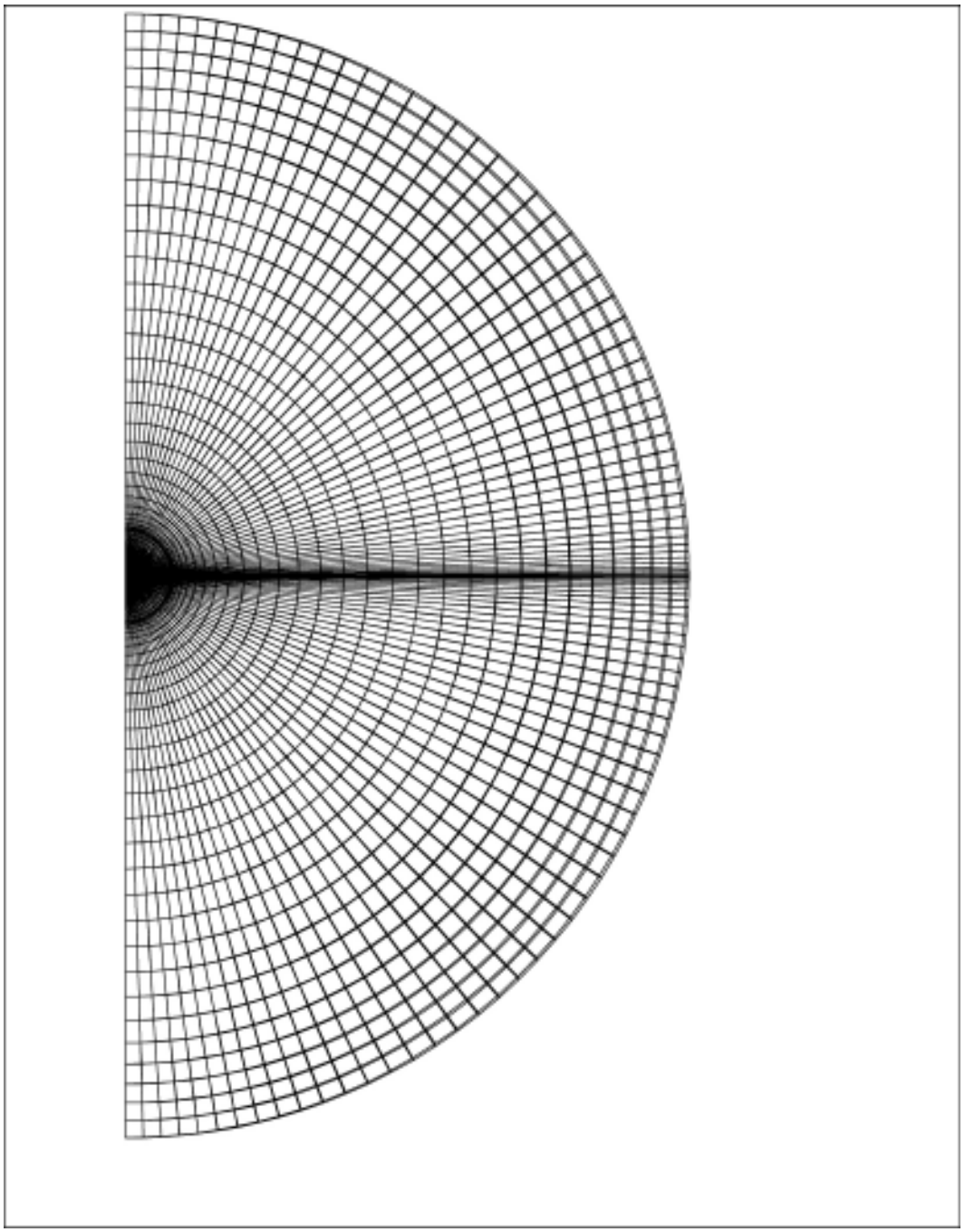

Figure F-5. *Test Case 3: the finite-element mesh used by CONNECTFLOW.*

The 3D mesh comprises 4,000 *CB81* finite elements, 40 elements in the radial direction along each of 100 arcs. The mesh was formed by mapping a block of 40×1×100 finite elements on to a segment of a sphere, and therefore has a hole (of radius 1 m) at its centre. The mesh has been refined near the repository boundary and also along the mid-plane of the repository.

The boundary conditions imposed are $P^R(r = 3{,}000\text{ m}) = 0$ Pa and $\Theta(r = 3{,}000\text{ m}) = 0$C.

With this model we have obtained good agreement with the analytical solution.

Figure F-6 and Figure F-7 and show the temperature and residual pressure rises as a function of time compared with the analytical solution. The temperature is in excellent agreement with the analytical solution. The residual pressure is in error by a few percent at the peak value, which is to be expected given the discrepancies in the equations; otherwise, there is again very good agreement.

Finally, as an example Figure F-8 shows pathlines from the mid-plane of the repository with radial starting positions $r = 0$ m, 125 m and 350 m, started at time $t = 10^2$ years. These pathlines match those calculated from the analytical solution. The travel times and radial co-ordinates for the pathlines to reach the plane z = 1,000 m are given in Table F-3, and compared with results from the analytical solution. The agreement is better than that obtained previously /International HYDROCOIN Project 1988/.

Table F-3. Travel times and final radial co-ordinates for pathlines starting at time t from position r on the mid-plane of the repository and ending on the plane z = 1,000 m.

Starting time [years]	Starting position [m]	Analytical travel time [years]	Simulated travel time [years]	Analytical final radial co-ordinate [m]	Simulated final radial co-ordinate [m]
100	0*	1,508.955	1,514.812	0.226	21.858
100	125	21,184.990	16,913.463	1,106.673	1,089.503
100	250	24,498.783	21,546.331	948.707	952.677
1,000	0*	2,287.476	2,245.710	0.081	11.448
1,000	125	2,895.950	2,871.925	323.149	331.530
1,000	250	5,531.358	5,393.588	634.490	637.627
10,000	0*	77,080.767	53,089.695	0.034	1.019
10,000	125	79,518.127	54,928.333	134.318	135.810
10,000	250	86,362.006	60,488.702	268.178	271.207

* The finite-element mesh has a small “hole” (of radius 1 m) at its centre, and therefore this pathline starting position was shifted to be on the surface of the “hole”. The analytical results were corrected to take this shift in the starting position into account.

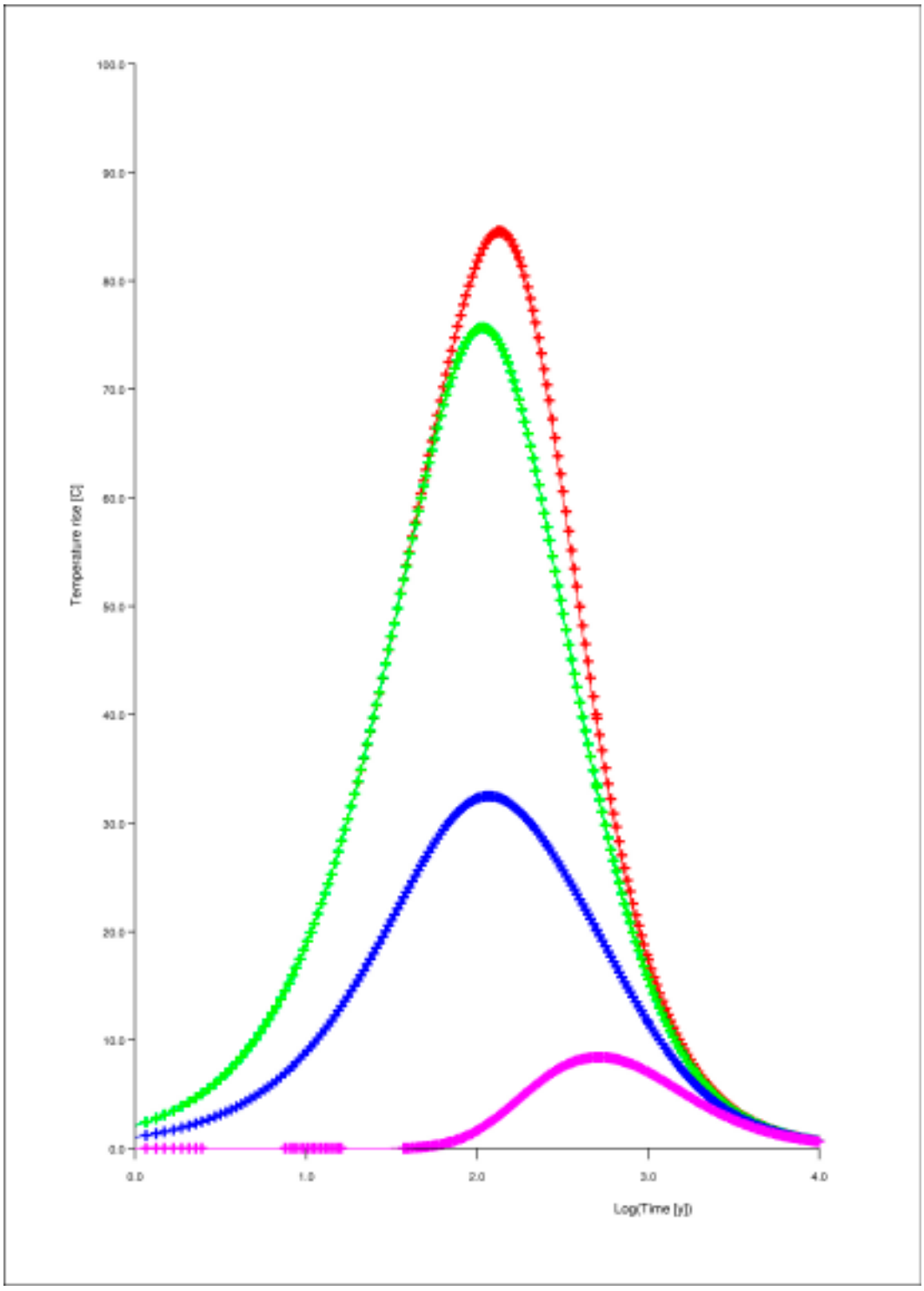

Figure F-6. *Test Case 3: the CONNECTFLOW prediction of the evolution of temperature at z = 0 m (red line), z = 125 m (green line), z = 250 m (blue line), and z = 375 m (violet line), is compared against a semi-analytical solution. The semi-analytical solution is expressed in terms of complex error functions.*

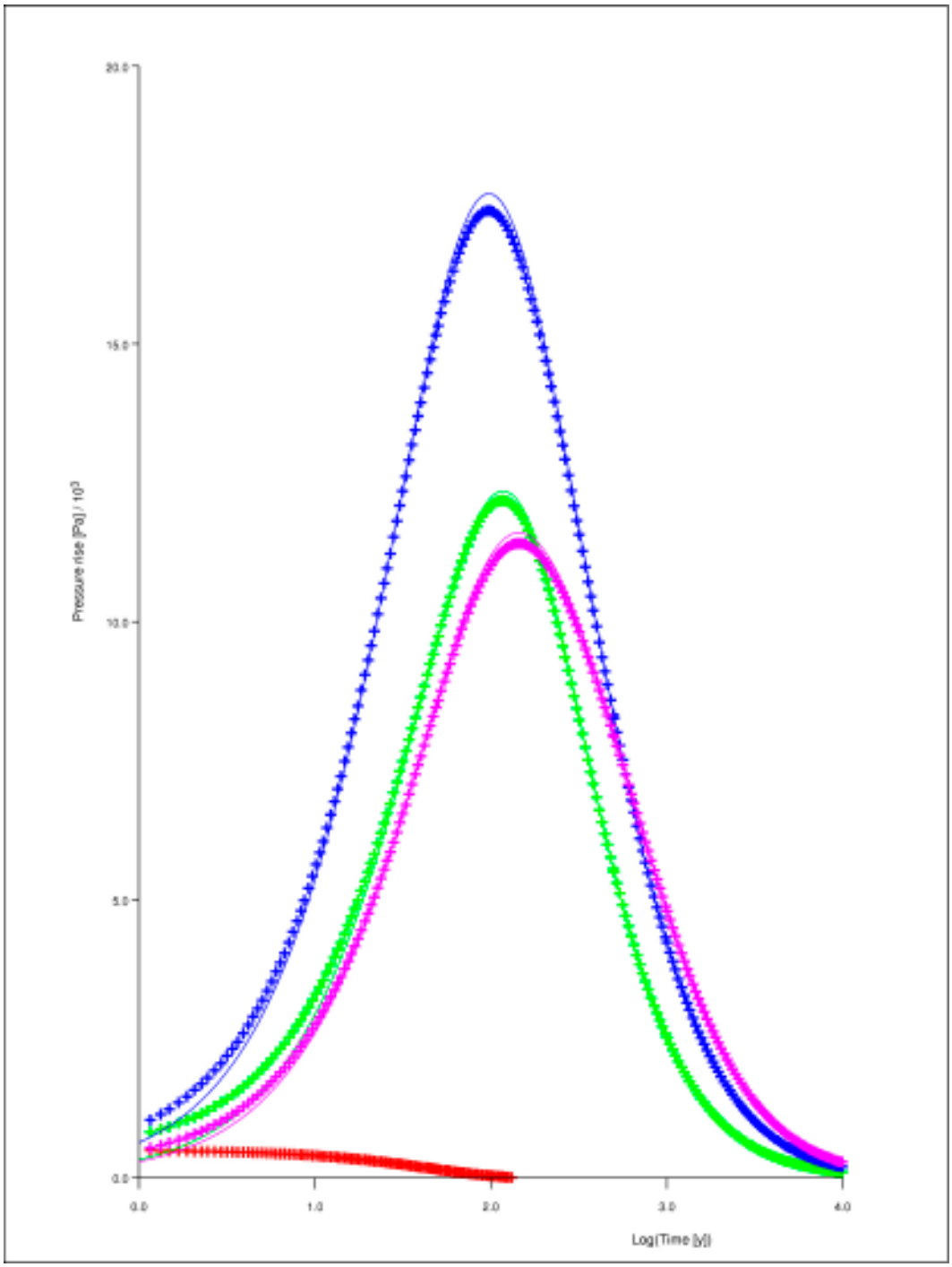

Figure F-7. *Test Case 3: the CONNECTFLOW prediction of the evolution of residual pressure at z = 0 m (red line), z = 125 m (green line), z = 250 m (blue line), and z = 375 m (violet line), is compared against a semi-analytical solution. The semi-analytical solution is expressed in terms of complex error functions.*

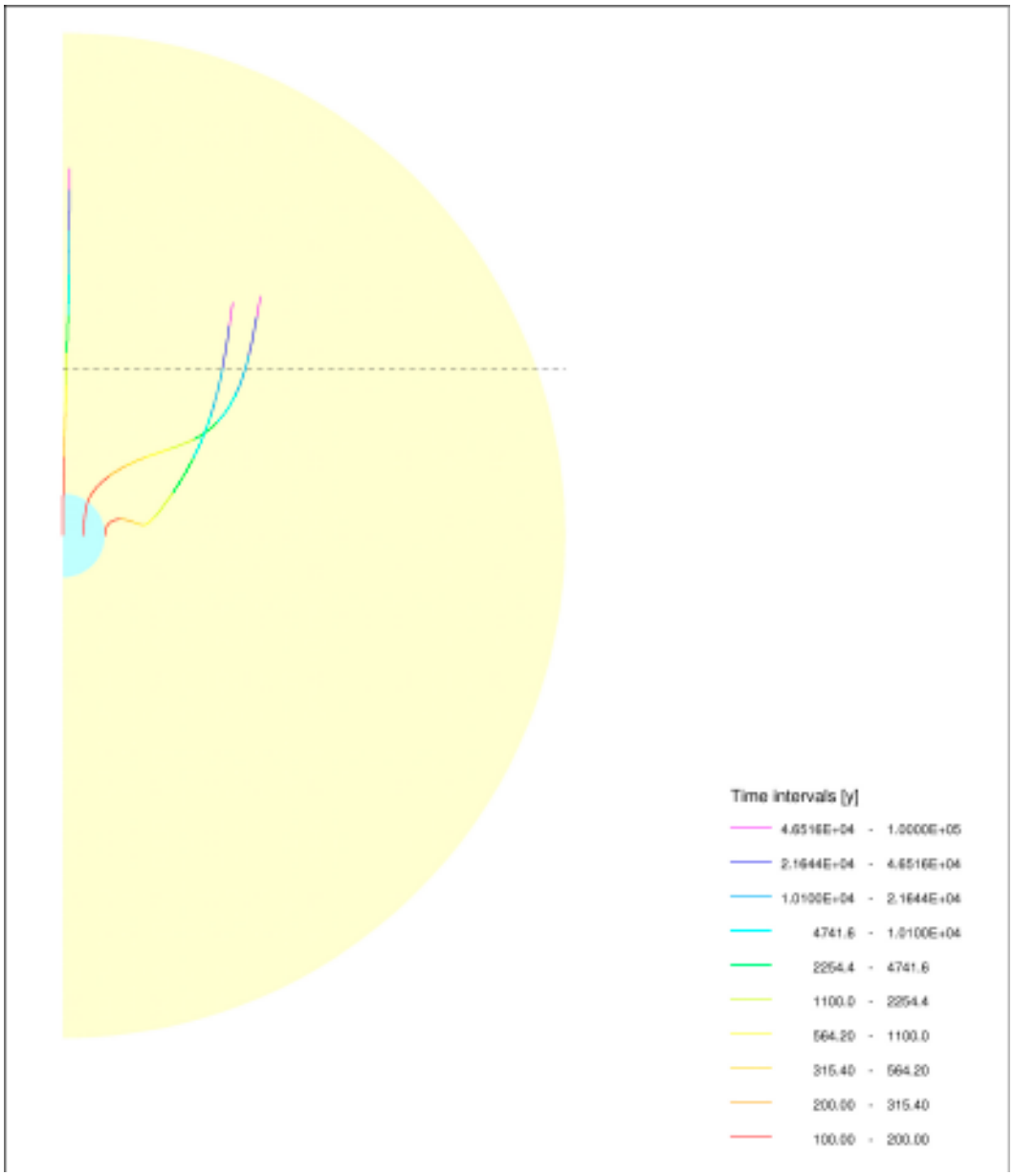

Figure F-8. *Test Case 3: the CONNECTFLOW prediction for pathlines with starting positions r ≈ 0 m, r = 125 m, and r = 250 m and starting time t = 100 y.*